Award Number: W81XWH-15-1-0271

TITLE: Low-Cost, High-Throughput 3-D Pulmonary Imager Using Hyperpolarized Contrast Agents and Low-Field MRI

PRINCIPAL INVESTIGATOR: Eduard Y. Chekmenev, Ph.D.

CONTRACTING ORGANIZATION: Vanderbilt University Medical Center, Nashville, TN 37240

REPORT DATE: October 2017

TYPE OF REPORT: Annual

PREPARED FOR: U.S. Army Medical Research and Materiel Command
Fort Detrick, Maryland, 21702-5012

REPORT DOCUMENTATION PAGE

Form Approved
OMB No. 0704-0188

1. REPORT DATE	2. REPORT TYPE	3. DATES COVERED
October 2017	Annual	09/30/2016–09/29/2017

4. TITLE AND SUBTITLE	5a. CONTRACT NUMBER
Low-Cost, High-Throughput 3-D Pulmonary Imager Using Hyperpolarized Contrast Agents and Low-Field MRI	
	5b. GRANT NUMBER W81XWH-15-1-0271
	5c. PROGRAM ELEMENT NUMBER

6. AUTHOR(S)	5d. PROJECT NUMBER
Eduard Y. Chekmenev, Ph.D.	
	5e. TASK NUMBER
E-Mail: eduard.chekmenev@vanderbilt.edu	**5f. WORK UNIT NUMBER**

7. PERFORMING ORGANIZATION NAME(S) AND ADDRESS(ES)	8. PERFORMING ORGANIZATION REPORT NUMBER
Vanderbilt University Medical Center 2201 W END AVE NASHVILLE, TN 37240-0001	

9. SPONSORING / MONITORING AGENCY NAME(S) AND ADDRESS(ES)	10. SPONSOR/MONITOR'S ACRONYM(S)
U.S. Army Medical Research and Materiel Command Fort Detrick, Maryland 21702-5012	
	11. SPONSOR/MONITOR'S REPORT NUMBER(S)

12. DISTRIBUTION / AVAILABILITY STATEMENT

Approved for Public Release; Distribution Unlimited

13. SUPPLEMENTARY NOTES

14. ABSTRACT
According to the original statement of work we have focused our activities on three specific aims. With regards to Aim #1, we have been working on the construction of ^{129}Xe automated hyperpolarizer & began device testing; The remaining efforts (for Year 3) will be focused on device construction complete, automation and optimization, and integrated use with the MRI scanner. With regards to Aim #2, we have focused a considerable amount of the effort on investigating the fundamental parameters of propane hyperpolarization and lifetimes in the gas and phase. In particular, we have studied the pressure dependence of the propane lifetimes at low magnetic fields, and we have identified the limits of the magnetic field for hyperpolarized propane technology (~0.4 T). These and Year 1 discoveries guided our efforts for the overall propane hyperpolarizer design. The prototype (which will likely remain the final design) is completed, and we are now waiting automation component for device automation. Regarding aim #3, we have worked with equipment vendors and finalized the design of the low-field MRI scanner (by using a new commercial vendor). See report for details. We also note that we are submitting a duplicating report for two partnering PI awards of the same project: W81XWH-15-1-0271 and W81XWH-15-1-0272.

15. SUBJECT TERMS
low-field MRI; pulmonary imaging, high-throughput; low cost

16. SECURITY CLASSIFICATION OF:			17. LIMITATION OF ABSTRACT	18. NUMBER OF PAGES	19a. NAME OF RESPONSIBLE PERSON USAMRMC
a. REPORT Unclassified	**b. ABSTRACT** Unclassified	**c. THIS PAGE** Unclassified	Unclassified	196	**19b. TELEPHONE NUMBER** *(include area code)*

Table of Contents

1. Introduction

We are developing clinical scale production of two gaseous hyperpolarized contrast agents and hyperpolarized MRI allowing for ultrafast (potentially sub-second) and high-throughput molecular imaging of lung function. The key additional focus of this project is on significantly lower cost of our imaging technology of low-field MRI compared to conventional high-field (1.5 T and beyond) MRI due to much higher patient throughput/much faster exams and the use of low field = low cost MRI. We focus our research effort on the high-risk and critical challenges that must be solved to enable clinical implementation of hyperpolarized gases for pulmonary imaging.

Specifically, the research efforts during Year 2 have focused on three specific aims as described in Statement of Work (Appendix 1):

Aim 1: Develop and construct a fully automated high-pressure low-cost stand-alone ^{129}Xe hyperpolarizer
Aim 2: Develop a large-scale hyperpolarization method for HP propane
Aim 3: Develop and construct a 0.05 T MRI scanner

It should also be noted that this report cites many recently published works, and the report is therefore significantly streamlined with references to relevant publications. All pertaining details can be found in the corresponding peer-reviewed publications and manuscripts, which are supplied in this progress report. We also note that 14 such publications, accepted manuscripts, 1 journal cover (with DOI), 1 cover story (with DOI and page number) have been produced during Year 2 of the funding period, which represents our commitment to research and overall progress tempo with regards to this project, and also demonstrates the fact that the work conducted under this funding is novel. The copies of all publications, submitted manuscripts and conference abstract are provided in the Appendix 2. They contain a significant amount of technical and specialized information.

2. Keywords

Low-field MRI, lung imaging, molecular imaging, functional imaging; propane; xenon-129; NMR; MRI; hyperpolarization.

3. ACCOMPLISHMENTS

Please, refer to Appendix 1 for the statement of work of the entire project. The following sections describe the specific areas/tasks of the project conducted during Year 1 of this project.

Task 1.1. Design of automated ^{129}Xe hyperpolarizer

Completed during Year 1.

Task 1.2. Prototyping of automated ^{129}Xe hyperpolarizer

Completed during Year 1.

Task 1.3. Prototype Construction and testing

Completed during Year 1.

We note that we have also looked at the alternative design of the optical pumping cell, where a metal cell was built using coated aluminum tubing. We designed and built the prototype cells. The cells were tested for optical pumping at SIUC site, where some hyperpolarization of ^{129}Xe was detected. We note that polarization numbers were generally significantly lower than those obtained in glass cells. Therefore, the project proceeded with optical pumping cell made of glass. We note that this design maybe potentially refined in the future if better surface coating will become feasible.

Task 1.4. Final Design

Final Design of the ^{129}Xe hyperpolarizer has been completed and we have placed all purchase orders for key components. Some components arrived and allowed us to begin the final construction of the ^{129}Xe hyperpolarizer. The final construction has begun during Year 2 (see below). The Section 1.5 (construction) will cover the aspects of device design, because the design features are best described by actual pictures and figures of merit (polarization, etc.).

Task 1.5. Final Construction

Final construction of the ^{129}Xe hyperpolarizer began in Year 2. It is nearly competed (as we already show (below) some device functionalities. Because of the delays (approximately 3 months) with construction, our team has worked on some aspects of polarizer optimization (part of Year 3 work) ahead of the schedule. The delays were largely due to delays of the key components from the vendors including driver module for automation and most critically for the high-power laser diode array (LDA). Overall, the activities and the tempo/progress of the project along aim 1 were along the lines of the original SOW.

The pictures below summarize the nearly completed construction of the xenon-129 hyperpolarizer.

Figure 1. The overall rendering of new-generation ^{129}Xe hyperpolarizer.
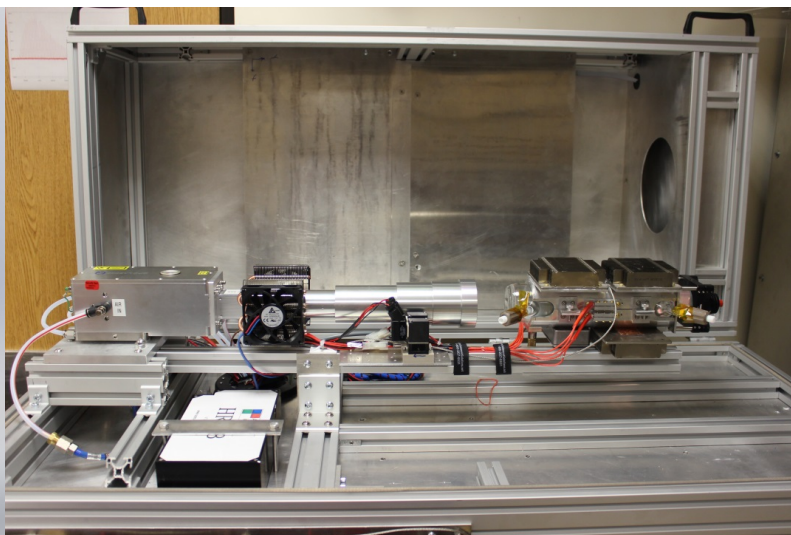
Figure 2. Photograph of the actual constructed upper (open) chassis of the ^{129}Xe hyperpolarizer. The magnet is removed to show the optical pumping cell and the optical train.
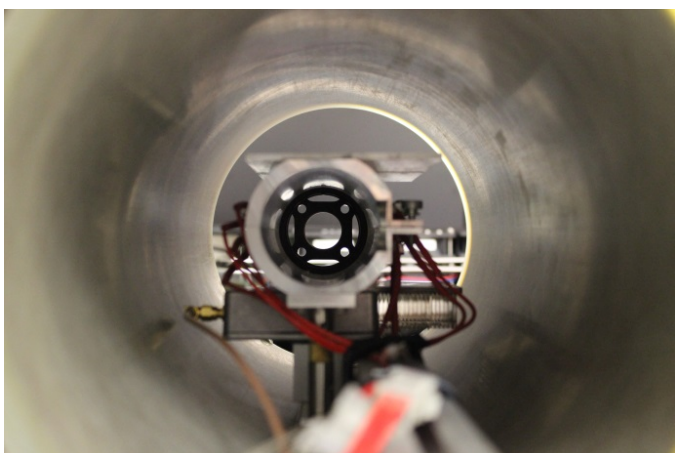
Figure 3. Photograph of the view from the back of the electromagnet (8" ID). Note, the optical-pumping cell is removed. Note the RF coil (for in situ NMR spectroscopy detection) at the bottom of the aluminum optical-pumping cell jacket.
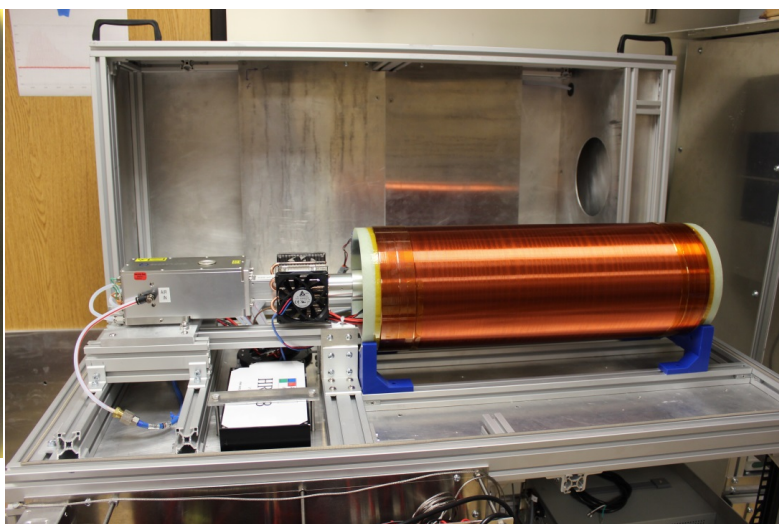
Figure 4. Photograph of the actual constructed upper (open) chassis of the ^{129}Xe hyperpolarizer. The magnet is ON.

The figures below show the photographs of the actual ^{129}Xe hyperpolarizer components
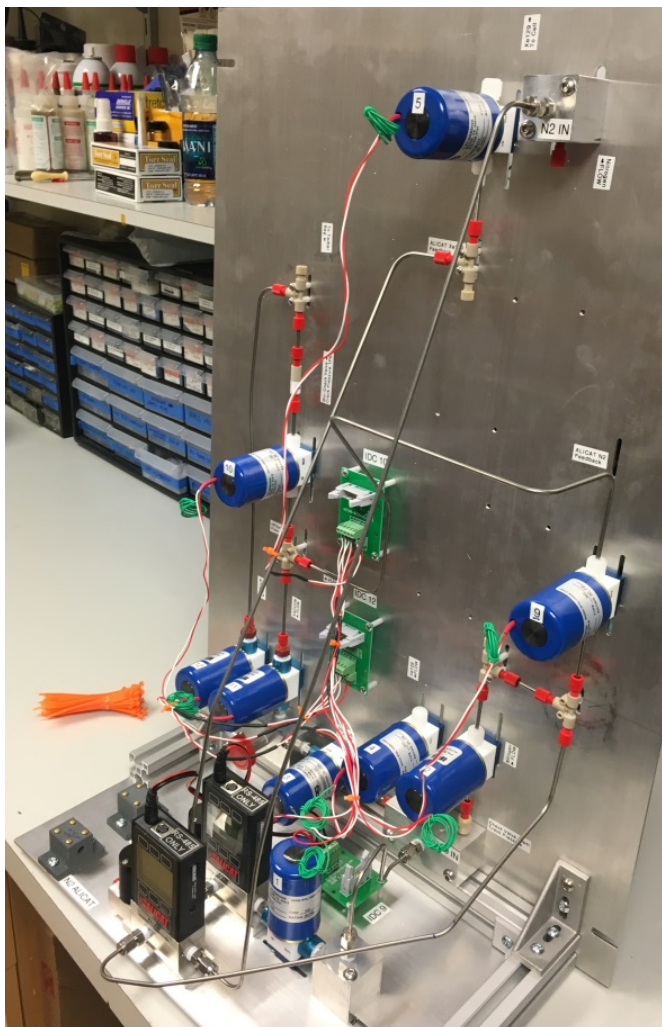
Figure 5. The photo of the gas-handling manifold.

Figure 6. The photo of the 220 V ADC relay board.

Figure 7. The photo of the driver module.
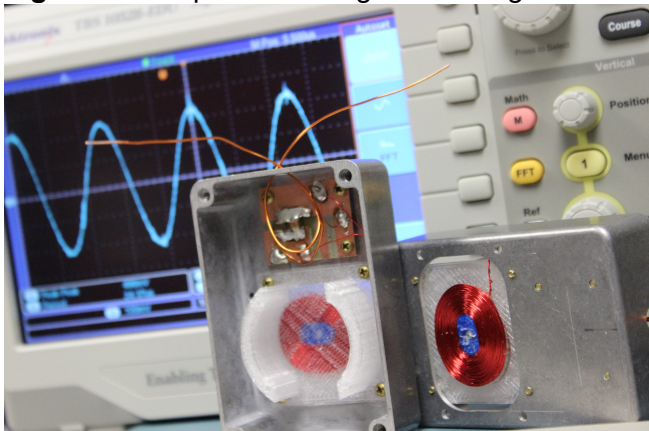
Figure 8. The close-up photograph of two RF coils (for *in situ* NMR polarimetry at 40.8 kHz) of the hyperpolarization equipment. The scope is used to measure the resonance frequency of the RF coil, because the coil is not matched to 50 Ohm.
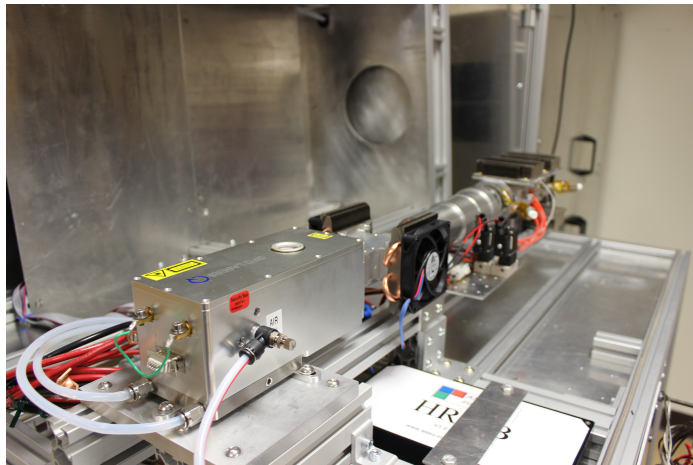
Figure 9. The photograph of the side view of the upper ^{129}Xe hyperpolarizer frame. The image shows the high-power LDA with 2" beam expander aiming at the optical pumping cell.

^{129}Xe hyperpolarizer features *ca*. 170 W LDA. The laser delivery was delayed causing the major shift in our construction schedule. We note that the laser performance has deteriorated from the nominal 170 W value to *ca*. 132 W value over the period of ~2 months, which does not meet the vendor's specifications (Figure 10). We will be contacting the vendor during Year 3 to remedy this issue. Figure 11 provides the spectral response

on the laser using the new IR spectrometer. We note that the current design (and its implementation) shows better spectral resolution of both the LDA (0.20 nm vs. 0.26 nm of the previous design) and the IR detector (0.07 nm vs. 0.10 nm).

Amps	7/13/2017 Laser Power (Watts)	10/23/2017 Laser Power (Watts)
15	22.06	
20	40.27	36
25	59.22	53
30	77.85	70
35	97.23	86
40	115.8	102
45	133.9	118
49	148.4	
50	152.6	132
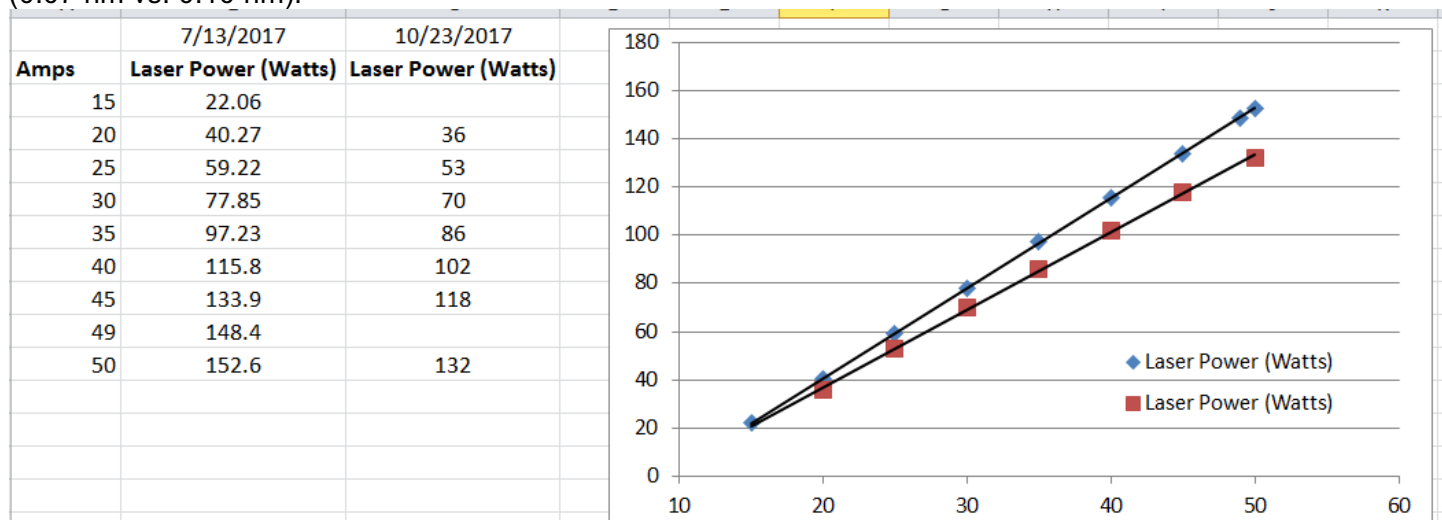
Figure 10. Laser power degradation with time. The laser was tested at 170 W by the vendor prior the installation. We now only get 132 W. We will work with vendor during Year 3 to remedy this issue.
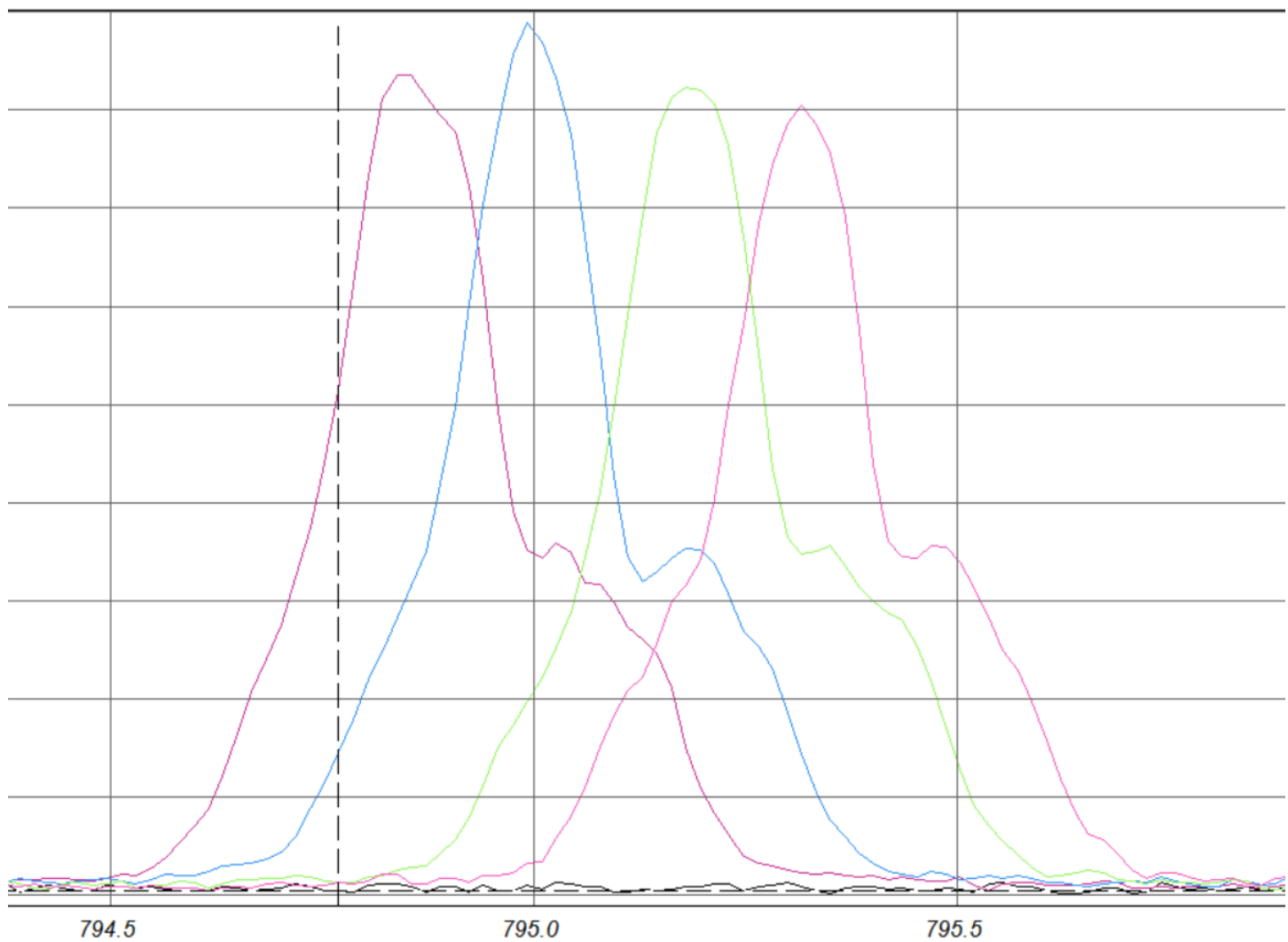
Figure 11. The spectral response of the LDA laser measured using IR spectrometer.

The construction of nearly all key components of ^{129}Xe hyperpolarizer is completed, and we are now in the process of testing, integration and automation. Figure 12A shows examples of *in situ* NMR polarimetry of ^{1}H (reference signal, right and middle) samples. The spectrum in the middle is recorded using water phantom (of similar shape at the sample of the optical pumping cell) recorded in ~ 5 mins. The intensity of this spectrum is then referenced vs. the intensity of hyperpolarized ^{129}Xe – also resonating at 40.8 kHz (achieved by increasing the magnetic field up by ~3.7 fold) allowing for computation of %P_{XE}. The spectrum on the left shows the spectrum of HP ^{129}Xe hyperpolarized to ^{129}Xe polarization (%P_{Xe}) of ca. 65%. Figure 12A(right) shows the spectrum of built-in proton referencing phantom. This phantom will allow for advanced quality assurance in the future: indirect signal calibration for computing %P_{Xe} (without removing the optical pumping cell as this was done to obtain the middle spectrum of Figure 12), setting the amperage of the magnet power supply to ensure the device is ON resonance in the presence of the fringe fields, and other more advanced tasks. Manuscript is in preparation to report on the new design of the aluminum jacket employed for temperature management of the optical pumping cell, which improves the overall device performance in terms of the speed of temperature cycling by approximately a factor of 3. It allows to decrease the production cycle for production of a batch of HP ^{129}Xe. Figure 12B shows the example of ^{129}Xe NMR *in situ* detection of P_{Xe} build-up and decay. Note the T_1 of ~168 mins (Figure 12B, right) is a clear sign of a good quality optical pumping cell, which additionally confirms that the new optical pumping cell design was an overall success.

The efforts during 3 will focus on completion of the construction, integration and automation of ^{129}Xe hyperpolarizer. Overall, we are thrilled to report that all initial design features have been materialized as expected/designed.

HP ^{129}Xe
%P_{Xe} = **65%**±13%

^{1}H Water Signal Reference
%P_H = 3.3×10^{-7}%

^{1}H Signal Reference
built-in the RF probe
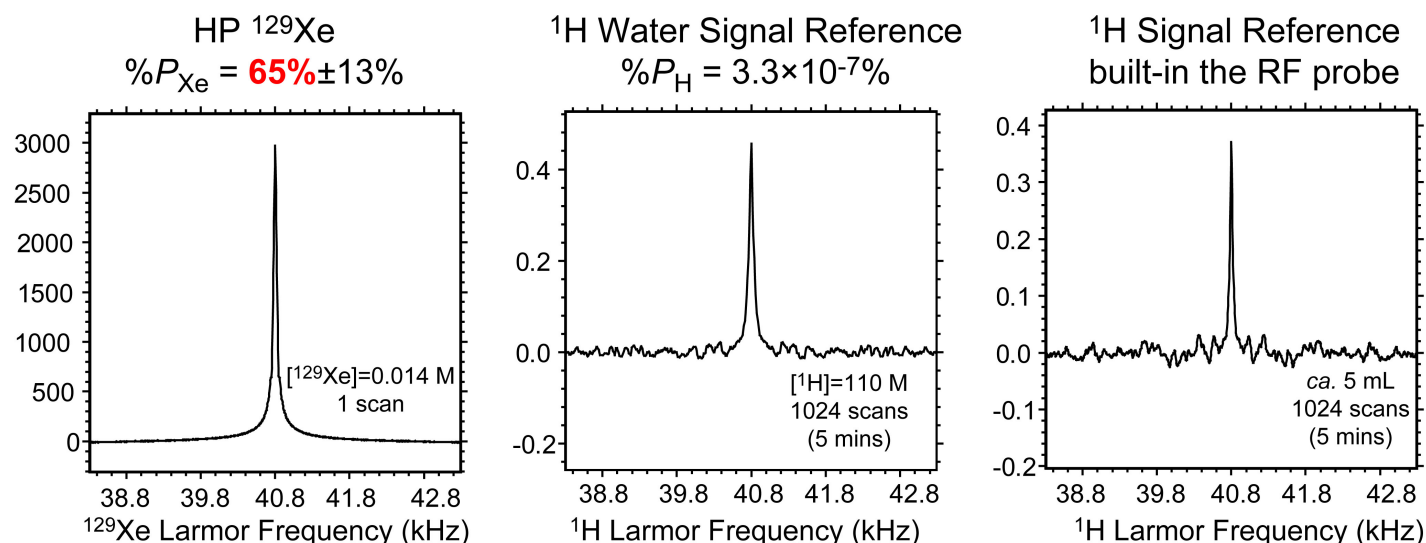
Figure 12A. *In situ* NMR spectroscopy at 40.8 kHz. (left) ^{129}Xe NMR spectrum of HP ^{129}Xe, the cell is filled with Rb and 50:50 mix of Xe and N$_2$ gases. (middle) ^{1}H NMR spectrum thermally polarized water.
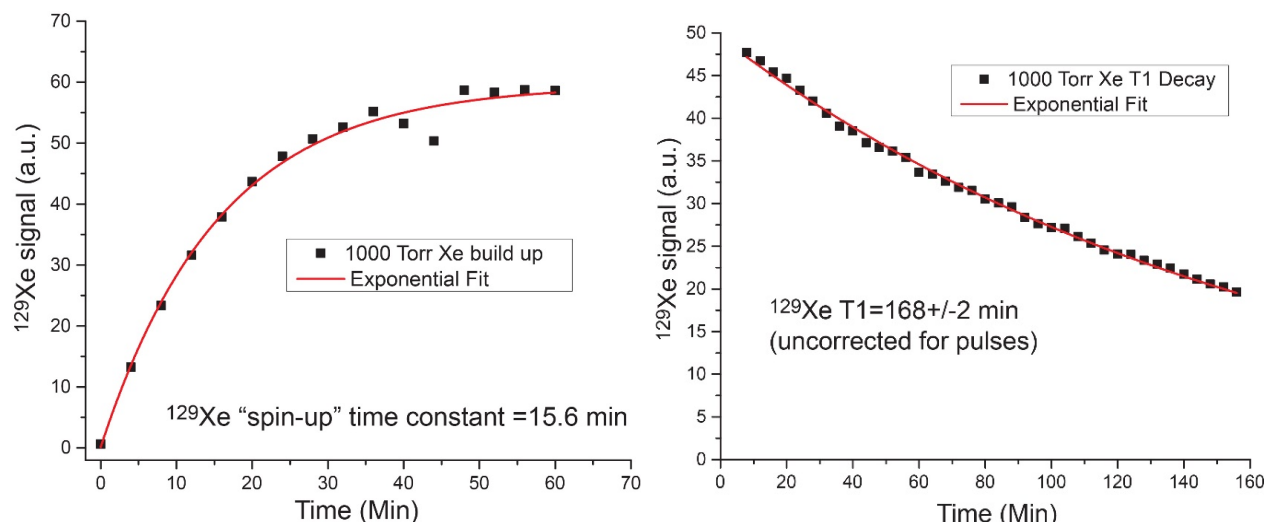
Figure 12B. *In situ* NMR spectroscopy at 40.8 kHz. (left) Detection of build-up of P_{Xe} during optical pumping process. (right) Detection of decay of P_{Xe} after optical pumping process was stopped (by rapid cool down and turning off the laser.

Aim 2. The activities during Year 2 of the project were focused around Task 2.3 Polarizer prototyping and Task 2.4. Prototype Optimization in accord with the original scope of work: see Appendix 1 for details.

Task 2.3 Polarizer prototyping

The heterogeneous PHIP polarizer prototype was created using a series of electronic valves, temperature sensors and controllers. It features several critical components:
1) Power supplies, switches, etc.
2) 24 VDC high-pressure valves;
3) mixing tank (to mix parahydrogen and propene substrate);
4) Stage 1 chamber for heating the gas mixture that enters the reactor;
5) Temperature-controlled heterogeneous reactor (stage 2);
6) Stage 3 chamber for cooling the gas mixture that exits the reactor;

The photograph of the prototype device is shown in Figure 13.

We note that the polarizer prototype operates with the same PID temperature controllers and the 24VDC valves. As a result, the replica driver module (from ^{129}Xe hyperpolarizer, see above) will be employed for this hyperpolarizer construction too. We note that while the prototype is controlled by manual electric switches (Figure 13), the driver and the relays will control the final polarizer in a completed automated and integrated fashion. All key components have been ordered, and being delivered. Once the prototype is validated/optimized, the final device will be completed by the adding the advanced automation hardware: relay board, driver module and optional NMR spectrometer (for feasibility of in situ quality assurance of the HP gas).
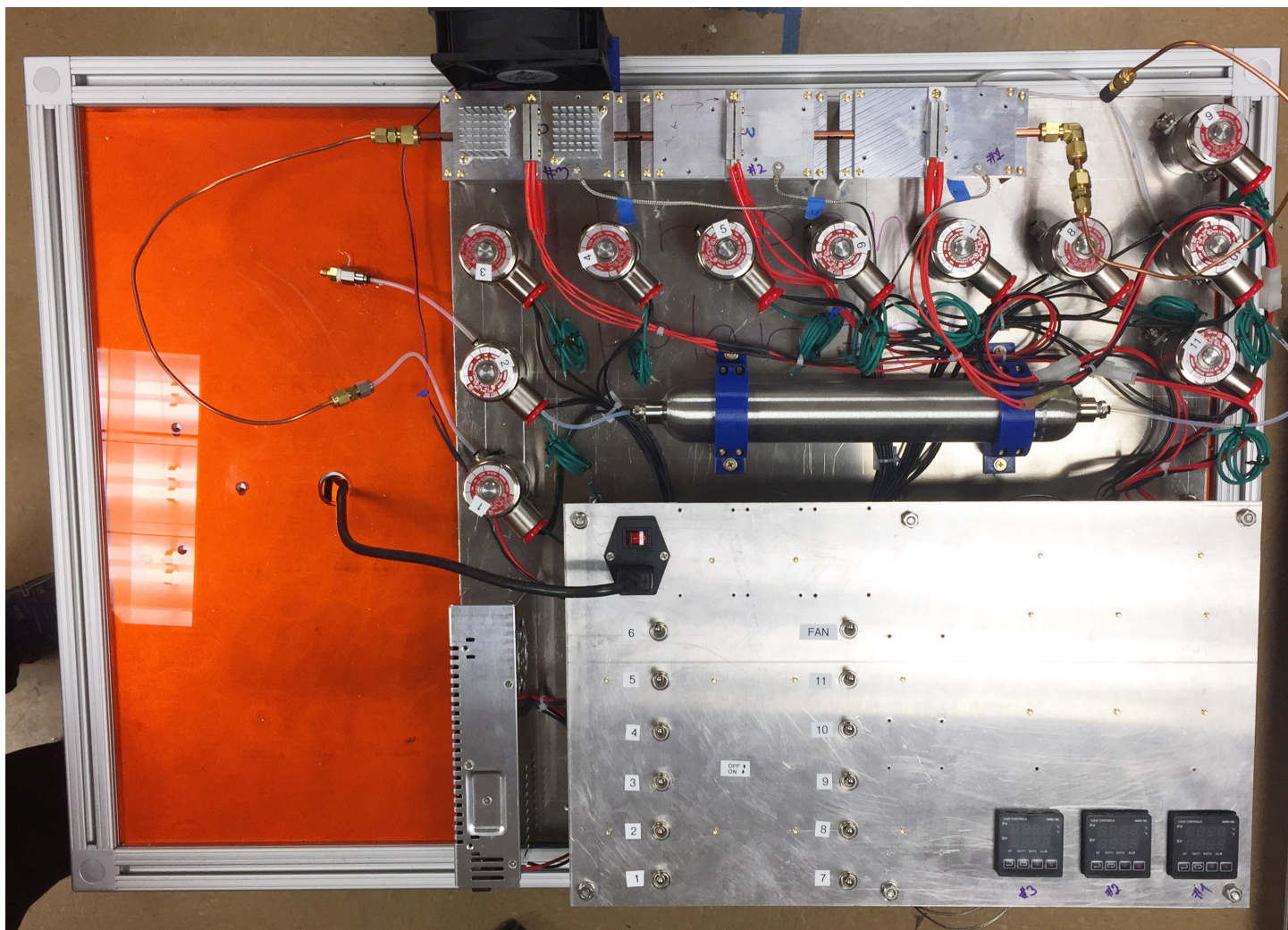
Figure 13. The photograph of the heterogeneous PHIP polarizer for hyperpolarization of propane gas via heterogeneous reaction of pairwise parahydrogen addition to propene substrate.

Task 2.4. Prototype Optimization

1) The prototype optimization was performed in part by performing catalyst performed optimization ahead of the the prototype construction (paper 7: Barskiy, D. A.; Kovtunov, K. V.; Gerasimov, E. Y.; Phipps, M. A.; Salnikov, O. G.; Coffey, A. M.; Kovtunova, L. M.; Prosvirin, I. P.; Bukhtiyarov, V. I.; Koptyug, I. V.et al. 2D Mapping of NMR Signal Enhancement and Relaxation for Heterogeneously Hyperpolarized Propane Gas. *J. Phys. Chem. C* **2017**, *121*, 10038–10046.). This paper (especially Figure 4 of the paper, see Appendix 2 for details) concluded that the reaction hyperpolarization yields (to optimize propane degree of hyperpolarization) require careful mapping of the conditions such as the ratio of the components, pressure, etc. As a result, these systematic studies guided the prototype (and future final design) construction, because the reaction will be performed at high pressure, which mitigated the polarization losses due to relaxation. We note that this work did not allow us for the temperature control of the catalyst, which is now possible in the prototype design (Figure 13). It will lead to improved polarization numbers for the produced HP propane gas.

2) The second area of tests was done with respect to the temperature management (up to 200 °C and potentially more as needed for gas temperature control;

3) The third area of tests was performed with regards to the flow of gas. The setup shown in Figure 13 allows the flow capable of delivering 1 L of gas in one go (<10 s cycle) or several liters per minute in continuous mode production.

4) The hyperpolarization tests were not completed (but planned) during Year 2 due to early departure of the postdoctoral fellow (moved to UC Berkeley for next phase career training) and issues with visas (Russian-USA sanctions) for our visiting collaborator, who will be performing the tests during Year 3. Overall, we are very exciting about our progress with this PHIP propane hyperpolarizer.

Aim 3. The activities during Year 2 of the project were focused on many tasks of Aim 3.

Task 3.1. Design low-field MRI system with commercial vendors

We originally aimed for using 0.05 T magnet (budgeted) with Tecmag console. We have good experience with it. But as we gained more experience with this system (funded by a separate DOD award, and this is where we leveraged the DOD funded support to make the best of both funding sources), we concluded that 0.05 T platform has a number of issues. One issue is the relatively low magnetic field, which could present a challenge for anatomical imaging (which we gather (after consultations with doctors and the end users) would be highly desirable). As a result, we focused some of our efforts at identifying the high possible field that would support the long-lived spin states of HP propane. According to our predictions, the long-lived spin state should be present at fields as high as ~0.4 T as $(\delta_A-\delta_B) \approx J_{AB}$ @ 0.4 T, where $(\delta_A-\delta_B)$ is the difference of chemical shifts between methyl (spin A) and methylene (spin B) protons at a given field in the scale of Hertz, and J_{AB} is the spin-spin coupling between methyl (spin A) and methylene (spin B) protons. This theoretical premise was tested experimentally. Figure 14 shows a diagram of T_1 values of HP propane, which shows that the gas is indeed long lived up to 0.37 T field (the highest field we could create conveniently using permanent magnets).

As result of these preliminary tests, we concluded that MRI magnets as high as 0.35 T can be employed. Several vendors make/can make clinical systems of with such characteristics. We contacted three vendors. Only two vendors were interested in working on/supplying the proton-based MRI system. Only one vendor agreed to supply / co-develop ^{1}H/[129]Xe MRI system, which is the goal of this project. This supplier (Time-Medical) already manufactures proton based MRI system, which is FDA approved in the USA. This scanner will have a huge benefit in terms of the potential clinical translation of propane MRI scan as the hardware is already FDA approved. Once the HP agent is approved, the entire scan can be easily translated to clinic. We are now working with the vendor on the logistics of the [129]Xe hardware/software frame. They can deliver the ^{1}H system in 2-3 months, which is the major strength. Moreover, we would be able to take advantage of all imaging sequences developed by the vendor.

This vendor also agreed to develop the [129]Xe hardware/software. We are now in discussion with the vendor. We expect to contact the PO of this award during Year 3 to approve the change of the budget to support the purchase of this instrument. We note that it will significantly and positively impact the future clinical translation of both HP propane and [129]Xe imaging modality, because no streamlined solution exists to perform [129]Xe and anatomical ^{1}H imaging. The ongoing and future work will represent a major technology breakthrough in the field of pulmonary imaging.
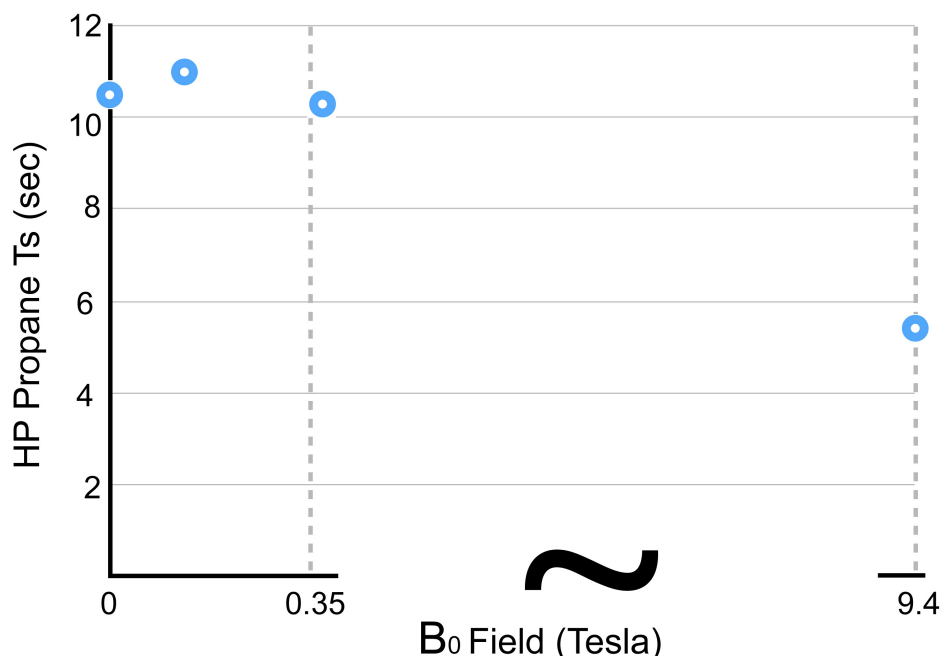
Figure 14. The exponential decay time constants of HP propane gas prepared by pairwise addition of parahydrogen to propene substrate at the Earth's magnetic field. Note that gas is long-lived at magnetic field as high as 0.37 T. The gas is no longer long lived at 9.4 T. The decay constant is significantly reduced. Note these data are preliminary and not published yet.

Moreover, the use of the higher field instrument (vs. 0.05 T) offers additional advantages in the context of MRI imaging of HP propane gas. See the corresponding discussion below.

Task 3.2. Low-field MRI system construction by Vendors

See the discussion above for the Task 3.1.

Task 3.3. Low-field MR system installation and fine-tuning at site (Vanderbilt)

The performance of this task is delayed.

Task 3.4. RF coils ([129]Xe and ^{1}H) construction for pulmonary imaging

Based on the discussions with the equipment vendor (Time-Medical), all RF coils will be made by the vendor. We will be filing the request for change in the budget (while keeping the overall numbers the same) in the first half of Year 3 of the project.

Task 3.5. Pulse-sequence development and installation

While naturally, we will be using primarily the imaging sequences provided by the MRI system vendor, we note that since some tasks of Aim 3 were delayed, the Vanderbilt team focused on the sequence aspects of HP propane imaging using already available low-field MRI equipment. We have used the installed 0.05 T MRI scanner, and have studied (experimentally and theoretically) the process of singlet state conversion of long-lived propane into observable magnetization. We note that this work was not possible before due to unavailability of sufficiently high B_0 homogeneity MRI magnet. The results were published in a paper #8 (Barskiy, D. A.; Salnikov, O. G.; Romanov, A. S.; Feldman, M. A.; Coffey, A. M.; Kovtunov, K. V.; Koptyug, I. V.; Chekmenev, E. Y. NMR Spin-Lock Induced Crossing (SLIC) Dispersion and Long-Lived Spin States of Gaseous Propane at Low Magnetic Field (0.05 T). Journal of Magnetic Resonance 2017, 276, 78-85). The figure 2e of this paper clearly shows a very good agreement between the experiment and the theory. We note that this demonstration allows us for careful planning of the MRI sequences, where the excitation RF pulse is a partial SLIC pulse (the corresponding experiments are in progress for Year 3 work). As a result, it would be possible to extract a fraction of magnetization and use it for one like of k-space sampling of the imaging. The process is then repeated. This strategy would simplify the RF pulse sequences for propane imaging a great deal, because conventional gradient echo imaging can be employed, where a strong RF excitation pulse is replaced by a weak (ca. 22 Hz or 15 Hz, see Figure 2e of that paper discussed above) RF pulse is all that is needed for excitation of the spin system. From the perspective of pulse sequence

acceleration, we have performed a theoretical study (see Supporting Information of the paper available at the publisher's web site) of the optimal duration of the SLIC pulse as a function of the field (Figure 15).

a

b
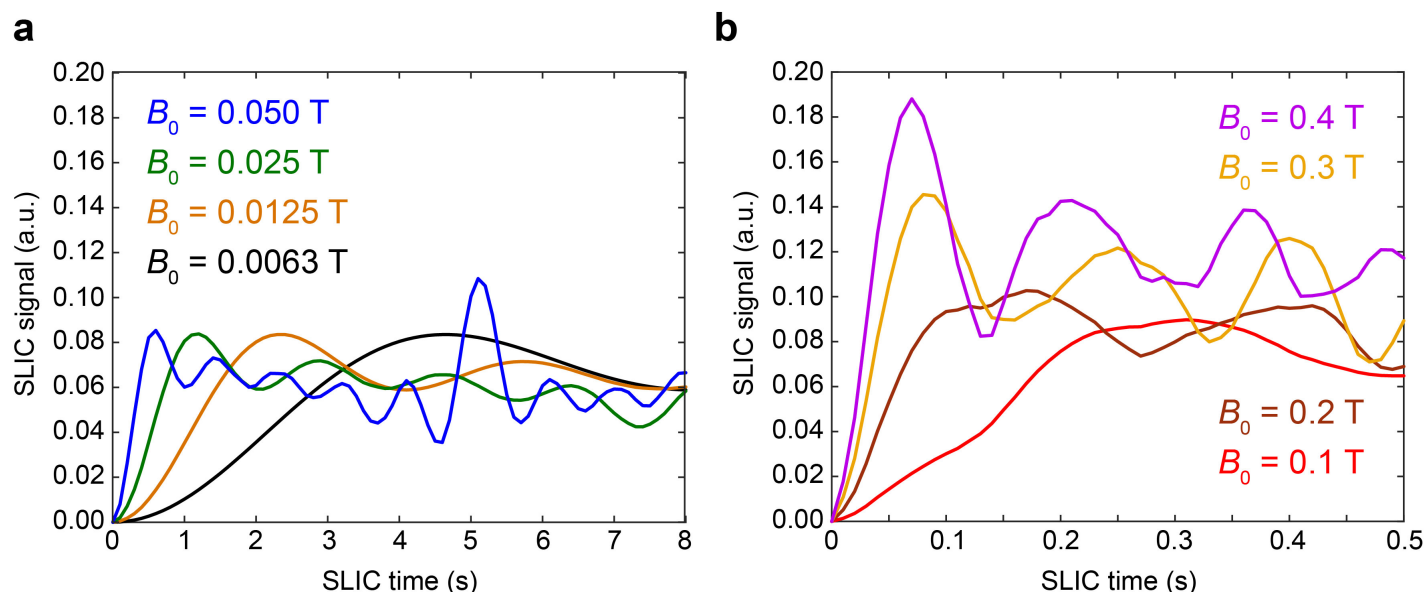
Figure 15. Simulation of ^{1}H NMR signal dependence for the 8-spin system of propane on SLIC pulse time (SLIC duration) at various static magnetic fields at zero RF pulse offset and B_1 of 22.2 Hz. Note that relaxation effects were not included into simulation. The picture is reproduced from supporting information file of Barskiy, D. A.; Salnikov, O. G.; Romanov, A. S.; Feldman, M. A.; Coffey, A. M.; Kovtunov, K. V.; Koptyug, I. V.; Chekmenev, E. Y. *J. Magn. Reson.* **2017**, *276*, 78.

Figure 15 clearly shows the advantage of using higher (than 0.05 T originally proposed) magnetic field. For example, the optimal SLIC duration at 0.3-0.4 T (our target with vendor) is *ca*. 60 ms vs. *ca*. 500 ms at 0.05T. Since we plan on using a partial SLIC pulse (i.e. ~1/30 of the optimal duration), it will be possible to excite the spin system in less than 2 ms. When the readout and gradient encoding are added, we expect to spend only 5 ms of time for each line of k-space at 0.35 T. As a result, it would be possible to record 1000 lines of k-space (sufficient for high quality 3D image, e.g. 8 slices with 128x128 matrix) in 5 seconds or a single patient breath-hold.

Second, Figure 15 also shows that the SLIC transformation efficiency is nearly doubled at 0.3-0.4T compared to that at 0.05 T (peak height). As a result, detection at 0.35 T would double the effective MRI signal, which is a clear practical advantage of performing imaging at 0.35 T vs. 0.05 T.

We have also studied the SLIC transformation of singlet state magnetization in a range of other compounds. The corresponding work is published in Paper #1 (Barskiy, D. A.; Salnikov, O. G.; Shchepin, R. V.; Feldman, M. A.; Coffey, A. M.; Kovtunov, K. V.; Koptyug, I. V.; Chekmenev, E. Y. NMR SLIC Sensing of Hydrogenation Reactions Using Parahydrogen in Low Magnetic Fields. J. Phys. Chem. C 2016, 120, 29098-29106). This work demonstrates the overall broad applicability of this approach, which goes well beyond HP propane gas.

What opportunities for training and professional development has the project provided?

This project provided numerous opportunities and enabled a great deal of career development.
1) Prof. Chekmenev received a very prestigious honor. He was named a Distinguished Investigator for accomplishments in the field of medical imaging from the Academy for Radiology & Biomedical Imaging Research.
2) A participating post-doctoral fellow, Dr. Panayiotis Nikolaou started his part-time position as a CEO of the start-up company XeUS Technologies, LTD. He will be 100% at the company after his planned departure at the end of 2017.
3) One of the PIs of this partnering PI award received an unrestricted funding in the form of a gift from ExxonMobil Research and Engineering Company: $25,000. This is the second gift from this company to support our research.

4) This project enabled research activity for numerous visiting scholars from collaborating labs (see the list of involved personnel) from SIUC. Trainees from each US site routinely visit the other site to perform experiments and work together in highly interdisciplinary environments; trainees also got the opportunity to work with (and learn from) visiting Russian collaborators.
5) Most trainees working on this project had an opportunity to attend at least one National or International Conference to publicize the work performed and also for their exposure to biomedical science. Dr. Aaron Coffey also additionally attended ISMRM conference in Hawaii in Spring 2017.

How were the results disseminated to communities of interest?

Yes. Several scientific conferences/meetings.

4. IMPACT

What was the impact on the development of the principal discipline(s) of the project?

Nothing to Report.

What was the impact on other disciplines?

Nothing to Report.

What was the impact on technology transfer?

There were two key areas of impact on the technology transfer:
1) The Vanderbilt team has filed a provisional application for detecting sulfur containing compounds using NMR hyperpolarization; this technology may take advantage of non-hydrogenative HET-PHIP catalysis in the future. The utility application was filed during Year 2 of this project.
2) More importantly, we provided the disclosure regarding the development of ^{129}Xe hyperpolarizers (for all three generations including the one funded by this award) to both SIUC and Vanderbilt University. Based on our preliminary discussions with the tech transfer office at Vanderbilt, VU (and most likely SIUC) will not file for patent protection for this technology. Instead, during Year 2 of the project, Dr. Chekmenev and his team received the ownership of the know-how (subject to the DOD regulations and approval). This tech transfer arrangement eventually allows a post-doctoral trainee of this project, Dr. Nikolaou, to lead the commercialization effort for this technology in XeUS Technologies LTD in Europe. The appeal of the low-cost and high-throughput was a key element proposed for this project, which we believe will be of significant benefit to the patients suffering from the lung disease once the technology is commercialized and once it is eventually available to the end users. The first device (from XeUS Technologies LTD) has already been pre-ordered – a true testament to our commitment for eventual technology transfer and commercialization of the work performed under this project.

What was the impact on society beyond science and technology?

Nothing to Report.

5. CHANGES / PROBLEMS

1) As described above we did not use the first prototype of full metal optical pumping cell for ^{129}Xe hyperpolarizer due to sub-par performance (but we discuss the work performed in this direction in the sections above). Instead, we developed an alternative solution, which we have demonstrated to work.

2) We have also experienced some technical issues with the high-power laser diode array (as discussed above). We will be resolving these issues with the equipment vendor during Year 3 of the project.

6. PRODUCTS

Oral Presentations

1. Chekmenev, E. Y. NMR Hyperpolarization Techniques of Gases. 2017. The 2017 International Workshop on Pulmonary Imaging, March 4; Philadelphia, PA, USA.
2. Chekmenev, E. Y. SABRE and PHIP hyperpolarization of contrast agents for molecular imaging, 25th International Society for Magnetic Resonance in Medicine (ISMRM) Conference, April 24; Honolulu, HI, 2017.

3. Chekmenev EY. NMR Hyperpolarized Contrast Agents for Molecular Imaging. 2017 March 21, Wayne State University (WSU), IBio Site-visit Seminar, Detroit, MI, USA.
4. Chekmenev EY. Hyperpolarized Contrast Agents for Molecular Imaging. 2017 March 22, Wayne State University (WSU), Department of Chemistry, Detroit, MI, USA.
5. Chekmenev EY. Hyperpolarized NMR Contrast Agents for Molecular Imaging. 2017 April 07, Beckman Research Institute Seminar Series and Department of Radiation Oncology, City of Hope, Duarte, CA, USA.
6. Chekmenev EY. Hyperpolarized Contrast Agents for Molecular Imaging. 2017 June 6, Wayne State University (WSU), Karmanos Cancer Center, Detroit, MI, USA.
7. Chekmenev EY. Hyperpolarized NMR Contrast Agents for Molecular Imaging. 2017 August 10, Beckman Research Institute Seminar Series, City of Hope, Duarte, CA, USA.
8. Goodson BM. PHIP, SABRE, and SEOP: Low(er)-Cost Alternatives for the Rapid Creation of Pure, Long-Lived Hyperpolarized Agents. In *58th Experimental ENC Conference* Pacific Grove, California, USA, 2017.
9. Goodson BM, Hyperpolarization of ^{129}Xe and ^{131}Xe by Clinical-Scale Stopped-Flow Spin-Exchange Optical Pumping. PiNG 2017 Conference, October 8-13, 2017, Park City Mountain Resort, Park City, UT.
10. Goodson BM, Methods for Enhancing NMR and MRI with Hyperpolarized Xenon and SABRE. 2017. The 2017 International Workshop on Pulmonary Imaging, March 4; Philadelphia, PA, USA.

Conference Abstracts

1) Barskiy, D. A.; Salnikov, O. G.; Romanov, A. S.; Feldman, M. A.; Coffey, A. M.; Kovtunov, K. V.; Koptyug, I. V.; Chekmenev, E. Y. Hyperpolarized Propane: Relaxation, Long-Lived Spin States, and Spin-Lock Induced Crossing (Slic) Dispersion. In *58th Experimental ENC Conference* Pacific Grove, California, USA, 2017.
2) Coffey, A. M.; Feldman, M. A.; Shchepin, R. V.; Barskiy, D. A.; Truong, M. L.; Pham, W.; Gore, J. C.; Chekmenev, E. Y. "Potential for High-Resolution Hyperpolarized in Vivo Metabolic Heteronuclear Spectroscopy at Low Magnetic Fields"; VUIIS Annual Retreat, 2017, Nashville, TN.
3) Coffey, A. M.; Feldman, M. A.; Shchepin, R. V.; Truong, M. L.; Pham, W.; Chekmenev, E. Y. "Resolving Spin-Spin Couplings in Hyperpolarized in Vivo Metabolic ^{13}C Spectroscopy at Low Magnetic Field Following Murine Tail-Vein Injection"; 25th International Society for Magnetic Resonance in Medicine (ISMRM) Conference, 2017, Honolulu, HI, USA.
4) Coffey, A. M.; Feldman, M. A.; Shchepin, R. V.; Truong, M. L.; Pham, W.; Chekmenev, E. Y. Feasibility of Low-Field Nmr (0.05t) Discrimination of Spin-Spin Couplings in Vivo for Murine ^{13}C Metabolic Spectroscopy. In *58th Experimental ENC Conference* Pacific Grove, California, USA, 2017.
5) Collel, J. F. P.; Emondts, M.; Logan, A. W. J.; Shen, K.; Shchepin, R. V.; Spannring, P.; Wang, Q.; Chekmenev, E. Y.; Malcolmson, S. J.; Feiters, M.et al. Hyperpolarization of ^{15}N in Aqueous Solution with Sabre Sheath. In *58th Experimental ENC Conference* Pacific Grove, California, USA, 2017.
6) Gemeinhardt, M.; Kovtunova, L. M.; Kovtunov, K. V.; Gesiorski, J.; Bales, L.; Koptyug, I. V.; Bukhtiyarov, V. I.; Chekmenev, E. Y.; Goodson, B. M. Enhancement of ^{15}N NMR Signals Via Heterogeneous SABRE-SHEATH. In *58th Experimental ENC Conference* Pacific Grove, California, USA, 2017.
7) Kidd, B. E.; Gemeinhardt, M.; Mashni, J.; Bales, L.; Gesiorski, J.; Chekmenev, E. Y.; Goodson, B. M. ^{1}H SABRE and ^{15}N Sabre-Sheath Enhancement and Competitive Binding of Primary DNA Nucleobases. In *58th Experimental ENC Conference* Pacific Grove, California, USA, 2017.
8) Murphy, M. N.; Porter, J.; Kidd, B. E.; Molway, M. J.; Basler, D.; Ranta, K.; Gemeinhardt, M.; Coffey, A. M.; Nikolaou, P.; Falola, B. D.et al. New Developments in Stopped-Flow Spin-Exchange Optical Pumping of ^{129}Xe and ^{131}Xe. In *58th Experimental ENC Conference* Pacific Grove, California, USA, 2017.
9) Nikolaou, P.; Coffey, A. M.; Chekmenev, E. Y. "3rd Generation Fully Automated Stopped-Flow Xenon-129 Hyperpolarizer"; VUIIS Annual Retreat, 2017, Nashville, TN.
10) Nikolaou, P.; Coffey, A. M.; Kidd, B. E.; Murphy, M. N.; Porter, J.; Barlow, M. J.; Goodson, B. M.; Chekmenev, E. Y. 3rd-Generation Fully-Automated Stopped-Flow Xenon-129 Hyperpolarizer. In *58th Experimental ENC Conference* Pacific Grove, California, USA, 2017.
11) Shchepin, R. V.; Barskiy, D. A.; Coffey, A. M.; Theis, T.; Kovtunov, K. V.; Kovtunova, L. M.; Koptyug, I. V.; Warren, W. S.; Goodson, B. M.; Chekmenev, E. Y. Toward Hypoxia and Ph Sensing ^{15}N Hyperpolarized Contrast Agents Using Sabre-Sheath. In *58th Experimental ENC Conference* Pacific Grove, California, USA, 2017.

12) Skinner, J. G.; Ranta, K.; Nikolaou, P.; Coffey, A. M.; Chekmenev, E. Y.; Goodson, B. M.; Barlow, M. J. Simulations of Xenon-Rich Stopped-Flow Spin-Exchange Optical Pumping at High Laser Fluxes. In *58th Experimental ENC Conference* Pacific Grove, California, USA, 2017.

Peer-Reviewed Manuscripts, Dissertation & Book Chapters

1) Barskiy, D. A.; Salnikov, O. G.; Shchepin, R. V.; Feldman, M. A.; Coffey, A. M.; Kovtunov, K. V.; Koptyug, I. V.; Chekmenev, E. Y. NMR SLIC Sensing of Hydrogenation Reactions Using Parahydrogen in Low Magnetic Fields. *J. Phys. Chem. C* **2016**, *120*, 29098-29106.

2) Kovtunov, K. V.; Barskiy, D. A.; Shchepin, R. V.; Salnikov, O. G.; Prosvirin, I. P.; Bukhtiyarov, A. V.; Kovtunova, L. M.; Bukhtiyarov, V. I.; Koptyug, I. V.; Chekmenev, E. Y. Production of Pure Aqueous ^{13}C-Hyperpolarized Acetate by Heterogeneous Parahydrogen-Induced Polarization. *Chem. Eur. J.* **2016**, *22*, 16446–16449.

3) Bales, L.; Kovtunov, K. V.; Barskiy, D. A.; Shchepin, R. V.; Coffey, A. M.; Kovtunova, L. M.; Bukhtiyarov, A. V.; Feldman, M. A.; Bukhtiyarov, V. I.; Chekmenev, E. Y.et al. Aqueous, Heterogeneous Parahydrogen-Induced ^{15}N Polarization. *J. Phys. Chem. C* **2017**, *121*, 15304–15309.

4) Barskiy, D. A.; Coffey, A. M.; Nikolaou, P.; Mikhaylov, D. M.; Goodson, B. M.; Branca, R. T.; Lu, G. J.; Shapiro, M. G.; Telkki, V.-V.; Zhivonitko, V. V.et al. NMR Hyperpolarization Techniques of Gases. *Chem. Eur. J.* **2017**, *23*, 724-724.

5) Barskiy, D. A.; Coffey, A. M.; Nikolaou, P.; Mikhaylov, D. M.; Goodson, B. M.; Branca, R. T.; Lu, G. J.; Shapiro, M. G.; Telkki, V.-V.; Zhivonitko, V. V.et al. Cover Picture: NMR Hyperpolarization Techniques of Gases (Chem. Eur. J. 4/2017). *Chem. Eur. J.* **2017**, *23*, 722-722.

6) Barskiy, D. A.; Coffey, A. M.; Nikolaou, P.; Mikhaylov, D. M.; Goodson, B. M.; Branca, R. T.; Lu, G. J.; Shapiro, M. G.; Telkki, V.-V.; Zhivonitko, V. V.et al. NMR Hyperpolarization Techniques of Gases. *Chem. Eur. J.* **2017**, *23*, 725–751.

7) Barskiy, D. A.; Kovtunov, K. V.; Gerasimov, E. Y.; Phipps, M. A.; Salnikov, O. G.; Coffey, A. M.; Kovtunova, L. M.; Prosvirin, I. P.; Bukhtiyarov, V. I.; Koptyug, I. V.et al. 2D Mapping of NMR Signal Enhancement and Relaxation for Heterogeneously Hyperpolarized Propane Gas. *J. Phys. Chem. C* **2017**, *121*, 10038–10046.

8) Barskiy, D. A.; Salnikov, O. G.; Romanov, A. S.; Feldman, M. A.; Coffey, A. M.; Kovtunov, K. V.; Koptyug, I. V.; Chekmenev, E. Y. NMR Spin-Lock Induced Crossing (SLIC) Dispersion and Long-Lived Spin States of Gaseous Propane at Low Magnetic Field (0.05 T). *Journal of Magnetic Resonance* **2017**, *276*, 78-85.

9) Burueva, D. B.; Romanov, A. S.; Salnikov, O. G.; Zhivonitko, V. V.; Chen, Y.-W.; Barskiy, D. A.; Chekmenev, E. Y.; Hwang, D. W.-H.; Kovtunov, K. V.; Koptyug, I. V. Extending the Lifetime of Hyperpolarized Propane Gas Via Reversible Dissolution. *J. Phys. Chem. C* **2017**, *121*, 4481–4487.

10) Coffey, A. M.; Feldman, M. A.; Shchepin, R. V.; Barskiy, D. A.; Truong, M. L.; Pham, W.; Chekmenev, E. Y. High-Resolution Hyperpolarized in Vivo Metabolic ^{13}C Spectroscopy at Low Magnetic Field (48.7 Mt) Following Murine Tail-Vein Injection. *Journal of Magnetic Resonance* **2017**, *281*, 246-252.

11) Colell, J. F. P.; Emondts, M.; Logan, A. W. J.; Shen, K.; Bae, J.; Shchepin, R. V.; Ortiz, G. X.; Spannring, P.; Wang, Q.; Malcolmson, S. J.et al. Direct Hyperpolarization of Nitrogen-15 in Aqueous Media with Parahydrogen in Reversible Exchange. *J. Am. Chem. Soc.* **2017**, *139*, 7761–7767.

12) Colell, J. F. P.; Logan, A. W. J.; Zhou, Z.; Shchepin, R. V.; Barskiy, D. A.; Ortiz, G. X.; Wang, Q.; Malcolmson, S. J.; Chekmenev, E. Y.; Warren, W. S.et al. Generalizing, Extending, and Maximizing Nitrogen-15 Hyperpolarization Induced by Parahydrogen in Reversible Exchange. *J. Phys. Chem. C* **2017**, *121*, 6626–6634.

13) Goodson, B. M.; Ranta, K.; Skinner, J.; Coffey, A. M.; Nikolaou, P.; Gemeinhardt, M. E.; Anthony, D.; Stephenson, S.; Hardy, S.; Owers-Bradley, J.et al. The Physics of Hyperpolarized Gas MRI (Invited Chapter). In *Hyperpolarized and Inert Gas MRI in Research and Medicine*; Albert, M., Hane, F., Eds.; Elsevier Inc.: San Diego, CA, United States, 2017; pp 23-46.

14) Kovtunov, K. V.; Kovtunova, L. M.; Gemeinhardt, M. E.; Bukhtiyarov, A. V.; Gesiorski, J.; Bukhtiyarov, V. I.; Chekmenev, E. Y.; Koptyug, I. V.; Goodson, B. M. Heterogeneous Microtesla Sabre Enhancement of ^{15}N NMR Signals. *Angew. Chem. Int. Ed.* **2017**, *56*, 10433–10437.

15) Shchepin, R. V.; Barskiy, D. A.; Coffey, A. M.; Feldman, M. A.; Kovtunova, L. M.; Bukhtiyarov, V. I.; Kovtunov, K. V.; Goodson, B. M.; Koptyug, I. V.; Chekmenev, E. Y. Robust Imidazole-^{15}N$_2$ Synthesis for High-Resolution Low-Field (0.05 T) ^{15}N hyperpolarized NMR Spectroscopy. *ChemistrySelect* **2017**, *2*, 4478–4483.

16) Zhou, Z.; Yu, J.; Colell, J. F. P.; Laasner, R.; Logan, A. W. J.; Barskiy, D. A.; Shchepin, R. V.; Chekmenev, E. Y.; Blum, V.; Warren, W. S.et al. Long-Lived $^{13}C_2$ Nuclear Spin States Hyperpolarized by Parahydrogen in Reversible Exchange at Microtesla Fields. *J. Phys. Chem. Lett.* **2017**, *8*, 3008–3014.

Inventions, patent applications and licenses: 1 Utility application filed

1) Chekmenev EY, Shchepin RV; Vanderbilt University, assignee. Methods of Detecting Sulfur-Containing Compounds. Publication Number US20170153218 A1. Application Number US 15/362,846. Priority date Nov. 30, 2015. Publication date Jun. 1, 2017.

7. PARTICIPANTS & OTHER COLLABORATING ORGANIZATIONS

Individuals worked on the project

The following personnel worked on the project

Name:	Eduard Chekmenev
Project Role:	Initiating PI (Vanderbilt)
Researcher Identifier (ORCID ID):	orcid.org/0000-0002-8745-8801
Nearest person month worked:	3
Contribution to Project:	Dr. Chekmenev was responsible for the overall progress of the project, performing some experiments with hyperpolarized propane and hyperpolarized xenon-129, developing RF coils, analyzing some of the data for the above-mentioned experiments, preparing the manuscripts.
Funding Support:	DOD W81XWH-12-1-0159/BC112431; NSF CHE-1416268; NIH 1R21EB018014; NIH 1R21EB020323; ExxonMobil Knowledge Build Award; NIH 1U01CA202229

Name:	Matthew S. Rosen
Project Role:	Consultant
Researcher Identifier (e.g. ORCID ID):	
Nearest person month worked:	1
Contribution to Project:	Prof. Rosen served as a consultant for RF pulse sequence design for TecMag MRI platform and on instrumentation for hyperpolarized Xe-129 production. He also actively participated in preparation of peer-reviewed manuscript.
Funding Support:	NIH R01-EB018976 NIH R21NS087344

Name:	Aaron M. Coffey
Project Role:	Postdoctoral Fellow
Researcher Identifier (e.g. ORCID ID):	
Nearest person month worked:	1
Contribution to Project:	Dr. Coffey participated in the design of ^{129}Xe hyperpolarizer and assisted with hyperpolarized propane experiments. Developed full metal optical pumping prototype, and RF coil prototypes. He also designed compensated electromagnet.
Funding Support:	NIH 1F32EB021840

Name:	Panayiotis Nikolaou
Project Role:	Postdoctoral Fellow
Researcher Identifier (e.g. ORCID ID):	
Nearest person month worked:	6
Contribution to Project:	Dr. Nikolaou led the design of ^{129}Xe hyperpolarizer. Developed optical pumping aluminum jacket prototype, made most of 3D drawings in the CAD software, placed

	most orders, and built RF coil & electromagnet prototypes. He also constructed prototype propane polarizer.
Funding Support:	DOD W81XWH-12-1-0159/BC112431

Name:	Roman V. Shchepin
Project Role:	Research Assistant Professor
Researcher Identifier (e.g. ORCID ID):	
Nearest person month worked:	1
Contribution to Project:	Dr. Shchepin helped with propane hyperpolarization experiments, equipment installation. He was also involved in some aspects of testing heterogeneous catalysts for PHIP hyperpolarization.
Funding Support:	DOD W81XWH-12-1-0159/BC112431; NIH 1R21EB018014; NIH 1R21EB020323; NIH 1U01CA202229

Name:	Danila A. Barskiy
Project Role:	Postdoctoral Fellow
Researcher Identifier (e.g. ORCID ID):	orcid.org/0000-0002-2819-7584
Nearest person month worked:	3
Contribution to Project:	Dr. Barskiy performed propane hyperpolarization experiments, built some RF coils. He was also tested heterogeneous catalysts for PHIP hyperpolarization.
Funding Support:	DOD W81XWH-12-1-0159/BC112431

Name:	Boyd M. Goodson
Project Role:	Partnering PI (SIUC)
Researcher Identifier (ORCID ID):	orcid.org/0000-0001-6079-5077
Nearest person month worked:	2
Contribution to Project:	Prof. Goodson was responsible for the overall progress of the project at the partnering site, performing some experiments with hyperpolarized xenon-129 and xenon-131, alternate cells designs, gas mixtures, etc., analyzing some of the data for the above-mentioned experiments, preparing manuscripts and presentations.
Funding Support:	SIUC DOD PRMRP W81XWH-15-1-0272 NSF-CHE-1416432 NSF-DMR-1461255 NIH-1R21EB018014 NIH-1R21EB020323

Name:	Michael Molway
Project Role:	MS student
Researcher Identifier (ORCID ID):	
Nearest person month worked:	6
Contribution to Project:	Michael Molway worked on many of the experiments concerning hyperpolarized

	xenon-129 and xenon-131, alternate cells designs, gas mixtures, etc., analyzing some of the data for the above-mentioned experiments, and helping to prepare manuscripts and presentations
Funding Support:	DOD PRMRP W81XWH-15-1-0272

Name:	Bryce Kidd
Project Role:	Postdoctoral fellow
Researcher Identifier (ORCID ID):	
Nearest person month worked:	3
Contribution to Project:	Dr. Kidd worked on many of the experiments concerning hyperpolarized xenon-129 and xenon-131, ODESR, alternate cells designs, gas mixtures, etc., as well as experiments involving high-power lasers, MR detection, etc. He also works with the Vanderbilt group with the clinical-scale polarizers. He also analyzed some of the data for the above-mentioned experiments, and helping to prepare manuscripts and presentations.
Funding Support:	NSF-CHE-1416432 DOD PRMRP W81XWH-15-1-0272 NIH-1R21EB018014, NIH-1R21EB020323

Name:	Megan Murphy
Project Role:	Undergraduate student researcher
Researcher Identifier (ORCID ID):	
Nearest person month worked:	3
Contribution to Project:	Ms. Murphy participated in most of (and now leads some of) the experiments concerning hyperpolarized xenon-129 and xenon-131, alternate cells designs (including metal cells), gas mixtures, etc., analyzing some of the data for the above-mentioned experiments, and helping to prepare manuscripts and presentations.
Funding Support:	DOD PRMRP W81XWH-15-1-0272

Name:	Justin Porter
Project Role:	Undergraduate student researcher
Researcher Identifier (ORCID ID):	
Nearest person month worked:	4
Contribution to Project:	Mr. Porter participated in some of the experiments concerning hyperpolarized xenon-129 and xenon-131, ODESR, alternate cells designs, gas mixtures, etc., analyzing some of the data for the above-mentioned experiments, and helping to prepare manuscripts and presentations.
Funding Support:	DOD PRMRP W81XWH-15-1-0272

Name:	Dustin Basler
Project Role:	Undergraduate student researcher
Researcher Identifier (ORCID ID):	

Nearest person month worked:	2
Contribution to Project:	Mr. Basler is now an intermediate-level undergraduate researcher. He participates in experiments investigating ODESR and 129Xe and 131Xe SEOP with high-power lasers.
Funding Support:	NIH/SIUC "Bridges to the Baccalaureate" Program; AF ROTC DOD PRMRP W81XWH-15-1-0272

Name:	Max Gemeinhardt
Project Role:	PhD chemistry graduate student
Researcher Identifier (ORCID ID):	
Nearest person month worked:	1
Contribution to Project:	Mr. Gemeinhardt assisted with some high-field 129Xe NMR experiments involving the testing of alternate cell designs (e.g. metal cells).
Funding Support:	SIUC / NMR Facility

Has there been a change in the active other support of the PD/PI(s) or senior/key personnel since the last reporting period?

One grant has been received at the very end of the period 2 of funding (retroactively started at 09/01/2017). Provided below is the detailed information:

1. NIH/NCI 1 R21 CA220137-01 (PI)   09/01/2017-08/31/2020
        $384,500 (USA Component)
   >$300,000 (Russian Component, co-PI: Prof. Igor V. Koptyug)
   "*Magnetic Resonance Spectroscopy and Molecular Imaging of Metabolic Pathways in Cancer*"

This proposal focuses on the development of hyperpolarized ^{13}C pyruvate using parahydrogen-based hyperpolarization technique for molecular imaging of elevated lactate metabolism, which is a universal hallmark of many cancers. This U.S.-Russia bilateral collaborative research partnership will allow bringing resources and expertise not otherwise fully available on either Russian or US side to develop this contrast agent, tools for its preparation (i.e. hyperpolarization methods and hardware) and validate it in cellular and rodent models of cancer. If this project is successful, it will enable fast (in 1 min), scalable (ranging from milli-gram to gram quantity) inexpensive (hyperpolarization hardware and ^{13}C-enriched compound) contrast agent production for molecular imaging of elevated lactate metabolism to monitor response to treatment and cancer screening in high-risk populations.

What other organizations were involved as partners?

In addition to the two performing sites (and consultant listed on the original application), we have, collaborating scientists engaged in this project for Aim 2.

Organization Name: International Tomography Center

Location of Organization: Novosibirsk, Russia

Partner's contribution to the project:

In-kind support: Our collaborators provided catalyst materials for propane hyperpolarizer development work as well as for the final polarizer design;

Collaboration: The Partners' staff work with project staff on the project, we planned for two-month visit with two collaborators visiting us at Vanderbilt site in the fall of 2017. We will perform collaborative experiments, analyzed the data, and prepared manuscripts for peer-reviewed publications.

Personnel exchanges:

1) See above.
2) Approximately 8 visits have been made between VUMC and SIUC sites for the collaborative research activities on both sites. The total duration of those visits was approximately 1 month.

8. SPECIAL REPORTING REQUIREMENTS

Collaborative Award

Since this is a collaborative award with two partnering PIs, we note that we are submitting a duplicating report for two partnering PI awards of the same project: W81XWH-15-1-0271 and W81XWH-15-1-0272. The responsibility of each PI is clearly marked in the Appendix 1.

9. APPENDICES

Appendix 1: Original Statement of work, Years 1-3

STATEMENT OF WORK – 10/10/2014
PROPOSED START DATE September 1, 2015

Site 1:	Vanderbilt University	Site 2:	Southern Illinois University
	1161 21st Ave South MCN AA-1105 Nashville, TN 37232-2310		900 SOUTH NORMAL AVENUE CARBONDALE, IL 62901
	PI: Chekmenev		Partnering PI: Goodson

Specific Aim 1	Timeline	Site 1 (Vanderbilt)	Site 2 (SIU)
Develop and construct a fully automated high-pressure low-cost stand-alone ^{129}Xe hyperpolarizer	Months		
1.1. Design	1-5	80%	20%
1.2. Prototyping	6-10	75%	25%
1.3. Prototype construction and testing	11-15	90%	10%
Milestone Achieved	Prototype ^{129}Xe polarizer constructed		
1.4. Final Design	16-20	80%	20%
1.5. Final Construction	21-24	90%	10%
1.6. Final Testing	25-30	75%	25%
1.7. Polarizer Integration with MRI scanner	31-34	90%	10%
Milestone Achieved	Final ^{129}Xe polarizer constructed		
1.8. Replica Polarizer Construction and Testing	31-36	50%	50%
Milestone Achieved	Replica ^{129}Xe polarizer constructed		

Specific Aim 2	Timeline	Site 1 (Vanderbilt)	Site 2 (SIU)
Develop a large-scale hyperpolarization method for HP propane			
2.1. Chemistry of Large Scale PHIP of propane	1-6	75%	25%
Milestone Achieved:	Clinical Scale Production of HP Propane is developed		
2.2. Initial Polarizer Design	7-12	100%	0%
2.3. Polarizer Prototyping	13-18	100%	0%
Milestone Achieved:	Prototype Polarizer Constructed		
2.4. Prototype Optimization	19-24	100%	0%
2.5. Final Polarizer Construction	25-30	100%	0%
2.6. Final Polarizer Testing and Integration with low-field MRI system	31-36	75%	25%
Milestone(s) Achieved:	Final Propane Polarizer Constructed		
Specific Aim 3	Timeline	Site 1 (Vanderbilt)	Site 2 (SIU)
Develop and construct a 0.05 T MRI scanner	Months		
3.1. Design low-field MRI system with commercial vendors	1-6	50%	50%
3.2. Low-field MRI system construction by Vendors	7-12	50%	50%
3.3. Low-field MRI system installation and fine-tuning at site 1 (Vanderbilt)	13-18	100%	0%

Milestone Achieved:	Clinical low-field MRI system for high-throughout pulmonary imaging is installed	25	
3.4. RF coils (^{129}Xe and ^{1}H) construction for pulmonary imaging	19-24	100%	0%
3.5. Pulse-sequence development and installation	25-30	50%	50%
Milestone Achieved:	Low-field MRI system is ready for use with contrast agents		
3.6. MRI system integration with Propane Hyperpolarizer	31-36	100%	0%
3.7. MRI system integration with Propane Hyperpolarizer	31-34	90%	10%
3.8. Demonstration of high-speed MRI and high-speed contrast agent production/ imaging scan	35-36	90%	10%
Milestones Achieved:	Functional high-speed MRI of hyperpolarized propane and ^{129}Xe; System ready for clinical trial.		

Appendix 2: Reports of characterization of new high-power laser diode array (LDA) and Abstracts Presented and Manuscripts Published and Accepted

14 manuscripts are reported: all are peer-reviewed manuscripts or peer-reviewed book chapters.
3 scientific conference/meeting presentations are reported.
Their non-confidential summaries are provided.
PDF files of these materials are provided below in the Appendix 2.
1 provisional patent application has been filed.

The laser reports are prepared as a part of our standard practices. When we receive this state of the art equipment from the vendors, we perform in-house quality assurance. The laser report are provided in the Appendix 2.

NMR SLIC Sensing of Hydrogenation Reactions Using Parahydrogen in Low Magnetic Fields

Danila A. Barskiy,[*,†] Oleg G. Salnikov,[‡,§] Roman V. Shchepin,[†] Matthew A. Feldman,[†] Aaron M. Coffey,[†] Kirill V. Kovtunov,[‡,§] Igor V. Koptyug,[‡,§] and Eduard Y. Chekmenev[*,†,‖]

[†]Vanderbilt University Institute of Imaging Sciences, Nashville, Tennessee 37232, United States
[‡]International Tomography Center SB RAS, Novosibirsk 630090, Russia
[§]Novosibirsk State University, Novosibirsk 630090, Russia
[‖]Russian Academy of Sciences, Moscow 119991, Russia

S *Supporting Information*

ABSTRACT: Parahydrogen-induced polarization (PHIP) is an NMR hyperpolarization technique that increases nuclear spin polarization by orders of magnitude, and it is particularly well-suited to study hydrogenation reactions. However, the use of high-field NMR spectroscopy is not always possible, especially in the context of potential industrial-scale reactor applications. On the other hand, the direct low-field NMR detection of reaction products with enhanced nuclear spin polarization is challenging due to near complete signal cancellation from nascent parahydrogen protons. We show that hydrogenation products prepared by PHIP can be irradiated with weak (on the order of spin−spin couplings of a few hertz) alternating magnetic field (called Spin-Lock Induced Crossing or SLIC) and consequently efficiently detected at low magnetic field (e.g., 0.05 T used here) using examples of several types of organic molecules containing a vinyl moiety. The detected hyperpolarized signals from several reaction products at tens of millimolar concentrations were enhanced by 10000-fold, producing NMR signals an order of magnitude greater than the background signal from protonated solvents.
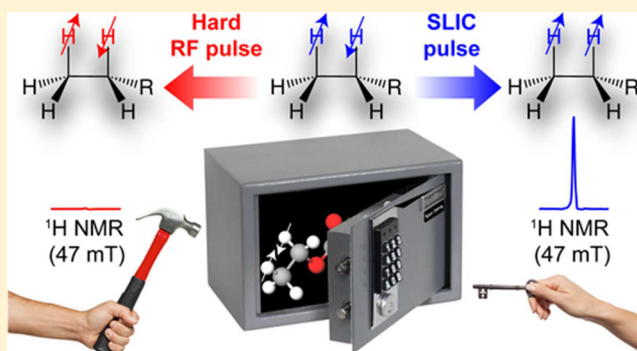
INTRODUCTION

Nuclear magnetic resonance (NMR) spectroscopy is a powerful analytical tool used for a broad range of applications.[1−3] One of the main limitations of NMR is low detection sensitivity dictated by the weak interaction energy of nuclear spins with the static magnetic field B_0.[4−6] Hence, methods for increasing the sensitivity of NMR detection are welcome because they decrease the detection limit and acquisition time. Nuclear spin hyperpolarization techniques such as dissolution dynamic nuclear polarization (d-DNP),[6] spin exchange optical pumping (SEOP) of noble gases,[7,8] and parahydrogen-induced polarization (PHIP)[5,9−11] can temporarily increase nuclear spin polarization (P) by several orders of magnitude (>10000 at high magnetic fields[6] and hundreds of millions at low fields[12]) and thus have become very popular in the past decade.[13,14] Motivated by biomedical applications, d-DNP and SEOP have been introduced into the clinical research realm to probe metabolism, function, response to treatment, etc.[13,15−17]

Recent PHIP innovations have demonstrated relatively inexpensive chemistries for production of contrast agents[18,19] and use of aqueous media[20] and heterogeneous catalysts,[10,21] making PHIP a promising means for generating new classes of hyperpolarized (HP) molecular contrast agents for in vivo

applications.[22] PHIP offers a number of advantages compared to d-DNP and SEOP, that is, (i) very fast (<1 min) hyperpolarization production speed, (ii) low cost, and (iii) straightforward scalability.[8] In addition, PHIP naturally employs hydrogenation reactions and therefore can find promising applications beyond biomedicine. For example, it could be a useful modality for in situ detection and imaging of industrial-scale hydrogenation and hydrogen-involving reactions,[23,24] which represent a significant fraction of all industrial chemical processes.[25]

In principle, while the PHIP hyperpolarization technique is inexpensive and high-throughput, high-resolution NMR spectroscopic detection is most often conducted at high fields using expensive superconducting magnets, which additionally have significant limitations of small sample size. Therefore, despite the low-cost nature of the PHIP hyperpolarization process, the high-field detection renders the entire analysis process generally expensive and limited to small samples—counter to the goals of industrial-scale applications.[26] Alternatively, cheap low-field

magnets can be efficiently used for PHIP signal detection[27−31] because detection sensitivity for HP states has a very weak ($B_0^{1/4}$) magnetic field dependence.[27,32] Moreover, low-field detection offers other advantages: (i) reduced B_0 susceptibility gradients, and (ii) the possibility of construction of relatively low-cost large homogeneous magnets that, in principle, can encompass large chemical reactors.[24,31−34]

However, the direct NMR detection of PHIP hyperpolarization in low magnetic fields is fundamentally challenging. Indeed, even if the magnetic equivalence of the parahydrogen (p-H$_2$) singlet state is broken during the hydrogenation reaction, two p-H$_2$-nascent spins will still reside in the nonobservable pseudo-singlet state[35,36] at low magnetic field (Figure 1a). In practice, this results in the collapse of the
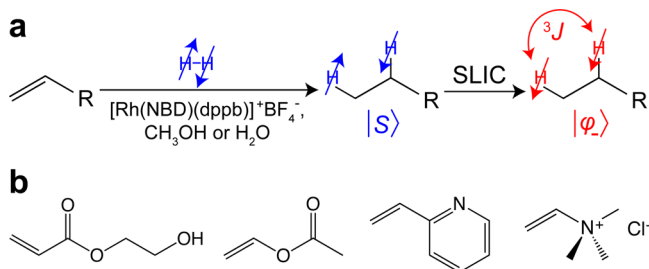

Figure 1. (a) Molecular diagram of unsaturated precursor hydrogenation by p-H$_2$, leading to the hydrogenated product with p-H$_2$-nascent protons residing in the pseudo-singlet state;[35] then, pseudo-singlet state is converted to observable magnetization by using spin-lock induced crossing (SLIC) sequence. (b) Chemical structures of investigated organic molecules containing vinyl moiety: 2-hydroxyethyl acrylate (HEA), vinyl acetate (VA), 2-vinylpyridine (VPy), and (vinyl)trimethylammonium chloride (VTMA).

NMR lines because the difference in the chemical shift of the two nascent protons is too small with respect to the spin−spin coupling (J_{HH}) and also with respect to the magnetic field homogeneity. As a result, the direct detection of PHIP products suffers from massive (more than 2 orders of magnitude) signal cancellation.[37−39]

Here, we show that application of spin-lock induced crossing (SLIC)[40] allows for direct proton readout of HP products at low magnetic field (e.g., 47.5 mT used here). The SLIC sequence is a simple low-power radio frequency (RF) pulse with B_1 strength on the order of J_{HH}. Specifically, more than 10000-fold NMR signal enhancement enabled direct ^{1}H low-field detection of 80 mM solutions of 2-hydroxyethyl propionate, ethyl acetate, 2-ethylpyridine, and (ethyl)-trimethylammonium chloride hyperpolarized via PHIP (Figure 1). The presented methodology of PHIP-enhanced milli-Tesla NMR with SLIC sensing (vs conventional NMR where a hard RF pulse is applied for signal detection) can be used for fast screening of potential HP contrast agents by PHIP and potentially without expensive high-field NMR instruments and isotopic labeling. Moreover, the presented methodology may be potentially conveniently applied to the visualization of industrial-scale processes in situ.

■ METHODS

Preparation of Catalyst/Precursor Solutions. Methanol (80 mL) was placed in four square bottles (431430, Corning Life Sciences, NY, USA) and degassed by the repetitive (three times) sequence: argon flushing, closing the cap, and vortexing

the solution. Rhodium catalyst [(bicyclo[2.2.1]hepta-2,5-diene)[1,4-bis(diphenylphosphino)butane]rhodium(I) tetrafluoroborate, 0.40 mmol, 0.150 g, 5.00 mM final concentration] was placed in each bottle. Vinyl acetate (6.40 mmol, 0.551 g, 80.0 mM final concentration), 2-hydroxyethyl acrylate (6.40 mmol, 0.742 g, 80.0 mM final concentration), trimethyl(vinyl)-ammonium chloride (6.40 mmol, 1.06 g, 80.0 mM final concentration), and 2-vinylpyridine (6.40 mmol, 0.672 g, 80.0 mM final concentration) were added to individual bottles. Water-soluble rhodium catalyst was prepared as described earlier.[20] Vinyl acetate (8.00 mmol, 0.688 g, 80.0 mM final concentration) and 2-hydroxyethyl acrylate (8.00 mmol, 0.928 g, 80.0 mM final concentration) were dissolved in the aqueous solution of rhodium catalyst (100 mL, 2.60 mM) each. Trimethyl(vinyl)ammonium chloride (4.00 mmol, 0.664 g, 80.0 mM final concentration) and 2-vinylpyridine (4.00 mmol, 0.420 g, 80.0 mM final concentration) were dissolved in aqueous rhodium catalyst solution (50 mL, 5.30 mM). Each bottle containing the catalyst/precursor solutions was connected to an automated PHIP polarizer[41] for further experiments.

Preparation of Parahydrogen Gas. For parahydrogen (p-H$_2$) preparation, normal hydrogen was passed through a spiral copper tube packed with FeO(OH) (Sigma-Aldrich, P/N 371254, 30−50 mesh) and immersed into a liquid N$_2$ Dewar. This procedure produces a stream of hydrogen enriched with ca. 50% $para$-isomer.[10]

PHIP Polarizer and Hydrogenation Reaction. A fully automated parahydrogen-based polarizer was employed for hydrogenation.[42] The prepared stock solutions containing catalyst and precursor molecule were connected to the heated injection loop of the polarizer. Hydrogenation of the unsaturated compounds (Figure 1b) was conducted in a chemical reactor (∼56 mL volume) of the polarizer at an ∼7.8 atm p-H$_2$ pressure by injecting the warmed solution from the injection loop and spraying it into the atmosphere of hot p-H$_2$ gas using the back pressure (∼17 atm) of N$_2$ gas (Figure 2a). Reactor temperature was held within the range of 55−60 °C. After a variable reaction time, t_R (Figure 2b), 2−2.5 mL of the solution was ejected from the polarizer into a ∼50 mL detection chamber located inside the RF probe within a 47.5 mT magnet. The magnet was located ∼0.5 m away from the polarizer, allowing very short (<1 s) ejection time of the reacted solution from the reactor to the detection chamber (Corning 50 mL PP centrifuge tube). A TTL microcontroller of the PHIP polarizer was used to switch solenoid valves that control gas and chemical delivery to the high-pressure reactor and ejection to the detection chamber. The detection chamber was cleaned after each NMR signal acquisition before a new portion of the solution from the polarizer was ejected.

Low-Field (2 MHz) NMR Detection. A commercially available MR Kea2 spectrometer (Magritek, Wellington, New Zealand) was used for NMR detection as described by Waddell et al.[43] The magnet (2 MHz Magritek core analyzer, Halbach array, radial field direction) had a homogeneity of 20 ppm over 4 cm diameter of spherical volume. The detection chamber was placed in the home-built ^{1}H RF coil[44] located in the magnet (Figure S1). Radio frequency calibration using a 5 mM aqueous solution of CuSO$_4$ in a 2.8 mL spherical phantom yielded a 90° ^{1}H excitation pulse width of 177 μs at 0.22 W.

SLIC RF Pulse Sequence. Spin order of the p-H$_2$ singlet state was converted to observable magnetization using the SLIC sequence developed by DeVience et al.[40] In order to generate
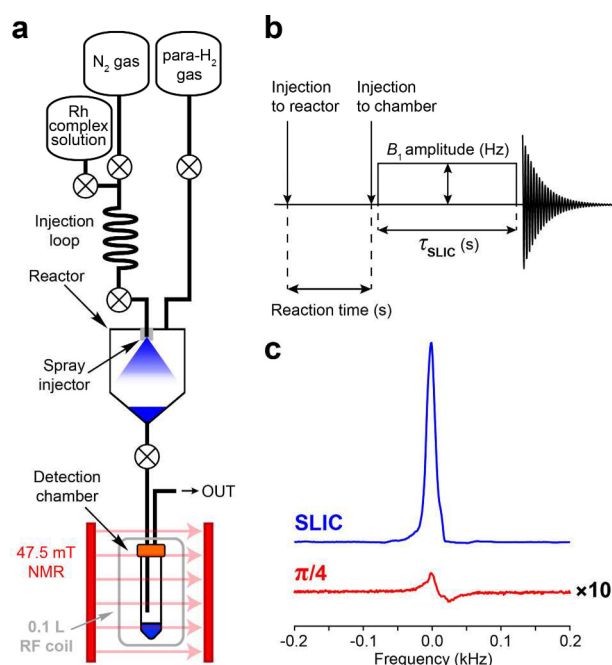
Figure 2. (a) Schematic diagram of experimental setup. The reactor was kept at 50−60 °C. (b) Sequence of events: injection of Rh complex solution (in CH_3OH or in H_2O) into reactor filled with ~7.8 atm of p-H_2, variable reaction time, injection into the detection chamber located inside a 47.5 mT magnet, subsequent application of SLIC pulse and signal acquisition. (c) ^1H NMR signal of HEP in methanol obtained after application of SLIC pulse (blue) and NMR signal obtained after application of a hard $\pi/4$ RF pulse (red); note the scaling by a factor of 10.

low-power (~1 μW) SLIC pulses, additional attenuators (Bird Technologies, 10 W, A series, male/female N connector, 30 and 20 dB) were inserted between the output of the Tomco RF amplifier (P/N BT00250-AlphaS-Dual, Tomco Technologies, Stepney, Australia) and TR switch of the spectrometer (Figure S1). The SLIC pulse amplitude was calibrated by measuring the TR switch voltage output on an oscilloscope (Tektronix, TDS 3034C) and comparing it to the measurements for the $\pi/2$ RF pulse calibrated by nutation experiment. Acquisition of the ^1H NMR signal started immediately after injection of the reactor content to the detection chamber followed by a SLIC pulse (Figure 2b). Optimization of SLIC parameters (B_1 amplitude and duration, τ_{SLIC}) was performed for the 2-hydroxyethyl propionate (the product of 2-hydroxyethyl acrylate hydrogenation), and then parameters found were used for the detection of all other substrates under study.

■ RESULTS

We carried out hydrogenation of several molecules containing a vinyl moiety (Figure 1): 2-hydroxyethyl acrylate (HEA), vinyl acetate (VA), 2-vinylpyridine (VPy), and (vinyl)-trimethylammonium chloride (VTMA), with p-H_2, using a home-built automated PHIP polarizer (Figure 2a). The compounds were chosen based on their importance in the context of potential PHIP applications. For example, ethyl acetate can be potentially employed to trace the metabolism of brain damage and cancer; 2-ethylpyridine (EPy) has shown the potential for ^{15}N pH mapping/imaging;[45] (ethyl)-trimethylammonium is structurally similar to choline, which is a key metabolic signature in many cancers;[46−48] 2-hydroxyethyl

propionate can be used for in vivo angiography, and it is also a typical test molecule for PHIP studies.[49,50] Hydrogenation of the vinyl motif ($-CH=CH_2$) by p-H_2 for the molecules studied leads to ethyl group ($-CH_2-CH_3$) formation, where two hydrogens come from the same p-H_2 molecule, and these nascent parahydrogen nuclei are incorporated into two chemically inequivalent positions. Due to the identical structure of the intentionally chosen hydrogenated motif for all substrates investigated (Figure 1b), their NMR parameters and J coupling patterns are relatively similar (Table S1).

Use of the automated home-built low-field PHIP polarizer made possible the fast conversion of 80 mM unsaturated substrates into hydrogenation reaction products. Reactions were carried out by fast (<4 s) injection of 3−5 mL of the catalyst/precursor solution into an atmosphere of p-H_2. Then reaction solutions were quickly (<1 s) pushed to the detection chamber located in the bore of a 47.5 mT magnet; the SLIC RF pulse was applied immediately, and it was followed by ^1H NMR signal acquisition (Figure 2a,b). The intensity of the NMR signal obtained after SLIC was at least 2 orders of magnitude greater than the signal intensity obtained after application of a hard $\pi/4$ pulse as typically employed in high-field PHIP experiments[11] (Figure 2c).

We note that the hydrogenation reactions were carried out in nondeuterated solvents, such as methanol and water. The NMR signal resulting from ~80 mM of hydrogenated material after SLIC was 10−30 times greater than the NMR signal originating from the solvent (Figure 3a,b). Besides providing a direct
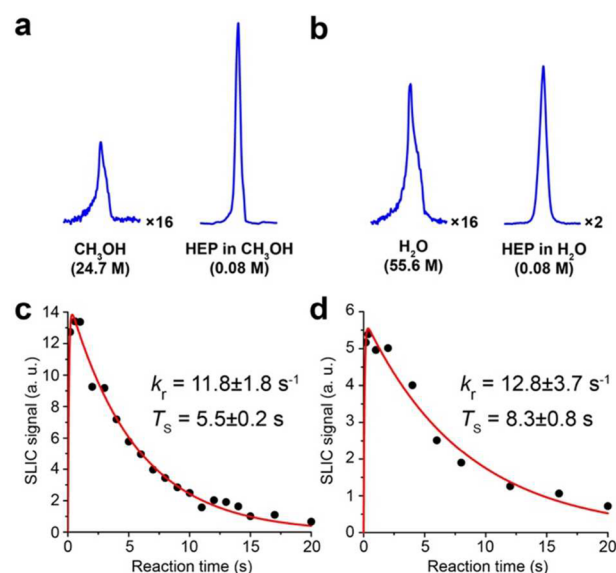
Figure 3. ^1H NMR spectroscopy of HEP at 47.5 mT. (a) Left: ^1H NMR signal of reaction mixture injected into the detection chamber at equilibrium nuclear spin polarization; the NMR signal originates primarily from methanol solvent. Right: ^1H HP NMR signal obtained after SLIC pulse applied to the reaction mixture (~0.08 M of 2-hydroxyetyl propionate (HEP) in methanol). (b) Left: ^1H NMR signal of reaction mixture injected into the detection chamber at equilibrium nuclear spin polarization; the NMR signal originates primarily from water solvent. Right: ^1H HP NMR signal obtained after SLIC pulse applied to the reaction mixture (~0.08 M of HEP in water). (c) Dependence of the SLIC signal (normalized to the thermal signal of the solvent) on the reaction time for HEP in methanol. (d) Dependence of the SLIC signal (normalized to the thermal signal of the solvent) on the reaction time for HEP in water.

comparison with the HP signal, utilization of nondeuterated solvents here advantageously allowed calibration of experimental parameters (e.g., RF pulses, B_1 frequency offset, and adjustments to account for minor magnetic field drift typical for low-field scanners based on permanent magnets and in the absence of a deuterium spin-lock apparatus). The signal enhancement of HP resonances was evaluated by computing the ratio of HP signal to the signal originating from the thermally polarized solvent (since the amount of material injected into the detection chamber each time may vary). Maximal apparent polarization percentage (P^{APP}) of ~0.23% was found for 2-hydroxyethyl propionate (HEP) when hydrogenation reaction of HEA was performed in methanol. Lower values were found for ethyl acetate and when water was used as a solvent. Hydrogenation of VPy and VTMA was also detected by SLIC, but their NMR signals were significantly lower (see Discussion).

Varying the reaction time allowed the build-up and decay of the hyperpolarized signal to be detected (Figure 3c,d). We found that the signal decayed with the time constant T_S ranging between 5 and 15 s depending on the studied molecule and the solvent. The T_S values obtained correlate well with prior results in the literature. For example, T_S of 6.4 ± 1.2 s was measured for EA at Earth's magnetic field in ALTADENA conditions,[18] while the present study yielded T_S of EA to be 7.2 ± 0.5 s in methanol (see Table 1 for the T_S values for all studied

Table 1. Kinetic and Relaxation Parameters Extracted from Fitting of the Build-up and Decay Curves for HEP, EA, ETMA, and EPy (Catalyst Concentration was 5 mM)

methanol	HEP	EA	ETMA	EPy
k_r (s^{-1})	11.8 ± 1.8	11.5 ± 2.3	14.1 ± 2.5	2.8 ± 0.5
T_S (s)	5.5 ± 0.2	7.2 ± 0.5	17.1 ± 1.2	
water	HEP	EA	ETMA	EPy
k_r (s^{-1})	12.8 ± 3.9	14.4 ± 5.9	21.9 ± 4.2	
T_S (s)	8.3 ± 0.8	4.3 ± 0.5	13.2 ± 1.4	

substrates in methanol and in water). One may also estimate the effective hydrogenation reaction kinetic constant k_r by fitting the experimental data with suitable analytical expression (eq S1) describing the build-up and decay of a hyperpolarized signal (Figure 3c,d and Supporting Information).

In principle, the use of an automated PHIP polarizer with a high-pressure injection reactor is not mandatory; that is, high-pressure NMR tubes with p-H$_2$ bubbling can be employed (similar to the recent studies of ^{13}C-VA hydrogenation and hyperpolarization with signal amplification by reversible exchange).[18,51] Nevertheless, the use of an automated PHIP polarizer benefited the present study because a series of experiments could be performed routinely and identically, which allowed us to quickly find optimal conditions for performing a singlet-to-magnetization transformation, that is, optimal RF pulse amplitude, frequency offset, and duration of the SLIC pulse (Figure 4).

■ DISCUSSION

The true singlet state of two spins (i.e., the state with a total spin of 0) is not NMR detectable because the singlet state has no magnetic moment.[52] The best example is the nuclear spin singlet state of p-H$_2$ that produces no NMR signal. Another way to explain the absence of the observable NMR signal is the realization that the transitions between exchange antisymmetric
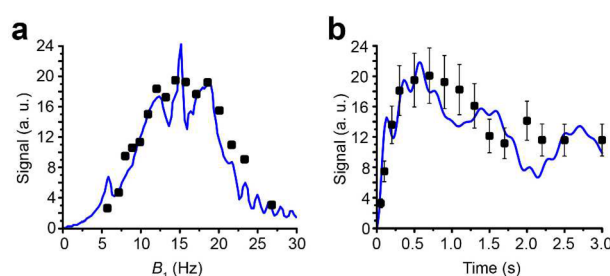
Figure 4. (a) Dependence of the SLIC signal of HEP in methanol (normalized to the thermal signal of the solvent) vs B_1 amplitude at the SLIC duration (τ_{SLIC}) of 0.6 s; black squares correspond to experimental results, and blue line corresponds to simulation assuming ±5 Hz RF pulse offset (i.e., simulating B_0 inhomogeneity). (b) Dependence of the SLIC signal vs SLIC duration (time) at B_1 amplitude of 15 Hz; black squares correspond to experimental results, and blue line corresponds to simulation.

singlet state and exchange symmetric triplet states are forbidden. However, once the magnetic equivalence of the two H atoms is broken (e.g., by introducing two hydrogen atoms from the same p-H$_2$ molecule into a nonsymmetric molecular environment), the spin order of the singlet state can be manifested as a nearly 100% nuclear spin polarization.[53] Hydrogenation reactions can be employed in a way that both hydrogen atoms from the same p-H$_2$ molecule are transferred to the product as a pair (pairwise addition), resulting in a canonical PHIP effect.[11,53,54] However, the singlet state is considered to be truly broken (i.e., resulting in two well-resolved resonances in the NMR spectrum) only if the chemical shift difference between p-H$_2$-nascent protons (δ_{HA} and δ_{HB}) is greater than the spin–spin coupling constant J_{HA-HB} between them (corresponding to the condition of a weak coupling regime).[55] Otherwise—in a strong coupling regime (sometimes referred to as inverse weak coupling regime[56]), that is, (δ_{HA} − δ_{HB}) < J_{HA-HB}—the two nascent protons reside in a pseudo-singlet state even after the act of pairwise addition of p-H$_2$.[35] For example, for the case where (δ_{HA} − δ_{HB}) is 3 ppm and J coupling is 7 Hz, the strong coupling regime occurs for magnetic fields below 0.055 T. The ethyl moiety (−CH$_2$−CH$_3$) is a chemical motif found in a wide range of organic molecules which has a typical J coupling constant of ~7 Hz between methylene and methyl groups, and the corresponding chemical shift difference ($\delta_{METHYLENE}$ − δ_{METHYL}) ranges from 0.5 to 3 ppm (Table S1). Since hydrogenation of vinyl or acrylate groups produces ethyl or propionate groups respectively (note that both cases are considered as an isolated five spin system −CH$_2$−CH$_3$), all four molecules studied form strongly coupled spin systems if hydrogenation by p-H$_2$ is carried out in the fields below 0.055 T.

Although the pseudo-singlet state is not directly detectable by NMR in the strong coupling regime,[38,56−58] the spin order from the pseudo-singlet spin state can be transformed into the observable magnetization using the SLIC sequence introduced by DeVience and co-workers.[40,59] They demonstrated that low-power continuous wave decoupling (with alternating magnetic field B_1 amplitude on the order of J_{HA-HB} and with frequency set at (δ_{HA} + δ_{HB})/2) enables coherent transfer of population between the singlet state $|S\rangle = (|\alpha\beta\rangle - |\beta\alpha\rangle)/\sqrt{2}$ and the state $|\varphi_-\rangle = (|\alpha\alpha\rangle - |\alpha\beta\rangle - |\beta\alpha\rangle + |\beta\beta\rangle)/2$. The latter term corresponds to magnetization aligned along the −x axis in a rotating frame, and it is readily observable by NMR.[52] The optimum duration of SLIC RF irradiation depends on the
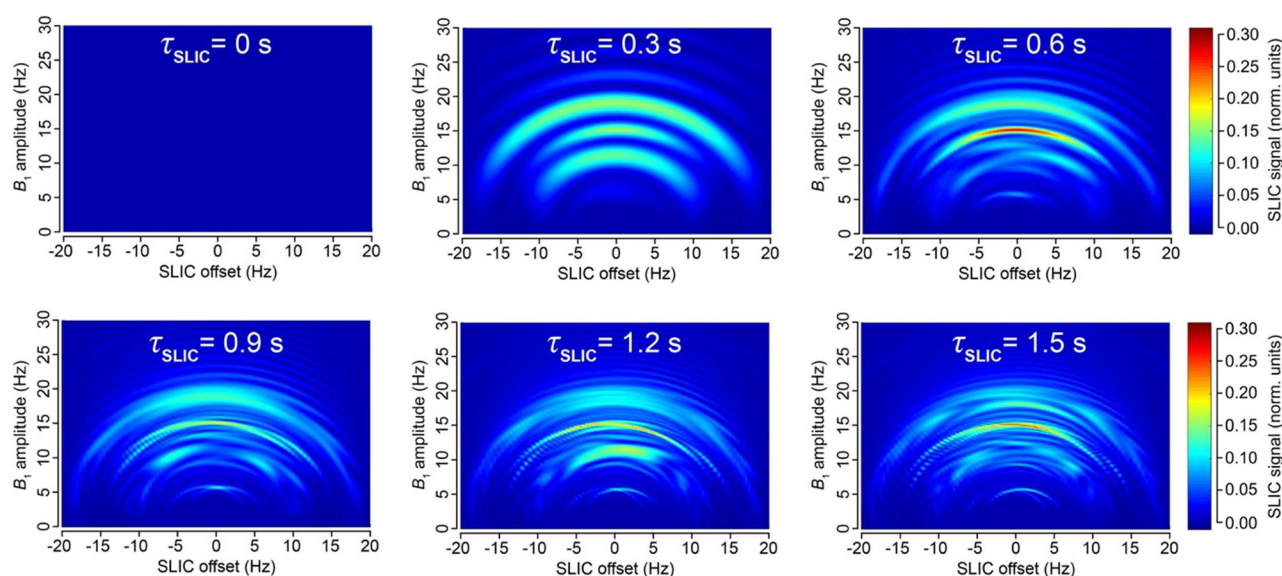
Figure 5. Simulation of ^1H NMR signal dependence in $-CH_2CH_3$ system on SLIC parameters: B_1 amplitude (Hz), SLIC pulse offset (Hz) (position of zero offset corresponds to the center frequency between CH_3 and CH_2 resonances), and SLIC pulse duration (τ_{SLIC}). Relaxation effects were not included in the simulation. See Supporting Information for animated gif files and the corresponding signal dependences for two-spin system.

combination of NMR resonance frequency, J_{HA-HB}, and ($\delta_{HA} - \delta_{HB}$). Advantageously, this transformation does not require any other RF pulses, making it relatively straightforward to implement from the hardware perspective.

However, we found that while the analytical model presented by DeVience et al. works well for the simple case of a two-spin system, it cannot properly describe the observed patterns obtained in the experiment with the five-spin systems of ethyl groups studied here. For example, our results show that instead of a relatively narrow maximum at $B_1 = J_{HA-HB}$ as predicted by the simple theory, there is a broad maximum at $B_1 \sim 2J_{HA-HB}$, and the optimal SLIC pulse duration is about $\sqrt{2}/\Delta v$ (where Δv is the chemical shift difference ($\delta_{METHYLENE} - \delta_{METHYL}$) expressed in Hz), that is, two times longer than that predicted for the two-spin model[40] (Figure 4). Here, detailed spin dynamics simulations were carried out (see Supporting Information), resulting in the graphs (Figure 5) where SLIC signal is plotted versus SLIC B_1 amplitude, SLIC B_1 offset, and SLIC duration, where NMR signal maxima form concentric waves with radii of approximately $3J_{HA-HB}/2$, $2J_{HA-HB}$, and $5J_{HA-HB}/2$. The pattern of the map also changes with SLIC duration, although there is a clear indication of an optimal pulse duration (τ_{SLIC}) yielding the global maximum of the produced signal. We note that the spin dynamics for five-spin systems is much more complex than that for two-spin systems but yet relatively easily predictable using the density matrix formalism.

Although low-field PHIP hyperpolarizers have been used previously to prepare HP molecules via pairwise p-H_2 addition,[43,49] prior attempts to perform direct ^1H NMR signal detection of nascent HP protons resulted in a very weak antiphase NMR signal.[60] Without SLIC or other singlet-to-magnetization pulse sequences,[61] direct proton detection at low fields is unlikely to yield high signal-to-noise ratio to study reaction conversion and pairwise selectivity. Building on our previous experience with SLIC detection of HP propane gas prepared via heterogeneous PHIP,[38] SLIC proton detection of HP liquid was employed in a low magnetic field of 47.5 mT, and the ^1H NMR signal obtained was approximately 2 orders of magnitude greater than the ^1H NMR signal obtained using

conventional hard (i.e., short duration and high amplitude) RF pulses (Figure 2c). To the best of our knowledge, the fact that the action of hard RF pulses on a spin system leads to NMR signal significantly lower than that obtained by low-frequency irradiation is somewhat unique in the field of NMR spectroscopy. Moreover, one can entertain an analogy with a safe, which is hard to open using brute force (e.g., a hammer), but a tiny key with appropriate symmetry can easily crack the lock. It should also be emphasized that unlike the vast majority of hyperpolarization techniques, where the preparation of singlet states requires additional preparation steps, direct creation of pseudo-singlet states is an inherent and unique feature of the PHIP technique.

By varying the "reaction" time (i.e., the time period that the reaction solution remains in the reactor following the injection), we measured singlet state lifetime (T_S) (Figure 3c,d). It was found that the NMR signal decays with a time constant of about 5−15 s depending on the solvent nature (i.e., methanol vs water) (Table 1 and Supporting Information). These values indicate that, despite the spin systems being in pseudo-singlet states, their lifetimes were not significantly longer compared to T_1; that is, they were not several fold greater. This is, however, not surprising because the existence of long-lived spin states requires specific symmetry properties, which may not be present in the systems studied here.[62−64] One should note, however, that such examples can occur, for example, in previously reported long-lived HP propane states.[38,65] Future studies are certainly warranted to identify other examples of long-lived HP spin states that could find use in biomedical and material science applications.[66]

The efficiency of a singlet-to-magnetization conversion by SLIC may be analyzed using the boundary transformation methodology presented by Levitt.[67] In the case of the two-spin system, it is possible to "extract" nearly 100% of the singlet spin order and transform it into observable magnetization (~91% when using the SLIC pulse sequence). At the same time for a five-spin system, such as $-CH_2-CH_3$, it is fundamentally possible to transform up to only 55% of spin order (Supporting Information). Our calculations for SLIC show ~27% trans-

formation efficiency (Figure 5), indicating that there could be a more efficient RF pulse sequence alternative to the SLIC implementation employed here.[68,69] This inefficiency partially explains the relatively low apparent polarization level of ~0.23% obtained for HEP and even lower values for other studied molecules. Other factors that likely had a significant negative impact on the efficiency of SLIC spin transformation include spin relaxation processes and B_0 magnetic field inhomogeneity. Indeed, our calculations show that the efficiency of spin order transfer depends dramatically on the B_1 RF frequency offset (Figure 5). Static B_0 magnetic field drifts and imperfections across the sample can therefore cause significant shifts away from the optimal transfer conditions, thus leaving a potentially large fraction of the population hidden in the "dark" unobservable nuclear pseudo-singlet state. The use of more homogeneous B_0 and B_1 fields can likely significantly improve SLIC efficiency and consequently P^{APP} in the future. Strong dependence of singlet-to-magnetization transformation on the magnetic field inhomogeneity is a substantial limitation of the presented SLIC-based low-field detection method.

Simple analysis also determines the limits of the B_0 magnetic field strength, which should be optimal for parahydrogen-based SLIC sensing presented here. First of all, the magnetic field should not be too high (the weakly coupled regime); otherwise, the singlet spin state is no longer an eigenstate of the nuclear spin Hamiltonian. The strong coupling condition can provide a quick estimate of the upper limit of the low magnetic field range, $B_0 < 2\pi J_{HA-HB}/\gamma \Delta v$, where γ is the proton gyromagnetic ratio. At the same time, very low magnetic fields can result in prohibitively long SLIC pulse duration (since, generally, $\tau_{SLIC} \sim 1/\Delta v$), resulting in significant relaxation losses and/or decoherences during an excessively long SLIC pulse. Thus, the magnetic field of 0.0475 T employed here lies in the "SLIC-safe range" for the studied spin systems; however, the optimal field should be calculated for a particular spin system under study.

We used ^{1}H and ^{13}C high-field (400 MHz) NMR spectroscopy to determine reaction conversion levels by taking aliquots of stock solutions before and after the reaction. One can see that measured conversion values were relatively high for all studied molecules (Figure 6). Lower levels for conversion of VPy and VTMA (25−40%) compared to nearly 100% conversion for HEA and VA can be explained by the presence of nitrogen in the former molecules. In case of VPy, the electron-donating N site can potentially compete with the double bond for a binding event to the Rh center, thereby lowering the probability of forming the active catalytic species and, consequently, decreasing reaction yields. For VTMA, the nitrogen atom possesses positive charge, which can lead to repulsion of the molecule from the positively charged cationic Rh center due to electrostatic interactions of charged ions. The determined conversion can be compared with the intensity of SLIC signal for the same experiments (Figure 6). The SLIC signal from reaction products does not linearly correlate with the conversion and decreases in the following order of substrates used in hydrogenation: HEA > VA > VTMA > VPy.

One should not find surprising that the different substrates show a different SLIC signal. This is a result of different chemical dynamics and pairwise addition behavior in hydrogenation reactions. It is known that the interplay between the substrate and the catalyst is very important, and variations of the substrate or catalyst structure that seem insignificant at the first glance may have drastic consequences on a pairwise
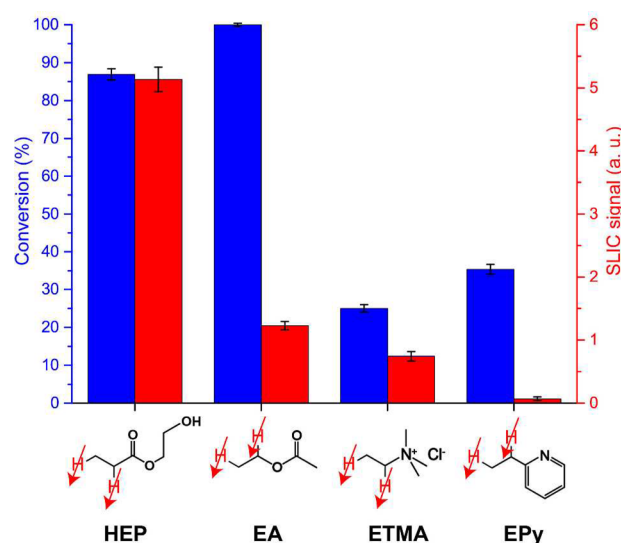
Figure 6. Hydrogenation reaction conversion and SLIC signal (normalized to the signal of the solvent) for substrates in water. Conversion was measured using high-resolution high-field ^{1}H 400 MHz NMR of aliquots before and after the reaction.

addition performance.[70] A good recent example supporting this statement is the homogeneous batch-mode hydrogenation of propylene in methanol using two Rh-based catalysts: [Rh-(COD)(dppb)]BF$_4$ and [Rh(NBD)(dppb)]BF$_4$ (where COD = 1,5-cyclooctadiene, NBD = norbornadiene, dppb = 1,4-bis(diphenylphosphino)butane).[71] Despite the fact that their structure is very similar and differ only in the structure of the ligand, PHIP effects observed for propane are 3−8 times higher when the latter catalyst is used. While discrepancy between the conversion and the SLIC signal can be treated as a disadvantage for a general applicability of the presented method for low-field monitoring of hydrogenation reactions, this observation is advantageous for probing the pairwise nature of p-H$_2$ addition (i.e., reaction selectivity) for HP NMR and MRI. This means that large libraries of compounds can be screened to identify promising candidates for PHIP HP contrast agents and for optimization of PHIP processes and hyperpolarization equipment. Moreover, since such selectivity probing does not require chemical shift dispersion (which is generally lacking at low magnetic fields), the low-field NMR modality presented here can be used to monitor the production of HP products in larger, more complex reactors operating with high pressures and temperatures; for example, the reactor used here already operated at >17 atm of gas pressure and >55 °C. We foresee that low-field NMR (and MRI) of large-scale industrial hydrogenation processes—hydrogenation of vegetable oils, hydrodesulfurization of petroleum, and other large-scale applications of hydrogenation in the industry—can become a useful spectroscopic and imaging tool.

■ CONCLUSIONS

In conclusion, we have shown that low-field NMR and low-amplitude RF irradiation termed spin-lock induced crossing can be used to detect the signal originating from HP molecules produced via hydrogenation reactions with p-H$_2$. Signal enhancement of more than 10000 allowed the build-up and decay of HP reaction products upon hydrogenation of several organic molecules (2-hydroxyethyl acrylate, vinyl acetate, 2-vinylpyridine, (vinyl)trimethylammonium chloride) to be

detected. Moreover, since the signal from ≤80 mM HP reaction products was significantly greater than the signal of thermally polarized solvents, direct proton detection was demonstrated in protonated solvents such as methanol and water, which can provide a significant potential application for molecular sensing of industrial-scale processes in the presence of large concentrations of background species. While it was shown that chemical conversion and SLIC signal are not directly correlated, this finding can be very useful for quick analysis of selectivity of hydrogen addition in catalysis and for production of HP contrast agents by PHIP technique; that is, despite the efficient overall hydrogenation, some compounds may exhibit a lower degree of p-H_2 pairwise addition. Moreover, the presented method allows for a quality assurance of the HP state of the molecules before performing experiments with more expensive isotopically enriched (e.g., ^{13}C) compounds[29,72] using polarization transfer schemes. Lastly, we showed that spin dynamics during the SLIC pulse for five-spin systems (e.g., molecules such as presented here, containing CH_3-CH_2- moiety) is much more complex than SLIC for two-spin systems. However, it is possible to adequately predict optimal detection parameters, such as B_1 amplitude, offset, and SLIC time. Low-field NMR signals are generally far less sensitive to susceptibility-induced magnetic field gradients (because these gradients scale linearly with B_0 strength), which is a useful property for studies of heterogeneous reactions (e.g., liquid/gas, liquid/solid, gas/solid) frequently practiced in industrial hydrogenation processes. Combined with greater penetration depth, which also scales inversely with B_0, low-field SLIC sensing may potentially provide a complementary analytical technology for analysis of hydrogenation reactions on a large scale.

■ ASSOCIATED CONTENT

ⓢ Supporting Information

The Supporting Information is available free of charge on the ACS Publications website at DOI: 10.1021/acs.jpcc.6b07555.

> Additional experimental details and theoretical calculations for singlet-to-magnetization conversion efficiency (PDF)
> Full simulation in animation mode for Figure S3 (GIF)
> Full simulation in animation mode for Figure S4 (GIF)

■ AUTHOR INFORMATION

Corresponding Authors

*E-mail: danila.barskiy@vanderbilt.edu. Phone: (615) 322-1329. Fax: (615) 322-0734.
*E-mail: eduard.chekmenev@vanderbilt.edu.

Notes

The authors declare no competing financial interest.

■ ACKNOWLEDGMENTS

■ REFERENCES

(1) Ernst, R. Nuclear Magnetic Resonance Fourier Transform Spectroscopy (Nobel Lecture). *Angew. Chem., Int. Ed. Engl.* **1992**, *31*, 805−823.

(2) Zalesskiy, S.; Danieli, E.; Bluemich, B.; Ananikov, V. Miniaturization of NMR Systems: Desktop Spectrometers, Microcoil Spectroscopy, and "NMR on a Chip" for Chemistry, Biochemistry, and Industry. *Chem. Rev.* **2014**, *114*, 5641−5694.

(3) Gladden, L. Magnetic Resonance in Reaction Engineering: Beyond Spectroscopy. *Curr. Opin. Chem. Eng.* **2013**, *2*, 331−337.

(4) Ardenkjaer-Larsen, J.; Boebinger, G.; Comment, A.; Duckett, S.; Edison, A.; Engelke, F.; Griesinger, C.; Griffin, R.; Hilty, C.; Maeda, H.; et al. Facing and Overcoming Sensitivity Challenges in Biomolecular NMR Spectroscopy. *Angew. Chem., Int. Ed.* **2015**, *54*, 9162−9185.

(5) Green, R.; Adams, R.; Duckett, S.; Mewis, R.; Williamson, D.; Green, G. The Theory and Practice of Hyperpolarization in Magnetic Resonance Using Parahydrogen. *Prog. Nucl. Magn. Reson. Spectrosc.* **2012**, *67*, 1−48.

(6) Ardenkjaer-Larsen, J.; Fridlund, B.; Gram, A.; Hansson, G.; Hansson, L.; Lerche, M.; Servin, R.; Thaning, M.; Golman, K. Increase in Signal-to-noise Ratio of > 10,000 Times in Liquid-state NMR. *Proc. Natl. Acad. Sci. U. S. A.* **2003**, *100*, 10158−10163.

(7) Goodson, B. Nuclear Magnetic Resonance of Laser-polarized Noble Gases in Molecules, Materials, and Organisms. *J. Magn. Reson.* **2002**, *155*, 157−216.

(8) Nikolaou, P.; Goodson, B.; Chekmenev, E. NMR Hyperpolarization Techniques for Biomedicine. *Chem. - Eur. J.* **2015**, *21*, 3156−3166.

(9) Natterer, J.; Bargon, J. Parahydrogen Induced Polarization. *Prog. Nucl. Magn. Reson. Spectrosc.* **1997**, *31*, 293−315.

(10) Kovtunov, K.; Zhivonitko, V.; Skovpin, I.; Barskiy, D.; Koptyug, I. Parahydrogen-Induced Polarization in Heterogeneous Catalytic Processes. *Top. Curr. Chem.* **2012**, *338*, 123−180.

(11) Bowers, C.; Weitekamp, D. Parahydrogen and Synthesis Allow Drammatically Enhanced Nuclear Alignment. *J. Am. Chem. Soc.* **1987**, *109*, 5541−5542.

(12) Nikolaou, P.; Coffey, A.; Barlow, M.; Rosen, M.; Goodson, B.; Chekmenev, E. Temperature-Ramped Xe-129 Spin-Exchange Optical Pumping. *Anal. Chem.* **2014**, *86*, 8206−8212.

(13) Kurhanewicz, J.; Vigneron, D.; Brindle, K.; Chekmenev, E.; Comment, A.; Cunningham, C.; DeBerardinis, R.; Green, G.; Leach, M.; Rajan, S.; et al. Analysis of Cancer Metabolism by Imaging Hyperpolarized Nuclei: Prospects for Translation to Clinical Research. *Neoplasia* **2011**, *13*, 81−97.

(14) Ardenkjaer-Larsen, J. On the Present and Future of Dissolution-DNP. *J. Magn. Reson.* **2016**, *264*, 3−12.

(15) Harzstark, A.; Weinberg, V.; Grycz, K.; Hurd, R.; Ardenkjaer-Larsen, J.; Murray, J.; Chen, A.; Ferrone, M.; Park, I.; Reed, G. A First-in-human Phase I Imaging Study Using Hyperpolarized (1)C-13 Pyruvate (H-Py) in Patients (Pts) With Localized Prostate Cancer (I-PCa). *J. Clin. Oncol.* **2012**, *30*, 4660.

(16) Nelson, S.; Kurhanewicz, J.; Vigneron, D.; Larson, P.; Harzstark, A.; Ferrone, M.; van Criekinge, M.; Chang, J.; Bok, R.; Park, I.; et al. Metabolic Imaging of Patients with Prostate Cancer Using Hyperpolarized [1-C-13]Pyruvate. *Sci. Transl. Med.* **2013**, *5*, 198ra108.

(17) Mugler, J.; Altes, T. Hyperpolarized 129Xe MRI of the Human Lung. *J. Magn. Reson. Imaging* **2013**, *37*, 313−331.

(18) Shchepin, R.; Barskiy, D.; Coffey, A.; Manzanera Esteve, I.; Chekmenev, E. Efficient Synthesis of Molecular Precursors for Para-Hydrogen-Induced Polarization of Ethyl Acetate-1−13C and Beyond. *Angew. Chem., Int. Ed.* **2016**, *55*, 6071−6074.

(19) Reineri, F.; Boi, T.; Aime, S. Parahydrogen-Induced Polarization of C-13 Carboxylate Resonance in Acetate and Pyruvate. *Nat. Commun.* **2015**, *6*, 5858.

(20) Shchepin, R.; Coffey, A.; Waddell, K.; Chekmenev, E. Parahydrogen Induced Polarization of 1-C-13-Phospholactate-d(2) for Biomedical Imaging with > 30,000,000-fold NMR Signal Enhancement in Water. *Anal. Chem.* **2014**, *86*, 5601−5605.

(21) Glöggler, S.; Grunfeld, A. M.; Ertas, Y. N.; McCormick, J.; Wagner, S.; Schleker, P. P. M.; Bouchard, L. S. A Nanoparticle Catalyst for Heterogeneous Phase Para-Hydrogen-Induced Polarization in Water. *Angew. Chem., Int. Ed.* **2015**, *54*, 2452–2456.

(22) Bhattacharya, P.; Harris, K.; Lin, A.; Mansson, M.; Norton, V. A.; Perman, W.; Weitekamp, D. P.; Ross, B. D. Ultra-fast Three Dimensional Imaging of Hyperpolarized 13C In Vivo. *MAGMA* **2005**, *18*, 245–256.

(23) Lysova, A.; Koptyug, I. Magnetic Resonance Imaging Methods for In Situ Studies in Heterogeneous Catalysis. *Chem. Soc. Rev.* **2010**, *39*, 4585–4601.

(24) Barskiy, D.; Kovtunov, K.; Koptyug, I.; He, P.; Groome, K.; Best, Q.; Shi, F.; Goodson, B.; Shchepin, R.; Truong, M.; et al. In Situ and Ex Situ Low-Field NMR Spectroscopy and MRI Endowed by SABRE Hyperpolarization. *ChemPhysChem* **2014**, *15*, 4100–4107.

(25) Ramachandran, R.; Menon, R. K. An Overview of Industrial Uses of Hydrogen. *Int. J. Hydrogen Energy* **1998**, *23*, 593–598.

(26) Blumich, B.; Casanova, F.; Appelt, S. NMR at Low Magnetic Fields. *Chem. Phys. Lett.* **2009**, *477*, 231–240.

(27) Gong, Q.; Gordji-Nejad, A.; Blumich, B.; Appelt, S. Trace Analysis by Low-Field NMR: Breaking the Sensitivity Limit. *Anal. Chem.* **2010**, *82*, 7078–7082.

(28) Gloggler, S.; Blumich, B.; Appelt, S.; Heise, H.; Matthews, S. NMR Spectroscopy for Chemical Analysis at Low Magnetic Fields. *Top. Curr. Chem.* **2011**, *335*, 1–22.

(29) Bhattacharya, P.; Chekmenev, E.; Reynolds, W.; Wagner, S.; Zacharias, N.; Chan, H.; Bunger, R.; Ross, B. Parahydrogen-Induced Polarization (PHIP) Hyperpolarized MR Receptor Imaging In Vivo: a Pilot Study of C-13 Imaging of Atheroma in Mice. *NMR Biomed.* **2011**, *24*, 1023–1028.

(30) Hovener, J.; Schwaderlapp, N.; Lickert, T.; Duckett, S.; Mewis, R.; Highton, L.; Kenny, S.; Green, G.; Leibfritz, D.; Korvink, J. A Hyperpolarized Equilibrium for Magnetic Resonance. *Nat. Commun.* **2013**, *4*, 2946.

(31) Suefke, M.; Liebisch, A.; Blumich, B.; Appelt, S. External High-quality-factor Resonator Tunes Up Nuclear Magnetic Resonance. *Nat. Phys.* **2015**, *11*, 767–771.

(32) Coffey, A.; Truong, M.; Chekmenev, E. Low-field MRI Can Be More Sensitive Than High-field MRI. *J. Magn. Reson.* **2013**, *237*, 169–174.

(33) Hovener, J.; Schwaderlapp, N.; Borowiak, R.; Lickert, T.; Duckett, S.; Mewis, R.; Adams, R.; Burns, M.; Highton, L.; Green, G.; et al. Toward Biocompatible Nuclear Hyperpolarization Using Signal Amplification by Reversible Exchange: Quantitative In Situ Spectroscopy and High-Field Imaging. *Anal. Chem.* **2014**, *86*, 1767–1774.

(34) Ruset, I.; Tsai, L.; Mair, R.; Patz, S.; Hrovat, M.; Rosen, M.; Muradian, I.; Ng, J.; Topulos, G.; Butler, J.; et al. A System for Open-access 3He Human Lung Imaging at Very Low Field. *Concepts Magn. Reson., Part B* **2006**, *29*, 210–221.

(35) Singlet and triplet spin states are eigenstates of the nuclear spin Hamiltonian for a two-spin system in the condition of a strong coupling regime (sometimes referred to as an inverse weak coupling regime). However, for multispin systems (e.g., a five-spin system studied here) versus two-spin systems, this "singlet–triplet" terminology is applicable only in qualitative terms, but it is still quite illustrative: indeed, at the magnetic field of 0.0475 T, the methyl and methylene proton spins of the studied molecular systems are strongly coupled and essentially represent a system of five almost magnetically equivalent spins. This is why we use the term "pseudo-singlet state" to describe the nuclear state of the of the $-CH_2CH_3$ system populated after molecular addition of p-H_2 to the unsaturated precursor.

(36) Olaru, A. M.; Roy, S. S.; Lloyd, L. S.; Coombes, S.; Green, G. G. R.; Duckett, S. B. Creating a Hyperpolarised Pseudo Singlet State Through Polarisation Transfer From Parahydrogen Under SABRE. *Chem. Commun.* **2016**, *52*, 7842–7845.

(37) Ratajczyk, T.; Gutmann, T.; Dillenberger, S.; Abdulhussaein, S.; Frydel, J.; Breitzke, H.; Bommerich, U.; Trantzschel, T.; Bernarding, J.; Magusin, P. C.; et al. Time Domain Parahydrogen Induced Polarization. *Solid State Nucl. Magn. Reson.* **2012**, *43*, 14–21.

(38) Kovtunov, K.; Truong, M.; Barskiy, D.; Koptyug, I.; Coffey, A.; Waddell, K.; Chekmenev, E. Long-Lived Spin States for Low-field Hyperpolarized Gas MRI. *Chem. - Eur. J.* **2014**, *20*, 14629–32.

(39) Prina, I.; Buljubasich, L.; Acosta, R. Parahydrogen Discriminated PHIP at Low Magnetic Fields. *J. Magn. Reson.* **2015**, *251*, 1–7.

(40) DeVience, S.; Walsworth, R.; Rosen, M. Preparation of Nuclear Spin Singlet States Using Spin-Lock Induced Crossing. *Phys. Rev. Lett.* **2013**, *111*, 173002.

(41) Coffey, A.; Kovtunov, K.; Barskiy, D.; Koptyug, I.; Shchepin, R.; Waddell, K.; He, P.; Groome, K.; Best, Q.; Shi, F.; et al. High-Resolution Low-Field Molecular Magnetic Resonance Imaging of Hyperpolarized Liquids. *Anal. Chem.* **2014**, *86*, 9042–9049.

(42) Coffey, A.; Shchepin, R.; Truong, M.; Wilkens, K.; Pham, W.; Chekmenev, E. An Open-Source Automated Parahydrogen Hyper-polarizer for Molecular Imaging Using 13C Metabolic Contrast Agents. *Anal. Chem.* **2016**, *88*, 8279–8288.

(43) Waddell, K.; Coffey, A.; Chekmenev, E. In Situ Detection of PHIP at 48 mT: Demonstration Using a Centrally Controlled Polarizer. *J. Am. Chem. Soc.* **2011**, *133*, 97–101.

(44) Coffey, A.; Shchepin, R.; Wilkens, K.; Waddell, K.; Chekmenev, E. A Large Volume Double Channel H-1-X RF Probe for Hyperpolarized Magnetic Resonance at 0.0475 T. *J. Magn. Reson.* **2012**, *220*, 94–101.

(45) Jiang, W.; Lumata, L.; Chen, W.; Zhang, S.; Kovacs, Z.; Sherry, A. D.; Khemtong, C. Hyperpolarized 15N-pyridine Derivatives as pH-sensitive MRI Agents. *Sci. Rep.* **2014**, *5*, 9104–9104.

(46) Kurhanewicz, J.; Vigneron, D. B.; Hricak, H.; Narayan, P.; Carroll, P.; Nelson, S. J. Three-dimensional H-1 MR Spectroscopic Imaging of the In Situ Human Prostate With High (0.24−0.7-cm3) Spatial Resolution. *Radiology* **1996**, *198*, 795–805.

(47) Gillies, R. J.; Morse, D. L. In vivo magnetic resonance spectroscopy in cancer. *Annu. Rev. Biomed. Eng.* **2005**, *7*, 287–326.

(48) Eliyahu, G.; Kreizman, T.; Degani, H. Phosphocholine as a Biomarker of Breast Cancer: Molecular and Biochemical Studies. *Int. J. Cancer* **2007**, *120*, 1721–1730.

(49) Goldman, M.; Johannesson, H.; Axelsson, O.; Karlsson, M. Design and Implementation of C-13 Hyperpolarization from Para-hydrogen, for New MRI Contrast Agents. *C. R. Chim.* **2006**, *9*, 357–363.

(50) Golman, K.; Axelsson, O.; Johannesson, H.; Mansson, S.; Olofsson, C.; Petersson, J. Parahydrogen-Induced Polarization in Imaging: Subsecond C-13 Angiography. *Magn. Reson. Med.* **2001**, *46*, 1–5.

(51) Truong, M.; Shi, F.; He, P.; Yuan, B.; Plunkett, K.; Coffey, A.; Shchepin, R.; Barskiy, D.; Kovtunov, K.; Koptyug, I.; et al. Irreversible Catalyst Activation Enables Hyperpolarization and Water Solubility for NMR Signal Amplification by Reversible Exchange. *J. Phys. Chem. B* **2014**, *118*, 13882–13889.

(52) Levitt, M. *Spin Dynamics: Basics of Nuclear Magnetic Resonance*; John Wiley & Sons, 2001.

(53) Bowers, C.; Weitekamp, D. Transformation of Symmetrization Order to Nuclear Spin Magnetization by Chemical Reaction and Nuclear Magnetic Resonance. *Phys. Rev. Lett.* **1986**, *57*, 2645–2648.

(54) Eisenschmid, T.; Kirss, R.; Deutsch, P.; Hommeltoft, S.; Eisenberg, R.; Bargon, J.; Lawler, R.; Balch, A. Parahydrogen Induced Polarization in Hydrogenation Reactions. *J. Am. Chem. Soc.* **1987**, *109*, 8089–8091.

(55) Appelt, S.; Hasing, F.; Sieling, U.; Gordji-Nejad, A.; Gloggler, S.; Blumich, B. Paths from Weak to Strong Coupling in NMR. *Phys. Rev. A: At., Mol., Opt. Phys.* **2010**, *81*, 023420.

(56) Colell, J.; Turschmann, P.; Gloggler, S.; Schleker, P.; Theis, T.; Ledbetter, M.; Budker, D.; Pines, A.; Blumich, B.; Appelt, S. Fundamental Aspects of Parahydrogen Enhanced Low-Field Nuclear Magnetic Resonance. *Phys. Rev. Lett.* **2013**, *110*, 137602.

(57) Turschmann, P.; Colell, J.; Theis, T.; Blumich, B.; Appelt, S. Analysis of Parahydrogen Polarized Spin System in Low Magnetic Fields. *Phys. Chem. Chem. Phys.* **2014**, *16*, 15411–15421.

(58) Bernarding, J.; Buntkowsky, G.; Macholl, S.; Hartwig, S.; Burghoff, M.; Trahms, L. J-coupling Nuclear Magnetic Resonance Spectroscopy of Liquids in nT Fields. *J. Am. Chem. Soc.* **2006**, *128*, 714−715.

(59) DeVience, S.; Walsworth, R.; Rosen, M. Probing Scalar Coupling Differences via Long-Lived Singlet States. *J. Magn. Reson.* **2016**, *262*, 42−49.

(60) Kovtunov, K.; Barskiy, D.; Shchepin, R.; Coffey, A.; Waddell, K.; Koptyug, I.; Chekmenev, E. Demonstration of Heterogeneous Parahydrogen Induced Polarization Using Hyperpolarized Agent Migration from Dissolved Rh(I) Complex to Gas Phase. *Anal. Chem.* **2014**, *86*, 6192−6.

(61) Tayler, M.; Levitt, M. Singlet Nuclear Magnetic Resonance of Nearly-Equivalent Spins. *Phys. Chem. Chem. Phys.* **2011**, *13*, 5556−60.

(62) Levitt, M. Singlet Nuclear Magnetic Resonance. *Annu. Rev. Phys. Chem.* **2012**, *63*, 89−105.

(63) Vinogradov, E.; Grant, A. K. Long-Lived States in Solution NMR: Selection Rules for Intramolecular Dipolar Relaxation in Low Magnetic Fields. *J. Magn. Reson.* **2007**, *188*, 176−182.

(64) Stevanato, G.; Roy, S. S.; Hill-Cousins, J.; Kuprov, I.; Brown, L. J.; Brown, R. C.; Pileio, G.; Levitt, M. H. Long-Lived Nuclear Spin States Far from Magnetic Equivalence. *Phys. Chem. Chem. Phys.* **2015**, *17*, 5913−5922.

(65) Kovtunov, K.; Truong, M.; Barskiy, D.; Salnikov, O.; Bukhtiyarov, V.; Coffey, A.; Waddell, K.; Koptyug, I.; Chekmenev, E. Propane-d(6) Heterogeneously Hyperpolarized by Parahydrogen. *J. Phys. Chem. C* **2014**, *118*, 28234−28243.

(66) Zhang, Y.; Duan, X.; Soon, P. C.; Sychrovský, V.; Canary, J. W.; Jerschow, A. Limits in Proton Nuclear Singlet-State Lifetimes Measured with Para-Hydrogen-Induced Polarization. *ChemPhysChem* **2016**, *17*, 2967.

(67) Levitt, M. Symmetry Constraints on Spin Dynamics: Application to Hyperpolarized NMR. *J. Magn. Reson.* **2016**, *262*, 91−99.

(68) Theis, T.; Feng, Y.; Wu, T.-l.; Warren, W. S. Composite and Shaped Pulses for Efficient and Robust Pumping of Disconnected Eigenstates in Magnetic Resonance. *J. Chem. Phys.* **2014**, *140*, 014201.

(69) Pravdivtsev, A. N.; Kiryutin, A. S.; Yurkovskaya, A. V.; Vieth, H.-M.; Ivanov, K. L. Robust Conversion of Singlet Spin Order in Coupled Spin-1/2 Pairs by Adiabatically Switched RF-fields. *arXiv:1607.00539* **2016**.

(70) Reineri, F.; Aime, S.; Gobetto, R.; Nervi, C. Role of the Reaction Intermediates in Determining PHIP (Parahydrogen Induced Polarization) Effect in the Hydrogenation of Acetylene Dicarboxylic Acid With the Complex [Rh(dppb)](+) (dppb: 1,4-bis-(diphenylphosphino)butane. *J. Chem. Phys.* **2014**, *140*, 094307.

(71) Salnikov, O. G.; Barskiy, D. A.; Coffey, A. M.; Kovtunov, K. V.; Koptyug, I. V.; Chekmenev, E. Y. Efficient Batch-Mode Parahydrogen-Induced Polarization of Propane. *ChemPhysChem* **2016**, DOI: 10.1002/cphc.201600564.

(72) Bhattacharya, P.; Chekmenev, E.; Perman, W.; Harris, K.; Lin, A.; Norton, V.; Tan, C.; Ross, B.; Weitekamp, D. Towards Hyperpolarized C-13-succinate Imaging of Brain Cancer. *J. Magn. Reson.* **2007**, *186*, 150−155.

NMR Spectroscopy

Production of Pure Aqueous ^{13}C-Hyperpolarized Acetate by Heterogeneous Parahydrogen-Induced Polarization

Kirill V. Kovtunov,*[a, b] Danila A. Barskiy,[c] Roman V. Shchepin,[c] Oleg G. Salnikov,[a, b] Igor P. Prosvirin,[b, d] Andrey V. Bukhtiyarov,[b, d] Larisa M. Kovtunova,[b, d] Valerii I. Bukhtiyarov,[b, d] Igor V. Koptyug,*[a, b] and Eduard Y. Chekmenev*[c, e]

Abstract: A supported metal catalyst was designed, characterized, and tested for aqueous phase heterogeneous hydrogenation of vinyl acetate with parahydrogen to produce ^{13}C-hyperpolarized ethyl acetate for potential biomedical applications. The Rh/TiO$_2$ catalyst with a metal loading of 23.2 wt% produced strongly hyperpolarized ^{13}C-enriched ethyl acetate-1-^{13}C detected at 9.4 T. An approximately 14-fold ^{13}C signal enhancement was detected using circa 50% parahydrogen gas without taking into account relaxation losses before and after polarization transfer by magnetic field cycling from nascent parahydrogen-derived protons to ^{13}C nuclei. This first observation of ^{13}C PHIP-hyperpolarized products over a supported metal catalyst in an aqueous medium opens up new possibilities for production of catalyst-free aqueous solutions of nontoxic hyperpolarized contrast agents for a wide range of biomolecules amenable to the parahydrogen induced polarization by side arm hydrogenation (PHIP-SAH) approach.

The methods based on magnetic resonance (NMR, MRI) are routinely used as sensitive analytical tools in chemistry and medicine. However, despite their impressive achievements, a potentially wider reach of these techniques is limited by their inherently limited sensitivity associated with the low nuclear spin polarization at thermal equilibrium. The advent of hyperpolarization NMR techniques significantly expands the range of potentially feasible MR applications.[1–9] One of these hyperpolarization techniques is dynamic nuclear polarization (DNP), which allows the hyperpolarization of a wide range of ^{13}C-labeled compounds[10,11] and their use for metabolic NMR/

MRI.[12–14] However, the main limitations of the DNP technique are: 1) a long hyperpolarization time and 2) the high cost of the hyperpolarizer. Parahydrogen-induced polarization (PHIP) is an alternative hyperpolarization technique using singlet spin order of parahydrogen.[15–17] Pairwise addition of parahydrogen (p-H$_2$), that is, addition of the two H atoms from one p-H$_2$ molecule to magnetically nonequivalent positions of a substrate molecule, creates hyperpolarization on the nascent protons in the product molecule. Importantly, the polarization transfer from nascent parahydrogen atoms through spin–spin couplings to heteronuclei (for example, to ^{13}C) results in hyperpolarized (HP) contrast agents with sufficiently long lifetimes for biomedical applications.[18–20]

PHIP allows the production of HP liquids that can be directly used for signal enhancement in various NMR/MRI applications.[18,20] Despite the relative complexity of the synthesis of ^{13}C-labeled PHIP precursor compounds, many successful examples with high polarization levels on ^{13}C nuclei ($P_{13C} > 10\%$) in biomolecules have been reported: ^{13}C-succinate,[21] ^{13}C-tetrafluoropropionate,[22] and more recently ^{13}C-phospholactate.[23] While the corresponding pioneering in vivo studies are encouraging,[22,24,25] they were performed using injections of a liquid HP contrast agent containing a homogeneous Rh-based catalyst,[26] which is potentially toxic and thus a definite roadblock for eventual application in humans. Two alternative approaches can potentially address this obstacle: 1) catalyst removal by filtration/extraction or 2) utilization of a heterogeneous catalyst for pairwise p-H$_2$ addition (HET-PHIP).[9,27–29] The second approach is more advantageous because it additionally allows catalyst recycling.

Importantly, the PHIP medium must be biocompatible, that is, aqueous. The first observation of heterogeneous PHIP effects in an aqueous medium was reported in 2010,[30] utilizing

[a] Dr. K. V. Kovtunov, O. G. Salnikov, Prof. I. V. Koptyug
Laboratory of Magnetic Resonance Microimaging
International Tomography Center, SB RAS
3A Institutskaya St., Novosibirsk 630090 (Russia)
E-mail: kovtunov@tomo.nsc.ru
koptyug@tomo.nsc.ru

[b] Dr. K. V. Kovtunov, O. G. Salnikov, Dr. I. P. Prosvirin, Dr. A. V. Bukhtiyarov,
Dr. L. M. Kovtunova, Prof. V. I. Bukhtiyarov, Prof. I. V. Koptyug
Novosibirsk State University
2 Pirogova St., Novosibirsk 630090 (Russia)

[c] Dr. D. A. Barskiy, Dr. R. V. Shchepin, Prof. E. Y. Chekmenev
Department of Radiology, Department of Biomedical Engineering
Department of Physics and Astronomy

Vanderbilt University Institute of Imaging Science (VUIIS)
Nashville, Tennessee, 37232-2310 (USA)
E-mail: eduard.chekmenev@vanderbilt.edu

[d] Dr. I. P. Prosvirin, Dr. A. V. Bukhtiyarov, Dr. L. M. Kovtunova,
Prof. V. I. Bukhtiyarov
Boreskov Institute of Catalysis SB RAS
5 Acad. Lavrentiev Pr., Novosibirsk 630090 (Russia)

[e] Prof. E. Y. Chekmenev
Russian Academy of Sciences
Leninskiy Prospekt 14, 119991 Moscow (Russia)

Supporting information for this article and ORCIDs for the author(s) are available on the WWW under: http://dx.doi.org/10.1002/chem.201603974.

supported metal catalysts. Recently, a similar observation (indicating the possibility of heterogeneous PHIP formation in water) was made using ligand-capped platinum nanoparticles.[31,32] Although the transfer of polarization from nascent parahydrogen protons to ^{13}C nuclei was accomplished at $P_{13C} = 0.013\%$,[31] subsequent applications of this system face serious challenges, because 1) separation of HP solution from 2-nm-sized nanoparticles is required, 2) very low conversion levels were achieved (ca. 0.03% after 15 s of reaction),[31] and 3) the reaction product 2-hydroxyethyl propionate (HEP) has no biomedical relevance beyond angiographic applications.[18]

Recently, an efficient procedure of polarization transfer from nascent parahydrogen protons to ^{13}C using the side arm hydrogenation (SAH) approach in combination with adiabatic magnetic field cycling was introduced. It was exemplified with a range of esters bearing an unsaturated alcoholic or carboxylic moiety, including vinyl acetate, which yielded HP ethyl acetate-1-^{13}C upon hydrogenation and magnetic field cycling.[33,34] However, these previous studies employed a homogeneous catalyst in an organic medium, which is incompatible with the long-term goal of in-human application of PHIP-SAH, which otherwise paves a straightforward and scalable route to efficient ^{13}C hyperpolarization of many biomolecules including ^{13}C-pyruvate.[33–35] Moreover, recent results based on the vinyl acetate heterogeneous hydrogenation in the gas phase with subsequent dissolution in aqueous phases and hydrolysis resulting in the production of a mixture of hyperpolarized ethane and thermally polarized acetic acid allow the generation of pure, biocompatible, and catalyst-free hyperpolarized fluid.[36]

In this work, we demonstrate that both previous shortcomings of PHIP-SAH can be resolved. Specifically, 2–3 mm beads of TiO_2 with supported rhodium nanoparticles were utilized for the aqueous phase heterogeneous hydrogenation of vinyl acetate-1-^{13}C with p-H_2, followed by polarization transfer to ^{13}C nuclei by means of magnetic field cycling.[33–35]

Recently, it was shown that decreasing the size of metal nanoparticles leads to an increase in the pairwise p-H_2 addition level;[9,37] therefore, the catalyst under investigation should have the smallest metal nanoparticles possible. However, large amounts of metal introduced upon impregnation of a porous support often lead to larger particle sizes, which are disadvantageous in terms of PHIP efficiency. Therefore, in the preparation of the 23.2 wt% Rh/TiO_2 catalyst, an aqueous rhodium nitrate solution was used to obtain relatively small metal particles even at the high rhodium loading. Rh was chosen as an active component because it usually provides the highest PHIP signal enhancements compared with other metals.[38] The catalyst was characterized in detail by transmission electron microscopy (TEM) and X-ray photoelectron spectroscopy (XPS) (Figure 1 and the Supporting Information, Figure S2). The average particle size of the 23.2 wt% Rh/TiO_2 catalyst was estimated from TEM data as circa 3 nm, which is favorable for the observation of PHIP effects.[39] Therefore, this catalyst was used for heterogeneous hydrogenation of vinyl acetate in an aqueous medium with subsequent polarization transfer from para-
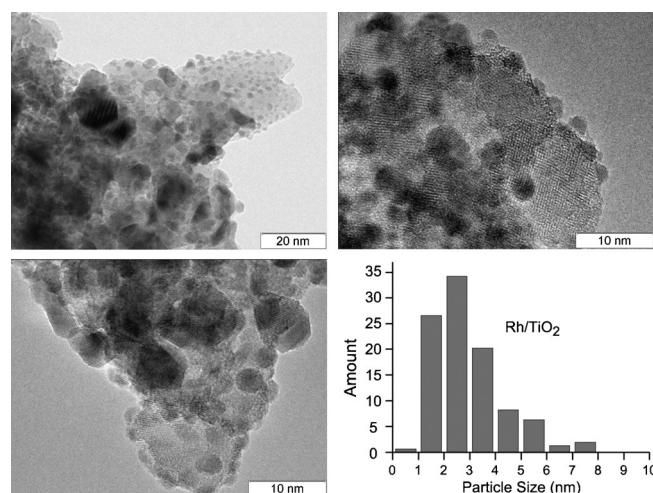
Figure 1. TEM images and metal particle size distribution for the 23.2 wt% Rh/TiO_2 catalyst obtained by wet impregnation from an aqueous rhodium nitrate solution. The average size of metal particles is ca. 3 nm.
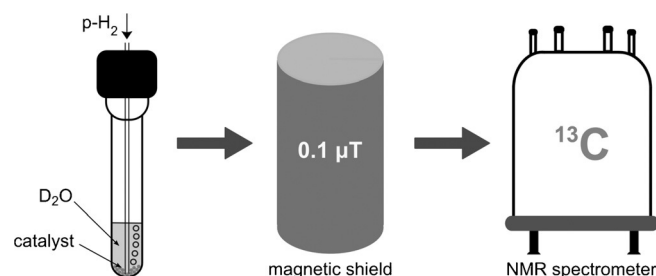
Figure 2. Experimental procedure for ^{13}C hyperpolarization and detection by NMR spectroscopy through PHIP-SAH and magnetic field cycling.

hydrogen-derived protons to ^{13}C nuclei and detection by ^{13}C NMR spectroscopy (Figure 2,3).

The catalyst's activity for vinyl acetate hydrogenation is expected to be lower in the aqueous medium (compared with that previously shown in organic solvents[40]), and the increase in the total available metal active centers by using 23.2 wt% Rh/TiO_2 catalyst was intended to compensate for this activity loss. Indeed, 20 s of hydrogen bubbling in our setup (ca. 0.5 mL of 0.08 M vinyl acetate-1-^{13}C solution, ca. 7.1 atm p-H_2 pressure at 150 standard cubic centimeters per minute (sccm) flow rate) was sufficient to reach a greater than 90% conversion of vinyl acetate to the reaction products (Figure 3 and the Supporting Information, Figure S3). An approximately 14-fold ^{13}C signal enhancement was observed under these conditions (see Figure 3).

Importantly, the hyperpolarized ^{13}C NMR signal was detected both when hydrogenation was carried out directly inside the magnetic shield and when the NMR tube with the hydrogenation products was briefly placed in the shield after the termination of the hydrogen bubbling. The latter approach generally resulted in greater ^{13}C polarization values. The size of the catalyst beads and the Rh loading can be potentially further optimized to maximize chemical conversion efficiency and the
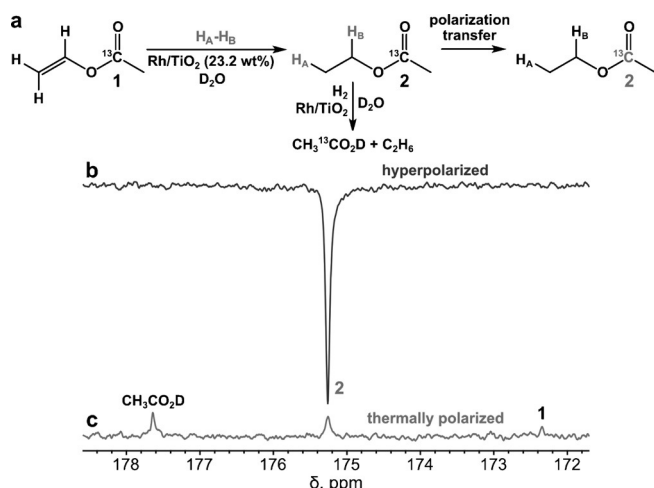
Figure 3. a) Scheme of vinyl acetate-1-^{13}C heterogeneous hydrogenation with parahydrogen (p-H$_2$) over 23.2 wt% Rh/TiO$_2$ catalyst in a D$_2$O solution with subsequent polarization transfer from protons to ^{13}C nuclei, b) ^{13}C NMR spectrum of HP ethyl acetate-1-^{13}C, and c) corresponding ^{13}C spectrum of thermally polarized sample after waiting for a time period longer than $5 \times T_1$. All spectra were acquired with one signal scan. NMR tube with the hydrogenation products was placed in a magnetic shield after termination of hydrogen bubbling. The ^{13}C signal enhancement (ε_{13C}) is ca. 14-fold and %P_{13C} is ca. 0.011%.

degree of pairwise addition, that is, to maximize the overall yield of ^{13}C hyperpolarization.

Figure 3 also shows that for the polarization transfer only the ^{13}C NMR signal from hyperpolarized ethyl acetate can be detected. However, in the ^{13}C NMR spectrum of the thermally polarized reaction products (Figure 3 c), the equilibrium signals of ^{13}C-labeled unreacted vinyl acetate, ethyl acetate, and acetic acid can be seen. Therefore, the formation of acetic acid by hydrogenolysis of ethyl acetate or by direct hydrogenation of vinyl acetate can be easily verified by ^{13}C NMR spectroscopy. Along with the acetic acid, ethane formed as a byproduct of the vinyl acetate heterogeneous hydrogenation with an estimated concentration of approximately 4 mM over the supported rhodium catalyst, and the corresponding ^{1}H NMR spectra before and after reaction are shown in the Supporting Information Figure S3.

It should also be emphasized that the circa 14-fold enhancement of the HET-PHIP ^{13}C signal (ε_{13C}) achieved here is a factor of circa 130 lower than that obtained under similar conditions using a homogeneous Rh catalyst in [D$_4$]MeOH.[35] However, the hydrogenation duration was 20 s in this study compared with 10 s in the previous report,[35] and additional T_1 relaxation losses have contributed to the lower ε_{13C} observed here (^{13}C T_1 of carboxyl ^{13}C sites is generally on the order of 30–60 s in vitro[21,22,33–35] and in vivo,[10,41] and T_1 of protons at low magnetic fields is generally on the order of 5–10 s[42,43]). It is likely that optimization of the catalyst structure and reaction conditions could lead to major improvements for the presented approach.

The stability of the catalyst under reactive conditions is also important, and XPS investigations of the catalyst before and after the reaction were carried out (see the Supporting Infor-

mation for details). It was successfully confirmed that the catalyst did not undergo any changes after the reaction and Rh nanoparticles are present at the surface of titania only in the metallic state (Supporting Information, Figure S2).

Glöggler et al.[31] utilized circa 2 nm beads that will likely be challenging to separate rapidly. In contrast, the 2–3 mm catalytically active beads used here can be easily separated, for example, by simple decantation of the hyperpolarized aqueous solution from the catalyst. For instance, the Supporting Information Figure S4 b shows that even during hydrogenation, the beads reside at the bottom of the NMR tube. Alternatively, if the average diameter of the beads is decreased to 0.1 mm, the catalyst suspension (Supporting Information, Figure S4 a) can be potentially filtered.

The ability to produce hyperpolarized compounds in water using solid catalysts opens up new possibilities for the production of catalyst-free aqueous solutions of nontoxic hyperpolarized contrast agents. Furthermore, polarization transfer from parahydrogen-derived protons to heteronuclei by magnetic field cycling increases the lifetime of hyperpolarization of the produced compounds and minimizes the signal background. All these factors are of paramount importance for in vivo applications.[18] Therefore, the first observation of ^{13}C hyperpolarized molecules formed by heterogeneous hydrogenation of vinyl acetate with p-H$_2$ over supported rhodium nanoparticles is a major step forward to biomedical applications of the HET-PHIP approach, and HET-PHIP-SAH in particular, because the latter can be used to hyperpolarize a wide range of biomolecules.[33–35]

In conclusion, we have presented a new approach to produce catalyst-free aqueous solutions of a biomolecule carrying ^{13}C hyperpolarization. The approach is based on the heterogeneous side arm hydrogenation (SAH) of a suitable precursor molecule with p-H$_2$ over supported metal catalysts with subsequent or simultaneous polarization transfer from parahydrogen-derived protons to ^{13}C nuclei by magnetic field cycling. The achieved circa 90% conversion in the heterogeneous hydrogenation reaction in water, which is comparable to the conversion achieved by homogenous PHIP hyperpolarization[23] for in vivo ^{13}C imaging,[24] can be further increased by increasing p-H$_2$ pressure and flow rate and the amount of catalytically active sites on the catalyst surface. We believe that combination of aqueous phase heterogeneous catalysis by supported metals with HET-PHIP-SAH and the polarization transfer approach offers a powerful tool for the production of hyperpolarized biocompatible contrast agents for MRI because the demonstrated method is scalable and does not require complex instrumentation.

Experimental Section

For the liquid phase heterogeneous hydrogenation 23.2 wt% Rh/TiO$_2$ solid catalyst was placed at the bottom of a 5 mm high-pressure medium-wall NMR tube, which was then filled with the solution of ^{13}C-labeled vinyl acetate in D$_2$O. Subsequently, the NMR tube was pressurized to ca. 7.1 atm of p-H$_2$ and heated to 90°C, and then p-H$_2$ was bubbled through the solution for 20 s at 150

sccm. The samples were not degassed before reaction and hyper-polarization process. As soon as bubbling was stopped, the NMR tube was transferred from the Earth's magnetic field to the very low magnetic field (ca. 0.1 μT) inside the magnetic shield and then adiabatically transferred to the 9.4 T high field of the NMR spectrometer, where ^{13}C NMR spectra were acquired (Figures 2,3). The detailed experimental setup is presented in the Supporting Information, Figure S1. The procedures for catalyst preparation, hydrogenation, and XPS experiments, and additional NMR spectra are given in the Supporting Information.

[1] P. Nikolaou, B. M. Goodson, E. Y. Chekmenev, *Chem. Eur. J.* **2015**, *21*, 3156–3166.

[2] J.-H. Ardenkjaer-Larsen, G. S. Boebinger, A. Comment, S. Duckett, A. S. Edison, F. Engelke, C. Griesinger, R. G. Griffin, C. Hilty, H. Maeda, *Angew. Chem. Int. Ed.* **2015**, *54*, 9162–9185; *Angew. Chem.* **2015**, *127*, 9292–9317.

[3] J. H. Ardenkjaer-Larsen, *J. Magn. Reson.* **2016**, *264*, 3–12.

[4] A. Comment, *J. Magn. Reson.* **2016**, *264*, 39–48.

[5] A. Comment, M. E. Merritt, *Biochemistry* **2014**, *53*, 7333–7357.

[6] K. M. Brindle, *J. Am. Chem. Soc.* **2015**, *137*, 6418–6427.

[7] B. M. Goodson, *J. Magn. Reson.* **2002**, *155*, 157–216.

[8] R. A. Green, R. W. Adams, S. B. Duckett, R. E. Mewis, D. C. Williamson, G. G. R. Green, *Prog. Nucl. Magn. Reson. Spectrosc.* **2012**, *67*, 1–48.

[9] K. V. Kovtunov, V. V. Zhivonitko, I. V. Skovpin, D. A. Barskiy, I. V. Koptyug, *Top. Curr. Chem.* **2012**, *338*, 123–180.

[10] J. H. Ardenkjaer-Larsen, B. Fridlund, A. Gram, G. Hansson, L. Hansson, M. H. Lerche, R. Servin, M. Thaning, K. Golman, *Proc. Natl. Acad. Sci. USA* **2003**, *100*, 10158–10163.

[11] J. Kurhanewicz, D. B. Vigneron, K. Brindle, E. Y. Chekmenev, A. Comment, C. H. Cunningham, R. J. DeBerardinis, G. G. Green, M. O. Leach, S. S. Rajan, R. R. Rizi, B. D. Ross, W. S. Warren, C. R. Malloy, *Neoplasia* **2011**, *13*, 81–97.

[12] K. M. Brindle, S. E. Bohndiek, F. A. Gallagher, M. I. Kettunen, *Magn. Reson. Med.* **2011**, *66*, 505–519.

[13] K. Brindle, *Nat. Rev. Cancer* **2008**, *8*, 94–107.

[14] K. Golman, R. in't Zandt, M. Thaning, *Proc. Natl. Acad. Sci. USA* **2006**, *103*, 11270–11275.

[15] C. R. Bowers, D. P. Weitekamp, *J. Am. Chem. Soc.* **1987**, *109*, 5541–5542.

[16] T. C. Eisenschmid, R. U. Kirss, P. P. Deutsch, S. I. Hommeltoft, R. Eisenberg, J. Bargon, R. G. Lawler, A. L. Balch, *J. Am. Chem. Soc.* **1987**, *109*, 8089–8091.

[17] M. G. Pravica, D. P. Weitekamp, *Chem. Phys. Lett.* **1988**, *145*, 255–258.

[18] K. Golman, O. Axelsson, H. Jóhannesson, S. Månsson, C. Olofsson, J. S. Petersson, *Magn. Reson. Med.* **2001**, *46*, 1–5.

[19] J.-B. Hövener, E. Y. Chekmenev, K. C. Harris, W. H. Perman, T. T. Tran, B. D. Ross, P. Bhattacharya, *Magn. Reson. Mater. Phys. Biol. Med.* **2009**, *22*, 123–134.

[20] M. Goldman, H. Jóhannesson, O. Axelsson, M. Karlsson, *C. R. Chim.* **2006**, *9*, 357–363.

[21] E. Y. Chekmenev, J. Hövener, V. A. Norton, K. Harris, L. S. Batchelder, P. Bhattacharya, B. D. Ross, D. P. Weitekamp, *J. Am. Chem. Soc.* **2008**, *130*, 4212–4213.

[22] P. Bhattacharya, E. Y. Chekmenev, W. F. Reynolds, S. Wagner, N. Zacharias, H. R. Chan, R. Bünger, B. D. Ross, *NMR Biomed.* **2011**, *24*, 1023–1028.

[23] R. V. Shchepin, A. M. Coffey, K. W. Waddell, E. Y. Chekmenev, *Anal. Chem.* **2014**, *86*, 5601–5605.

[24] A. M. Coffey, R. V. Shchepin, M. L. Truong, K. Wilkens, W. Pham, E. Y. Chekmenev, *Anal. Chem.* **2016**, *88*, 8279–8288.

[25] N. M. Zacharias, H. R. Chan, N. Sailasuta, B. D. Ross, P. Bhattacharya, *J. Am. Chem. Soc.* **2012**, *134*, 934–943.

[26] P. Bhattacharya, K. Harris, A. P. Lin, M. Mansson, V. A. Norton, W. H. Perman, D. P. Weitekamp, B. D. Ross, *Magn. Reson. Mater. Phys. Biol. Med.* **2005**, *18*, 245–256.

[27] K. V. Kovtunov, I. E. Beck, V. I. Bukhtiyarov, I. V. Koptyug, *Angew. Chem. Int. Ed.* **2008**, *47*, 1492–1495; *Angew. Chem.* **2008**, *120*, 1514–1517.

[28] A. M. Balu, S. B. Duckett, R. Luque, *Dalton Trans.* **2009**, 5074–5076.

[29] M. Irfan, N. Eshuis, P. Spannring, M. Tessari, M. C. Feiters, F. P. J. T. Rutjes, *J. Phys. Chem. C* **2014**, *118*, 13313–13319.

[30] I. V. Koptyug, V. V. Zhivonitko, K. V. Kovtunov, *ChemPhysChem* **2010**, *11*, 3086–3088.

[31] S. Glöggler, A. M. Grunfeld, Y. N. Ertas, J. Mccormick, S. Wagner, P. P. M. Schleker, L.-S. Bouchard, *Angew. Chem. Int. Ed.* **2015**, *54*, 2452–2456; *Angew. Chem.* **2015**, *127*, 2482–2486.

[32] S. Glöggler, A. M. Grunfeld, Y. N. Ertas, J. McCormick, S. Wagner, L.-S. Bouchard, *Chem. Commun.* **2016**, *52*, 605–608.

[33] F. Reineri, T. Boi, S. Aime, *Nat. Commun.* **2015**, *6*, 5858.

[34] E. Cavallari, C. Carrera, T. Boi, S. Aime, F. Reineri, *J. Phys. Chem. B* **2015**, *119*, 10035–10041.

[35] R. V. Shchepin, D. A. Barskiy, A. M. Coffey, I. V. Manzanera Esteve, E. Y. Chekmenev, *Angew. Chem. Int. Ed.* **2016**, *55*, 6071–6074; *Angew. Chem.* **2016**, *128*, 6175–6178.

[36] O. G. Salnikov, K. V. Kovtunov, I. V. Koptyug, *Sci. Rep.* **2015**, *5*, 13930.

[37] A. Corma, O. G. Salnikov, D. A. Barskiy, K. V. Kovtunov, I. V. Koptyug, *Chem. Eur. J.* **2015**, *21*, 7012–7015.

[38] K. V. Kovtunov, D. A. Barskiy, A. M. Coffey, M. L. Truong, O. G. Salnikov, A. K. Khudorozhkov, E. A. Inozemtseva, I. P. Prosvirin, V. I. Bukhtiyarov, K. W. Waddell, *Chem. Eur. J.* **2014**, *20*, 11636–11639.

[39] V. P. Ananikov, L. L. Khemchyan, Y. V. Ivanova, V. I. Bukhtiyarov, A. M. Sorokin, I. P. Prosvirin, S. Z. Vatsadze, A. V. Medved'ko, V. N. Nuriev, A. D. Dilman, *Russ. Chem. Rev.* **2014**, *83*, 885–985.

[40] K. V. Kovtunov, D. A. Barskiy, O. G. Salnikov, R. V. Shchepin, A. M. Coffey, L. M. Kovtunova, V. I. Bukhtiyarov, I. V. Koptyug, E. Y. Chekmenev, *RSC Adv.* **2016**, *6*, 69728–69732.

[41] R. E. Hurd, Y.-F. Yen, D. Mayer, A. Chen, D. Wilson, S. Kohler, R. Bok, D. Vigneron, J. Kurhanewicz, J. Tropp, D. Spielman, A. Pfefferbaum, *Magn. Reson. Med.* **2010**, *63*, 1137–1143.

[42] R. V. Shchepin, A. M. Coffey, K. W. Waddell, E. Y. Chekmenev, *J. Phys. Chem. Lett.* **2012**, *3*, 3281–3285.

[43] D. A. Barskiy, K. V. Kovtunov, I. V. Koptyug, P. He, K. A. Groome, Q. A. Best, F. Shi, B. M. Goodson, R. V. Shchepin, M. L. Truong, A. M. Coffey, K. W. Waddell, E. Y. Chekmenev, *ChemPhysChem* **2014**, *15*, 4100–4107.

2D Mapping of NMR Signal Enhancement and Relaxation for Heterogeneously Hyperpolarized Propane Gas

Danila A. Barskiy,[†] Kirill V. Kovtunov,*[,‡,§] Evgeny Y. Gerasimov,[§,||] M. Anthony Phipps,[†] Oleg G. Salnikov,[‡,§] Aaron M. Coffey,[†] Larisa M. Kovtunova,[§,||] Igor P. Prosvirin,[§,||] Valerii I. Bukhtiyarov,[§,||] Igor V. Koptyug,[‡,§] and Eduard Y. Chekmenev*[,†,⊥,#]

[†]Vanderbilt University Institute of Imaging Science (VUIIS), Department of Radiology, Vanderbilt University Medical Center, Nashville, Tennessee 37232, United States
[‡]International Tomography Center SB RAS, Novosibirsk 630090, Russia
[§]Novosibirsk State University, Novosibirsk 630090, Russia
[||]Boreskov Institute of Catalysis SB RAS, Novosibirsk 630090, Russia
[⊥]Department of Biomedical Engineering, Department of Physics, Vanderbilt-Ingram Cancer Center (VICC), Nashville, Tennessee 37232, United States
[#]Russian Academy of Sciences, 19991 Moscow, Russia

S Supporting Information

ABSTRACT: Hyperpolarized (HP) propane is a promising contrast agent for magnetic resonance imaging (MRI) of lungs and for studying porous media. The parahydrogen-induced polarization (PHIP) technique is a convenient approach to produce pure propane gas with enhanced proton polarization, when hydrogenation of propylene with parahydrogen is performed over heterogeneous catalysts. Here, we present a new approach of multidimensional mapping of the efficiency of pairwise parahydrogen addition using PHIP-echo pulse sequence. We use this approach to study the performance of three model heterogeneous Rh/TiO$_2$ catalysts in the production of HP propane gas. The three catalysts with 1.0, 13.7, and 23.2 wt % of supported rhodium nanoparticles have been characterized by X-ray photoelectron spectroscopy (XPS) and high resolution transition electron microscopy (HRTEM). By varying the fractions of parahydrogen and propylene in the reactant mixture as well as the gas mixture pressure, 2D maps of PHIP-echo NMR signal and 2D maps of HP propane NMR signal enhancement were obtained. These maps clearly indicate that lower metal coverage results in more efficient pairwise hydrogen addition, producing greater levels of proton polarization of propane gas. The presented method can be extended to multidimensional characterization of the influence of other key parameters of PHIP reaction process including temperature or addition of an inert carrier gas. A 2D T_1 relaxation map of propane at 9.4 T is also reported as a function of propane fraction (in the mixture with hydrogen) and gas mixture pressure.
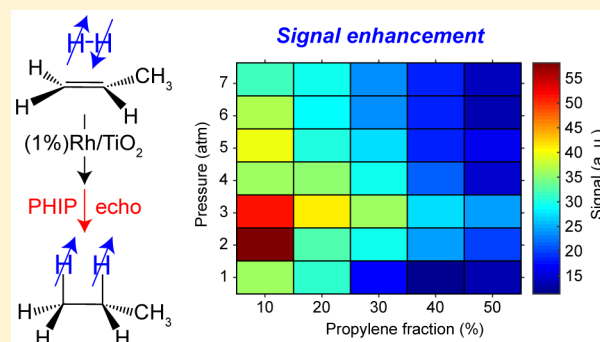
INTRODUCTION

Hyperpolarization techniques are revolutionizing the field of nuclear magnetic resonance (NMR) spectroscopy and magnetic resonance imaging (MRI) because they allow significant increase of nuclear spin polarization by several orders of magnitude.[1−3] This immense polarization gain renders concomitant gains in the NMR/MRI detection sensitivity by 4−8 orders of magnitude[4−6] depending on the static magnetic field of the detector, thus enabling new applications in various fields including biomedicine. Biomedical applications of hyperpolarization are the main driving forces for the fundamental and applied scientific development of hyperpolarization methods.[1,7−11] Hyperpolarized (HP) compounds are prepared exogenously, and once administered in

vivo (via intravenous injection or inhalation), they act as contrast agents for probing metabolism and organ function. Historically, hyperpolarization of noble gases (i.e., ^{129}Xe and ^{3}He)[3,12,13] has been developed first, and they have been readily applied for functional pulmonary imaging.[2,14−17] Numerous clinical trials have been completed and are ongoing or pending.[18]

The vast majority of HP contrast agents incorporate HP heteronuclei (e.g., ^{13}C, ^{129}Xe, etc.), which typically have significantly longer spin−lattice relaxation times T_1 compared

to those of proton sites. This allows increasing the lifetime of HP contrast agents to tens of seconds or minutes. However, despite the significant progress in the HP MRI field, it faces one critical translational challenge; that is, conventional clinical MRI scanners do not have heteronuclear detection capability and cannot be easily upgraded. The relatively recent advent of long-lived spin states (LLSS) by the seminal works of Levitt,[19−25] Bodenhausen,[26,27] and Warren[28−31] revolutionized our understanding of nuclear spin relaxation and provided an alternative approach for storing nuclear spin order. Indeed, hyperpolarization can be stored directly on protons allowing HP states to undergo relaxation on a significantly longer time scale (characterized by the exponential decay constant T_{LLSS}) compared to that governed by spin−lattice T_1 relaxation.

While a significant amount of work has been historically focused on the LLSS of heteronuclei, LLSS on protons sites[19,32,33] have been shown, too. Moreover, we have recently demonstrated the existence of LLSS between methyl and methylene protons of propane. It has been shown that HP propane lifetime (T_{LLSS}) is ca. 3 times greater than T_1 measured at the same conditions, and T_{LLSS} can exceed 13 s in the gas phase.[34] As a result, long-lived HP propane can potentially be used as an inhalable HP contrast agent in a manner similar to HP ^{129}Xe. While the first demonstration of HP propane (and other hydrocarbon gases, which in principle can have LLSS) and its imaging has been done almost a decade ago,[35−37] the demonstration of its long lifetime and the perceived potential as an inhalable contrast agent have rekindled a significant interest in efficient hyperpolarization of propane[38−44] and other hydrocarbon gases.[45]

Parahydrogen-induced polarization (PHIP)[46−48] is naturally a very attractive approach for preparing HP propane possessing LLSS (although dynamic nuclear polarization (DNP) of hydrocarbons has been recently reported as well[45]) because it offers the possibility of overpopulating LLSS directly via pairwise addition of parahydrogen (p-H$_2$) and in principle with preserving 100% of the singlet spin order (Figure 1a). While efficient homogeneous pairwise p-H$_2$ addition to propylene has been demonstrated,[49] the heterogeneous (HET) PHIP is more attractive[35,36,50−52] because it allows preparing HP contrast medium free from catalyst and solvent contamination and catalyst removal. When the chemical conversion of the PHIP precursor is complete, the produced HP agent can be potentially administered via inhalation for biomedical imaging without additional purification steps.

Improving the efficiency of HET-PHIP to prepare HP propane (and other compounds) to maximize the nuclear spin polarization (P_H) in the regime of nearly complete conversion is mandatory for successful clinical translation of HP propane and HP hydrocarbon gases in general. Designing such catalyst is a challenge at the moment: while P_H of 1−3% has been demonstrated,[41,53] there is certainly a lot of room for improvement since P_H of up to 100% is theoretically possible.[46,47] In particular, the performance of the catalyst for pairwise (vs dissociative) p-H$_2$ addition required for singlet spin state preservation in the resulting HP product (Figure 1a) depends on many factors: pressure, gas mixture composition, temperature, etc. Here, we report on the systematic study of three model Rh/TiO$_2$[41,54] catalysts with different Rh loadings (1.0, 13.7, and 23.2 wt %) in hydrogenation reaction of propylene with p-H$_2$ at various reactant proportions and total gas pressure. This catalytic system has been chosen for the study because (i) it is stable and (ii) it allows producing HP propane and overpopulating its LLSS with high level of polarization at high levels of chemical conversion.[2,42]

We present a 2D mapping approach to study PHIP-echo HP signal of propane in situ in a 9.4 T NMR spectrometer. The presented PHIP-echo pulse sequence mitigates the challenges of PASADENA NMR spectroscopy of HP compounds because the detected signal is no longer antiphase. Moreover, the 2D mapping approach (which can potentially be extended to a multidimensional approach) provides direct insights for optimization of the catalyst performance for production of HP gases by PHIP. Here, propane gas PHIP-echo signal was mapped as a function of propylene fraction and pressure of the reaction mixture. It was found that Rh/TiO$_2$ with the lowest Rh metal content (1.0 wt %) provided the highest signal enhancements for propane in HET-PHIP while all three catalysts maintained high levels of reaction conversion (~95%) in hydrogenation reaction. We show that maximal signal enhancement is observed for high p-H$_2$ fraction (~90%) and low or intermediate total gas pressure (1−3 atm). This result is in qualitative agreement with the previous studies where approximately linear increase of PHIP signal of propane with p-H$_2$ partial pressure was observed in hydrogenation of propyne over Pt/TiO$_2$ catalyst.[55]

■ MATERIALS AND METHODS

Catalysts Preparation and Characterization. For the preparation of Rh/TiO$_2$ catalysts with 1.0 and 13.7 wt % metal loadings, the acidic solution of Rh(NO$_3$)$_3$ (Rh concentration 38 mg/mL) in H$_2$O was used. 0.54 mL of Rh(NO$_3$)$_3$ solution in the case of 1.0 wt % Rh/TiO$_2$ and 8.4 mL of Rh(NO$_3$)$_3$ solution in the case of 13.7 wt % Rh/TiO$_2$ were evaporated to dryness via rotary evaporator (BUCHI) and then diluted in water to a total volume of 1.6 mL. 2 g of TiO$_2$ (Hombifine N, S_{BET} = 107 m^2/g) was impregnated with the aqueous solution of rhodium for 1 h at room temperature. The excess solvent was evaporated, and formed catalysts were dried in air at 120 °C for 4 h. Then the samples were calcined at 400 °C in air for 3 h with subsequent reduction in H$_2$ flow at 330 °C for 3 h. For the preparation of Rh/TiO$_2$ catalyst with 23.2 wt % Rh metal loading, acidic solution of Rh(NO$_3$)$_3$ (metal concentration 98 mg/mL) was used. 6.2 mL of Rh(NO$_3$)$_3$ solution was evaporated to dryness and diluted with water to a total volume of 2 mL, and then 5 drops of tetramethylammonium hydroxide,
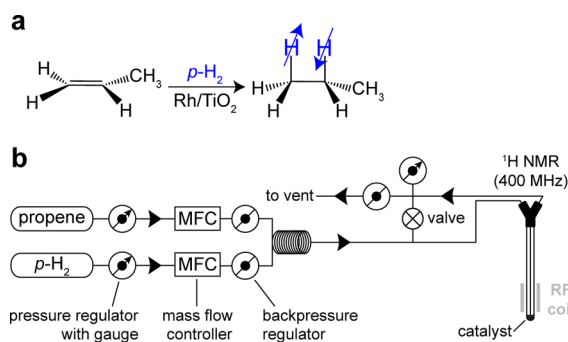
Figure 1. (a) Molecular diagram of heterogeneous pairwise hydrogenation of propylene to propane with parahydrogen (p-H$_2$) over Rh/TiO$_2$ catalyst with preservation of p-H$_2$ spin order in the final HP product. (b) Schematic diagram of the experimental setup employed to perform p-H$_2$ addition to propylene with the detection of produced HP propane in high-field NMR spectrometer (400 MHz Bruker Avance III NMR spectrometer).

25 wt % in H_2O (Acros, CAS: 75-59-2), were added. 2 g of TiO_2 was impregnated with the aqueous solution of rhodium for 2.5 h at room temperature. The excess solvent was evaporated and formed catalyst was dried in air at 120 °C for 4 h. Then calcination of the sample was performed at 400 °C in air for 3 h with subsequent reduction in H_2 flow at 330 °C for 3 h.

The X-ray photoelectron spectroscopy (XPS) measurements were performed on a SPECS (Germany) photoelectron spectrometer equipped with a PHOIBOS-150 hemispherical energy analyzer and Al $K\alpha$ irradiation ($h\nu$ = 1486.6 eV, 200 W). The binding energy (BE) scale was precalibrated using the positions of the photoelectron of Au $4f_{7/2}$ (BE = 84.0 eV) and Cu $2p_{3/2}$ (BE = 932.67 eV) core level peaks. The binding energy of peaks was calibrated by the position of the Ti 2p peak (BE = 458.8 eV) corresponding to the Ti^{4+} from the TiO_2. The sample loading process has never exceeded 1 min in order to minimize sample contact with air.

HRTEM analysis was performed with JEM-2010 (JEOL, Japan) operating at line resolution of 0.14 nm. For X-ray dispersive microanalysis of elemental composition, the energy dispersive spectrometer EDX with Si(Li) detector at 130 eV energy resolution was used (EDAX, USA). For the preparation of sample for the HRTEM analysis, the sample of the catalyst was dispersed in ethanol using an ultrasonic disperser and deposited on copper grids coated with a holey carbon film.

Heterogeneous Hydrogenation and NMR Experiments. The schematics of the experimental setup are shown in Figure 1b. Propylene (>99%, Sigma-Aldrich, #295663) and ultrapure hydrogen (>99.999%, A-L Compressed Gases Inc., Nashville, TN) were used as received. Hydrogen gas was enriched with p-H_2 to ~50% $para$-state using a home-built parahydrogen generator by passing normal H_2 through FeO(OH) powder (Sigma-Aldrich, P/N 371254, 30−50 mesh) maintained at liquid N_2 temperature (77 K). The degree of $para$-fraction in produced p-H_2 gas was confirmed by ^1H NMR spectroscopy using a Bruker Avance III 400 MHz NMR spectrometer using a previously described procedure.[56] Gas flow rates of p-H_2 and propylene (see Table S13 in the Supporting Information for details regarding flow rates for different pressures) were regulated by mass flow controllers (Sierra Instruments, Monterey, CA, model #C50L-AL-DD-2-PV2-V0). The gases flowed through a long 1/8 in. outside diameter (o.d.) and 1/16 in. inner diameter (i.d.) Teflon tubing to ensure their efficient mixing and then through a 1/16 in. o.d. Teflon tubing (1/32 in. i.d.) to the bottom of a 5 mm NMR tube where the catalyst was placed. The NMR tube residing in the NMR instrument (400 MHz Bruker Avance III NMR spectrometer) was heated to 100 °C to initiate the *in situ* hydrogenation. The gas mixture could be readily directed either to the NMR tube for detection or directly to the vent using a manual shut-off valve (Western Analytical Products, #P-733). In the latter case the NMR spectrum of a stopped (thermally polarized) gas was recorded. The total pressure was controlled using a backpressure regulator (Figure 1b).

T_1 relaxation measurements have been performed using the same experimental setup with the exception of propane cylinder (>99 wt %, Sigma-Aldrich, #536172) being connected instead of a propylene cylinder. The percentage of hydrogen and propane gases was controlled by mass flow controllers (see Table S13). When equilibrium mixture composition has been reached (as monitored by NMR signal of flowing gas), the flow rate through the NMR tube was stopped by directing the gas to the vent. T_1 was measured using inversion−recovery sequence for the stopped gas mixture.

■ RESULTS AND DISCUSSION

The Holy Grail in the field of HET-PHIP is the development of a catalytic system, capable of producing HP fluid with theoretically maximum nuclear spin polarization at nearly 100% conversion efficiency, thereby producing pure and highly hyperpolarized contrast agent suitable for biomedical and other applications.[2] However, very often high polarization P_H (and pairwise selectivity) is observed either for deactivated catalysts[57,58] or when the hydrogenation reaction is performed at very low (i.e., ≪10%) conversion values.[55] Here, the study is performed at >95% conversion efficiency in the light of the potential use of HP propane as a contrast agent. Rh/TiO_2 was chosen for this study because it has been shown previously to be one of the most promising systems to provide efficient pairwise hydrogenation of propylene to propane accompanied by the high reaction conversion, with the final goal of HP propane production.[41,59] In the present study, we have investigated Rh/TiO_2 catalysts with three different percentages of loaded Rh metal: 1.0, 13.7, and 23.2 wt %. The preparation procedures are described in the Materials and Methods section.

XPS and HRTEM Analysis. Figure 2a−c presents Rh 3d core-level spectra obtained for the Rh/TiO_2 samples with low (1.0 wt %), intermediate (13.7 wt %), and high (23.2 wt %) rhodium metal loading before reaction. The Rh $3d_{5/2}$ peak at 307.2 ± 0.1 eV can be attributed to metallic Rh^0, proving the presence of Rh in all studied samples.[60,61] According to the high-resolution transition electron microscopy (HRTEM) data, at the low metal loading (1.0 wt %) Rh nanoparticles are not observed as the dispersed unique particles (Figure 2d). Moreover, observed interplanar distances are related to the TiO_2 anatase phase only. Nevertheless, EDX spectra of the different sample areas contain peaks corresponding to the L-line of Rh (Figure S1). This observation confirms that Rh exists on the surface of TiO_2 as clusters with the size less than 0.5 nm or as Rh atoms incorporated into the structure of TiO_2. For intermediate metal coverage (13.7 wt % of Rh) HRTEM images show the presence of RhO_x particles with the average size of 1.2 nm (Figure 2e). A part of supported rhodium forms a metallic layer on the surface of TiO_2 and the layer thickness varies from 0.5 to 3 nm. The interplanar distances for the metallic rhodium are slightly increased indicating partial oxidation of Rh. According to the HRTEM data the catalyst with the highest percentage (23.2 wt %) of supported Rh contains a broad distribution of metal particles sizes with the average size of about 2.4 nm (Figure 2f). According to the measured interplanar distances, the particles can be attributed to metallic Rh.

PHIP-Echo Sequence. The conventional PHIP[48] effect at high magnetic fields is known as the PASADENA[46,47] effect (Figure 3a). When two hydrogen atoms of p-H_2 are added to the precursor molecule in a pairwise manner (i.e., added together as a pair), thus conserving their singlet spin correlation, the NMR spectrum of such hydrogenation product is manifested as absorptive−emissive multiplets (Figure 3b,c). On the one hand, these multiplets have conventionally been the characteristic signature of the PHIP phenomenon enabling many mechanistic studies in homogeneous and heterogeneous catalysis.[50,62,63] Moreover, the enhanced antiphase multiplets of nascent protons allow unambiguous identification of two-spin order derived from p-H_2 protons and distinguishing these
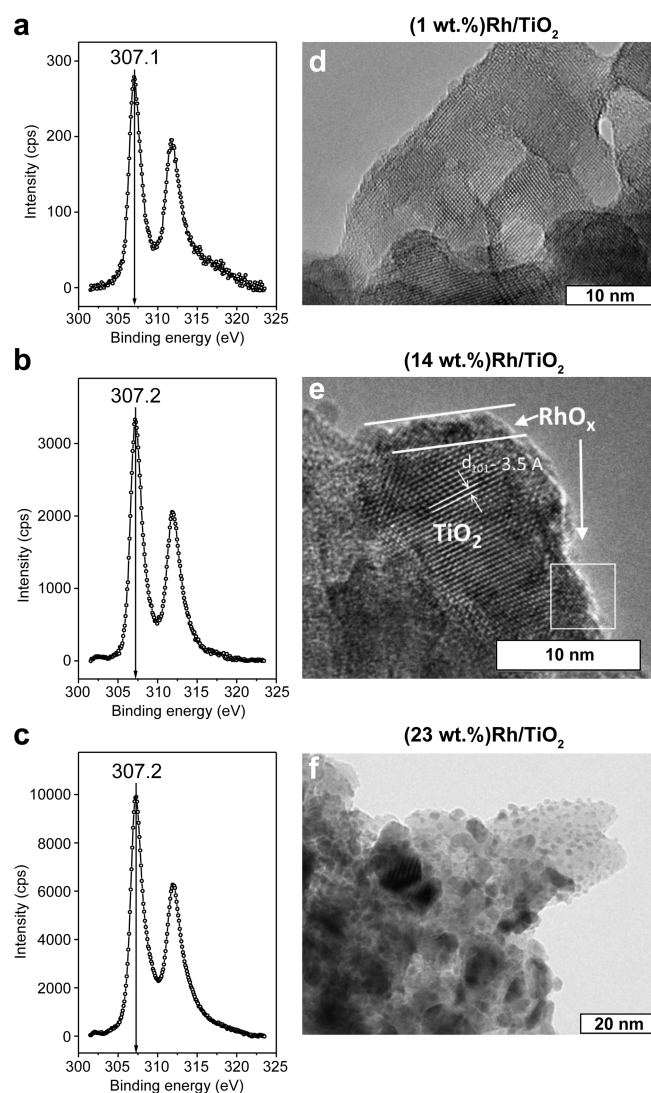
Figure 2. Characterization of the Rh/TiO₂ samples with different rhodium metal percentages. Left: Rh 3d core-level XPS spectra of Rh/TiO₂ catalysts before propylene hydrogenation reaction: (a) 1.0 wt % of Rh, (b) 13.7 wt % of Rh, (c) 23.2 wt % of Rh. Binding energies are correlated to data from the XPS handbook.[61] Right: HRTEM images of Rh/TiO₂ catalyst samples: (d) 1.0 wt % of Rh, (e) 13.7 wt % of Rh, (f) 23.2 wt % of Rh.

Figure 3. (a) ^1H NMR pulse sequence used for direct detection of antiphase nuclear spin order of HP propane: 45° excitation pulse followed by acquisition of the free induction decay (FID). The hydrogenation reaction and the detection are performed at high magnetic field (PASADENA[46,47] experiment). (b) ^1H NMR spectrum of HP propane (produced via hydrogenation of propylene with p-H_2 over Rh/TiO₂ catalyst) recorded under the PASADENA conditions using pulse sequence shown in (a). (c) Simulation of ^1H NMR spectrum of HP propane obtained under the PASADENA conditions using pulse sequence shown in (a). (d) ^1H NMR PHIP-echo pulse sequence (note that 45° pulse is used here instead of 90° pulse in conventional spin echo experiments). PHIP-echo can be used to convert antiphase nuclear spin order of PHIP-derived nuclei into in-phase spin order directly at high magnetic field. (e) ^1H NMR spectrum of HP propane acquired using PHIP-echo pulse sequence shown in (d). (f) Simulation of ^1H NMR spectrum of HP propane acquired using PHIP-echo pulse sequence shown in (d). Note that residual peak labeled with open circle in (b) and (e) belongs to the CH₃ group of unreacted propylene.

signatures from those of thermally polarized nuclei. On the other hand, the spectral appearance of such antiphase multiplets has certain experimental disadvantages. Indeed, the NMR signal intensity of antiphase multiplets is greatly affected by B_0 inhomogeneities, and this NMR signal is also significantly reduced when the PASADENA signal is detected from a continuously flowing HP gas.[59] Moreover, in-phase magnetization is typically required for MRI;[37] otherwise, the frequency-encoding process will lead to the partial self-cancellation of antiphase spectral lines.[41,43]

Here we present a simple solution to overcome the above-mentioned challenge by using the so-called PHIP-echo radio frequency (RF) pulse sequence (Figure 3d). PHIP-echo is a spin-echo-based RF pulse sequence, where the first pulse is 45° hard pulse instead of typically employed 90° pulse. This type of RF pulse sequence has been previously used in the context of time-domain NMR spectroscopy[64] and MRI.[65] Moreover, the first two pulses are often employed as a part of sequences used

in the J-coupling spectroscopy[66−68] and other spin order transformation/filtering schemes.[69,70] The main advantage of PHIP-echo (compared to other schemes listed above) for analysis of gaseous PHIP-reaction products is its short duration; thus, relaxation losses due to T_2^* signal decay are minimized. In addition, the proper choice of interpulse delay, Δ (Figure 3d), allows concentrating most of the detectable signal in only one resonance line (e.g., −CH₃ resonance instead of both −CH₂− and −CH₃ as shown in Figure 3e,f in the case of propane),

Figure 4. 2D mapping of PHIP-echo NMR signal for optimization of the effective ^{1}H NMR signal enhancement of HP propane for three Rh/TiO$_2$ catalysts with different Rh metal loadings: 1.0 wt % (left column), 13.7 wt % (central column), and 23.2 wt % (right column). Top row: 2D maps of ^{1}H NMR PHIP-echo propane signals (the sum of both H$_A$ and H$_B$ signals of Figure 3e) as a function of propylene fraction in the reactant mixture and as a function of the reaction mixture pressure. Central row: 2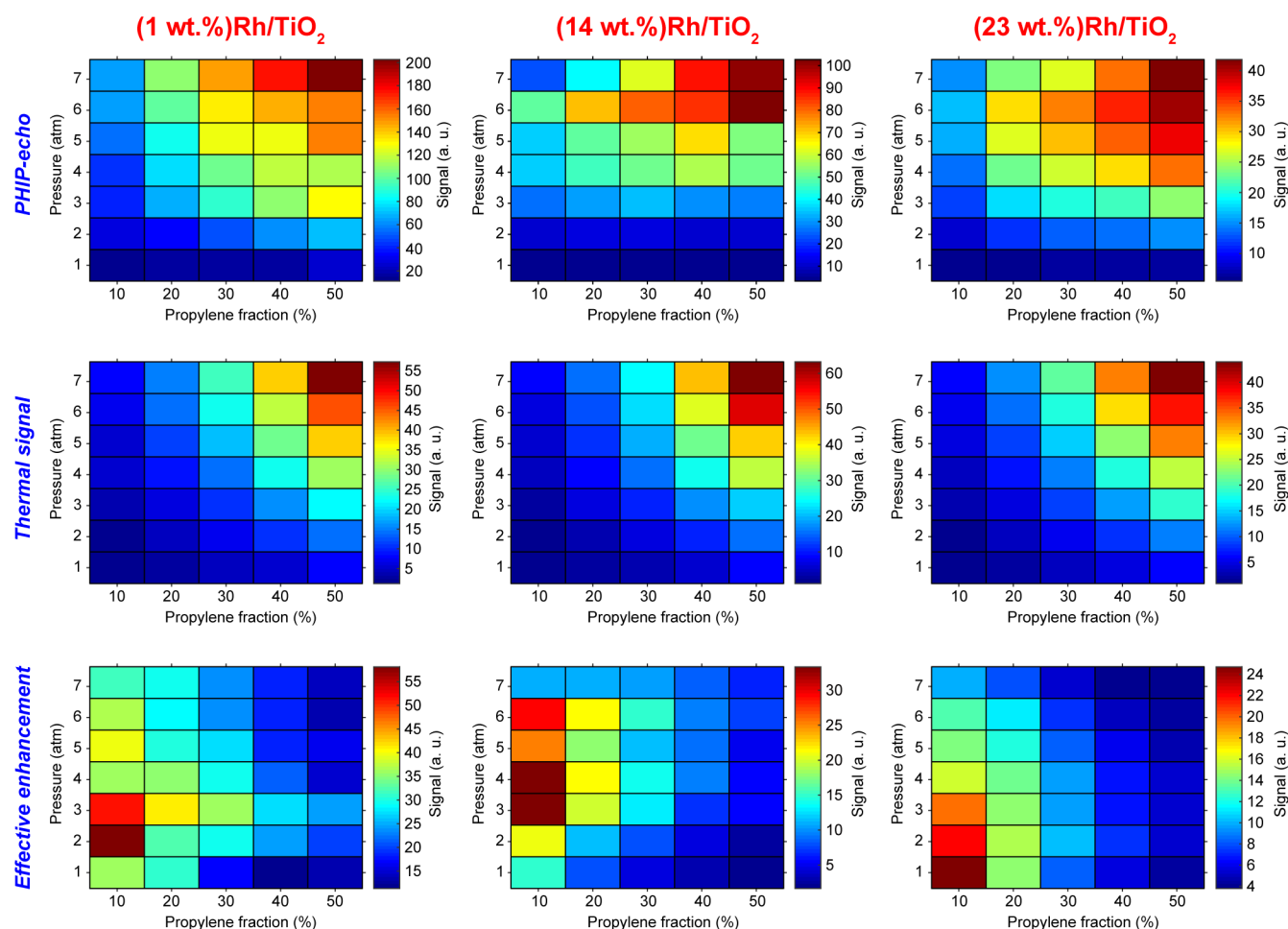D maps of thermal ^{1}H NMR signal of propane (sum of integrals corresponding to all 8 protons in propane molecule) as a function of propylene fraction in the reactant mixture and as a function of the reaction mixture pressure; spectra were acquired after cessation of gas flow through the NMR tube and complete relaxation of nuclear spins to equilibrium. Bottom row: 2D maps of effective ^{1}H NMR signal enhancement as a function of propylene fraction in the reactant mixture and as a function of the reaction mixture pressure. Effective signal enhancement was calculated as a ratio of PHIP-echo signal (top row) and thermal signal (central row) taking into account the number of protons, which give rise to the observable signal (2 in the case of polarization and 8 for the thermally polarized one). We note that the computed in this fashion (see Supporting Information for details) signal enhancement ε reports on the signal enhancement of the two (out of eight) protons of propane spin system: H$_A$ and H$_B$ as shown in Figure 3. The maximum observed ε in the experiments presented in Figure 4 was ~55 corresponding to %P$_H$ ~ 0.18% (see Supporting Information for details). We note that while the enhancement factor ε is field dependent, the %P$_H$ is field independent because it takes into account the equilibrium nuclear spin polarization at the field of reference.

which makes it more suitable for high-field gas MRI[71] under PASADENA[47] conditions.

In this study, the time delay, Δ, between pulses and free induction decay (FID) acquisition was chosen to be 17 ms, which is approximately $1/(8J)$, where J (=7.4 Hz) is a spin–spin coupling constant between methyl and methylene protons in propane molecule (experimentally found position of the maximum is in agreement with simulations, Figure S4). Experimentally recorded spectra for PASADENA and PHIP-echo conditions (Figure 3b,e) are in excellent agreement with simulations performed using spin density matrix formalism (Figure 3c,f).

Analysis of Signal Enhancement for Propane. The PHIP-echo pulse sequence was used to search for maximum signal enhancement of HP propane at variable reactant compositions (propylene/p-H$_2$ ratios) and total gas pressure. 2D maps of PHIP-echo signal (i.e., total integral of ^{1}H NMR

signals for −CH$_2$− and −CH$_3$ groups of propane), corresponding thermal signal (total integral of ^{1}H NMR signals for −CH$_2$− and −CH$_3$ groups of propane), and their ratio, i.e., the actual signal enhancement (ε), are presented in Figure 4. It is seen that the signal intensity in the PHIP-echo experiment increases with the increase of propylene fraction (in the initial reactant mixture) and total gas pressure for all three studied catalysts. This is not surprising since the concentration of propane gas increases with the pressure increase and the increase of initial percentage of hydrocarbon in the mixture under condition of nearly complete chemical conversion (of propylene to propane). However, Rh/TiO$_2$ catalyst with 1.0 wt % metal loading shows the best performance among three catalysts studied, i.e., ca. factor of 2 greater signal of HP propane than that for the catalyst with 13.7 wt % loading and ca. factor of 5 higher signal than that for the catalyst with 23.2 wt % loading (Figure 4, top row).

We additionally analyzed whether the performance of 1 wt % Rh loaded catalyst improves with increase of reaction conversion, and 2D maps of thermally polarized propane signals have been plotted. Figure 4 (middle row) shows that thermal NMR signal increases with the increase of propylene fraction in the initial mixture and total gas pressure and that the observed signal is approximately the same for all three catalysts studied. This data can be used to analyze reaction conversion (using integrals of ^{1}H NMR signal for the reaction product propane and the reactant propylene). The Supporting Information shows that conversion level of 95 ± 5% is achieved for each point of 2D map (Figure S5). These high conversion values are the result of the high catalysts' performance in propylene hydrogenation.

The ratio of ^{1}H NMR signal of propane obtained using PHIP-echo detection to the thermal NMR signal is plotted in Figure 4, bottom row, and can be seen as an element-wise division of the 2D maps from the top row by those of the middle row. Interestingly, this plot unambiguously shows that the maximum signal enhancement of propane is observed for low propylene fraction in the reaction mixture (10% propylene and 90% p-H$_2$) and low or intermediate pressures (depending on the percentage of metal loading), 1−4 atm.

We note that the propylene fraction in the initial mixture has never exceeded 50% in our experiments because otherwise unreacted propylene would be inevitably present in the final gas mixture. Surplus propylene is undesirable primarily in the light of the potential biomedical translation of this work. Moreover, propylene excess can potentially lead to reduced performance of heterogeneous catalysts by blocking active catalytic sites.

During the delay of 2Δ (34 ms) required for PHIP-echo acquisition (Figure 3d), HP propane magnetization decays due to T_2-relaxation process. We note that this magnetization attenuation represents a relatively negligible contribution. Following additional measurements, T_2 ranges from 0.6 s (∼1 atm propane pressure) to 2.2 s (at ∼7 atm propane pressure) (Figure S6). Consequently, the corresponding HP NMR signal would be attenuated by a factor 0.94 to 0.98, respectively. Given that the effect of T_2 relaxation is relatively insignificant (and T_2 may be additionally influenced by p-H$_2$ fraction and the % conversion, which would consequently require very complex mapping of such potential T_2 correction factor), we have not included T_2-correction in our maps (Figure 4). However, generally speaking, the T_1- and T_2-associated relaxation losses may require special consideration for such multidimensional mapping of catalyst performance.

The 2D plots presented in Figure 4 show the actual enhancement factors, not corrected for the spin-polarization relaxation losses during the free flow. While the spin order responsible for the observed p-H$_2$-derived NMR signal, i.e., $\hat{I}_{1z}\hat{I}_{2z}$, is not reduced at high flow rates (unlike the spin order $(\hat{I}_{1z} - \hat{I}_{2z})$ responsible for the observed NMR signal in ALTADENA[72] experiments), NMR signal intensity is likely to be affected by the conditions of the experiment, where FID is detected directly during the flow of the reagents through the detection zone of the spectrometer. This phenomenon in the context of PHIP was discussed in detail previously.[59] The gas flow contributes significantly to the HP state relaxation because time delay between gas production and detection is comparable to that of T_1. Indeed, if the gas flow rate is low, HP propane molecules have more time to relax after their production before being detected. If the gas flow rate is high, the NMR signal is greater since the molecules have less time for relaxation. Since

the mass flow rates of reagents have been the same for different pressures (for each propylene/p-H$_2$ ratio) due to the experimental design (Table S13), it is obvious that volume flow rates decreased with increased gas pressure. This flow rate decrease likely has led to the increased NMR signal losses due to the relaxation as discussed above. However, increased reaction pressure should naturally lead to the increase of propane relaxation time, thus compensating for the losses.

In order to show that this is indeed the case, we have performed the additional measurements to investigate propane relaxation time T_1 in the mixtures with hydrogen and at different gas pressures and different propane fraction. The results are summarized in 2D relaxation map (Figure 5a). T_1
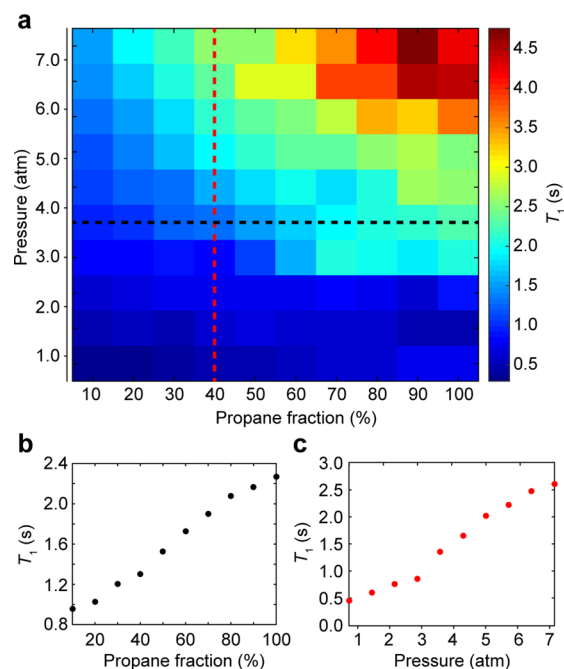
Figure 5. (a) 2D map of longitudinal relaxation time (T_1) for −CH$_3$ group of propane as a function of pressure and propane fraction in the mixture with hydrogen. Each data point is a separate T_1 measurement obtained using inversion−recovery pulse sequence. (b) Cross section of the 2D map presented in (a) at ∼3.7 atm pressure (40 psig). (c) Cross section of the 2D map presented in (a) at the propane fraction of 40% (the rest ∼60% is hydrogen).

relaxation time was measured using inversion−recovery technique for thermally polarized propane mixed with hydrogen at different pressures. T_1 relaxation times indeed increase with the increasing propane fraction and pressure corresponding to the major contribution of spin-rotational mechanism to nuclear spin relaxation of propane in the gas phase. In the triple gas mixture (propylene, hydrogen and propane), the propane T_1 will be governed by the combined fraction of (propane + propylene) rather than by the propane fraction alone because T_1 increases when collisions of molecules become more frequent and efficient. Collisions of propane with H$_2$ are less efficient in the context of T_1 relaxation compared to those of propane−propane and propane−propylene, with the latter two likely being very similar in efficiency given the similar size and mass of the two molecules. Therefore, the effect of chemical conversion (propylene to propane) on propane T_1 under these conditions should be relatively small compared to the overall increase in T_1 due to (propylene + propane) fraction increase.

Overall, the interplay between two opposite effects—increase of T_1 (Figure 5b,c) and HP propane transport time along NMR tube (under conditional of constant flow rate in units of sccm) with reaction pressure increase—somewhat cancels these two opposite trends, although these two effects may have some influence on the map appearance and may potentially require more careful consideration in the future studies especially those involving multidimensional mapping. Alternatively, more thorough future mapping studies may benefit from minimizing the transportation time (ideally to achieve condition when transport time is $\ll T_1$) and implementation of fixed flow rate in units of cm^3/min rather than sccm.

Here, we assume that the above two effects have relatively negligible effect on the maps appearance, and we speculate that the most efficient pairwise hydrogen addition to propylene occurs in the regime when Rh catalyst particles have the lowest coverage by the adsorbed propylene species.[73] It is indeed supported by deuterium tracer studies with propylene, which showed that deuterium excess leads to formation of propane-d_2 as the major product.[74] Moreover, it is known that the rate of alkene exchange with H_2/D_2 is typically proportional to the concentration of adsorbed alkene, and it will therefore increase as the propylene/H_2 ratio increases.[75] Since the exchange process can only lead to the loss of nuclear spin correlation between p-H_2-nascent protons (or even result in their complete separation), it manifests itself as a decrease of ^{1}H NMR signal enhancement at elevated propylene fractions. While the actual causes of the observed phenomena can be very complex, and certainly warrant additional future investigations, the end result of the mapping method is straightforward—the maximal P_H is observed at specific reaction conditions, namely, low pressures and high p-H_2 fraction. Importantly, mapping approach allows unambiguous and visual presentation.

Here, we demonstrated the use of 2D mapping technique for optimization of the HP propane production for three catalytic systems. While all three systems enable near 100% chemical conversion, they produce markedly different P_H. 2D mapping technique is very insightful because optimal catalyst performance clearly varies from one catalyst to another. Only two parameters (pressure and gas mixture composition) were systematically mapped although temperature (and potentially other parameters, e.g., addition of inert carrier gas) will likely have a significant effect on the P_H. We note that the temperature control was very challenging in the presented study due to hardware limitations, but it should be certainly studied in the future.

CONCLUSION

We reported the first systematic study of HP propane production for potential biomedical applications. We used parahydrogen-induced polarization (PHIP) technique to produce HP propane and detect it at high magnetic field using PHIP-echo pulse sequence. PHIP-echo transforms antiphase multiplets of HP propane generated at high field into in-phase NMR signal, thus, allowing for more practical and quantitative NMR spectroscopy of gaseous reaction products. Moreover, we mapped ^{1}H NMR signal and ^{1}H NMR signal enhancement as a function of propylene/p-H_2 gas mixture composition and pressure for three model catalysts Rh/TiO$_2$ with different Rh loadings (1.0, 13.7, and 23.2 wt %). We found that Rh/TiO$_2$ catalysts with lowest percentage of loaded Rh metal (1 wt %) provide the highest level of signal enhancement (and the best pairwise addition selectivity). Relaxation of

propane in propane/H_2 mixtures with propane percentage ranging from 10% to 100% was also systematically studied at various pressures (1−7 atm). It is shown that relaxation time increases nearly linearly with pressure and propane percentage, substantiating the major contribution of spin rotational mechanism for propane relaxation in the gas phase. The demonstrated experimental approaches pave the way to future multidimensional mapping of HP propane production by PHIP and toward future biomedical applications.

ASSOCIATED CONTENT

Ⓢ Supporting Information

The Supporting Information is available free of charge on the ACS Publications website at DOI: 10.1021/acs.jpcc.7b02506.

Additional information about Rh/TiO$_2$ catalysts; additional information about PHIP-echo pulse sequence; reaction conversion and ^{1}H NMR signal enhancement calculation; tabulated measured ^{1}H NMR signal values and calculated conversion and signal enhancement factors; reactants flow rates used to control propylene percentage in the reaction mixture; experimental T_1 relaxation data for thermally polarized propane gas in the mixture with H_2 at various pressures; TEM images and XPS spectra of catalysts; NMR experimental data (PDF)

AUTHOR INFORMATION

Corresponding Authors
*E-mail: kovtunov@tomo.nsc.ru (K.V.K.).
*E-mail: eduard.chekmenev@vanderbilt.edu (E.Y.C.).

ORCID
Danila A. Barskiy: 0000-0002-2819-7584
Kirill V. Kovtunov: 0000-0001-7577-9619
Igor P. Prosvirin: 0000-0002-0351-5128
Igor V. Koptyug: 0000-0003-3480-7649
Eduard Y. Chekmenev: 0000-0002-8745-8801

Notes
The authors declare no competing financial interest.

REFERENCES

(1) Nikolaou, P.; Goodson, B. M.; Chekmenev, E. Y. NMR Hyperpolarization Techniques for Biomedicine. *Chem. - Eur. J.* **2015**, *21*, 3156−3166.
(2) Barskiy, D. A.; Coffey, A. M.; Nikolaou, P.; Mikhaylov, D. M.; Goodson, B. M.; Branca, R. T.; Lu, G. J.; Shapiro, M. G.; Telkki, V.-V.; Zhivonitko, V. V.; et al. NMR Hyperpolarization Techniques of Gases. *Chem. - Eur. J.* **2017**, *23*, 725−751.
(3) Goodson, B. M. Nuclear Magnetic Resonance of Laser-Polarized Noble Gases in Molecules, Materials, and Organisms. *J. Magn. Reson.* **2002**, *155*, 157−216.

(4) Nikolaou, P.; Coffey, A. M.; Barlow, M. J.; Rosen, M.; Goodson, B. M.; Chekmenev, E. Y. Temperature-Ramped ^{129}Xe Spin Exchange Optical Pumping. *Anal. Chem.* **2014**, *86*, 8206−8212.

(5) Ardenkjaer-Larsen, J. H.; Fridlund, B.; Gram, A.; Hansson, G.; Hansson, L.; Lerche, M. H.; Servin, R.; Thaning, M.; Golman, K. Increase in Signal-to-Noise Ratio of > 10,000 Times in Liquid-State NMR. *Proc. Natl. Acad. Sci. U. S. A.* **2003**, *100*, 10158−10163.

(6) Blümich, B. Virtual Special Issue: Magnetic Resonance at Low Fields. *J. Magn. Reson.* **2017**, *274*, 145−147.

(7) Kurhanewicz, J.; Vigneron, D. B.; Brindle, K.; Chekmenev, E. Y.; Comment, A.; Cunningham, C. H.; DeBerardinis, R. J.; Green, G. G.; Leach, M. O.; Rajan, S. S.; et al. Analysis of Cancer Metabolism by Imaging Hyperpolarized Nuclei: Prospects for Translation to Clinical Research. *Neoplasia* **2011**, *13*, 81−97.

(8) Brindle, K. M. Imaging Metabolism with Hyperpolarized ^{13}C-Labeled Cell Substrates. *J. Am. Chem. Soc.* **2015**, *137*, 6418−6427.

(9) Comment, A.; Merritt, M. E. Hyperpolarized Magnetic Resonance as a Sensitive Detector of Metabolic Function. *Biochemistry* **2014**, *53*, 7333−7357.

(10) Schroder, L. Xenon for NMR Biosensing - Inert but Alert. *Phys. Medica* **2013**, *29*, 3−16.

(11) Witte, C.; Schroder, L. NMR of Hyperpolarised Probes. *NMR Biomed.* **2013**, *26*, 788−802.

(12) Walker, T. G.; Happer, W. Spin-Exchange Optical Pumping of Noble-Gas Nuclei. *Rev. Mod. Phys.* **1997**, *69*, 629−642.

(13) Goodson, B. M.; Ranta, K.; Skinner, J.; Coffey, A. M.; Nikolaou, P.; Gemeinhardt, M. E.; Anthony, D.; Stephenson, S.; Hardy, S.; Owers-Bradley, J.; et al. The Physics of Hyperpolarized Gas MRI (Invited Chapter). In *Hyperpolarized and Inert Gas MRI in Research and Medicine*; Albert, M., Hane, F., Eds.; Elsevier Inc.: San Diego, CA, 2017; pp 23−46.

(14) Mugler, J. P.; Altes, T. A. Hyperpolarized ^{129}Xe MRI of the Human Lung. *J. Magn. Reson. Imaging* **2013**, *37*, 313−331.

(15) Branca, R. T.; Cleveland, Z. I.; Fubara, B.; Kumar, C. S. S. R.; Maronpot, R. R.; Leuschner, C.; Warren, W. S.; Driehuys, B. Molecular MRI for Sensitive and Specific Detection of Lung Metastases. *Proc. Natl. Acad. Sci. U. S. A.* **2010**, *107*, 3693−3697.

(16) Branca, R. T.; He, T.; Zhang, L.; Floyd, C. S.; Freeman, M.; White, C.; Burant, A. Detection of Brown Adipose Tissue and Thermogenic Activity in Mice by Hyperpolarized Xenon MRI. *Proc. Natl. Acad. Sci. U. S. A.* **2014**, *111*, 18001−18006.

(17) Albert, M. S.; Cates, G. D.; Driehuys, B.; Happer, W.; Saam, B.; Springer, C. S.; Wishnia, A. Biological Magnetic-Resonance-Imaging Using Laser Polarized Xe-129. *Nature* **1994**, *370*, 199−201.

(18) Walkup, L. L.; Woods, J. C. Translational Applications of Hyperpolarized ^{3}He and ^{129}Xe. *NMR Biomed.* **2014**, *27*, 1429−1438.

(19) Carravetta, M.; Levitt, M. H. Long-Lived Nuclear Spin States in High-Field Solution NMR. *J. Am. Chem. Soc.* **2004**, *126*, 6228−6229.

(20) Pileio, G.; Carravetta, M.; Hughes, E.; Levitt, M. H. The Long-Lived Nuclear Singlet State of ^{15}N-Nitrous Oxide in Solution. *J. Am. Chem. Soc.* **2008**, *130*, 12582−12583.

(21) Pileio, G.; Levitt, M. H. Theory of Long-Lived Nuclear Spin States in Solution Nuclear Magnetic Resonance. II. Singlet Spin Locking. *J. Chem. Phys.* **2009**, *130*, 214501.

(22) Levitt, M. H. Singlet Nuclear Magnetic Resonance. *Annu. Rev. Phys. Chem.* **2012**, *63*, 89−105.

(23) Dumez, J.-N.; Håkansson, P.; Mamone, S.; Meier, B.; Stevanato, G.; Hill-Cousins, J. T.; Roy, S. S.; Brown, R. C. D.; Pileio, G.; Levitt, M. H. Theory of Long-Lived Nuclear Spin States in Methyl Groups and Quantum-Rotor Induced Polarisation. *J. Chem. Phys.* **2015**, *142*, 044506.

(24) Stevanato, G.; Singha Roy, S.; Hill-Cousins, J.; Kuprov, I.; Brown, L. J.; Brown, R. C. D.; Pileio, G.; Levitt, M. H. Long-Lived Nuclear Spin States Far from Magnetic Equivalence. *Phys. Chem. Chem. Phys.* **2015**, *17*, 5913−5922.

(25) Levitt, M. H. Symmetry Constraints on Spin Dynamics: Application to Hyperpolarized NMR. *J. Magn. Reson.* **2016**, *262*, 91−99.

(26) Vasos, P. R.; Comment, A.; Sarkar, R.; Ahuja, P.; Jannin, S.; Ansermet, J.-P.; Konter, J. A.; Hautle, P.; van den Brandt, B.; Bodenhausen, G. Long-Lived States to Sustain Hyperpolarized Magnetization. *Proc. Natl. Acad. Sci. U. S. A.* **2009**, *106*, 18469−18473.

(27) Ahuja, P.; Sarkar, R.; Jannin, S.; Vasos, P. R.; Bodenhausen, G. Proton Hyperpolarisation Preserved in Long-Lived States. *Chem. Commun.* **2009**, *46*, 8192−8194.

(28) Warren, W. S.; Jenista, E.; Branca, R. T.; Chen, X. Increasing Hyperpolarized Spin Lifetimes through True Singlet Eigenstates. *Science* **2009**, *323*, 1711−1714.

(29) Theis, T.; Ortiz, G. X.; Logan, A. W. J.; Claytor, K. E.; Feng, Y.; Huhn, W. P.; Blum, V.; Malcolmson, S. J.; Chekmenev, E. Y.; Wang, Q.; et al. Direct and Cost-Efficient Hyperpolarization of Long-Lived Nuclear Spin States on Universal ^{15}N$_2$-Diazirine Molecular Tags. *Sci. Adv.* **2016**, *2*, e1501438.

(30) Feng, Y. S.; Theis, T.; Liang, X. F.; Wang, Q.; Zhou, P.; Warren, W. S. Storage of Hydrogen Spin Polarization in Long-Lived C-13(2) Singlet Order and Implications for Hyperpolarized Magnetic Resonance Imaging. *J. Am. Chem. Soc.* **2013**, *135*, 9632−9635.

(31) Feng, Y.; Theis, T.; Wu, T.-L.; Claytor, K.; Warren, W. S. Long-Lived Polarization Protected by Symmetry. *J. Chem. Phys.* **2014**, *141*, 134307.

(32) Franzoni, M. B.; Buljubasich, L.; Spiess, H. W.; Munnemann, K. Long-Lived H-1 Singlet Spin States Originating from Para-Hydrogen in Cs-Symmetric Molecules Stored for Minutes in High Magnetic Fields. *J. Am. Chem. Soc.* **2012**, *134*, 10393−10396.

(33) Carravetta, M.; Johannessen, O. G.; Levitt, M. H. Beyond the T_1 Limit: Singlet Nuclear Spin States in Low Magnetic Fields. *Phys. Rev. Lett.* **2004**, *92*, 153003.

(34) Barskiy, D. A.; Salnikov, O. G.; Romanov, A. S.; Feldman, M. A.; Coffey, A. M.; Kovtunov, K. V.; Koptyug, I. V.; Chekmenev, E. Y. NMR Spin-Lock Induced Crossing (SLIC) Dispersion and Long-Lived Spin States of Gaseous Propane at Low Magnetic Field (0.05 T). *J. Magn. Reson.* **2017**, *276*, 78−85.

(35) Bouchard, L. S.; Kovtunov, K. V.; Burt, S. R.; Anwar, M. S.; Koptyug, I. V.; Sagdeev, R. Z.; Pines, A. Para-Hydrogen-Enhanced Hyperpolarized Gas-Phase Magnetic Resonance Imaging. *Angew. Chem., Int. Ed.* **2007**, *46*, 4064−4068.

(36) Koptyug, I. V.; Kovtunov, K. V.; Burt, S. R.; Anwar, M. S.; Hilty, C.; Han, S. I.; Pines, A.; Sagdeev, R. Z. Para-Hydrogen-Induced Polarization in Heterogeneous Hydrogenation Reactions. *J. Am. Chem. Soc.* **2007**, *129*, 5580−5586.

(37) Bouchard, L. S.; Burt, S. R.; Anwar, M. S.; Kovtunov, K. V.; Koptyug, I. V.; Pines, A. Nmr Imaging of Catalytic Hydrogenation in Microreactors with the Use of Para-Hydrogen. *Science* **2008**, *319*, 442−445.

(38) Zhao, E. W.; Zheng, H.; Zhou, R.; Hagelin-Weaver, H. E.; Bowers, C. R. Shaped Ceria Nanocrystals Catalyze Efficient and Selective Para-Hydrogen-Enhanced Polarization. *Angew. Chem., Int. Ed.* **2015**, *54*, 14270−14275.

(39) Zhou, R.; Zhao, E. W.; Cheng, W.; Neal, L. M.; Zheng, H.; Quiñones, R. E.; Hagelin-Weaver, H. E.; Bowers, C. R. Parahydrogen-Induced Polarization by Pairwise Replacement Catalysis on Pt and Ir Nanoparticles. *J. Am. Chem. Soc.* **2015**, *137*, 1938−1946.

(40) Zhao, E. W.; Zheng, H.; Ludden, K.; Xin, Y.; Hagelin-Weaver, H. E.; Bowers, C. R. Strong Metal−Support Interactions Enhance the Pairwise Selectivity of Parahydrogen Addition over Ir/TiO$_2$. *ACS Catal.* **2016**, *6*, 974−978.

(41) Kovtunov, K. V.; Barskiy, D. A.; Coffey, A. M.; Truong, M. L.; Salnikov, O. G.; Khudorozhkov, A. K.; Inozemtseva, E. A.; Prosvirin, I. P.; Bukhtiyarov, V. I.; Waddell, K. W.; et al. High-Resolution 3D Proton Hyperpolarized Gas MRI Enabled by Parahydrogen and Rh/TiO$_2$ Heterogeneous Catalyst. *Chem. - Eur. J.* **2014**, *20*, 11636−11639.

(42) Kovtunov, K. V.; Truong, M. L.; Barskiy, D. A.; Koptyug, I. V.; Coffey, A. M.; Waddell, K. W.; Chekmenev, E. Y. Long-Lived Spin States for Low-Field Hyperpolarized Gas MRI. *Chem. - Eur. J.* **2014**, *20*, 14629−14632.

(43) Kovtunov, K. V.; Truong, M. L.; Barskiy, D. A.; Salnikov, O. G.; Bukhtiyarov, V. I.; Coffey, A. M.; Waddell, K. W.; Koptyug, I. V.;

Chekmenev, E. Y. Propane-D₆ Heterogeneously Hyperpolarized by Parahydrogen. *J. Phys. Chem. C* **2014**, *118*, 28234−28243.

(44) Burueva, D. B.; Romanov, A. S.; Salnikov, O. G.; Zhivonitko, V. V.; Chen, Y.-W.; Barskiy, D. A.; Chekmenev, E. Y.; Hwang, D. W.-H.; Kovtunov, K. V.; Koptyug, I. V. Extending the Lifetime of Hyperpolarized Propane Gas Via Reversible Dissolution. *J. Phys. Chem. C* **2017**, *121*, 4481−4487.

(45) Vuichoud, B.; Canet, E.; Milani, J.; Bornet, A.; Baudouin, D.; Veyre, L.; Gajan, D.; Emsley, L.; Lesage, A.; Copéret, C.; et al. Hyperpolarization of Frozen Hydrocarbon Gases by Dynamic Nuclear Polarization at 1.2 K. *J. Phys. Chem. Lett.* **2016**, *7*, 3235−3239.

(46) Bowers, C. R.; Weitekamp, D. P. Transformation of Symmetrization Order to Nuclear-Spin Magnetization by Chemical-Reaction and Nuclear-Magnetic-Resonance. *Phys. Rev. Lett.* **1986**, *57*, 2645−2648.

(47) Bowers, C. R.; Weitekamp, D. P. Para-Hydrogen and Synthesis Allow Dramatically Enhanced Nuclear Alignment. *J. Am. Chem. Soc.* **1987**, *109*, 5541−5542.

(48) Eisenschmid, T. C.; Kirss, R. U.; Deutsch, P. P.; Hommeltoft, S. I.; Eisenberg, R.; Bargon, J.; Lawler, R. G.; Balch, A. L. Para Hydrogen Induced Polarization in Hydrogenation Reactions. *J. Am. Chem. Soc.* **1987**, *109*, 8089−8091.

(49) Salnikov, O. G.; Barskiy, D. A.; Coffey, A. M.; Kovtunov, K. V.; Koptyug, I. V.; Chekmenev, E. Y. Efficient Batch-Mode Parahydrogen-Induced Polarization of Propane. *ChemPhysChem* **2016**, *17*, 3395−3398.

(50) Kovtunov, K. V.; Zhivonitko, V. V.; Skovpin, I. V.; Barskiy, D. A.; Koptyug, I. V. Parahydrogen-Induced Polarization in Heterogeneous Catalytic Processes. *Top. Curr. Chem.* **2012**, *338*, 123−180.

(51) Kovtunov, K. V.; Zhivonitko, V. V.; Skovpin, I. V.; Barskiy, D. A.; Salnikov, O. G.; Koptyug, I. V. Toward Continuous Production of Catalyst-Free Hyperpolarized Fluids Based on Biphasic and Heterogeneous Hydrogenations with Parahydrogen. *J. Phys. Chem. C* **2013**, *117*, 22887−22893.

(52) Kovtunov, K. V.; Barskiy, D.; Shchepin, R. V.; Coffey, A. M.; Waddell, K. W.; Koptyug, I. V.; Chekmenev, E. Y. Demonstration of Heterogeneous Parahydrogen Induced Polarization Using Hyperpolarized Agent Migration from Dissolved Rh(I) Complex to Gas Phase. *Anal. Chem.* **2014**, *86*, 6192−6196.

(53) Kovtunov, K. V.; Beck, I. E.; Bukhtiyarov, V. I.; Koptyug, I. V. Observation of Parahydrogen-Induced Polarization in Heterogeneous Hydrogenation on Supported Metal Catalysts. *Angew. Chem., Int. Ed.* **2008**, *47*, 1492−1495.

(54) Salnikov, O. G.; Burueva, D. B.; Gerasimov, E. Y.; Bukhtiyarov, A. V.; Khudorozhkov, A. K.; Prosvirin, I. P.; Kovtunova, L. M.; Barskiy, D. A.; Bukhtiyarov, V. I.; Kovtunov, K. V.; et al. The Effect of Oxidative and Reductive Treatments of Titania-Supported Metal Catalysts on the Pairwise Hydrogen Addition to Unsaturated Hydrocarbons. *Catal. Today* **2017**, *283*, 82−88.

(55) Zhou, R.; Cheng, W.; Neal, L. M.; Zhao, E. W.; Ludden, K.; Hagelin-Weaver, H. E.; Bowers, C. R. Parahydrogen Enhanced NMR Reveals Correlations in Selective Hydrogenation of Triple Bonds over Supported Pt Catalyst. *Phys. Chem. Chem. Phys.* **2015**, *17*, 26121−26129.

(56) Feng, B.; Coffey, A. M.; Colon, R. D.; Chekmenev, E. Y.; Waddell, K. W. A Pulsed Injection Parahydrogen Generator and Techniques for Quantifying Enrichment. *J. Magn. Reson.* **2012**, *214*, 258−262.

(57) Sharma, R.; Bouchard, L. S. Strongly Hyperpolarized Gas from Parahydrogen by Rational Design of Ligand-Capped Nanoparticles. *Sci. Rep.* **2012**, *2*, 5.

(58) Gloggler, S.; Grunfeld, A. M.; Ertas, Y. N.; McCormick, J.; Wagner, S.; Bouchard, L. S. Surface Ligand-Directed Pair-Wise Hydrogenation for Heterogeneous Phase Hyperpolarization. *Chem. Commun.* **2016**, *52*, 605−608.

(59) Barskiy, D. A.; Salnikov, O. G.; Kovtunov, K. V.; Koptyug, I. V. NMR Signal Enhancement for Hyperpolarized Fluids Continuously Generated in Hydrogenation Reactions with Parahydrogen. *J. Phys. Chem. A* **2015**, *119*, 996−1006.

(60) Larichev, Y. V.; Netskina, O. V.; Komova, O. V.; Simagina, V. I. Comparative XPS Study of Rh/Al₂O₃ and Rh/TiO₂ as Catalysts for NaBH₄ Hydrolysis. *Int. J. Hydrogen Energy* **2010**, *35*, 6501−6507.

(61) Moulder, J. F.; Stickle, W. F.; Sobol, P. E.; Bomben, K. D. *Handbook of X-Ray Photoelectron Spectroscopy*; Perkin-Elmer: Eden Prairie, MN, 1992.

(62) Blazina, D.; Duckett, S. B.; Dunne, J. P.; Godard, C. Applications of the Parahydrogen Phenomenon in Inorganic Chemistry. *Dalton Trans.* **2004**, 2601−2609.

(63) Duckett, S. B.; Newell, C. L.; Eisenberg, R. Observation of New Intermediates in Hydrogenation Catalyzed by Wilkinson's Catalyst, RhCl(PPh₃)₃, Using Parahydrogen-Induced Polarization. *J. Am. Chem. Soc.* **1994**, *116*, 10548−10556.

(64) Ratajczyk, T.; Gutmann, T.; Dillenberger, S.; Abdulhussaein, S.; Frydel, J.; Breitzke, H.; Bommerich, U.; Trantzschel, T.; Bernarding, J.; Magusin, P. C. M. M.; et al. Time Domain Para Hydrogen Induced Polarization. *Solid State Nucl. Magn. Reson.* **2012**, *43−44*, 14−21.

(65) Dechent, J. F.; Buljubasich, L.; Schreiber, L. M.; Spiess, H. W.; Muennemann, K. Proton Magnetic Resonance Imaging with Para-Hydrogen Induced Polarization. *Phys. Chem. Chem. Phys.* **2012**, *14*, 2346−2352.

(66) Prina, I.; Buljubasich, L.; Acosta, R. H. High-Resolution Hyperpolarized J-Spectra with Parahydrogen Discrimination. *J. Phys. Chem. Lett.* **2013**, *4*, 3924−3928.

(67) Acosta, R. H.; Prina, I.; Buljubasich, L. In *Gas Phase NMR*; The Royal Society of Chemistry: 2016; Chapter 9, pp 304−335.

(68) Buljubasich, L.; Prina, I.; Franzoni, M. B.; Münnemann, K.; Spiess, H. W.; Acosta, R. H. High Resolution Para-Hydrogen Induced Polarization in Inhomogeneous Magnetic Fields. *J. Magn. Reson.* **2013**, *230*, 155−159.

(69) Pravdivtsev, A. N.; Ivanov, K. L.; Yurkovskaya, A. V.; Vieth, H.-M.; Sagdeev, R. Z. New Pulse Sequence for Robust Filtering of Hyperpolarized Multiplet Spin Order. *Dokl. Phys. Chem.* **2015**, *465*, 267−269.

(70) Ivanov, K. L.; Petrova, M. V.; Lukzen, N. N.; Sagdeev, R. Z. Separation of Integral and Multiplet Nuclear Polarization by Means of Spin Echo Magnetization Phase Analysis. *Dokl. Phys. Chem.* **2009**, *427*, 121−124.

(71) Kovtunov, K. V.; Romanov, A. S.; Salnikov, O. G.; Barskiy, D. A.; Chekmenev, E. Y.; Koptyug, I. V. Gas Phase UTE MRI of Propane and Propene. *Tomography* **2016**, *2*, 49−55.

(72) Pravica, M. G.; Weitekamp, D. P. Net NMR Alighnment by Adiabatic Transport of Parahydrogen Addition Products to High Magnetic Field. *Chem. Phys. Lett.* **1988**, *145*, 255−258.

(73) Bond, G. C. *Metal-Catalysed Reactions of Hydrocarbons*; Springer: 2005; Vol. 2.

(74) Bond, G. C.; Turkevich, J. The Reaction of Propylene with Deuterium over a Platinum Catalyst. *Trans. Faraday Soc.* **1953**, *49*, 281−291.

(75) Bond, G. C.; Phillipson, J. J.; Wells, P. B.; Winterbottom, J. M. Hydrogenation of Olefins. Part 1.-Hydrogenation of Ethylene, Propylene and the N-Butenes over Alumina-Supported Platinum and Iridium. *Trans. Faraday Soc.* **1964**, *60*, 1847−1864.

Aqueous, Heterogeneous *para*-Hydrogen-Induced ^{15}N Polarization

Liana B. Bales,[†] Kirill V. Kovtunov,[*,‡,§] Danila A. Barskiy,[○] Roman V. Shchepin,[○] Aaron M. Coffey,[○] Larisa M. Kovtunova,[§,‖] Andrey V. Bukhtiyarov,[‖] Matthew A. Feldman,[○] Valerii I. Bukhtiyarov,[§,‖] Eduard Y. Chekmenev,[*,⊥,#,○] Igor V. Koptyug,[‡,§] and Boyd M. Goodson[*,†,▽]

[†]Department of Chemistry and Biochemistry, and [▽]Materials Technology Center, Southern Illinois University, Carbondale, Illinois 62901, United States

[‡]International Tomography Center SB RAS, Novosibirsk 630090, Russia

[§]Novosibirsk State University, Novosibirsk 630090, Russia

[‖]Boreskov Institute of Catalysis SB RAS, Novosibirsk 630090, Russia

[⊥]Department of Biomedical Engineering and Physics, Vanderbilt-Ingram Cancer Center (VICC), and [○]Vanderbilt Institute of Imaging Science (VUIIS), Department of Radiology, Vanderbilt University Medical Center, Nashville, Tennessee 37232, United States

[#]Russian Academy of Sciences, Moscow 119991, Russia

S *Supporting Information*

ABSTRACT: The successful transfer of *para*-hydrogen-induced polarization to ^{15}N spins using heterogeneous catalysts in aqueous solutions was demonstrated. Hydrogenation of a synthesized unsaturated ^{15}N-labeled precursor (neurine) with *para*hydrogen (p-H$_2$) over Rh/TiO$_2$ heterogeneous catalysts yielded a hyperpolarized structural analogue of choline. As a result, ^{15}N polarization enhancements of over 2 orders of magnitude were achieved for the ^{15}N-labeled ethyltrimethylammonium ion product in deuterated water at elevated temperatures. Enhanced ^{15}N NMR spectra were successfully acquired at 9.4 and 0.05 T. Importantly, long hyperpolarization lifetimes were observed at 9.4 T, with a ^{15}N T_1 of ~6 min for the product molecules, and the T_1 of the deuterated form exceeded 8 min. Taken together, these results show that this approach for generating hyperpolarized species with extended lifetimes in aqueous, biologically compatible solutions is promising for various biomedical applications.
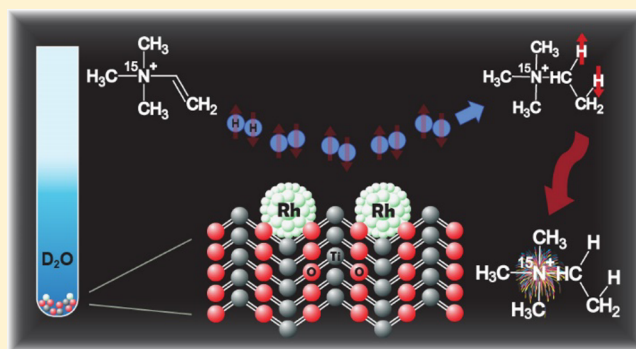
■ INTRODUCTION

Hyperpolarization—the creation of highly nonequilibrium nuclear spin polarization—has been investigated for years as a way to dramatically improve the detection sensitivity of NMR and MRI.[1−8] Although many hyperpolarization methods have been developed, dissolution dynamic nuclear polarization (d-DNP)[9,10] has become increasingly dominant for biomedical applications because of advanced technology enabling the preparation of hyperpolarized (HP) nuclear spins within a wide range of chemical and biological systems, including metabolic MRI contrast agents now under investigation in clinical trials.[11−13] However, the high costs and infrastructure associated with d-DNP technology, combined with relatively slow production rates, present a challenge for many potential applications.

Approaches exploiting *para*-hydrogen-induced polarization (PHIP)[14−17] could be attractive alternatives because of their dramatically lower costs and instrumentation demands, much greater hyperpolarization rates (minutes to seconds, even allowing continuous agent production), and potential for

scalability. In "traditional" PHIP,[15,18] the pure spin order from *para*hydrogen (p-H$_2$) gas is transferred to a molecular substrate via the pairwise hydrogenation of asymmetric unsaturated bonds, a process that is typically facilitated with a catalyst. Key recent PHIP developments for biomedical applications include the demonstration of PHIP in aqueous media[19−25] and PHIP using heterogeneous catalysts (HET-PHIP).[26−30] The latter approach enables facile separation of the catalyst from the target molecule and, hence, the potential preparation of "pure" HP agents and catalyst reuse. However, also of great importance is the transfer of spin order from the nascent protons to substrate heteronuclei (e.g., ^{13}C), providing greater hyperpolarization lifetimes compared to ^{1}H spins. ^{13}C hyperpolarization via PHIP has been achieved via both RF-driven polarization transfer[31−36] and polarization transfer in a magnetic shield (i.e., field cycling),[37,38] an approach that very

recently has been extended to HET-PHIP conditions to produce aqueous solutions of highly polarized ^{13}C-containing molecules free from the catalyst.[27,39]

Translation of this approach to ^{15}N spins could have many advantages; indeed, Aime and co-workers have recently demonstrated ^{15}N hyperpolarization of propargylcholine-^{15}N via homogeneous PHIP and field cycling in a mixture of acetone and methanol or in water.[40] In addition to greatly increasing agent diversity, agents with HP ^{15}N spins can be spectrally sensitive to the local biochemical environment.[41−43] Importantly, ^{15}N T_1 values are often considerably longer than corresponding ^{13}C values,[43−45] thereby enabling longer hyperpolarization storage (either for direct readout or for transfer to ^{1}H for more sensitive detection);[46−52] such T_1 values are expected to be even longer at lower magnetic fields.[53,54]

Herein, we report ^{15}N NMR hyperpolarization of a structural analogue of choline via heterogeneous, aqueous-phase hydrogenation of ^{15}N-trimethyl(vinyl)-ammonium (i.e., neurine-^{15}N) bromide over solid Rh/TiO$_2$ catalysts. The PHIP-derived ^{15}N nuclear spin polarization achieved in these experiments is the first reported to date involving heterogeneous catalysis and yielded ^{15}N enhancements of ∼2 × 10^2-fold and a long relaxation time of ∼350 s at 9.4 T; deuterating the substrate yielded weaker enhancements but a longer relaxation time (^{15}N T_1 ≈ 500 s). Finally, significant signal enhancement is shown for the first time to enable detection at low (0.05 T)[55] magnetic field of the ^{15}N resonance for molecules polarized using PHIP. For most of the heterogeneous hydrogenation reactions in this work, hydrogen gas was used with 50% p-H$_2$ enrichment (the normal room-temperature ratio of $para$- to $ortho$-hydrogen is 25/75) prepared with a home-built generator (more details concerning experiments, chemical synthesis, and characterization are provided in the Supporting Information (SI)).

■ RESULTS AND DISCUSSION

In one experiment, freshly produced p-H$_2$ was bubbled at 90 psi into a medium-wall NMR tube (using a previously developed setup)[27,39] containing the target substrate (neurine-^{15}N bromide) and the heterogeneous catalyst Rh/TiO$_2$ in water (D$_2$O) at 90 °C, causing the unsaturated substrate to be hydrogenated via pairwise addition. The reaction was performed under ALTADENA[56] conditions (i.e., wherein the hydrogenation reaction was performed outside of the magnet at low field), and results are shown in Figure 1 (see also Figures S5 and S8). In order to effect the transfer of spin order from nascent ^{1}H substrate spins to ^{15}N, the hydrogenation reaction was performed by using a magnetic shield, similar to the recently reported procedure—also know as the magnetic field cycling (MFC) approach,[27,57−59] but in our case, the hydrogenation reaction was carried out directly in the magnetic shield. The level of polarization achieved is strongly dependent upon the speed of the sample transfer from the low (micro-Tesla) field to the Earth's field;[40] therefore, to avoid related issues, the hydrogenation reaction was performed directly in the magnetic shield, and only after the termination of p-H$_2$ bubbling was the sample quickly transferred to the high-field NMR for analysis. A strong ^{15}N NMR signal was observed for the HP product (Figure 1B); however, no ^{15}N signal was observed prior to p-H$_2$ bubbling (Figure 1A).

This ^{15}N NMR enhancement was achieved using Rh/TiO$_2$ catalyst with 1.0% Rh loading. Importantly, utilization of Rh/TiO$_2$ solid catalyst for heterogeneous PHIP[60,61] can, in principle, allow one to alter the conversion rate by varying
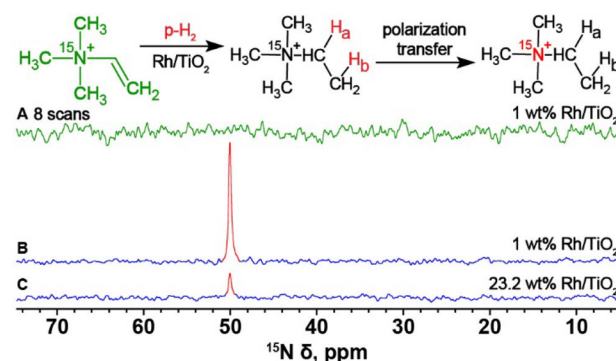

Figure 1. (A) ^{15}N NMR spectrum of a 0.25 M ^{15}N-neurine substrate in the presence of 1.0% Rh/TiO$_2$ before reaction with p-H$_2$ in D$_2$O, recorded with eight scans and a 30 s repetition delay; no signal of reactant is observed at 58 ppm under these conditions. ^{15}N NMR spectrum of the hyperpolarized product using the same acquisition parameters as those used for spectrum acquisition shown in (A) but taken with 1 scan after transfer of spin order to ^{15}N, achieved with 30 s 50%-enriched p-H$_2$ bubbling inside of the magnetic shield. (C) Same as (B) but with hydrogenation occurring over 23.2% Rh/TiO$_2$. HP ^{15}N spectra are shown with an absorptive phase (i.e., sharing the same phase as a thermally polarized ^{15}N sample); note that the field cycling was not optimized for polarization transfer.

the Rh fraction[62] of the catalytic material without decreasing the achieved polarization level of the products.[27] To investigate this possibility for the present reaction, a second Rh/TiO$_2$ catalyst with 23.2% Rh loading was also used (Figure 1C). Although an enhanced ^{15}N signal of the product is observed with the 23.2% Rh/TiO$_2$ catalyst, the signal is ∼3.7-fold weaker than that observed with the 1.0% Rh catalyst. The explanation comes from the corresponding ^{1}H HET-PHIP spectra (Figure S8), which indicate that, while the 23.2% Rh catalyst does indeed yield much higher reaction rates (in fact, providing essentially complete conversion of the substrate in 30 s), a smaller ^{1}H polarization enhancement is achieved, giving rise to the weaker ^{15}N enhancement in Figure 1 (possibly reflecting either reduced pairwise H$_2$ addition or different ^{1}H relaxation of species adsorbed onto catalyst particles). Thus, the 1.0% Rh catalyst was used for the subsequent experiments in this work. In any case, these observations are the first reported to date for hyperpolarization of ^{15}N-containing molecules via heterogeneous catalysis with ^{15}N polarization derived from the spin order from p-H$_2$.

The effects of substrate deuteration and increased p-H$_2$ fraction on ^{15}N signal enhancement were also separately investigated. Deuteration has previously been shown to increase heteronuclear (e.g., ^{13}C) T_1 in the context of PHIP[63,64] and DNP.[65] Here, following successful observation of ^{1}H HET-PHIP with the fully deuterated substrate (neurine-^{15}N-d_{12} bromide; see the SI for synthesis and Figure S9 for spectra), the approach described above was used to demonstrate ^{15}N enhancement of the product in the aqueous phase following heterogeneous hydrogenation (Figure 2A). However, the intensity of this ^{15}N line was slightly lower than that of the fully protonated substrate studied under the same conditions (Figure 2B). This reduced ^{15}N enhancement with deuterated substrates is analogous to that observed with ^{15}N SABRE-SHEATH (Signal Amplification By Reversible Exchange in SHield Enables Alignment to Heteronuclei)[66] and likely reflects either enhanced ^{15}N relaxation in the μT regime (i.e. within the
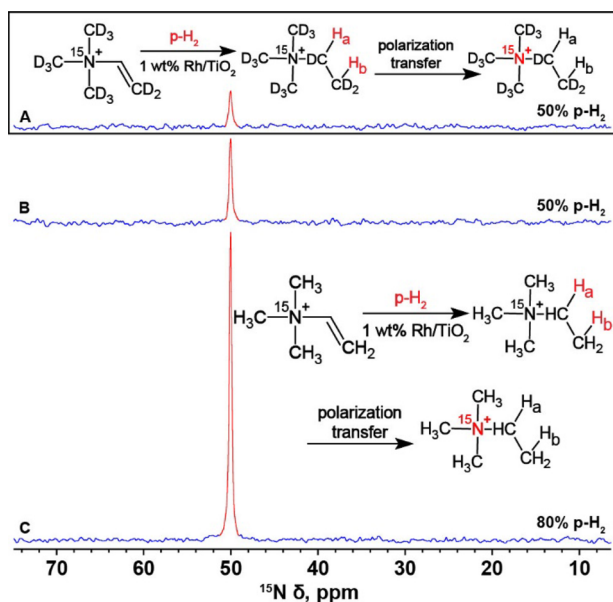
Figure 2. (A) Single-shot ^{15}N NMR spectrum of the fully deuterated substrate (0.125 M) solution in D_2O obtained after 30 s of $p\text{-}H_2$ bubbling (50% $p\text{-}H_2$ fraction) and polarization transfer to ^{15}N using the magnetic shield. (B) Same as (A) but with the protonated substrate (0.125 M). (C) Same as (B) but with an 80% $p\text{-}H_2$ fraction.

magnetic shield) or a more direct loss of spin order into the ^2H spin degrees of freedom under those conditions.

On the other hand, use of a greater $p\text{-}H_2$ fraction with the protonated substrate did yield an expected increase in ^{15}N signal enhancement (Figure 2C). For this experiment, the $p\text{-}H_2$ fraction was increased to 80% using a cryocooler-based $p\text{-}H_2$ generator operating at a temperature lower than the 77 K of lN_2 (see the SI for details). Increasing the ratio of *para-* to *ortho*-H_2 from ~50/50 (Figure 2B) to ~80/20 (Figure 2C) yielded an improvement in the product's ^{15}N signal enhancement by nearly 3-fold, approaching the full 3-fold increase that would be theoretically expected if 100% $p\text{-}H_2$ had been used. Taking the results from Figures 1 and 2 together, the greatest signal enhancement was achieved using 80% $p\text{-}H_2$ on the protonated substrate in the presence of 1.0% Rh/TiO_2.

In PHIP, quantification of the sensitivity gain provided by the polarization level requires not only comparison with a signal from a thermally polarized sample but also an estimation of the efficiency of the hydrogenation reaction (and hence, the concentration of the product) at the time of detection. Here, the HP ^{15}N signal was compared to the thermally polarized signal obtained from a 3.2 M $^{15}NH_4Cl$ aqueous solution. Note that the spectrum in Figure 2C was obtained after the first 30 s of $p\text{-}H_2$ bubbling; comparison with thermal ^{15}N (and ^1H) spectra obtained with different bubbling times allowed the conversion level of the reagent to the product to be estimated at ~10% (see Figure S10C). Therefore, the concentration of the product in Figure 2C is approximately 0.0125 M, yielding a corresponding ^{15}N signal enhancement of $\varepsilon \approx 2 \times 10^2$ (attempts to detect polarization of ^{15}N nuclei at natural abundance were unsuccessful).

While the ^{15}N signal increased steadily with $p\text{-}H_2$ bubbling time for the first 30 s of reaction, after that point, the signal tended to level off until the hydrogenation reaction yield reached 100% (not shown). This behavior could be potentially explained by changes in relaxation of species adsorbed onto the

catalyst particles. Importantly, the ^{15}N hyperpolarization was found to be long-lived at 9.4 T for both the protonated and deuterated substrates, with T_1 decay constants of 348 ± 10 and 494 ± 13 s, respectively (Figure 3), values that are roughly 1–2
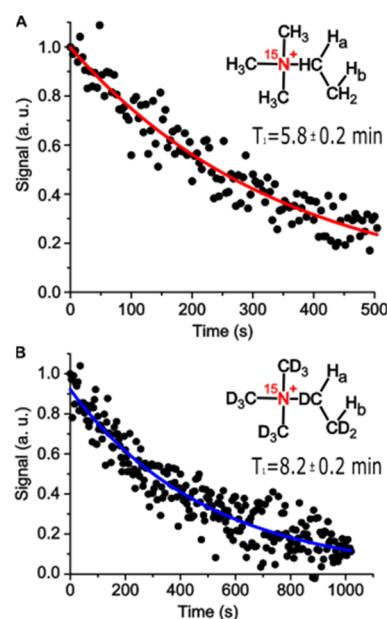

Figure 3. HP ^{15}N T_1 relaxation curves measured at 9.4 T for the protonated (A) and deuterated product (B); curves are exponential fits, giving the ^{15}N T_1 values (not corrected for ~10° tipping-angle pulses) and error margins. Note the >2-fold time axis scale difference.

orders of magnitude longer that the corresponding lifetimes of ^1H hyperpolarization and a factor of 2 larger than that recently reported for ^{15}N derivatives of choline.[40]

Finally, because the magnetization of HP species is not endowed by the NMR/MRI magnet, in principle, strong magnets are not required for detection. To investigate the feasibility of performing low-field NMR/MRI with ^{15}N spins hyperpolarized by HET-PHIP, hydrogenation reaction products for both protonated and deuterated substrates were detected at 0.05 T, Figure 4. Indeed, ^{15}N NMR resonances were successfully detected via low-field ^{15}N NMR spectroscopy at a 210 kHz resonance frequency, with slightly greater signal observed for the protonated versus the deuterated product, which is qualitatively consistent with the high-field results. Higher polarization enhancements enabled by future experimental refinements should boost the signal to noise ratio to allow measurement of the ^{15}N T_1 at low field, where even longer hyperpolarization lifetimes would be expected,[54] thereby improving storage of the HP state.

■ CONCLUSIONS

In summary, heterogeneous Rh/TiO_2 catalysts and MFC were used to achieve ^{15}N hyperpolarization via HET-PHIP for the first time; previous transfers of spin order from $p\text{-}H_2$ to ^{15}N spins had only been achieved under homogeneous catalytic conditions via PHIP/MFC[40] or SABRE-SHEATH.[67,68] ^{15}N nuclear spin polarization enhancements of ~2×10^2 fold (at 9.4 T) were observed in aqueous solutions following hydrogenation of neurine-^{15}N bromide with $p\text{-}H_2$, which yielded a structural analogue of the biological molecule choline (the HP form of which has been shown promising in vivo[45] because of
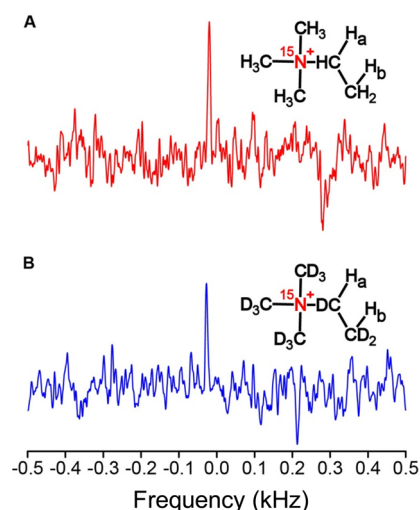
Figure 4. Single-shot low-field (0.05 T) HP ^{15}N NMR spectra of (A) the fully protonated product and (B) the fully deuterated product obtained via heterogeneous hydrogenation of neurine-^{15}N bromide over a 1.0% Rh/TiO$_2$ catalyst with 80% p-H$_2$. Peaks of interest are at an offset of ~(−)0.025 kHz.

the widespread function of choline in cellular metabolism and its significantly upregulated metabolism in cancer).[69,70] Larger enhancements were observed with 1.0 versus 23.2% Rh/TiO$_2$ as well as with higher p-H$_2$ fractions; however, deuteration of the substrate yielded lower enhancements but a longer hyperpolarization lifetime. Indeed, very long ^{15}N T_1 values were observed at 9.4 T for both the protonated and deuterated substrates, ~6 and >8 min, respectively. The ^{15}N hyperpolarization via HET-PHIP also enabled observation of ^{15}N signals at low (0.05 T) field, where even longer hyperpolarization lifetimes are expected, further demonstrating the potential for wider applicability of the approach. Moreover, these results also expand the range of molecules (including biomolecules) amenable to HET-PHIP hyperpolarization. While the molecule hyperpolarized here lacks the −OH moiety found in choline, PHIP precursors for choline hyperpolarization have been previously described.[71] It should also be noted that the heterogeneous catalysts used (Rh/TiO$_2$) are very stable and do not undergo any modifications during reaction (as was confirmed by XPS analysis; see the SI). Therefore, the absence of leaching of the active component of the catalyst material into solution, combined with the ability to use such supported metal catalysts for aqueous-phase heterogeneous hydrogenation (given their potential for facile separation), should allow not only catalyst recycling and reuse but also the preparation of pure HP substances free from the presence of the catalyst. Although the reported polarization values need to be increased further, taken together, these results open a door to the rapid and inexpensive creation of pure agents with long hyperpolarization lifetimes for various biomedical applications, including in vivo molecular MR imaging.

ASSOCIATED CONTENT

Ⓢ Supporting Information

The Supporting Information is available free of charge on the ACS Publications website at DOI: 10.1021/acs.jpcc.7b05912.

Experimental procedures, synthesis of protonated and deuterated substrate molecules, catalyst synthesis,

catalyst characterization (before and after hydrogenation reaction), and additional figures (PDF)

AUTHOR INFORMATION

Corresponding Authors
*E-mail: kovtunov@tomo.nsc.ru (K.V.K.).
*E-mail: eduard.chekmenev@vanderbilt.edu (E.Y.C.).
*E-mail: bgoodson@chem.siu.edu (B.M.G.).

ORCID Ⓞ
Kirill V. Kovtunov: 0000-0001-7577-9619
Danila A. Barskiy: 0000-0002-2819-7584
Andrey V. Bukhtiyarov: 0000-0002-0199-8111
Eduard Y. Chekmenev: 0000-0002-8745-8801
Igor V. Koptyug: 0000-0003-3480-7649
Boyd M. Goodson: 0000-0001-6079-5077

Notes
The authors declare no competing financial interest.

ACKNOWLEDGMENTS

REFERENCES

(1) Green, R. A.; Adams, R. W.; Duckett, S. B.; Mewis, R. E.; Williamson, D. C.; Green, G. G. R. The Theory and Practice of Hyperpolarization in Magnetic Resonance Using Parahydrogen. *Prog. Nucl. Magn. Reson. Spectrosc.* **2012**, *67*, 1−48.

(2) Nikolaou, P.; Goodson, B. M.; Chekmenev, E. Y. NMR Hyperpolarization Techniques for Biomedicine. *Chem. - Eur. J.* **2015**, *21*, 3156−3166.

(3) Bowers, C. R. Sensitivity Enhancement Utilizing Parahydrogen. *Encycl. Magn. Reson.* **2007**, *9*, 4365−4384.

(4) Barskiy, D. A.; Coffey, A. M.; Nikolaou, P.; Mikhaylov, D. M.; Goodson, B. M.; Branca, R. T.; Lu, G. J.; Shapiro, M. G.; Telkki, V.; Zhivonitko, V. V.; et al. NMR Hyperpolarization Techniques of Gases. *Chem. - Eur. J.* **2017**, *23*, 725−751.

(5) Koptyug, I. V. Spin Hyperpolarization in NMR to Address Enzymatic Processes in Vivo. *Mendeleev Commun.* **2013**, *23*, 299−312.

(6) Goodson, B. M. Nuclear Magnetic Resonance of Laser-Polarized Noble Gases in Molecules, Materials, and Organisms. *J. Magn. Reson.* **2002**, *155*, 157−216.

(7) Brindle, K. M. Imaging Metabolism with Hyperpolarized ^{13}C-Labeled Cell Substrates. *J. Am. Chem. Soc.* **2015**, *137*, 6418−6427.

(8) Schroder, L. Xenon for NMR Biosensing - Inert but Alert. *Phys. Medica* **2013**, *29*, 3−16.

(9) Ardenkjaer-Larsen, J. H.; Fridlund, B.; Gram, A.; Hansson, G.; Hansson, L.; Lerche, M. H.; Servin, R.; Thaning, M.; Golman, K. Increase in Signal-to-Noise Ratio of > 10,000 Times in Liquid-State NMR. *Proc. Natl. Acad. Sci. U. S. A.* **2003**, *100*, 10158−10163.

(10) Maly, T.; Debelouchina, G. T.; Bajaj, V. S.; Hu, K.-N.; Joo, C.-G.; Mak-Jurkauskas, M. L.; Sirigiri, J. R.; van der Wel, P. C. A.; Herzfeld, J.; Temkin, R. J.; et al. Dynamic Nuclear Polarization at High Magnetic Fields. *J. Chem. Phys.* **2008**, *128*, 052211.

(11) Nelson, S. J.; Kurhanewicz, J.; Vigneron, D. B.; Larson, P. E. Z.; Harzstark, A. L.; Ferrone, M.; van Criekinge, M.; Chang, J. W.; Park, I.; et al. Metabolic Imaging of Patients with Prostate Cancer Using Hyperpolarized [1-13C]Pyruvate. *Sci. Transl. Med.* **2013**, *5*, 198ra108.

(12) Keshari, K. R.; Wilson, D. M. Chemistry and Biochemistry of 13C Hyperpolarized Magnetic Resonance Using Dynamic Nuclear Polarization. *Chem. Soc. Rev.* **2014**, *43*, 1627−1659.

(13) Kurhanewicz, J.; Vigneron, D. B.; Brindle, K.; Chekmenev, E. Y.; Comment, A.; Cunningham, C. H.; Deberardinis, R. J.; Green, G. G.; Leach, M. O.; Rajan, S. S.; et al. Analysis of Cancer Metabolism by Imaging Hyperpolarized Nuclei: Prospects for Translation to Clinical Research. *Neoplasia* **2011**, *13*, 81−97.

(14) Koptyug, I. V.; Kovtunov, K. V.; Burt, S. R.; Anwar, M. S.; Hilty, C.; Han, S. I.; Pines, A.; Sagdeev, R. Z. Para-Hydrogen-Induced Polarization in Heterogeneous Hydrogenation Reactions. *J. Am. Chem. Soc.* **2007**, *129*, 5580−5586.

(15) Bowers, C. R.; Weitekamp, D. P. Parahydrogen and Synthesis Allow Dramatically Enhanced Nuclear Alignment. *J. Am. Chem. Soc.* **1987**, *109*, 5541−5542.

(16) Adams, R. W.; Aguilar, J. A.; Atkinson, K. D.; Cowley, M. J.; Elliott, P. I. P.; Duckett, S. B.; Green, G. G. R.; Khazal, I. G.; López-Serrano, J.; Williamson, D. C. Reversible Interactions with Para-Hydrogen Enhance NMR Sensitivity by Polarization Transfer. *Science* **2009**, *323*, 1708−1711.

(17) Bowers, C. R.; Weitekamp, D. P. Transformation of Symmetrization Order to Nuclear-Spin Magnetization by Chemical Reaction and Nuclear Magnetic Resonance. *Phys. Rev. Lett.* **1986**, *57*, 2645−2648.

(18) Eisenschmid, T. C.; Kirss, R. U.; Deutsch, P. P.; Hommeltoft, S. I.; Eisenberg, R.; Bargon, J.; Lawler, R. G.; Balch, A. L. Para Hydrogen Induced Polarization in Hydrogenation Reactions. *J. Am. Chem. Soc.* **1987**, *109*, 8089−8091.

(19) Shchepin, R. V.; Coffey, A. M.; Waddell, K. W.; Chekmenev, E. Y. Parahydrogen Induced Polarization of 1-13C-Phospholactate-d_2 for Biomedical Imaging with > 30,000,000-Fold NMR Signal Enhancement in Water. *Anal. Chem.* **2014**, *86*, 5601−5605.

(20) Zacharias, N. M.; Chan, H. R.; Sailasuta, N.; Ross, B. D.; Bhattacharya, P. Real-Time Molecular Imaging of Tricarboxylic Acid Cycle Metabolism in Vivo by Hyperpolarized 1-13C Diethyl Succinate. *J. Am. Chem. Soc.* **2012**, *134*, 934−943.

(21) Shchepin, R. V.; Pham, W.; Chekmenev, E. Y. Dephosphorylation and Biodistribution of 1-13C-Phospholactate in Vivo. *J. Labelled Compd. Radiopharm.* **2014**, *57*, 517−524.

(22) Shchepin, R. V.; Coffey, A. M.; Waddell, K. W.; Chekmenev, E. Y. PASADENA Hyperpolarized 13C Phospholactate. *J. Am. Chem. Soc.* **2012**, *134*, 3957−3960.

(23) Coffey, A. M.; Shchepin, R. V.; Truong, M. L.; Wilkens, K.; Pham, W.; Chekmenev, E. Y. Open-Source Automated Parahydrogen Hyperpolarizer for Molecular Imaging Using 13C Metabolic Contrast Agents. *Anal. Chem.* **2016**, *88*, 8279−8288.

(24) Hövener, J.-B.; Chekmenev, E. Y.; Harris, K. C.; Perman, W. H.; Tran, T. T.; Ross, B. D.; Bhattacharya, P. Quality Assurance of PASADENA Hyperpolarization for 13C Biomolecules. *MAGMA* **2009**, *22*, 123−134.

(25) Bhattacharya, P.; Chekmenev, E. Y.; Reynolds, W. F.; Wagner, S.; Zacharias, N.; Chan, H. R.; Bunger, R.; Ross, B. D. Parahydrogen-Induced Polarization (PHIP) Hyperpolarized MR Receptor Imaging in Vivo: A Pilot Study of 13C Imaging of Atheroma in Mice. *NMR Biomed.* **2011**, *24*, 1023−1028.

(26) Zhou, R.; Zhao, E. W.; Cheng, W.; Neal, L. M.; Zheng, H.; Quiñones, R. E.; Hagelin-Weaver, H. E.; Bowers, C. R. Parahydrogen-Induced Polarization by Pairwise Replacement Catalysis on Pt and Ir Nanoparticles. *J. Am. Chem. Soc.* **2015**, *137*, 1938−1946.

(27) Kovtunov, K. V.; Barskiy, D. A.; Salnikov, O. G.; Shchepin, R. V.; Coffey, A. M.; Kovtunova, L. M.; Bukhtiyarov, V. I.; Koptyug, I. V.; Chekmenev, E. Y. Toward Production of Pure 13C Hyperpolarized Metabolites Using Heterogeneous Parahydrogen-Induced Polarization of Ethyl [1-13C]Acetate. *RSC Adv.* **2016**, *6*, 69728−69732.

(28) Koptyug, I. V.; Zhivonitko, V. V.; Kovtunov, K. V. New Perspectives for Parahydrogen-Induced Polarization in Liquid Phase Heterogeneous Hydrogenation: An Aqueous Phase and ALTADENA Study. *ChemPhysChem* **2010**, *11*, 3086−3088.

(29) Kovtunov, K. V.; Zhivonitko, V. V.; Skovpin, I. V.; Barskiy, D. A.; Koptyug, I. V. Parahydrogen-Induced Polarization in Heterogeneous Catalytic Processes. *Top. Curr. Chem.* **2012**, *338*, 123−180.

(30) Gloggler, S.; Grunfeld, A. M.; Ertas, Y. N.; McCormick, J.; Wagner, S.; Schleker, P. P. M.; Bouchard, L. S. A Nanoparticle Catalyst for Heterogeneous Phase Para-Hydrogen-Induced Polarization in Water. *Angew. Chem., Int. Ed.* **2015**, *54*, 2452−2456.

(31) Goldman, M.; Jóhannesson, H. Conversion of a Proton Pair Para Order into C-13 Polarization by Rf Irradiation, for Use in MRI. *C. R. Phys.* **2005**, *6*, 575−581.

(32) Siddiqui, S.; Kadlecek, S.; Pourfathi, M.; Xin, Y.; Mannherz, W.; Hamedani, H.; Drachman, N.; Ruppert, K.; Clapp, J.; Rizi, R. The Use of Hyperpolarized Carbon-13 Magnetic Resonance for Molecular Imaging. *Adv. Drug Delivery Rev.* **2016**, DOI: 10.1016/j.addr.2016.08.011.

(33) Kadlecek, S.; Emami, K.; Ishii, M.; Rizi, R. Optimal Transfer of Spin-Order between a Singlet Nuclear Pair and a Heteronucleus. *J. Magn. Reson.* **2010**, *205*, 9−13.

(34) Haake, M.; Natterer, J.; Bargon, J. Efficient NMR Pulse Sequences to Transfer the Parahydrogen-Induced Polarization to Hetero Nuclei. *J. Am. Chem. Soc.* **1996**, *118*, 8688−8691.

(35) Bär, S.; Lange, T.; Leibfritz, D.; Hennig, J.; von Elverfeldt, D.; Hövener, J. On the Spin Order Transfer from Parahydrogen to Another Nucleus. *J. Magn. Reson.* **2012**, *225*, 25−35.

(36) Cai, C.; Coffey, A. M.; Shchepin, R. V.; Chekmenev, E. Y.; Waddell, K. W. Efficient Transformation of Parahydrogen Spin Order into Heteronuclear Magnetization. *J. Phys. Chem. B* **2013**, *117*, 1219−1224.

(37) Jóhannesson, H.; Axelsson, O.; Karlsson, M. Transfer of Para-Hydrogen Spin Order into Polarization by Diabatic Field Cycling. *C. R. Phys.* **2004**, *5*, 315−324.

(38) Reineri, F.; Boi, T.; Aime, S. Parahydrogen Induced Polarization of 13C Carboxylate Resonance in Acetate and Pyruvate. *Nat. Commun.* **2015**, *6*, 5858.

(39) Kovtunov, K. V.; Barskiy, D. A.; Shchepin, R. V.; Salnikov, O. G.; Prosvirin, I. P.; Bukhtiyarov, A. V.; Kovtunova, L. M.; Bukhtiyarov, V. I.; Koptyug, I. V.; Chekmenev, E. Y. Production of Pure Aqueous 13C-Hyperpolarized Acetate by Heterogeneous Parahydrogen-Induced Polarization. *Chem. - Eur. J.* **2016**, *22*, 16446−16449.

(40) Reineri, F.; Viale, A.; Ellena, S.; Alberti, D.; Boi, T.; Giovenzana, G. B.; Gobetto, R.; Premkumar, S. S. D.; Aime, S. 15N Magnetic Resonance Hyperpolarization via the Reaction of Parahydrogen with 15N-Propargylcholine. *J. Am. Chem. Soc.* **2012**, *134*, 11146−11152.

(41) Shchepin, R. V.; Barskiy, D. A.; Coffey, A. M.; Theis, T.; Shi, F.; Warren, W. S.; Goodson, B. M.; Chekmenev, E. Y. 15N Hyperpolarization of Imidazole-15N2 for Magnetic Resonance pH Sensing via SABRE-SHEATH. *ACS Sensors* **2016**, *1*, 640−644.

(42) Jiang, W.; Lumata, L.; Chen, W.; Zhang, S.; Kovacs, Z.; Sherry, A. D.; Khemtong, C. Hyperpolarized 15N-Pyridine Derivatives as pH-Sensitive MRI Agents. *Sci. Rep.* **2015**, *5*, 9104.

(43) Nonaka, H.; Hirano, M.; Imakura, Y.; Takakusagi, Y.; Ichikawa, K.; Sando, S. Design of a 15N Molecular Unit to Achieve Long Retention of Hyperpolarized Spin State. *Sci. Rep.* **2017**, *7*, 40104.

(44) Nonaka, H.; Hata, R.; Doura, T.; Nishihara, T.; Kumagai, K.; Akakabe, M.; Tsuda, M.; Ichikawa, K.; Sando, S. A Platform for Designing Hyperpolarized Magnetic Resonance Chemical Probes. *Nat. Commun.* **2013**, *4*, 2411.

(45) Slichter, C. P. The Discovery and Demonstration of Dynamic Nuclear Polarization—a Personal and Historical Account. *Phys. Chem. Chem. Phys.* **2010**, *12*, 5741−5751.

(46) Wang, J.; Kreis, F.; Wright, A. J.; Hesketh, R. L.; Levitt, M. H.; Brindle, K. M. Dynamic 1H Imaging of Hyperpolarized [1-13C]Lactate In Vivo Using a Reverse INEPT Experiment. *Magn. Reson. Med.* **2017**, DOI: 10.1002/mrm.26725.

(47) Chekmenev, E. Y.; Norton, V. A.; Weitekamp, D. P.; Bhattacharya, P. Hyperpolarized ^{1}H NMR Employing Low Nucleus for Spin Polarization Storage. *J. Am. Chem. Soc.* **2009**, *131*, 3164−3165.

(48) Sarkar, R.; Comment, A.; Vasos, P. R.; Jannin, S.; Gruetter, R.; Bodenhausen, G.; Hall, H. H.; Kirik, D.; Denisov, V. P. Proton NMR of ^{15}N-Choline Metabolites Enhanced by Dynamic Nuclear Polarization. *J. Am. Chem. Soc.* **2009**, *131*, 16014−16015.

(49) Pfeilsticker, J. A.; Ollerenshaw, J. E.; Norton, V. A.; Weitekamp, D. P. A Selective ^{15}N-to-^{1}H Polarization Transfer Sequence for More Sensitive Detection of ^{15}N-Choline. *J. Magn. Reson.* **2010**, *205*, 125−129.

(50) Norton, V. A.; Weitekamp, D. P. Communication: Partial Polarization Transfer for Single-Scan Spectroscopy and Imaging. *J. Chem. Phys.* **2011**, *135*, 141107.

(51) Truong, M. L.; Coffey, A. M.; Shchepin, R. V.; Waddell, K. W.; Chekmenev, E. Y. Sub-Second Proton Imaging of ^{13}C Hyperpolarized Contrast Agents in Water. *Contrast Media Mol. Imaging* **2014**, *9*, 333−341.

(52) Mishkovsky, M.; Comment, A.; Gruetter, R. In Vivo Detection of Brain Krebs Cycle Intermediate by Hyperpolarized Magnetic Resonance. *J. Cereb. Blood Flow Metab.* **2012**, *32*, 2108−2113.

(53) Theis, T.; Ortiz, G. X.; Logan, A. W. J.; Claytor, K. E.; Feng, Y.; Huhn, W. P.; Blum, V.; Malcolmson, S. J.; Chekmenev, E. Y.; Wang, Q.; et al. Direct and Cost-Efficient Hyperpolarization of Long-Lived Nuclear Spin States on Universal ^{15}N$_2$-Diazirine Molecular Tags. *Sci. Adv.* **2016**, *2*, e1501438−e1501438.

(54) Colell, J. F. P.; Logan, A. W. J.; Zhou, Z.; Shchepin, R. V.; Barskiy, D. A.; Ortiz, G. X.; Wang, Q.; Malcolmson, S. J.; Chekmenev, E. Y.; Warren, W. S.; et al. Generalizing, Extending, and Maximizing Nitrogen-15 Hyperpolarization Induced by Parahydrogen in Reversible Exchange. *J. Phys. Chem. C* **2017**, *121*, 6626−6634.

(55) Barskiy, D. A.; Salnikov, O. G.; Romanov, A. S.; Feldman, M. A.; Coffey, A. M.; Kovtunov, K. V.; Koptyug, I. V.; Chekmenev, E. Y. NMR Spin-Lock Induced Crossing (SLIC) Dispersion and Long-Lived Spin States of Gaseous Propane at Low Magnetic Field (0.05 T). *J. Magn. Reson.* **2017**, *276*, 78−85.

(56) Pravica, M. G.; Weitekamp, D. P. Net NMR Alignment by Adiabatic Transport of Parahydrogen Addition Products to High Magnetic Field. *Chem. Phys. Lett.* **1988**, *145*, 255−258.

(57) Golman, K.; Axelsson, O.; Johannesson, H.; Mansson, S.; Olofsson, C.; Petersson, J. S. Parahydrogen-Induced Polarization in Imaging: Subsecond ^{13}C Angiography. *Magn. Reson. Med.* **2001**, *46*, 1−5.

(58) Cavallari, E.; Carrera, C.; Boi, T.; Aime, S.; Reineri, F. Effects of Magnetic Field Cycle on the Polarization Transfer from Parahydrogen to Heteronuclei through Long-Range J-Couplings. *J. Phys. Chem. B* **2015**, *119*, 10035−10041.

(59) Shchepin, R. V.; Barskiy, D. A.; Coffey, A. M.; Esteve, I. V. M; Chekmenev, E. Y. Efficient Synthesis of Molecular Precursors for Para-Hydrogen-Induced Polarization of Ethyl Acetate-1-^{13}C and Beyond. *Angew. Chem., Int. Ed.* **2016**, *55*, 6071−6074.

(60) Kovtunov, K. V.; Barskiy, D. A.; Coffey, A. M.; Truong, M. L.; Salnikov, O. G.; Khudorozhkov, A. K.; Inozemtseva, E. A.; Prosvirin, I. P.; Bukhtiyarov, V. I.; Waddell, K. W.; et al. High-Resolution 3D Proton MRI of Hyperpolarized Gas Enabled by Parahydrogen and Rh/TiO$_2$ Heterogeneous Catalyst. *Chem. - Eur. J.* **2014**, *20*, 11636−11639.

(61) Kovtunov, K. V.; Barskiy, D. A.; Salnikov, O. G.; Burueva, D. B.; Khudorozhkov, A. K.; Bukhtiyarov, A. V.; Prosvirin, I. P.; Gerasimov, E. Y.; Bukhtiyarov, V. I.; Koptyug, I. V. Strong Metal-Support Interactions for Palladium Supported on TiO$_2$ Catalysts in the Heterogeneous Hydrogenation with Parahydrogen. *ChemCatChem* **2015**, *7*, 2581−2584.

(62) Burueva, D. B.; Salnikov, O. G.; Kovtunov, K. V.; Romanov, A. S.; Kovtunova, L. M.; Khudorozhkov, A. K.; Bukhtiyarov, A. V.; Prosvirin, I. P.; Bukhtiyarov, V. I.; Koptyug, I. V. Hydrogenation of Unsaturated Six-Membered Cyclic Hydrocarbons Studied by the Parahydrogen-Induced Polarization Technique. *J. Phys. Chem. C* **2016**, *120*, 13541−13548.

(63) Chekmenev, E. Y.; Hövener, J.-B.; Norton, V. A.; Harris, K.; Batchelder, L. S.; Bhattacharya, P.; Ross, B. D.; Weitekamp, D. P. PASADENA Hyperpolarization of Succinic Acid for MRI and NMR Spectroscopy. *J. Am. Chem. Soc.* **2008**, *130*, 4212−4213.

(64) Bhattacharya, P.; Chekmenev, E. Y.; Perman, W. H.; Harris, K. C.; Lin, A. P.; Norton, V. A.; Tan, C. T.; Ross, B. D.; Weitekamp, D. P. Towards Hyperpolarized ^{13}C-Succinate Imaging of Brain Cancer. *J. Magn. Reson.* **2007**, *186*, 150−155.

(65) Allouche-Arnon, H.; Lerche, M. H.; Karlsson, M.; Lenkinski, R. E.; Katz-Brull, R. Deuteration of a Molecular Probe for DNP Hyperpolarization - A New Approach and Validation for Choline Chloride. *Contrast Media Mol. Imaging* **2011**, *6*, 499−506.

(66) Shchepin, R. V.; Truong, M. L.; Theis, T.; Coffey, A. M.; Shi, F.; Waddell, K. W.; Warren, W. S.; Goodson, B. M.; Chekmenev, E. Y. Hyperpolarization of "Neat" Liquids by NMR Signal Amplification by Reversible Exchange. *J. Phys. Chem. Lett.* **2015**, *6*, 1961−1967.

(67) Barskiy, D. A.; Shchepin, R. V.; Coffey, A. M.; Theis, T.; Warren, W. S.; Goodson, B. M.; Chekmenev, E. Y. Over 20% ^{15}N Hyperpolarization in Under One Minute for Metronidazole, an Antibiotic and Hypoxia Probe. *J. Am. Chem. Soc.* **2016**, *138*, 8080−8083.

(68) Theis, T.; Truong, M. L.; Coffey, A. M.; Shchepin, R. V.; Waddell, K. W.; Shi, F.; Goodson, B. M.; Warren, W. S.; Chekmenev, E. Y. Microtesla SABRE Enables 10% Nitrogen-15 Nuclear Spin Polarization. *J. Am. Chem. Soc.* **2015**, *137*, 1404−1407.

(69) Sharma, U.; Baek, H. M.; Su, M. Y.; Jagannathan, N. R. In Vivo ^{1}H MRS in the Assessment of the Therapeutic Response of Breast Cancer Patients. *NMR Biomed.* **2011**, *24*, 700−711.

(70) Dorrius, M. D.; Pijnappel, R. M.; Jansen-van der Weide, M. C.; Jansen, L.; Kappert, P.; Oudkerk, M.; Sijens, P. E. Determination of Choline Concentration in Breast Lesions: Quantitative Multivoxel Proton MR Spectroscopy as a Promising Noninvasive Assessment Tool to Exclude Benign Lesions. *Radiology* **2011**, *259*, 695−703.

(71) Shchepin, R. V.; Chekmenev, E. Y. Synthetic Approach for Unsaturated Precursors for Parahydrogen Induced Polarization of Choline and Its Analogs. *J. Labelled Compd. Radiopharm.* **2013**, *56*, 655−662.

Long-Lived $^{13}C_2$ Nuclear Spin States Hyperpolarized by Parahydrogen in Reversible Exchange at Microtesla Fields

Zijian Zhou,[†] Jin Yu,[†] Johannes F. P. Colell,[†] Raul Laasner,[‡] Angus Logan,[†] Danila A. Barskiy,[§] Roman V. Shchepin,[∥] Eduard Y. Chekmenev,[∥,⊥] Volker Blum,[†,‡] Warren S. Warren,[†,∥] and Thomas Theis*,[†]

[†]Department of Chemistry, Duke University, Durham, North Carolina 27708, United States

[‡]Department of Mechanical Engineering and Materials Science, Duke University, Durham, North Carolina 27708, United States

[§]Departments of Radiology, Biomedical Engineering, and Physics, Vanderbilt University, Institute of Imaging Science (VUIIS), Nashville, Tennessee 37232, United States

[∥]Departments of Radiology, Physics, and Biomedical Engineering, Duke University, Durham, North Carolina 27708, United States

[⊥]Russian Academy of Sciences, 19991 Moscow, Russia

S *Supporting Information*

ABSTRACT: Parahydrogen is an inexpensive and readily available source of hyperpolarization used to enhance magnetic resonance signals by up to four orders of magnitude above thermal signals obtained at ∼10 T. A significant challenge for applications is fast signal decay after hyperpolarization. Here we use parahydrogen-based polarization transfer catalysis at microtesla fields (first introduced as SABRE-SHEATH) to hyperpolarize $^{13}C_2$ spin pairs and find decay time constants of 12 s for magnetization at 0.3 mT, which are extended to 2 min at that same field, when long-lived singlet states are hyperpolarized instead. Enhancements over thermal at 8.5 T are between 30 and 170 fold (0.02 to 0.12% polarization). We control the spin dynamics of polarization transfer by choice of microtesla field, allowing for deliberate hyperpolarization of either magnetization or long-lived singlet states. Density functional theory calculations and experimental evidence identify two energetically close mechanisms for polarization transfer: First, a model that involves direct binding of the $^{13}C_2$ pair to the polarization transfer catalyst and, second, a model transferring polarization through auxiliary protons in substrates.
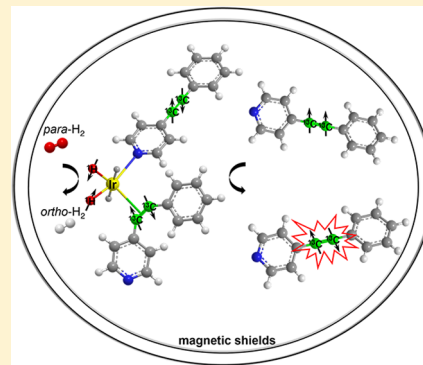
Nuclear spin hyperpolarization is an intriguing research area because of its ability to enhance nuclear magnetic resonance (NMR) and magnetic resonance imaging (MRI) signals by multiple orders of magnitude.[1−5] Hyperpolarization methods are particularly useful if they can enhance signals from heteronuclei such as ^{13}C or ^{15}N because they can be installed in a wide range of biomolecules, and they retain hyperpolarization on extended time scales.[6−14] At the same time, hyperpolarization of protons also has particular advantages, which stem from higher sensitivity and nearly 100% natural abundance. A particularly simple hyperpolarization technique is *para*-H_2-induced polarization (PHIP).[15,16] In particular, when implemented as Signal Amplification By Reversible Exchange (SABRE) it allows for continuous and rapid hyperpolarization directly in solutions.[17,18] In the SABRE procedure, *para*-H_2 and the target (i.e., to-be-hyperpolarized) molecules bind reversibly with an iridium-based hexacoordinate catalyst.[19] At specific magnetic fields, polarization will transfer from *para*-H_2 to spins on the target molecule driven by *J*-coupling interactions; for example ∼6.5 mT is ideal to hyperpolarize proton spins.[17,18] On the contrary, heteronuclei (e.g., ^{15}N, ^{31}P, ^{13}C, ^{19}F) are best magnetized in microtesla fields established in magnetically

shielded environments,[20−2223] an approach that was coined SABRE-SHEATH (SABRE in Shield Enable Alignment Transfer to Heteronuclei).

However, if the goal is to hyperpolarize long-lived singlet states,[6,24−28] then the picture changes slightly because the conditions for the transfer of scalar order have a different field dependence. For example, it has been shown that the singlet state of the $^{15}N_2$ spin pair of diazirines is hyperpolarized over a relatively wide range of magnetic fields between a few microtesla to ∼100 mT.[29] These hyperpolarized nuclear spin singlet states of $^{15}N_2$ diazirines display relaxation time constants of >20 min. Similarly, SABRE was used to hyperpolarize long-lived singlet states on $^1H_2$ pairs,[30,31] where polarization decay time constants of >4 min were observed.[32] Such long hyperpolarization lifetime promises biomolecular tracking and imaging of low-concentration analytes on significantly extended time scales. In this article, we use SABRE-SHEATH to hyperpolarize magnetization as well as long-lived nuclear
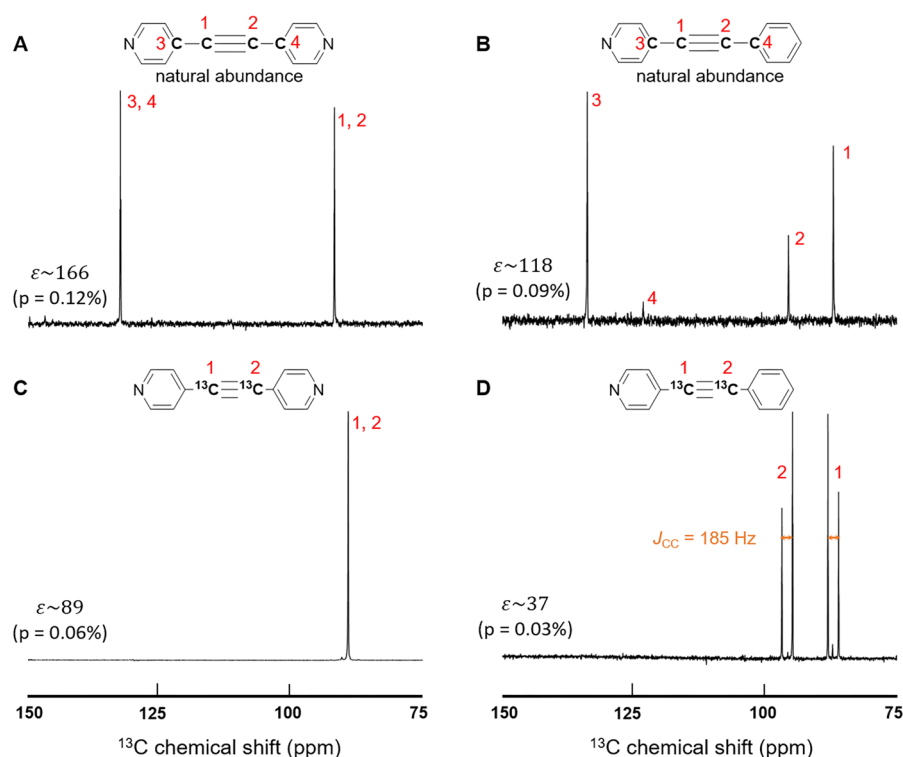
Figure 1. ^{13}C spectra of naturally abundant (A,B) and ^{13}C-labeled (C,D) substrates used in experiments. Panels A and C show results for the symmetrically substituted 1,2-di(4-pyridyl)acetylene. Panels B and D are from the asymmetrically substituted 1-phenyl-2-(4-pyridyl) acetylene. For the naturally abundant substrates the bridge carbons on the pyridyl rings (3,4 in panel A, 3 in panel B) show significant enhancement, while the one on the benzene ring (4 in panel B) is only slightly hyperpolarized. The ^{13}C–^{13}C coupling, J_{CC}, read from the line-splitting in panel D is 185 Hz. (The SI also provides a thermal spectrum in Figure S2.)
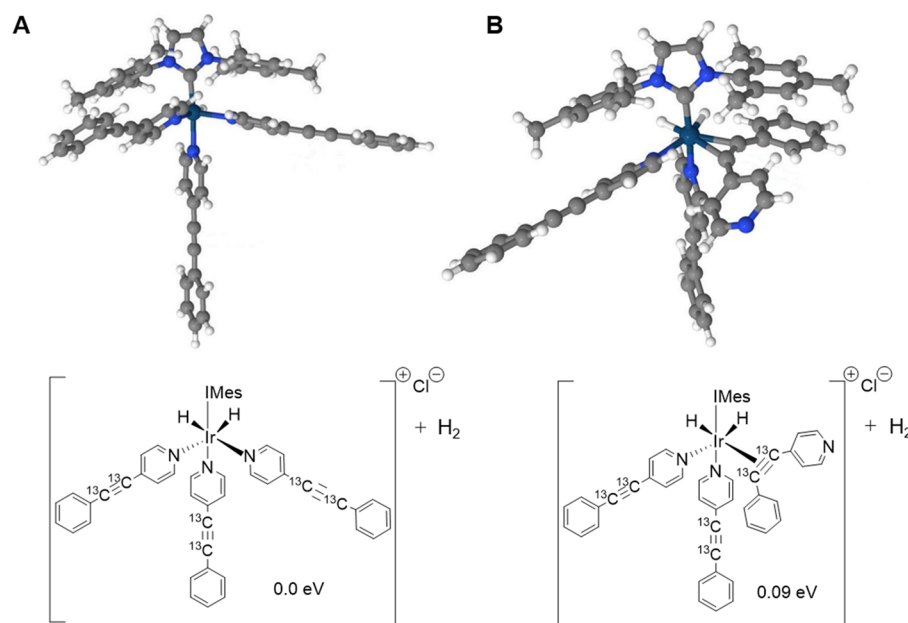
Figure 2. Two possible polarization transfer catalysts (PTCs). Top: 3D models obtained after energy minimization in the all electron code FHI-aims. Bottom: Structural formulas of the PTCs for clarity. (A) Substrate is bound to all Ir binding sites via nitrogen. (B) One of the molecules' triple bond binds to the iridium catalyst, which has a higher energy than the structure in panel A. DFT calculations reveal that the energy difference between the two proposed complexes is relatively small (0.09 eV). Other possible complexes (with higher energies) are discussed in the SI.

singlet states in carbon-13 spin pairs and find lifetime T_1 of 12 s for magnetization and T_S of 2 min for long-lived singlet states at 0.3 mT. Here it is important to note that the current record of a long-lived singlet state is held by a ^{13}C$_2$ spin pair (hyperpolarized by DNP, not SABRE) with lifetime, T_S, of >1 h.[6]

For the presented experiments, we designed two molecules with various isotopic labeling schemes. We synthesized 1,2-(4-pyridyl) acetylene, with symmetric structure, and 1-phenyl-2-(4-pyridyl) acetylene, with asymmetric structure. For both, we consider isotopomers with naturally abundant ^{13}C as well as
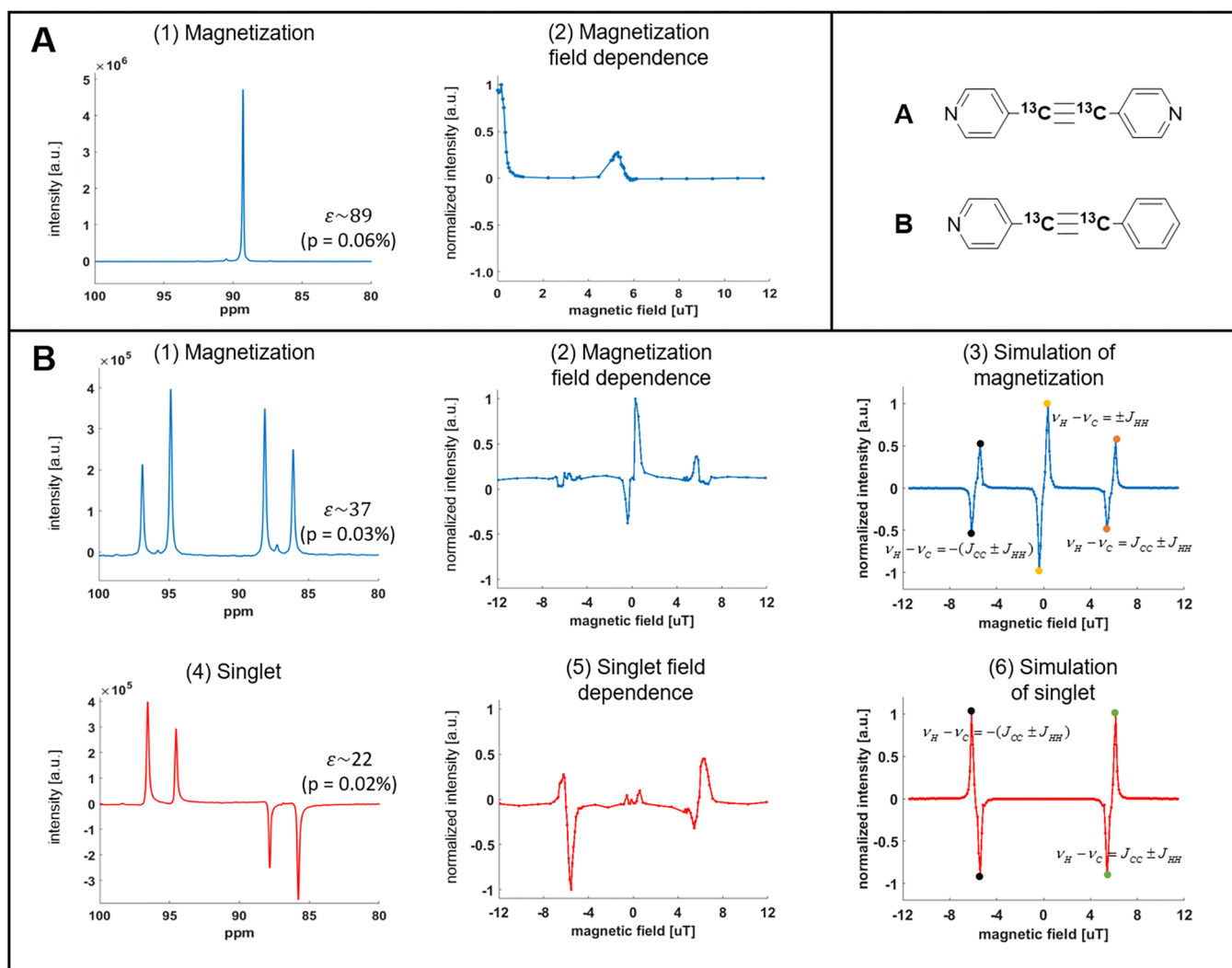
Figure 3. Field-dependent hyperpolarization for the two substrates. (A) (1) a hyperpolarized magnetization spectrum hyperpolarized at 0.17 μT (and acquired at 8.45 T) for the symmetric substrate and (2) its field dependence in the microtesla range. (B) Experimental and simulated results of creating magnetization and singlet order for the asymmetric substrate as a function of magnetic field: (1) Magnetization spectrum hyperpolarized at 0.28 μT. (2) Experimental and (3) simulated field dependence for magnetization. (4) Singlet spectrum hyperpolarized at 6.2 μT. (5) Experimental and (6) simulated field dependence for singlet order. In (B3) and (B6), the highlighted points are the local maxima for polarization transfer labeled by analytically derived resonance conditions from careful inspection of the nuclear-spin Hamiltonian provided in the SI.

doubly ^{13}C-labeled substrates at the triple bond. The results presented in Figure 1 indicate that the acetylene carbon spins as well as the aromatic bridge carbon spins are hyperpolarized. The enhancements are between 30 and 170 fold (0.02 to 0.12% polarization) when compared with thermal signals acquired at 8.45 T. The molecules with ^{13}C at natural abundance show two to three times higher enhancements compared with ^{13}C enriched sites. This is likely due to faster T_1 relaxation in ^{13}C$_2$ pairs as opposed to T_1 of isolated ^{13}C spins. An additional cause may simply be the higher ratio of polarization source (p-H$_2$) to target spins in the naturally abundant case.[33]

The hyperpolarization transfer from para-H$_2$ to these substrates occurs via iridium-based polarization transfer catalysts (PTCs). We used the standard precatalyst [IrCl(IMes)(COD)] (IMes = 1,3-bis(2,4,6-trimethylphenyl)imidazole-2-ylidene; COD = cyclooctadiene).[18,19] We used substrate concentrations of 30 or 160 mM and catalyst concentrations of 2 or 10 mM for the symmetric and asymmetric compounds, respectively. The solvent was methanol-d_4, and the precatalyst was activated by bubbling para-H$_2$ through the sample for 15

min at a pressure of 7 bar and a fractional parahydrogen enrichment of ~85%. Thereafter, hyperpolarization was performed according to the SABRE-SHEATH procedure:[10,20,29] The sample is exposed to para-H$_2$ in a magnetically shielded environment outfitted with a small solenoid coil to obtain a controllable microtesla magnetic field. One minute of exposure to para-H$_2$ is sufficient to equilibrate polarization. Subsequently, the sample is transferred manually as quickly as possible (~8 s) to a Bruker 360 MHz (8.45T) magnet for read out. The manual transfer time of 8 s is relatively consistent, with variations of ~1 s.

The polarization transfer occurs in catalytically active PTCs. Two possible energetically low PTC species are depicted in Figure 2. The ground-state energies were determined by density functional theory (DFT) calculations using the all-electron FHI-aims code.[34] The geometries were optimized using the PBE parametrization of exchange and correlation[35] with a van der Waals correction[36] and the *tier 2* basis sets.[34,37] Scalar relativity was handled in the atomic ZORA approximation.[34] Additional possible configurations and the corre-

sponding PTC-energy landscape are provided in the Supporting Information (SI). Furthermore, we provide ^{1}H NMR spectra of the hyperpolarized hydrides bound to the iridium center, demonstrating the presence of at least two catalytic species (see Figure S2C in the SI). In this first study, we were not able to detect hyperpolarized ^{13}C signals from molecules bound to the iridium molecules. Therefore, we rely on more indirect evidence coupled to ab initio calculations to determine likely PTC structures.

In the first PTC model (Figure 2A), all substrate molecules bind to the Ir center via nitrogen. This is the energetically lowest PTC species identified by us. Here polarization transfers from *para*-H$_2$ to the pyridyl protons first and finally arrives at the acetylenic carbons ("indirect transfer mechanism"). In the second PTC model (Figure 2B), the catalyst binds with the triple bond and polarization is transferred directly to ^{13}C sites ("direct transfer mechanism").

The spectra displayed in Figure 1 could quickly lead to the conclusion that the active PTC must be the directly binding model (Figure 2B) because we do not observe hyperpolarization from the ring carbons, other than from those in the bridge to the acetylene bond. Moreover, we observe hydrogenation, which most certainly requires binding of the triple bond to the iridium center. Hydrogenation rates depend on the ratio of substrate to catalyst: At 3:1 hydrogenation completes in <30 min, however at above 15:1, hydrogenation takes >12 h. In a single SABRE experiment (with 1 min of bubbling) we estimate significantly less than 1% hydrogenation at the 15:1 ratio, which was used for most experiments. We even observe hyperpolarized hydrogenation products that display typical ALTADENA type enhancements due to incorporation of *para*-H$_2$ (spectra provided in the SI), still, keeping in mind that the displayed spectra of Figure 1 must all result from SABRE because they are uniquely associated with the intact, non-hydrogenated substrates.

However, these conclusions may be premature. First, the PTC on of Figure 2A is energetically lower. Furthermore, notice that all nondetected ^{13}C spins are directly bound to protons. This leads to much faster ^{13}C relaxation (a typical T_1 relaxation time for aromatic ^{13}C directly bound to a proton is ~5 s (see ref 38), whereas T_1 relaxation constants of the bridge carbons are found to be 11(1) s and T_1 of the acetylenic carbons is 12(0.5) s at low fields) with two important consequences. First, the hyperpolarization buildup at these ^{13}C sites will be much less efficient, and second, a small amount of hyperpolarization may quickly relax during the ~8 s sample transfer from polarization region into the magnet. In addition, we performed SABRE under optimized condition for ^{1}H polarization transfer at 6.5 mT, and this resulted in strong enhancement of the pyridyl ring protons, while enhancement of ^{13}C was negligible and ^{1}H enhancements on the distant phenyl ring were much smaller. Although bound species are never observed from the ^{13}C spectra, the hydride peaks are available in the SI. We observe a small chemical shift difference of the hydride peaks (~0.2 ppm, which would be much larger for the binding mode in Figure 2B based on DFT calculation). Finally, we attempted to hyperpolarize diphenyl-^{13}C$_2$-acetylene (no ring nitrogens) in the SABRE-SHEATH mode and did not observe enhancements. All of these considerations point to a strong contribution of the PTC shown in Figure 2A.

To investigate this in more detail, we performed a careful characterization of hyperpolarization transfer as a function of microtesla field using the doubly ^{13}C-labeled molecules. As depicted in Figure 3, we varied the magnetic field between −12 and +12 μT, accompanied by simulations of the hyperpolarization transfer process.

The first important finding is that we can directly choose to polarize different states of the ^{13}C pair, magnetization or singlet, which are easily distinguishable by their spectra. Magnetization is easily detected from both molecules (Figure 3A1,B1), whereas singlet order can only be detected immediately from the asymmetric 1-phenyl-2-(4-pyridyl) acetylene because the acetylenic carbons have a chemical shift difference (Figure 1C). For this asymmetric compound, the acetylenic carbons are strongly coupled at low fields (J_{CC} is ~185 Hz, whereas their chemical shift difference, $\Delta\nu_C$, is <0.5 mHz). Upon transfer to the high field in the magnet (8.45 T) for read out, the chemical shift difference becomes significantly larger than the J_{CC} coupling ($\Delta\nu_C \approx 770$ Hz), the carbons are now weakly coupled, and the singlet state is no longer an eigenstate. The sample transfer from low to high field transforms $I_1 \cdot I_2$ singlet order into detectable ($I_{1z} - I_{2z}$), which gives antiphase signals in a pulse acquire experiment, as shown in Figure 3B4. (Full analysis of singlet order transfer is provided in the SI.) However, for the symmetric molecule, because the two carbons will remain symmetric at high field, the singlet state cannot be accessed immediately. In principle, access to the singlet can be accomplished by specialized pulse sequences such as singlet-to-magnetization (S2M)[39,40] or SLIC,[41,42] yet this is beyond the scope of the present work.

To understand the polarization transfer dynamics at microtesla fields in detail, we consider resonance conditions dictated by the Hamiltonian of the doubly ^{13}C labeled molecule. As detailed in the SI, at low fields of <0.6 μT we encounter a resonance condition to polarize magnetization, given as

$$|\nu_H - \nu_C| = \pm J_{HH} \qquad (1)$$

where ν_H and ν_C are the frequencies of protons and carbons and J_{HH} is the J-coupling between the two *para*-H$_2$ derived hydrides on the iridium. When solved for the magnetic field using $\nu = -\gamma B$, we obtain the magnetization transfer field as

$$B_{trans} = \pm J_{HH}/(\gamma_H - \gamma_C) \qquad (2)$$

where $\gamma_H = 42.577$ Hz/μT and $\gamma_C = 10.705$ Hz/μT. When the field is increased to a few microtesla, additional resonance conditions to create magnetization or singlet are encountered. The Hamiltonian reveals overlapping conditions to create magnetization and singlet given as

$$|\nu_H - \nu_C| = \pm(J_{CC} \pm J_{HH}) \qquad (3)$$

where J_{CC} is the acetylenic ^{13}C J-coupling. Again, solving for the transfer field we obtain

$$B_{trans} = \pm(J_{CC} \pm J_{HH})/(\gamma_H - \gamma_C) \qquad (4)$$

Equations 1 and 2 and 3 and 4 fully encompass the behavior observed in Figure 3. In the low-field region, maximum magnetization transfer is observed at ~±0.34(0.1) μT, whereas there is negligible singlet buildup. At slightly elevated fields, both magnetization and singlet have local maxima/minima at ~±5.6(0.2) and ~±6.4(0.2) μT (see Figure 3B). These values are consistent with $J_{HH} \approx 10(3)$ Hz and $J_{CC} \approx 190(5)$ Hz. J_{CC} can also be estimated from the hyperpolarized NMR spectrum of the free form where we find $J_{CC} = 185$ Hz (see Figure 1D).

By numerical simulations of the spin dynamics, we confirm that the general behavior is largely independent of the polarization transfer mechanism (direct to $^{13}C_2$ (Figure 2B) versus indirect via auxiliary protons (Figure 2A); see the SI for details). However, the numerical value of J_{CC} strongly depends on the exact nature of the PTC. We have performed first-principles calculations of the relevant J-couplings using the FHI-aims code.[34] We used the PBE[35] parametrization for exchange and correlation and the fully uncontracted cc-PvSZ[43] basis sets (*tier 2* for iridium[34]). The ab initio calculations predict a J_{CC} of ∼191 Hz for substrate bound via nitrogen (Figure 2A) versus a J_{CC} of 120 Hz for substrate bound directly via the acetylenic bond (see full details in the SI). On the basis of the measurements shown in Figure 3, we can now conclude with more confidence that the primary PTC is the energetically favored species shown in Figure 2A because for the PTC in Figure 2B we would expect efficient hyperpolarization at significantly lower fields of 3.5 ± 0.3 μT, which is not observed.

Finally, because the asymmetric molecule allows for easy read out of both singlet state and magnetization, we can measure their lifetimes T_S or T_1. As displayed in Figure 4, we measured
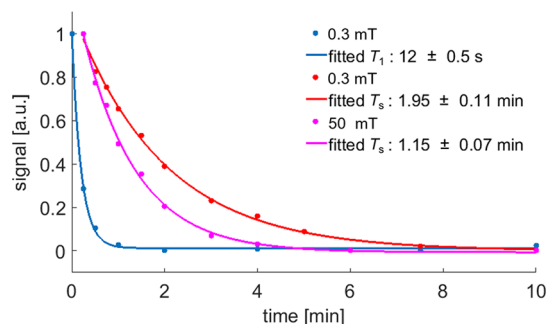

Figure 4. T_1 and T_S measurements of 1-phenyl-2-(4-pyridyl) acetylene. For all measurements, the sample was first hyperpolarized in the shield using 0.4 μT (polarize magnetization)/6 μT (polarize singlet order) then positioned at 0.3 mT or 50 mT. After varying delay times the sample was transferred to the magnet quickly to measure the remaining signal. The data points were sampled randomly to eliminate the effect of the slow triple bond hydrogenation, and the lifetime constants were obtained using single exponential fit.

T_S at 0.3 and 50 mT and fit with exponential decay constants of 117(7) and 69(4) s, respectively. For comparison, we measured T_1 at the field where it has longer T_S (0.3 mT) and find that magnetization decays much more rapidly with exponential decay constant T_1 of 12(0.5) s. The T_1 lifetime of the $^{13}C_2$ pair at 8.45 T is measured as 8(0.4) s.

In conclusion, we demonstrated that both magnetization and long-lived singlet order can be induced on $^{13}C_2$ using SABRE-SHEATH. Hyperpolarization lifetime is extended to ∼2 min, or 10 times T_1. Furthermore, we describe direct hyperpolarization of long-lived singlet order by SABRE-SHEATH when the J-coupling in the targeted spin pair is much larger than the J_{HH} coupling between the hydrides. This is in contrast with the first demonstration, of heteronuclear ($^{15}N_2$) long-lived states hyperpolarized by SABRE, where J_{NN} and J_{HH} were comparable in size, leading to a resonance condition that is matched at a broad range of fields,[29] raising the question if long-lived states could be hyperpolarized when J_{NN} or J_{CC} are much larger. Here we have shown that specific microtesla fields work in that case. Hyperpolarization levels and enhancements remained relatively low in this first demonstration. A likely culprit are the

quadrupolar ^{14}N nuclei, as we are finding that quadrupoles act as highly efficient polarization sinks at microtesla fields.[44] Therefore, we could likely boost hyperpolarization by additional ^{15}N labeling of our substrates and other strategies detailed in the literature.[45−47] Finally, we have also assembled clear evidence of at least two potential PTC species that simultaneously exist in solution. (For example, hydrogenation occurs, which requires direct binding of the $^{13}C_2$ triple bond to Ir. At the same time, the ^1H SABRE experiments presented in Figure S2B of the SI show strongest ^1H enhancements of the ortho protons, which requires polarization transfer in N-bound substrates.) Unraveling these questions, we presented arguments that lead us to believe that polarization transfer to $^{13}C_2$ is primarily mediated indirectly via protons in the substrates. Overall, the presented results illustrate an avenue toward simple and fast hyperpolarization of long-lived ^{13}C hyperpolarization with potential applications in biomolecular MRI or the observation of slower processes by hyperpolarized NMR. The presented advances can be translated to biomolecules already shown to be amenable to heteronuclear SABRE hyperpolarization including nicotinamide,[20,48] in vivo pH sensor imidazole,[49] hypoxia sensor metronidazole,[45] and others.[10,50] While the current work was performed in methanol solutions, recent advances in heterogeneous[51,52] and water-soluble[53−59] SABRE catalysis may lead to in vivo translation of the presented approach for fast hyperpolarization of long-lived ^{13}C molecular probes.

■ ASSOCIATED CONTENT

ⓢ Supporting Information

The Supporting Information is available free of charge on the ACS Publications website at DOI: 10.1021/acs.jpclett.7b00987.

Details of substrate synthesis, experimental setup, ^1H spectra, Matlab simulations (Spinach package) and DFT calculations. (PDF)

■ AUTHOR INFORMATION

Corresponding Author

*E-mail: thomas.theis@duke.edu.

ORCID ⓞ

Johannes F. P. Colell: 0000-0001-9020-344X

Danila A. Barskiy: 0000-0002-2819-7584

Eduard Y. Chekmenev: 0000-0002-8745-8801

Volker Blum: 0000-0001-8660-7230

Thomas Theis: 0000-0001-6779-9978

Notes

The authors declare no competing financial interest.

■ REFERENCES

(1) Ardenkjær-Larsen, J. H.; Fridlund, B.; Gram, A.; Hansson, G.; Hansson, L.; Lerche, M. H.; Servin, R.; Thaning, M.; Golman, K. Increase in signal-to-noise ratio of > 10,000 times in liquid-state NMR. *Proc. Natl. Acad. Sci. U. S. A.* **2003**, *100* (18), 10158−10163.

(2) Ardenkjaer-Larsen, J.-H.; Boebinger, G. S.; Comment, A.; Duckett, S.; Edison, A. S.; Engelke, F.; Griesinger, C.; Griffin, R. G.; Hilty, C.; Maeda, H.; Parigi, G.; Prisner, T.; Ravera, E.; van Bentum, J.; Vega, S.; Webb, A.; Luchinat, C.; Schwalbe, H.; Frydman, L. Facing and Overcoming Sensitivity Challenges in Biomolecular NMR Spectroscopy. *Angew. Chem., Int. Ed.* **2015**, *54* (32), 9162−9185.

(3) Walker, T. G.; Happer, W. Spin-exchange optical pumping of noble-gas nuclei. *Rev. Mod. Phys.* **1997**, *69* (2), 629−642.

(4) Zheng, Y.; Miller, G. W.; Tobias, W. A.; Cates, G. D. A method for imaging and spectroscopy using γ-rays and magnetic resonance. *Nature* **2016**, *537* (7622), 652−655.

(5) Nelson, S. J.; Kurhanewicz, J.; Vigneron, D. B.; Larson, P. E.; Harzstark, A. L.; Ferrone, M.; van Criekinge, M.; Chang, J. W.; Bok, R.; Park, I.; Reed, G.; Carvajal, L.; Small, E. J.; Munster, P.; Weinberg, V. K.; Ardenkjaer-Larsen, J. H.; Chen, A. P.; Hurd, R. E.; Odegardstuen, L. I.; Robb, F. J.; Tropp, J.; Murray, J. A. Metabolic imaging of patients with prostate cancer using hyperpolarized [1-(1)(3)C]pyruvate. *Sci. Transl. Med.* **2013**, *5* (198), 198ra108.

(6) Stevanato, G.; Hill-Cousins, J. T.; Håkansson, P.; Roy, S. S.; Brown, L. J.; Brown, R. C. D.; Pileio, G.; Levitt, M. H. A Nuclear Singlet Lifetime of More than One Hour in Room-Temperature Solution. *Angew. Chem., Int. Ed.* **2015**, *54* (12), 3740−3743.

(7) Keshari, K. R.; Wilson, D. M. Chemistry and biochemistry of 13C hyperpolarized magnetic resonance using dynamic nuclear polarization. *Chem. Soc. Rev.* **2014**, *43* (5), 1627−59.

(8) Tee, S. S.; DiGialleonardo, V.; Eskandari, R.; Jeong, S.; Granlund, K. L.; Miloushev, V.; Poot, A. J.; Truong, S.; Alvarez, J. A.; Aldeborgh, H. N.; Keshari, K. R. Sampling Hyperpolarized Molecules Utilizing a 1 T Permanent Magnetic Field. *Sci. Rep.* **2016**, *6*, 32846.

(9) Nonaka, H.; Hirano, M.; Imakura, Y.; Takakusagi, Y.; Ichikawa, K.; Sando, S. Design of a ^{15}N Molecular Unit to Achieve Long Retention of Hyperpolarized Spin State. *Sci. Rep.* **2017**, *7*, 40104.

(10) Colell, J. F. P.; Logan, A. W. J.; Zhou, Z.; Shchepin, R. V.; Barskiy, D. A.; Ortiz, G. X.; Wang, Q.; Malcolmson, S. J.; Chekmenev, E. Y.; Warren, W. S.; Theis, T. Generalizing, Extending, and Maximizing Nitrogen-15 Hyperpolarization Induced by Parahydrogen in Reversible Exchange. *J. Phys. Chem. C* **2017**, *121* (12), 6626−6634.

(11) Nikolaou, P.; Goodson, B. M.; Chekmenev, E. Y. NMR Hyperpolarization Techniques for Biomedicine. *Chem. - Eur. J.* **2015**, *21* (8), 3156−3166.

(12) Kurhanewicz, J.; Vigneron, D. B.; Brindle, K.; Chekmenev, E. Y.; Comment, A.; Cunningham, C. H.; Deberardinis, R. J.; Green, G. G.; Leach, M. O.; Rajan, S. S.; Rizi, R. R.; Ross, B. D.; Warren, W. S.; Malloy, C. R. Analysis of cancer metabolism by imaging hyperpolarized nuclei: prospects for translation to clinical research. *Neoplasia* **2011**, *13* (2), 81−97.

(13) Brindle, K. M. Imaging Metabolism with Hyperpolarized ^{13}C-Labeled Cell Substrates. *J. Am. Chem. Soc.* **2015**, *137* (20), 6418−6427.

(14) Comment, A.; Merritt, M. E. Hyperpolarized Magnetic Resonance as a Sensitive Detector of Metabolic Function. *Biochemistry* **2014**, *53* (47), 7333−7357.

(15) Bowers, C. R.; Weitekamp, D. P. Transformation of Symmetrization Order to Nuclear-Spin Magnetization by Chemical-Reaction and Nuclear-Magnetic-Resonance. *Phys. Rev. Lett.* **1986**, *57* (21), 2645−2648.

(16) Eisenschmid, T. C.; Kirss, R. U.; Deutsch, P. P.; Hommeltoft, S. I.; Eisenberg, R.; Bargon, J.; Lawler, R. G.; Balch, A. L. Para Hydrogen Induced Polarization in Hydrogenation Reactions. *J. Am. Chem. Soc.* **1987**, *109* (26), 8089−8091.

(17) Adams, R. W.; Aguilar, J. A.; Atkinson, K. D.; Cowley, M. J.; Elliott, P. I.; Duckett, S. B.; Green, G. G.; Khazal, I. G.; Lopez-Serrano, J.; Williamson, D. C. Reversible interactions with para-hydrogen enhance NMR sensitivity by polarization transfer. *Science* **2009**, *323* (5922), 1708−11.

(18) Cowley, M. J.; Adams, R. W.; Atkinson, K. D.; Cockett, M. C. R.; Duckett, S. B.; Green, G. G. R.; Lohman, J. A. B.; Kerssebaum, R.; Kilgour, D.; Mewis, R. E. Iridium N-Heterocyclic Carbene Complexes as Efficient Catalysts for Magnetization Transfer from para-Hydrogen. *J. Am. Chem. Soc.* **2011**, *133* (16), 6134−6137.

(19) Vazquez-Serrano, L. D.; Owens, B. T.; Buriak, J. M. The search for new hydrogenation catalyst motifs based on N-heterocyclic carbene ligands. *Inorg. Chim. Acta* **2006**, *359* (9), 2786−2797.

(20) Theis, T.; Truong, M. L.; Coffey, A. M.; Shchepin, R. V.; Waddell, K. W.; Shi, F.; Goodson, B. M.; Warren, W. S.; Chekmenev, E. Y. Microtesla SABRE Enables 10% Nitrogen-15 Nuclear Spin Polarization. *J. Am. Chem. Soc.* **2015**, *137* (4), 1404−1407.

(21) Truong, M. L.; Theis, T.; Coffey, A. M.; Shchepin, R. V.; Waddell, K. W.; Shi, F.; Goodson, B. M.; Warren, W. S.; Chekmenev, E. Y. ^{15}N Hyperpolarization by Reversible Exchange Using SABRE-SHEATH. *J. Phys. Chem. C* **2015**, *119* (16), 8786−8797.

(22) Zhivonitko, V. V.; Skovpin, I. V.; Koptyug, I. V. Strong ^{31}P nuclear spin hyperpolarization produced via reversible chemical interaction with parahydrogen. *Chem. Commun.* **2015**, *51* (13), 2506−2509.

(23) Shchepin, R. V.; Goodson, B. M.; Theis, T.; Warren, W. S.; Chekmenev, E. Y. Toward Hyperpolarized ^{19}F Molecular Imaging Via Reversible Exchange with Parahydrogen. *ChemPhysChem* **2017**, DOI: 10.1002/cphc.201700594.

(24) Carravetta, M.; Johannessen, O. G.; Levitt, M. H. Beyond the T1 limit: Singlet nuclear spin states in low magnetic fields. *Phys. Rev. Lett.* **2004**, *92*, 153003.

(25) Carravetta, M.; Levitt, M. H. Long-lived nuclear spin states in high-field solution NMR. *J. Am. Chem. Soc.* **2004**, *126* (20), 6228−6229.

(26) Levitt, M. H. Singlet Nuclear Magnetic Resonance. *Annu. Rev. Phys. Chem.* **2012**, *63*, 89−105.

(27) Warren, W. S.; Jenista, E.; Branca, R. T.; Chen, X. Increasing Hyperpolarized Spin Lifetimes Through True Singlet Eigenstates. *Science* **2009**, *323* (5922), 1711−1714.

(28) Vasos, P. R.; Comment, A.; Sarkar, R.; Ahuja, P.; Jannin, S.; Ansermet, J. P.; Konter, J. A.; Hautle, P.; van den Brandt, B.; Bodenhausen, G. Long-lived states to sustain hyperpolarized magnetization. *Proc. Natl. Acad. Sci. U. S. A.* **2009**, *106* (44), 18469−18473.

(29) Theis, T.; Ortiz, G. X.; Logan, A. W. J.; Claytor, K. E.; Feng, Y.; Huhn, W. P.; Blum, V.; Malcolmson, S. J.; Chekmenev, E. Y.; Wang, Q.; Warren, W. S. Direct and cost-efficient hyperpolarization of long-lived nuclear spin states on universal ^{15}N$_2$-diazirine molecular tags. *Sci. Adv.* **2016**, *2* (3), e1501438.

(30) Roy, S. S.; Rayner, P. J.; Norcott, P.; Green, G. G.; Duckett, S. B. Long-lived states to sustain SABRE hyperpolarised magnetisation. *Phys. Chem. Chem. Phys.* **2016**, *18* (36), 24905−24911.

(31) Olaru, A. M.; Roy, S. S.; Lloyd, L. S.; Coombes, S.; Green, G. G. R.; Duckett, S. B. Creating a hyperpolarised pseudo singlet state through polarisation transfer from parahydrogen under SABRE. *Chem. Commun.* **2016**, *52* (50), 7842−7845.

(32) Roy, S. S.; Norcott, P.; Rayner, P. J.; Green, G. G. R.; Duckett, S. B. A Hyperpolarizable ^{1}H Magnetic Resonance Probe for Signal Detection 15 minutes after Spin Polarization Storage. *Angew. Chem.* **2016**, *128* (50), 15871−15874.

(33) Shchepin, R. V.; Truong, M. L.; Theis, T.; Coffey, A. M.; Shi, F.; Waddell, K. W.; Warren, W. S.; Goodson, B. M.; Chekmenev, E. Y. Hyperpolarization of "Neat" Liquids by NMR Signal Amplification by Reversible Exchange. *J. Phys. Chem. Lett.* **2015**, *6* (10), 1961−1967.

(34) Blum, V.; Gehrke, R.; Hanke, F.; Havu, P.; Havu, V.; Ren, X.; Reuter, K.; Scheffler, M. Ab initio molecular simulations with numeric atom-centered orbitals. *Comput. Phys. Commun.* **2009**, *180* (11), 2175−2196.

(35) Perdew, J. P.; Burke, K.; Ernzerhof, M. Generalized Gradient Approximation Made Simple. *Phys. Rev. Lett.* **1996**, *77* (18), 3865−3868.

(36) Tkatchenko, A.; Scheffler, M. Accurate Molecular Van Der Waals Interactions from Ground-State Electron Density and Free-Atom Reference Data. *Phys. Rev. Lett.* **2009**, *102* (7), 073005.

(37) Jensen, S. R.; Saha, S.; Flores-Livas, J. A.; Huhn, W.; Blum, V.; Goedecker, S.; Frediani, L. The Elephant in the Room of Density Functional Theory Calculations. *J. Phys. Chem. Lett.* **2017**, *8* (7), 1449−1457.

(38) Barskiy, D. A.; Shchepin, R. V.; Tanner, C. P. N.; Colell, J. F. P.; Goodson, B. M.; Theis, T.; Warren, W. S.; Chekmenev, E. Y. The Absence of Quadrupolar Nuclei Facilitates Efficient ^{13}C Hyperpolarization via Reversible Exchange with Parahydrogen. *ChemPhysChem* **2017**, DOI: 10.1002/cphc.201700416.

(39) Tayler, M. C. D.; Levitt, M. H. Singlet nuclear magnetic resonance of nearly-equivalent spins. *Phys. Chem. Chem. Phys.* **2011**, *13* (13), 5556−5560.

(40) Feng, Y.; Theis, T.; Liang, X.; Wang, Q.; Zhou, P.; Warren, W. S. Storage of hydrogen spin polarization in long-lived $^{13}C_2$ singlet order and implications for hyperpolarized magnetic resonance imaging. *J. Am. Chem. Soc.* **2013**, *135* (26), 9632−5.

(41) Devience, S.; Walsworth, R.; Rosen, M. In *Spin-Locking Induced Crossing: J-Coupling Spectroscopy at High and Low Fields*, Experimental NMR Conference, Pacific Grove, CA, 2013.

(42) Theis, T.; Feng, Y.; Wu, T.; Warren, W. S. Composite and shaped pulses for efficient and robust pumping of disconnected eigenstates in magnetic resonance. *J. Chem. Phys.* **2014**, *140* (1), 014201.

(43) Dunning, T. H. Gaussian basis sets for use in correlated molecular calculations. I. The atoms boron through neon and hydrogen. *J. Chem. Phys.* **1989**, *90* (2), 1007−1023.

(44) Barskiy, D. A.; Shchepin, R. V.; Tanner, P. N.; Colell, J. F. P.; Goodson, B. M.; Theis, T.; Warren, W. S.; Chekmenev, E. Y. The Absence of Quadrupolar Nuclei Facilitates Efficient ^{13}C Hyperpolarization via Reversible Exchange with Parahydrogen. *ChemPhysChem* **2017**, DOI: 10.1002/cphc.201700416.

(45) Barskiy, D. A.; Shchepin, R. V.; Coffey, A. M.; Theis, T.; Warren, W. S.; Goodson, B. M.; Chekmenev, E. Y. Over 20% ^{15}N Hyperpolarization in Under One Minute for Metronidazole, an Antibiotic and Hypoxia Probe. *J. Am. Chem. Soc.* **2016**, *138* (26), 8080−8083.

(46) Rayner, P. J.; Burns, M. J.; Olaru, A. M.; Norcott, P.; Fekete, M.; Green, G. G. R.; Highton, L. A. R.; Mewis, R. E.; Duckett, S. B. Delivering strong ^1H nuclear hyperpolarization levels and long magnetic lifetimes through signal amplification by reversible exchange. *Proc. Natl. Acad. Sci. U. S. A.* **2017**, *114* (16), E3188−E3194.

(47) Eshuis, N.; Hermkens, N.; van Weerdenburg, B. J. A.; Feiters, M. C.; Rutjes, F. P. J. T.; Wijmenga, S. S.; Tessari, M. Toward Nanomolar Detection by NMR Through SABRE Hyperpolarization. *J. Am. Chem. Soc.* **2014**, *136* (7), 2695−2698.

(48) Shchepin, R. V.; Barskiy, D. A.; Mikhaylov, D. M.; Chekmenev, E. Y. Efficient Synthesis of Nicotinamide-1−^{15}N for Ultrafast NMR Hyperpolarization Using Parahydrogen. *Bioconjugate Chem.* **2016**, *27* (4), 878−882.

(49) Shchepin, R. V.; Barskiy, D. A.; Coffey, A. M.; Theis, T.; Shi, F.; Warren, W. S.; Goodson, B. M.; Chekmenev, E. Y. ^{15}N Hyperpolarization of Imidazole-$^{15}N_2$ for Magnetic Resonance pH Sensing Via SABRE-SHEATH. *ACS Sens.* **2016**, *1*, 640.

(50) Logan, A. W.; Theis, T.; Colell, J. F.; Warren, W. S.; Malcolmson, S. J. Hyperpolarization of Nitrogen-15 Schiff Bases by Reversible Exchange Catalysis with para-Hydrogen. *Chem. - Eur. J.* **2016**, *22* (31), 10777−81.

(51) Shi, F.; Coffey, A. M.; Waddell, K. W.; Chekmenev, E. Y.; Goodson, B. M. Nanoscale Catalysts for NMR Signal Enhancement by Reversible Exchange. *J. Phys. Chem. C* **2015**, *119* (13), 7525−7533.

(52) Shi, F.; Coffey, A. M.; Waddell, K. W.; Chekmenev, E. Y.; Goodson, B. M. Heterogeneous Solution NMR Signal Amplification by Reversible Exchange. *Angew. Chem., Int. Ed.* **2014**, *53* (29), 7495−7498.

(53) Spannring, P.; Reile, I.; Emondts, M.; Schleker, P. P. M.; Hermkens, N. K. J.; van der Zwaluw, N. G. J.; van Weerdenburg, B. J. A.; Tinnemans, P.; Tessari, M.; Blümich, B.; Rutjes, F. P. J. T.; Feiters, M. C. A New Ir-NHC Catalyst for Signal Amplification by Reversible Exchange in D_2O. *Chem. - Eur. J.* **2016**, *22* (27), 9277−9282.

(54) Shi, F.; He, P.; Best, Q.; Groome, K. A.; Truong, M. L.; Coffey, A. M.; Zimay, G.; Shchepin, R. V.; Waddell, K. W.; Chekmenev, E. Y.; Goodson, B. M. Aqueous NMR Signal Enhancement by Reversible Exchange in a Single Step Using Water-Soluble Catalysts. *J. Phys. Chem. C* **2016**, *120* (22), 12149−12156.

(55) Hövener, J.-B.; Schwaderlapp, N.; Borowiak, R.; Lickert, T.; Duckett, S. B.; Mewis, R. E.; Adams, R. W.; Burns, M. J.; Highton, L. A. R.; Green, G. G. R.; Olaru, A.; Hennig, J.; von Elverfeldt, D. Toward Biocompatible Nuclear Hyperpolarization Using Signal Amplification by Reversible Exchange: Quantitative in Situ Spectroscopy and High-Field Imaging. *Anal. Chem.* **2014**, *86* (3), 1767−1774.

(56) Rovedo, P.; Knecht, S.; Baumlisberger, T.; Cremer, A. L.; Duckett, S. B.; Mewis, R. E.; Green, G. G.; Burns, M.; Rayner, P. J.; Leibfritz, D.; Korvink, J. G.; Hennig, J.; Putz, G.; von Elverfeldt, D.; Hovener, J. B. Molecular MRI in the Earth's Magnetic Field Using Continuous Hyperpolarization of a Biomolecule in Water. *J. Phys. Chem. B* **2016**, *120* (25), 5670−7.

(57) Zeng, H.; Xu, J.; McMahon, M. T.; Lohman, J. A. B.; van Zijl, P. C. M. Achieving 1% NMR polarization in water in less than 1 min using SABRE. *J. Magn. Reson.* **2014**, *246*, 119−121.

(58) Truong, M. L.; Shi, F.; He, P.; Yuan, B.; Plunkett, K. N.; Coffey, A. M.; Shchepin, R. V.; Barskiy, D. A.; Kovtunov, K. V.; Koptyug, I. V.; Waddell, K. W.; Goodson, B. M.; Chekmenev, E. Y. Irreversible Catalyst Activation Enables Hyperpolarization and Water Solubility for NMR Signal Amplification by Reversible Exchange. *J. Phys. Chem. B* **2014**, *118* (48), 13882−13889.

(59) Colell, J. F. P.; Emondts, M.; Logan, A. W. J.; Shen, K.; Bae, J.; Shchepin, R. V.; Ortiz, G. X.; Spannring, P.; Wang, Q.; Malcolmson, S. J.; et al. Direct Hyperpolarization of Nitrogen-15 in Aqueous Media with Parahydrogen in Reversible Exchange. *J. Am. Chem. Soc.* **2017**, DOI: 10.1021/jacs.7b00569.

Generalizing, Extending, and Maximizing Nitrogen-15 Hyperpolarization Induced by Parahydrogen in Reversible Exchange

Johannes F. P. Colell,[†] Angus W. J. Logan,[†] Zijian Zhou,[†] Roman V. Shchepin,[‡] Danila A. Barskiy,[‡] Gerardo X. Ortiz, Jr.,[†] Qiu Wang,[†] Steven J. Malcolmson,[†] Eduard Y. Chekmenev,[‡,§] Warren S. Warren,*[,†,‖] and Thomas Theis*[,†]

[†]Department of Chemistry, Duke University, Durham, North Carolina 27708, United States

[‡]Vanderbilt University Institute of Imaging Science (VUIIS), Department of Radiology, Department of Biomedical Engineering, Vanderbilt Ingram Cancer Center (VICC), Vanderbilt University, Nashville, Tennessee 37232, United States

[§]Russian Academy of Sciences, Moscow, Russia

[‖]Departments of Physics, Radiology and Biomedical Engineering, Duke University, Durham, North Carolina 27707, United States

S Supporting Information

ABSTRACT: Signal Amplification by Reversible Exchange (SABRE) is a fast and convenient NMR hyperpolarization method that uses cheap and readily available *para*-hydrogen as a hyperpolarization source. SABRE can hyperpolarize protons and heteronuclei. Here we focus on the heteronuclear variant introduced as SABRE-SHEATH (SABRE in SHield Enables Alignment Transfer to Heteronuclei) and nitrogen-15 targets in particular. We show that ^{15}N-SABRE works more efficiently and on a wider range of substrates than ^{1}H-SABRE, greatly generalizing the SABRE approach. In addition, we show that nitrogen-15 offers significantly extended T_1 times of up to 12 minutes. Long T_1 times enable higher hyperpolarization levels but also hold the promise of hyperpolarized molecular imaging for several tens of minutes. Detailed characterization and optimization are presented, leading to nitrogen-15 polarization levels in excess of 10% on several compounds.
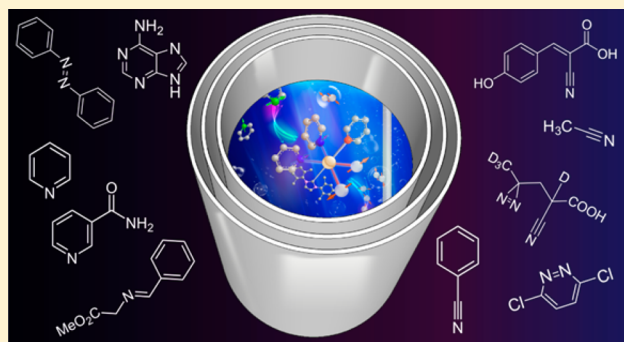
INTRODUCTION

Hyperpolarization techniques enhance nuclear polarization and nuclear magnetic resonance (NMR) signals by 4 to 8 orders of magnitude.[1−11] The concomitant increase of signal-to-noise (S/N) has opened new opportunities for *in vitro* NMR studies such as nanomolar detection[12−15] and *in vivo* MRI with direct access to metabolic activity on the molecular level.[16−20]

Signal Amplification By Reversible Exchange (SABRE)[21] is the nonhydrogenative variant of *para*-hydrogen induced polarization (PHIP).[22−25] A hydrogenation reaction is not required, and substrates can be hyperpolarized continuously or repeatedly. Furthermore, SABRE occurs in the liquid state at room temperature and requires only inexpensive equipment.[21,26,27] As depicted in Scheme 1, SABRE uses a transition metal catalyst to establish contact between the polarization source, *para*-H$_2$, and the target nuclei.

Specifically, magnetic contact is established by the *J*-coupling of the *para*-H$_2$-derived hydrides to the target nuclei across the iridium center. Reversible exchange of hydrides and substrate leads to continuous hyperpolarization buildup on the substrate as long as fresh *para*-H$_2$ is supplied. Accordingly, SABRE has also been referred to as polarization transfer catalysis (PTC).[28]

Scheme 1. Reversible Exchange of *para*-H$_2$ and Substrate on the Polarization Transfer Catalyst Leads to Continuous Buildup of Polarization on the Free Substrate[a]
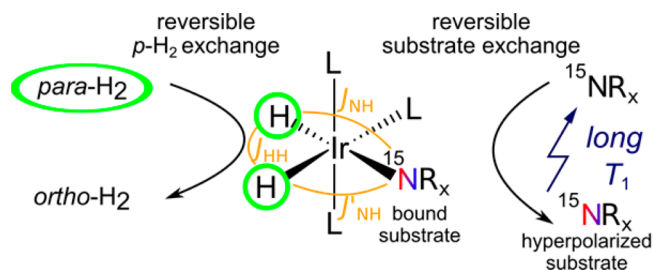
[a]The *J*-couplings in the polarization transfer complex drive the polarization transfer. L: Ligands. Rx: arbitrary group.

Until recently, SABRE was primarily focused on ^{1}H nuclei, where T_1 is typically short (several seconds), and high ^{1}H polarization levels (1%) are observed predominantly for Lewis

basic N-heterocyclic molecules. On the other hand, hetero-nuclei (e.g., ^{15}N, ^{13}C, ^{31}P) offer long T_1 relaxation times, in particular at low magnetic fields, and allow for large polarization levels for a wider variety of structural motifs. As demonstrated recently, heteronuclei are most efficiently targeted when conducting SABRE at magnetic fields of a few μT inside magnetically shielded environments (SABRE-SHEATH).[29−31] Here we focus on the direct hyperpolarization of nitrogen-15 at μT magnetic evolution fields. The relatively simple exper-imental procedure is shown in the Supporting Information video.

The present contribution presents three major points. First, we demonstrate that the substrate scope is significantly expanded with SABRE-SHEATH. This is because nitrogen is directly bound to iridium, unlike the protons in the R-groups. Second, we show that long T_1 lifetimes, in excess of 10 min, can be obtained at relatively low fields in 1 T permanent magnets. This is significant because the combination of low cost hyperpolarization with low cost NMR detection sets the stage for affordable and highly sensitive NMR spectroscopy and molecular magnetic resonance imaging (MRI). Lastly, we optimize the SABRE-SHEATH process in detail leading to nitrogen-15 hyperpolarization in excess of 10%.
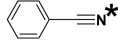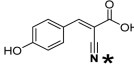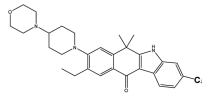
■ METHODS
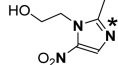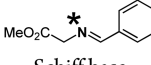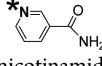
Methanol-d_4 solutions with defined concentrations of precata-lyst ([IrCl(COD)(IMes)]; COD = 1,5-cyclooctadiene; IMes = 1,3-bis(2,4,6-trimethylphenyl)-imidazol-2-ylidene, substrate (Sub), and coligand (L) were converted to catalytically active solutions of ([Ir(H)$_2$(IMes)L$_x$Sub$_{3−x}$]) by bubbling hydrogen gas through these solutions. The pressure was regulated to 10 bar. The pressure gradient across the sample was negligible (<0.1 bar), just enough to establish the desired flow rate (typically 60 sccm ≈ 6 ccm at 10 bar). The flow rate is set with a needle valve at the outlet after the bubbling stage, directly venting the hydrogen gas into a hood.

The sample volume was 500 μL inside a medium-walled 5 mm pressure NMR tube (Wilmad 524-PV-8). The para-H$_2$ fraction was 80−90% unless noted otherwise. After a suitable activation period (10 min to 1 h), samples were placed in a defined magnetic evolution field B_{evo} in the μT range. Evolution time in the shield exceeded the build-up time to yield maximal signal intensity. The T_1 measurements were performed from a single hyperpolarization process by a sequence of small tip angle (6°) pulses. Measurements at 1 T were performed in a benchtop NMR instrument (Magritek 15N-Spinsolve). Meas-urements at 8.45 T were carried out on a Bruker Avance DX360 NMR spectrometer. See Supporting Information (SI) for additional experimental details, a theoretical model of SABRE-SHEATH, as well as a video illustrating experiments.

■ RESULTS AND DISCUSSION

I. Expansion of Substrate Range. The generalized substrate scope is illustrated in Table 1. (Full experimental details are provided in the SI). The results suggest that, in general, sp and sp^2-hybridized ^{15}N sites can be hyperpolarized. This is significant because sp and sp^2 hybridized nitrogens are found in a wide range of metabolites and drugs.[32] It is noteworthy that ^{1}H enhancements are negligible, except for Entries 5 and 8, formally imidazole and pyridine derivatives. Table 1 includes T_1 values, where available; however, they vary

Table 1. ^{15}N-SABRE-SHEATH Enhancements (ε) over Thermal Measurements at 8.5 T, Polarization Levels, and T_1 in Methanol-d_4 for Diverse Molecular Motifs^d

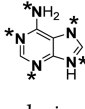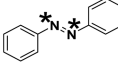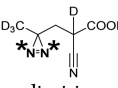| Entry	Substrate	ε	P [%]	T_1 [min]
1	acetonitrile	4,400	1.3	3.5 @ 1 T
2	benzonitrile	21,000	6.8	12 @ 1 T
3	CHCA	3,600	1.1	1.2 @ 1 T in D2O
4	alectinib	5,000	1.5	N/A
5	metronidazole	72,000	24	0.6 @ 9.4 T
6	Schiff base	7,200	2.1	2.2 @ 1 T
7	dichloropyridazine	12,000	3.5	0.25 T$_S$: 0.6 @8.5 T
8	nicotinamide	11,000[a]	3.4	2.1 @ 1 T in D2O
9	imidazole	2,000[a]	0.58[a]	0.4 @9.4 T
10	adenine	200[b]	0.06	N/A
11	diphenyldiazene	> 40[c]	>0.01	0.15 T$_S$: 1 @ 8.5 T
12	diazirine	15,000	4.4	5 T$_S$: 23 @0.3 mT

^{a}Data obtained with 50% para-H2. ^{b}Enhancements averaged over all ^{15}N sites. ^{c}SABRE hyperpolarizes the Z-isomer. See SI for additional information. ^{d}∗ indicates hyperpolarized site.

strongly with concentration, solvent, and magnetic field (see below).

The first four entries are nitriles (sp-hybrid ^{15}N), commonly encountered in biologically active molecules and drugs.[32] Nitriles have been reported as ^{1}H-SABRE substrates, but enhancements did not exceed ∼60-fold (over 9.4 T).[33] In contrast, with SABRE-SHEATH, nitriles consistently show polarization levels of several percent (see Table 1). Nitriles are particularly versatile; polarization levels remain large irrespec-

Table 2. Comparison of Spin−Lattice Relaxation Times T_1 and Signal-to-Noise in a Single 90°-Acquired Experiment of Dilute (Methanol-d_4) and Neat Solutions at 8.5 and 1 T[a]

compound	conc. [mM]	T_1 @ 8.5 T [min]	T_1 @ 1 T [min]	S/N @ 8.5 T	S/N @ 1 T
^{15}N-pyridine	50	1.05 ± 0.02	2.06 ± 0.13	5700	1500
^{15}N-acetonitrile	50	2.05 ± 0.02	3.73 ± 0.05	5000	2900
^{15}N-benzonitrile	50	2.15 ± 0.02	11.95 ± 0.35	7300	1400
^{15}N$_2$-diazirine	50	0.16 ± 0.002	4.35 ± 0.1	1200	1300
pyridine	neat (12.4 M)	1.5 ± 0.05	3.31 ± 0.3	300	300
pyridine-d_5	neat (12.4 M)	1.6 ± 0.02	3.68 ± 0.45	1300	400
acetonitrile	neat (19.1 M)	2.2 ± 0.05	2.3 ± 0.4	1000	200
acetonitrile-d_3	neat (19.1 M)	2.36 ± 0.03	2.01 ± 0.1	1900	400
benzonitrile	neat (9.7 M)	2.88 ± 0.03	10.5 ± 1	7100	2600

[a]Neat solutions have ^{15}N at natural abundance (0.36%).

tive of the backbone structure or system composition. Many substituents, including unsaturated bonds, hydroxyl and carboxylic acid groups are tolerated. Examples are α-cyano-4-hydroxycinnamic acid (CHCA, entry 3) with potentiating effects for chemotherapy[34] and alectinib (entry 4), a potent inhibitor of anaplastic lymphoma kinase (ALK) also used for the treatment of nonsmall cell lung cancer.

The remaining entries in Table 1 (entries 6−12) all contain sp²-hybridized ^{15}N. As a first example, metronidazole (entry 5) is an antibiotic also used as a hypoxia probe.[35−39] Very high polarization levels are observed for this molecule, when nitrogen is at its natural abundance of 0.36%. Next, we found that ^{15}N nuclei in a wide range of Schiff bases (entry 6), which included biologically relevant scaffolds, such as pyridoxal phosphate analogues and retinal with critical roles in visual signaling, hyperpolarize well.[40−42]

Dichloropyridazine (entry 7) also illustrates the basic principle: the ^{15}N sites hyperpolarize well, whereas the protons do not because they do not directly interact with the catalyst. This molecule also is the first example with two adjacent ^{15}N nuclei, offering the opportunity to store hyperpolarization in long-lived singlet states characterized by extended decay time constants T_S.[43]

A further interesting substrate is nicotinamide (vitamin B$_3$, entry 8) with its important functions in mammalian metabolism.[44−47] A significant opportunity in current medical imaging is presented by imidazole (entry 9) which has a pK_A of ∼7.1, ideal for in vivo pH sensing.[48] Furthermore, nucleobases, such as adenine (entry 10), are also amendable to hyperpolarization. Surprisingly, enhancements can be detected for all nitrogen positions including the amino group, presumably due to the existence of the enamine−imine tautomer, which is structurally similar to Schiff bases (or indirect polarization transfer). Diphenyldiazene (entry 11) exhibits E/Z isomerism induced optically,[49,50] or chemically.[51] Interestingly the Z form is hyperpolarized exclusively despite the fact that the E form is thermodynamically stable. Enhancements of the Z-form, in presently unknown low concentration, significantly exceed 40-fold (see SI). The last entry, a diazirine (entry 12), stands out as it offers particularly long decay time constants, T_1 of 5 min and T_S of above 20 min, allowing for detection of enhanced signal for hours after polarization buildup. These diazirine moieties can readily be incorporated in a wide range of drugs or biomolecules replacing CH$_2$− groups.[52]

The lowest enhancements are recorded for imidazole (entry 9)[48] and adenine (entry 10) with exchanging protons at the ^{15}N sites. This causes shorter T_1 times and significant polarization losses during transfer to the detection field (∼8 s in our

experiments). For substrates with exchanging protons higher pH values are associated with larger enhancements because deprotonated forms bind to the catalyst more easily and because T_1 is longer on deprotonated ^{15}N.

II. Extended Relaxation Times. Nitrogen-15 SABRE is particularly appealing because many substrates show large T_1 times, which enables the observation of slow processes, such as diffusion, biochemical reactions, or downstream metabolic processes. Table 2 lists T_1 times and S/N (signal-to-noise) for various substrates at two different magnetic fields, 8.5 and 1 T. Measurements at 1 T were performed in an inexpensive, portable benchtop NMR instrument (Magritek 15N-Spinsolve), illustrating the potential of low-cost high-sensitivity NMR when combining SABRE hyperpolarization with permanent magnet-based technology. Since most clinical MRI scanners operate in the 1−3 T range, measurements at 1 T are useful for future biomedical translation.

The results clearly show that T_1 times strongly depend on the magnetic field and molecular structure. The molecular environment of the respective spin determines which relaxation mechanism is relevant. Usually, NMR relaxation is dominated by dipolar relaxation, caused by other nearby spins, and has a relatively weak field dependence. However, nitrogen-15, which is often far removed from other spins, can be dominated by chemical shift anisotropy (CSA) relaxation. Under these circumstances a strong field dependence is expected because CSA relaxation scales with B_0^2.[53]

This is best exemplified by ^{15}N-benzonitrile and ^{15}N$_2$-diazirine. In benzonitrile dipolar relaxation is minimized, as protons are far away from the nitrogen nucleus. We observe $T_1 \approx 2.15$ min at 8.5 T and $T_1 \approx 11.95$ min at 1 T; CSA dominates relaxation. In the ^{15}N$_2$-diazirine the field dependence is even more pronounced. At 8.5 T we measure T_1 of ∼10 s, but at 1 T, $T_1 \approx 4.35$ min. Note that we recently also reported the relaxation time constant of the long-lived singlet state in diazirine with T_S in excess of 20 min at $B_0 = 0.3$ mT.[52]

Now we focus our attention on the S/N comparison between the investigated magnetic fields. In NMR with thermally polarized spins, signal scales with B_0^2, as, both, polarization and induction are proportional to B_0.[53,54]

The noise, on the other hand (in the coil noise dominated regime), scales with $B_0^{1/4}$; hence S/N scales with $B_0^{7/4}$.[54−56] However, if the polarization source is an external hyperpolarizer, spin polarization is no longer determined by B_0 and S/N scales as $B_0^{3/4}$. The expected signal loss in our experiments when going from 8.5 to 1 T is thus $(8.5/1)^{3/4} \approx 5$. However, it is evident from Table 2 that measurements at 1 T are on average only 2.8 times less sensitive than at 8.5 T. This can be

attributed to different pickup-coil design, where coil sensitivity is higher at 1 T as the inductance in solenoid coils (used at 1 T) is larger than in saddle coils (used at 8.5 T).[57] An additional factor is relaxation during sample transfer from the hyper-polarization region to detection fields (∼1 s to 1 T, ∼8 s to 8.5 T). The latter effect is best exemplified by the molecule with the most pronounced field dependence of the relaxation time ($^{15}N_2$ diazirine). In this case, the S/N is better at 1 T than at 8.5 T because of reduced relaxation losses in 1 T experiments. Notice that the S/N comparisons were performed without additional delays before acquisition. With additional delays, the low-field experiments would be more favorable because of extended T_1.

For future applications, an important scenario is body-noise-dominated magnetic resonance, as is the case for human MRI. Here body-noise (dielectric loss) dominates, and the S/N with thermal magnetization is proportional to B_0.[55,58] Accordingly, for hyperpolarized MRI, S/N is expected to be directly proportional to hyperpolarization level and independent of B_0.[57,59] Therefore, NMR and MRI in low fields are of great general interest as magnet and RF-circuit design is more flexible, and devices are portable and relatively cheap.[59,60] For example, recent advances in low-field MRI have already enabled high performance ^1H-MRI at fields as low as 6.5 mT, even using thermal magnetization.[61] The newest advances, such as "External High-Quality-factor-Enhanced NMR" (EHQE-NMR)[62] and others,[63] lead to independence of B_0, even for spectroscopic applications of hyperpolarized MR.

Both the presented T_1 lifetime and S/N results suggest that NMR and MRI with hyperpolarized heteronuclei can benefit from low fields. Especially, the combination of a simple hyperpolarization technique like SABRE with low-field detection appears as a powerful approach. Costs go down, and relaxation times go up without sacrificing S/N. With SABRE-SHEATH, ^{15}N-labeled markers can be hyperpolarized continuously or repeatedly, directly in room-temperature solutions. Thus, low-field NMR and MRI with SABRE may enable high sensitivity NMR and MRI for a large audience at moderate cost with many applications.[64,65]

III. Analysis of Temperature and Field Dependence.
Enhancements and polarization levels reported in Table 1 are not optimized with respect to all variables affecting efficiency, i.e., catalyst and substrate concentrations, coligand concentration, para-H_2 pressure/flow rate, temperature, magnetic field, etc. The experimental efforts involved in globally optimizing this multidimensional parameter space would not be practicable for all substrates.

Here we focus on the dependence of polarization on magnetic evolution field B_{evo} and average complex lifetime τ_{life} using a suitable model system. This model system needs to exhibit large, stable enhancements over many experiments and have a relatively quick polarization buildup (<5 min), and continuous repetition of experiments must be possible. We use a system similar to Mewis et al.,[33] i.e., acetonitrile-15N (100 mM), IrCl(IMes) (COD) (5 mM), and pyridine (33 mM) in methanol-d_4. (Pyridine is added for stability; without this coligand experiments were inconsistent.) Note that ^1H enhancements did not exceed 60-fold (over thermal polarization at 9 T),[33] whereas ^{15}N exhibits more than 4000-fold enhancement. This particular system composition yields large S/N and long-term stability, not maximum ^{15}N-polarization (vide infra).
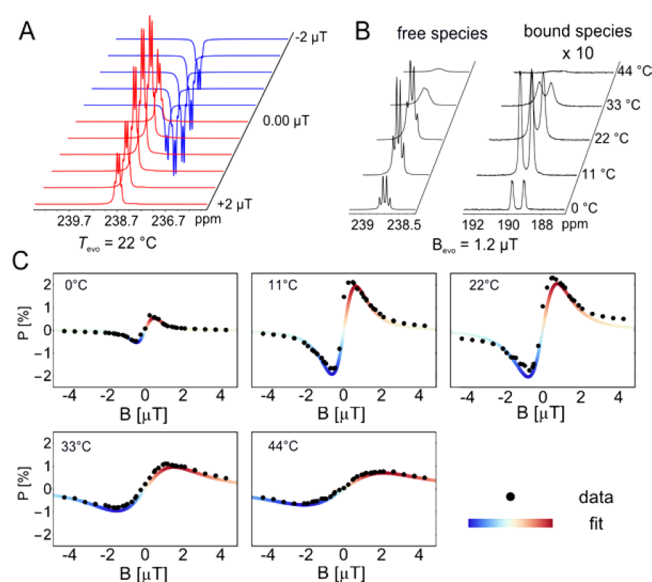
Figure 1. Temperature and field dependence of SABRE-SHEATH. (A) Excerpt of the experimental ^{15}N spectra at different magnetic evolution fields at a temperature of 22 °C. (B) NMR spectra at constant magnetic field but different temperatures. (C) Free substrate ^{15}N polarization at different magnetic evolution fields and temperatures. The data are fit to a simple theoretical model derived from the three-spin model as shown in Scheme 1 and Figure 2A. Red vs blue highlights the 180° phase shift.

In Figure 1 we show that ^{15}N polarization strongly depends on magnetic field (Figure 1A) and temperature during evolution in the shield (Figure 1B). We observe that the phase of the hyperpolarized signal (with respect to a fixed detector phase) can be controlled by the magnetic evolution field (i.e., 180° phase shift is observed upon B_{evo} inversion; see Figure 1, A and C). This is a useful feature for hyper-polarization experiments because it allows for simple difference measurements, as well as easy distinction of hyperpolarized signals from the thermal background. This inversion is associated with the existence of the two matching con-ditions.[66,67]

In the absence of chemical exchange we obtain

$$B_{evo} = \pm[J_{HH} + (J_{NH} + J'_{NH})/4]/(\gamma_H - \gamma_N) \quad (1)$$

where the J coupling parameters are defined in Figure 2. The expected optimal field is $B_{evo} = \pm0.3\ \mu T$. However, the experimental data from Figure 1C clearly show that the maxima are shifted to higher magnetic fields and scale with the temperature. These shifts are caused by broadening of the resonance conditions as a result of chemical exchange. Shorter catalyst/substrate complex lifetimes, at elevated temperatures, cause broader resonance conditions and more overlap. In the SI we develop a theory that includes the exchange and obtains an analytical expression that only depends on the J-coupling parameters, the magnetic field, and the average catalyst lifetime. We use this expression to fit the data as illustrated in Figure 1C and obtain excellent qualitative agreement; however, quantita-tive agreement with experimental lifetime is not obtained. Experimentally, it is easy to determine the J-couplings and the average lifetime τ_{life} as depicted in Figure 2B. Specifically, the substrate dissociation limited catalyst lifetime[68] is monitored by the change in NMR line width $\Delta\nu_i$ of the catalyst bound and free species[69]

Figure 2. *J*-coupling and line width analysis. (A) Exchange between bound and free species (^{15}N−CH$_3$CN, H$_2$) and *J*-coupling definitions. (B) Lineshape analysis of ^{15}N spectra (blue: individual Lorentzians, black: experimental trace, pink: overall fit, red: residual error optimized to rms-noise level). (C) ^{1}H spectra of the hydride region taken under PASADENA conditions.[25]

$$\tau_{\text{life}} = 1/(\pi(\Delta\nu_{\text{bound}} - \Delta\nu_{\text{free}})) \qquad (2)$$

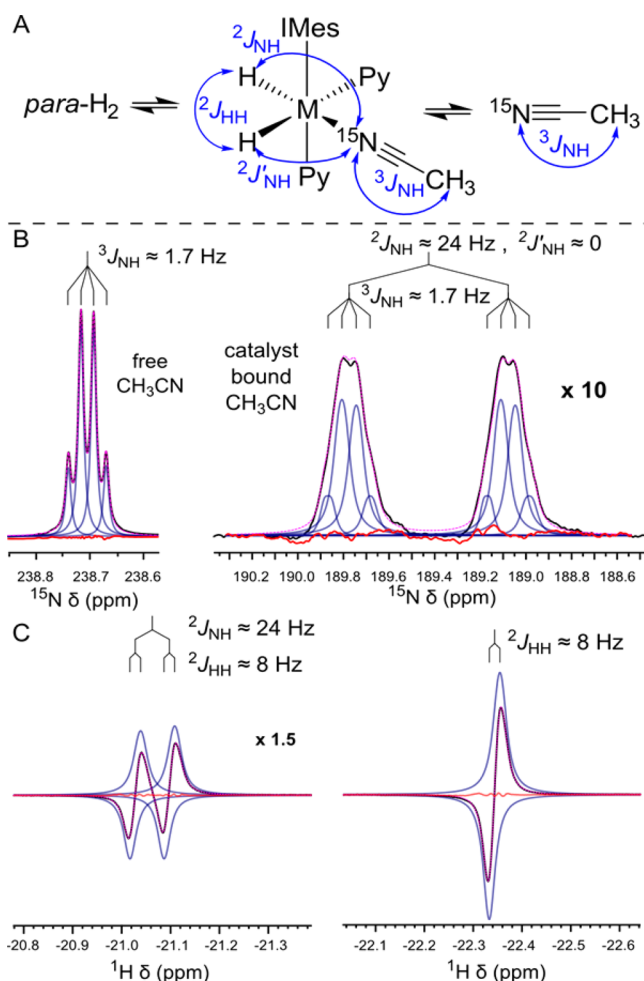At the temperature corresponding to maximum enhancement (22 °C), we experimentally determine a lifetime of 44−46 ms. At low temperature of 0 °C line widths are small enough to determine relevant *J*-coupling constants ($^2J_{HH'} = 8$ Hz, $^3J_{NH} = 1.71$ Hz, $^3J_{NH,\text{bound}} = 1.69$ Hz, $\Delta J_{NH} = {}^2J_{NH} - {}^2J_{NH'} = 24$ Hz). The couplings were used as fixed parameters to determine the individual line positions for evaluation of the line widths at higher temperatures. The experimental data also indicate that the major chemical species under our experimental conditions is indeed the system illustrated in Figure 2A because the nonequivalent hydrides indicate different ligands (pyridine and ^{15}N−CH$_3$CN) in the equatorial plane.

IV. Maximizing Polarization. After the above study of hyperpolarization as a function of temperature and magnetic field, further optimization requires inspection of concentrations of catalyst, substrate, and coligand, as well as *para*-H$_2$ pressure/flow rate. Here we performed a careful study to determine optimum catalyst concentration by conducting a dilution series at fixed catalyst loading ($c_{\text{sub}}/c_{\text{cat}} = 20$, see Figure 3A). We find maximum enhancement at 0.25 mM [IrCl(IMes)(COD)] and 5 mM ^{15}N−CH$_3$CN in the presence of 0.25 mM pyridine as
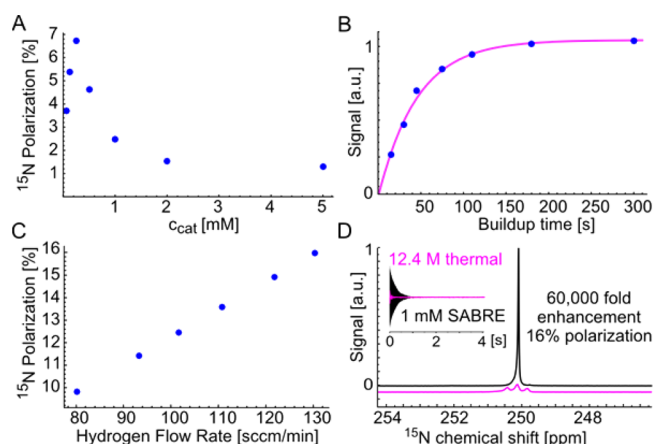
Figure 3. (A) ^{15}N polarization of ^{15}N−CH$_3$CN as a function of the catalyst concentration at fixed catalyst loading of 5 mol%. (B) ^{15}N signal as a function of the buildup time (T_b = 40.8 s). (C) ^{15}N polarization as a function of the hydrogen flow rate ($c_{\text{Catalyst}} = 0.25$ mM, $c_{\text{Pyridine}} = 0.25$ mM, $c_{\text{Benzonitrile}} = 1$ mM). (D) Comparison of a neat ^{15}N pyridine reference ($c = 12.4$ M, pink, thermal 8.45 T, shifted by 63 ppm) and ^{15}N spectrum of hyperpolarized benzonitrile ($c = 1$ mM, conditions as in C).

stabilizing coligand, corresponding to $P_{15N} = 7\%$ (enhancement of 23 000-fold at 8.5 T). It is noteworthy that the maximum polarization is observed at the same catalyst concentration experimentally determined for ^{15}N pyridine in methanol[30] and neat pyridine.[70]

For further optimization, it is reasonable to expect that large T_1, specifically, a T_1 that is large at the magnetic evolution field, will increase polarization levels. As reported in Table 2, benzonitrile stands out in terms of long T_1. Therefore, we tested benzonitrile at optimized concentrations. Figure 3B shows a buildup curve for benzonitrile where we find a relatively long buildup time constant of 40.8 s. Specifically, for this system we observe the highest hyperpolarization levels at a catalyst loading of 25 mol% (0.25 mM [IrCl(IMes)(COD)] activated in the presence of one catalyst equivalent of pyridine 0.25 mM and four catalyst equivalents ^{15}N-benzonitrile (1 mM)). Note that in absence of stabilizing coligand (pyridine) enhancements drop by ∼50%. Large catalyst loading ($c_{\text{sub}}/c_{\text{cat}} = 4$) leads to high levels of polarization because a low excess of substrate increases the likelihood of a polarization event per substrate molecule; this is consistent with theoretical predictions by Barskiy et al.[67] and experimental findings by Appleby et al.[71]

On this system, we examined the influence of *para*-H$_2$ flow rate at maximized pressure (limited to 10 bar by the experimental setup) as depicted in Figure 3C. In the investigated range, hyperpolarization levels are linearly dependent on the flow rate—in line with previous studies.[70] At even higher flow rates the sample volume ($V_{\text{bubbles}} + V_{\text{liquid}}$) is larger than the homogeneous μT magnetic field region, and polarization levels drop. The highest polarization was obtained at 130 sccm at 10 bar of 85% *para*-H$_2$. We obtain 16% ^{15}N polarization as illustrated in Figure 3D. The results indicate that hyperpolarization levels are limited by the hydrogen exchange from gas to liquid phase; i.e., the interface area between bubbles and solution. We believe that improvements over the reported 16% are within reach by more efficient dispersion of *para*-H$_2$.

In summary, we propose the following sequence of experiments: First, optimization of magnetic field and temper-

ature, followed by a dilution series at a given c_{sub}/c_{cat} ratio to choose the best catalyst concentration c_{cat}. At the identified c_{cat}, substrate concentration should be optimized. Typically, we find that optimal c_{sub} is about 4 to 5 times c_{cat} such that the catalysts are coordinatively saturated but an excess of free substrate remains. Finally, $para$-H_2 pressure and flow should be chosen as high as possible for a given setup. We acknowledge that all parameters are interdependent such that multiple cycles through these optimization steps may lead to even higher hyperpolarization level.

CONCLUSION AND OUTLOOK

In this article we have shown that SABRE-SHEATH can hyperpolarize a wide range of nitrogen-containing compounds, often outside the reach of ^{1}H-SABRE. The presented results suggest that sp and sp^2 hybridized nitrogens can be hyperpolarized, and ^{15}N polarization of at least several percent can be obtained easily and rapidly (30 s to 1 min) if no impeding factors such as steric hindrance or proton exchange inhibit polarization buildup.[42,48,70]

Furthermore, we have shown that ^{15}N T_1 times may be extraordinarily long and can in special cases exceed 10 min. We obtain extended relaxation times at relatively low magnetic fields of 1 T, using a permanent magnet-based spectrometer. The results are contrasted to measurements at 8.5 T where one may observe only slightly higher S/N ($\sim$3) if relaxation delays are neglected. The extended T_1 times at low field quickly compensate for the S/N losses when tracking hyperpolarized species on longer time scales. Moreover, the demonstrated hyperpolarization levels allow for ^{15}N imaging[30,72,73] (likely even in low magnetic fields). The cited demonstrations show images with 2×2 mm^2 resolution acquired in less than a second.[30]

In addition, polarization transfer strategies from ^{15}N to ^{1}H have been developed avoiding detection on the low gyromagnetic ratio ^{15}N for read-out.[74−77] Such polarization transfer strategies may increase S/N by another order of magnitude.

Finally, we present a systematic strategy to optimize SABRE-SHEATH experiments for maximum hyperpolarization. The sequence consists of optimization of temperature and μT magnetic fields, a dilution series to determine the optimal catalyst concentration, and use of high $para$-H_2 pressure and flow.

The present contribution elucidates upon the interplay of kinetic parameters and system compositions, as well as extrinsic parameters on the polarization levels. This is a significant stepping stone for optimization of heterogeneous SABRE,[78,79] SABRE in biocompatible aqueous media,[80−83] and modes to continuously supply polarized substrates. Such advances, in combination with low-cost, low-field MRI, let us envision hyperpolarized biomolecular MRI in the near future.

ASSOCIATED CONTENT

Ⓢ Supporting Information
The Supporting Information is available free of charge on the ACS Publications website at DOI: 10.1021/acs.jpcc.6b12097.

Detailed descriptions of 1) Characteristics of chemical exchange, 2) Experimental determination of complex lifetimes, 3) Hyperpolarization Transfer Theory, 4) Experimental Details, and 5) Spectral data and miscellaneous information (PDF)

Video showing the experimental procedure (AVI)

AUTHOR INFORMATION

Corresponding Authors
*E-mail: thomas.theis@duke.edu.
*E-mail: warren.warren@duke.edu.

ORCID Ⓞ
Johannes F. P. Colell: 0000-0001-9020-344X
Danila A. Barskiy: 0000-0002-2819-7584
Qiu Wang: 0000-0002-6803-9556
Steven J. Malcolmson: 0000-0003-3229-0949
Eduard Y. Chekmenev: 0000-0002-8745-8801
Thomas Theis: 0000-0001-6779-9978

Author Contributions
All authors have given approval to the final version of the manuscript.

Notes
The authors declare no competing financial interest.

ABBREVIATIONS

SABRE: Signal Amplification by Reversible Exchange
SHEATH: Shield Enables Alignment Transfer to Hetero-nuclei
$para$-H_2: $para$-hydrogen
PHIP: $para$-hydrogen-induced polarization
CSA: Chemical Shift Anisotropy
CHCA: α-Cyano-4-hydroxycinnamic acid
S/N: signal-to-noise ratio
SI: Supporting Information
MRI: Magnetic Resonance Imaging
NMR: Nuclear Magnetic Resonance
rms: root-mean-square

REFERENCES

(1) Ardenkjaer-Larsen, J. H.; Fridlund, B.; Gram, A.; Hansson, G.; Hansson, L.; Lerche, M. H.; Servin, R.; Thaning, M.; Golman, K. Increase in signal-to-noise ratio of > 10,000 times in liquid-state NMR. *Proc. Natl. Acad. Sci. U. S. A.* **2003**, *100*, 10158−10163.
(2) Nikolaou, P.; Coffey, A. M.; Barlow, M. J.; Rosen, M.; Goodson, B. M.; Chekmenev, E. Y. Temperature-Ramped ^{129}Xe Spin Exchange Optical Pumping. *Anal. Chem.* **2014**, *86*, 8206−8212.
(3) Griffin, R. G.; Prisner, T. F. High field dynamic nuclear polarization-the renaissance. *Phys. Chem. Chem. Phys.* **2010**, *12*, 5737−5740.
(4) Ardenkjaer-Larsen, J.-H.; Boebinger, G. S.; Comment, A.; Duckett, S.; Edison, A. S.; Engelke, F.; Griesinger, C.; Griffin, R. G.; Hilty, C.; Maeda, H.; et al. Facing and Overcoming Sensitivity Challenges in Biomolecular NMR Spectroscopy. *Angew. Chem., Int. Ed.* **2015**, *54*, 9162−9185.
(5) Walker, T. G.; Happer, W. Spin-exchange optical pumping of noble-gas nuclei. *Rev. Mod. Phys.* **1997**, *69*, 629−642.

(6) Freeman, M. S.; Emami, K.; Driehuys, B. Characterizing and modeling the efficiency limits in large-scale production of hyperpolarized ^{129}Xe. *Phys. Rev. A: At., Mol., Opt. Phys.* **2014**, *90*, 023406.

(7) Chen, W. C.; Gentile, T. R.; Ye, Q.; Walker, T. G.; Babcock, E. On the limits of spin-exchange optical pumping of ^{3}He. *J. Appl. Phys.* **2014**, *116*, 014903.

(8) Barskiy, D. A.; Coffey, A. M.; Nikolaou, P.; Mikhaylov, D. M.; Goodson, B. M.; Branca, R. T.; Lu, G. J.; Shapiro, M. G.; Telkki, V.-V.; Zhivonitko, V. V.; et al. NMR Hyperpolarization Techniques of Gases. *Chem. - Eur. J.* **2017**, *23*, 725−751.

(9) Zheng, Y.; Miller, G. W.; Tobias, W. A.; Cates, G. D. A method for imaging and spectroscopy using γ-rays and magnetic resonance. *Nature* **2016**, *537*, 652−655.

(10) Ward, H. R.; Lawler, R. G. Nuclear magnetic resonance emission and enhanced absorption in rapid organometallic reactions. *J. Am. Chem. Soc.* **1967**, *89*, 5518−5519.

(11) Kaptein, R. Chemically induced dynamic nuclear polarization in five alkyl radicals. *Chem. Phys. Lett.* **1968**, *2*, 261−267.

(12) Hermkens, N. K. J.; Eshuis, N.; van Weerdenburg, B. J. A.; Feiters, M. C.; Rutjes, F. P. J. T.; Wijmenga, S. S.; Tessari, M. NMR-Based Chemosensing via pH$_2$ Hyperpolarization: Application to Natural Extracts. *Anal. Chem.* **2016**, *88*, 3406−3412.

(13) Eshuis, N.; van Weerdenburg, B. J. A.; Feiters, M. C.; Rutjes, F. P. J. T.; Wijmenga, S. S.; Tessari, M. Quantitative Trace Analysis of Complex Mixtures Using SABRE Hyperpolarization. *Angew. Chem., Int. Ed.* **2015**, *54*, 1372−1372.

(14) Eshuis, N.; Aspers, R. L. E. G.; van Weerdenburg, B. J. A.; Feiters, M. C.; Rutjes, F. P. J. T.; Wijmenga, S. S.; Tessari, M. 2D NMR Trace Analysis by Continuous Hyperpolarization at High Magnetic Field. *Angew. Chem., Int. Ed.* **2015**, *54*, 14527−14530.

(15) Eshuis, N.; Hermkens, N.; van Weerdenburg, B. J. A.; Feiters, M. C.; Rutjes, F. P. J. T.; Wijmenga, S. S.; Tessari, M. Toward Nanomolar Detection by NMR Through SABRE Hyperpolarization. *J. Am. Chem. Soc.* **2014**, *136*, 2695−2698.

(16) Rodrigues, T. B.; Serrao, E. M.; Kennedy, B. W.; Hu, D. E.; Kettunen, M. I.; Brindle, K. M. Magnetic resonance imaging of tumor glycolysis using hyperpolarized 13C-labeled glucose. *Nat. Med.* **2014**, *20*, 93−7.

(17) Nelson, S. J.; Kurhanewicz, J.; Vigneron, D. B.; Larson, P. E.; Harzstark, A. L.; Ferrone, M.; van Criekinge, M.; Chang, J. W.; Bok, R.; Park, I.; et al. Metabolic imaging of patients with prostate cancer using hyperpolarized [1-(13)C]pyruvate. *Sci. Transl. Med.* **2013**, *5*, 198ra108.

(18) Keshari, K. R.; Wilson, D. M. Chemistry and biochemistry of ^{13}C hyperpolarized magnetic resonance using dynamic nuclear polarization. *Chem. Soc. Rev.* **2014**, *43*, 1627−59.

(19) Keshari, K. R.; Wilson, D. M.; Sai, V.; Bok, R.; Jen, K.-Y.; Larson, P.; Van Criekinge, M.; Kurhanewicz, J.; Wang, Z. J. Non-invasive in vivo imaging of diabetes-induced renal oxidative stress and response to therapy using hyperpolarized ^{13}C dehydroascorbate magnetic resonance. *Diabetes* **2015**, *64*, 344.

(20) Merritt, M. E.; Harrison, C.; Sherry, A. D.; Malloy, C. R.; Burgess, S. C. Flux through hepatic pyruvate carboxylase and phosphoenolpyruvate carboxykinase detected by hyperpolarized 13C magnetic resonance. *Proc. Natl. Acad. Sci. U. S. A.* **2011**, *108*, 19084−9.

(21) Adams, R. W.; Aguilar, J. A.; Atkinson, K. D.; Cowley, M. J.; Elliott, P. I. P.; Duckett, S. B.; Green, G. G. R.; Khazal, I. G.; Lopez-Serrano, J.; Williamson, D. C. Reversible Interactions with para-Hydrogen Enhance NMR Sensitivity by Polarization Transfer. *Science* **2009**, *323*, 1708−1711.

(22) Eisenschmid, T. C.; Kirss, R. U.; Deutsch, P. P.; Hommeltoft, S. I.; Eisenberg, R.; Bargon, J.; Lawler, R. G.; Balch, A. L. Para Hydrogen Induced Polarization in Hydrogenation Reactions. *J. Am. Chem. Soc.* **1987**, *109*, 8089−8091.

(23) Golman, K.; Axelsson, O.; Johannesson, H.; Mansson, S.; Olofsson, C.; Petersson, J. S. Parahydrogen-induced polarization in imaging: Subsecond C-13 angiography. *Magn. Reson. Med.* **2001**, *46*, 1−5.

(24) Bowers, C. R.; Weitekamp, D. P. Parahydrogen and synthesis allow dramatically enhanced nuclear alignment. *J. Am. Chem. Soc.* **1987**, *109*, 5541−5542.

(25) Bowers, C. R.; Weitekamp, D. P. Transformation of Symmetrization Order to Nuclear-Spin Magnetization by Chemical Reaction and Nuclear Magnetic Resonance. *Phys. Rev. Lett.* **1986**, *57*, 2645−2648.

(26) Hövener, J.-B.; Knecht, S.; Schwaderlapp, N.; Hennig, J.; von Elverfeldt, D. Continuous Re-hyperpolarization of Nuclear Spins Using Parahydrogen: Theory and Experiment. *ChemPhysChem* **2014**, *15*, 2451−2457.

(27) Nikolaou, P.; Goodson, B. M.; Chekmenev, E. Y. NMR Hyperpolarization Techniques for Biomedicine. *Chem. - Eur. J.* **2015**, *21*, 3156−3166.

(28) Cowley, M. J.; Adams, R. W.; Atkinson, K. D.; Cockett, M. C. R.; Duckett, S. B.; Green, G. G. R.; Lohman, J. A. B.; Kerssebaum, R.; Kilgour, D.; Mewis, R. E. Iridium N-Heterocyclic Carbene Complexes as Efficient Catalysts for Magnetization Transfer frompara-Hydrogen. *J. Am. Chem. Soc.* **2011**, *133*, 6134−6137.

(29) Theis, T.; Truong, M. L.; Coffey, A. M.; Shchepin, R. V.; Waddell, K. W.; Shi, F.; Goodson, B. M.; Warren, W. S.; Chekmenev, E. Y. Microtesla SABRE Enables 10% Nitrogen-15 Nuclear Spin Polarization. *J. Am. Chem. Soc.* **2015**, *137*, 1404−1407.

(30) Truong, M. L.; Theis, T.; Coffey, A. M.; Shchepin, R. V.; Waddell, K. W.; Shi, F.; Goodson, B. M.; Warren, W. S.; Chekmenev, E. Y. ^{15}N Hyperpolarization by Reversible Exchange Using SABRE-SHEATH. *J. Phys. Chem. C* **2015**, *119*, 8786−8797.

(31) Zhivonitko, V. V.; Skovpin, I. V.; Koptyug, I. V. Strong ^{31}P nuclear spin hyperpolarization produced via reversible chemical interaction with parahydrogen. *Chem. Commun.* **2015**, *51*, 2506−2509.

(32) Fleming, F. F.; Yao, L.; Ravikumar, P. C.; Funk, L.; Shook, B. C. Nitrile-Containing Pharmaceuticals: Efficacious Roles of the Nitrile Pharmacophore. *J. Med. Chem.* **2010**, *53*, 7902−7917.

(33) Mewis, R. E.; Green, R. A.; Cockett, M. C. R.; Cowley, M. J.; Duckett, S. B.; Green, G. G. R.; John, R. O.; Rayner, P. J.; Williamson, D. C. Strategies for the Hyperpolarization of Acetonitrile and Related Ligands by SABRE. *J. Phys. Chem. B* **2015**, *119*, 1416−1424.

(34) Wang, H.; Lanks, K. W. 2-Cyanocinnamic Acid Sensitization of L929 Cells to Killing by Hyperthermia. *Cancer research* **1986**, *46*, 5349−5352.

(35) Barskiy, D. A.; Shchepin, R. V.; Coffey, A. M.; Theis, T.; Warren, W. S.; Goodson, B. M.; Chekmenev, E. Y. Over 20% ^{15}N Hyperpolarization in Under One Minute for Metronidazole, an Antibiotic and Hypoxia Probe. *J. Am. Chem. Soc.* **2016**, *138*, 8080−8083.

(36) Halestrap, A. P.; Denton, R. M. Specific inhibition of pyruvate transport in rat liver mitochondria and human erythrocytes by α-cyano-4-hydroxycinnamate. *Biochem. J.* **1974**, *138*, 313−316.

(37) Morais-Santos, F.; Miranda-Goncalves, V.; Pinheiro, S.; Vieira, A. F.; Paredes, J.; Schmitt, F. C.; Baltazar, F.; Pinheiro, C. Differential sensitivities to lactate transport inhibitors of breast cancer cell lines. *Endocr.-Relat. Cancer* **2014**, *21*, 27−38.

(38) McKeage, K. Alectinib: A Review of Its Use in Advanced ALK-Rearranged Non-Small Cell Lung Cancer. *Drugs* **2015**, *75*, 75−82.

(39) Santarpia, M.; Altavilla, G.; Rosell, R. Alectinib: a selective, next-generation ALK inhibitor for treatment of ALK-rearranged non-small-cell lung cancer. *Expert Rev. Respir. Med.* **2015**, *9*, 255−268.

(40) Conti, P.; Tamborini, L.; Pinto, A.; Blondel, A.; Minoprio, P.; Mozzarelli, A.; De Micheli, C. Drug Discovery Targeting Amino Acid Racemases. *Chem. Rev.* **2011**, *111*, 6919−6946.

(41) Eliot, A. C.; Kirsch, J. F. Pyridoxalphophateenzymes: Mechanistic, Structural, and Evolutionary Considerations. *Annu. Rev. Biochem.* **2004**, *73*, 383−415.

(42) Logan, A. W.; Theis, T.; Colell, J. F.; Warren, W. S.; Malcolmson, S. J. Hyperpolarization of Nitrogen-15 Schiff Bases by Reversible Exchange Catalysis with para-Hydrogen. *Chem. - Eur. J.* **2016**, *22*, 10777−81.

(43) Feng, Y.; Theis, T.; Wu, T.-L.; Claytor, K.; Warren, W. S. Long-lived polarization protected by symmetry. *J. Chem. Phys.* **2014**, *141*, 134307.

(44) Ellinger, P.; Kader, M. M. A. Nicotinamide metabolism in mammals. *Biochem. J.* **1949**, *44*, 77−87.

(45) Cantó, C.; Houtkooper; Riekelt, H.; Pirinen, E.; Youn; Dou, Y.; Oosterveer; Maaike, H.; Cen, Y.; Fernandez-Marcos; Pablo, J.; Yamamoto, H.; Andreux; Pénélope, A.; Cettour-Rose, P.; et al. The NAD+ Precursor Nicotinamide Riboside Enhances Oxidative Metabolism and Protects against High-Fat Diet-Induced Obesity. *Cell Metab.* **2012**, *15*, 838−847.

(46) Sauve, A. A. NAD+ and vitamin B3: from metabolism to therapies. *J. Pharmacol. Exp. Ther.* **2008**, *324*, 883−893.

(47) Shchepin, R. V.; Barskiy, D. A.; Mikhaylov, D. M.; Chekmenev, E. Y. Efficient Synthesis of Nicotinamide-1−^{15}N for Ultrafast NMR Hyperpolarization Using Parahydrogen. *Bioconjugate Chem.* **2016**, *27*, 878−882.

(48) Shchepin, R. V.; Barskiy, D. A.; Coffey, A. M.; Theis, T.; Shi, F.; Warren, W. S.; Goodson, B. M.; Chekmenev, E. Y. ^{15}N Hyper-polarization of Imidazole-^{15}N$_2$ for Magnetic Resonance pH Sensing Via SABRE-SHEATH. *ACS Sens.* **2016**, *1*, 640.

(49) Hartley, G. S. The Cis-form of Azobenzene. *Nature* **1937**, *140*, 281−281.

(50) Merino, E.; Ribagorda, M. Control over molecular motion using thecis−transphotoisomerization of the azo group. *Beilstein J. Org. Chem.* **2012**, *8*, 1071−1090.

(51) Bohle, D. S.; Rosadiuk, K. A. Nitric Oxide Catalysis of Diazene E/Z Isomerization. *Inorg. Chem.* **2015**, *54*, 7145−7151.

(52) Theis, T.; Ortiz, G. X.; Logan, A. W. J.; Claytor, K. E.; Feng, Y.; Huhn, W. P.; Blum, V.; Malcolmson, S. J.; Chekmenev, E. Y.; Wang, Q.; et al. Direct and cost-efficient hyperpolarization of long-lived nuclear spin states on universal ^{15}N$_2$-diazirine molecular tags. *Sci. Adv.* **2016**, *2*, e1501438.

(53) Abragam, A. *The principles of nuclear magnetism*; Clarendon Press: Oxford, 1961.

(54) Hoult, D. I.; Richards, R. E. The signal-to-noise ratio of the nuclear magnetic resonance experiment. *J. Magn. Reson.* **1976**, *24*, 71−85.

(55) Hoult, D. I.; Lauterbur, P. C. The sensitivity of the zeugmatographic experiment involving human samples. *J. Magn. Reson.* **1979**, *34*, 425−433.

(56) Hoult, D. I. Sensitivity of the NMR Experiment. In *eMagRes.*; John Wiley & Sons, Ltd: 2007.

(57) Hoult, D. I.; Richards, R. E. The signal-to-noise ratio of the nuclear magnetic resonance experiment. *J. Magn. Reson.* **1976**, *24*, 71−85.

(58) Hoult, D. I. Sensitivity of Whole Body MRI Experiments. *Enc. Magn. Reson.* **2007**, DOI: 10.1002/9780470034590.emrstm0491.

(59) Minard, K. R.; Wind, R. A. Solenoidal microcoil design—Part II: Optimizing winding parameters for maximum signal-to-noise perform-ance. *Concepts Magn. Reson.* **2001**, *13*, 190−210.

(60) Danieli, E.; Perlo, J.; Blümich, B.; Casanova, F. Highly Stable and Finely Tuned Magnetic Fields Generated by Permanent Magnet Assemblies. *Phys. Rev. Lett.* **2013**, *110*, 180801.

(61) Sarracanie, M.; LaPierre, C. D.; Salameh, N.; Waddington, D. E. J.; Witzel, T.; Rosen, M. S. Low-Cost High-Performance MRI. *Sci. Rep.* **2015**, *5*, 15177.

(62) Suefke, M.; Liebisch, A.; Blumich, B.; Appelt, S. External high-quality-factor resonator tunes up nuclear magnetic resonance. *Nat. Phys.* **2015**, *11*, 767−771.

(63) Coffey, A. M.; Truong, M.; Chekmenev, E. Y. Low-field MRI can be more sensitive than high-field MRI. *J. Magn. Reson.* **2013**, *237*, 169−174.

(64) Hata, R.; Nonaka, H.; Takakusagi, Y.; Ichikawa, K.; Sando, S. Design of a hyperpolarized ^{15}N NMR probe that induces a large chemical-shift change upon binding of calcium ions. *Chem. Commun.* **2015**, *51*, 12290−12292.

(65) Clavijo Jordan, M. V.; Lo, S.-T.; Chen, S.; Preihs, C.; Chirayil, S.; Zhang, S.; Kapur, P.; Li, W.-H.; De Leon-Rodriguez, L. M.; Lubag, A. J. M.; et al. Zinc-sensitive MRI contrast agent detects differential release of Zn(II) ions from the healthy vs. malignant mouse prostate. *Proc. Natl. Acad. Sci. U. S. A.* **2016**, *113*, E5464−E5471.

(66) Knecht, S.; Pravdivtsev, A. N.; Hövener, J.-B.; Yurkovskaya, A. V.; Ivanov, K. L. Quantitative description of the SABRE process: rigorous consideration of spin dynamics and chemical exchange. *RSC Adv.* **2016**, *6*, 24470−24477.

(67) Barskiy, D. A.; Pravdivtsev, A. N.; Ivanov, K. L.; Kovtunov, K. V.; Koptyug, I. V. Simple analytical model for Signal Amplification by Reversible Exchange (SABRE) process. *Phys. Chem. Chem. Phys.* **2016**, *18*, 89−93.

(68) Cowley, M. J.; Adams, R. W.; Atkinson, K. D.; Cockett, M. C. R.; Duckett, S. B.; Green, G. G. R.; Lohman, J. A. B.; Kerssebaum, R.; Kilgour, D.; Mewis, R. E. Iridium N-Heterocyclic Carbene Complexes as Efficient Catalysts for Magnetization Transfer from para-Hydrogen. *J. Am. Chem. Soc.* **2011**, *133*, 6134−6137.

(69) Günther, H. *NMR Spectroscopy: Basic Principles, Concepts and Applications in Chemistry*, 3rd ed.; Wiley-VCH: Weinheim, Germany, 2013.

(70) Shchepin, R. V.; Truong, M. L.; Theis, T.; Coffey, A. M.; Shi, F.; Waddell, K. W.; Warren, W. S.; Goodson, B. M.; Chekmenev, E. Y. Hyperpolarization of "Neat" Liquids by NMR Signal Amplification by Reversible Exchange. *J. Phys. Chem. Lett.* **2015**, *6*, 1961−1967.

(71) Appleby, K. M.; Mewis, R. E.; Olaru, A. M.; Green, G. G. R.; Fairlamb, I. J. S.; Duckett, S. B. Investigating pyridazine and phthalazine exchange in a series of iridium complexes in order to define their role in the catalytic transfer of magnetisation from para-hydrogen. *Chem. Sci.* **2015**, *6*, 3981−3993.

(72) Jiang, W.; Lumata, L.; Chen, W.; Zhang, S.; Kovacs, Z.; Sherry, A. D.; Khemtong, C. Hyperpolarized ^{15}N-pyridine Derivatives as pH-Sensitive MRI Agents. *Sci. Rep.* **2015**, *5*, 9104.

(73) Cudalbu, C.; Comment, A.; Kurdzesau, F.; van Heeswijk, R. B.; Uffmann, K.; Jannin, S.; Denisov, V.; Kirik, D.; Gruetter, R. Feasibility of in vivo ^{15}N MRS detection of hyperpolarized ^{15}N labeled choline in rats. *Phys. Chem. Chem. Phys.* **2010**, *12*, 5818−5823.

(74) Sarkar, R.; Comment, A.; Vasos, P. R.; Jannin, S.; Gruetter, R.; Bodenhausen, G.; Hall, H.; Kirik, D.; Denisov, V. P. Proton NMR of ^{15}N-Choline Metabolites Enhanced by Dynamic Nuclear Polarization. *J. Am. Chem. Soc.* **2009**, *131*, 16014−16015.

(75) Mishkovsky, M.; Cheng, T.; Comment, A.; Gruetter, R. Localized in vivo hyperpolarization transfer sequences. *Magn. Reson. Med.* **2012**, *68*, 349−352.

(76) Truong, M. L.; Coffey, A. M.; Shchepin, R. V.; Waddell, K. W.; Chekmenev, E. Y. Sub-second proton imaging of ^{13}C hyperpolarized contrast agents in water. *Contrast Media Mol. Imaging* **2014**, *9*, 333−341.

(77) Chekmenev, E. Y.; Norton, V. A.; Weitekamp, D. P.; Bhattacharya, P. Hyperpolarized ^{1}H NMR Employing Low γ Nucleus for Spin Polarization Storage. *J. Am. Chem. Soc.* **2009**, *131*, 3164−3165.

(78) Shi, F.; Coffey, A. M.; Waddell, K. W.; Chekmenev, E. Y.; Goodson, B. M. Heterogeneous Solution NMR Signal Amplification by Reversible Exchange. *Angew. Chem., Int. Ed.* **2014**, *53*, 7495−7498.

(79) Shi, F.; Coffey, A. M.; Waddell, K. W.; Chekmenev, E. Y.; Goodson, B. M. Nanoscale Catalysts for NMR Signal Enhancement by Reversible Exchange. *J. Phys. Chem. C* **2015**, *119*, 7525−7533.

(80) Shi, F.; He, P.; Best, Q.; Groome, K. A.; Truong, M. L.; Coffey, A. M.; Zimay, G.; Shchepin, R. V.; Waddell, K. W.; Chekmenev, E. Y.; et al. Aqueous NMR Signal Enhancement by Reversible Exchange in a Single Step Using Water-Soluble Catalysts. *J. Phys. Chem. C* **2016**, *120*, 12149.

(81) Zeng, H.; Xu, J.; McMahon, M. T.; Lohman, J. A. B.; van Zijl, P. C. M. Achieving 1% NMR polarization in water in less than 1 min using SABRE. *J. Magn. Reson.* **2014**, *246*, 119−121.

(82) Hövener, J.-B.; Schwaderlapp, N.; Borowiak, R.; Lickert, T.; Duckett, S. B.; Mewis, R. E.; Adams, R. W.; Burns, M. J.; Highton, L. A. R.; Green, G. G. R.; et al. Toward Biocompatible Nuclear Hyperpolarization Using Signal Amplification by Reversible Exchange: Quantitative in Situ Spectroscopy and High-Field Imaging. *Anal. Chem.* **2014**, *86*, 1767−1774.

(83) Truong, M. L.; Shi, F.; He, P.; Yuan, B.; Plunkett, K. N.; Coffey, A. M.; Shchepin, R. V.; Barskiy, D. A.; Kovtunov, K. V.; Koptyug, I. V.; et al. Irreversible Catalyst Activation Enables Hyperpolarization and Water Solubility for NMR Signal Amplification by Reversible Exchange. *J. Phys. Chem. B* **2014**, *118*, 13882−13889.

2

The Physics of Hyperpolarized Gas MRI

B.M. Goodson, K. Ranta, J.G. Skinner, A.M. Coffey, P. Nikolaou,
M. Gemeinhardt, D. Anthony, S. Stephenson, S. Hardy,
J. Owers-Bradley, M.J. Barlow and E.Y. Chekmenev

INTRODUCTION

Hyperpolarized (HP) gases have helped realize a growing list of potential applications—particularly within the biomedical and clinical realms. Integral to their use are the properties of such gaseous agents, as well as how they are prepared, stored, and delivered to the sample or subject. For example, arguably the most important property of a HP gas—besides its biological compatibility—is the lifetime of its highly nonequilibrium nuclear spin polarization ("hyperpolarization"). Such lifetimes must be sufficiently long to allow hyperpolarization to accumulate so that it lasts long enough for the agent to be delivered to the sample or target organ for imaging or spectroscopy. In turn, this crucial lifetime requirement dramatically limits the types of gases that can serve effectively as HP gas agents, and places practical constraints on how the gases are handled to best preserve and utilize the hyperpolarization. On the other hand, once delivered the polarization lifetime provides a powerful means of contrast—along with other key properties like density, position, motion, spectral frequency, and signal dynamics from chemical exchange.

The available methods of hyperpolarization are also vitally important. Although such methods were originally created and developed as part of fundamental physics or chemistry research with generally quite different—if any—uses in mind, biomedical applications have now grown to comprise a strong force driving the development of hyperpolarization technology. Additionally, such methods not only determine the amounts of HP gases produced and polarization levels that can be attained, but also further limit the viable choices of HP gas agents for potential biomedical applications. To date, virtually all biomedical HP gas studies have involved noble gases, with small hydrocarbons and other small-molecule gases showing promise. Such HP gases may be generated via either spin-exchange optical pumping (SEOP), metastability exchange optical pumping (MEOP), "brute-force" polarization (BFP), dynamic nuclear polarization (DNP), and/or parahydrogen-induced polarization (PHIP). Each of these approaches has advantages and limitations, and understanding how they work to produce and deliver a given HP gas is thus necessary for integration with a desired biomedical application.

This chapter is organized as follows. First, we describe the properties and behavior of HP gases. Following an introduction of the general properties of these substances, particular attention is given to modes of relaxation, general rules for care and handling of these gases, and some considerations on how best to utilize them in magnetic resonance (MR) studies (e.g., with respect to pulse sequences). Then we discuss the aforementioned methods of generating HP gases, with particular focus on SEOP, MEOP, DNP, and PHIP. The principles of each method are introduced, along with key design features and production performance of select gas "hyperpolarizers." Finally, we provide a summary and conclude with an outlook for HP gas approaches and technological development.

TABLE 2.1   MR Properties of Selected Gases of Interest for Hyperpolarized MRI

HP gas	Isotopes of interest	Nuclear spin (I)	Isotope natural abundance	Gyromagnetic ratio (relative to ^{1}H)	Most effective HP methods
Xenon	^{129}Xe	1/2	26.44%,	(−)0.27856	SEOP & DNP
	^{131}Xe	3/2	21.18%	0.08257	
Helium	^{3}He	1/2	0.00014%	(−)0.76181	MEOP & SEOP
Krypton	^{83}Kr	9/2	11.55%	(−)0.03862	SEOP
Propane, d_6-propane	^{1}H	1/2	99.985%,	(1)	PHIP
	^{13}C	1/2	1.11%	0.25145	
Nitrous oxide	^{15}N	1/2	0.37%	(−)0.10137	DNP

HP GASES: PROPERTIES AND CONSIDERATIONS

General Properties

The physical properties that define the gas phase have significant implications for how HP gases are prepared and administered. For example, the weak intermolecular forces between gas particles give rise to characteristically low densities under ambient conditions—roughly three orders of magnitude lower than for condensed phases. In comparison to standard magnetic resonance imaging (MRI), such low densities represent a major limitation for MR detection and imaging, but this limitation is more than compensated by hyperpolarization. The low viscosity and high compressibility of gases facilitate rapid transport, storage, and delivery of HP gases to the subject via the lungs, and the miscibility of gases enables rapid and facile preparation of arbitrary admixtures. In terms of biological interactions the gases investigated for use in HP MRI are considered "simple" asphyxiants, although many possess varying degrees of anesthetic properties. Dilution and/or mixing with O_2 for respiration may be required for some applications, which may in turn impact signal strength and the lifetime of the HP state. On the other hand, the same solubility of some gases (e.g., xenon) in tissues that gives rise in part to anesthetic effects also can enable MR applications beyond gas-space imaging (particularly those that exploit chemical exchange between different environments), as discussed elsewhere in this book.

How gases move and interact with each other (and their surroundings) on the atomic level has significant implications for nuclear spin relaxation, as discussed in the next subsection. The restriction of free diffusive motion, often quantified by the apparent diffusion coefficient, can reflect microscale changes in lung structure. On the macroscopic level, because gases expand to adopt the shape of their containers, HP gas imaging allows investigation of lung void-space dynamics and the absence of signal can map pathological obstruction of gas flow. Moreover, agent dose is readily calculated using the ideal gas law (with quantities often measured in L · atm, referring to the volume and pressure of the gas). Nevertheless, HP gases must ultimately be delivered to subjects under ambient conditions (∼1 atm)—often requiring that the gas be expanded, compressed, condensed, and/or sublimated prior to agent administration. Finally, MR detection of HP gases obviously requires the presence of HP-storing nuclear spins, and thus the ready availability of clinical-scale quantities of a given gas with sufficient (naturally abundant or enriched) spins can influence the viability of an approach under consideration. Some key MR properties of selected gases discussed in this chapter are provided in Table 2.1.

Spin Relaxation Mechanisms of HP Gases

Gas-phase nuclear spin relaxation is one of the primary determinants of a prospective HP gaseous agent's viability. It not only determines the lifetime of the HP state, but also limits the level of polarization that can be achieved. Contributions to the nuclear spin relaxation rate of a gas can be categorized into intrinsic (i) and extrinsic (e) processes (e.g., Ref. [1]):

$$T_1^{-1} = \Gamma_i + \Gamma_e.$$

For example, the ^{129}Xe T_1 is commonly disassembled into five dominating contributions [2]:

$$T_1^{-1} = \Gamma_{it} + \Gamma_{ip} + \Gamma_{eo} + \Gamma_{eg} + \Gamma_{ew},$$

where contributions to the intrinsic rate are from (t)ransient Xe_2 dimers and (p)ersistent Xe_2 dimers, and extrinsic processes comprise paramagnetic (o)xygen interactions, diffusion through magnetic field (g)radients, and (w)all collisions. The first three terms can be quantified by [1,3]

$$\frac{1}{T_1} = \frac{[Xe]}{56.1 \text{ h}} + \frac{1 + (3.65 \times 10^{-3})}{4.59 \text{ h}\left(1 + r_B \frac{[B]}{[Xe]}\right)} + 0.4 \text{ s}^{-1} \text{ amg}^{-1} \times n_{O_2},$$

where r_B is the persistent dimer breakup efficiency of a secondary gas B in the mixture relative to that of xenon, and n_{O2} is the oxygen concentration in amagats. In the absence of O_2 contamination, typical ^{129}Xe T_1 values are limited to a few hours and are dominated by spin rotation suffered during persistent dimer relaxation and paramagnetic relaxation from wall collisions. Variations in glass, coatings, and container geometry have made wall relaxation contributions notoriously difficult to quantitatively predict, but with careful preparation and protection, they can be as long as tens of hours [1,4]. Wall relaxation is commonly mitigated with siloxane glass coatings such as SurfaSil, and is also reduced at fields near a few Tesla [1].

In general, intrinsic relaxation for molecular gases is typically dominated by spin-rotation interactions. For example, for partially deuterated propane a T_1 of ~6 s has been measured at low field [5], necessitating rapid transfer to samples when using HP propane. The T_1 for (ortho-)hydrogen is even shorter, on the millisecond time-scale (although HP ortho-H_2 has been created in solution [6]). However, loss of the pure spin order of the singlet state of para-hydrogen requires interconversion with ortho-hydrogen, which can take weeks if proper precautions are taken with the storage vessel. Intrinsic relaxation of ^{3}He is known to be slow as well ($T_1 \sim$ days) so that hyperpolarization lifetime is typically limited by the presence of paramagnetic centers such as oxygen contamination or wall impurities. Indeed, ^{3}He relaxation times of hundreds of hours have been reported [7].

Intrinsic relaxation of quadrupolar noble gas nuclei (e.g., ^{131}Xe, ^{83}Kr) is much faster and is usually dominated by quadrupolar contributions suffered during Xe−Xe or Kr−Kr binary exchange [8]:

$$1/T_1^{131Xe} = 0.0395 \text{ s}^{-1} \text{ amg}^{-1} \times n_{Xe},$$

$$1/T_1^{83Kr} = 0.0016 \text{ s}^{-1} \text{ amg}^{-1} \times n_{Kr},$$

where the n values are in density units of amagat (1 amg is the number of gas particles per unit volume at 1 atm and 0 °C). These lifetimes can be orders of magnitude faster than the corresponding intrinsic effects measured in spin 1/2 nuclei—therefore limiting the densities that can be effectively polarized or stored [9]. In fact, quadrupolar contributions from van der Waals complexes and wall collisions make actual relaxation rates even higher. On the other hand, the low gyromagnetic ratio for ^{83}Kr makes it less susceptible to dipolar relaxation from the presence of oxygen in biological environments. While fast depolarization limits the achievable hyperpolarization magnitude and storage times for quadrupolar noble gases, it has also been shown to be useful as a form of contrast to probe surfaces, and fast relaxation may allow sufficiently rapid signal averaging to potentially support the utility of thermal polarizations in some circumstances [10].

Finally, extrinsic relaxation of each of these species can also be brought about by diffusion through magnetic field gradients, and thus care should be taken to ensure that fields used to produce or store HP gases are kept homogeneous [2]—particularly important for ^{3}He, because of its high gyromagnetic ratio ($\Gamma_{eg} \propto \gamma^2$) and otherwise ultralong relaxation times—with no zero-field crossings [11].

Storage and Delivery Considerations for HP Gases

Besides ensuring its biological compatibility and safe administration, the most important considerations for using any HP gas involve experimental design to maximize nuclear spin polarization and agent throughput, achieve efficient HP agent delivery, and maintain polarization levels as much as possible throughout the study.

First, any contributors to hyperpolarization destruction need to be addressed within and "downstream" of the polarization chamber. Although the lifetime of a given gas's polarization is physically capped by its intrinsic T_1 relaxation rate, this source of spin destruction is often small compared to extrinsic sources of polarization loss while transporting and delivering HP gas for imaging experiments. Indeed, gas polarizations can be unintentionally destroyed via a number of ways in an experimental setup, including paramagnetic relaxation, diffusion through magnetic field gradients, and movement of the gas through magnetic "zero-field" crossings. Paramagnetic relaxation can be mitigated first by ensuring that all polarizer materials that can come in contact with the HP gas have minimal magnetic impurities (e.g., PFA/PTFE vs stainless steel), and that gas lines are well

evacuated and/or purged with ultrapure gases to minimize O_2 exposure. When it comes to HP gas MRI on aerobic organisms, oxygen exposure will be unavoidable, but addition of O_2 to create breathable admixtures with HP gas should be performed only at the last possible step prior to agent administration. For HP [129]Xe, borosilicate glass components are often coated with silicon-based polymers (SurfraSil, etc.) [12,13], thereby limiting paramagnetic wall relaxation and increasing hyperpolarization lifetimes. However, for the smaller [3]He atoms, such coatings may hurt more than they help—and thus it can be important to choose glass with minimal paramagnetic impurities (e.g., GE180) [7]. For quadrupolar nuclei, hydrophobic coatings can accelerate relaxation [14] by enhancing physisorption, and thus uncoated (naturally hydrophilic) clean glass surfaces are desired.

Permanent magnets or smaller auxiliary fields are sometimes used to accumulate or transport gases to avoid field relaxation. Particularly for [3]He, minimizing field gradients using homogeneous fields (e.g., Helmholtz coils or other arrangements) [15] can be important for minimizing polarization losses. During the transfer of a prepared HP gas sample to a subject, special attention needs to be placed toward keeping the applied magnetic field as uniform as possible, and avoiding areas of zero-field crossings. For [3]He cells, degaussing may need to be performed [16] on occasion to remove weak permanent fields that have developed owing to impurities embedded in the glass. Automation of gas hyperpolarizers is highly desirable for maximizing throughput, maintaining reproducibility, and minimizing errors during HP gas preparation and delivery, but fields produced by some solenoid valve designs can be problematic [17]. Transit through a given gas's phase diagram can also be a source of relaxation. For example, the T_1 of solid [129]Xe at liquid-N_2 temperature (77K) can be several hours [18,19] (facilitating purification and storage [20]), but only if kept from warming too close to the Xe melting point (where the T_1 can drop to seconds). Polarized solid xenon needs to be maintained in a strong field ($>500\,G$) in order to suppress (1) dipolar relaxation from lattice vacancy hopping [21] and (2) thermal mixing with fast-relaxing [131]Xe present in the lattice [19]. Freezing or dissolving quadrupolar gases results in immediate loss of hyperpolarization because of subsecond T_1s in condensed phases unless at cryogenic temperatures. Thus, in addition to the fact that hyperpolarization processes themselves need to be monitored for consistent production of HP substances, the seemingly endless ways to destroy hard-won polarization necessitates that polarizers are designed to include in situ polarimetry for quality assurance of the HP agent.

Finally, although the physical mechanisms themselves underlying the hyperpolarization processes in SEOP, MEOP, DNP, and PHIP are sufficiently different that few generalizations about polarizer design are discussed here (the reader is instead directed to subsections below), the use of *gases* does provide some advantages regardless of hyperpolarization mechanism. Importantly, HP gases are relatively easy to physically separate from auxiliary substances (e.g., alkali metals (AMs), radicals, or catalysts) found in polarizers that may be toxic or otherwise undesirable if administered in significant dosage to a patient. Additionally, HP gases are relatively easy to administer to a living subject via inhalation—although alternative approaches wherein the agent is dissolved in a biocompatible liquid prior to administration (e.g., Ref. [22]) would ultimately be subject to similar sterile-path considerations needed for condensed-phase HP agents [23].

Pulse Sequence Considerations

HP gas delivered by inhalation enters the lungs as a bolus, whereas in chemical exchange saturation transfer using hyperpolarized nuclei (Hyper-CEST) applications (see chapter: Xenon Biosensor HyperCEST MRI) a steady-state supply of HP [129]Xe is desired/maintained in other organs and tissues for CEST-based sensing. In both cases, the ultimate goal is to maximize the SNR through optimization of MRI pulse sequences used in conventional MRI. Unlike in conventional MRI, where the consumed (through the RF excitation) magnetization recovers via thermal equilibration with the external magnetic field, a HP magnetization pool can only decay after in vivo administration—i.e., the hyperpolarization can only be refreshed by using a new bolus. As a result, pulse sequences used in HP gas MRI eliminate the "recovery" steps typically found in conventional MRI, and primarily focus on signal "encoding" and "detection" steps, which typically results in RF sequences with very short repetition time (TR) [24]. The latter is highly desirable, because HP gaseous agents have an in vivo T_1 on the order of seconds to tens of seconds resulting in a relatively narrow imaging time window. On the other hand, the greatly increased signal strength provided by hyperpolarization also obviates the need for signal averaging. As a result, multislice 2D and 3D images of HP gases in the lungs can be recorded in seconds and on a single breath-hold [25]. In addition to TR reduction, compressed sensing, where only a small fraction of k-space is sampled during imaging acquisition, can be employed—thereby significantly reducing the total scan time even further. This practice is especially advantageous for 3D sequences [26].

An additional complication of the "nonrenewable" nature of the HP magnetization is that each RF pulse consumes a nonlinear fraction of the remaining HP magnetization. One approach is to use small-angle excitation RF pulses for each line of k-space [27]. The resulting MRI signal is significantly lower than that recorded using a maximum RF pulse angle (i.e., 90°) with the benefit that the bulk of magnetization is preserved for further RF excitations. Nevertheless, the accumulating loss of magnetization from the application of many constant—even if small—flip-angle pulses over the course of image acquisition can lead to image blurring or other artifacts. Therefore, versions of this approach often use variable-tipping-angle pulses calculated to compensate for signal loss and thereby provide approximately the same amount of signal for each scan [27].

An alternative strategy is to use fast imaging with steady precession (FISP) [28] sequences [29], where near-90° RF pulses can be used for excitation, and nearly the entire magnetization pool contributes to the signal formation for each line of k-space [30]. Once the signal is recorded during the "detection" step, the magnetization is quickly "rewound" back to the z-axis for use in the next k-space step. The advantage of this second approach is the significantly greater SNR. However, these sequences require that the T_2 value of the HP gas be significantly larger than the "detection" time period (i.e., in order to take full advantage of the long T_2 of the HP contrast media). Furthermore, FISP sequences are more susceptible to B_1 and B_0 inhomogeneities [31], potentially resulting in imaging artifacts.

For further special pulse sequence considerations related to Hyper-CEST, please refer to Chapter 17, Xenon Biosensor HyperCEST MRI.

METHODS FOR GENERATING HP GASES

Dynamic Nuclear Polarization

For nuclear spin $I = \frac{1}{2}$ nuclei such as ^{129}Xe (or ^{1}H, ^{13}C, ^{15}N, etc.), nuclear spin polarization P in the high-temperature limit is approximately given by the following equation: $|P| \approx \gamma \hbar B_0 / 2kT$, where $\hbar$ is the reduced Planck's constant, k is Boltzmann's constant, T is temperature in Kelvin, and γ is the gyromagnetic ratio of the nucleus in question. From this equation it follows that a change in temperature from 310K (body temperature) to liquid helium at 4.2K can enhance ^{129}Xe P (e.g.) by $\sim$75-fold. Fig. 2.1 also reveals that sufficiently low temperatures in static magnetic fields of several Tesla lead to electronic spin polarization reaching order of unity. For example, for $B_0 = 3.35T$ and $T = 1K$, electronic polarization is $\sim$98% as electrons possess a very high gyromagnetic ratio compared to protons, or $|\gamma_e / \gamma_{1H}| \sim 658$, $|\gamma_e / \gamma_{129Xe}| \sim 2380$. Conversely, ^{129}Xe nuclear polarization is only 0.0947% for these conditions! In order for nuclear spin polarization to reach $\geq$10% under thermal equilibrium conditions, a sample at high field (several Tesla) would generally need to be stored at milliKelvin temperatures (e.g., using a ^{3}He/^{4}He dilution refrigerator). Indeed, such time-consuming BFP approaches have been used to achieve high nuclear spin polarizations in different systems, including noble gases [32−35].

In a seminal theoretical paper published in 1953 Albert Overhauser proposed to use electron spins to enhance nuclear spin polarization, which was shortly thereafter confirmed experimentally by Carver and Slichter [36].
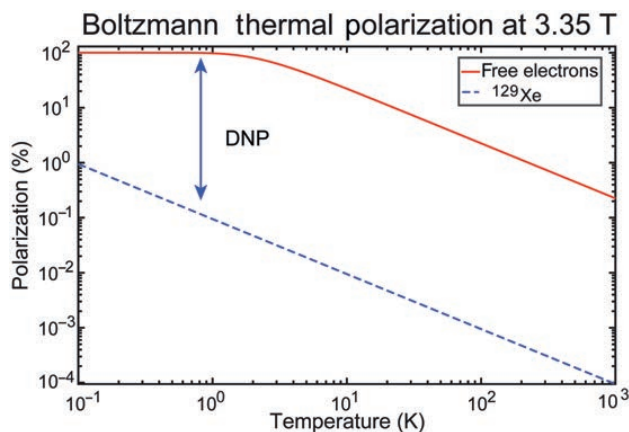
FIGURE 2.1 Boltzmann thermal polarization of electrons and ^{129}Xe nuclear spins for $B_0 = 3.35T$ as a function of temperature. RF fields facilitate transfer of polarization from electron spins to surrounding nuclear spins (e.g., ^{129}Xe).

The process of DNP utilizes the very high Boltzmann polarization of unpaired electrons attained at very low temperatures and magnetic field strengths of several Tesla described above, and transfers this polarization via dipolar or scalar couplings to nuclear spins (e.g., ^{1}H, ^{13}C, ^{15}N, ^{129}Xe, etc.), thereby dramatically enhancing the nuclear spin polarization of the target substances. The requisite unpaired electrons are typically introduced into a sample by adding persistent radicals [37].

Dissolution DNP (d-DNP) is the DNP approach typically employed for small molecules that may be used in biomedical applications. d-DNP is often explained in terms of the cross effect, a three-spin (two-electron, one-nucleus) process in which the electron spin transitions are driven by resonant microwaves and the difference in energy of the electron spin flips roughly matches the energy needed to flip the nuclear spin [38,39]. In the cross effect, the electron linewidth generally exceeds the nuclear spin Larmor frequency. The d-DNP hyperpolarizer instrumentation was first introduced in 2003 [37], primarily for production of liquid ^{13}C-HP contrast agents. The device consists of three major components: (1) a superconducting magnet establishing the B_0 field strength; (2) a helium cryostat connected to vacuum pumps to cool the sample to ∼1K; and (3) a microwave source enabling polarization transfer from unpaired electron spins to nuclear spins. Such hyperpolarizers include the commercial platforms of the HyperSense [37] by Oxford Instruments operating at $3.35T$ and $1.2-1.6$K, the SPINlab [23] for clinical use developed by GE Healthcare operating at $5T$ and 1.1K, as well as numerous home-built solutions.

In addition to substances that comprise liquid solutions at room temperatures, DNP has also garnered recent attention as a means to hyperpolarize gases. For example, DNP devices have recently been shown to be effective for hyperpolarization of ^{129}Xe, reaching $P_{Xe} \sim 30\%$ in about 90 min at ∼1K [40] despite a previously identified spin-diffusion (e→^{129}Xe) bottleneck [41]. Other experiments have investigated the potential of hyperpolarizing ^{15}N-labeled N$_2$O, with the idea being to exploit the long-lived singlet-state lifetime at low field, quantified by an exponential time constant T_S, of 26 min [42,43]. However, to date the production has been modest—achieving polarizations of $P_{15N} \sim 10\%$ over 37 h in ∼25 cc volumes [42].

The DNP technique is capable of efficient ^{129}Xe hyperpolarization using homogeneous mixing of ^{129}Xe and radical agents when a cosolvent (e.g., ethanol or propanol) is employed [40]. Once ^{129}Xe is HP in the solid state, it is sublimated to leave the hyperpolarizer as a pure gas, and the process is therefore termed sublimation DNP [40]. A key strength of this approach is a relatively widespread network of DNP hyperpolarizers. Limitations of using DNP for hyperpolarizing gases include (1) the relatively high costs associated with device purchase, operation, and maintenance and (2) relatively low throughput (≪100 scc/h) and scalability (e.g., the ease by which production could be scaled by an order of magnitude). For ^{129}Xe, polarization levels are also generally lower than what can be achieved with available SEOP polarizers, although the aforementioned improvements in the technology for producing HP ^{129}Xe via DNP [40] may ultimately allow ^{129}Xe polarizations to approach unity using this technique.

Spin-Exchange Optical Pumping

SEOP History and Theoretical Background

SEOP is a method of generating high polarizations in noble gas nuclei. Spin order is derived from circularly polarized laser light used to selectively deplete one of the electronic ground states of an alkali metal (AM), typically Rb, Cs, or K. Gas-phase collisions then transfer polarization from the AM electrons to the noble gas nuclei via Fermi-contact interactions.

It was in Kastler's pioneering work [44] where the ability to use light to polarize electron spins was first demonstrated. Polarization of the nuclei of noble gases via spin exchange with optically pumped AM vapors was later demonstrated by Bouchiat et al. [45] and Grover [46], leading to detailed study and advancement of the SEOP approach by Happer, Cates, Walker, and many others (e.g., Refs. [47−51]).

SEOP is most commonly used to polarize nuclear spin $^1/_2$ ^{129}Xe and ^{3}He, though it is also possible to polarize the quadrupolar species ^{21}Ne [52,53], ^{83}Kr [14], and ^{131}Xe [9] (where $I=3/2, 9/2, 3/2$, respectively). Rb is often the AM of choice due to its low melting point [54] facilitating vaporization, and the availability of high-powered, frequency-narrowed lasers tunable to the D_1 transition [55,56].

The polarization of the AM electrons (Fig. 2.2A), P_{AM}, is determined by the optical pumping rate γ_{OP} and the rate of spin-destruction lost to nonangular-momentum-conserving interactions, Γ_{SD} [52]:

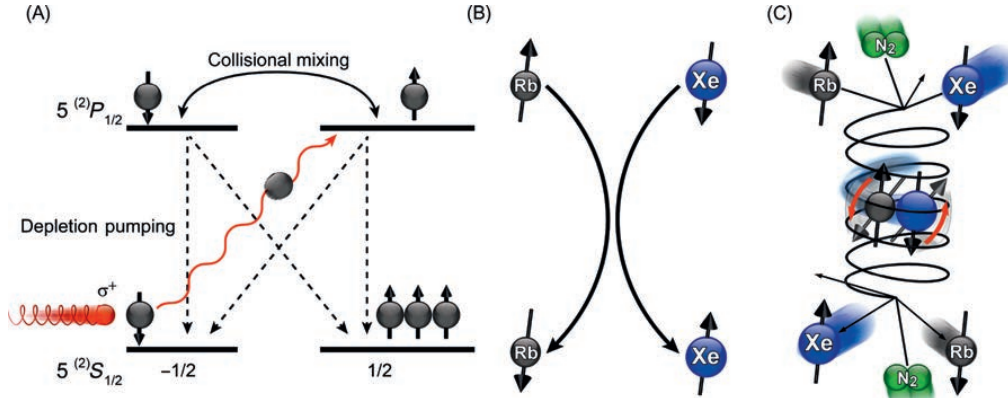$$P_{AM}(z,r) = \frac{\gamma_{OP}(z,r)}{\gamma_{OP}(z,r) + \Gamma_{SD}},$$

FIGURE 2.2 The two-step process of SEOP. (A) First step: Optical pumping of the electronic spins of an AM vapor (Rb); hyperfine splittings caused by the presence of the Rb nuclear spins are omitted for clarity. (B,C) Second step: Spin exchange between the Rb electron and noble gas (here, Xe) nuclear spin during binary (B) and/or three-body (C) gas-phase collisions.

where both P_{AM} and γ_{OP} are a function of position within the OP cell. γ_{OP} is determined by the frequency overlap between the laser's spectral profile and the pressure-broadened AM D_1 transition line, and Γ_{SD} is the electronic spin-destruction rate [52]:

$$\Gamma_{SD} = \sum_i k^i_{SD} \cdot [M_i],$$

where k^i_{SD} quantifies the rate of spin-destroying collisions with each of the ith gas species present in the cell and $[M_i]$ is the number density of that species. At any significant distance from the cell walls, collisions with Xe typically dominate the AM electronic spin destruction; k^{Xe}_{SD} has been measured to be orders of magnitude greater than $k^{N_2}_{SD}$ and k^{He}_{SD} [57,58]—a fact that makes it more difficult to hyperpolarize ^{129}Xe at higher xenon densities (alkali−alkali collisions may also be relevant during ^{3}He pumping).

Once the AM vapor is polarized, angular momentum may be transferred from the AM electron spins to the nuclei of the noble gas (NG) through gas-phase collisions. This spin-exchange process may be mediated by two distinct mechanisms: "two-body" transient dimers (brief AM−NG interactions—simple collisions, Fig. 2.2B) or "three-body" persistent dimers (longer interactions between an AM atom and a heavy NG atom, where a third species facilitates the formation and destruction of van der Waals complexes; Fig. 2.2C). For example, for ^{3}He only two-body collisions contribute to spin exchange, but for ^{129}Xe, more complex collision mechanisms can contribute significantly—with the more-efficient three-body term dominating under conditions of low gas density (particularly Xe density) [48]. Since AM/Xe interactions are often not spin-conserving, the probability of the AM electron spin order being transferred to the noble gas nuclei in any one collision is low. However, AM polarization lost to collisions is quickly recovered by photon reabsorption, so that order lost to spin-rotation interactions is quickly regained—provided the resonant photon flux is sufficiently high.

The AM electron spin polarization reaches steady state on a timescale much faster than the spin-exchange rate (γ_{SE}), and thus the nuclear spin polarization of the NG accumulates over time according to simple exponential behavior. For example, for ^{129}Xe the time-dependent polarization is governed by [52]

$$P_{Xe} = \langle P_{AM}(z,r) \rangle \cdot \left(\frac{\gamma_{SE}}{\gamma_{SE} + \Gamma_{Xe}} \right) \cdot \left\{ 1 - \exp \left[-(\gamma_{SE} + \Gamma_{Xe})t \right] \right\},$$

where $\langle P_{AM}(z,r) \rangle$ is the spatially averaged AM polarization, $\Gamma_{Xe} = (T_1^{Xe})^{-1}$, and γ_{SE} is given by [52]

$$\gamma_{SE} = [AM] \cdot \left\{ \frac{\gamma_{AMXe}}{[Xe]} \left(\frac{1}{1 + br} \right) + \langle \sigma \nu \rangle \right\},$$

where [AM], [Xe] are number densities, γ_{AMXe} is the three-body interaction rate, $\langle \sigma \nu \rangle$ is the velocity-averaged binary SE cross-section, and the factor $1/(1 + br)$ accounts for the ratio of nitrogen to xenon in the cell and their

relative efficiencies in facilitating formation/breakup of persistent dimers (br $= 0.275 \cdot$ (N$_2$ pressure)/(Xe pressure)). Thus, the SE rate γ_{SE} is proportional to the AM density. Moreover, as discussed above the relaxation rates of ^{129}Xe and ^{3}He are typically much slower than the SE rates during SEOP, allowing the NG polarization to ultimately approach $\langle P_{AM}(z,r) \rangle$ in some circumstances. These long relaxation times also facilitate HP gas storage and transport.

SEOP Instrumentation

A number of essential experimental components are required to conduct an SEOP experiment (illustrated in Fig. 2.1): (1) an optical pumping cell made typically of borosilicate (Pyrex) glass, containing a small quantity of AM and the noble gas to be polarized; (2) an oven to vaporize the AM and control the temperature during (and between) SEOP runs; (3) a magnetic field of tens of Gauss; and (4) a source of circularly polarized laser light tuned to the optical D_1 transition of the AM [49].

Polarizers harness the SEOP process to produce large quantities of HP gas for use in further applications. In these applications it is often high magnetization—the product of the HP noble gas (HPNG) polarization and concentration—that is desired. Polarizers are therefore often designed to optimize these parameters. Broadly, these SEOP devices are typically divided into two categories based on their modes of operation and design features—stopped-flow polarizers and continuous-flow polarizers—as described below.

STOPPED-FLOW POLARIZERS

In stopped-flow polarizers [11,25,59−66] (Fig. 2.3A−C) the optical cell is sealed during SEOP and holds a static quantity of gas mixture that is heated using an oven and optically pumped with a high-powered laser source. Steady-state nuclear polarization is typically achieved within minutes or tens of minutes for ^{129}Xe [25], ^{83}Kr [10], ^{131}Xe [9,69], and ^{21}Ne [70], and hours for ^{3}He [71], at which point the cell can be cooled within the oven—thereby condensing the AM vapor on the inner surface of the optical cell, and allowing for the extraction of the HP gas mixture for use in experiments [25,65].

CONTINUOUS-FLOW POLARIZERS

In continuous-flow polarizers [20,68,72−78] the gas mixture flows through a heated optical pumping cell where it undergoes SEOP with AM vapors during transit through the cell. The now-polarized gas can then be flowed continuously into an experiment, recirculated through the polarizer [75,78], or—in the case of xenon—cryogenically collected using a cold finger submerged in liquid nitrogen at high field [21]. At 77K ^{129}Xe solidifies while largely maintaining its polarization. The accumulation time is constrained however by the T_1 of xenon in the solid phase ($\sim$3 h at 77K) [19−21]. Cryogenic collection is not practical for the quadrupolar HP nuclei, as the T_1 values are far too short in the solid state. A diagram of one continuous-flow design is provided in Fig. 2.3D [68]. This variant employs a "counterflow" design wherein the premixed gas (containing ^{129}Xe to be HP) flows toward the incident laser light, such that the gas mixes with the most highly polarized Rb vapor before leaving the OP cell. To mitigate deleterious Rb-induced thermal runaway [73,79,80]—and possibly the formation of Rb clusters [81]—the majority of the Rb within the system resides outside of the pump beam within a Rb presaturator located upstream of the OP cell, saturating the gas mixture as it flows through—even at high flow rates.

SEOP Gas Mixes and Operating Regimes

There are substantial differences in the gas mixes and operating regimes employed in stopped-flow and continuous-flow polarizers. The first continuous-flow polarizer was operated at high pressure ($\sim$10 atm) to optimally couple the Rb D_1 line to the broadband pump laser via collisional broadening [20]; note that broadband LDAs have spectral linewidths of $\sim$2−3 nm (FWHM). However, in order to maximize P_{Xe} the xenon fraction was kept low (typically 1%) to minimize Rb-Xe spin destruction, thus, helium became a major constituent of the mixture due to its low Rb spin-destruction cross-section. In order to suppress radiation trapping [82] (i.e., to suppress radiative decay of the excited Rb), a small fraction of nitrogen was added to the mix. High concentrations and substantial volumes of HP xenon could then be obtained by cryo-accumulation of the xenon gas, a process which separates it from the rest of the gas mix [20]. The continuous-flow pressure polarizer in Fig. 2.3D [68] operates within an atypical, lower pressure—so called "long-lived" or van der Waals—regime in order to exploit the faster SE rates that prevail there. This shift in approach was made possible in part by the high-power pump laser (90 W, with moderate linewidth of $\sim$1.5 nm FWHM) it employed.

Likewise, stopped-flow polarizers have progressed significantly with the advent of frequency-narrowed high-power lasers (with spectral typical widths of $\sim$0.2−0.4 nm) [56,62,64]. Most notably, these lasers have enabled
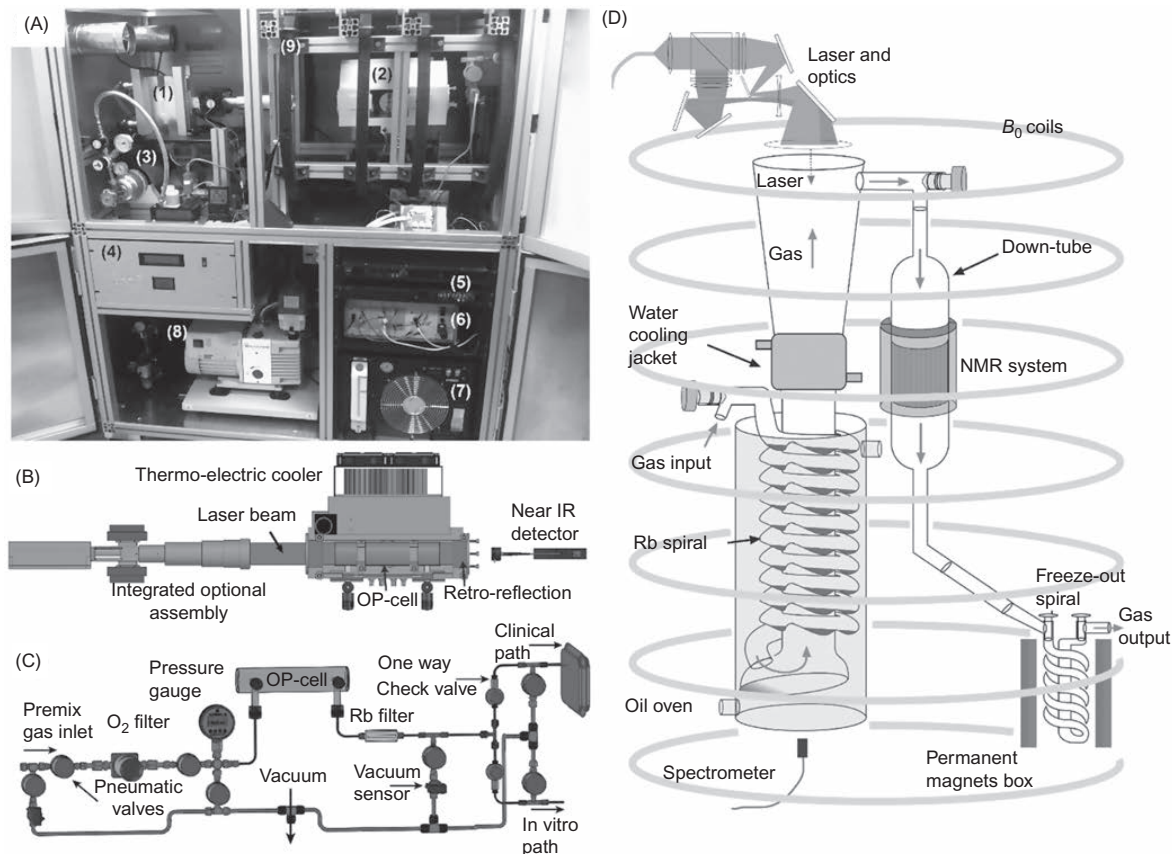
FIGURE 2.3 Examples of ^{129}Xe hyperpolarizers. (A−C) Our Consortium's second-generation stopped-flow (SF) Xe hyperpolarizer. The photo in (A) shows the principal components of the device ((1) laser; (2) 3D-printed oven; (3) Xe gas supply; (4) microcontroller box; (5) power supplies; (6) low-frequency NMR spectrometer; (7) water chiller; (8) vacuum pumps; (9) electromagnetic coils). Diagrams showing the oven/optical path and gas manifold are shown respectively in (B) and (C). (D) Diagram showing the continuous-flow (CF) design of Ruset and colleagues [68]. *Source: For (C) from Nikolaou P, Coffey AM, Barlow MJ, Rosen MS, Goodson BM, Chekmenev EY. Temperature-ramped 129Xe spin exchange optical pumping. Anal Chem 2014;19:8206−12 [67]. For (D) figure courtesy of W. Hersman.*

operational regimes to be found where high polarizations can be achieved with relatively high xenon densities in cells that no longer required helium for pressure broadening [17,25,80,83]. Indeed, where higher xenon densities are used this approach can obviate the need for cryo-collection while still obtaining high concentrations of highly polarized xenon in sufficient quantities for clinical lung imaging [25].

SEOP Characterization

A number of diagnostic techniques have been applied to SEOP over the years, driven by a desire to deconvolute the complex interplay among the relevant experimental parameters—thereby aiding both the understanding of fundamental SEOP phenomena and the optimization of polarizer performance. Of these, the most easily employed are in situ (low-field) NMR and IR spectroscopies. Based on NMR and IR data alone, one can detect and quantify the HPNG magnetization (via NMR), obtain spin-exchange and spin-destruction rates (using fits to build up T_1 decay curves from the HPNG NMR), observe spatial variations in the noble gas nuclear spin polarization, monitor optical absorption by the AM (via IR [25]), and estimate the globally averaged AM polarization using a simple field cycling method, now described [25,83]. In this approach, the simplest and most readily implemented for obtaining a measure of P_{AM}, one compares absorption spectra of the pump laser transmitted through the cell when the magnetic field is cycled [25,62]. The technique utilizes a simplistic Beer's law approach

and the "bleaching" of the IR absorption spectrum resulting from the depletion pumping of the ground-state magnetic sublevels. The first step of the OP process—whereby the Rb electrons become spin-polarized—leaves a smaller concentration of Rb atoms in the laser-absorbing m_J state. In turn, this population reduction allows more laser light to be transmitted through the cell, allowing P_{AM} to be estimated from the difference [62].

To monitor the buildup of P_{Xe} via in situ NMR, single-shot "pulse-acquire" experiments suffice, and the ability to signal average is only needed if a calibration of the signal against water is required. Thus, a number of groups have constructed low-field spectrometers [84–87], though commercial systems (such as Magritek's Kea and Aurora spectrometers) exist. Requirements for the IR spectrometer are governed by the line width and tunability of the laser source, and are met by devices that are commercially available (e.g., Ocean Optics HR4000).

Nevertheless, these probes provide only part of the picture of what occurs within an SEOP cell during optical pumping. For example, it is often desired to have a direct measure of the AM electronic polarization. Such measurements can be made using optically detected electron spin resonance (ODESR) [88], measurement of collisional frequency shifts [89], and Faraday rotations [70,90,91]. Such measurements can provide insight into limitations of the nuclear spin polarization (since it is ultimately bound by P_{AM}).

An ODESR experimental setup is illustrated in Fig. 2.4A and B [88]. This method probes the AM electronic sublevels using (1) a transverse RF field tuned to the Rb EPR resonance frequency; (2) a low-power circularly polarized D_1 (or D_2) probe laser (usually) orthogonal to the pump beam; and (3) a photodetector coupled to a lock-in amplifier which detects the modulation of the probe laser transmission caused by the precessing Rb magnetization. By sweeping B_0 across the Zeeman sublevels one can obtain a spectrum in which the relative intensity of the peaks provides a direct measure of the relative populations of the sublevels [76,88,92–94]. When combined with gradients the peaks can be spatially encoded and high-resolution AM polarization images of less than 1 mm can be obtained [88,93,94].

Another approach for probing spin polarization within SEOP cells involves precise measurement of polarization-dependent shifts of the Larmor frequency of the NG—and vice versa: collisional frequency shifts in He and Xe NMR spectra (Fig. 2.4C–E) have been shown to be a function of Rb magnetization, thereby providing a simultaneous measure of HPNG and AM polarization [89]. The effect arises directly from the Fermi-contact interaction and its magnitude is characterized by the dimensionless enhancement factor κ_0, measured as $(\kappa_0)_{RbHe} = 4.52 + 0.00934T$ (with T in °C) [95,96] and, more recently, $(\kappa_0)_{RbXe} = 493 \pm 31$ [89]. These values, when combined with a measurement of the frequency shift of the NG in question (and an estimate of the AM density, discussed below), can be used to obtain a volume-averaged expectation value for the z-component of the AM electron spin $\langle S_z \rangle$ (where Rb magnetization is proportional to $[Rb]\langle S_z \rangle$) according to the relation given in Ref. [89].

Faraday rotation—the rotation of the plane of polarization of nearly resonant light as it traverses the SEOP cell—provides another method for the determination of AM polarization. This approach exploits the fact that the B_0-induced Zeeman splitting of the AM metal vapor induces a phase shift between the circular components of the linearly plane-polarized light, resulting in a rotation in the plane of polarization [70,90,91,97,98].

In an alternative configuration, Faraday rotation can also be used to measure the AM vapor density—another key parameter governing SEOP [98]. The spin-exchange rate increases as a function of the AM density, and knowledge of the AM density is thus necessary in order to extract (per-atom) spin-exchange cross-sections. A simpler (and older) route for measuring the AM density utilizes the empirical thermionic emission data published by Killian [99]. The AM density can be roughly predicted from the cell temperature using AM density curves (see, e.g., Ref. [54]); other such formulae can be used (e.g., Ref. [100]) and may achieve better quantitative agreement when compared to results from other methods [101]. Alternatively, relatively simple optical absorption methods can be used for the direct measurement of AM density during SEOP by monitoring absorption of light from (for instance) a 421.5 nm source by the $5S_{1/2}-6P_{1/2}$ Rb transition [102], though other transitions may be used [103].

Finally, temperature is another important parameter governing SEOP. In addition to determining the AM density, temperature can affect the values of many parameters mentioned above. Exterior cell wall temperatures and oven air temperatures can be measured trivially via thermocouples; however, measurement of the internal gas temperature can be challenging. As mentioned previously, nitrogen buffer gas is often present in the HPNG mix, making it possible to monitor the in-cell temperature of the gas mixture by Raman spectroscopy [104,105]. Nitrogen collisionally deexcites the excited Rb atoms via radiationless, two-body quenching collisions and concomitantly accumulates energy in its rovibrational manifolds. Irradiating the gas with a probe laser causes Raman scattering. The relative peak intensities of the resulting Raman spectra reveal the distribution of energy across the rotational states and is a function of temperature [106]. To date, the method has shown that temperatures within the OP cell can be elevated by hundreds of degrees above ambient [104], particularly when Xe
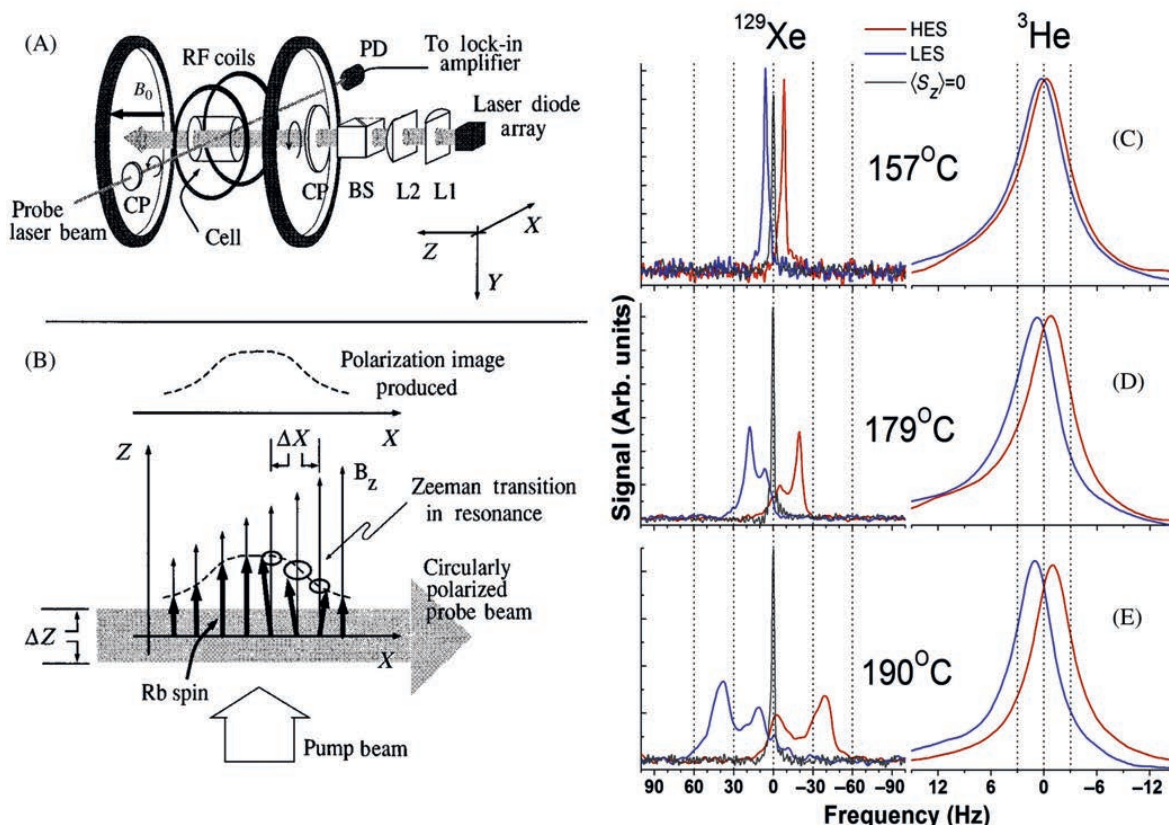
FIGURE 2.4 ODESR and collisional frequency shifts. (A) ODESR experimental apparatus, described in text and in full in Ref. [88]. The total magnetic field B is the resultant of a uniform field B_0 and a linear gradient field $(r\nabla B)$, both along the z axis. Not depicted are the coils used to generate the gradient fields and the oven. (B) Schematic sketch of imaging with a linear gradient. The signal arises solely from the Rb spins in resonance. As B_0 is swept linearly in time, the volume element in resonance is swept along the x axis. (C), (D), and (E) Typical ^{3}He and ^{129}Xe collisional shift spectra from cell 155B acquired one-after-the-other under steady-state SEOP conditions. The narrow ^{129}Xe peak at 0 Hz was acquired with the laser blocked (such that the ^{129}Xe was still HP whereas the Rb was not); it has been amplitude normalized to appear on the same graph. The double peak, in the ^{129}Xe spectra at all but the lowest temperatures, represents regions of highly polarized and nearly unpolarized Rb vapor; the lines are broadened and begin to coalesce due to diffusion of ^{129}Xe between these two regions. For ^{3}He, the much smaller frequency-shift dispersion and more rapid diffusion yield a single narrow peak in all cases. The respective shifts in the spectral "center of mass" upon reversal of the Rb magnetization were used to extract $(\kappa_0)_{RbXe}$. LES and HES (low and high Zeeman polarization energy state) respectively appear on the left and right in each of the plots in (C), (D), and (E). Alternation between LES and HES was achieved by inverting the quarter wave plate of the pump laser.

density is high [107]; convection plays a key role in the heat transport within the cell [104]; and there is impact of narrowed versus broadband sources on the thermal dynamics within the OP cell [105]. Raman spectroscopy is well-placed to provide further insight into the deleterious "rubidium runaway" [73,79,80] and Rb cluster formation [81] phenomena, which may become critical issues as ever more powerful pump lasers are used.

Applications of SEOP-Prepared HP Gases

HPNGs continue to be utilized in an ever-growing number of fields. For example, ^{3}He has been widely adopted for applications varying from biomedical imaging [108−111] and apparent diffusion coefficient (ADC) measurements of the lungs [112,113]; studies of fundamental symmetries [114,115]; and in polarized neutron spin filters and targets for electron scattering experiments [116−120]. However, the main supply of ^{3}He is through tritium decay in nuclear warheads, and with diminishing stockpiles the price of ^{3}He is becoming prohibitively expensive [121], likely limiting its future use.
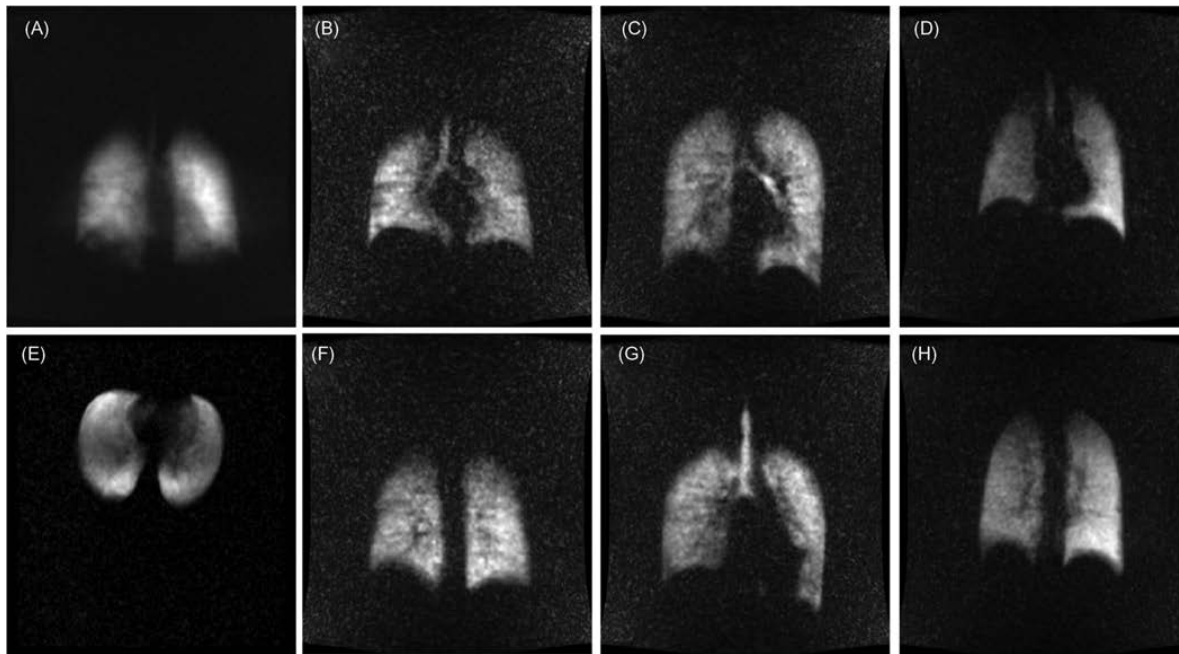
FIGURE 2.5 Examples of xenon MR images of heathy human lungs taken during a breath-hold. (A) Infinite coronal slice in a 26-year-old male. (E) Infinite axial slice in a 23-year-old female. (B,F), (C,G), and (D,H) pairs of coronal images from three healthy volunteers: a 26-year-old male, a 22-year-old male, and a 29-year-old male, respectively. HP Xe gas was produced on a GE2000 Polarizer using a 2% Xe natural-abundance mix. ^{129}Xe polarization was typically $\sim 9\% \pm 0.5\%$. FGRE sequence used for all images, FOV = 48 cm $\times$ 48 cm, TE = 4.2 ms, TR = 9 ms, FA = $\sim 5.5°$, Res = 128 $\times$ 128, Slice thickness = Inf. for (A,E); 25 mm for (B,C,D,F,G,H). *Source: University of Nottingham.*

Unlike ^{3}He, xenon is naturally abundant and is a by-product of oxygen production. ^{129}Xe is mildly soluble in blood and organic solvents and has a broad chemical-shift range that makes it attractive for a number of applications. To date, these features have been exploited in studies of porous materials (e.g., Ref. [122]) and surface interactions (e.g., Ref. [59]); and extensively in a variety of chemical, biophysical, and biomedical applications, including those involving cryptophane-based host systems and void-space imaging (reviewed in Refs. [123−128]); extensively in studies of the lungs (e.g., Refs. [111,129−140] and Fig. 2.5); the brain (e.g., Refs. [24,141−151]); and other bodily tissues [152] including the blood [153−156]. Indeed, the biomedical applications of HP ^{129}Xe and ^{3}He will dominate most of the remaining book chapters.

Contrary to ^{129}Xe and ^{3}He, the quadrupolar species ^{21}Ne, ^{83}Kr, and ^{131}Xe undergo rapid spin relaxation, as mentioned above. This rapid relaxation makes many applications challenging, but also provides—particularly in the cases of ^{83}Kr and ^{131}Xe—a unique and complementary sensitivity to the chemical composition of surfaces in porous media and the shape, size, and symmetry of void spaces [69,157−160], including (in the case of ^{83}Kr) the lungs [14,161]. ^{21}Ne, the least studied of the HPNGs, has potential for use as a navigational gyroscope [70], and in precision tests of Lorentz and CTP symmetries as a comagnetometer [162].

Metastability Exchange Optical Pumping

MEOP History and Theoretical Background

An alternative to SEOP is MEOP, an approach that relies on optical pumping of an atom's metastable state possessing nonzero spin angular momentum. Optical pumping had already been successfully applied to vapors of AMs and mercury to polarize the electronic and nuclear magnetic moments of such atoms [163], but it was not until 1960 that the technique was applied to the electronic ^{4}He $2^{3}S_1$ metastable state [164], and then to ^{3}He in 1962 [165]. The technique has also been successfully applied to polarize the electronic and nuclear states of ^{21}Ne [166], ^{83}Kr [167], and ^{131}Xe [168], the latter using an electron beam for pumping instead of an optical source.
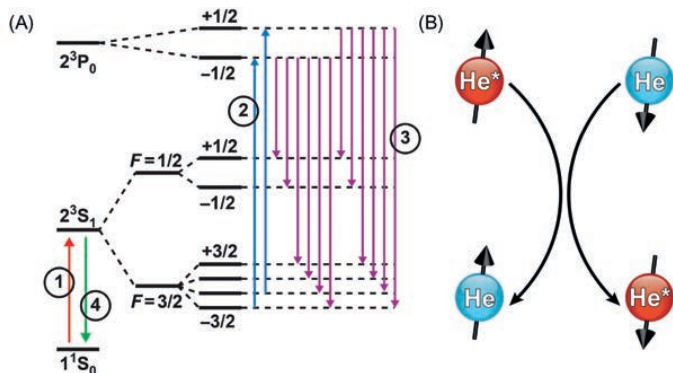
FIGURE 2.6 (A) Energy transitions involved in metastable optical pumping of helium. (1) Excitation due to RF discharge. (2) Excitation due to pumping light. (3) Decay back to all metastable states. (4) Decay due to metastability exchange collision. (B) Metastability exchange Collision. Nuclear orientation is represented by an arrow, and polarized metastable electronic states by an asterisk (*).

MEOP has also been used to polarize the electronic states of ^{129}Xe [169], but nuclear polarization was not seen, likely due to strong nuclear relaxation mechanisms.

Fig. 2.6A shows the energy levels involved in the optical pumping of the helium metastable states. An RF discharge placed across a low-pressure sample (e.g., within a glass cell) excites a small fraction of the He atoms from the 1^1S_0 ground state to the long-lived 2^3S_1 metastable state (label 1). Resonant circularly polarized light then excites population from the 2^3S_1 to the 2^3P_0 state, according to the selection rule $\Delta m = +1$ (label 2). This selectivity means that the pumping light only excites atoms from the metastable $m = -^1/_2$ and $m = -^3/_2$ sublevels to the $m = +^1/_2$ and $m = -^1/_2$ sublevels, respectively. The population then decays back to all 2^3S_1 sublevels with roughly equal probability (label 3). The net result is the transfer of atoms from the lower magnetic quantum numbers ($m = -^1/_2, -^3/_2$) to the higher magnetic quantum numbers ($m = +^1/_2, +^3/_2$). Unlike He^4, He^3 has a nonzero nuclear spin, and there is efficient coupling between the nucleus and the electrons (the hyperfine interaction)—resulting in an entanglement of electronic and nuclear spin states. Because of this interaction, optical pumping of the electronic angular momentum simultaneously induces nuclear orientation as well [170]. Finally the metastable and ground-state sublevels are coupled via metastability exchange collisions (label 4). Fig. 2.6B shows a representation of the metastability exchange interaction between metastable atoms (denoted He*) and ground state atoms, with the arrows representing their nuclear spin states.

It was realized that as a consequence of hyperfine interaction and the metastability exchange collisions in ^{3}He atoms, the emerging ground-state atom has a polarized nucleus. It was found that the metastability exchange collision dominates the ground-state ^{3}He nuclear magnetic relaxation rate (T_1), leading to a polarization of the ground-state ^{3}He nuclei—matching the degree of polarization of the electronic spins of the metastable atoms [165]. Typical polarization rates have been reported as 10^{18} atoms/s (e.g., Refs. [171,172]); in those examples, steady-state polarization was achieved in $\sim 0.5-3$ min for low-pressure (<10 Torr), small cells (<300 cm^3).

Initially, there were two limitations of the MEOP technique. The first was the type of polarizing light source that was available. Early experiments were performed using helium discharge lamps, leading to low polarizations. To get higher levels of metastable (and hence nuclear) pumping, a more powerful source is required. The second limitation was the low pressure, around 1 mbar required by the RF discharge. For any experiment or application requiring HP ^{3}He at greater than 1 mbar pressures, a polarization-preserving compressor is needed. New techniques developed in 2002 [173] using high magnetic fields have allowed polarization at higher pressures. However, even then a compressor is required before the polarized gas can be used experimentally. These issues are discussed in greater detail below.

MEOP Laser Technology

Helium discharge lamps are inefficient sources for the 1083 nm circularly polarized light required for the 2^3S_1 to 2^3P_0 excitation; e.g., a 10 W helium discharge lamp generates less than 1 mW of useful pumping light at 1083 nm. Nevertheless, these early studies reported polarizations from $\sim 20\%$ to $\sim 40\%$, typically using 5 cm diameter spherical cells of ^{3}He at ~ 10 Torr [165].

It was not until the advent of tunable laser sources at 1083 nm that ^{3}He and ^{4}He MEOP became more viable. In the late 1980s a laser with a medium comprised of a crystal of La$_{1-x}$Nd$_x$MgAl$_{11}$O$_{19}$ (known as LNA) became readily available [174], allowing for higher polarizations of $\sim 60\%$ (110 cm^3 cell at 0.3 Torr) [175] and even $\sim 85\%$ (70$-$300 cm^3 cells at 0.1$-$1.0 Torr) [171] for HP ^{3}He. However the LNA lasers still had notable limitations,

including significant variations in the quality of the LNA crystals, thermal conductivity and gradient issues within the LNA, as well as nontrivial space, cooling, and power requirements.

The mid-1990s saw the advent of low-power laser diodes capable of operating at the required 1083 nm. It was found that polarizations approaching the theoretical limit of 100% could be routinely achieved using such lasers, albeit within low-volume collimated beams [176]. However, the output power is low compared to the LNA lasers (only ~ 50 mW) and as such these sources have generally been unable to polarize clinically relevant quantities of ^{3}He in a sufficiently short period of time. MEOP of ^{3}He using a newer compact, high-efficiency tunable 1083 nm source based on a ytterbium (Yb) fiber laser was first reported in 1997 [177]. These air-cooled table-top lasers can have electrical input/optical output efficiencies of >25% [177]. Yb fiber laser powers of 1.5 W have been used to achieve polarizations of up to 82% (260 cm^3 at 0.3 Torr) [172], matching that of equivalent LNA lasers. Since then, the optical power of commercial Yb fiber lasers has greatly increased, enabling higher polarization values while also allowing for more HP ^{3}He to be prepared in a given time [178].

MEOP Compressor Technology

There are several fields of research that utilize dense samples of HP He^3 gas, such as a target in nuclear physics [179], medical imaging [129], and neutron scattering [180]. Such applications have thus required a method of compressing the low-pressure HP ^{3}He polarized via MEOP with minimal polarization loss in order to achieve gas densities required for these uses.

The earliest solution reported was by Daniels and Timsit [181] who used a Toepler pump to compress the polarized ^{3}He. A Toepler pump is comprised entirely of glass, and uses a reservoir of mercury that when raised and lowered acts as a piston to compress the ^{3}He gas. The main issue with the Toepler pump is that its valves suffer from sticking and/or leaking problems, and its slow pumping speed (15–30 s per "stroke") [182]—much slower than a conventional piston pump.

The 1990s saw developments in new compression methods with the advent of titanium-based piston pumps [183]. It was found that the ^{3}He T_1 relaxation time for contact with certain materials (Pyrex, titanium, copper, brass, aluminum, glass, etc.) was long enough (~ 60 min) that their use would not lead to large ^{3}He depolarization losses. Since then other groups have built upon this work, creating optimized pumping systems to increase the speed of compression and the maximum pressure attainable, while also lessening the impact of the pump on the polarization losses of the gas [178,184]. Simpler and more compact compression solutions include modified diaphragm pumps [185] and peristaltic pumps, with which continuous flow polarization has been reported [186].

MRI Applications of MEOP-Polarized Gases

Following the first reported use of HP ^{129}Xe MRI on ex vivo air spaces in 1994 [129], HP ^{3}He was tested as a potential alternative [187]. ^{3}He has several advantages over ^{129}Xe, namely that it has a higher gyromagnetic ratio and can be inhaled in larger quantities without substantial risk, as it is not absorbed by the tissue of the lungs— as is known from deep sea diving and special lung function tests [188]. Until recently, it was also easier to achieve higher polarizations in ^{3}He than ^{129}Xe. Initial images obtained with HP ^{3}He prepared were taken on excised guinea pigs [187]. MEOP-prepared HP ^{3}He has since been successfully used to take images of human lungs [108], with considerable research into finer more detailed images, and the differences in the ventilation of the lungs afflicted by various illnesses.

HP ^{3}He has also been used to assess the lung's microstructure by making use of diffusion weighting gradients to measure the ADC of the smaller airways [189]. This technique has been used to explore the progression and effect of thoracic diseases such as COPD [190], asthma [191], emphysema [113], and pulmonary fibrosis [189] at the alveolar level (Fig. 2.7). However, owing to the ever-increasing expense of ^{3}He because of the worldwide shortage of this isotope [192], future research into lung MRI is likely to concentrate on naturally abundant alternatives, such as ^{129}Xe and quadrupolar species such as ^{83}Kr and ^{131}Xe [193].

Parahydrogen-Induced Polarization

Principles

The production of macroscopic quantities of gases with high spin order—a key topic of this entire book—arguably owes its origin to the studies of the spin isomers of molecular hydrogen (H_2) gas by Bonhoeffer and Harteck [194]. Because ^{1}H nuclei are fermions, the overall wave function for H_2 must be antisymmetric with respect to exchange. All H_2 molecules in the (symmetric) ground rotational state ($J = 0$) must be in the (antisymmetric)
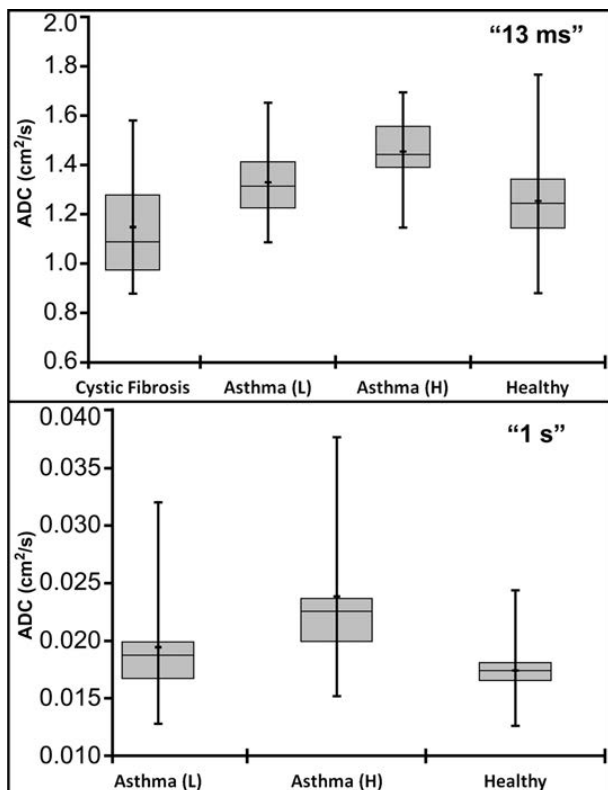
FIGURE 2.7 Apparent diffusion coefficients measurements using HP ^{3}He. Top Graph: Short timescale ADC results (13 ms). Bottom Graph: Long timescale ADC results (1 s). *Source: The University of Nottingham. Data was acquired using relatively small quantities of HP ^{3}He (0.5 L of 1:18 ^{3}He:^{4}He mix) prepared via MEOP, at two different diffusion timescales, on a total of 317 volunteers (18 with CF, 33 with Asthma (Low S_{acin}), 15 with Asthma (High S_{acin}), and 251 healthy).*

singlet spin state [$\propto (|\uparrow\downarrow\rangle - |\downarrow\uparrow\rangle)$] (a.k.a. "para-hydrogen," *para*-H$_2$), and all H$_2$ molecules in the antisymmetric $J = 1$ state must be in the (symmetric) triplet nuclear spin state [$\propto (|\uparrow\downarrow\rangle + |\downarrow\uparrow\rangle), |\uparrow\uparrow\rangle, |\downarrow\downarrow\rangle)$] (a.k.a. "ortho-hydrogen"). Thus, the significant energy difference between the ground and excited rotational states provides the means to prepare and separate *para*-H$_2$: although the ratio of *para*-H$_2$:*ortho*-H$_2$ is about 25%:75% at room temperature, reduction to liquid-N$_2$ temperature (77K) with concomitant exposure to a paramagnetic catalyst that accelerates the ortho-para conversion (like iron oxide) enriches *para*-H$_2$ to 50% of the mixture, and reduction to 20K can enrich the *para*-H$_2$ fraction to well over 90%. Importantly, in the absence of exposure to paramagnetic centers (e. g., from O$_2$ gas or those within container walls) the exchange between *para*-H$_2$ and *ortho*-H$_2$ is extremely inefficient—allowing *para*-H$_2$ to be stored effectively for weeks [195].

However, the pure spin order of the singlet state of *para*-H$_2$ is actually NMR-invisible. Instead, HP gases may be produced using PHIP, where PHIP-prepared HP gases have been demonstrated initially in the context of void-space imaging [196]. This process still fundamentally relies on the singlet of *para*-H$_2$ molecule to be the source of spin order, which can be transformed into observable nuclear spin polarization by the process of symmetry breaking typically conduced via a process of pairwise chemical addition of *para*-H$_2$ to an unsaturated precursor molecule [197]—as shown schematically in Fig. 2.8; a key requirement is that the unsaturated bond must be structurally asymmetric, such that the nascent ^{1}H positions following hydrogenation are magnetically inequivalent. While the process underlying PHIP has been known for many decades, it was not until the advent of efficient heterogeneous catalysts promoting significant fractional pairwise addition of *para*-H$_2$ (vs radical addition [196]) that efficient (high P), relatively large-scale production of PHIP HP gases became possible. Notably, the *radical* addition of *para*-H$_2$ does not lead to PHIP, because *para*-H$_2$ singlet order is scrambled. $P_H \sim 1\%$ has been recently demonstrated in HP propane, enabling submillimeter 3D MRI of the flowing propane gas [198]. The propane molecule represents the shortest hydrocarbon framework for breaking *para*-H$_2$ symmetry without deuterium or ^{13}C enrichment. Furthermore, propane is an otherwise nontoxic "simple" asphyxiant with anesthetic properties qualitatively similar to those of xenon. Despite achieving $P_H \sim 1\%$ in seconds, HP propane gas cannot be easily used for biomedical applications, because its T_1 is on the order of 1 s at high magnetic fields. However,
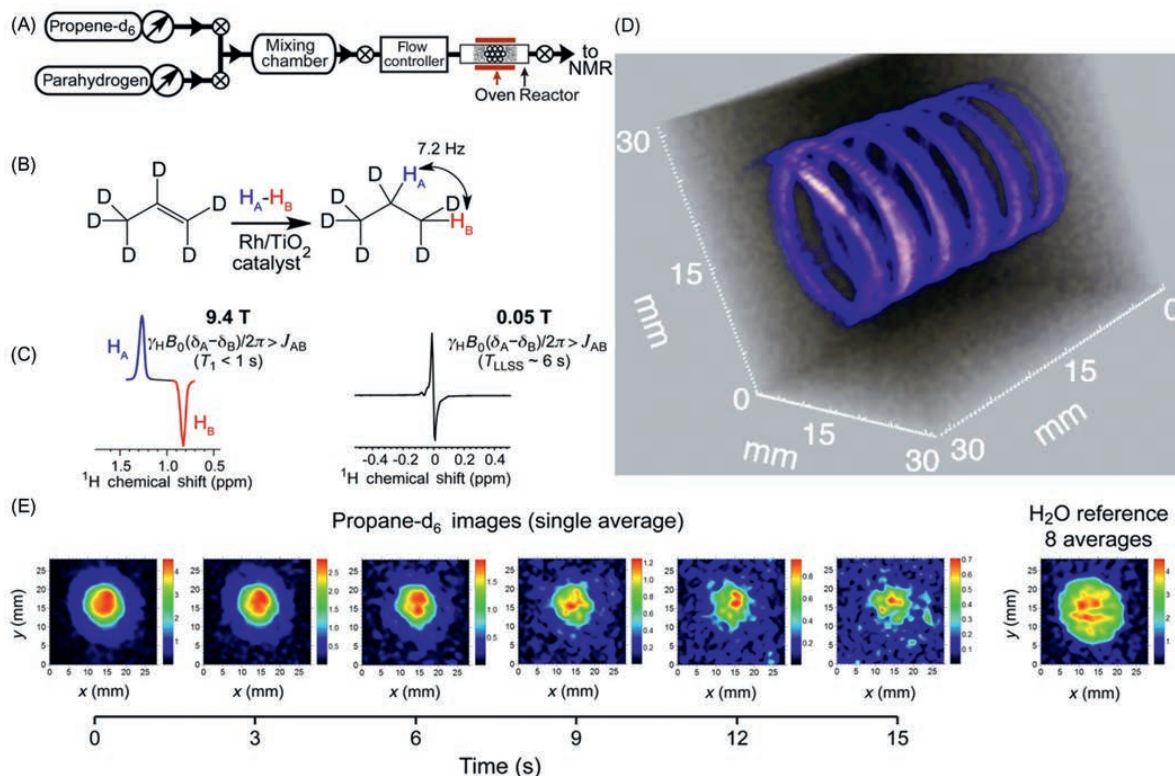
FIGURE 2.8   (A) The schematic representation of PHIP hyperpolarization hardware required for preparation of HP propane gas. (B) The schematics of pairwise addition of parahydrogen gas to an unsaturated precursor molecule resulting in hyperpolarization of propane-d_6 gas via the PHIP approach. (C) Spectroscopic appearance of HP propane-d_6 gas under conditions of high and low magnetic fields corresponding to the two regimes of chemical-shift dominance and J-coupling dominance, respectively. (D) 3D 4.7T MRI of "flowing" (where a constantly renewing bolus of polarization is delivered) propane-d_6 gas with $0.5 \times 0.5 \times 0.5$ mm^3 spatial resolution. (E) 2D subsecond molecular imaging of "stopped" (i.e., gas is no longer flowing to renew the hyperpolarization pool for signal encoding and readout) HP propane-d_6 gas at 0.05T (pixel size 0.88×0.88 mm^2). All images are recorded using the same batch of HP propane-d_6 with apparent $P_H \sim 0.1\%$ [5].

the use of low magnetic fields has been shown to be efficient for extending the lifetime of HP propane through the use of long-lived spin states (LLSS) [199,200] in HP propane [201] and propane-d_6 [5]. The latter exhibits the longest $T_{LLSS} \sim 6$ s [5], which is sufficiently long for imaging of "stopped" gas (i.e., gas that is not flowing and without freshly delivered boluses of hyperpolarization), Fig. 2.8 [5].

PHIP Instrumentation

Besides the hardware needed to create the supply of *para*-H$_2$ (discussed briefly above), the hardware prerequisites are relatively simple for PHIP hyperpolarization of propane and other hydrocarbons. The setup shown in Fig. 2.8 requires mixing two gases: *para*-H$_2$ and propene precursor stored in separate containers. The prepared mix passes through a high-temperature reactor containing the heterogeneous catalyst bed, where the hydrogenation reaction takes place to enable pairwise addition of *para*-H$_2$ to unsaturated precursor. Once prepared in this fashion, the HP propane is ready for use. The setup does not require the use of any alternating or static fields, representing one of the key advantages of this technology: simplicity, scalability, and relatively low-cost production of an HP gaseous agent.

Potential for Biomedical Applications of HP Propane

While efficient production of HP gases by PHIP has been demonstrated only on a relatively small scale of ~ 10 scc/s this approach can be potentially scaled to meet preclinical and clinical requirements. Potential

applications include high-resolution lung imaging given propane's status as a nontoxic gas [202]. Indeed, while propane is flammable, it has lower flammability level and upper flammability level values of $\sim 2.4\%$ and $\sim 9.6\%$, respectively, and a relatively high ignition temperature of $>920°$F. Thus, in addition to other favorable properties (see Ref. [203] for details), the range of conditions required to ignite propane are relatively narrow compared to many other species, making propane more difficult to accidentally ignite—and as a consequence help make propane relatively safe. As a result, flammability is not anticipated here to be an unsurmountable translational challenge. Indeed cyclopropane, which has similar properties to propane, has been used previously as an anesthetic (e.g., Ref. [204], which also discusses accidental but preventable ignitions); and unlike the case with anesthetic use, any propane used for MRI applications could be administered in a variable concentration range and with appropriate mixtures (e.g., coadministered with N_2 gas) to ensure safety. Furthermore, the P_H can also be potentially improved to further enhance the detection sensitivity of HP propane. HP propane offers two other key advantages over HP ^{129}Xe and other noble gases. First, the gyromagnetic ratio of ^{1}H is ~ 3.6 times greater than that of ^{129}Xe, and each propane molecule can carry at least two HP protons, making HP propane nearly an order of magnitude more sensitive than HP ^{129}Xe at the same level of polarization. Second, clinical translation of HP propane will likely be significantly faster, because proton detection capability is universally available on all MRI scanners, unlike the requirement for heteronuclear MRI scanner capability for HP ^{129}Xe and other noble gas isotopes. Furthermore, conventional MRI sequences and MRI coils could be employed for HP propane readout, taking advantage of already available infrastructure. The key disadvantage of HP propane is the requirement of using a low-field MRI scanner rather than a high-field MRI device (in order to exploit the significantly longer hyperpolarization lifetime at low field). However, next-generation low-field MRI instruments are currently under development; moreover, low-field MRI can offer more SNR for imaging HP contrast agents than high-field MRI [205], thereby potentially providing further sensitivity benefits for HP propane technology.

HP GASES: SUMMARY AND OUTLOOK

Examples of nominal polarization values and production rates for several of the HP gases discussed in this chapter are summarized and compared in Table 2.2. A number of HP gases can be prepared with a significant degree of polarization P at quantities (approaching ~ 1 L dose) sufficient for lung imaging and other in vivo imaging applications—including ^{3}He, ^{129}Xe, propane, and ^{83}Kr. Multiple factors determine the practicality of their in vivo and clinical effectiveness as HP contrast agents: (1) the availability and cost of the involved substances; (2) the cost and production throughput of hyperpolarization equipment; (3) the lifetime of the HP gas state; and (4) the availability of suitable MRI imaging hardware (e.g., heteronuclear MRI scanner capability is required for most HP gases). Moreover, some hyperpolarization techniques for gases (e.g., SEOP) have been

TABLE 2.2 Summary of Hyperpolarization Methods, Polarization Results, and Production Rates for Various Gases

Agent	Hyperpolarization method	Nominal/peak polarization values (%)	Estimated production rates (L · atm/h)	Selected references
Xenon-129	SEOP, CF[a]	$P_{Xe} \sim 30-60$	$\sim 1-5$	[206−208]
	SEOP, SF[a]	$P_{Xe} \sim 30-90$	$\sim 0.1-1.2$[b]	[25,67,80]
	d-DNP	$P_{Xe} \sim 30$	<0.1	[40]
Xenon-131	SEOP, SF[a]	$P_{Xe} \leq 2.2$	~ 0.04[b,c]	[9]
Helium-3	SEOP, SF[a]	$P_{He} \sim 60-85$	~ 0.1	[7,180,209]
	MEOP	$P_{He} \sim 65-80$	$\sim 1-3$	[120]
Krypton-83	SEOP, SF[a]	$P_{Kr} \sim 4-27$	$\sim 0.015-0.4$[b,c]	[65]
N_2O	d-DNP	$P_N \sim 10$	~ 0.001	[42]
d_6-propane	PHIP	$P_H \sim 1$	~ 27[b,c]	[198]

[a]CF, continuous flow; SF, stopped flow.
[b]Estimated production rate of the gaseous agent in question at STP, not counting the additional presence of diluting gases (N_2, He, and/or H_2), varying from 25% to 95% of the mixture.
[c]Extrapolated from small amounts quoted with short production times.

available for $>$30 years (and therefore are more robust), whereas others (DNP and PHIP) are newcomers to the field of gas hyperpolarization, providing opportunities for improvement.

Historically, human lung MRI with ^{3}He has been demonstrated first, which was relatively quickly followed by lung MRI demonstration with ^{129}Xe. Other agents with sufficient hyperpolarization lifetime will likely follow this trend—i.e., demonstration of in vivo and human MRI feasibility despite the aforementioned challenges—because these new agents may provide additional (and frequently complementary) biomedical information to what is already feasible with the established HP gases, clinically available imaging modalities, and other tests. For example, while ^{3}He drove the initial feasibility demonstrations of ventilation and diffusion imaging, the advent of clinical-scale production of HP ^{129}Xe enabled the expansion of biomedical HP gas applications to include gas-perfusion imaging, brown fat imaging [210], and brain imaging. Thus, it is not unreasonable to expect that HP propane, ^{83}Kr, and others may provide other benefits to the research community as they are developed, embodying new tools in biomedical research. Indeed, the HP gas research field will likely enjoy substantial growth benefiting from the advent of new HP agents, more advanced instrumentation, and corresponding applications.

However, despite the breakthroughs in science and technology, the in vivo and human demonstrations, and the number of successfully completed clinical trials with HP ^{129}Xe and ^{3}He, HP gases are not yet being used for clinical diagnosis, primarily due to the combinations of the factors outlined above. Therefore, the widespread clinical use of HP agents relies on addressing these translational challenges. While it is not yet clear which of the agents and type(s) of hyperpolarization technique will enjoy clinical adaptation, fundamental changes in MR hardware may be required to achieve clinical use. For example, multinuclear upgrade of 1.5T or 3T clinical scanners is costly ($>$\$0.5 M) and cumbersome (i.e., most hardware vendors are not providing the required software) for HP ^{129}Xe, ^{3}He, ^{83}Kr, or other heteronuclei. As an alternative approach, a dedicated low-field (LF) MRI scanner may have unique advantages as a platform for the clinical adaptation of HP gases. LF-MRI scanners are fundamentally less expensive than high-field superconductive MRI scanners; yet, LF-MRI can yield more SNR for HP applications [205]; furthermore, LF-MRI can provide enhanced patient safety due to significantly lower specific absorption rate at low RF frequencies [211], and significantly higher patient throughput—because patient-tailored magnet shimming and RF coil calibration steps can be obviated. Moreover, LF-MRI is also ideally suited for HP propane imaging, because of the longer-lived HP state.

To conclude, while HP gas MRI is an established field, new advances in preparation and imaging of HP gases continue to emerge and may significantly and positively impact this field. While there are no *fundamental* barriers for clinical translation and adaptation of HP gas MRI, which can be useful for a number of functional MRI applications, significant clinical translation challenges remain and must be addressed before one can expect to see this promising family of approaches become routinely available in the clinic.

References

[1] Anger BC, Schrank G, Schoeck A, Butler KA, Solum MS, Pugmire RJ, et al. Gas-phase spin relaxation of Xe129. Phys Rev A 2008;78.

[2] Saam B. T1 relaxation of 129Xe and how to keep it long. In: Meersmann T, Brunner E, editors. Hyperpolarized xenon-129 magnetic resonance: concepts, production, techniques and applications. London: Royal Soc Chem; 2015. p. 122−41.

[3] Jameson CJ, Jameson AK, Hwang JK. Nuclear spin relaxation by intermolecular dipole coupling in the gas phase. 129Xe in oxygen. J Chem Phys 1988;89:4074−81.

[4] Repetto M, Babcock E, Blümler P, Heil W, Karpuk S, Tullney K. Systematic T1 improvement for hyperpolarized 129xenon. J Magn Reson 2015;252:163.

[5] Kovtunov KV, Truong ML, Barskiy DA, Salnikov OG, Bukhtiyarov VI, Coffey AM, et al. Propane-d₆ heterogeneously hyperpolarized by parahydrogen. J Phys Chem C 2014;118:28234−43.

[6] Barskiy DA, Kovtunov KV, Koptyug IV, He P, Groome KA, Best QA, et al. The feasibility of formation and kinetics of NMR signal amplification by reversible exchange (SABRE) at high magnetic field (9.4 T). J Am Chem Soc 2014;136:3322−5.

[7] Chen WC, Gentile TR, Ye Q, Walker TG, Babcock E. On the limits of spin-exchange optical pumping of 3He. J Appl Phys 2014;116:014903.

[8] Meersmann T, Pavlovskaya GE. Beyond spin $I = 1/2$; hyperpolarized 131Xe and 83Kr magnetic resonance. Hyperpolarized xenon-129 magnetic resonance. Hyperpolarized xenon-129 magnetic resonance : concepts, production, techniques and applications. London: R Soc Chem; 2015.

[9] Stupic KF, Cleveland ZI, Pavlovskaya GE, Meersmann T. Hyperpolarized 131Xe NMR spectroscopy. J Magn Reson 2011;208:58−69.

[10] Stupic KF, Cleveland ZI, Pavlovskaya GE, Meersmann T. Quadrupolar relaxation of hyperpolarized krypton-83 as a probe for surfaces. Solid State Nucl Magn Reson 2006;29:79−84.

[11] Ruth U, Hof T, Schmidt J, Fick D, Jänsch HJ. Production of nitrogen-free, hyperpolarized 129Xe gas. Appl Phys B 1999;68:93−7.

[12] Breeze SR, Lang S, Moudrakovski I, Ratcliffe CI, Ripmeester JA, Simard B, et al. Coatings for optical pumping cells and extending the lifetime of hyperpolarized xenon. J Appl Phys 1999;86:4040−2.

[13] Breeze SR, Lang S, Moudrakovski I, Ratcliffe CI, Ripmeester JA, Santyr G, et al. Coatings for optical pumping cells and short-term storage of hyperpolarized xenon. J Appl Phys 2000;87:8013−17.

[14] Pavlovskaya GE, Cleveland ZI, Stupic KF, Basaraba RJ, Meersmann T. Hyperpolarized krypton-83 as a contrast agent for magnetic resonance imaging. Proc Natl Acad Sci USA 2005;102:18275−9.

[15] Barker JR. New coil systems for the production of uniform magnetic fields. J Sci Instrum 1949;26:273−5.

[16] Jacob RE, Morgan SW, Saam B, Leawoods JC. Wall relaxation of He3 in spin-exchange cells. Phys Rev Lett 2001;87:143004.

[17] Nikolaou P, Coffey AM, Walkup LL, Gust BM, Whiting N, Newton H, et al. XeNA: An automated 'open-source' 129Xe hyperpolarizer for clinical use. Magn Reson Imag 2014;32:541−50.

[18] Cates GD, Benton DR, Gatzke M, Happer W, Hasson KC, Newbury NR. Laser production of large nuclear-spin polarization in frozen xenon. Phys Rev Lett 1990;65:2591−4.

[19] Gatzke M, Cates GD, Driehuys B, Fox D, Happer W, Saam B. Extraordinarily slow nuclear spin relaxation in frozen laser-polarized 129Xe. Phys Rev Lett 1993;70:690−3.

[20] Driehuys B, Cates G, Miron E, Sauer K, Walter D, Happer W. High-volume production of laser-polarized 129Xe. Appl Phys Lett 1996;69:1668−70.

[21] Kuzma N, Patton B, Raman K, Happer W. Fast nuclear spin relaxation in hyperpolarized solid 129 Xe. Phys Rev Lett 2002;88:147602.

[22] Goodson BM. Using injectable carriers of laser-polarized noble gases for enhancing NMR and MRI. Concepts Magn Reson 1999;11:203−23.

[23] Ardenkjaer-Larsen JH, Leach AM, Clarke N, Urbahn J, Anderson D, Skloss TW. Dynamic nuclear polarization polarizer for sterile use intent. NMR Biomed 2011;24:927−32.

[24] Nikolaou P, Goodson BM, Chekmenev EY. NMR hyperpolarization techniques for biomedicine. Chemistry 2015;21:3156−66.

[25] Nikolaou P, Coffey AM, Walkup LL, Gust BM, Whiting N, Newton H, et al. Near-unity nuclear polarization with an open-source 129Xe hyperpolarizer for NMR and MRI. Proc Natl Acad Sci USA 2013;110:14150−5.

[26] Sarracanie M, Armstrong BD, Stockmann J, Rosen MS. High speed 3D Overhauser-enhanced MRI using combined b-SSFP and compressed sensing. Magn Reson Med 2014;71:735−45.

[27] Zhao L, Mulkern R, Tseng CH, Williamson D, Patz S, Kraft R, et al. Gradient-Echo imaging considerations for hyperpolarized 129Xe MR. J Magn Reson B 1996;113:179−83.

[28] Oppelt A, Graumann R, Barfuss H, Fischer H, Hartl W, Schajor W. Fast imaging with steady precession a new fast magnetic resonance imaging sequence. Electromedica (English edition) 1986;54:15−18.

[29] Wild JM, Teh K, Woodhouse N, Paley MNJ, Fichele S, De Zanche N, et al. Steady-state free precession with hyperpolarized He-3: Experiments and theory. J Magn Reson 2006;183:13−24.

[30] Svensson J, Månsson S, Johansson E, Petersson JS, Olsson LE. Hyperpolarized 13C MR angiography using trueFISP. Magn Reson Med 2003;50:256−62.

[31] Haacke EM, Tkach JA. Fast MR imaging: techniques and clinical applications. Am J Roentgenol 1990;155:951−96.

[32] Frossati G. Polarization of He-3, D-2 and (eventually) Xe-129 using low temperatures and high magnetic fields. J Low Temp Phys 1998;111:521−32.

[33] Tanaka M, Kunimatsu T, Fujiwara M, Kohri H, Ohta T, Utsuro M, et al. Nuclear spin imaging with hyperpolarized nuclei created by brute force method. J Phys: Conf Ser 2011;295:012167.

[34] O'Neill JD, Krjukov EV, Owers-Bradley JR, Xia Y. NMR spectroscopy of adsorbed Xe-129 at low temperatures and high magnetic fields. J Low Temp Phys 2007;146:563−79.

[35] Krjukov EV, O'Neill JD, Owers-Bradley JR. Brute force polarization of Xe-129. J Low Temp Phys 2005;140:397−408.

[36] Carver TR, Slichter CP. Polarization of Nuclear Spins in Metals. Phys Rev 1953;92:212−13.

[37] Ardenkjær-Larsen JH, Fridlund B, Gram A, Hansson G, Hansson L, Lerche MH, et al. Increase in signal-to-noise ratio of >10,000 times in liquid-state NMR. Proc Natl Acad Sci USA 2003;100:10158−63.

[38] Hu K-N, Bajaj VS, Rosay M, Griffin RG. High-frequency dynamic nuclear polarization using mixtures of TEMPO and trityl radicals. J Chem Phys 2007;126:044512.

[39] Thurber KR, Tycko R. Theory for cross effect dynamic nuclear polarization under magic-angle spinning in solid state nuclear magnetic resonance: the importance of level crossings. J Chem Phys 2012;137:084508.

[40] Capozzi A, Roussel C, Comment A, Hyacinthe JN. Optimal glass-forming solvent brings sublimation dynamic nuclear polarization to Xe-129 hyperpolarization biomedical imaging standards. J Phys Chem C 2015;119:5020−5.

[41] Pourfathi M, Kuzma NN, Kara H, Ghosh RK, Shaghaghi H, Kadlecek SJ, et al. Propagation of dynamic nuclear polarization across the xenon cluster boundaries: elucidation of the spin-diffusion bottleneck. J Magn Reson 2013;253:71−6.

[42] Kuzma NN, Håkansson P, Pourfathi M, Ghosh RK, Kara H, Kadlecek SJ, et al. Lineshape-based polarimetry of dynamically-polarized (N2O)-N-15 in solid-state mixtures. J Magn Reson 2013;234:90−4.

[43] Levitt MH. Singlet nuclear magnetic resonance. Annu Rev Phys Chem 2012;63:89−105.

[44] Brossel J, Kastler A. La detection de la resonance magnetique des niveaux excites − l'effet de depolarization des radiations de resonance optique et de fluorescence. C R Acad Sci 1949;229:1213−15.

[45] Bouchiat MR, Carver TR, Varnum CM. Nuclear polarization in He3 gas induced by optical pumping and dipolar exchange. Phys Rev Lett 1960;5:373−5.

[46] Grover BC. Noble-gas NMR detection through noble-gas-rubidium hyperfine contact interaction. Phys Rev Lett 1978;40:391.

[47] Happer W, Miron E, Schaefer S, Schreiber D, Wijngaarden WAV, Zeng X. Polarization of the nuclear spins of noble-gas atoms by spin exchange with optically pumped alkali-metal atoms. Phys Rev A 1984;29:3092−110.

[48] Cates GD, Fitzgerald RJ, Barton AS, Bogorad P, Gatzke M, Newbury NR, et al. Rb-129Xe spin-exchange rates due to binary and three-body collisions at high Xe pressures. Phys Rev A 1992;45:4631−9.

[49] Walker TG, Happer W. Spin-exchange optical pumping of noble-gas nuclei. Rev Mod Phys 1997;69:629.

[50] Walker TG. Fundamentals of Spin-Exchange Optical Pumping. J Phys: Conf Ser 2011;294:012001.

[51] Chupp TE, Wagshul ME, Coulter KP, Mcdonald AB, Happer W. Polarized, high-density, gaseous He 3 targets. Phys Rev C 1987;36:2244−51.

[52] Chupp T, Coulter K. Polarization of 21Ne by spin exchange with optically pumped Rb vapor. Phys Rev Lett 1985;55:1074.

[53] Stoner R, Walsworth R. Measurement of the 21Ne Zeeman frequency shift due to Rb − 21Ne collisions. Phys Rev A 2002;66:032704.

[54] D. Steck. Rubidium 85 D line data, Rubidium 87 D line data. (2008), http://steck.us/alkalidata/rubidium87numbers.pdf.

[55] Babcock E, Chann B, Nelson IA, Walker TG. Frequency-narrowed diode array bar. Appl Opt 2005;44:3098−104.

[56] Whiting N, Nikolaou P, Eschmann N, Barlow M, Lammert R, Ungar J, et al. Using frequency-narrowed, tunable laser diode arrays with integrated volume holographic gratings for spin-exchange optical pumping at high resonant fluxes and xenon densities. Appl Phys B 2012;106:775−88.

[57] Nelson IA, Walker TG. Rb-Xe spin relaxation in dilute Xe mixtures. Phys Rev A 2001;65:012712.

[58] Bouchiat MA, Brossel J, Pottier LC. Experimental methods for the study of relaxation in an optically oriented alkali metal vapour. J Chem Phys 1972;56:3703−14.

[59] Raftery D, Long H, Meersmann T, Grandinetti PJ, Reven L, Pines A. High-field NMR of adsorbed xenon polarized by laser pumping. Phys Rev Lett 1991;66:584.

[60] Rosen MS, Chupp TE, Coulter KP, Welsh RC, Swanson SD. Polarized 129Xe optical pumping/spin exchange and delivery system for magnetic resonance spectroscopy and imaging studies. Rev Sci Instrum 1999;70:1546.

[61] Desvaux H, Gautier T, Le Goff G, Pétro M, Berthault P. Direct evidence of a magnetization transfer between laser-polarized xenon and protons of a cage-molecule in water. Eur Phys J B 2000;12:289−96.

[62] Nikolaou P, Whiting N, Eschmann NA, Chaffee KE, Goodson BM. Generation of laser-polarized xenon using fiber-coupled laser-diode arrays narrowed with integrated volume holographic gratings. J Magn Reson 2009;197:249−54.

[63] Parnell SR, Deppe MH, Parra-Robles J, Wild JM. Enhancement of 129Xe polarization by off-resonant spin exchange optical pumping. J Appl Phys 2010;108:064908.

[64] Whiting N, Nikolaou P, Eschmann NA, Goodson BM, Barlow MJ. Interdependence of in-cell xenon density and temperature during Rb/129Xe spin-exchange optical pumping using VHG-narrowed laser diode arrays. J Magn Reson 2011;208:298−304.

[65] Six JS, Hughes-Riley T, Stupic KF, Pavlovskaya GE, Meersmann T. Pathway to cryogen free production of hyperpolarized krypton-83 and xenon-129. PloS ONE 2012;7:49927.

[66] Hughes-Riley T, Six JS, Lilburn DM, Stupic KF, Dorkes AC, Shaw DE, et al. Cryogenics free production of hyperpolarized 129Xe and 83Kr for biomedical MRI applications. J Magn Reson 2013;237:23−33.

[67] Nikolaou P, Coffey AM, Barlow MJ, Rosen MS, Goodson BM, Chekmenev EY. Temperature-ramped 129Xe spin exchange optical pumping. Anal Chem 2014;19:8206−12.

[68] Ruset IC, Ketel S, Hersman FW. Optical pumping system design for large production of hyperpolarized Xe-129. Phys Rev Lett 2006;96:053002.

[69] Wu Z, Happer W, Kitano M, Daniels J. Experimental studies of wall interactions of adsorbed spin-polarized Xe131 nuclei. Phys Rev A 1990;42:2774.

[70] Ghosh RK. Spin exchange optical pumping of neon and its applications. Princeton, NJ: Department of Physics, Princeton University; 2009.

[71] Fain S, Schiebler ML, McCormack DG, Parraga G. Imaging of lung function using hyperpolarized helium-3 magnetic resonance imaging: review of current and emerging translational methods and applications. J Magn Reson Imaging 2010;32:1398−408.

[72] Haake M, Pines A, Reimer JA, Seydoux R. Surface-enhanced NMR using continuous-flow laser-polarized xenon. J Am Chem Soc 1997;119:11711−12.

[73] Zook AL, Adhyaru BB, Bowers CR. High capacity production of >65% spin polarized xenon-129 for NMR spectroscopy and imaging. J Magn Reson 2002;159:175−82.

[74] Mortuza MG, Anala S, Pavlovskaya GE, Dieken TJ, Meersmann T. Spin-exchange optical pumping of high-density xenon-129. J Chem Phys 2003;181:1581.

[75] Knagge K, Prange J, Raftery D. A continuously recirculating optical pumping apparatus for high xenon polarization and surface NMR studies. Chem Phys Lett 2004;397:11−16.

[76] Schrank G, Ma Z, Schoeck A, Saam B. Characterization of a low-pressure high-capacity 129Xe flow-through polarizer. Phys Rev A 2009;80:063424.

[77] Norquay G, Parnell SR, Xu X, Parra-Robles J, Wild JM. Optimized production of hyperpolarized 129Xe at 2 bars for in vivo lung magnetic resonance imaging. J Appl Phys 2013;113:044908.

[78] Nossov A, Haddad E, Guenneaua F, Gédéon A. Application of continuously circulating flow of hyperpolarized (HP) 129Xe-NMR on mesoporous materials. Phys Chem Chem Phys 2003;5:4473−8.

[79] Witte C, Kunth M, Rossella F, Schröder L. Observing and preventing rubidium runaway in a direct-infusion xenon-spin hyperpolarizer optimized for high-resolution hyper-CEST (chemical exchange saturation transfer using hyperpolarized nuclei) NMR. J Chem Phys 2014;140:084203.

[80] Nikolaou P, Coffey AM, Ranta K, Walkup LL, Gust BM, Barlow MJ, et al. Multidimensional mapping of spin-exchange optical pumping in clinical-scale batch-mode 129Xe hyperpolarizers. J Phys Chem B 2014;118:4809−16.

[81] Freeman MS, Emami K, Driehuys B. Characterizing and modeling the efficiency limits in large-scale production of hyperpolarized 129Xe. Phys Rev A 2014;90:023406.

[82] Saha I, Nikolaou P, Whiting N, Goodson BM. Characterization of violet emission from Rb optical pumping cells used in laser-polarized xenon NMR experiments. Chem Phys Lett 2006;428:268−76.

[83] Nikolaou P, Coffey AM, Walkup LL, Gust BM, LaPierre CD, Koehnemann E, et al. A 3D-printed high power nuclear spin polarizer. J Am Chem Soc 2014;136:1636−42.

[84] Parnell SR, Woolley EB, Boag S, Frost CD. Digital pulsed NMR spectrometer for nuclear spin-polarized 3He and other hyperpolarized gases. Meas Sci Technol 2008;19:045601.

[85]   Korchak SE, Kilian W, Mitschang L. Configuration and performance of a mobile 129Xe polarizer. Appl Magn Reson 2013;44:65−80.
[86]   Saam BT, Conradi MS. Low frequency NMR polarimeter for hyperpolarized gases. J Magn Reson 1998;134:67−71.
[87]   Borowiak R, Schwaderlapp N, Huethe F, Lickert T, Fischer E, Bär S, et al. A battery-driven, low-field NMR unit for thermally and hyperpolarized samples. Magn Reson Matter Phy 2013;26:491−9.
[88]   Young AR, Appelt S, Ben-Amar Baranga A, Erickson C, Happer W. Three-dimensional imaging of spin polarization of alkali-metal vapor in optical pumping cells. Appl Phys Lett 1997;70:3081−3.
[89]   Ma Z, Sorte E, Saam B. Collisional 3He and 129Xe Frequency Shifts in Rb−Noble-Gas Mixtures. Phys Rev Lett 2011;106:193005.
[90]   Mort J, Lüty F, Brown FC. Faraday rotation and spin-orbit splitting of the F center in alkali halides. Phys Rev 1965;137:A566−73.
[91]   Erickson CJ, Levron D, Happer W, Kadlecek S, Chann B, Anderson LW, et al. Spin relaxation resonances due to the spin-axis interaction in dense rubidium and cesium vapor. Phys Rev Lett 2000;85:4237.
[92]   Babcock E, Nelson I, Kadlecek S, Driehuys B, Anderson LW, Hersman FW, et al. Hybrid spin-exchange optical pumping of 3He. Phys Rev Lett 2003;91:123003.
[93]   Baranga AB-A, Appelt S, Erickson CJ, Young AR, Happer W. Alkali-metal-atom polarization imaging in high-pressure optical-pumping cells. Phys Rev A 1998;58:2282.
[94]   Shah NJ, Unlü T, Wegener HP, Halling H, Zilles K, Appelt S. Measurement of rubidium and xenon absolute polarization at high temperatures as a means of improved production of hyperpolarized 129Xe. NMR Biomed 2000;13:214−19.
[95]   Romalis M, Cates G. Accurate 3He polarimetry using the Rb Zeeman frequency shift due to the Rb − 3He spin-exchange collisions. Phys Rev A 1998;58:3004.
[96]   Babcock E, Nelson IA, Kadlecek S, Walker TG. He3 polarization-dependent EPR frequency shifts of alkali-metal−He3 pairs. Phys Rev A 2005;71:013414.
[97]   Babcock ED. Spin-exchange optical pumping with alkali-metal vapors. Madison, MI: University of Wisconsin-Madison: Physics; 2005.
[98]   Stenger J, Beckmann M, Nagengast W, Rith K. A compact Faraday rotation monitor for density and polarization of optically pumped alkali atoms. Nucl Instrum Meth A 1997;384:333−6.
[99]   Killian TJ. Thermionic phenomena caused by vapors of rubidium and potassium. Phys Rev 1926;27:578.
[100] Lide D. Handbook of chemistry and physics. 85th ed. Boca Raton, FL: CRC Press; 2004.
[101] Shao W, Wang G, Hughes EW. Measurement of spin-exchange rate constants between Xe 129 and alkali metals. Phys Rev A 2005;72:022713.
[102] Dregely IM, Ruset IC, Kotkowski EJ, Hersman FW. Scaling up 129Xe Hyperpolarization—a diagnostic tools system *International Society for Magnetic Resonance in Medicine*. Proc Intl Soc Mag Reson Med, Vol. 15. Berlin: ICC; 2007. p. 1265.
[103] Gallagher A, Lewis E. Determination of the vapor pressure of rubidium by optical absorption. J Opt Soc Am 1973;63:864−9.
[104] Walter D, Griffith W, Happer W. Energy transport in high-density spin-exchange optical pumping cells. Phys Rev Lett 2001;86:3264−7.
[105] Newton H, Walkup LL, Whiting N, West L, Carriere J, Havermeyer F, et al. Comparative study of in situ N2 rotational Raman spectroscopy methods for probing energy thermalisation processes during spin-exchange optical pumping. Appl Phys B 2014;115:167−72.
[106] Hickman R, Liang L. Rotational temperature measurement in nitrogen using Raman spectroscopy. Rev Sci Instrum 1972;43:796−9.
[107] Whiting N, Newton H, Morris P, Barlow MJ, Goodson BM. Observation of energy thermalization and ∼1000 K gas temperatures during spin-exchange optical pumping at high xenon densities. Phys Rev A 2014;118(18):4809−16.
[108] Ebert M, Grossmann T, Heil W, Otten WE, Surkau R, Leduc M, et al. Nuclear magnetic resonance imaging with hyperpolarised helium-3. Lanclet 1996;11:9011.
[109] Leawoods JC, Yablonskiy DA, Saam B, Gierada DS, Conradi MS. Hyperpolarized 3He gas production and MR imaging of the lung. Concepts Magn Reson 2001;13:277−93.
[110] Möller HE, Chen XJ, Saam B, Hagspiel KD, Johnson GA, Altes TA, et al. MRI of the lungs using hyperpolarized noble gases. Magn Reson Med 2002;47:1029−51.
[111] Wild JM, Marshall H, Xu X, Norquay G, Parnell SR, Clemence M, et al. Simultaneous imaging of lung structure and function with triple-nuclear hybrid MR imaging. Radiology 2013;267:251−5.
[112] Saam BT, Yablonskiy DA, Kodibagkar VD, Leawoods JC, Gierada DS, Cooper JD, et al. MR imaging of diffusion of 3He gas in healthy and diseased lungs. Magn Reson Med 2000;44:174−9.
[113] Salerno M, de Lange EE, Altes TA, Truwit JD, Brookeman JR, Mugler III JP. Emphysema: hyperpolarized helium 3 diffusion MR imaging of the lungs compared with spirometric indexes—initial experience 1. Radiology 2002;222:252−60.
[114] Chupp TE, Hoare RJ, Walsworth RL, Wu B. Spin-exchange-pumped 3He and 129Xe Zeeman masers. Phys Rev Lett 1994;72:2363.
[115] Newbury NR, Barton AS, Bogorad P, Cates GD, Gatzke M, Saam B, et al. Laser polarized muonic helium. Phys Rev Lett 1991;67:3219.
[116] Thompson AK, Bernstein AM, Chupp TE, DeAngelis DJ, Dodge GE, Dodson G, et al. Quasielastic scattering of polarized electrons from polarized 3he and measurement of the neutron's form factors. Phys Rev Lett 1992;68:2901.
[117] Singh JT, Dolph PAM, Tobias WA, Kelleher A, Mooney KE, et al. Development of high performance alkali-hybrid polarized 3He targets for electron scattering. Phys Rev C 2015;91:055205.
[118] Lelievre-Berna E. Mid-term report of the NMI3 neutron spin filter project. Physica B Cond Mat 2007;397:162−7.
[119] Gentile TR, Chen WC. Polarized 3He spin filters for neutron science. Proc Sci (PSTP) 2013;022:1−11.
[120] Karpuk S, Allmendinger F, Burghoff M, Gemmel C, Güldner M, Heil W, et al. Spin polarized 3He: from basic research to medical applications. Phys Partic Nucl 2013;44:904−8.
[121] J.C. Woods, Subcommittee on Investigations and Oversight Committee of Science and Technology United States House of Representatives. Congressional hearing: "caught by surprise: causes and consequences of the helium-3 supply crisis"; 2010.
[122] Terskikh VV, Moudrakovski IL, Breeze SR, Lang S, Ratcliffe CI, Ripmeester JA, et al. A general correlation for the 129Xe NMR chemical shift-pore size relationship in porous silica-based materials. Langmuir 2002;18:5653−6.
[123] Goodson BM. Nuclear magnetic resonance of laser-polarized noble gases in molecules, materials, and organisms. J Magn Reson 2002;155:157−216.
[124] Cherubini A, Bifone A. Hyperpolarised xenon in biology. Prog Nucl Magn Reson Spectrosc 2003;42:1−30.

[125] Lilburn DML, Pavlovskaya GE, Meersmann T. Perspectives of hyperpolarized noble gas MRI beyond 3He. J Magn Reson 2013;229:173−86.

[126] Taratula O, Dmochowski IJ. Functionalized 129Xe contrast agents for magnetic resonance imaging. Curr Opin Chem Biol 2010;14:97−104.

[127] Berthault P, Huber G, Desvaux H. Biosensing using laser-polarized xenon NMR/MRI. Prog Nucl Magn Reson Spectrosc 2009;55:35−60.

[128] Schroder L. Xenon for NMR biosensing—inert but alert. Phys Med 2013;29:3−16.

[129] Albert MS, Cates GD, Driehuys B, Happer W, Saam B, Springer CS, et al. Biological magnetic resonance imaging using laser-polarized 129Xe. Nature 1994;370:199−201.

[130] Patz S, Muradyan I, Hrovat MI, Dabaghyan M, Washko GR, Hatabu H, et al. Diffusion of hyperpolarized 129Xe in the lung: a simplified model of 129Xe septal uptake and experimental results. New J Phys 2011;13:015009.

[131] Mugler III JP, Altes TA. Hyperpolarized 129Xe MRI of the human lung. J Magn Reson Imaging 2013;37:313−31.

[132] Mugler III JP, Driehuys B, Brookeman JR, Cates GD, Berr SS, Bryant RG, et al. MR imaging and spectroscopy using hyperpolarized 129Xe gas: preliminary human results. Magn Reson Med 1997;37:809−15.

[133] Patz S, Hersman FW, Muradian I, Hrovat MI, Ruset IC, Ketel S, et al. Hyperpolarized 129Xe MRI: a viable functional lung imaging modality? Eur J Radiol 2007;64:335−44.

[134] Dregely I, Mugler JP, Ruset IC, Altes TA, Mata JF, Miller GW, et al. Hyperpolarized Xenon-129 gas-exchange imaging of lung microstructure: first case studies in subjects with obstructive lung disease. J Magn Reson Imaging 2011;33:1052−62.

[135] Kaushik SS, Cleveland ZI, Cofer GP, Metz G, Beaver D, Nouls J, et al. Diffusion-weighted hyperpolarized 129Xe MRI in healthy volunteers and subjects with chronic obstructive pulmonary disease. Magn Reson Med 2011;65:1154−65.

[136] Matsuoka S, Patz S, Albert MS, Sun Y, Rizi RR, Gefter WB, et al. Hyperpolarized gas MR imaging of the lung: current status as a research tool. J Thorac Imaging 2009;24:181−8.

[137] Lilburn DML, Hughes-Riley T, Six JS, Stupic KF, Shaw DE, Pavlovskaya GE, et al. Validating excised rodent lungs for functional hyperpolarized xenon-129 MRI. PloS ONE 2013;8:e73468.

[138] Kadlecek S, Mongkolwisetwara P, Xin Y, Ishii M, Profka H, Emami K, et al. Regional determination of oxygen uptake in rodent lungs using hyperpolarized gas and an analytical treatment of intrapulmonary gas redistribution. NMR Biomed 2011;24:1253−63.

[139] Mugler III JP, Altes TA, Ruset IC, Dregely IM, Mata JF, Miller GW, et al. Simultaneous magnetic resonance imaging of ventilation distribution and gas uptake in the human lung using hyperpolarized xenon-129. Proc Nat Acad Sci USA 2010;107:21707−12.

[140] Walkup LL, Woods JC. Translational applications of hyperpolarized He-3 and Xe-129. NMR Biomed 2014;27:1429−38.

[141] Duhamel G, Choquet P, Grillon E, Lamalle L, Leviel JL, Ziegler A, et al. MR imaging and spectroscopy of rat brain using arterial delivery of hyperpolarized xenon in a lipid emulsion. Magn Reson Med 2001;46:208−12.

[142] Swanson SD, Rosen MS, Agranoff BW, Coulter KP, Welsh RC, Chup TE. Brain MRI with laser-polarized 129Xe. Magnetic resonance in medicine. Magn Reson Med 1997;38:695−8.

[143] Mazzanti ML, Walvick RP, Zhou X, Sun Y, Shah N, Mansour J, et al. Distribution of hyperpolarized xenon in the brain following sensory stimulation: preliminary MRI findings. PloS ONE 2011;6:e21607.

[144] Imai H, Kimura A, Akiyama K, Ota C, Okimoto K, Fujiwara H. Development of a fast method for quantitative measurement of hyperpolarized 129Xe dynamics in mouse brain. NMR Biomed 2012;25:210−17.

[145] Kershaw J, Nakamura K, Kondoh Y, Wakai A, Suzuki N, Kanno I. Confirming the existence of five peaks in 129Xe rat head spectra. Magn Reson Med 2007;57:791−7.

[146] Kimura A, Imai H, Wakayama T, Fujiwara H. A simple method for quantitative measurement and analysis of hyperpolarized 129Xe uptake dynamics in mouse brain under controlled flow. Magn Reson Med 2008;7:179−85.

[147] Nakamura K, Kondoh Y, Wakai A, Kershaw J, Wright D, Kanno I. 129Xe spectra from the heads of rats with and without ligation of the external carotid and pterygopalatine arteries. Magn Reson Med 2005;53:528−34.

[148] Wakai A, Nakamura K, Kershaw J, Kondoh Y, Wright D, Kanno I. A method for measuring the decay time of hyperpolarized 129Xe magnetization in rat brain without estimation of RF flip angles. Magn Reson Med Sci 2005;4:19−25.

[149] Wakai A, Nakamura K, Kershaw J, Kanno I. In vivo MR spectroscopy of hyperpolarized 129Xe in rat brain. International Congress Series 2004;1265:139−43.

[150] M. Rao, N. Stewart, G. Norquay, Wild J. Proc Intl Soc Mag Reson Med Milan, Italy; 2014. p. 3532.

[151] M. Rao, N. Stewart, G. Norquay, Wild J. COST Hyperpol. Vol 4. Zurich, Switzerland; 2014.

[152] Swanson SD, Rosen MS, Coulter KP, Welsh RC, Chupp TE. Distribution and dynamics of laser-polarized 129Xe magnetization in vivo. Magn Reson Med 1999;24:1137−45.

[153] Norquay G, Leung G, Stewart NJ, Tozer GM, Wolber J, Wild JM. Relaxation and exchange dynamics of hyperpolarized 129Xe in human blood. Magn Reson Med 2014;74:303−11.

[154] Chen RY, Fan FC, Kim D, Jan KM, Usami S, Chien S. Tissue-blood partition coefficient for xenon: temperature and hematocrit dependence. J Appl Physiol 1980;49:178−83.

[155] Bifone A, Song Y-Q, Seydoux R, Taylor RE, Goodson BM, Pietrass T, et al. NMR of laser-polarized xenon in human blood. Proc Nat Acad Sci USA 1996;93:1232−12936.

[156] Albert MS, Schepkin VD, Budinger TF. Measurement of 129Xe T1 in blood to explore the feasibility of hyperpolarized 129Xe MRI. J Comput Assist Tomogr 1995;19:975−8.

[157] Moudrakovski IL, Ratcliffe CI, Ripmeester JA. 131Xe, a new NMR probe of void space in solids. J Am Chem Soc 2001;123:2066−7.

[158] Meersmann T, Smith SA, Bodenhausen G. Multiple-quantum filtered xenon-131 NMR as a surface probe. Phys Rev Lett 1998;80:1398.

[159] Millot Y, Man PP, Springuel-Huet M-A, Fraissard J. Quantification of electric-field gradient in the supercage of Y zeolites with 131Xe (I = 3/2) NMR. C R Acad Sci Ser II C 2001;4:815−18.

[160] Horton-Garcia CF, Pavlovskaya GE, Meersmann T. Introducing krypton NMR spectroscopy as a probe of void space in solids. J Am Chem Soc 2005;127:1958−62.

[161] Six JS, Hughes-Riley T, Lilburn DM, Dorkes AC, Stupic KF, Shaw DE, et al. Pulmonary MRI contrast using Surface Quadrupolar Relaxation (SQUARE) of hyperpolarized (83)Kr. Magn Reson Imag 2014;32:48—53.

[162] R. Stoner Testing Local Lorentz Invariance with Zeeman Masers. *1st Meeting on CPT and Lorentz Symmetry (CPT 98)*. Bloomington, IN: CPT and Lorentz Symmetry: Proceedings; 1991.

[163] Kastler A. Optical methods of atomic orientation and of magnetic resonance. J Opt Soc Am 1957;47:460—5.

[164] Colegrove FD, Franken PA. Optical pumping of helium in the 3S1 metastable state. Phys Rev 1960;119:680—90.

[165] Colegrove FD, Scheare LD, Walters GK. Polarization of He3 gas by optical pumping. Phys Rev 1963;132:2561—72.

[166] Schearer LD. Optical pumping of neon P 2 3 metastable atoms. Phys Rev 1969;180:83—90.

[167] Young L, Yang D, Dunford RW. Optical production of metastable krypton. J Phys B 2002;35:2985—92.

[168] Hadeishi T, Chung-Heng L. Nuclear alignment of the 1S0 ground state of 131Xe by electron pumping and metastability-exchange collisions. Phys Rev Lett 1967;19:211.

[169] Lefevre-Seguin V, Leduc M. Metastability-exchange and depolarising collisions in xenon and krypton. J Phys B 1977;10:2157.

[170] Batz M, Nacher PJ, Tastevin G. Fundamentals of metastability exchange optical pumping in helium. J Phys Conf Series 2011;294.

[171] Gentile TR, McKeown RD. Spin-polarizing He nuclei with an arc-lamp-pumped neodymium-doped lanthanum magnesium hexaluminate laser. Phys Rev 1993;47:456.

[172] Gentile TR, Hayden ME, Barlow MJ. Comparison of metastability-exchange optical pumping sources. J Opt Soc Am 2003;33:265—6.

[173] Courtade E, Marion F, Nacher PJ, Tastevin G, Kiersnowski K, Dohnalik T. Magnetic field effects on the 1083 nm atomic line of helium. J Eur Phys D 2002;21:25—55.

[174] Schearer LD, Padetha T. Tunable lasers at 1080 nm for helium optical pumping. J Appl Phys 1990;68:943—9.

[175] Daniels JM, Schearer LD, Leduc M, Nacher PJ. Polarizing 3He nuclei with neodymium La 1-xNdxMgAl 11 O 19 lasers. J Opt Soc Am B 1987;4:1133—5.

[176] Wallace CD, Bixler DL, Monroe TJ, Dunning FB, Walters GK. Optical pumping of a He(23S) metastable atom beam using a diode laser. Rev Sci Instrum 1995;66:265—6.

[177] Chernikov SV, Taylor JR, Platonov NS, Gapontsev VP, Nacher PJ, Tastevin G, et al. 1083 nm ytterbium doped fibre amplifier for optical pumping of helium. Electronic Lett 1997;33:787—9.

[178] Batz M, Baeßler S, Heil W, Otten EW, Rudersdorf D, Schmiedeskamp J, et al. 3He spin filter for neutrons. J Res Natl Inst Stand Technol 2005;110:293—8.

[179] Phillips GC, Perry RR, Windham PM, Walters GK, Schearer LD, Colegrove FD. Demonstration of a polarized He3 target for nuclear reactions. Phys Rev lett 1962;9:502—4.

[180] Chen WC, Gentile TR, Fu CB, Watson S, Jones GL, McIver JW, et al. Polarized 3He cell development and application at NIST. J Phys Conf Series 2011;294:012003.

[181] Timsit RS, Daniels JM, Dennig EI, Kiang AKC, May AD. An experiment to compress polarized 3He gas. J Cand Phys 1971;49:508—16.

[182] Timsit RS, Hilger W, Daniels JM. A gas circulation system, using a Toepler pump, for the construction of a polarized 3He target. Rev Sci Instrum 1973;44:508—16.

[183] Becker J, Heil W, Krug B, Leduc M, Meyerhoff M, Nacher PJ, et al. Study of mechanical compression of spin-polarized 3He gas. Nucl Instrum Meth A 1994;346:45—51.

[184] Hussey DS, Rich DR, Belov AS, Tong X, Yang H, Bailey C, et al. Polarized 3He gas compression system using metastability-exchange optical pumping. Rev Sci Instrum 2005;76:053503.

[185] Gentile TR, Rich DR, Thompson AK, Snow WM, Jones GL. Compressing spin-polarized 3He with a modified diaphragm pump. J Res Natl Inst Stand Technol 2001;106:709—29.

[186] Nacher PJ, Tastevin G, Maitre X, Dollat X, Lemaire B, Olejnik J. A peristaltic compressor for hyperpolarized helium. Eur J Radiol 1999; 9:b18.

[187] Middleton H, Black RD, Saam B, Cates GD, Cofer GP, Guenther R, et al. MR Imaging with Hyperpolarized 3He Gas. Magn Reson Med 1995;33:271—5.

[188] Kauczor HU, Hofmann D, Kreitner KF, Nilgens H, Surkau R, Heil W, et al. Normal and abnormal pulmonary ventilation: visualization at hyperpolarized He-3 MR imaging. Radiology 1996;2:564—8.

[189] Yablonskiy DA, Sukstanskii AL, Leawoods JC, Gierada DS, Bretthorst GL, Lefrak SS, et al. Quantitative in vivo assessment of lung microstructure at the alveolar level with hyperpolarized 3He diffusion MRI. Proc Nat Acad Sci USA 2002;99:3111—16.

[190] Swift AJ, Wild JM, Fichele S, Woodhouse N, Fleming S, Waterhouse J, et al. Emphysematous changes and normal variation in smokers and COPD patients using diffusion 3 He MRI. Eur J Radiol 2005;54:352—8.

[191] Wang C, Altes TA, Mugler III JP, Miller GW, Ruppert K, Mata JF, et al. Assessment of the lung microstructure in patients with asthma using hyperpolarized 3He diffusion MRI at two time scales: comparison with healthy subjects and patients with COPD. J Magn Reson Imaging 2008;28:80—8.

[192] D.A. Shea, D. Morgan The helium-3 shortage: supply, demand, and options for Congress. In: Service Cr, ed. CRS; 2010.

[193] Cleveland ZI, Pavlovskaya GE, Elkins ND, Stupic KF, Repine JE, Meersmann T. Hyperpolarized 83 Kr MRI of lungs. J Magn Reson 2008;195:232—7.

[194] Farkas A. Orthohydrogen, parahydrogen, and heavy hydrogen. Cambridge: Cambridge University Press; 1935.

[195] Feng B, Coffey AM, Colona RD, Chekmenev EY, Waddell KW. A pulsed injection parahydrogen generator and techniques for quantifying enrichment. J Magn Reson 2012;214:258—62.

[196] Bouchard LS, Burt SR, Anwar MS, Kovtunov KV, Koptyug IV, Pines A. NMR imaging of catalytic hydrogenation in microreactors with the use of para-hydrogen. Science 2008;319:442—5.

[197] Bowers CR, Weitekamp DP. Para-hydrogen and synthesis allow dramatically enhanced nuclear alignment. J Am Chem Soc 1987;109:5541—2.

[198] Kovtunov KV, Barskiy DA, Coffey AM, Truong ML, Salnikov OG, Khudorozhkov AK, et al. High-resolution 3D proton hyperpolarized gas MRI enabled by parahydrogen and Rh/TiO2 heterogeneous catalyst. Chem Eur J 2014;20:11636—9.

[199] Carravetta M, Levitt MH. Long-lived nuclear spin states in high-field solution NMR. J Am Chem Soc 2004;126:1711−14.

[200] Warren WS, Jenista E, Branca RT, Chen X. Increasing hyperpolarized spin lifetimes through true singlet eigenstates. Science 2009;323:1711−14.

[201] Kovtunov KV, Truong ML, Barskiy DA, Koptyug IV, Coffey AM, Waddell KW, et al. Long-lived spin states for low-field hyperpolarized gas MRI. Chem Eur J 2014;20:14629−32.

[202] McKee RH, Herron D, Saperstein M, Podhasky P, Hoffman GM, Roberts L. The toxicological properties of petroleum gases. Int J Toxicol 2014;33:28S−51S.

[203] All Gas Inc. Propane Gas Properties. 2015. http://www.allgasinc.com/propane-gas-properties.php.

[204] Greene BA. The hazards of fire and explosion in anesthesia: Report of a clinical investigation in 230 cases. Anesthesiology 1941;2:144−60.

[205] Coffey AM, Truong ML, Chekmenev EY. Low-field MRI can be more sensitive than high-field MRI. J Magn Reson 2013;237:169−74.

[206] Polarian Inc. (2015) www.polarean.com.

[207] Xemed LLC. (2015) https://www.xemed.com/.

[208] Rao M, Wild JM. RF instrumentation for same-breath triple nuclear lung MR imaging of 1H and hyperpolarized 3He and 129Xe at 1.5T. Magn Reson Med 2015;75(4):1841−8.

[209] Chen WC, Gentile TR, Walker TG, Babcock E. Spin-exchange optical pumping of 3He with Rb-K mixtures and pure K. Phys Rev A 2007;75:013416.

[210] Branca RT, He T, Zhang L, Floyd CS, Freeman M, White C, et al. Detection of brown adipose tissue and thermogenic activity in mice by hyperpolarized xenon MRI. Proc Natl Acad Sci USA 2014;111:18001−6.

[211] Hayden ME, Bidinosti CP, Chapple EM. Specific absorption rates and signal-to-noise ratio limitations for MRI in very-low magnetic fields. Concepts Magn Reson 2012;40A:281−94.

CHEMISTRY
A **European** Journal

Front Cover Picture:
*E. Y. Chekmenev et al.*
NMR Hyperpolarization Techniques of Gases

■ NMR Spectroscopy

NMR Hyperpolarization Techniques of Gases

Danila A. Barskiy,[a] Aaron M. Coffey,[a] Panayiotis Nikolaou,[a] Dmitry M. Mikhaylov,[b] Boyd M. Goodson,[c] Rosa T. Branca,[d] George J. Lu,[e] Mikhail G. Shapiro,[e] Ville-Veikko Telkki,[f] Vladimir V. Zhivonitko,[g, h] Igor V. Koptyug,[g, h] Oleg G. Salnikov,[g, h] Kirill V. Kovtunov,[g, h] Valerii I. Bukhtiyarov,[i] Matthew S. Rosen,[j] Michael J. Barlow,[k] Shahideh Safavi,[k] Ian P. Hall,[k] Leif Schröder,[l] and Eduard Y. Chekmenev*[a, m]
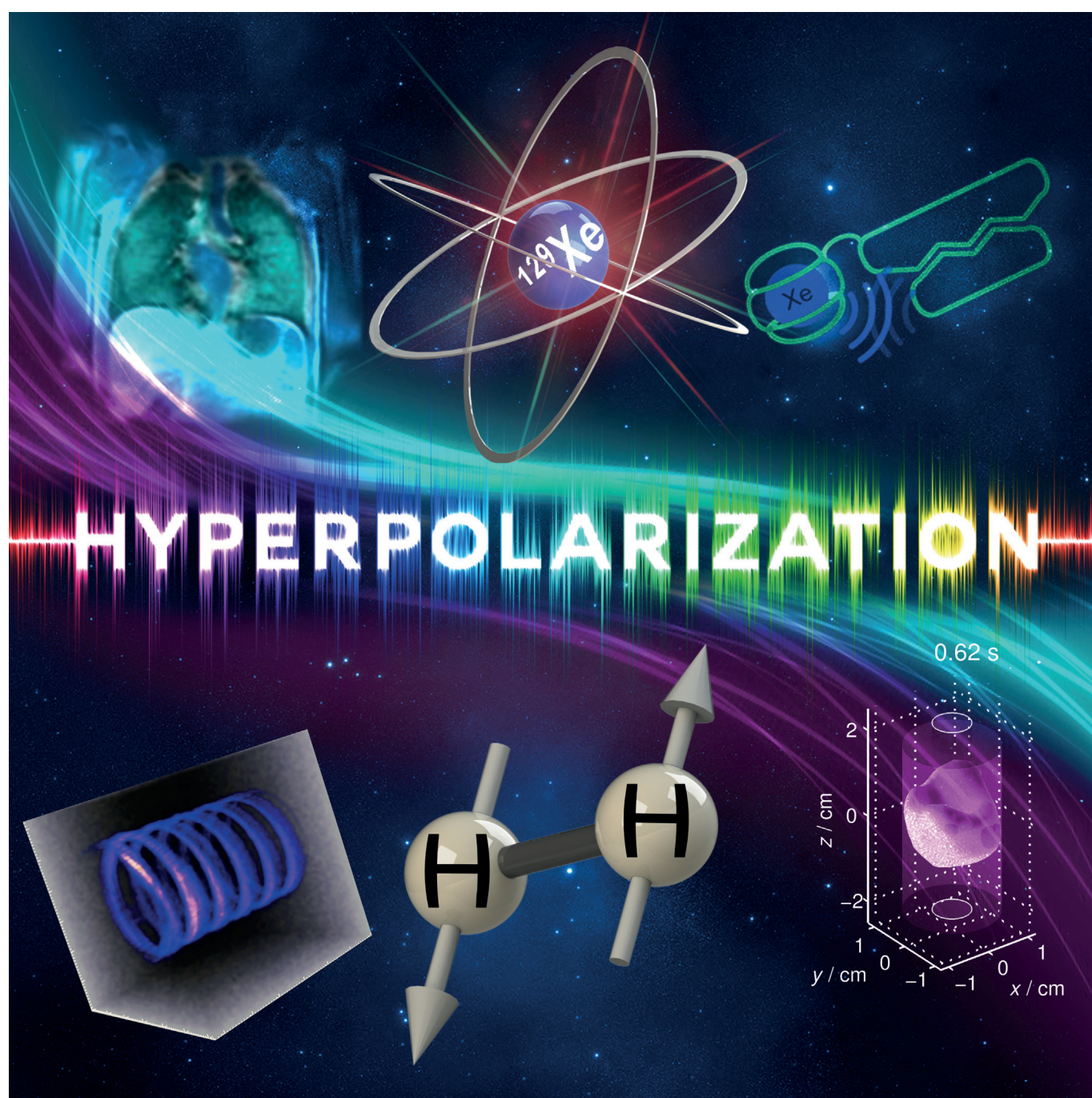
Abstract: Nuclear spin polarization can be significantly increased through the process of hyperpolarization, leading to an increase in the sensitivity of nuclear magnetic resonance (NMR) experiments by 4–8 orders of magnitude. Hyperpolarized gases, unlike liquids and solids, can often be readily separated and purified from the compounds used to mediate the hyperpolarization processes. These pure hyperpolarized gases enabled many novel MRI applications including the visualization of void spaces, imaging of lung function, and remote detection. Additionally, hyperpolarized gases can be dissolved in liquids and can be used as sensitive molecular probes and reporters. This Minireview covers the fundamentals of the preparation of hyperpolarized gases and focuses on selected applications of interest to biomedicine and materials science.

1. Introduction

The use of techniques to enhance nuclear spin polarization (P) to order unity (i.e., nearly 100%) results in corresponding gains in NMR sensitivity by 4–8 orders of magnitude.[1] This process of significant polarization enhancement-well above that achieved at thermal equilibrium-is termed *hyperpolarization*. Hyperpolarization of solids, liquids, and gases[2] has been demonstrated via a number of techniques including Brute Force Polarization (BFP),[3] Spin Exchange Optical Pumping (SEOP),[4] Dynamic Nuclear Polarization (DNP),[1c] Chemically-Induced Dynamic Nuclear Polarization (CIDNP)[5] photo-CIDNP,[6] Parahydrogen Induced Polarization (PHIP),[7] and Signal Amplification By Reversible Exchange (SABRE).[8] A wide range of nuclei can be hyperpolarized, including ^1H,[9] ^3He,[10] ^7Li,[11] ^{13}C,[1c,12] ^{15}N,[13] ^{19}F,[14] ^{31}P,[15] ^{83}Kr,[16] and ^{129}Xe,[4,17] among others.[18] Hyperpolarized (HP) substances are revolutionizing the fields of NMR spectroscopy and magnetic resonance imaging (MRI), because many applications that were previously impractical because of weak NMR signals (e.g., from sub-mM metabolites) are now becoming possible. Moreover, the enormous gain in attainable signal-to-noise ratio (SNR) allows spectroscopic detection and imaging of HP compounds to be performed in seconds, obviating the need for time-consuming signal averaging and thermal recovery of the spin magnetization. The ability to rapidly acquire signals with very high SNR from HP systems is the inherent feature that is greatly desirable for in vivo gas imaging applications: that is, images can be acquired during a single breath hold; sufficient signal can be attained despite the low density of gas compared to liquid. While liquid HP contrast agents are injected in vivo to probe metabolism[19] (extensively discussed in many recent reviews)[20] or used otherwise,[21] they typically cannot be used to probe gas-phase processes in vitro or in vivo. This Minireview focuses on the techniques allowing the production of HP gases with particular application to their use in biomedical applications, and explores some examples from materials science.

We begin with the fundamentals of SEOP in the context of NMR hyperpolarization of ^{129}Xe gas. Although other noble gases have been hyperpolarized, none are as widely used for magnetic resonance as HP ^{129}Xe, which has a relatively large natural abundance (ca. 26%) and is relatively cheap (ca. USD 20 per L). The selected applications described here include functional lung imaging,[22] metabolic brown fat imaging,[23]

[a] Dr. D. A. Barskiy, Dr. A. M. Coffey, Dr. P. Nikolaou, Prof. E. Y. Chekmenev
Department of Radiology, Department of Biomedical Engineering
Department of Physics, Vanderbilt-Ingram Cancer Center (VICC)
Vanderbilt University Institute of Imaging Science (VUIIS)
Vanderbilt University, Nashville, TN 37232 (USA)
E-mail: eduard.chekmenev@vanderbilt.edu

[b] Prof. D. M. Mikhaylov
Huazhong University of Science and Technology
Wuhan, 100044 (China)

[c] Prof. B. M. Goodson
Southern Illinois University
Department of Chemistry and Biochemistry, Materials Technology Center
Carbondale, IL 62901 (USA)

[d] Prof. R. T. Branca
Department of Physics and Astronomy
Biomedical Research Imaging Center
University of North Carolina at Chapel Hill
Chapel Hill, NC 27599 (USA)

[e] Dr. G. J. Lu, Prof. M. G. Shapiro
Division of Chemistry and Chemical Engineering
California Institute of Technology, Pasadena, CA 91125 (USA)

[f] Dr. V.-V. Telkki
NMR Research Unit, University of Oulu
90014 Oulu (Finland)

[g] Dr. V. V. Zhivonitko, Prof. I. V. Koptyug, O. G. Salnikov, Dr. K. V. Kovtunov
International Tomography Center SB RAS
630090 Novosibirsk (Russia)

[h] Dr. V. V. Zhivonitko, Prof. I. V. Koptyug, O. G. Salnikov, Dr. K. V. Kovtunov
Novosibirsk State University
Pirogova St. 2, 630090 Novosibirsk (Russia)

[i] Prof. V. I. Bukhtiyarov
Boreskov Institute of Catalysis SB RAS
5 Acad. Lavrentiev Pr., 630090 Novosibirsk (Russia)

[j] Prof. M. S. Rosen
MGH/A.A. Martinos Center for Biomedical Imaging
Boston, MA 02129 (USA)

[k] Dr. M. J. Barlow, Dr. S. Safavi, Prof. I. P. Hall
Respiratory Medicine Department, Queen's Medical Centre
University of Nottingham Medical School
Nottingham NG7 2UH (UK)

[l] Dr. L. Schröder
Molecular Imaging, Department of Structural Biology
Leibniz-Institut für Molekulare Pharmakologie (FMP)
13125 Berlin (Germany)

[m] Prof. E. Y. Chekmenev
Russian Academy of Sciences
119991 Moscow (Russia)

ORCID(s) from the author(s) for this article are available on the WWW under http://dx.doi.org/10.1002/chem.201603884.

Boyd M. Goodson graduated from Princeton University in 1995 (thesis research with Warren Warren and Herschel Rabitz) and earned his Ph.D. in chemistry in 1999 with Alexander Pines at the University of California, Berkeley/LBNL. Following postdoctoral work with Ahmed Zewail at Caltech, in 2002 Goodson joined the faculty at Southern Illinois University Carbondale and was promoted to full professor in 2014. His research and teaching have been recognized by an NSF CAREER award, Research Innovation and Cottrell Scholar Awards from the Research Corporation for Science Advancement, the ORAU Powe Junior Faculty Award, and the Kaplan Award for Research, Sigma Xi Society (SIUC Chapter). Goodson's research interests concern magnetic resonance and optical spectroscopies, NMR/MRI sensitivity enhancement, and hyperpolarization.

Matthew S. Rosen received his Ph.D. in Physics at the University of Michigan in 2001, where he developed the first ^{129}Xe high-volume hyperpolarizer for in vivo use, and with it demonstrated the first use of ^{129}Xe as a MRI tracer in vivo. His career bridges the spectrum from fundamental physics to applied bioimaging work. He is Assistant Professor of Radiology at Harvard Medical School and the Director of the Low-Field MRI and Hyperpolarized Media Laboratory at the MGH/Martinos Center for Biomedical Imaging. He currently leads an effort to develop tools and techniques for robust ultra-low-magnetic-field implementations of MRI.

Dr. Danila A. Barskiy studied Chemistry in Novosibirsk State University where he obtained a Ph.D. in 2015. He is currently pursuing his research interests as a Postdoctoral Fellow at the Vanderbilt University Institute of Imaging Science in the laboratory of Prof. Eduard Chekmenev. His research interests include spin dynamics and chemical kinetics of parahydrogen-based nuclear spin hyperpolarization techniques (SABRE and PHIP) and applications of these techniques for NMR spectroscopy and imaging of biomedical and industrial processes.

Prof. Dmitry Mikhaylov studied applied physics at the National Research Nuclear University MEPHI (NRNU MEPHI). He got his Ph.D. in 2011 under the guidance of Prof. M. Ivanov. In 2012 he became the head of Engineering Science Center of NRNU MEPHI, one of the biggest R&D centers in Russia. In 2012 he received one of the biggest Russian State research grants for research in the area of endoscopy. In 2013, he started collaboration with Vanderbilt University for research in field of endoscopy and nanomaterials. In 2015, he received an award from Russian Airspace Agency to conduct research in gravity free biological processes. In 2016, he moved to China to continue research.

Panayiotis Nikolaou studied Chemistry with a primary focus on (i) developing and applying new technologies to understand and improve hyperpolarized ^{129}Xe production and (ii) studying the host-guest dynamics of ^{29}Xe-cryptophane inclusion complexes at Southern Illinois University Carbondale (under the guidance of Prof. Boyd M. Goodson), where he earned his Ph.D. in 2010. He is currently a Post-Doctoral fellow with Prof. Eduard Chekmenev at Vanderbilt, where he has designed and built two automated clinical-scale xenon polarizers. Current Research interests include the development of fully-automated xenon hyperpolarizer technology, hyperpolarized contrast agents, and their biomedical application in MR.

Eduard Y. Chekmenev, b 1977, Ph.D. in Physical Chemistry (supervisor Prof. Richard J. Wittebort) 2003, University of Louisville, KY, USA. Postdoctoral Fellow at NHMFL to work on structural biology of membrane proteins in Tallahassee, FL, USA (with Prof. Timothy Cross) and in NMR hyperpolarization at Caltech (with Prof. Daniel P. Weitekamp) and hyperpolarized in vivo imaging at HMRI (with Dr. Brian D. Ross). In 2009, Dr. Chekmenev started his hyperpolarization program at Vanderbilt University Institute of Imaging Science (VUIIS), and he was tenured in 2015. In 2016, he was elected as a Professor of the Russian Academy of Sciences. Research interests include development of methods of hyperpolarization and their Biomedical and industrial applications.

Shahideh Safavi studied Medicine at St George's University of London, graduating in 2008. She undertook her general medicine training in London, followed by specialist training in respiratory medicine in London and Nottingham. She is currently pursuing her research interests at University of Nottingham, as a clinical research fellow, under the supervision of Prof. Ian Hall and Dr. Michael Barlow. Her research is focused on development and use of novel functional MRI techniques in respiratory medicine.

Michael Barlow studied Physics at Essex University where he obtained his Ph.D. in the study of hot electron transport in semiconductor quantum wells. His interest in optical pumping arose from work on helium magnetometers when he was instrument manager for the NASA Cassini MAG team. This work continues to the present day with optical pumping and Raman techniques to explore spin exchange optical pumping for the production of hyperpolarized xenon. He is currently lead physicist for the Nottingham xenon Lung imaging team.

Professor Ian Hall is currently the Boots' Professor of Therapeutics and Director of the Centre for Biomolecular Sciences at the University of Nottingham. His main clinical interest is in respiratory medicine. He completed his clinical studies at the University of Oxford before moving to Nottingham for specialist and research training. Subsequently he was an MRC travelling fellow at the University of Pennsylvania and National Asthma Campaign Senior Research Fellow back in Nottingham. Current research interests include the genetic basis of lung disease and novel imaging approaches.

Rosa Tamara Branca studied Physics at the University of Rome La Sapienza, where she obtained her Bachelors of Science and Masters degree in 2002. In 2006 she obtained her Ph.D. in Biophysics under the guidance of Dr. B. Maraviglia and Dr. W. Warren while studying non-linear MR effects due to dipolar-dipolar interactions and radiation damping. In 2006 she moved to Duke University, first as a Post-Doctoral Fellow and then as an Assistant Research Professor (2009). She began working with hyperpolarized gases in 2009, while working on a project to detect targeted lung metastases with HP Helium. In 2012 she moved to the University of North Carolina at Chapel Hill, where she holds a faculty appointment in the Department of Physics and Astronomy and in the Biomedical Research Imaging Center. Her current research interests include applications of hyperpolarized gases in lung and brown fat imaging.

Leif Schröder studied Physics in Göttingen and Heidelberg where he obtained a Ph.D. in Physics while being affiliated with the German Cancer Research Center to investigate the quantum mechanical fine structure of in vivo NMR spectra. His subsequent stay at the University of California at Berkeley and Lawrence Berkeley National Laboratory was supported by an Emmy Noether fellowship from the German Research Foundation to work hyperpolarized xenon biosensors. He is a co-developer of the Hyper-CEST technique for which he received national and international prizes, including the IUPAP Young Scientist Award in Medical Physics. He further received an Emmy Noether fellowship to start his own group at the FMP, Berlin, where he also managed the ERC Project Biosensorlmaging and is currently heading the Molecular Imaging Group.

Mikhail G. Shapiro is an Assistant Professor of Chemical Engineering and a Heritage Principal Investigator at the California Institute of Technology. His laboratory works on biomolecular technologies for non-invasive imaging and control of biological function. He received his Ph.D. in Biological Engineering from MIT and held post-doctoral fellowships at the University of Chicago and the University of California, Berkeley. He has pioneered protein-based MRI sensors of neurotransmission, reporter genes for several forms of MRI, including xenon and diffusion, and genetically encoded reporters for ultrasound. His awards include the Burroughs Wellcome Career Award, the DARPA Young Faculty Award, the Pew Biomedical Scholarship and the Technology Review's TR35 list of the top innovators under age 35.

Dr. George J. Lu obtained his B.S. degree at University of Alberta, Canada, where he worked with Prof. Brian Sykes and Prof. Michael James on protein NMR and X-ray crystallography. He received his Ph.D. at the University of California, San Diego (UCSD), where he studied solid-state NMR methodology and membrane protein structural biology with Prof. Stanley Opella. He is currently a postdoctoral fellow at Caltech with Prof. Mikhail Shapiro, and his research applies the technique of protein engineering to the development of MRI contrast agents and new imaging and therapeutic methods.

Dr. Aaron M. Coffey conducted undergraduate studies in Electrical Engineering at the University of Arizona, Tucson. He completed a Ph.D. in Biomedical Engineering in 2014 at Vanderbilt University under the guidance of Prof. Eduard Chekmenev in the area of hyperpolarized and low-field NMR and MRI, where he continued as a postdoctoral fellow. He recently received the Ruth L. Kirschstein postdoctoral fellowship 1F32EB021840-01 for 'Ultra-fast molecular MRI of human adipose tissue with hyperpolarized xenon-129 contrast agent.' His research interests include advancing MR detection hardware and utilizing hyperpolarization techniques to enable MR contrast agents for molecular imaging and high sensitivity spectroscopic NMR studies.

Prof. Igor V. Koptyug received his Ph.D. degree in 1991; in 1992–1995 he was a postdoctoral researcher in the photochemistry group of Professor N. J. Turro (Columbia University, New York). He earned his Dr. Sci. (Habilitation) degree in catalysis in 2003 and a title of Professor in 2006; currently, he is the head of the Laboratory of Magnetic Resonance Microimaging at the International Tomography Center, Siberian Branch of the Russian Academy of Sciences, Novosibirsk. His research interests include signal enhancement in NMR and applications of NMR and MRI in catalysis and biological studies in vivo and in vitro.

Dr. Kirill V. Kovtunov studied chemistry at the Novosibirsk State University, Russia. He completed a Ph.D. in Physical Chemistry in 2008 at the International Tomography Center under the supervision of Prof. Igor Koptyug in the area of utilization of parahydrogen in heterogeneous processes, where he obtained heterogeneous PHIP effects for the first time. His research interests include heterogeneous catalysis and utilization of parahydrogen-induced polarization techniques to produce highly polarized contrast agents for NMR/MRI and mechanistic studies of heterogeneous reactions involving hydrogen. Currently, he is a senior scientific researcher in the group of Prof. Igor Koptyug.
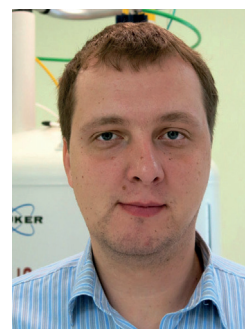
Valerii I. Bukhtiyarov received his Ph.D. degree in 1989. In 1993, Valeriy I. Bukhtiyarov held a post-doc position at University of Wales College of Cardiff (UK) supervised by Professor M. Wyn Roberts. He earned his Dr. Sci. (Habilitation) degree in catalysis in 1998 and a title of Professor in 2003. Since 2000, he is the head of the Surface Science Laboratory in the Boreskov Institute of Catalysis (BIC) of the Siberian Branch of the Russian Academy of Sciences, Novosibirsk; since July 2015, he is the director of BIC. His scientific interests include bridging between surface science and heterogeneous catalysis; application of physical methods to study adsorption and surface chemical reactions, including in situ measurements; and application of nanoscience approaches for modeling and study of heterogeneous catalysts.

Oleg G. Salnikov completed his undergraduate studies in chemistry at Novosibirsk State University in 2014 and continued there as a Ph.D. student. In 2012, he started working on the HET-PHIP project in the group of Prof. Igor Koptyug at the International Tomography Center SB RAS under the supervision of Dr. Kirill Kovtunov. His research interests include the application of PHIP for mechanistic studies of heterogeneous catalytic reactions and development of MR contrast agents using HET-PHIP.

Ville-Veikko Telkki studied physics at the University of Oulu, Finland. He completed his Ph.D. studies in 2006 under the guidance of Prof. Jukka Jokisaari. In 2005, before the final dissertation, he joined the research group of Prof. Alex Pines in UC Berkeley, concentrating on remote detection MRI. In 2007, he returned back to University of Oulu. Currently, he is a Research Fellow of Academy of Finland, and he is leading the Experimental NMR Research Group, focusing on the development and application of advanced NMR methods for materials research.

Dr. Vladimir V. Zhivonitko graduated from Novosibirsk State University, Russia, in 2005, where he studied chemistry. In the same year he started his Ph.D. studies under supervision of Prof. Igor V. Koptyug at the International Tomography Center SB RAS. In 2008 he defended his Ph.D. thesis concerning MRI of nonlinear chemical processes in model catalytic reactors. Thereafter, he joined the HET-PHIP project conducted in Prof. Koptyug's lab as a postdoctoral researcher. His interests include basic NMR research with hyperpolarized substances, development of catalytic systems for PHIP and NMR micro-imaging of catalytic reactors. Currently, he works as a senior scientific researcher at the same location.

and biosensors[24] (including those enabled by genetic encoding).[25] A recent demonstration of the DNP process to hyperpolarize ^{129}Xe[26] and hydrocarbon gases[27] is also described.

HP gases can also be efficiently produced via PHIP, when parahydrogen gas is added in a pairwise manner to a multiple chemical bond (C≡C or C≡C) in an unsaturated molecule, resulting in a gaseous HP product. This process can be performed in heterogeneous fashion,[9a, 28] and despite low T_1 of the HP states, this powerful scalable technique allows for cheap preparation of HP hydrocarbons on demand. Moreover, because protons are being directly hyperpolarized and detected, it is inexpensive and straightforward to perform (since expensive isotopic enrichment and heteroatom-specific instrumentation can be obviated) and thus is readily applied with conventional clinical MRI scanners. This Minireview describes the fundamentals of PHIP for production of HP gases,[29] selected recent developments to extend the lifetime of the HP state through the use of the long-lived spin states (LLSS),[30] and HP gas application for void space imaging, remote sensing, time of flight imaging, and micro-fluidic imaging.

In all cases, the separation from other compounds required for hyperpolarization processes (e.g., Rb in case of SEOP of HP ^{129}Xe, free radicals in the case of DNP, and homogeneous or heterogeneous catalysts in the case of PHIP) is readily achievable, and experiments can be performed with HP gases in a chemically pure form.

2. Fundamentals of Noble Gas Hyperpolarization

2.1. SEOP

The most commonly employed method for generating HP noble gases is spin-exchange optical pumping (SEOP). The development of SEOP is rooted in the pioneering work of Kastler,[31] who was recognized with the Nobel Prize in physics for demonstrating that electronic spin order can be created in alkali metal vapors using circularly polarized laser light. Later Bouchiat, Carver, and Varnum[32] showed that the addition of ^{3}He to the gas mixture permitted helium nuclear spins to be polarized by spin-exchange collisions with the optically pumped alkali vapor atoms-work that was extended to ^{129}Xe by Grover.[33] The rich physics of SEOP has been extensively explored by Happer, Cates, Chupp, Walker, and many others (e.g., refs. [4, 17b, 34]), ultimately leading to the ability to produce large quantities of HP noble gases with nuclear spin polarization levels approaching unity for use in a variety of applications-including those described throughout this Mini-Review.

The underlying phenomenon of SEOP has been reviewed extensively elsewhere,[4, 35] but can be briefly described as follows (Figure 1): First, a heated alkali metal vapor is irradiated with resonant circularly polarized light. Angular momentum conservation results in population being driven from appropriate spin-state ground states (e.g., $mJ = -1/2$ with σ+ light, neglecting nuclear spin degrees of freedom). The ground-state levels are repopulated at roughly the same rates, resulting in depletion of one-spin state and population accumulation in
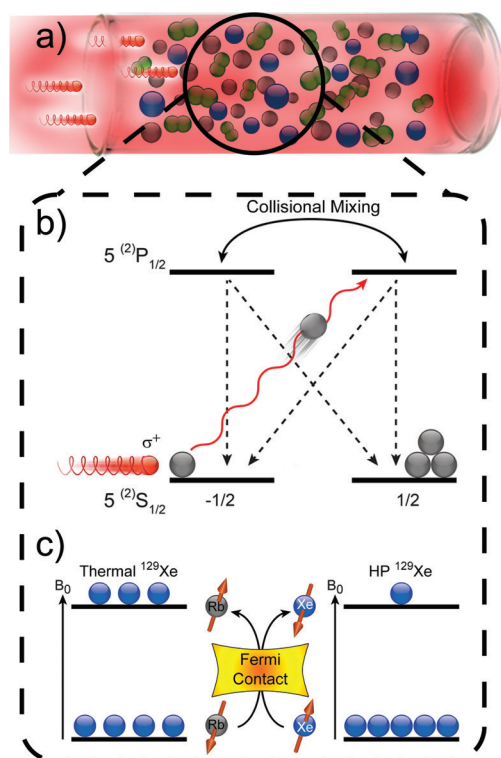
Figure 1. Schematic representations of SEOP.[2b,4] (a) SEOP cell containing a noble gas (here, Xe), buffer gases (e.g. N_2), and a small quantity of vaporized alkali metal (here, Rb); the cell is irradiated by circularly polarized laser light that can be absorbed by the alkali metal atoms. (b) The first step of SEOP: in order to conserve angular momentum, photon absorption results in selective population depletion from one Rb ground electronic state (neglecting Rb nuclear spin for simplicity). Although gas-phase collisions work to equalize the excited-state populations (and hence, the ground-state repopulation rates), continuous depletion of one state by the laser leaves the alkali metal vapor electronically spin-polarized. (c) The second step of SEOP: Gas-phase collisions occasionally allow spin order to be transferred from the alkali metal atom electrons to the noble gas nuclei via Fermi contact hyperfine interactions, thereby hyperpolarizing the noble gas over time. Reproduced with permission from Ref. [2b] John Wiley & Sons, Ltd., 2015.

the other-rendering the alkali metal vapor electronically spin polarized. Gas-phase collisions then transfer polarization from the electrons of the alkali metal to the spins of the noble gas nuclei via Fermi-contact interactions.

This process is allowed to continue so that the nuclear spin polarization can accumulate over time, ultimately yielding a steady-state nuclear spin polarization given by Equation (1):

$$P_N = \langle P_{AM} \rangle \cdot \left(\frac{\gamma_{SE}}{\gamma_{SE} + \Gamma_N} \right) \qquad (1)$$

where $\langle P_{AM} \rangle$ is the spatially averaged polarization of the alkali metal vapor, Γ_N is the noble gas nuclear longitudinal relaxation rate ($1/T_1$) in the optical pumping cell, and γ_{SE} is the spin-exchange rate (i.e., the rate at which polarization can be transferred from alkali metal to the noble gas).

Although the vast majority of SEOP experiments have employed the spin $I = 1/2$ noble gas isotopes ^{129}Xe and ^{3}He, the quadrupolar species ^{21}Ne ($I = 3/2$),[36] ^{83}Kr ($I = 9/2$),[37] and ^{131}Xe[38] ($I = 3/2$) can also be polarized via this method. For the

alkali metal vapor, Rb is most-commonly employed for practical reasons-including its low melting point[39] (facilitating vaporization) and the availability of high-powered lasers resonant with its D_1 transition;[40] however, K and Cs are also utilized (particularly for ^{3}He[41] and ^{129}Xe,[42] respectively).

Technological developments for SEOP have been extensively reviewed elsewhere,[35] and only a brief description is given here. Devices for preparing HP noble gases may be grouped into two types: "stopped-flow" and "continuous-flow". In a stopped-flow device,[43] a batch of a desired gas mixture is loaded into an OP cell (which contains a quantity of alkali metal) and is heated and optically pumped with a laser; once the gas is hyperpolarized, OP is stopped and the gas is transferred to the sample (usually after the cell has cooled to condense the alkali metal); alternatively, multiple batches may be systematically polarized and collected to accumulate the HP gas prior to transfer. In a continuous-flow device,[44] a desired gas mixture is allowed to flow from its source continuously through a heated cell while it is irradiated by the laser; the flow rate is chosen to allow sufficient average residency of noble gas atoms in the cell to enable the gas to be hyperpolarized "on the fly". The HP gas mixture can then either be directed into the sample or a cryo-condenser (to collect the otherwise-dilute HP noble gas and deliver it purely and with high density, following sublimation).[44a]

All of the noble gas isotopes are amenable to the stopped-flow design,[38,43h,i,45] whereas the relatively high spin-exchange rates and facile cryo-storage of ^{129}Xe's polarization[46] make it the best choice for use in a continuous-flow device. Both device designs have evolved considerably over the years, achieving ever-greater gas polarizations and production amounts/throughputs-benefiting in particular from the advent of compact, high-power, relatively low-cost light sources embodied by spectrally-narrowed laser diode arrays.[40,43e,g,44f,47]

2.2. Other Methods for Hyperpolarizing Noble gases: MEOP, "Brute Force", and DNP

In addition to SEOP, HP noble gases can be prepared by metastability exchange optical pumping (MEOP), "brute force", and dynamic nuclear polarization (DNP), and we briefly describe these approaches here.

In MEOP,[48] an electrical discharge is used to create metastable (electronically excited) atoms in a dilute gas. The unpaired electrons of these metastable atoms can be spin-polarized via optical pumping with a laser. The angular momentum of the electron spin may then be transferred to the nuclear spin of another gas atom in the cell during a metastability-exchange collision. The process is allowed to continue until a bulk nuclear spin polarization develops across the cell. Finally, a pump is used to compress the HP gas to a sufficient density prior to use.[49] MEOP works well for ^{3}He[48] and has been highly effective at producing clinical-scale amounts for biomedical imaging experiments (e.g., [50]); MEOP is generally less effective for the heavier noble gas isotopes because of stronger relaxation mechanisms.[51]

Next, to understand the so-called brute-force (BF) approach, one should first consider the relation determining the equilibrium ("thermal") nuclear spin polarization (for $I = 1/2$ nuclei), see Equation (2):

$$P_N^{eq} \doteq \tanh\left(\frac{\gamma \hbar B_0}{2kT}\right) \tag{2}$$

where γ is the nuclear gyromagnetic ratio, B_0 quantifies the strength of the magnetic field, T is the absolute temperature, $\hbar$ is Planck's constant divided by 2π, and k is Boltzmann's constant. At room temperature and in a typical superconducting magnet, P_N^{eq} will be $\approx 10^{-5}$–10^{-6}. Thus, if the sample temperature were lowered to milli-Kelvin temperatures (and enough time were allowed for the nuclear spins to relax to their new equilibrium conditions), the nuclear spin polarization would exceed 10%. Although the approach can be time consuming, such BF approaches have used ^{3}He/^{4}He dilution refrigerators to polarize the nuclear spins in different substances, including noble gases.[52]

Finally, noble gases can also be hyperpolarized via DNP.[53] Here, the approach is essentially the same as that of dissolution DNP (d-DNP), introduced by Golman and co-workers in 2003.[1c] Briefly, the approach requires the substance to be hyperpolarized (here, ^{129}Xe) to be mixed in a glassy frozen matrix containing molecules with unpaired electron spins (e.g., a stable radical or a photoinduced, non-persistent radical).[53c] With the matrix placed at very low temperatures (~1 K) and at high magnetic field (several T), the unpaired electrons obtain a near-unity spin polarization. The matrix is then irradiated with microwaves in order to drive the high spin polarization to surrounding nuclei in the matrix, allowing a high bulk nuclear spin polarization to accumulate over time. The matrix is then rapidly warmed, sublimating the HP xenon as a pure gas-hence the name "sublimation DNP" given for this approach.[53b] Using DNP, polarization values of ~30% have been achieved in ~1.5 h,[53b] despite identified issues with a spin-diffusion bottleneck between electron and ^{129}Xe spins.[53a] Although the amounts and polarization values achieved thus far with DNP are not as high as corresponding values achieved with SEOP, the advantages are the increasing availability and general applicability of dissolution DNP polarizers in biomedical facilities-including Oxford's HyperSense[1c] and more recently, GE Healthcare's SPINlab.[54]

2.3. The Rise of Magnetic Resonance Applications of Hyperpolarized Noble Gases

Prior to finding their way into magnetic resonance, HP gases found their first applications in fundamental physics experiments (work that of course continues, see for example, refs. [55,56]). And although the portions of this Mini-Review that are dedicated to HP noble gases are largely concerned with biomedical applications of ^{129}Xe, the first MR applications actually involved studies of materials (as well as investigations of the use of HP ^{129}Xe as a source of hyperpolarization for other spins).

Soon after the demonstration of ultra-long ^{129}Xe relaxation times for frozen solid xenon,[46] Pines and co-workers used HP ^{129}Xe NMR to probe the surfaces of powdered substances[43a] (and high-field gas-phase spectroscopy was also demonstrated by performing SEOP within an NMR magnet).[42a] Soon afterwards, the exquisite sensitivity of the ^{129}Xe chemical shift was investigated for probing surfaces of a number of porous materials and particles[57]-as was the ability to transfer the ^{129}Xe hyperpolarization to the nuclear spins of other substances.[58] The advent of continuous-flow production of HP ^{129}Xe[44a] was soon applied to greatly facilitate studies of materials surfaces,[59] including under conditions of magic angle spinning.[60] Since that work, HP xenon has been used to study diffusion in confined spaces or porous media;[61–63] image such systems as a function of gas flow[64] or ^{129}Xe chemical shift;[65] or spectroscopically probe single-crystal surfaces,[66] liquid crystals,[67] or combustion processes.[68] However, the greatest body of materials-related work has concerned the effort to probe void spaces and surfaces in microporous or nanoporous materials with HP ^{129}Xe, thereby providing information about pore size, pore shape, and gas dynamics in: nanochanneled organic, organometallic, and peptide-based molecular materials[69] (including in macroscopically oriented single crystals);[70] multi-walled carbon nanotubes;[71] gas hydrate clathrates;[72] porous polymeric materials and aerogels;[73] metal-organic frameworks;[74] calixarene-based materials and nanoparticles;[75] organoclays;[76] mesoporous silicas;[77] and zeolites and related materials[78]—efforts that have been aided by computational studies of xenon in confined spaces (e.g., ref. [79]). For a more in-depth review of HP ^{129}Xe in microporous and nanoporous materials, see ref. [80].

Indeed, ^{129}Xe has found the widest NMR/MRI application of the HP noble gases-a fact that is at least partially due to its significant natural abundance (26.44%) and ready recoverability from air during oxygen production. While ^{3}He does have the advantage of a roughly three-fold greater gyromagnetic ratio, its weak chemical shift dependence and lack of significant interaction with other substances make it a poor probe of other substances. More importantly, the lack of natural abundance (most ^{3}He comes from tritium decay) will limit the future use of this isotope for wide-scale magnetic resonance applications.[81] The rapid relaxation suffered by the quadrupolar isotopes (^{21}Ne, ^{83}Kr, and ^{131}Xe) presents a challenge for most HP NMR applications, although as pointed out by Meersmann and co-workers, the quadrupolar interaction also endows a unique sensitivity of HP ^{83}Kr to surface chemistry and local geometry that can be complementary to the information provided by ^{129}Xe chemical shift—a feature that can prove useful for probing porous materials, lung tissues, and other systems.[37,68b,82]

3. Clinical Application of Hyperpolarized Xenon-129 MRI

HP xenon-129 MRI (^{129}Xe-MRI) is an MRI modality first developed in the 1990s for enhanced lung imaging of ventilation and perfusion and regional information on gas exchange. It

has been used to image patients with a number of respiratory diseases, including asthma, COPD, and pulmonary fibrosis. In addition to its use in disease assessment and long-term management, in vivo gas-phase ^{129}Xe-MRI has the potential to provide imaging biomarkers of drug efficacy, which could be used to stratify treatment, improve patients' quality of life, and cut down healthcare costs. It can also be potentially employed by pharmaceutical companies to speed up decision-making in proof-of-concept studies in drug development.

3.1. From Mice to Men

Identified by British chemists William Ramsay and Morris Travers in 1898[83] (following their discovery of neon and krypton a few months earlier), xenon is a colorless and odorless noble gas. Xenon initially captured the attention of clinicians as a general anesthetic agent when Albert Behnke, a US Navy physician, investigated the cause for "drunkenness" observed in deep-sea divers.[84] Interestingly, Behnke also happened to be the clinician who had studied the anesthetic effects of nitrogen and helium in humans.[85] It was Lawrence et al.[85] who first published experimental data on the general anesthetic effects of xenon with mice as their test subjects. It took clinicians 5 years to put xenon to use in clinical settings,[86] and xenon has continued to be used as a general anesthetic since.

3.2. The Motivation for Hyperpolarized Xenon-129 MRI

The next major clinical application of xenon-129 came in 1994 in the form of its use as an inhalational contrast agent for magnetic resonance imaging (MRI).[87]

Plain radiograph and computed tomography (CT) are currently the main modalities used to image the lungs in clinical settings. Despite their ability to provide detailed anatomical data, in particular with high resolution CT, their main drawbacks are the risks involved with repeated radiation exposure and the inability to provide physiological information on regional lung function. Although conventional MRI has been a game-changer in both neuro and hepatic imaging, its dependence on the protons of water molecules in tissue to provide nuclear magnetic resonance (NMR) signal[87] has meant that it is of little value in imaging the lungs due to poor image quality because of three factors: 1- low proton abundance within the lung parenchyma, 2- air-tissue interface causing magnetic field heterogeneity, and 3- image degradation secondary to cardiac and respiratory motion.[88]

The NMR signal strength of a given species depends on its nuclear spin, that is, polarization, concentration, and the volume of the element. Except for those in water and fat, the concentrations of all other protons and nuclear species are too low to be of use in conventional MRI. However, hyperpolarization can be used to overcome the otherwise low detection sensitivity for low-concentration spins. For example, by delivering HP ^{129}Xe to excised mouse lungs, Albert and colleagues were able to obtain improved MR lung images compared to those obtained with conventional MRI.[87]

3.3. Hyperpolarized Xenon-129 MRI—There and Back Again

HP xenon-129 MRI of human lungs, which are obviously much larger than those of mice, proved challenging; it took physicists three years following Albert's paper in 1994 to be able to publish data on human studies.[89] The challenge was due to the need to produce much larger quantities of HP ^{129}Xe and to achieve adequate levels of polarization. Furthermore, conventional MR imaging sequences had to be modified as the polarization of the noble gas is non-renewable, and some polarization is lost every time an MR excitation pulse is applied.[90] These issues led to a shift in interest from ^{129}Xe to helium-3 (^{3}He), a fellow noble gas, whose larger gyromagnetic ratio and larger achievable polarization compared to ^{129}Xe at the time allowed for better signal intensity and image resolution for a given amount of HP gas.[91]

Interest in ^{129}Xe was reignited in the early 2010s; this resurgence was due to the fact that contrary to ^{129}Xe, which is naturally occurring, ^{3}He is a byproduct of tritium decay. ^{3}He had become scarce as the US sequestered ^{3}He for ^{3}He-based neutron detectors for national security, leading to extremely low availability of ^{3}He for scientific research and an exponential rise in its price.[91b] As a result, it was unlikely that ^{3}He-MRI would become a routine imaging modality in clinical settings, and so interest in ^{129}Xe-MRI was rekindled.

3.4. Safety & Tolerability Profile in Patient Groups

Over the past two decades, ^{129}Xe-MRI has been improved and utilized in imaging a wide range of respiratory diseases, including asthma,[92] chronic obstructive pulmonary disease (COPD),[92b, 93] cystic fibrosis (CF),[92a] and pulmonary fibrosis.[94] Studies specifically designed to investigate the safety and tolerability of ^{129}Xe-MRI have not shown major common side effects in various patient groups, including those with asthma,[92a] and mild-moderate COPD,[92a, 95] with light-headedness of very short duration as the main reported minor side effect.

3.5. Ventilation Imaging

Ventilation imaging provides valuable clinically relevant information relevant to regional lung function. Regions with normal ventilation typically appear bright and homogenous on ^{129}Xe-MRI, and in a healthy subject with normal lung function, both lungs show relatively homogenous ventilation except for two regions (as seen in Figure 2 and discussed in the caption). In those with diseased lungs where regional ventilation is impaired, the abnormal regions will appear darker; these regions are called "ventilation defects".

Compared to healthy volunteers, ^{129}Xe distribution has been shown to be regionally heterogeneous with ventilation defects in a number of different patient groups, including those with asthma, COPD, and CF.[92a, 93c,d] Ventilation imaging has also been shown to correlate with spirometry[93c] and CT findings[96] in patients with COPD.

Additionally, ventilation imaging has been used to assess the efficacy of drug therapy. Studying the impact of Salbuta-
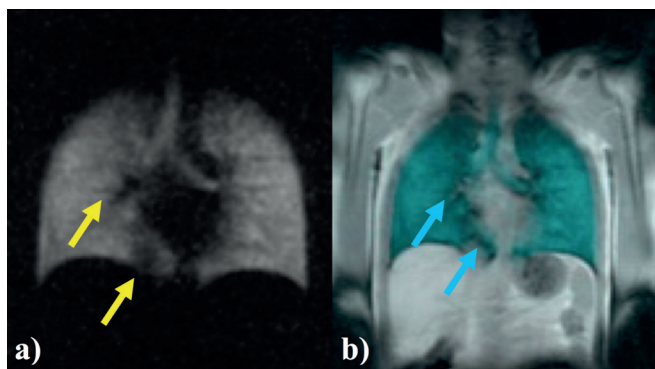
Figure 2. ^{129}Xe-MRI of a healthy volunteer. a) Coronal plane 25 mm slice ^{129}Xe-MR ventilation image of a healthy adult male, with ^{129}Xe appearing bright. The upper airways are visualized and delineated. b) Coronal plane 25 mm slice fused ^{129}Xe-MR ventilation and proton co-registration image, with ^{129}Xe appearing blue-green. The two black regions pointed out in the fused image (yellow arrows) are due to a diaphragmatic eventration and pulmonary vasculature, clearly defined on the fused image (blue arrows). J. Thorpe, B. Haywood, M. Barlow, S. Safavi & I. Hall—University of Nottingham (Unpublished work).

mol in patients with asthma, Parragra's group[92b] has reported a significant reduction in ventilation defects after Salbutamol administration.

Hence ^{129}Xe-MR ventilation imaging, although appearing simple, can be used to not only assess disease, but to also assess drug efficacy and monitor disease progression.

3.6. Diffusion Imaging

The apparent diffusion coefficient (ADC) of gas within lung is a function of alveolar size and geometry. This can be assessed using ^{129}Xe-MRI to characterize pulmonary microstructure at the alveolar level, as seen in Figure 3.

^{129}Xe-MRI derived ADC mapping has been shown to correlate well with pulmonary function tests,[93d, 95] including total diffusing capacity for the lung (TLco). This is of important clinical significance, as it clearly illustrates the ability of ^{129}Xe-MRI to provide regional quantitative lung function data. In addition
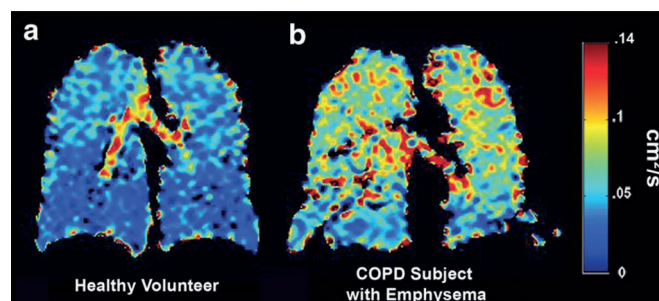

Figure 3. ADC map of a healthy volunteer and a patient with COPD. a) Healthy volunteer with a low mean ADC of 0.037 ± 0.021 cm^2 s^{-1}, indicating normal alveolar microstructure. b) Patient with COPD with high ADC values (0.068 ± 0.028 cm^2 s^{-1}) in the parenchyma, indicating alveolar destruction. Reproduced with permission from Ref. [95] John Wiley & Sons, Ltd., 2011.

to its potential use in disease diagnosis, monitoring and assessing therapeutic drug efficacy, diffusion imaging can also be used to plan surgery, including tumor resection and lung volume reduction surgery for emphysema, as it can aid prediction of post-surgery lung function. The predicted post-surgery lung function is currently calculated using ventilation or perfusion scintigraphy and quantitative CT; however, there is a risk that scintigraphy, the most commonly used imaging modality, may underestimate post-operative lung function,[97] thereby, preventing the patient from undergoing potentially curative surgery.

3.7. Dissolved Phase Imaging

^{129}Xe (in contrast to ^{3}He) is highly lipophilic and soluble in biological tissues and thus is able to provide information on gas exchange and pulmonary perfusion, which can be particularly interesting in the context of functional lung imaging.[98] It is the associated persistent exchange of ^{129}Xe between the gas and dissolved compartments, each with its own different resonance frequencies, that is central to assessing gas exchange using ^{129}Xe-MRI.[99] Therefore, combined imaging of the gas phase ^{129}Xe and the dissolved phase ^{129}Xe would permit ventilation/perfusion (V/Q) imaging-and consequently a more direct mapping of lung function.[87] Hence, although ^{129}Xe-MRI initially lagged behind ^{3}He-MRI, developmentally, this capability provides another reason why ^{129}Xe-MRI is likely to be the pragmatic HP noble gas MRI modality of choice.

Although the majority of the inhaled ^{129}Xe remains in the airspaces, where it exhibits its primary gas-phase resonance, a portion dissolves in alveolar septa and crosses the alveolar-capillary barrier to dissolve in the blood. The resulting shift in the resonance frequency leads to the appearance of two additional distinct resonances: 1) the barrier resonance, and 2) the hemoglobin-associated ^{129}Xe resonance, as seen in Figure 4 (We note the intensity differences between the two spectra are due primarily to the variation in the amount and speed at which hyperpolarised xenon gas was inhaled by the two vol-
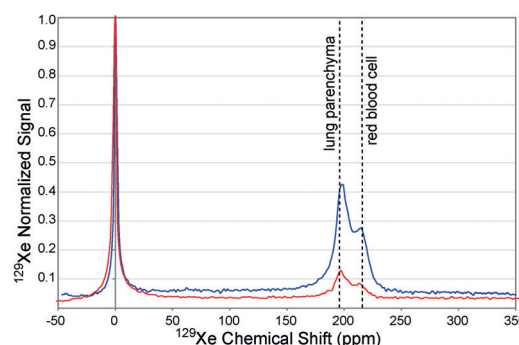

Figure 4. ^{129}Xe NMR spectra recorded from two healthy volunteers. Two dotted lines have been placed to represent the expected dissolved state peaks, the left most line representing the expected ~196 ppm lung parenchyma peak, and the right most line representing the expected 216 ppm red blood cell peak. S. Hardy, B. Haywood, M. Barlow, S. Safavi & I. Hall—University of Nottingham (Unpublished work).

unteers. As volunteers became more familiar with the breathing protocol, the improvements in both ventilatory image quality and dissolved phase signal/noise were noted). This transfer pathway is identical to that followed by oxygen; therefore, in addition to being a ventilation probe, ^{129}Xe is also a gas diffusion transfer probe.[94a]

The signal intensity of the dissolved phase ^{129}Xe is approximately 2% of that remaining in the alveolar spaces, which presents a challenge to obtaining good quality images.[94a] However, as the alveolar space, alveolar septa, and capillary blood are in dynamic exchange, it is possible to use nearly all of the inhaled gas to generate 3D images of dissolved ^{129}Xe in a single breath-hold, as demonstrated in a number of studies.[94a, 100]

Another challenge is to distinguish between xenon dissolved in the alveolar septa and that dissolved in the blood. Various teams have used the chemical shift and the change in resonance frequency to distinguish xenon in these two compartments[98a,101] as the dissolved-phase ^{129}Xe signal splits into two distinct peaks in alveolar septa and blood. These methods, known as the Xenon Polarization Transfer Contrast (XTC)[98a,101b,c] and the Model of Xenon Exchange (MOXE),[101a,d,e] have been assessed in healthy volunteers[102] and patients with obstructive lung disease,[102a] with promising results.

Further testing these methods, Kaushik et al.[94a] hypothesized that there will be a reduction in ^{129}Xe signal intensity in the hemoglobin:alveolar septum ratio in patients with idiopathic pulmonary fibrosis (IPF), due to the thickening of the alveolar septa in this condition. MR spectroscopy was used to demonstrate the change in relative signal intensity in patients with IPF compared to healthy volunteers. The ratio was significantly lower in the IPF group compared to the healthy volunteer group, due to a 52% reduction in the hemoglobin signal and a 58% increase in the alveolar septa signal. There was a strong correlation between the hemoglobin:alveolar septum ratio and TLco. Therefore, this technique appears to provide a non-invasive measure of diffusion limitation and gas-transfer impairment.

These findings suggest that ^{129}Xe-MRI has the potential to detect subtle lung function deterioration before irreversible structural changes become apparent, providing clinicians with the chance to offer therapy (when available), at an earlier stage in order to delay, halt or reverse disease progression.

3.8. Neuroimaging

^{129}Xe-MR brain imaging is emerging as a distinct possibility. Just as xenon can be used as a gas exchange probe due to its ability to dissolve across the alveolar-capillary barrier, it can also be used as a cerebral blood flow (CBF) probe, as it can cross the blood–brain barrier and accumulate in the brain.[103] First utilized in its non-polarized form for CBF measurement using CT in 1982,[104] Swanson et al.[105] were the first group to publish data on brain MR imaging using HP ^{129}Xe as an inhaled neuroimaging contrast agent, albeit in rats. Animal studies have continued over the past two decades, using HP ^{129}Xe as both an inhalational[106] and injectable contrast agent.[107]

Diseased states have also been imaged in the rat model. Xenon signal in the brain is proportional to CBF, hence a decrease in the signal is expected to occur in areas of decreased CBF, such as those expected in ischemic stroke. Working on this principle, Zhou et al.[108] created a rat model of cerebral ischemia by using an intraluminal suture to occlude the middle cerebral artery, and demonstrated ^{129}Xe-MRI is able to detect the hypo-perfused area of focal cerebral ischemia, which was also confirmed on biopsy. Mazzanti et al.[109] further demonstrated the capacity of ^{129}Xe-MRI for functional neuroimaging by inducing pain in the rat's forepaw, and obtaining ^{129}Xe-MR images, which showed 13–28% increase in signal compared to the pre-stimulus images; these regions of increased signal corresponded to areas previously demonstrated by conventional functional MRI (f-MRI) as being activated by a forepaw pain stimulus.

It remains to be seen whether ^{129}Xe-MR neuro-imaging is feasible in humans and of value but developmental work is on-going.

3.9. Conclusion

Biomarkers of disease can be classified into diagnostic, prognostic, and theranostic. The ideal biomarker encompasses all groups, and ^{129}Xe-MRI has the potential to provide diagnostic, prognostic, and theranostic biomarkers.

4. Brown-Fat MRI using Dissolved Hyperpolarized ^{129}Xe

For biological MR applications, one of the most interesting properties of HP xenon is its high tissue solubility and its chemical shift sensitivity to its molecular environment. However, MR imaging and spectroscopy applications of dissolved-phase HP xenon have been limited to brain and lung tissues (as described in the sections above), as the concentration of dissolved-phase xenon in other tissues is rarely high enough to yield good signal after the typical single breath-hold protocol used for human studies. Neglecting nuclear spin relaxation and magnetization loss due to NMR pulsing, the time dependence of xenon concentration in tissues $C_i(t)$ is well described by the Kety–Schmidt, Equation (3):[110]

$$C_i(t) = \lambda_i C_a \left(1 - e^{-\frac{F_i}{\lambda_i}t} \right) \tag{3}$$

where λ_i, is the xenon partition coefficient between tissue and blood, C_a is the arterial concentration of the inert gas, and F_i is the blood flow to the tissue of interest. For most tissues, λ_i, which determines both the maximum concentration achievable in a given tissue and the time it takes to achieve maximum concentration, is close to unity.[111] However, F_i, which also determines wash-in rate, varies widely. For example, blood flow to the brain is very high (~ 0.5 L min^{-1} kg^{-1}) and the maximum xenon concentration in this tissue can be reached after a few seconds from the beginning of gas inhalation. On the other hand, while the solubility of xenon in fatty tissues is almost

20 times higher than in blood, because of the low tissue-perfusion ($\sim0.01\,L\,min^{-1}\,kg^{-1}$), saturation can only be reached after several minutes. For HP ^{129}Xe gas, this is a clear limitation, as gas depolarization would limit the amount of detectable signal even under continuous HP xenon inhalation (because of short in vivo T_1 relaxation times).

It was recently shown that the intensity of the xenon dissolved-phase signal could reach much higher levels than in the brain in a tissue called Brown Adipose Tissue (BAT).[112] Brown adipose tissue is a fatty tissue found in most mammals, including humans, and its primary function is to generate heat through a process called non-shivering thermogenesis.[113] During stimulation of non-shivering thermogenesis in this tissue, intracellular triglyceride oxidation is decoupled from ATP production so that triglycerides are mainly burned to produce heat. To support this metabolic activity, BAT is richly vascularized. During non-shivering thermogenesis, tissue perfusion increases by several fold as blood flow is needed to support the tissue's oxygen demand and to quickly dissipate the heat produced.

Aside from its thermoregulatory function, BAT has recently gained a great deal of interest because of its presumed role in the regulation of body weight and blood glucose level. For example, a series of studies in rodents have clearly shown that BAT function can directly regulate body weight and improve insulin sensitivity.[114] However, the detection of this tissue still remains a challenge, especially in humans,[115] where it is sparsely distributed and not easy to detect by standard MR techniques. In the paper by Branca et al.,[23] a strong enhancement of the intensity of the xenon-dissolved phase signal was reported in mice inhaling HP ^{129}Xe right after stimulation of non-shivering thermogenic activity in BAT, an effect which was ascribed to the strong enhancement in blood flow to BAT.[116] Blood flow to this tissue during stimulation can reach values as high as $5\,L\,min^{-1}\,kg^{-1}$,[116] considerably increasing xenon wash-in rate and allowing it to reach an in-tissue concentration of tens of mM. Since the increase in blood flow is specific to brown fat cells, background free maps of this tissue could be generated.

More interestingly, it was also shown that xenon chemical shift information can provide a measure of the relative tissue hydration and tissue temperature. Specifically, two major peaks were observed in these studies. One signal, at ~197 ppm, corresponds to xenon dissolved in cell cytoplasm/blood, and one signal at ~190 ppm corresponds to xenon dissolved in the lipid droplets of the tissue. The lipid-dissolved peak was shown to have a temperature-sensitive chemical shift ($-0.2\,ppm\,^{\circ}C^{-1}$), which enabled direct measurement of the increase in tissue temperature (Figure 5) during non-shivering thermogenesis.[23] In addition, during non-shivering thermogenesis, a relative decrease of the lipid-dissolved phase peak was observed with respect to the cytoplasm/blood peak, yielding direct evidence of this tissue's oxidative metabolism of internal triglycerides.

More recently, the feasibility of BAT detection in humans during a single breath hold of HP xenon was demonstrated, with validation by FDG-PET.[117] As in mice, a strong increase in the lipid dissolved xenon signal was seen in the same glucose-
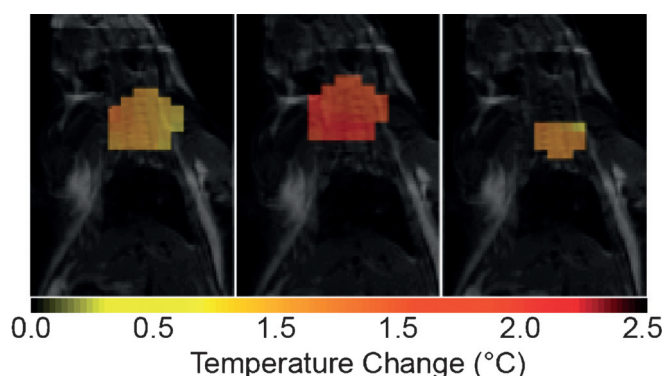

Figure 5. ^{129}Xe brown adipose tissue (BAT) temperature map overlaid on a sagittal ^{1}H image. These temperature maps were obtained by using the lipid-dissolved xenon signal as a temperature probe. The temperature coefficient of the lipid-dissolved xenon chemical shift was measured to be $-0.2\,ppm\,^{\circ}C^{-1}$.

avid area of the supraclavicular fat depot. More interestingly, xenon spectra showed, in addition to the lipid-dissolved phase peak, a nearby peak around 200 ppm that was attributed to xenon dissolved in red blood cells (RBCs), a signal that provided direct evidence of the strong increase in tissue blood flow as the main drive for the increase in xenon tissue uptake.

By being a highly vascularized fatty tissue, BAT is clearly an easy target for the lipophilic xenon. In this case, HP ^{129}Xe gas MRI is a "one-stop shop" for human BAT studies as it is capable of providing both morphological and functional information.

5. ^{129}Xe Cages and Hyper-CEST MRI

5.1. Bound xenon and molecular hosts

In addition to the NMR study of HP Xe in the gas phase and the studies of tissue-dissolved Xe as described above, the affinity of xenon to reside in hydrophobic pockets enables additional insights. This phenomenon made xenon a tool for exploring binding sites on protein surfaces[2c] with some effort being put on spin polarization transfer to nuclei in nearby residues that form the catalytic site of enzymes. Hence, detection of proton signals with and without adding HP nuclei could identify the pocket-related residues.[111] Xe NMR spectra themselves can also show signals indicative of bound atoms. Such a population could either cause a shift of the dissolution peak or a distinct signal given the exchange rate would fall into the right regime.[112] An example are red blood cells[113] where the signal of "bound" Xe is ascribed to the interaction with hemoglobin.[118] Several experiments first used lyophilized protein powder samples, for example, of lipoxygenases.[119] NMR of dissolved Xe has been applied to identify binding pockets of lipid transfer protein,[120] and for observation of conformational changes in maltose binding protein,[121] and chemotaxis Y protein.[122] Besides specific site affinity for native structures, protein engineering also allowed for the design of conformation-sensitive binding pockets as demonstrated with the ribose binding protein.[123]

The binding of Xe to synthetic hosts where the cavity has a simpler design than in proteins can be even more pronounced. α-cyclodextrin[124] still comes with fast exchange but cucurbit[n]urils[125] (CBn, n = 5, 6) show distinct peaks for bound Xe, as do cryptophanes, a family of molecular cages with some members that show rather high Xe affinity (K > 10^3 M^{-1}).[126] It has been shown that different members of this group show distinct signals of bound xenon (Figure 6 a). In particular cryptophane-A, CrA, is often used for conferring a distinct chemical shift to bound Xe ca. 130 ppm upfield from the signal of free Xe in aqueous solution.
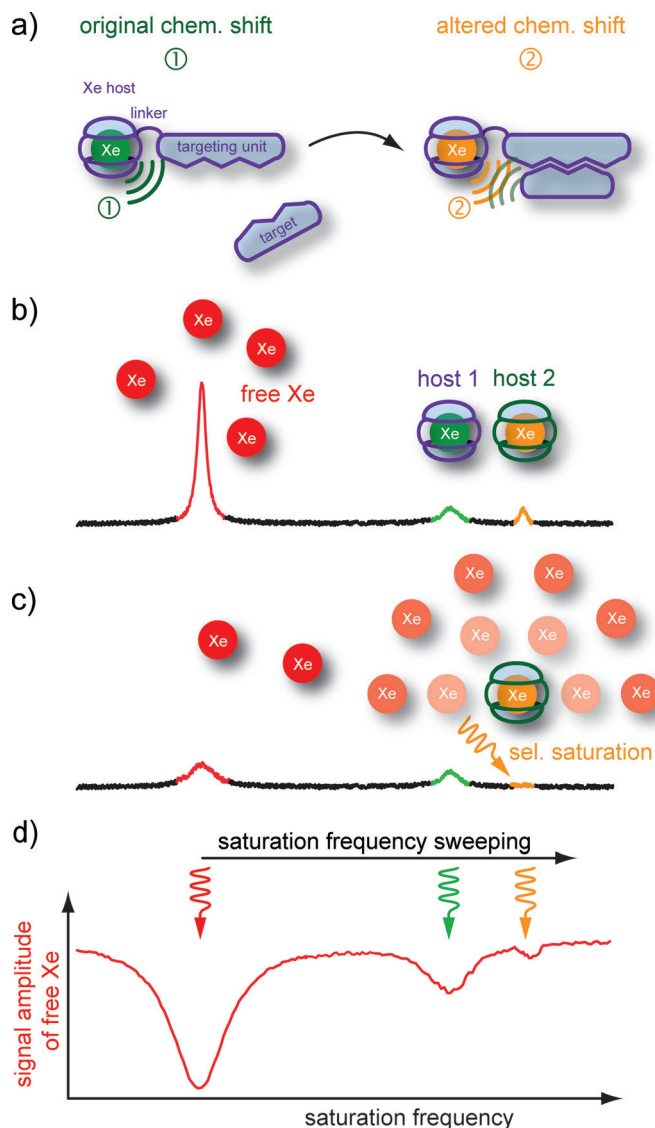
Figure 6. Caged Xe biosensor concept, and Hyper-CEST detection. a) Different Xe hosts confer different chemical shifts to the bound atoms that enable readout at distinct resonance frequencies. b) Xe inside a molecular host changes its resonance frequency upon binding to a target structure. c) Selective Hyper-CEST saturation at one of these frequencies causes a cloud of depolarized Xe around the respective host. The reduced signal from free Xe represents an amplified information from the small amount of cages. d) Sweeping the saturation pulse over a certain frequency range and subsequent observation of the magnetization from free Xe yields a Hyper-CEST spectrum for comparing the performance of different hosts.

5.2. Xenon biosensor concept

These molecular cages triggered the field of Xe biosensors where (for example) a variant of CrA is used as the NMR-active reporter being tethered to a binding unit to reveal the presence of a certain analyte (Figure 6 b). The first implementation was shown with the biotin–avidin system.[127] This original publication also introduced the multiplexing option that this concept offers. This feature is inherent to the different cage types (like in Figure 6 a), but also small chemical modifications on the cage, for example, deuteration,[127b] already provide a host-guest system with a different resonance frequency. Thus the combination of different hosts with different targeting units would allow for detecting multiple analytes simultaneously.

The sensing capability initially relied on a change in chemical shift and direct detection of the bound Xe signal-a concept that was later partially revised due to anticipated loss of spectral resolution in cells and live animals. Optimization for this concept included first and foremost increasing the Xe affinity and maximizing the detected chemical shifts. It is obvious that the cage size impacts the binding constant as illustrated in a comparative review,[128] but substitutions on CrA and cryptophane-111 can also increase the affinity.[129] Understanding the details behind the complexation of Xe revealed induced fit properties[130] and displacement of water[131] as contributing forces. The linker length between cage and targeting unit is a critical parameter for enabling the right balance between sufficient mobility required for narrow resonances and desired surface contact with the target to shift the signal.[132] Another relevant aspect of cryptophane-based sensors is the poor water solubility of the host. While many cages were first characterized in organic solvents, various synthesis studies succeeded to improve solubility.[129c,131,133]

5.3. Hyper-CEST signal amplification

The focus on the binding properties somewhat shifted with the advent of MR imaging protocols for such sensors. The low concentration of caged atoms (typically < 10^{-5} M) requires extensive signal averaging for conventional detection. Initial imaging applications were slow and limited to selected spatial dimensions.[134] To improve this situation, the chemical exchange of Xe became an important parameter. One method for enhanced sensitivity in spectroscopy applications uses selective read-out of the caged Xe signal while the pool of dissolved Xe serves as a polarization reservoir.[135] This principle was also used in imaging[136] but has its limitations due to the timing that comes with frequency selective excitation pulses with defined flip angles.

However, inverting the roles of the participating pools, that is, manipulating the dilute pool and detecting the abundant solution pool, enables significant signal enhancements. The method with selectively saturating the magnetization from the dilute pool (either through cw irradiation, or by using a train of shaped excitation pulses) and observing the signal decrease of the other pool (Figure 6 c) is called chemical exchange saturation transfer (CEST), first introduced by Balaban and co-work-

ers.[137] Combining CEST with HP nuclei was first demonstrated by the Pines lab for an imaging application and coined Hyper-CEST.[138] With Hyper-CEST, host concentrations as low as ~10^{-8} M become accessible-even for imaging.[139] The effect strongly depends on the exchange rate and therefore it can also sense system parameters like ambient temperature.[140] The spectral dimension can be recovered by performing a series of experiments in which the saturation pulse is swept over a certain frequency range (Figure 6d), thus providing another method to sense parameters that influence the chemical shift.[141] It also preserves the multiplexing option mentioned early on.

5.4. Xe Biosensor Applications in Cell Biology

The improved detection limits for imaging made it possible to address problems under more biologically realistic conditions. To date, cryptophane-based sensors that use specific binding to the target have been implemented for sensing the enzyme MMP7,[142] nucleotides,[143] human carbonic anhydrase,[144] MHC class II,[145] zinc ions,[146] the glycoprotein CD14[147] and the receptors for integrin,[148] transferrin,[149] EGF,[150] and folate.[151] An indirect binding approach was pursued through in situ click chemistry with metabolically labeled cell surface glycans.[152] Conformational changes of the sensor induced by changes in pH represent an approach for stimulus-induced binding.[153]

As part of these studies, cell uptake and toxicity evaluations set the bar for target concentrations of functionalized hosts.[148,154] Xe itself passes the cell membrane[149] and does not require further attention to reach intracellular targets. Cell-penetrating peptides proved to be a valuable measure for achieving micromolar intracellular concentrations. However, they are not an absolute requirement since the hydrophobic character of CrA can mediate membrane association and therefore enables certain types of cellular labeling.[155] Sensors with highly specific binding motifs (e.g., antibodies[147,150] or bioorthogonal reaction partners)[152] only require sample-averaged concentrations of 10^{-8} M for MRI.

Critically, the membrane affinity of CrA can be clearly identified by a ca. 10 ppm downfield shift for Xe in membrane-associated CrA.[156] This property proved primarily useful to identify cell-associated cages in the first live-cell experiments.[149,155a] A closer look in combination with FRET data revealed partitioning coefficients on the order 10^2–10^3 for different membrane compositions.[157] This work also initiated a new class of Hyper-CEST experiments for investigating membrane fluidity and integrity: Due to the accelerated exchange, Xe signals from membrane-embedded cages do only differ marginally in chemical shift. However, build-up of the CEST effect can be very different depending on membrane fluidity. Comparative studies are possible when irradiating a pool of caged Xe at fixed saturation power and frequency but increasing saturation time. Evaluating the (multi-)exponential depolarization with an inverse Laplace transformation yields characteristic time constants for different environments.[158] The method called DeLTA (depolarization Laplace transform analysis) can also be used to

discriminate cholesterol content and the onset of lipid domain fluctuations.[159]

5.5. Host Optimization

In order to explore a large chemical shift range of different sensors, the impact of metal ion chelation in close proximity to the cage provides a means to diversify signals.[160] Along this line, attached Gd-chelates can serve as relaxation switches for ^{129}Xe which are detachable through chemical reactions.[161] Regarding Hyper-CEST detection, improved efficiency depends on the exchange properties, which are sub-optimal for CrA. Faster exchanging hosts such as CB6[162] and CB7[163] are currently under investigation. Their binding properties for competitive guests must be taken into account but this versatile binding phenomenon on the other hand enables the option to implement detection of other guests via displacements approaches. An example is the mapping of lysine decarboxylase (LDC) activity where the enzymatic product cadaverine quenches the Hyper-CEST effect.[163] Related to this is an implementation of a sensor relay in which the cavity becomes accessible for Xe as soon as another host recruits the original guest from the CB6 cavity.[164] The macrocyclic host also allows construction of rotaxanes that keep the cavity blocked. Cleaving one of the rotaxane stoppers releases the thread and makes CB6 available for Hyper-CEST detection.[165] This recent design could serve as a development platform for various sensors based on cleavage reactions.

Many dilute targets will only be accessible with an increased number of CEST sites per targeting unit. For this purpose, multivalent carriers with 10^2–10^3 Xe hosts will be the right tool. They have been implemented with scaffolds such as bacterial phages,[150,166] viral capsids,[167] and liposomes.[168] Alternatively, nano-compartments absorbing small amounts of Xe gas can be used, one example being PFOB nanodroplets.[169] The first imaging experiments with the latter substance also included the first multi-channel read-out of different host classes.[155b] Similar host compartments such as gas vesicles[170] and bacterial spores[171] will be discussed separately in the following section.

5.6. Hyper CEST Analysis and Data Encoding

Stable and reproducible HP Xe delivery with shot-to-shot noise <1% achieved through temperature stabilization of the pumping cell[172] allows one to further investigate the predicted line-shape for Hyper-CEST spectra, that is, an Lorentzian.[173] Linked to this theoretical description is an approximation for the Bloch–McConnell equations that allows prediction of the build-up of the Hyper-CEST effect and quantification of the exchange parameters.[174] Comparison of hosts can then be done by using the gas turnover rate.[162b] The exchange dynamics also set the boundary conditions for maximum signal contrast and an orientation for optimum saturation parameters.[175] It is important to achieve the saturation transfer before the intrinsic T_1 relaxation dominates with its signal loss.

For imaging, the CEST information needs to be encoded as fast as possible. Fast imaging sequences can replace the original point-wise encoding[138] given that sufficient magnetization is available. Echo planar imaging (EPI) allows sub-second imaging,[139] with particular application to hyperpolarized imaging using variable flip-angle excitation in an approach called smashCEST. These rapid imaging approaches enable time-resolved studies, including the monitoring of diffusion.[139] Image quality can be improved by exploiting redundancies in the spectral domain[176] during encoding and post-processing. Spin-echo encoding is an alternative for cases where T_2* relaxation makes EPI encoding impractical.[155a] Interest in Hyper-CEST agents has led to the development of fast strategies for gradient-encoded CEST spectra at up to 40-fold reduced scan times.[177]

6. Genetically Encodable Hyperpolarized ^{129}Xe MRI Contrast Agents

Genetically encoded MRI reporters are contrast agents that can be produced by genetically transfected cells to enable the tracking of cells, imaging of gene expression, or sensing of specific aspects of cellular function. Among the advantages of these reporters over synthetic agents are that they can be introduced into cells using established gene-delivery techniques, avoid dilution with cell division, and that a large genetic engineering toolbox can be used to modify and optimize protein-based reporter performance. Furthermore, these agents leverage the recent boom in molecular biology methods to manipulate and deliver genetic materials to animals, such as transgenic mouse lines, viral therapy, RNA interference, and genome editing.

Most existing genetic reporters have been designed for ^{1}H MRI. Examples include enzymes or transporters that can act on synthetic contrast agents,[178] proteins that naturally contain paramagnetic metals, including ferritin,[179] MagA,[180] MntR,[181] tyrosinase,[182] and cytochrome P450,[183] and diamagnetic CEST agents such as lysine rich-protein,[184] human protamine sulfate[185] and proteins that alter water diffusivity in tissue.[186] Comparatively fewer contrast agents have been designed for heteronuclear MRI, all of them based on enzymatic or transporter interactions with ^{19}F compounds,[187] HP ^{13}C compounds,[187c,188] or ^{31}P substrates.[189] A major challenge of all of these agents is their relatively low molecular sensitivity, typically of the micromolar or higher order, which limits their range of in vivo applications. Several excellent reviews have been written on these classes of MRI reporters.[190]

Given the sensitivity gains of HP ^{129}Xe MRI and in particular HyperCEST, there is a strong incentive to develop genetically encoded MRI reporters acting on xenon. However, this prospect is challenging due to the weak interaction of xenon with most proteins. Xenon-binding proteins have been identified through X-ray crystallography, wherein xenon is used as a heavy atom marker to aide in structure elucidation,[191] and NMR, wherein the ^{129}Xe chemical shift can probe proteins' confirmation and ligand binding.[192] Examples of proteins shown to interact with xenon include myoglobin[193] and hemoglobin,

maltose-binding protein[112] and lysozyme.[119] These interactions are attributed primarily to enthalpic Debye and London interactions, with a smaller entropic contribution from xenon dehydration as it enters a hydrophobic cavity.[192b] Unfortunately, although protein binding was shown to shift the resonance frequency of xenon by several ppm mm^{-1}, these proteins are not suitable as ^{129}Xe-MRI contrast agents because their xenon affinities ($\sim$10 mM) would require unrealistic quantities of protein to be present to achieve significant direct contrast, while their xenon exchange rates (dissociation constant $\sim 10^5$ s^{-1})[193] are too fast compared to the induced xenon chemical shift ($\Delta\omega \sim 10^3$–10^4 s^{-1}) to enable efficient HyperCEST contrast.

A major advance in the development of genetically encoded reporters for Xe-MRI was made in 2014, when Shapiro et al. reported that an unusual class of gas-filled protein nanostructures called gas vesicles (GVs) could produce efficient HyperCEST contrast at picomolar concentrations.[25] GVs, which evolved in photosynthetic microbes as a means to regulate buoyancy, comprise hollow gas compartments at hundreds of nm in size and possess a 2 nm protein shell that is permeable to gas but excludes liquid water[194] (Figure 7 a,b). Shapiro et al. showed that GVs can interact with xenon to produce HyperCEST contrast with peak saturation approximately 175 ppm upfield from dissolved ^{129}Xe (Figure 7 c,d). The large chemical shift separation enables the contrast to be extremely efficient, with
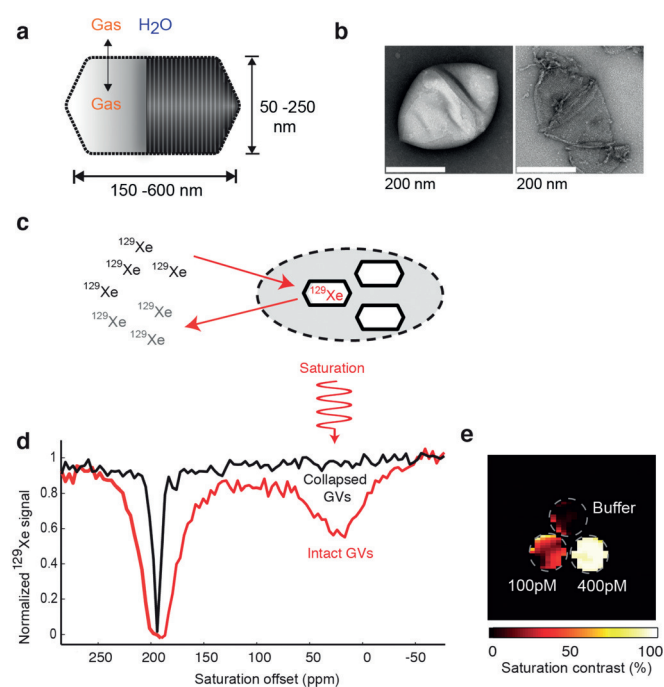

Figure 7. Gas vesicles as genetically encodable HyperCEST reporters detectable at pM concentrations. (a) Diagram of a gas vesicle: a hollow gas nanocompartment (solid shading) surrounded by a gas-permeable protein shell (ribbed shading). (b) Transmission electron micrographs of individual GVs purified from *Halobacterium* NRC-1 in their intact (left) and collapsed (right) state. (c) Diagram of ^{129}Xe CEST between bulk aqueous solvent (left) and GVs (hexagons) either in isolation or inside a cell (gray). (d) Frequency-dependent saturation spectra for intact (red) and collapsed (black) GVs. (e) Saturation contrast image of a three-compartment phantom containing 400 pM GVs, 100 pM GVs and buffer. Reprinted by permission from Macmillan Publishers Ltd: Nature Chemistry,[170] copyright 2014.

a GV detection limit in the picomolar range (Figure 7 e), orders of magnitude lower than comparable proton contrast agents. Furthermore, GVs formed by different species of bacteria and archaea, in which these nanostructrues differ in size and shape, produce HyeprCEST saturation at different chemical shifts, thereby enabling multiplexed imaging. In their initial study, Shapiro et al. provided proofs of concept for GVs as antibody-functionalized markers of cancer cells and as reporters of gene expression in *E. coli*. In addition to GVs, other biological structures may be able to serve as HyperCEST agents. For example, bacterial spores, a dormant cellular state comprising a multi-layered structure of ~1.5 μm size, were recently demonstrated for HyperCEST at a chemical shift 4.5 ppm downfield from aqueous xenon.[171]

The discovery of GVs as highly efficient biomolecular reporters for HyperCEST leads to several interesting questions and possibilities that merit further investigation. If we assume that an optimal CEST saturation can always be achieved with sufficient RF power and that the relaxation of ^{129}Xe is minimal during CEST experiment, then HyperCEST sensitivity is determined by (a) the chemical shift difference and (b) the exchange rate between the contrast-agent-bound and the dissolved ^{129}Xe spins.[195] Regarding the chemical shift, each GV has a several-attoliter gas chamber containing thousands of gas atoms or molecules, where ^{129}Xe atoms presumably experience an environment similar to gas phase, and consequently compared to the synthetic contrast agents, GV-associated ^{129}Xe chemical shift is usually closer to that of the gas phase. Intriguingly, the specific value of chemical shift appears to be genetically determined.[25] It will be interesting to study how this chemical shift relates to other genetically encoded GV properties, including their size, shape and aggregation state, and the extent to which these properties can be tuned at the genetic level. In terms of the exchange rate, when the Z spectra (i.e., the frequency-dependent saturation effects are visualized similar to conventional magnetization transfer spectra by plotting the water saturation (S_{sat}) normalized by the signal without saturation (S_0) as a function of saturation frequency) acquired with intact and collapsed GV are compared with those acquired with synthetic agents, both the GV-bound and the dissolved ^{129}Xe peaks appear to be broader, suggesting the exchange rate is in the intermediate regime. It will be interesting to define quantitatively the optimal RF saturation parameters for the specific exchange rate of GVs. On the molecular level, though the atomic-level structure of the GV wall has not been solved, some hypotheses have been proposed regarding the channels on the protein shell that allow gas exchange in and out of the nanostructure;[194b] it is possible that variation (natural or engineered) in the amino acid sequence of GV proteins could alter the permeability of these putative pores. Taken together, GVs present a wide dynamic range for ^{129}Xe chemical shifts and exchange rates, and these two properties are likely amenable to protein engineering for new and optimized forms of ^{129}Xe HyperCEST.

It is also worth noting that in addition to serving as HyperCEST reporters, GVs produce contrast in at least two complementary imaging modalities. First, they are the first genetically encodable imaging agents for ultrasound,[196] where their low density and high elasticity relative to surrounding media allows them to scatter sound waves. Secondly, their gas-filled interior, which has a different magnetic susceptibility from surrounding solution, allows GVs to produce ^{1}H MRI contrast in susceptibility-weighted imaging.[197]

The list of genetically encoded ^{129}Xe-based HyperCEST reporters has been recently expanded to include β-lactamase by Dmochowski and co-workers.[198] As a small protein encoded by a single gene, this reporter may be easier to use in some settings than GVs, albeit with somewhat lower molecular sensitivity.

7. Parahydrogen

Hydrogen exists in two nuclear spin isomers, denoted as *ortho*- and *para*-, corresponding to the nuclear triplet and singlet states, respectively: here parahydrogen corresponds to the states with an even rotational quantum number J whereas orthohydrogen corresponds to odd values of J. The ratio of the two isomers is determined by the Boltzmann thermal equilibrium for the given temperature, Figure 8.[199] For a more detailed discussion of the physics and applications of parahydrogen beyond the scope of this Minireview, we refer the interested reader to the 1935 book by Farkas on hydrogen[199] or various excellent discussions.[200]

Importantly, conversion between the two states occurs extremely slowly due to the transition being forbidden by the selection rules of quantum mechanics, leaving only statistically unlikely naturally occurring processes of sufficient energy (radiation, molecular collisions, etc.) to foment interconversion. Therefore, after its production (and provided lack of exposure to sources of paramagnetic impurities in the storage vessel), parahydrogen may be stored for long periods before use, as the relaxation rate of the parahydrogen back to room-temperature equilibrium can be on the order of months.[201] Production rates are significantly faster, however, since as discovered in 1929 by Bonhoeffer and Harteck, the use of paramagnetic catalysts (i.e., activated charcoal, nickel, hydrated iron(III) oxide) promotes establishment of Boltzmann thermodynamic equilibrium between *ortho*-H$_2$/*para*-H$_2$ states for a given temperature at greatly accelerated rates. In practice, normal hydrogen gas (i.e., equilibrium ratio at room temperature) consisting of 75% *ortho*- and 25% *para*- isomers is passed through chamber filled with paramagnetic catalyst and maintained at cryogenic temperatures, where the equilibration to the isomer ratio governed by the Boltzmann distribution occurs. For example, a parahydrogen generator operating at 77 K (obtained conveniently by a liquid-N$_2$ bath) yields a mixture with ~50% parahydrogen, whereas the designs based on cryo-chillers (e.g. $T \leq 20$ K) yield ≥ 99% parahydrogen (Figure 8).

8. Fundamentals of Parahydrogen-Induced Polarization (PHIP)

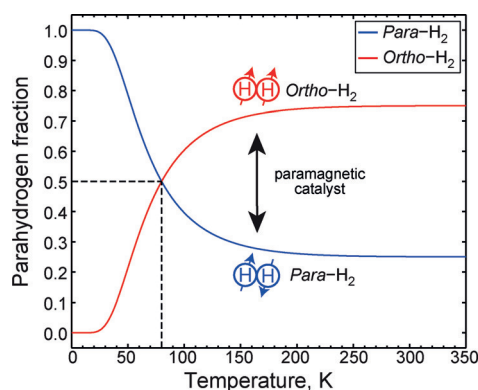In 1986 Bowers and Weitekamp proposed a method for achieving very high nuclear polarizations using parahydrogen.[7a]

Figure 8. Parahydrogen conversion. Passage of H_2 gas over a paramagnetic catalyst, given sufficient contact time, converts the *ortho*-H_2 fraction to *para*-H_2 fraction as a function of temperature.

tion strongly depends on the magnetic field at which the hydrogenation reaction takes place. If hydrogenation is performed at high magnetic field B_0 (i.e., wherein the chemical shift difference between the two *para*-H_2-nascent protons, $\Delta\delta$, is much greater than the spin-spin coupling J between them ($\gamma\Delta\delta B_0 > 2\pi J$)), then the population of the singlet spin state ($\alpha\beta - \beta\alpha$) of *para*-$H_2$ is transferred to the population of spin states $\alpha\beta$ and $\beta\alpha$ of the formed weakly coupled AX spin system (PASADENA effect, Figure 9b).[7b] The NMR spectrum of the AX system populated in this way will contain four peaks grouped in two antiphase multiplets (Figure 9b).
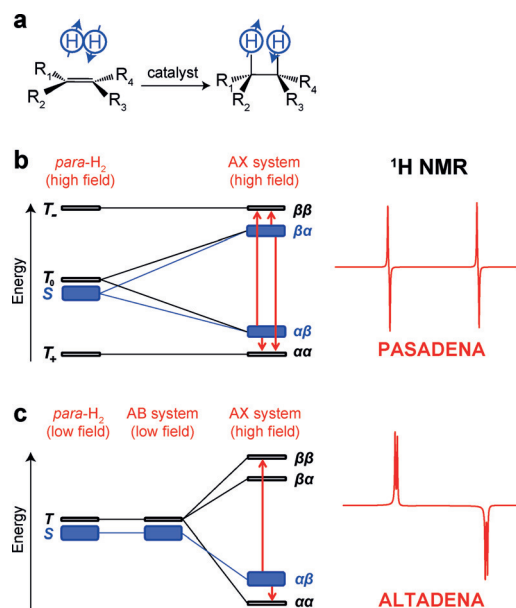
Dubbed PASADENA (Parahydrogen And Synthesis Allow Dramatically Enhanced Nuclear Alignment), the effect predicted strongly enhanced ^1H NMR signals for hydrogenation reaction products when unsaturated molecular precursors are hydrogenated with parahydrogen. Later they demonstrated the effect experimentally by hydrogenating acrylonitrile with parahydrogen using Wilkinson's catalyst.[7b] Anti-phase ^1H NMR multiplets were demonstrated for the reaction product, propionitrile, and for dihydride rhodium complex—the reaction intermediate. It was later realized that experimental demonstrations of the PASADENA effect had already been published,[202] but had been misinterpreted as chemically induced dynamic nuclear polarization.[7c] PASADENA and (the later discovered) ALTADENA[203] are collectively referred to as parahydrogen-induced polarization (PHIP).[11c] This seminal discovery of Bowers and Weitekamp opened up a new strategy for hyperpolarization of various compounds, and currently PHIP and its recent modification, SABRE (Signal Amplification By Reversible Exchange),[8] are used to obtain HP molecules with ^1H,[11c, 200b] ^{13}C,[12] ^{15}N,[13d] ^{19}F,[14] and ^{31}P[15] nuclei in a hyperpolarized state.

Detailed explanation of the spin dynamics and chemical kinetics behind PHIP can be found in several comprehensive reviews.[11c, 200, 204] Here we briefly discuss the main principles of PHIP to qualitatively describe the phenomena discussed below. As an example, we take the simplest two-spin system. The two-spin system of the hydrogen molecule gives rise to four nuclear spin energy levels. As described above, three of these energy levels correspond to orthohydrogen, the state with total nuclear spin 1 (triplet state), whereas the remaining fourth energy level corresponds to parahydrogen (singlet state), the state with zero total nuclear spin. Transitions between singlet and triplet spin states are forbidden by symmetry;[7a] and the spin 0 parahydrogen is NMR-silent.

Bowers and Weitekamp's idea was to break the magnetic equivalence of two hydrogen nuclei by using parahydrogen in a hydrogenation reaction (Figure 9a), thus, making prohibited transitions allowed. Indeed, upon incorporation of a parahydrogen molecule into an asymmetric molecular precursor, the symmetry of the *para*-H_2 molecule becomes broken. This situa-

Figure 9. a) Molecular diagram of parahydrogen (*para*-H_2) addition to the substrate performed with a homogeneous or heterogeneous catalyst. b) PASADENA effect: nuclear spin energy level diagram of *para*-H_2 at high magnetic field (left). An AX spin system is formed upon pairwise addition of *para*-H_2 to the unsaturated substrate at high magnetic field and corresponding ^1H NMR spectrum is shown on the right. c) ALTADENA effect: nuclear spin energy level diagram of *para*-H_2 at low magnetic field (left). An AB spin system is formed after pairwise *para*-H_2 addition to the unsaturated substrate at low magnetic field. An AX spin system is obtained after adiabatic transfer of the reaction product from low to high magnetic field. The corresponding ^1H NMR spectrum is shown on the right.

Two lines (positive-negative or negative-positive, depending on the sign of spin–spin coupling constant J) in each multiplet are separated by J Hz in the case of isotropic liquids and/or gases.[205] The PASADENA-hyperpolarized organic molecules are typically manifested in ^1H NMR spectra as positive-negative multiplets, whereas multiplets for hydride intermediates are negative-positive, since J couplings are usually negative for metal hydrides.[206] Interestingly, the signal intensity of PASADENA spectrum is maximized when a 45° (instead of 90°) pulse is applied for signal acquisition, which may be shown using a density operator description of the PHIP process.[204]

On the other hand, if the hydrogenation reaction takes place at low magnetic field (such that $\gamma\Delta\delta B_0 \leq 2\pi J$; e.g., at the Earth's magnetic field), and afterwards the hydrogenation

product is adiabatically transferred to a high magnetic field, then there is a single state that is overpopulated, that is, $\alpha\beta$ or $\beta\alpha$-depending on the sign of the *J*-coupling constant between the nuclei (ALTADENA effect, Figure 9c).[203] In this case after a 90° pulse the spectral pattern will consist of four lines grouped in two "integral multiplets" simply corresponding to one spin "up" and second spin "down" state (Figure 9c).

In order to be able to observe PHIP for the molecule of interest several key conditions must be fulfilled:[11c]

1. The addition of parahydrogen to the unsaturated precursor should occur in a pairwise manner. Pairwise addition implies that two hydrogen atoms from the same H_2 molecule are included in the product molecule together as a pair, thus preserving spin correlation between the two proton spins.
2. The characteristic nuclear spin relaxation time for *para*-H_2-nascent protons should be longer than the time needed to complete the pairwise hydrogenation process.
3. The magnetic equivalence of the two correlated nuclear spins should be broken during the hydrogenation[207] or in the product of the hydrogenation reaction.[7b]

If all of the above-mentioned conditions are fulfilled, the product of the hydrogenation reaction will possess a non-equilibrium population distribution of its nuclear spin energy levels owing to either the PASADENA or ALTADENA process.

One should note that the final polarization of the hydrogenation reaction product does not depend on the magnetic field strength, and the polarization obtained by PHIP in principle can reach 100% (neglecting spin relaxation and/or decoherence).[7a, 204] In principle, enhancement of the NMR signal can be as high as several thousand-fold above ordinary thermal signals from high-field NMR spectrometers and even a million-fold at low magnetic fields.

Since the hydrogenation reactions have a significant activation energy barrier, the key component of the system is a catalyst (Figure 9a), which (i) enables the hydrogenation reaction, and (ii) provides efficient pairwise addition of molecular hydrogen to the substrate. All hydrogenation catalysts can be classified as homogeneous or heterogeneous depending on their phase relative to the substrate. Homogeneous catalysts are present in the same phase as the to-be-hydrogenated substrate (typically, liquid phase), whereas heterogeneous catalysts are present in a phase different from the phase of the substrate (usually, a solid catalyst and a gaseous or liquid substrate). Since the first demonstration by Bowers and Weitekamp,[7b] homogeneous catalysts have become widely used to produce PHIP, which is reasonable: it is known that hydrogenation mechanisms using metal complexes can usually provide an efficient route for pairwise hydrogen addition. For a long time, the feasibility of using heterogeneous catalysts for production of PHIP was rejected based on the known mechanism of heterogeneous hydrogenation, that is, the Horiuti-Polanyi mechanism. According to Horiuti and Polanyi,[208] hydrogen molecules dissociate on metals (typically used as heterogeneous hydrogenation catalysts) and form a pool of randomly

moving free hydrogen atoms, thus ostensibly not fulfilling condition 1 (pairwise addition) above.[209] Nevertheless, it was shown that various classes of heterogeneous catalysts, that is, immobilized metal complexes,[9a] supported metal nanoparticles,[28b] etc., can enable the PHIP effect. In the current minireview both classes of catalysts are considered.

9. Gases Hyperpolarized via PHIP

As mentioned in the introduction, MRI of gases suffers from poor sensitivity due to their low molecular density combined with the low thermal polarization of their nuclear spins. These problems can make it challenging to image gas-filled void spaces due to the very low signal-to-noise ratio (SNR) and the usually long signal-averaging times, which can be prohibitive for many clinical applications. HP noble gases[210] can be used to address these issues. However, the production of HP noble gases is relatively expensive, necessitating costly hyperpolarizer equipment. Moreover, imaging of HP noble gases requires a dedicated X-band channel (for the heteronucleus of interest) and radio-frequency probe, which are not standard features of clinical MRI scanners (although they are becoming increasingly prevalent). Therefore, production of non-toxic HP proton-containing gases via PHIP could be a promising alternative that avoids the above technical requirements of HP noble gases.

9.1. Production of Hyperpolarized Gases Using PHIP

Historically, experiments with parahydrogen were predominantly conducted in the liquid phase, wherein fluids hyperpolarized by PHIP reside in a solution along with a homogeneous hydrogenation catalyst.[200b] Heterogeneous catalysts can be used to separate the HP product from the catalyst.[29, 211] At the same time, it is also possible to produce catalyst-free HP gases by combining the main advantage of homogeneous (high selectivity) and heterogeneous catalysis (easiest catalyst separation) by using gas-liquid biphasic hydrogenation. Utilization of a homogeneous catalyst dissolved in the liquid phase for biphasic hydrogenation of unsaturated gases with *para*-H_2 allows one to produce HP gas that is free from contamination by the catalyst. In the demonstration of this approach it was shown that the reaction product can return to the gas phase while retaining a significant degree of hyperpolarization.[212] This feature significantly extends the range of gases that can be hyperpolarized. It was shown that utilization of a simple experimental procedure allows one to achieve signal enhancements of 300 for propyne hydrogenation to propylene using the bidentate cationic complex [Rh(PPh$_2$-(CH$_2$)$_4$-PPh$_2$)(COD)]BF$_4$.[212] Another approach for HP gas production is the use of homogeneous catalysts based on a careful choice of the metal complex (homogeneous hydrogenation catalyst) in which the desired unsaturated substrate is coordinated to the metal center.[213] In that case hydrogenation of the substrate with parahydrogen allows the product to leave the metal center and to migrate to a different phase with preservation of the spin order of the two nascent protons derived from the *para*-H_2 molecule. Indeed, it was shown that PHIP-hyperpolar-

ized gas can be obtained in a catalysis-free regime using a chemical reaction with molecular addition of parahydrogen to a water-soluble Rh(I) complex carrying a payload of a compound with double (C=C) bonds.[213] Hydrogenation of the norbornadiene ligand leads to the formation of norbornene, which is expelled from the Rh^I complex to the aqueous phase, but due to its insolubility in water HP norbornene migrates from the solution to the gas phase (Figure 10).[213]
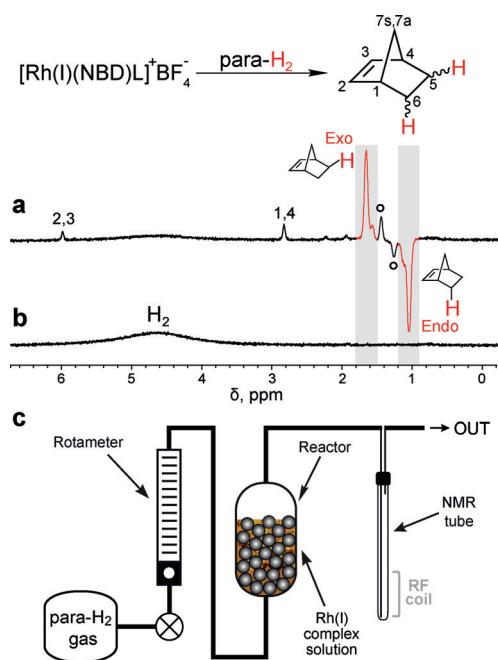

Figure 10. ALTADENA ^{1}H NMR spectra of a gaseous stream during bubbling of parahydrogen (a) and normal H_2 (b) through the solution of [Rh(I)(NBD)L]$^+$BF$_4^-$ in D_2O at 70–80 °C. The broad signal labeled "H_2" belongs to ortho-H_2 gas: the resonances labeled with open circles correspond to norbornane. c) Diagram of the experimental setup with the NMR detection performed in the high field. Reprinted with permission from ref. [213], Copyright (2014) American Chemical Society.

As soon as PHIP was successfully demonstrated in heterogeneous hydrogenations over immobilized[9a] and supported metal catalysts,[28b] the production of HP gases over these catalysts became an important area of PHIP-related investigations. Many different heterogeneous catalysts were used for the production of HP gases in the past eight years, with the aim to find the catalyst with the highest level of pairwise hydrogen addition for a given substrate.[29, 214] Without doubt the utilization of a solid catalyst allows one to produce HP gases in the continuous-flow regime by passing a mixture of an unsaturated substrate with para-H_2 through the catalyst layer. In this approach, hydrogenation occurs at the Earth's magnetic field and corresponds to the ALTADENA[203] type of PHIP experiment. Note that the nature of the heterogeneous solid catalyst can have a significant impact on the polarization level, and titania-supported metal catalysts were shown to exhibit larger PHIP effects compared to metals on other supports.[215] The polarization level for HP gases produced over supported metal catalysts can be several percent,[28b, 216] and it can change with the

variation of the size of the supported metal nanoparticles.[217] Larger polarizations are observed for smaller Pt particles, but for Pd there is an opposite trend.

9.2. MRI of Hyperpolarized Hydrocarbon Gases

Continuous production of HP gases via heterogeneous hydrogenation paves the way to the potential practical applications for imaging of void spaces by MRI. The first experiments were related to MRI visualization of HP propane in a NMR tube with a cross-shaped partition or with a series of capillaries.[9b] For that work, a mixture of para-H_2 and propene gas was flowed through a reactor cell with the heterogeneous catalyst (e.g., Wilkinson's catalyst immobilized on silica). After that the product (HP propane gas) was transferred to the NMR magnet and the ALTADENA enhancement was evident in the MR images.

For both model samples, detection of the NMR signal of a thermally polarized gas did not produced observable images, whereas the use of PHIP-polarized propane gas allowed one to visualize the corresponding structures of the objects used in the experiments.[9b] Importantly, the demonstrated 300-fold signal enhancement in the gas-phase MRI is sufficient to image gases with a similar spatial resolution as that in corresponding liquid-phase MRI experiments. The subsequent development of the strategies for ^{1}H MRI visualization of both hyperpolarized (Figures 11 and 12) and thermally polarized propane gas
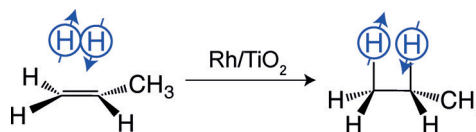

Figure 11. Heterogeneous pairwise hydrogenation of propene to propane with para-H_2 over Rh/TiO$_2$ catalyst with preservation of spin order of parahydrogen in the final HP product.

for high-resolution MRI applications allowed one to significantly decrease the imaging time. Compared to FLASH MRI[218] (Figure 12), the use of UTE MRI[219] decreases the total imaging time significantly, down to the regime sufficient for MRI of a patient within a single breath-hold in a future clinical translation. It was shown that utilization of UTE MRI makes it possible to obtain 2D images of thermally polarized propane gas with ca. 0.9×0.9 mm^2 spatial resolution in ca. 2 s (and potentially with better resolution for HP gases).[220]

Recently, HP propane gas produced by heterogeneous hydrogenation of propene over supported metal catalysts was utilized for 3D ^{1}H MRI with micro-scale spatial resolution (625× 625×625 μm^3), large imaging matrix size (128×128×32) and short (17.4 s) image acquisition time.[215a]

Utilization of a fully deuterated substrate (propene-d_6) in the heterogeneous hydrogenation with para-H_2 permitted acquisition of a high-resolution 3D MRI image of flowing HP [D_6]-propane gas with 0.5×0.5×0.5 mm^3 spatial and ~18 s temporal resolution (Figure 13 a).[221] It was shown that the signal-to-noise ratio in the 3D images of HP [D_6]-propane gas (Fig-
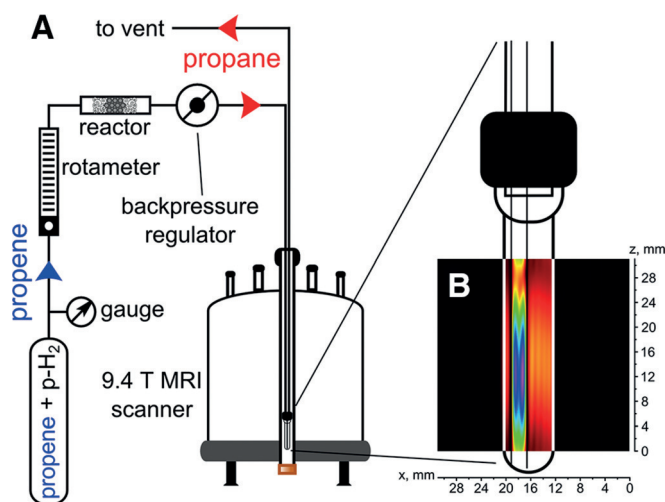
Figure 12. (a) Schematic representation of the experimental setup for using PHIP to produce HP propane via heterogeneous hydrogenation of propene with parahydrogen. (b) ^{1}H MRI FLASH image of HP propane flowing into a 10 mm NMR tube via 1/16 in. OD Teflon capillary. Note that the NMR tube is shown schematically and its length does not match the actual scale of the 2D MR image. Reprinted with permission from ref. [220].
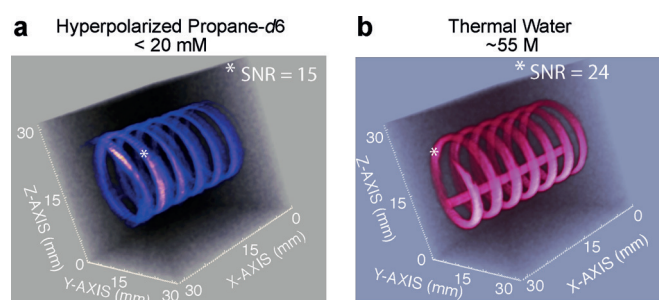

Figure 13. High-resolution 3D gradient echo (GRE) MRI at 4.7 T. a) 3D MRI of flowing HP propane gas (~20 mM concentration) with $0.5 \times 0.5 \times 0.5$ mm^3 spatial and 17.7 s temporal resolution and $32 \times 32 \times 32$ mm^3 field of view. b) The corresponding image of (stationary) thermally polarized tap water (55 M). Reprinted with permission from ref. [221], Copyright (2014) American Chemical Society.

ure 13 a) and water (Figure 13 b) are similar. This observation confirms that the utilization of a gas hyperpolarized by PHIP

allows one to obtain MR images with quality similar to that obtained with water as the signal source.

Utilization of HP gases produced by PHIP is not limited only to void space imaging. Indeed, it was shown that a catalytic reactor positioned inside an NMR magnet can be imaged in situ during heterogeneous hydrogenation of propene to propane with parahydrogen.[28a] In situ MRI of a catalytic reaction allows one to visualize the regions in the catalyst layer where the hydrogenation reaction occurs. Importantly, based on the significant signal enhancement the velocity map for HP gas forming in and flowing through the catalyst bed was obtained.[28a]

Given the above results, PHIP is clearly becoming an important technique for signal enhancement in both basic science and biomedical MRI investigations. Moreover, the use of PHIP to produce HP gases can be useful for their potential utilization in medical MRI applications.

10. Remote-Detection MRI of Hyperpolarized Gases

MRI of gases in small voids, such as in porous media, microreactors, and microfluidic devices, suffers from particularly low sensitivity due to an additional exacerbating factor: low filling factor of the NMR coil, which may be less than 10^{-5} in some cases. While HP methods partially compensate for the low sensitivity, an additional sensitivity boost provided by alternative detection methods may be required. These methods include, for example, surface RF microcoils, RF microslots, and remote detection (RD), to name a few.[222]

In RD MRI,[223] encoding of spatial information and signal detection are performed with different coils in different locations (see Figure 14 a). The encoding RF coil is a large coil around the whole sample, so that all spins can be excited. Signal detection is performed outside the sample with a much smaller and more sensitive RF coil, with an optimized filling factor.[224] The technique requires that the encoded spins are transported to the detector before the magnetization is fully relaxed, and it inflicts one additional dimension as compared to conventional MRI, because it is based on phase encoding only. Nevertheless, it provides a substantial sensitivity boost as an ultrasensitive detection solenoid may be hundreds of times more sensitive than the encoding coil.[225] Furthermore, the flow delivers spins
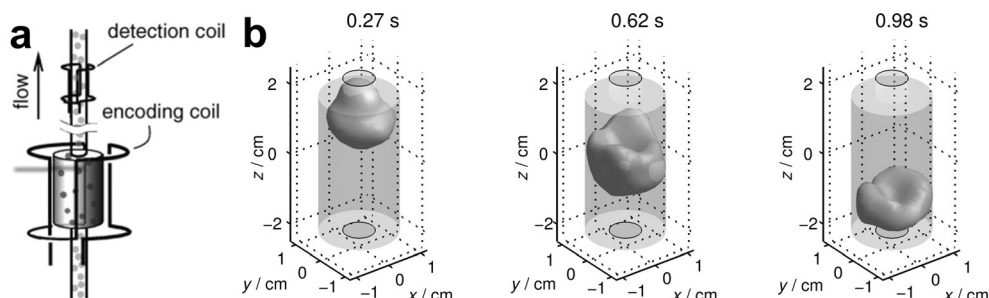

Figure 14. RD MRI of flow of HP [129]Xe through a rock sample. a) The rock sample is inside a large RF coil used to encode spatial information into spin coherences, and the signal is read out by a smaller and more sensitive coil around the outlet tubing, with optimized filling factor. b) 3D TOF images. The silhouettes represent the rock sample. TOF, i.e., the time instant the signal is detected after the encoding, is shown above the images. Reprinted with permission from J. Granwehr, E. Harel, S. Han, S. Garcia, A. Pines, P. N. Sen, Y. Q. Song, *Phys. Rev. Lett.* **2005**, *95*, 075503. Copyright (2005) by the American Physical Society.

from the different parts of the sample to the detector at different times, and this inherent time dimension can be utilized to produce time-of-flight (TOF) flow images.[226]

10.1. Time-of-Flight Flow Imaging with HP Gases

HP Xe is an ideal probe fluid in RD MRI experiments, because the T_1 relaxation time of ^{129}Xe can be extremely long, allowing correspondingly long transport times from the sample to the detector. HP Xe RD MRI has been used for imaging flow through porous materials,[223, 227] rocks,[226] microfluidic devices,[225] and wood,[228] as well as for quantifying diffusion through membranes.[229] Figure 14 b shows a remarkable example of 3D TOF images of HP Xe flowing through a rock sample. The shortest TOF image (TOF = 0.27 s) shows spins that were at the top of the encoding region, because they arrived first to the detector, and the longest TOF image (TOF = 0.98 s) shows the spins at the sample bottom.

Gaseous HP hydrocarbons produced by PHIP have been used in RD MRI experiments as well.[230] T_1 values for spins of hydrocarbons are typically much shorter (~1 s) than that of ^{129}Xe, limiting the transport time of fluid from the sample to the detector; however, if the sample coil and the detection coil are close enough and the flow rate is sufficiently high, the experiments are feasible. Because the gyromagnetic ratio and the natural abundance of ^1H is much higher than that of ^{129}Xe, the sensitivity in PHIP experiments may be greater.

As an example, Figure 15 b shows 2D RD MR images of HP propane, which was produced by propene hydrogenation with *para*-H$_2$ over an Rh catalyst, flowing in a microfluidic capillary.[230a] Overall, the combined sensitivity gain provided by the RD scheme and PHIP was 48 000-fold, and the experiments turned out to be one to two orders of magnitude more sensitive than the corresponding RD experiments with HP Xe. Comparison of the TOF images of a gas and a liquid (Figures 15 b,c) nicely depicts different flow behavior of these phases; laminar flow of a liquid translates the encoded liquid molecules over a large distance (Figure 15 c), whereas for a gas the three orders of magnitude faster diffusion causes efficient mixing of the flow lamellas, leading to a significantly less dispersed, plug-like flow behavior (Figure 15 b).[230a,b]

Experiments with model microfluidic chips have supported the viability of the RD-PHIP approach for visualization of complex microfluidic geometries and flow quantification, Figure 16.[230a] Moreover, these experiments exposed the manufacturing imperfections of the chips. The gas flow in different channels varied in an irregular manner, and the signal amplitude profiles revealed an inhomogeneous distribution of the gas, implying that the channel depth varied from one channel to another.

10.2. Microfluidic Reactor Imaging

The natural ability of *para*-H$_2$ to participate in many important chemical reactions, including those performed with the use of microfluidic devices, opens an avenue for studies using HP gases. Combined RD MRI and PHIP methodologies in such
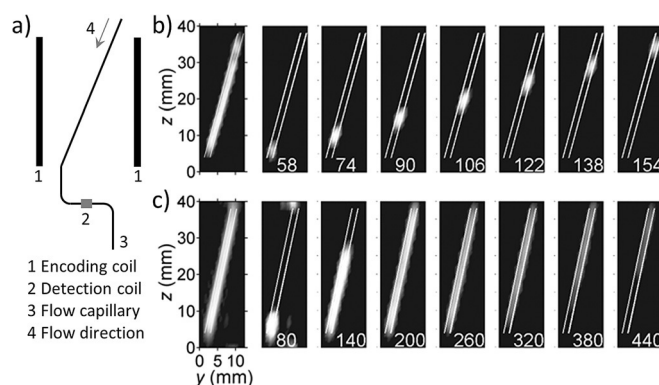

Figure 15. a) RD MRI setup of a simplified microfluidic system consisting of a capillary leading through the encoding and detection coils. TOF RD MRI visualization of (a) HP propane and b) water flow in the capillary (outlined in white), revealing much more extensive dispersion of liquid than that of gas molecules. TOF (ms) is shown at the bottom of the panels. The panels on the left are sums of the other panels.[230a]
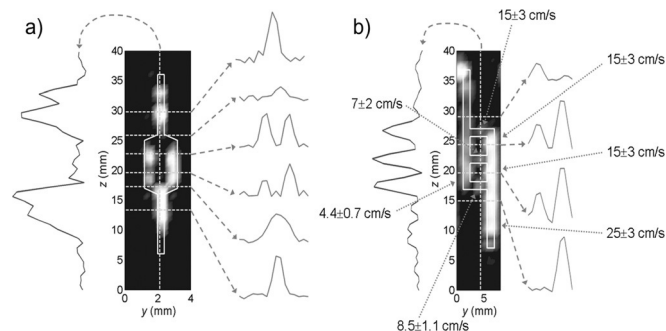

Figure 16. RD MRI of HP propane in microfluidic chips with a) a widened channel in the middle part and b) ladder-like channels (outlined in white). These images are the sum of the panels measured at different TOF instances, and they expose, e.g., manufacturing imperfections. Flow velocities extracted from TOF data are shown in b). Reproduced with permission from Ref. [230a] John Wiley & Sons, Ltd., 2010.

studies were exemplified by the demonstration of catalytic reaction imaging of microscale catalyst layers.[230c] Tiny layers of heterogeneous Rh catalyst packed in thin capillaries (150–800 µm in diameter) served as model microfluidic reactors. It was shown that the RD-PHIP methodology can be used for visualization of mass transport and progress of gas-phase propene hydrogenation reaction inside the microreactors.

The white dashed rectangles in Figure 17 highlight the locations of the catalyst layers. The accumulation of produced HP propane with the distance that gas mixture travels inside the catalyst layer is visualized by the increased signal amplitude in the lower part of the reactor. It was shown that under the given conditions (relatively short travel times), the signal decay due to nuclear spin relaxation was quite insignificant, and the amplitude of the HP propane signal was directly proportional to reaction yield, allowing the determination of the rate of propene hydrogenation.

In addition, the experiments enabled the observation of gas adsorption effects in the microfluidic reactors during their in situ operation, and an elegant approach for quantifying the
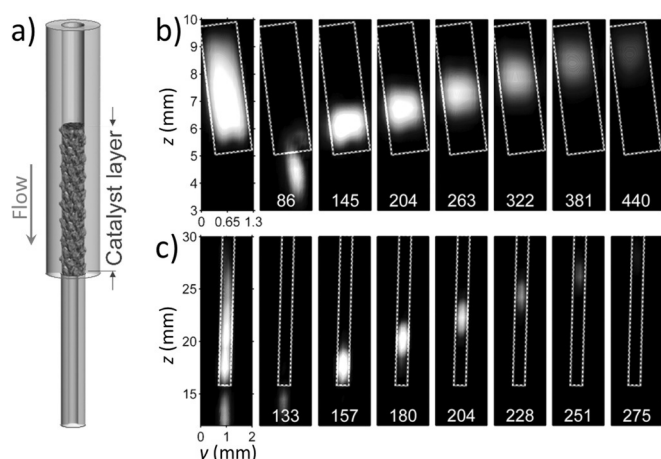
Figure 17. RD MRI visualization of reaction progress inside a catalyst layer packed in a thin capillary. a) Sample setup. 2D TOF images of HP propane resulting from the hydrogenation reaction in the reactors of a) 800 and b) 150 μm in diameter. The reactors are outlined by a white dashed line in the figures. TOF (ms) is shown at the bottom of the panels. The panels on the left are the sums of all other panels in each series.[230c]

amount of absorbed gas using RD NMR was proposed. The authors also introduced the concept of a microfluidic nuclear polarizer based on their findings about PHIP produced in the microscale heterogeneous catalytic hydrogenation.

Further efforts were directed to the development of the concept by employing micro-engineering technologies to produce micro-structured lab-on-a-chip reactors with the catalyst (sputtered Pt) deposited on the inner surface of the channels.[231] It was found that these reactors did not provide PHIP. However, these studies provided a platform for further development of RD NMR for future HP applications, for example, by using Hadamard encoding to achieve a better chemical resolution.[231b]

10.3. Outcome and Perspectives

The current advances and future prospects in RD MRI with HP gases already offer many interesting applications as highlighted above. The major issues concerning the methodology are related to the availability of HP gases and the lifetime of hyperpolarization. HP ^{129}Xe is typically more expensive than the ^{1}H HP hydrocarbon gases produced using PHIP. On the other hand, the nuclear spin relaxation causes more severe problems in the case of HP hydrocarbons. Recent developments in the field of long-lived nuclear spin states,[232] however, may alleviate (or at least mitigate) the latter problem. For instance, it has been shown that a long-lived HP state in ethylene gas can survive for ca. 15 min.[233] The further RD NMR development could concern utilization of such extremely long-lived HP states. In addition, the progress achieved in the field of single-scan ultrafast NMR techniques[234] also offers new capabilities in the context of NMR hyperpolarization. For example, recent work demonstrates the feasibility of single-scan 2D Laplace NMR experiments of dissolved HP propene,[235] and the method should be applicable, e.g., for the investigation of dynamics and physical

environments of HP gases in porous media, both with high-field and low-field (mobile) NMR instruments.[235–236]

11. Conclusion

The development and applications of HP gases continue to advance, and show no sign of slowing down. In addition to SEOP hyperpolarization for production of HP ^{3}He and ^{129}Xe, (i) the SEOP HP technique has been expanded to several other noble gases, (ii) the heterogeneous PHIP[28a] technique has enabled production of HP hydrocarbons in pure form (free from contamination by the catalyst), and (iii) the dissolution DNP technique was demonstrated for production of HP ^{129}Xe[26, 53a] and ^{15}N$_2$O gases.[237] Thus, many other gases could be potentially amenable to DNP hyperpolarization.

As a result of these fundamental advances in the physics, chemistry and engineering of hyperpolarization processes, which enabled more efficient production of established HP gases (e.g., higher throughput and greater polarization in ^{129}Xe hyperpolarizers)[43i, 238] and other advances that enabled the production of new HP gases, it was possible to significantly expand the reach of applications of HP gases in biomedicine and other fields. For example, as described in this mini-review, HP ^{129}Xe is now being employed for in vivo thermometry, brown fat imaging, targeted biosensors, and many other exciting applications, whereas HP hydrocarbons are already used for high-resolution 3D imaging, remote detection, and microfluidic imaging. Many other new applications will likely emerge given that HP gases are becoming more available to researchers, because hyperpolarization equipment is becoming more readily available through commercial sources (as opposed to custom made in the research labs of specialists, as was generally the case only one decade ago). So far, basic and translational scientists have been the main driving force behind the development of MRI of hyperpolarized gases. However, before their entry into routine clinical practice, further research is needed to improve image quality and validate its use, qualitatively and quantitatively, in respiratory disease. This will undoubtedly require collaboration between physicists, chemists and clinicians. Moreover, the better-established applications (e.g., lung imaging using HP ^{129}Xe) will likely continue to be more fully developed, to the point when studies will be driven by medical doctors (the ultimate users of this technology) rather than by the physicists and chemists who pioneered the technology and helped bring it from the proof-of-principle stage to the clinical scale. We look forward to all of these developments with great excitement.

Acknowledgements

Keywords: gas · hyperpolarization · MRI · NMR · propane · Xe-129

[1] a) P. Nikolaou, A. Coffey, M. Barlow, M. Rosen, B. Goodson, E. Chekmenev, *Anal. Chem.* **2014**, *86*, 8206–8212; b) C. Witte, L. Schröder, *NMR Biomed.* **2013**, *26*, 788–802; c) J. Ardenkjaer-Larsen, B. Fridlund, A. Gram, G. Hansson, L. Hansson, M. Lerche, R. Servin, M. Thaning, K. Golman, *Proc. Natl. Acad. Sci. USA* **2003**, *100*, 10158–10163.

[2] a) B. M. Goodson, N. Whiting, A. M. Coffey, P. Nikolaou, F. Shi, B. Gust, M. E. Gemeinhardt, R. V. Shchepin, J. G. Skinner, J. R. Birchall, M. J. Barlow, E. Y. Chekmenev in *Hyperpolarization Methods for MRS, Vol. 4* (Eds.: J. Griffiths, P. Bottomley, R. E. Wasylishen), Wiley, Chichester, **2015**, pp. 797–810; b) P. Nikolaou, B. Goodson, E. Chekmenev, *Chem. Eur. J.* **2015**, *21*, 3156–3166; c) B. Goodson, *J. Magn. Reson.* **2002**, *155*, 157–216.

[3] M. L. Hirsch, N. Kalechofsky, A. Belzer, M. Rosay, J. G. Kempf, *J. Am. Chem. Soc.* **2015**, *137*, 8428–8434.

[4] T. Walker, W. Happer, *Rev. Mod. Phys.* **1997**, *69*, 629.

[5] H. R. Ward, *Acc. Chem. Res.* **1972**, *5*, 18–24.

[6] K. H. Mok, P. J. Hore, *Methods* **2004**, *34*, 75–87.

[7] a) C. Bowers, D. Weitekamp, *Phys. Rev. Lett.* **1986**, *57*, 2645–2648; b) C. Bowers, D. Weitekamp, *J. Am. Chem. Soc.* **1987**, *109*, 5541–5542; c) T. Eisenschmid, R. Kirss, P. Deutsch, S. Hommeltoft, R. Eisenberg, J. Bargon, R. Lawler, A. Balch, *J. Am. Chem. Soc.* **1987**, *109*, 8089–8091.

[8] R. Adams, J. Aguilar, K. Atkinson, M. Cowley, P. Elliott, S. Duckett, G. Green, I. Khazal, J. Lopez-Serrano, D. Williamson, *Science* **2009**, *323*, 1708–1711.

[9] a) I. V. Koptyug, K. V. Kovtunov, S. R. Burt, M. S. Anwar, C. Hilty, S.-I. Han, A. Pines, R. Z. Sagdeev, *J. Am. Chem. Soc.* **2007**, *129*, 5580–5586; b) L. S. Bouchard, K. V. Kovtunov, S. R. Burt, M. S. Anwar, I. V. Koptyug, R. Z. Sagdeev, A. Pines, *Angew. Chem. Int. Ed.* **2007**, *46*, 4064–4068; *Angew. Chem.* **2007**, *119*, 4142–4146.

[10] B. M. Goodson, *J. Magn. Reson.* **2002**, *155*, 157–216.

[11] a) T. R. Carver, C. P. Slichter, *Phys. Rev.* **1953**, *92*, 212–213; b) A. Overhauser, *Phys. Rev.* **1953**, *92*, 411–415; c) J. Natterer, J. Bargon, *Prog. Nucl. Magn. Reson. Spectrosc.* **1997**, *31*, 293–315.

[12] K. Golman, O. Axelsson, H. Johannesson, S. Mansson, C. Olofsson, J. Petersson, *Magn. Reson. Med.* **2001**, *46*, 1–5.

[13] a) C. Gabellieri, S. Reynolds, A. Lavie, G. S. Payne, M. O. Leach, T. R. Eykyn, *J. Am. Chem. Soc.* **2008**, *130*, 4598–4599; b) F. Reineri, A. Viale, S. Ellena, D. Alberti, T. Boi, G. Giovenzana, R. Gobetto, S. Premkumar, S. Aime, *J. Am. Chem. Soc.* **2012**, *134*, 11146–11152; c) T. Theis, M. Truong, A. Coffey, E. Chekmenev, W. Warren, *J. Magn. Reson.* **2014**, *248*, 23–26; d) T. Theis, M. Truong, A. Coffey, R. Shchepin, K. Waddell, F. Shi, B. Goodson, W. Warren, E. Chekmenev, *J. Am. Chem. Soc.* **2015**, *137*, 1404–1407.

[14] M. Plaumann, U. Bommerich, T. Trantzschel, D. Lego, S. Dillenberger, G. Sauer, J. Bargon, G. Buntkowsky, J. Bernarding, *Chem. Eur. J.* **2013**, *19*, 6334–6339.

[15] V. V. Zhivonitko, I. V. Skovpin, I. V. Koptyug, *Chem. Commun.* **2015**, *51*, 2506–2509.

[16] G. E. Pavlovskaya, Z. I. Cleveland, K. F. Stupic, R. J. Basaraba, T. Meersmann, *Proc. Natl. Acad. Sci. USA* **2005**, *102*, 18275–18279.

[17] a) B. Goodson, *Concepts Magn. Reson.* **1999**, *11*, 203–223; b) T. Walker, *J. Phys. Conf. Ser.* **2011**, 012001.

[18] D. Lilburn, G. E. Pavlovskaya, T. Meersmann, *J. Magn. Reson.* **2013**, *229*, 173–186.

[19] K. Golman, R. in't Zandt, M. Thaning, *Proc. Natl. Acad. Sci. USA* **2006**, *103*, 11270–11275.

[20] a) J. Kurhanewicz, D. Vigneron, K. Brindle, E. Chekmenev, A. Comment, C. Cunningham, R. DeBerardinis, G. Green, M. Leach, S. Rajan, R. Rizi, B. Ross, W. Warren, C. Malloy, *Neoplasia* **2011**, *13*, 81–97; b) K. M. Brindle, *J. Am. Chem. Soc.* **2015**, *137*, 6418–6427; c) A. Comment, M. E. Merritt, *Biochemistry* **2014**, *53*, 7333–7357; d) A. Comment, *J. Magn. Reson.* **2016**, *264*, 39–48; e) K. R. Keshari, D. M. Wilson, *Chem. Soc. Rev.* **2014**, *43*, 1627–1659; f) I. V. Koptyug, *Mendeleev Commun.* **2013**, *23*, 299–312; g) S. Meier, P. R. Jensen, M. Karlsson, M. H. Lerche, *Sensors* **2014**, *14*, 1576–1597; h) M. H. Lerche, P. R. Jensen, M. Karlsson, S. Meier, *Anal. Chem.* **2015**, *87*, 119–132.

[21] a) N. Eshuis, B. van Weerdenburg, M. Feiters, F. Rutjes, S. Wijmenga, M. Tessari, *Angew. Chem. Int. Ed.* **2015**, *54*, 1481–1484; *Angew. Chem.* **2015**, *127*, 1501–1504; b) C. Hilty, M. Ragavan, *Anal. Chem.* **2015**, *87*, 1004–1008.

[22] J. Mugler, T. Altes, *J. Magn. Reson. Imaging* **2013**, *37*, 313–331.

[23] R. Branca, T. He, L. Zhang, C. Floyd, M. Freeman, C. White, A. Burant, *Proc. Natl. Acad. Sci. USA* **2014**, *111*, 18001–18006.

[24] L. Schröder, *Physica Medica-Eur. J. Med. Phys.* **2013**, *29*, 3–16.

[25] M. G. Shapiro, R. M. Ramirez, L. J. Sperling, G. Sun, J. Sun, A. Pines, D. V. Schaffer, V. S. Bajaj, *Nat. Chem.* **2014**, *6*, 629–634.

[26] a) A. Comment, S. Jannin, J.-N. Hyacinthe, P. Miéville, R. Sarkar, P. Ahuja, P. R. Vasos, X. Montet, F. Lazeyras, J.-P. Vallée, *Phys. Rev. Lett.* **2010**, *105*, 018104; b) N. Kuzma, M. Pourfathi, H. Kara, P. Manasseh, R. Ghosh, J. Ardenkjaer-Larsen, S. Kadlecek, R. Rizi, *J. Chem. Phys.* **2012**, *137*, 104508.

[27] B. Vuichoud, E. Canet, J. Milani, A. Bornet, D. Baudouin, L. Veyre, D. Gajan, L. Emsley, A. Lesage, C. Copéret, C. Thieuleux, G. Bodenhausen, I. Koptyug, S. Jannin, *J. Phys. Chem. Lett.* **2016**, *7*, 3235–3239.

[28] a) L.-S. Bouchard, S. R. Burt, M. S. Anwar, K. V. Kovtunov, I. V. Koptyug, A. Pines, *Science* **2008**, *319*, 442–445; b) K. V. Kovtunov, I. E. Beck, V. I. Bukhtiyarov, I. V. Koptyug, *Angew. Chem. Int. Ed.* **2008**, *47*, 1492–1495; *Angew. Chem.* **2008**, *120*, 1514–1517.

[29] K. Kovtunov, V. Zhivonitko, I. Skovpin, D. Barskiy, I. Koptyug, *Top. Curr. Chem.* **2013**, *338*, 123–180.

[30] M. Carravetta, O. G. Johannessen, M. H. Levitt, *Phys. Rev. Lett.* **2004**, *92*, 153003.

[31] J. Brossel, A. Kastler, *C. R. Acad. Sci.* **1949**, *229*, 1213–1215.

[32] M. R. Bouchiat, T. R. Carver, C. M. Varnum, *Phys. Rev. Lett.* **1960**, *5*, 373–375.

[33] B. C. Grover, *Phys. Rev. Lett.* **1978**, *40*, 391.

[34] a) W. Happer, E. Miron, S. Schaefer, D. Schreiber, W. V. Wijngaarden, X. Zeng, *Phys. Rev. A* **1984**, *29*, 3092–3110; b) G. D. Cates, R. J. Fitzgerald, A. S. Barton, P. Bogorad, M. Gatzke, N. R. Newbury, B. Saam, *Phys. Rev. A* **1992**, *45*, 4631–4639; c) T. E. Chupp, M. E. Wagshul, K. P. Coulter, A. B. Mcdonald, W. Happer, *Phys. Rev. C* **1987**, *36*, 2244–2251.

[35] T. Meersmann, E. Brunner in *Hyperpolarized Xenon-129 Magnetic Resonance: Concepts, Production, Techniques and Applications*, RSC, Cambridge, **2015**.

[36] a) T. E. Chupp, K. P. Coulter, *Phys. Rev. Lett.* **1985**, *55*, 1074; b) R. Stoner, R. Walsworth, *Phys. Rev. A* **2002**, *66*, 032704.

[37] Ref. [16].

[38] K. F. Stupic, Z. I. Cleveland, G. E. Pavlovskaya, T. Meersmann, *J. Magn. Reson.* **2011**, *208*, 58–69.

[39] D. Steck in Rubidium 85 D line data, Rubidium 87 D line data (revision 2.1.5, 13 January 2015), Vol.

[40] a) E. Babcock, B. Chann, I. A. Nelson, T. G. Walker, *Appl. Opt.* **2005**, *44*, 3098–3104; b) N. Whiting, P. Nikolaou, N. Eschmann, M. Barlow, R. Lammert, J. Ungar, W. Hu, L. Vaissie, B. Goodson, *Appl. Phys. B* **2012**, *106*, 775–788.

[41] E. Babcock, I. Nelson, S. Kadlecek, B. Driehuys, L. W. Anderson, F. W. Hersman, T. G. Walker, *Phys. Rev. Lett.* **2003**, *91*, 123003.

[42] a) X. Z. Zeng, C. J. Wu, M. X. Zhao, S. L. Li, L. Y. Li, X. T. Zhang, Z. D. Liu, W. Y. Liu, *Chem. Phys. Lett.* **1991**, *182*, 538–540; b) N. Whiting, N. A. Eschmann, B. M. Goodson, M. J. Barlow, *Phys. Rev. A* **2011**, *83*, 053428.

[43] a) D. Raftery, H. Long, T. Meersmann, P. J. Grandinetti, L. Reven, A. Pines, *Phys. Rev. Lett.* **1991**, *66*, 584–587; b) M. S. Rosen, T. E. Chupp, K. P. Coulter, R. C. Welsh, S. D. Swanson, *Rev. Sci. Instrum.* **1999**, *70*, 1546; c) U. Ruth, T. Hof, J. Schmidt, D. Fick, H. J. Jänsch, *Appl. Phys. B* **1999**, *68*, 93–97; d) H. Desvaux, T. Gautier, G. Le Goff, M. Pétro, P. Berthault, *Eur. Phys. J. B* **2000**, *12*, 289–296; e) P. Nikolaou, N. Whiting, N. A. Eschmann, K. E. Chaffee, B. M. Goodson, *J. Magn. Reson.* **2009**, *197*, 249–254; f) S. R. Parnell, M. H. Deppe, J. Parra-Robles, J. M. Wild, *J. Appl. Phys.* **2010**, *108*, 064908; g) N. Whiting, P. Nikolaou, N. A. Eschmann, B. M. Goodson, M. J. Barlow, *J. Magn. Reson.* **2011**, *208*, 298–304; h) J. S. Six, T. Hughes-Riley, K. F. Stupic, G. E. Pavlovskaya, T. Meersmann, *PLoS One* **2012**, *7*, e49927; i) P. Nikolaou, A. Coffey, L. Walkup, B. Gust, N. Whiting, H. Newton, S. Barcus, I. Muradyan, M. Dabaghyan, G. Moroz, M. Rosen, S. Patz, M. Barlow, E. Chekmenev, B. Goodson, *Proc. Natl. Acad. Sci. USA* **2013**, *110*, 14150–14155; j) T. Hughes-Riley, J. S. Six, D. M. Lilburn, K. F. Stupic, A. C. Dorkes, D. E. Shaw, G. E. Pavlovskaya, T. Meersmann, *J. Magn. Reson.* **2013**, *237*, 23–33; k) P. Nikolaou, A. M. Coffey, L. L. Walkup, B. M. Gust, N. R. Whiting, H. Newton, I. Muradyan, M. Dabaghyan, K. Ranta, G. Moroz, S. Patz, M. S. Rosen, M. J. Barlow, E. Y. Chekmenev, B. M. Goodson, *Magn. Reson. Imaging* **2014**, *32*, 541–550; l) P. Nikolaou, A. M. Coffey, L. L. Walkup, B. Gust, C. LaPierre, E. Koehnemann, M. J. Barlow, M. S. Rosen, B. M. Goodson, E. Y. Chekmenev, *J. Am. Chem. Soc.* **2014**, *136*, 1636–1642; m) P. Nikolaou, A. M. Coffey, K. Ranta, L. L. Walkup, B. Gust, M. J. Barlow, M. S. Rosen, B. M. Goodson, E. Y. Chekmenev, *J. Phys. Chem. B* **2014**, *118*, 4809–4816.

[44] a) B. Driehuys, G. Cates, E. Miron, K. Sauer, D. Walter, W. Happer, *Appl. Phys. Lett.* **1996**, *69*, 1668–1670; b) M. Haake, A. Pines, J. A. Reimer, R. Seydoux, *J. Am. Chem. Soc.* **1997**, *119*, 11711–11712; c) A. L. Zook, B. B. Adhyaru, C. R. Bowers, *J. Magn. Reson.* **2002**, *159*, 175–182; d) M. G. Mortuza, S. Anala, G. E. Pavlovskaya, T. J. Dieken, T. Meersmann, *J. Chem. Phys.* **2003**, *118*, 1581; e) K. Knagge, J. Prange, D. Raftery, *Chem. Phys. Lett.* **2004**, *397*, 11–16; f) I. C. Ruset, S. Ketel, F. W. Hersman, *Phys. Rev. Lett.* **2006**, *96*, 053002; g) G. Schrank, Z. Ma, A. Schoeck, B. Saam, *Phys. Rev. A* **2009**, *80*, 063424; h) G. Norquay, S. R. Parnell, X. Xu, J. Parra-Robles, J. M. Wild, *J. Appl. Phys.* **2013**, *113*, 044908; i) A. Nossov, E. Haddad, F. Guenneaua, A. Gédéon, *Phys. Chem. Chem. Phys.* **2003**, *5*, 4473–4478.

[45] a) K. F. Stupic, Z. I. Cleveland, G. E. Pavlovskaya, T. Meersmann, *Solid State Nucl. Magn. Reson.* **2006**, *29*, 79–84; b) Z. Wu, W. Happer, M. Kitano, J. Daniels, *Phys. Rev. A* **1990**, *42*, 2774; c) R. K. Ghosh in *Spin Exchange Optical Pumping of Neon and its Applications*, Princeton University, Princeton, **2009**; d) S. Fain, M. L. Schiebler, D. G. McCormack, G. Parraga, *J. Magn. Reson. Imaging* **2010**, *32*, 1398–1408.

[46] G. D. Cates, D. R. Benton, M. Gatzke, W. Happer, K. C. Hasson, N. R. Newbury, *Phys. Rev. Lett.* **1990**, *65*, 2591–2594.

[47] a) B. Chann, I. Nelson, T. G. Walker, *Opt. Lett.* **2000**, *25*, 1352–1354; b) J. N. Zerger, M. J. Lim, K. P. Coulter, T. E. Chupp, *Appl. Phys. Lett.* **2000**, *76*, 1798–1800.

[48] F. D. Colegrove, L. D. Scheare, G. K. Walters, *Phys. Rev.* **1963**, *132*, 2561–2572.

[49] a) T. R. Gentile, D. R. Rich, A. K. Thompson, W. M. Snow, G. L. Jones, *J. Res. Natl. Inst. Stand. Technol.* **2001**, *106*, 709–729; b) P. J. Nacher, G. Tastevin, X. Maitre, X. Dollat, B. Lemaire, J. Olejnik, *Eur. J. Radiol.* **1999**, *9*, b18.

[50] M. Ebert, T. Grossmann, W. Heil, W. E. Otten, R. Surkau, M. Leduc, P. Bachert, M. V. Knopp, L. R. Schad, M. Thelen, *Lancet* **1996**, *11*, 9011.

[51] a) L. D. Schearer, *Phys. Rev.* **1969**, *180*, 83–90; b) L. Young, D. Yang, R. W. Dunford, *J. Phys. B* **2002**, *35*, 2985–2992; c) T. Hadeishi, L. Chung-Heng, *Phys. Rev. Lett.* **1967**, *19*, 211; d) V. Lefevre-Seguin, M. Leduc, *J. Phys. B* **1977**, *10*, 2157.

[52] a) G. Frossati, *J. Low Temp. Phys.* **1998**, *111*, 521–532; b) M. Tanaka, T. Kunimatsu, M. Fujiwara, H. Kohri, T. Ohta, M. Utsuro, M. Yosoi, S. Ono, K. Fukuda, K. Takamatsu, K. Ueda, J.-P. Didelez, G. Frossati, A. D. Waard, *J. Phys. Conf. Ser.* **2011**, *295*, 012167; c) J. D. O'Neill, E. V. Krjukov, J. R. Owers-Bradley, Y. Xia, *J. Low Temp. Phys.* **2007**, *146*, 563–579; d) E. V. Krjukov, J. D. O'Neill, J. R. Owers-Bradley, *J. Low Temp. Phys.* **2005**, *140*, 397–408.

[53] a) M. Pourfathi, N. N. Kuzma, H. Kara, R. K. Ghosh, H. Shaghaghi, S. J. Kadlecek, R. R. Rizi, *J. Magn. Reson.* **2013**, *235*, 71–76; b) A. Capozzi, C. Roussel, A. Comment, J. N. Hyacinthe, *J. Phys. Chem. C* **2015**, *119*, 5020–5025; c) A. Capozzi, J. N. Hyacinthe, T. Cheng, T. R. Eichhorn, G. Boero, C. Roussel, J. J. van der Klink, A. Comment, *J. Phys. Chem. C* **2015**, *119*, 22632–22639.

[54] J. H. Ardenkjaer-Larsen, A. M. Leach, N. Clarke, J. Urbahn, D. Anderson, T. W. Skloss, *NMR Biomed.* **2011**, *24*, 927–932.

[55] a) T. E. Chupp, R. J. Hoare, R. L. Walsworth, B. Wu, *Phys. Rev. Lett.* **1994**, *72*, 2363; b) N. R. Newbury, A. S. Barton, P. Bogorad, G. D. Cates, M. Gatzke, B. Saam, L. Han, R. Holmes, P. A. Souder, J. Xu, D. Benton, *Phys. Rev. Lett.* **1991**, *67*, 3219.

[56] a) A. K. Thompson, A. M. Bernstein, T. E. Chupp, D. J. DeAngelis, G. E. Dodge, G. Dodson, K. A. Dow, M. Farkhondeh, W. Fong, J. Y. Kim, R. A. Loveman, J. M. Richardson, H. Schmieden, D. R. Tieger, T. C. Yates, M. E. Wagshul, J. D. Zumbro, *Phys. Rev. Lett.* **1992**, *68*, 2901; b) J. T. Singh, P. A. M. Dolph, W. A. Tobias, T. D. Averett, A. Kelleher, K. E. Mooney, V. V. Nelyubin, Y. Wang, Y. Zheng, G. D. Cates, *Phys. Rev. C* **2015**, *91*, 055205; c) E. Lelievre-Berna, *Phys. B* **2007**, *397*, 162–167; d) T. R. Gentile, W. C. Chen, *Proc. Sci. (PSTP)* **2013**, *022*, 1–11; e) S. Karpuk, F. Allmendinger, M. Burghoff, C. Gemmel, M. Güldner, W. Heil, W. Kilian, S. Knappe-Grüneberg, C. Mrozik, W. Müller, E. W. Otten, M. Repetto, Z. Salhi, U. Schmidt, A. Schnabel, F. Seifert, Y. Sobolev, L. Trahms, K. Tullney, *Phys. Part. Nucl.* **2013**, *44*, 904–908.

[57] a) D. Raftery, L. Reven, H. Long, A. Pines, P. Tang, J. A. Reimer, *J. Phys. Chem.* **1993**, *97*, 1649–1655; b) C. R. Bowers, T. Pietrass, E. Barash, A. Pines, R. K. Grubbs, A. P. Alivisatos, *J. Phys. Chem.* **1994**, *98*, 9400–9404; c) T. Pietrass, A. Bifone, A. Pines, *Surf. Sci.* **1995**, *334*, L730–L734.

[58] a) C. R. Bowers, H. W. Long, T. Pietrass, H. C. Gaede, A. Pines, *Chem. Phys. Lett.* **1993**, *205*, 168–170; b) B. Driehuys, G. D. Cates, W. Happer, H. Mabuchi, B. Saam, M. S. Albert, A. Wishnia, *Phys. Lett. A* **1993**, *184*, 88–92; c) H. W. Long, H. C. Gaede, J. Shore, L. Reven, C. R. Bowers, J. Kritzenberger, T. Pietrass, A. Pines, P. Tang, J. A. Reimer, *J. Am. Chem. Soc.* **1993**, *115*, 8491–8492; d) B. Driehuys, G. D. Cates, W. Happer, *Phys. Rev. Lett.* **1995**, *74*, 4943–4946; e) H. C. Gaede, Y. Q. Song, R. E. Taylor, E. J. Munson, J. A. Reimer, A. Pines, *Appl. Magn. Reson.* **1995**, *8*, 373–384; f) T. Room, S. Appelt, R. Seydoux, E. L. Hahn, A. Pines, *Phys. Rev. B* **1997**, *55*, 11604–11610; g) G. Navon, Y. Q. Song, T. Room, S. Appelt, R. E. Taylor, A. Pines, *Science* **1996**, *271*, 1848–1851; h) R. J. Fitzgerald, K. L. Sauer, W. Happer, *Chem. Phys. Lett.* **1998**, *284*, 87–92; i) T. Pietrass, R. Seydoux, A. Pines, *J. Magn. Reson.* **1998**, *133*, 299–303; j) S. Appelt, F. Haesing, S. Baer-Lang, N. Shah, B. Blumich, *Chem. Phys. Lett.* **2001**, *348*, 263–269.

[59] a) M. Haake, A. Pines, J. A. Reimer, R. Seydoux, *J. Am. Chem. Soc.* **1997**, *119*, 11711–11712; b) R. Seydoux, A. Pines, M. Haake, J. A. Reimer, *J. Phys. Chem. B* **1999**, *103*, 4629–4637; c) ref. [44b].

[60] a) D. Raftery, E. MacNamara, G. Fisher, C. V. Rice, J. Smith, *J. Am. Chem. Soc.* **1997**, *119*, 8746–8747; b) E. Brunner, M. Haake, A. Pines, J. A. Reimer, R. Seydoux, *Chem. Phys. Lett.* **1998**, *290*, 112–116; c) E. Brunner, R. Seydoux, M. Haake, A. Pines, J. A. Reimer, *J. Magn. Reson.* **1998**, *130*, 145–148; d) E. MacNamara, G. Fisher, C. V. Rice, S. J. Hwang, D. Raftery, *J. Phys. Chem. B* **1999**, *103*, 1158–1160.

[61] a) B. Saam, N. Drukker, W. Happer, *Chem. Phys. Lett.* **1996**, *263*, 481–487; b) D. M. Schmidt, J. S. George, S. I. Penttila, A. Caprihan, E. Fukushima, *J. Magn. Reson.* **1997**, *129*, 184–187; c) Y. Song, B. Goodson, B. Sheridan, T. de Swiet, A. Pines, *J. Chem. Phys.* **1998**, *108*, 6233–6239.

[62] a) R. W. Mair, D. G. Cory, S. Peled, C. H. Tseng, S. Patz, R. L. Walsworth, *J. Magn. Reson.* **1998**, *135*, 478–486; b) R. W. Mair, G. P. Wong, D. Hoffmann, M. D. Hurlimann, S. Patz, L. M. Schwartz, R. L. Walsworth, *Phys. Rev. Lett.* **1999**, *83*, 3324–3327; c) S. Peled, C. H. Tseng, A. A. Sodickson, R. W. Mair, R. L. Walsworth, D. G. Cory, *J. Magn. Reson.* **1999**, *140*, 320–324.

[63] a) I. L. Moudrakovski, A. Sanchez, C. I. Ratcliffe, J. A. Ripmeester, *J. Phys. Chem. B* **2000**, *104*, 7306–7310; b) G. P. Wong, R. W. Mair, R. L. Walsworth, D. G. Cory, *Phys. Rev. Lett.* **2001**, *86*, 4156–4159.

[64] a) E. Brunner, M. Haake, L. Kaiser, A. Pines, J. A. Reimer, *J. Magn. Reson.* **1999**, *138*, 155–159; b) L. G. Kaiser, T. Meersmann, J. W. Logan, A. Pines, *Proc. Natl. Acad. Sci. USA* **2000**, *97*, 2414–2418.

[65] a) I. L. Moudrakovski, S. Lang, C. I. Ratcliffe, B. Simard, G. Santyr, J. A. Ripmeester, *J. Magn. Reson.* **2000**, *144*, 372–377; b) G. Pavlovskaya, J. Six, T. Meersman, N. Gopinathan, S. P. Rigby, *AIChE J.* **2015**, *61*, 4013–4019.

[66] a) H. J. Jänsch, T. Hof, U. Ruth, J. Schmidt, D. Stahl, D. Fick, *Chem. Phys. Lett.* **1998**, *296*, 146–150; b) H. J. Jansch, P. Gerhard, M. Koch, *Proc. Natl. Acad. Sci. USA* **2004**, *101*, 13715–13719.

[67] a) X. X. Li, C. Newberry, I. Saha, P. Nikolaou, N. Whiting, B. M. Goodson, *Chem. Phys. Lett.* **2006**, *419*, 233–239; b) A. E. Truxal, C. C. Slack, M. D. Gomes, C. C. Vassiliou, D. E. Wemmer, A. Pines, *Angew. Chem. Int. Ed.* **2016**, *55*, 4666; *Angew. Chem.* **2016**, *128*, 4744.

[68] a) S. Anala, G. E. Pavlovskaya, P. Pichumani, T. J. Dieken, M. D. Olsen, T. Meersmann, *J. Am. Chem. Soc.* **2003**, *125*, 13298–13302; b) N. J. Rogers, F. Hill-Casey, K. F. Stupic, J. S. Six, C. Lesbats, S. P. Rigby, J. Fraissard, G. E. Pavlovskaya, T. Meersmann, *Proc. Natl. Acad. Sci. USA* **2016**, *113*, 3164–3168.

[69] a) T. Meersmann, J. W. Logan, R. Simonutti, S. Caldarelli, A. Comotti, P. Sozzani, L. G. Kaiser, A. Pines, *J. Phys. Chem. A* **2000**, *104*, 11665–11670; b) P. Sozzani, A. Comotti, R. Simonutti, T. Meersmann, J. W. Logan, A. Pines, *Angew. Chem. Int. Ed.* **2000**, *39*, 2695–2698; *Angew. Chem.* **2000**, *112*, 2807–2810; c) I. Moudrakovski, D. V. Soldatov, J. A. Ripmeester, D. N. Sears, C. J. Jameson, *Proc. Natl. Acad. Sci. USA* **2004**, *101*, 17924–17929; d) D. V. Soldatov, I. L. Moudrakovski, E. V. Grachev, J. A. Ripmeester, *J. Am. Chem. Soc.* **2006**, *128*, 6737–6744; e) C. Y. Cheng, C. R. Bowers, *J. Am. Chem. Soc.* **2007**, *129*, 13997–14002; f) C. Y. Cheng, C. R. Bowers, *ChemPhysChem* **2007**, *8*, 2077–2081; g) C. Y. Cheng, T. C. Stamatatos, G. Christou, C. R. Bowers, *J. Am. Chem. Soc.* **2010**, *132*, 5387–5393; h) C. R. Bowers, M. Dvoyashkin, S. R. Salpage, C. Akel, H. Bhase, M. F. Geer, L. S. Shimizu, *ACS Nano* **2015**, *9*, 6343–6353; i) R. Anedda, D. V. Soldatov, I. L. Moudrakovski, M. Casu, J. A. Ripmeester, *Chem. Mater.* **2008**, *20*, 2908–2920.

[70] A. Comotti, S. Bracco, L. Ferretti, M. Mauri, R. Simonutti, P. Sozzani, *Chem. Commun.* **2007**, 350–352.

[71] J. M. Kneller, R. J. Soto, S. E. Surber, J. F. Colomer, A. Fonseca, J. B. Nagy, G. Van Tendeloo, T. Pietrass, *J. Am. Chem. Soc.* **2000**, *122*, 10591–10597.

[72] I. L. Moudrakovski, A. A. Sanchez, C. I. Ratcliffe, J. A. Ripmeester, *J. Phys. Chem. B* **2001**, *105*, 12338–12347.

[73] a) A. V. Nossov, D. V. Soldatov, J. A. Ripmeester, *J. Am. Chem. Soc.* **2001**, *123*, 3563–3568; b) J. P. Butler, R. W. Mair, D. Hoffmann, M. I. Hrovat, R. A. Rogers, G. P. Topulos, R. L. Walsworth, S. Patz, *J. Phys. Condens. Matter* **2002**, *14*, L297–L304; c) I. L. Moudrakovski, L. Q. Wang, T. Baumann, J. H. Satcher, G. J. Exarhos, C. I. Ratcliffe, J. A. Ripmeester, *J. Am. Chem. Soc.* **2004**, *126*, 5052–5053; d) I. L. Moudrakovski, C. I. Ratcliffe, J. A. Ripmeester, L. Q. Wang, G. J. Exarhos, T. F. Baumann, J. H. Satcher, *J. Phys. Chem. B* **2005**, *109*, 11215–11222; e) R. Simonutti, S. Bracco, A. Comotti, M. Mauri, P. Sozzani, *Chem. Mater.* **2006**, *18*, 4651–4657; f) A. Comotti, S. Bracco, P. Sozzani, S. Horike, R. Matsuda, J. Chen, M. Takata, Y. Kubota, S. Kitagawa, *J. Am. Chem. Soc.* **2008**, *130*, 13664–13672.

[74] a) K. Campbell, K. J. Ooms, R. E. Wasylishen, R. R. Tykwinski, *Org. Lett.* **2005**, *7*, 3397–3400; b) K. J. Ooms, R. E. Wasylishen, *Microporous Mesoporous Mater.* **2007**, *103*, 341–351; c) S. Pawsey, I. Moudrakovski, J. Ripmeester, L. Q. Wang, G. J. Exarhos, J. L. C. Rowsell, O. M. Yaghi, *J. Phys. Chem. C* **2007**, *111*, 6060–6067.

[75] a) A. Dubes, I. L. Moudrakovski, P. Shahgaldian, A. W. Coleman, C. I. Ratcliffe, J. A. Ripmeester, *J. Am. Chem. Soc.* **2004**, *126*, 6236–6237; b) G. S. Ananchenko, I. L. Moudrakovski, A. W. Coleman, J. A. Ripmeester, *Angew. Chem. Int. Ed.* **2008**, *47*, 5616–5618; *Angew. Chem.* **2008**, *120*, 5698–5700.

[76] P. Sozzani, S. Bracco, A. Comotti, M. Mauri, R. Simonutti, P. Valsesia, *Chem. Commun.* **2006**, 1921–1923.

[77] a) A. Nossov, E. Haddad, F. Guenneau, C. Mignon, A. Gedeon, D. Grosso, F. Babonneau, C. Bonhomme, C. Sanchez, *Chem. Commun.* **2002**, 2476–2477; b) V. V. Terskikh, I. L. Moudrakovski, S. R. Breeze, S. Lang, C. I. Ratcliffe, J. A. Ripmeester, A. Sayari, *Langmuir* **2002**, *18*,

5653–5656; c) A. Nossov, E. Haddad, F. Guenneau, A. Galarneau, F. Di Renzo, F. Fajula, A. Gedeon, *J. Phys. Chem. B* **2003**, *107*, 12456–12460; d) A. Comotti, S. Bracco, P. Valsesia, L. Ferretti, P. Sozzani, *J. Am. Chem. Soc.* **2007**, *129*, 8566–8576; e) A. Galarneau, M. Nader, F. Guenneau, F. Di Renzo, A. Gedeon, *J. Phys. Chem. C* **2007**, *111*, 8268–8277.

[78] a) A. Nossov, F. Guenneau, M. A. Springuel-Huet, E. Haddad, V. Montouillout, B. Knott, F. Engelke, C. Fernandez, A. Gedeon, *Phys. Chem. Chem. Phys.* **2003**, *5*, 4479–4483; b) A. Sakthivel, S. J. Huang, W. H. Chen, Z. H. Lan, K. H. Chen, T. W. Kim, R. Ryoo, A. S. T. Chiang, S. B. Liu, *Chem. Mater.* **2004**, *16*, 3168–3175; c) A. Sakthivel, S. J. Huang, W. H. Chen, Z. H. Lan, K. H. Chen, H. P. Lin, C. Y. Mou, S. B. Liu, *Adv. Funct. Mater.* **2005**, *15*, 253–258; d) Y. Liu, W. P. Zhang, Z. C. Liu, S. T. Xu, Y. D. Wang, Z. K. Xie, X. W. Han, X. H. Bao, *J. Phys. Chem. C* **2008**, *112*, 15375–15381; e) Y. Liu, W. P. Zhang, S. J. Xie, L. Xu, X. W. Han, X. H. Bao, *J. Phys. Chem. B* **2008**, *112*, 1226–1231; f) L. Itani, Y. Liu, W. P. Zhang, K. N. Bozhilov, L. Delmotte, V. Valtchev, *J. Am. Chem. Soc.* **2009**, *131*, 10127–10139; g) H. C. Xin, J. Zhao, S. T. Xu, J. P. Li, W. P. Zhang, X. W. Guo, E. J. M. Hensen, Q. H. Yang, C. Li, *J. Phys. Chem. C* **2010**, *114*, 6553–6559; h) K. K. Zhu, J. M. Sun, J. Liu, L. Q. Wang, H. Y. Wan, J. Z. Hu, Y. Wang, C. H. F. Peden, Z. M. Nie, *ACS Catal.* **2011**, *1*, 682–690; i) C. Z. Jin, G. Li, X. S. Wang, L. X. Zhao, L. P. Liu, H. O. Liu, Y. Liu, W. P. Zhang, X. W. Han, X. H. Bao, *Chem. Mater.* **2007**, *19*, 1664–1670; j) X. J. Li, W. P. Zhang, S. L. Liu, L. Y. Xu, X. W. Han, X. H. Bao, *J. Catal.* **2007**, *250*, 55–66.

[79] a) C. J. Jameson, *J. Chem. Phys.* **2002**, *116*, 8912–8929; b) C. J. Jameson, A. C. de Dios, *J. Chem. Phys.* **2002**, *116*, 3805–3821.

[80] E. Weiland, M. A. Springuel-Huet, A. Nossov, A. Gédéon, *Microporous Mesoporous Mater.* **2016**, *225*, 41–65.

[81] J. C. Woods in Congressional Hearing: "Caught by Surprise: Causes and Consequences of the Helium-3 Supply Crisis", Vol. **2010**.

[82] a) J. S. Six, T. Hughes-Riley, D. M. Lilburn, A. C. Dorkes, K. F. Stupic, D. E. Shaw, P. G. Morris, I. P. Hall, G. E. Pavlovskaya, T. Meersmann, *Magn. Reson. Imaging* **2014**, *32*, 48–53; b) Z. I. Cleveland, K. F. Stupic, G. E. Pavlovskaya, J. E. Repine, J. B. Wooten, T. Meersmann, *J. Am. Chem. Soc.* **2007**, *129*, 1784–1792.

[83] W. Ramsay, *Nobel Lecture*, Dec **1904**, *12*, 1901–1921.

[84] T. Marx, M. Schmidt, U. Schirmer, H. Reinelt, *J. R. Soc. Med.* **2000**, *93*, 513–517.

[85] J. Lawrence, W. Loomis, C. Tobias, F. Turpin, *J. Physiol.* **1946**, *105*, 197.

[86] S. C. Cullen, E. G. Gross, *Science* **1951**, *113*, 580–582.

[87] M. Albert, G. Cates, B. Driehuys, W. Happer, B. Saam, C. Springer, A. Wishnia, *Nature* **1994**, *370*, 199–201.

[88] a) R. Edelman, H. Hatabu, E. Tadamura, W. Li, P. Prasad, *Nat. Med.* **1996**, *2*, 1236–1239; b) H. Kauczor, K. Kreitner, *Eur. Radiol.* **1999**, *9*, 1755–1764.

[89] J. Mugler, B. Driehuys, J. Brookeman, G. Cates, S. Berr, R. Bryant, T. Daniel, E. deLange, J. Downs, C. Erickson, W. Happer, D. Hinton, N. Kassel, T. Maier, C. Phillips, B. Saam, K. Sauer, M. Wagshul, *Magn. Reson. Med.* **1997**, *37*, 809–815.

[90] L. Zhao, M. Albert, *Nucl. Instrum. Methods Phys. Res. Sect. A* **1998**, *402*, 454–460.

[91] a) H. Middleton, R. Black, B. Saam, G. Cates, G. Cofer, R. Guenther, W. Happer, L. Hedlund, G. Johnson, K. Juvan, J. Swartz, *Magn. Reson. Med.* **1995**, *33*, 271–275; b) L. Walkup, J. Woods, *NMR Biomed.* **2014**, *27*, 1429–1438.

[92] a) Y. Shukla, A. Wheatley, M. Kirby, S. Svenningsen, A. Farag, G. Santyr, N. Paterson, D. McCormack, G. Parraga, *Acad. Radiol.* **2012**, *19*, 941–951; b) S. Svenningsen, M. Kirby, D. Starr, D. Leary, A. Wheatley, G. N. Maksym, D. G. McCormack, G. Parraga, *J. Magn. Reson. Imaging* **2013**, *38*, 1521–1530.

[93] a) S. S. Kaushik, Z. I. Cleveland, G. P. Cofer, G. Metz, D. Beaver, J. Nouls, M. Kraft, W. Auffermann, J. Wolber, H. P. McAdams, *Magn. Reson. Med.* **2011**, *65*, 1154–1165; b) B. Driehuys, S. Martinez-Jimenez, Z. Cleveland, G. Metz, D. Beaver, J. Nouls, S. Kaushik, R. Firszt, C. Willis, K. Kelly, J. Wolber, M. Kraft, H. McAdams, *Radiology* **2012**, *262*, 279–289; c) M. Kirby, S. Svenningsen, A. Owrangi, A. Wheatley, A. Farag, A. Ouriadov, G. Santyr, R. Etemad-Rezai, H. Coxson, D. McCormack, G. Parraga, *Radiology* **2012**, *265*, 600–610; d) M. Kirby, S. Svenningsen, N. Kanhere, A. Owrangi, A. Wheatley, H. Coxson, G. Santyr, N. Paterson, D. McCormack, G. Parraga, *J. Appl. Physiol.* **2013**, *114*, 707–715.

[94] a) S. Kaushik, M. Freeman, S. Yoon, M. Liljeroth, J. Stiles, J. Roos, W. Foster, C. Rackley, H. McAdams, B. Driehuys, *J. Appl. Physiol.* **2014**, *117*, 577–585; b) N. J. Stewart, G. Leung, G. Norquay, H. Marshall, J. Parra-Robles, P. S. Murphy, R. F. Schulte, C. Elliot, R. Condliffe, P. D. Griffiths, *Magn. Reson. Med.* **2015**, *74*, 196–207.

[95] S. Kaushik, Z. Cleveland, G. Cofer, G. Metz, D. Beaver, J. Nouls, M. Kraft, W. Auffermann, J. Wolber, H. McAdams, B. Driehuys, *Magn. Reson. Med.* **2011**, *65*, 1154–1165.

[96] M. Kirby, G. Parraga, *Acad. Radiol.* **2013**, *20*, 1344–1356.

[97] B. G. Zeiher, T. J. Gross, J. A. Kern, L. A. Lanza, M. W. Peterson, *Chest* **1995**, *108*, 68–72.

[98] a) K. Ruppert, J. Brookeman, K. Hagspiel, J. Mugler, *Magn. Reson. Med.* **2000**, *44*, 349–357; b) J. Butler, R. Mair, D. Hoffmann, M. Hrovat, R. Rogers, G. Topulos, R. Walsworth, S. Patz, *J. Phys. Condens. Matter* **2002**, *14*, L297; c) ref. [73b].

[99] K. Qing, K. Ruppert, Y. Jiang, J. Mata, W. Miller, Y. Shim, C. Wang, I. Ruset, F. Hersman, T. Altes, J. Mugler, *J. Magn. Reson. Imaging* **2014**, *39*, 346–359.

[100] Z. Cleveland, G. Cofer, G. Metz, D. Beaver, J. Nouls, S. Kaushik, M. Kraft, J. Wolber, K. Kelly, H. McAdams, B. Driehuys, *PLoS One* **2010**, *5*, e12192.

[101] a) J. Mugler, T. Altes, I. Ruset, I. Dregely, J. Mata, G. Miller, S. Ketel, J. Ketel, F. Hersman, K. Ruppert, *Proc. Natl. Acad. Sci. USA* **2010**, *107*, 21707–21712; b) Y. V. Chang, J. D. Quirk, I. C. Ruset, J. J. Atkinson, F. W. Hersman, J. C. Woods, *Magn. Reson. Med.* **2014**, *71*, 339–344; c) K. Ruppert, J. Mata, J. Brookeman, K. Hagspiel, J. Mugler, *Magn. Reson. Med.* **2004**, *51*, 676–687; d) K. Ruppert, J. Mata, H. Wang, W. Tobias, G. Cates, J. Brookeman, K. Hagspiel, J. Mugler, *Magn. Reson. Med.* **2007**, *57*, 1099–1109; e) Y. Chang, J. Mata, T. Altes, J. Mugler III, K. Ruppert, *Proceedings of the Joint Annual Meeting of ISMRM-ESMRMB*, Stockholm, Sweden **2010**, p. 4602.

[102] a) Y. V. Chang, *Magn. Reson. Med.* **2013**, *69*, 884–890; b) I. Dregely, I. Ruset, J. Mata, J. Ketel, S. Ketel, J. Distelbrink, T. Altes, J. Mugler, G. Miller, F. Hersman, K. Ruppert, *Magn. Reson. Med.* **2012**, *67*, 943–953; c) I. Dregely, J. Mugler, I. Ruset, T. Altes, J. Mata, G. Miller, J. Ketel, S. Ketel, J. Distelbrink, F. Hersman, K. Ruppert, *J. Magn. Reson. Imaging* **2011**, *33*, 1052–1062.

[103] R. Chen, F.-C. Fan, S. Kim, K. Jan, S. Usami, S. Chien, *J. Appl. Physiol.* **1980**, *49*, 178–183.

[104] D. Gur, W. F. Good, S. K. Wolfson, H. Yonas, L. Shabason, *Science* **1982**, *215*, 1267–1268.

[105] S. D. Swanson, M. S. Rosen, B. W. Agranoff, K. P. Coulter, R. C. Welsh, T. E. Chupp, *Magn. Reson. Med.* **1997**, *38*, 695–698.

[106] a) A. Wakai, K. Nakamura, J. Kershaw, D. Wright, I. Kanno, *Magn. Reson. Med. Sci.* **2005**, *4*, 19–25; b) X. Zhou, M. Mazzanti, J. Chen, Y. S. Tzeng, J. Mansour, J. Gereige, A. Venkatesh, Y. Sun, R. Mulkern, M. Albert, *NMR Biomed.* **2008**, *21*, 217–225.

[107] G. Duhamel, P. Choquet, J.-L. Leviel, J. Steibel, L. Lamalle, C. Julien, F. Kober, E. Grillon, J. Derouard, M. Décorps, *C. R. Acad. Sci.* **2000**, *323*, 529–536.

[108] X. Zhou, Y. Sun, M. Mazzanti, N. Henninger, J. Mansour, M. Fisher, M. Albert, *NMR Biomed.* **2011**, *24*, 170–175.

[109] M. Mazzanti, R. Walvick, X. Zhou, Y. Sun, N. Shah, J. Mansour, J. Gereige, M. Albert, *PLoS One* **2011**, *6*, e21607.

[110] S. S. Kety, *Pharmacol. Rev.* **1951**, *3*, 1–41.

[111] C. Landon, P. Berthault, F. Vovelle, H. Desvaux, *Protein Sci.* **2001**, *10*, 762–770.

[112] S. M. Rubin, S.-Y. Lee, E. J. Ruiz, A. Pines, D. E. Wemmer, *J. Mol. Biol.* **2002**, *322*, 425–440.

[113] A. Bifone, Y. Song, R. Seydoux, R. Taylor, B. Goodson, T. Pietrass, T. Budinger, G. Navon, A. Pines, *Proc. Natl. Acad. Sci. USA* **1996**, *93*, 12932–12936.

[114] a) S. C. Gunawardana, D. W. Piston, *Diabetes* **2012**, *61*, 674–682; b) X. Liu, S. Wang, Y. You, M. Meng, Z. Zheng, M. Dong, J. Lin, Q. Zhao, C. Zhang, X. Yuan, *Endocrinology* **2015**, *156*, 2461–2469.

[115] A. M. Cypess, C. R. Haft, M. R. Laughlin, H. H. Hu, *Cell Metab.* **2014**, *20*, 408–415.

[116] P. Thurlby, P. Trayhurn, *Pflügers Arch.* **1980**, *385*, 193–201.

[117] R. Branca, L. Zhang, A. Burant, L. Katz, A. McCallister, *Proceedings of the 24th Annual Meeting ISMRM* (Singapore) **2016**, p. 1054.

[118] B. P. Schoenborn, H. C. Watson, J. C. Kendrew, *Nature* **1965**, *207*, 28–30.

[119] C. Bowers, V. Storhaug, C. E. Webster, J. Bharatam, A. Cottone, R. Gianna, K. Betsey, B. Gaffney, *J. Am. Chem. Soc.* **1999**, *121*, 9370–9377.

[120] L. Dubois, P. Da Silva, C. Landon, J. G. Huber, M. Ponchet, F. Vovelle, P. Berthault, H. Desvaux, *J. Am. Chem. Soc.* **2004**, *126*, 15738–15746.

[121] S. M. Rubin, M. M. Spence, I. E. Dimitrov, E. J. Ruiz, A. Pines, D. E. Wemmer, *J. Am. Chem. Soc.* **2001**, *123*, 8616–8617.

[122] T. J. Lowery, M. Doucleff, E. J. Ruiz, S. M. Rubin, A. Pines, D. E. Wemmer, *Protein Sci.* **2005**, *14*, 848–855.

[123] T. J. Lowery, S. M. Rubin, E. J. Ruiz, A. Pines, D. E. Wemmer, *Angew. Chem. Int. Ed.* **2004**, *43*, 6320–6322; *Angew. Chem.* **2004**, *116*, 6480–6482.

[124] Y. Song, B. Goodson, R. Taylor, D. Laws, G. Navon, A. Pines, *Angew. Chem. Int. Ed. Engl.* **1997**, *36*, 2368–2370; *Angew. Chem.* **1997**, *109*, 2464–2466.

[125] a) M. El Haouaj, M. Luhmer, Y. H. Ko, K. Kim, K. Bartik, *J. Chem. Soc. Perkin Trans. 2* **2001**, 804–807; b) G. Huber, F. X. Legrand, V. Lewin, D. Baumann, M. P. Heck, P. Berthault, *ChemPhysChem* **2011**, *12*, 1053–1055.

[126] a) K. Bartik, M. Luhmer, J.-P. Dutasta, A. Collet, J. Reisse, *J. Am. Chem. Soc.* **1998**, *120*, 784–791; b) M. Luhmer, B. Goodson, Y. Song, D. Laws, L. Kaiser, M. Cyrier, A. Pines, *J. Am. Chem. Soc.* **1999**, *121*, 3502–3512.

[127] a) M. M. Spence, S. M. Rubin, I. E. Dimitrov, E. J. Ruiz, D. E. Wemmer, A. Pines, S. Q. Yao, F. Tian, P. G. Schultz, *Proc. Natl. Acad. Sci. USA* **2001**, *98*, 10654–10657; b) T. Brotin, A. Lesage, L. Emsley, A. Collet, *J. Am. Chem. Soc.* **2000**, *122*, 1171–1174.

[128] T. Brotin, J.-P. Dutasta, *Chem. Rev.* **2009**, *109*, 88–130.

[129] a) P. A. Hill, Q. Wei, R. G. Eckenhoff, I. J. Dmochowski, *J. Am. Chem. Soc.* **2007**, *129*, 9262–9263; b) P. A. Hill, Q. Wei, T. Troxler, I. J. Dmochowski, *J. Am. Chem. Soc.* **2009**, *131*, 3069–3077; c) G. Huber, T. Brotin, L. Dubois, H. Desvaux, J.-P. Dutasta, P. Berthault, *J. Am. Chem. Soc.* **2006**, *128*, 6239–6246.

[130] a) D. R. Jacobson, N. S. Khan, R. Collé, R. Fitzgerald, L. Laureano-Pérez, Y. Bai, I. J. Dmochowski, *Proc. Natl. Acad. Sci. USA* **2011**, *108*, 10969–10973; b) O. Taratula, P. A. Hill, N. S. Khan, P. J. Carroll, I. J. Dmochowski, *Nat. Commun.* **2010**, *1*, 148.

[131] L. Gao, W. Liu, O.-S. Lee, I. J. Dmochowski, J. G. Saven, *Chem. Sci.* **2015**, *6*, 7238–7248.

[132] T. J. Lowery, S. Garcia, L. Chavez, E. J. Ruiz, T. Wu, T. Brotin, J. P. Dutasta, D. S. King, P. G. Schultz, A. Pines, *ChemBioChem* **2006**, *7*, 65–73.

[133] a) J. Canceill, L. Lacombe, A. Collet, *J. Chem. Soc. Chem. Commun.* **1987**, 219–221; b) R. M. Fairchild, A. I. Joseph, K. T. Holman, H. A. Fogarty, T. Brotin, J.-P. Dutasta, C. Boutin, G. Huber, P. Berthault, *J. Am. Chem. Soc.* **2010**, *132*, 15505–15507; c) T. Traoré, G. Clavé, L. Delacour, N. Kotera, P.-Y. Renard, A. Romieu, P. Berthault, C. Boutin, N. Tassali, B. Rousseau, *Chem. Commun.* **2011**, *47*, 9702–9704; d) Y. Bai, P. A. Hill, I. J. Dmochowski, *Anal. Chem.* **2012**, *84*, 9935–9941; e) E. Dubost, N. Kotera, S. Garcia-Argote, Y. Boulard, E. Léonce, C. Boutin, P. Berthault, C. Dugave, B. Rousseau, *Org. Lett.* **2013**, *15*, 2866–2868; f) R. Tyagi, C. Witte, R. Haag, L. Schröder, *Org. Lett.* **2014**, *16*, 4436–4439.

[134] C. Hilty, T. J. Lowery, D. E. Wemmer, A. Pines, *Angew. Chem. Int. Ed.* **2006**, *45*, 70–73; *Angew. Chem.* **2006**, *118*, 76–79.

[135] S. Garcia, L. Chavez, T. J. Lowery, S.-I. Han, D. E. Wemmer, A. Pines, *J. Magn. Reson.* **2007**, *184*, 72–77.

[136] N. Kotera, N. Tassali, E. Léonce, C. Boutin, P. Berthault, T. Brotin, J. P. Dutasta, L. Delacour, T. Traoré, D. A. Buisson, *Angew. Chem. Int. Ed.* **2012**, *51*, 4100–4103; *Angew. Chem.* **2012**, *124*, 4176–4179.

[137] K. Ward, A. Aletras, R. Balaban, *J. Magn. Reson.* **2000**, *143*, 79–87.

[138] L. Schröder, T. J. Lowery, C. Hilty, D. E. Wemmer, A. Pines, *Science* **2006**, *314*, 446–449.

[139] M. Kunth, J. Dopfert, C. Witte, F. Rossella, L. Schröder, *Angew. Chem. Int. Ed.* **2012**, *51*, 8217–8220; *Angew. Chem.* **2012**, *124*, 8341–8344.

[140] a) L. Schröder, T. Meldrum, M. Smith, T. J. Lowery, D. E. Wemmer, A. Pines, *Phys. Rev. Lett.* **2008**, *100*, 257603; b) L. Schröder, L. Chavez, T. Meldrum, M. Smith, T. J. Lowery, D. E. Wemmer, A. Pines, *Angew. Chem. Int. Ed.* **2008**, *47*, 4316–4320; *Angew. Chem.* **2008**, *120*, 4388–4392.

[141] F. Schilling, L. Schröder, K. Palaniappan, S. Zapf, D. Wemmer, A. Pines, *ChemPhysChem* **2010**, *11*, 3529–3533.

[142] Q. Wei, G. K. Seward, P. A. Hill, B. Patton, I. E. Dimitrov, N. N. Kuzma, I. J. Dmochowski, *J. Am. Chem. Soc.* **2006**, *128*, 13274–13283.

[143] V. Roy, T. Brotin, J. P. Dutasta, M. H. Charles, T. Delair, F. Mallet, G. Huber, H. Desvaux, Y. Boulard, P. Berthault, *ChemPhysChem* **2007**, *8*, 2082 – 2085.

[144] J. M. Chambers, P. A. Hill, J. A. Aaron, Z. Han, D. W. Christianson, N. N. Kuzma, I. J. Dmochowski, *J. Am. Chem. Soc.* **2009**, *131*, 563 – 569.

[145] A. Schlundt, W. Kilian, M. Beyermann, J. Sticht, S. Günther, S. Höpner, K. Falk, O. Roetzschke, L. Mitschang, C. Freund, *Angew. Chem. Int. Ed.* **2009**, *48*, 4142 – 4145; *Angew. Chem.* **2009**, *121*, 4206 – 4209.

[146] Ref. [136].

[147] H. M. Rose, C. Witte, F. Rossella, S. Klippel, C. Freund, L. Schröder, *Proc. Natl. Acad. Sci. USA* **2014**, *111*, 11697 – 11702.

[148] G. K. Seward, Y. Bai, N. S. Khan, I. J. Dmochowski, *Chem. Sci.* **2011**, *2*, 1103 – 1110.

[149] C. Boutin, A. Stopin, F. Lenda, T. Brotin, J.-P. Dutasta, N. Jamin, A. Sanson, Y. Boulard, F. Leteurtre, G. Huber, *Bioorg. Med. Chem.* **2011**, *19*, 4135 – 4143.

[150] K. K. Palaniappan, R. M. Ramirez, V. S. Bajaj, D. E. Wemmer, A. Pines, M. B. Francis, *Angew. Chem. Int. Ed.* **2013**, *52*, 4849 – 4853; *Angew. Chem.* **2013**, *125*, 4949 – 4953.

[151] N. S. Khan, B. A. Riggle, G. K. Seward, Y. Bai, I. J. Dmochowski, *Bioconjugate Chem.* **2015**, *26*, 101 – 109.

[152] C. Witte, V. Martos, H. Rose, S. Reinke, S. Klippel, L. Schröder, C. Hackenberger, *Angew. Chem. Int. Ed.* **2015**, *54*, 2806 – 2810; *Angew. Chem.* **2015**, *127*, 2848 – 2852.

[153] B. A. Riggle, Y. Wang, I. J. Dmochowski, *J. Am. Chem. Soc.* **2015**, *137*, 5542 – 5548.

[154] G. K. Seward, Q. Wei, I. J. Dmochowski, *Bioconjugate Chem.* **2008**, *19*, 2129 – 2135.

[155] a) S. Klippel, J. Dopfert, J. Jayapaul, M. Kunth, F. Rossella, M. Schnurr, C. Witte, C. Freund, L. Schröder, *Angew. Chem. Int. Ed.* **2014**, *53*, 493 – 496; *Angew. Chem.* **2014**, *126*, 503 – 506; b) S. Klippel, C. Freund, L. Schröder, *Nano Lett.* **2014**, *14*, 5721 – 5726; c) F. Rossella, H. Rose, C. Witte, J. Jayapaul, L. Schröder, *ChemPlusChem* **2014**, *79*, 1463 – 1471.

[156] T. Meldrum, L. Schröder, P. Denger, D. Wemmer, A. Pines, *J. Magn. Reson.* **2010**, *205*, 242 – 246.

[157] J. Sloniec, M. Schnurr, C. Witte, U. Resch-Genger, L. Schröder, A. Hennig, *Chem. Eur. J.* **2013**, *19*, 3110 – 3118.

[158] M. Schnurr, C. Witte, L. Schröder, *Phys. Chem. Chem. Phys.* **2013**, *15*, 14178 – 14181.

[159] a) M. Schnurr, C. Witte, L. Schröder, *Biophys. J.* **2014**, *106*, 1301 – 1308; b) M. Schnurr, C. Witte, L. Schröder in *Caged Xenon in Phospholipid Membrane Environments* (Eds.: T. Meersmann, E. Brunner), **2015**, Chap. 16, pp. 288 – 300.

[160] K. Jeong, C. C. Slack, C. C. Vassiliou, P. Dao, M. D. Gomes, D. J. Kennedy, A. E. Truxal, L. J. Sperling, M. B. Francis, D. E. Wemmer, *ChemPhysChem* **2015**, *16*, 3573 – 3577.

[161] F. Zamberlan, C. Lesbats, N. J. Rogers, J. L. Krupa, G. E. Pavlovskaya, N. R. Thomas, H. M. Faas, T. Meersmann, *ChemPhysChem* **2015**, *16*, 2294 – 2298.

[162] a) Y. Wang, I. J. Dmochowski, *Chem. Commun.* **2015**, *51*, 8982 – 8985; b) M. Kunth, C. Witte, A. Hennig, L. Schröder, *Chem. Sci.* **2015**, *6*, 6069 – 6075.

[163] M. Schnurr, J. Sloniec-Myszk, J. Döpfert, L. Schröder, A. Hennig, *Angew. Chem. Int. Ed.* **2015**, *54*, 13444 – 13447; *Angew. Chem.* **2015**, *127*, 13645 – 13648.

[164] Y. Wang, B. W. Roose, E. J. Palovcak, V. Carnevale, I. J. Dmochowski, *Angew. Chem. Int. Ed.* **2016**, *55*, 8984 – 8987; *Angew. Chem.* **2016**, *128*, 9130 – 9133.

[165] J. A. Finbloom, C. C. Slack, C. J. Bruns, K. Jeong, D. E. Wemmer, A. Pines, M. B. Francis, *Chem. Commun.* **2016**, *52*, 3119 – 3122.

[166] T. K. Stevens, K. K. Palaniappan, R. M. Ramirez, M. B. Francis, D. E. Wemmer, A. Pines, *Magn. Reson. Med.* **2013**, *69*, 1245 – 1252.

[167] T. Meldrum, K. L. Seim, V. S. Bajaj, K. K. Palaniappan, W. Wu, M. B. Francis, D. E. Wemmer, A. Pines, *J. Am. Chem. Soc.* **2010**, *132*, 5936 – 5937.

[168] M. Schnurr, K. Sydow, H. Rose, M. Dathe, L. Schröder, *Adv. Healthcare Mater.* **2015**, *4*, 40 – 45.

[169] T. K. Stevens, R. M. Ramirez, A. Pines, *J. Am. Chem. Soc.* **2013**, *135*, 9576 – 9579.

[170] M. Shapiro, R. Ramirez, L. Sperling, G. Sun, J. Sun, A. Pines, D. Schaffer, V. Bajaj, *Nat. Chem.* **2014**, *6*, 629 – 634.

[171] Y. Bai, Y. Wang, M. Goulian, A. Driks, I. J. Dmochowski, *Chem. Sci.* **2014**, *5*, 3197 – 3203.

[172] C. Witte, M. Kunth, F. Rossella, L. Schröder, *J. Chem. Phys.* **2014**, *140*, 084203.

[173] M. Zaiss, M. Schnurr, P. Bachert, *J. Chem. Phys.* **2012**, *136*, 144106.

[174] M. Kunth, C. Witte, L. Schröder, *J. Chem. Phys.* **2014**, *141*, 194202.

[175] M. Kunth, C. Witte, L. Schröder, *NMR Biomed.* **2015**, *28*, 601 – 606.

[176] J. Döpfert, C. Witte, M. Kunth, L. Schröder, *Contrast Media Mol. Imaging* **2014**, *9*, 100 – 107.

[177] a) J. Döpfert, C. Witte, L. Schröder, *ChemPhysChem* **2014**, *15*, 261 – 264; b) C. Boutin, E. Léonce, T. Brotin, A. Jerschow, P. Berthault, *J. Phys. Chem. Lett.* **2013**, *4*, 4172 – 4176.

[178] a) A. Y. Louie, M. M. Hüber, E. T. Ahrens, U. Rothbächer, R. Moats, R. E. Jacobs, S. E. Fraser, T. J. Meade, *Nat. Biotechnol.* **2000**, *18*, 321 – 325; b) R. Weissleder, A. Moore, U. Mahmood, R. Bhorade, H. Benveniste, E. A. Chiocca, J. P. Basilion, *Nat. Med.* **2000**, *6*, 351 – 354; c) B. B. Bartelle, C. A. Berríos-Otero, J. J. Rodriguez, A. E. Friedland, O. Aristizábal, D. H. Turnbull, *Circ. Res.* **2012**, *110*, 938 – 947; d) P. S. Patrick, J. Hammersley, L. Loizou, M. I. Kettunen, T. B. Rodrigues, D.-E. Hu, S.-S. Tee, R. Hesketh, S. K. Lyons, D. Soloviev, *Proc. Natl. Acad. Sci. USA* **2014**, *111*, 415 – 420; e) G. G. Westmeyer, Y. Emer, J. Lintelmann, A. Jasanoff, *Chem. Biol.* **2014**, *21*, 422 – 429.

[179] a) G. Genove, U. DeMarco, H. Xu, W. F. Goins, E. T. Ahrens, *Nat. Med.* **2005**, *11*, 450 – 454; b) B. Cohen, H. Dafni, G. Meir, A. Harmelin, M. Neeman, *Neoplasia* **2005**, *7*, 109 – 117.

[180] O. Zurkiya, A. W. S. Chan, X. Hu, *Magn. Reson. Med.* **2008**, *59*, 1225 – 1231.

[181] B. B. Bartelle, M. D. Mana, G. A. Suero-Abreu, J. J. Rodriguez, D. H. Turnbull, *Magn. Reson. Med.* **2015**, *74*, 1750 – 1757.

[182] R. Weissleder, M. Simonova, A. Bogdanova, S. Bredow, W. S. Enochs, J. A. Bogdanov, *Radiology* **1997**, *204*, 425 – 429.

[183] M. G. Shapiro, G. G. Westmeyer, P. A. Romero, J. O. Szablowski, B. Kuster, A. Shah, C. R. Otey, R. Langer, F. H. Arnold, A. Jasanoff, *Nat. Biotechnol.* **2010**, *28*, 264 – U120.

[184] A. A. Gilad, M. T. McMahon, P. Walczak, P. T. Winnard, V. Raman, H. W. van Laarhoven, C. M. Skoglund, J. W. Bulte, P. C. van Zijl, *Nat. Biotechnol.* **2007**, *25*, 217 – 219.

[185] A. Bar-Shir, G. Liu, K. W. Chan, N. Oskolkov, X. Song, N. N. Yadav, P. Walczak, M. T. McMahon, P. C. van Zijl, J. W. Bulte, *ACS Chem. Biol.* **2014**, *9*, 134 – 138.

[186] A. Mukherjee, D. Wu, H. C. Davis, M. G. Shapiro, *bioRxiv* **2016**, 037515.

[187] a) V. D. Kodibagkar, J. Yu, L. Liu, H. P. Hetherington, R. P. Mason, *Magn. Reson. Imaging* **2006**, *24*, 959 – 962; b) L. Liu, V. D. Kodibagkar, J.-X. Yu, R. P. Mason, *FASEB J.* **2007**, *21*, 2014 – 2019; c) Y. Jamin, C. Gabellieri, L. Smyth, S. Reynolds, S. P. Robinson, C. J. Springer, M. O. Leach, G. S. Payne, T. R. Eykyn, *Magn. Reson. Med.* **2009**, *62*, 1300 – 1304.

[188] a) A. P. Chen, R. E. Hurd, Y.-p. Gu, D. M. Wilson, C. H. Cunningham, *NMR Biomed.* **2011**, *24*, 514 – 520; b) P. S. Patrick, M. I. Kettunen, S.-S. Tee, T. B. Rodrigues, E. Serrao, K. N. Timm, S. McGuire, K. M. Brindle, *Magn. Reson. Med.* **2015**, *73*, 1401 – 1406.

[189] a) A. P. Koretsky, B. A. Traxler, *FEBS Lett.* **1989**, *243*, 8 – 12; b) A. P. Koretsky, M. J. Brosnan, L. H. Chen, J. D. Chen, T. Van Dyke, *Proc. Natl. Acad. Sci. USA* **1990**, *87*, 3112 – 3116; c) G. Walter, E. R. Barton, H. L. Sweeney, *Proc. Natl. Acad. Sci. USA* **2000**, *97*, 5151 – 5155.

[190] a) A. K. Srivastava, D. K. Kadayakkara, A. Bar-Shir, A. A. Gilad, M. T. McMahon, J. W. Bulte, *Dis. Models Mech.* **2015**, *8*, 323 – 336; b) A. A. Gilad, K. Ziv, M. T. McMahon, P. C. Van Zijl, M. Neeman, J. W. Bulte, *J. Nucl. Med.* **2008**, *49*, 1905 – 1908; c) A. Jasanoff, *Curr. Opin. Neurobiol.* **2007**, *17*, 593 – 600.

[191] T. Prangé, M. Schiltz, L. Pernot, N. Colloc'h, S. Longhi, W. Bourguet, R. Fourme, *Proteins Struct. Funct. Bioinf.* **1998**, *30*, 61 – 73.

[192] a) E. Locci, Y. Dehouck, M. Casu, G. Saba, A. Lai, M. Luhmer, J. Reisse, K. Bartik, *J. Magn. Reson.* **2001**, *150*, 167 – 174; b) A. Cherubini, A. Bifone, *Prog. Nucl. Magn. Reson. Spectrosc.* **2003**, *42*, 1 – 30.

[193] R. Tilton, Jr., I. Kuntz, Jr., *Biochemistry* **1982**, *21*, 6850 – 6857.

[194] a) F. Pfeifer, *Nat. Rev. Microbiol.* **2012**, *10*, 705 – 715; b) A. Walsby, *Microbiol. Rev.* **1994**, *58*, 94 – 144.

[195] a) E. Harel, L. Schröder, S. Xu, *Annu. Rev. Anal. Chem.* **2008**, *1*, 133 – 163; b) P. van Zijl, N. N. Yadav, *Magn. Reson. Med.* **2011**, *65*, 927 – 948.

[196] M. G. Shapiro, P. W. Goodwill, A. Neogy, M. Yin, F. S. Foster, D. V. Schaffer, S. M. Conolly, *Nat. Nanotechnol.* **2014**, *9*, 311 – 316.

[197] G. J. Lu, A. Farhadi, J. O. Szablowski, S. R. Barnes, A. Lakshmanan, R. W. Bourdeau, M. G. Shapiro, in preparation.

[198] Y. Wang, B. W. Roose, E. J. Palovcak, V. Carnevale, I. J. Dmochowski, *Angew. Chem. Int. Ed.* **2016**, DOI: 10.1002/anie.201604055; *Angew. Chem.* **2016**, DOI: 10.1002/ange.201604055.

[199] A. Farkas, *Ortho-hydrogen, para-Hydrogen, and Heavy Hydrogen*, Cambridge University Press, Cambridge, **1935**.

[200] a) L. Buljubasich, M. B. Franzoni, K. Munnemann, *Top. Curr. Chem.* **2013**, *338*, 33–74; b) R. Green, R. Adams, S. Duckett, R. Mewis, D. Williamson, G. Green, *Prog. Nucl. Magn. Reson. Spectrosc.* **2012**, *67*, 1–48.

[201] a) B. Feng, A. Coffey, R. Colon, E. Chekmenev, K. Waddell, *J. Magn. Reson.* **2012**, *214*, 258–262; b) J. B. Hövener, S. Bar, J. Leupold, K. Jenne, D. Leibfritz, J. Hennig, S. B. Duckett, D. von Elverfeldt, *NMR Biomed.* **2013**, *26*, 124–131; c) S. Kadlecek, V. Vahdat, T. Nakayama, D. Ng, K. Emami, R. Rizi, *NMR Biomed.* **2011**, *24*, 933–942.

[202] a) P. F. Seidler, H. E. Bryndza, J. E. Frommer, L. S. Stuhl, R. G. Bergman, *Organometallics* **1983**, *2*, 1701–1705; b) S. I. Hommeltoft, D. H. Berry, R. Eisenberg, *J. Am. Chem. Soc.* **1986**, *108*, 5345–5347.

[203] M. G. Pravica, D. P. Weitekamp, *Chem. Phys. Lett.* **1988**, *145*, 255–258.

[204] C. R. Bowers, *eMagRes* **2007**, DOI: 10.1002/9780470034590.emrstm9780470030489.

[205] M. Levitt, *Spin Dynamics: Basics of Nuclear Magnetic Resonance*, Wiley, Chichester, **2001**.

[206] J. K. Gregory, *Acc. Chem. Res.* **1988**, *21*, 120–128.

[207] F. Reineri, S. Aime, R. Gobetto, C. Nervi, *J. Chem. Phys.* **2014**, *140*, 094307.

[208] I. Horiuti, M. Polanyi, *Trans. Faraday Soc.* **1934**, *30*, 1164–1172.

[209] A. Eichhorn, A. Koch, J. Bargon, *J. Mol. Catal. A* **2001**, *174*, 293–295.

[210] D. M. Lilburn, G. E. Pavlovskaya, T. Meersmann, *J. Magn. Reson.* **2013**, *229*, 173–186.

[211] a) R. Zhou, E. Zhao, W. Cheng, L. Neal, H. Zheng, R. Quinones, H. Hagelin-Weaver, C. Bowers, *J. Am. Chem. Soc.* **2015**, *137*, 1938–1946; b) A. M. Balu, S. B. Duckett, R. Luque, *Dalton Trans.* **2009**, 5074–5076.

[212] K. Kovtunov, V. Zhivonitko, I. Skovpin, D. Barskiy, O. Salnikov, I. Koptyug, *J. Phys. Chem. C* **2013**, *117*, 22887–22893.

[213] K. Kovtunov, D. Barskiy, R. Shchepin, A. Coffey, K. Waddell, I. Koptyug, E. Chekmenev, *Anal. Chem.* **2014**, *86*, 6192–6196.

[214] V. V. Zhivonitko, K. V. Kovtunov, I. V. Skovpin, D. A. Barskiy, O. G. Salnikov, I. V. Koptyug in *Understanding Organometalic Reaction Mechanisms and Catalysis*, Wiley-VCH, Weinheim (Germany), **2014**.

[215] a) K. Kovtunov, D. Barskiy, A. Coffey, M. Truong, O. Salnikov, A. Khudorozhkov, E. Inozemtseva, I. Prosvirin, V. Bukhtiyarov, K. Waddell, E. Chekmenev, I. Koptyug, *Chem. Eur. J.* **2014**, *20*, 11636–11639; b) E. Zhao, H. Zheng, K. Ludden, Y. Xin, H. Hagelin-Weaver, C. Bowers, *ACS Catal.* **2016**, *6*, 974–978; c) K. Kovtunov, D. Barskiy, O. Salnikov, D. Burueva, A. Khudorozhkov, A. Bukhtiyarov, I. Prosvirin, E. Gerasimov, V. Bukhtiyarov, I. Koptyug, *ChemCatChem* **2015**, *7*, 2581–2584.

[216] D. Barskiy, O. Salnikov, K. Kovtunov, I. Koptyug, *J. Phys. Chem. A* **2015**, *119*, 996–1006.

[217] A. Corma, O. Salnikov, D. Barskiy, K. Kovtunov, I. Koptyug, *Chem. Eur. J.* **2015**, *21*, 7012–7015.

[218] A. Haase, J. Frahm, D. Matthaei, W. Hanicke, K.-D. Merboldt, *J. Magn. Reson.* **1986**, *67*, 258–266.

[219] M. D. Robson, P. D. Gatehouse, M. Bydder, G. M. Bydder, *J. Comput. Assist. Tomogr.* **2003**, *27*, 825–846.

[220] K. V. Kovtunov, A. S. Romanov, O. G. Salnikov, D. A. Barskiy, E. Y. Chekmenev, I. V. Koptyug, *Tomography* **2016**, *2*, 49–55.

[221] K. Kovtunov, M. Truong, D. Barskiy, O. Salnikov, V. Bukhtiyarov, A. Coffey, K. Waddell, I. Koptyug, E. Chekmenev, *J. Phys. Chem. C* **2014**, *118*, 28234–28243.

[222] E. Harel, *Lab Chip* **2009**, *9*, 17–23.

[223] A. J. Moulé, M. M. Spence, S.-I. Han, J. A. Seeley, K. L. Pierce, S. Saxena, A. Pines, *Proc. Natl. Acad. Sci. USA* **2003**, *100*, 9122–9127.

[224] a) J. A. Seeley, S. I. Han, A. Pines, *J. Magn. Reson.* **2004**, *167*, 282–290; b) X. Zhou, D. Graziani, A. Pines, *Proc. Natl. Acad. Sci. USA* **2009**, *106*, 16903–16906.

[225] C. Hilty, E. E. McDonnell, J. Granwehr, K. L. Pierce, S.-I. Han, A. Pines, *Proc. Natl. Acad. Sci. USA* **2005**, *102*, 14960–14963.

[226] J. Granwehr, E. Harel, S. Han, S. Garcia, A. Pines, P. N. Sen, Y.-Q. Song, *Phys. Rev. Lett.* **2005**, *95*, 075503.

[227] E. Harel, J. Granwehr, J. A. Seeley, A. Pines, *Nat. Mater.* **2006**, *5*, 321–327.

[228] V. Telkki, J. Saunavaara, J. Jokisaari, *J. Magn. Reson.* **2010**, *202*, 78–84.

[229] V. Telkki, C. Hilty, S. Garcia, E. Harel, A. Pines, *J. Phys. Chem. B* **2007**, *111*, 13929–13936.

[230] a) V. Telkki, V. Zhivonitko, S. Ahola, K. Kovtunov, J. Jokisaari, I. Koptyug, *Angew. Chem. Int. Ed.* **2010**, *49*, 8363–8366; *Angew. Chem.* **2010**, *122*, 8541–8544; b) V. Telkki, V. Zhivonitko, *J. Magn. Reson.* **2011**, *210*, 238–245; c) V. Zhivonitko, V. Telkki, I. Koptyug, *Angew. Chem. Int. Ed.* **2012**, *51*, 8054–8058; *Angew. Chem.* **2012**, *124*, 8178–8182.

[231] a) V. Zhivonitko, V. Telkki, J. Leppaniemi, G. Scotti, S. Franssila, I. Koptyug, *Lab Chip* **2013**, *13*, 1554–1561; b) V. Telkki, V. Zhivonitko, A. Selent, G. Scotti, J. Leppaniemi, S. Franssila, I. Koptyug, *Angew. Chem. Int. Ed.* **2014**, *53*, 11289–11293; *Angew. Chem.* **2014**, *126*, 11471–11475.

[232] M. Levitt, *Annu. Rev. Phys. Chem.* **2012**, *63*, 89–105.

[233] V. Zhivonitko, K. Kovtunov, P. Chapovsky, I. Koptyug, *Angew. Chem. Int. Ed.* **2013**, *52*, 13251–13255; *Angew. Chem.* **2013**, *125*, 13493–13497.

[234] A. Tal, L. Frydman, *Prog. Nucl. Magn. Reson. Spectrosc.* **2010**, *57*, 241–292.

[235] S. Ahola, V. Zhivonitko, O. Mankinen, G. Zhang, A. Kantola, H. Chen, C. Hilty, I. Koptyug, V. Telkki, *Nat. Commun.* **2015**, *6*, 8363.

[236] a) S. Ahola, V. Telkki, *ChemPhysChem* **2014**, *15*, 1687–1692; b) J. King, V. Lee, S. Ahola, V. Telkki, T. Meldrum, *Angew. Chem. Int. Ed.* **2016**, *55*, 5040–5043; *Angew. Chem.* **2016**, *128*, 5124–5127.

[237] a) N. N. Kuzma, P. Hakansson, M. Pourfathi, R. K. Ghosh, H. Kara, S. J. Kadlecek, G. Pileio, M. H. Levitt, R. R. Rizi, *J. Magn. Reson.* **2013**, *234*, 90–94; b) R. K. Ghosh, N. N. Kuzma, S. J. Kadlecek, R. R. Rizi, *Magn. Reson. Med.* **2016**, *75*, 1822–1830.

[238] M. S. Freeman, K. Emami, B. Driehuys, *Phys. Rev. A* **2014**, *90*, 023406.

Communication

NMR Spin-Lock Induced Crossing (SLIC) dispersion and long-lived spin states of gaseous propane at low magnetic field (0.05 T)

CrossMark

Danila A. Barskiy [a,b,*], Oleg G. Salnikov [c,d], Alexey S. Romanov [c,d], Matthew A. Feldman [a,b], Aaron M. Coffey [a,b], Kirill V. Kovtunov [c,d], Igor V. Koptyug [c,d], Eduard Y. Chekmenev [a,b,e,f,g,*]

[a] Vanderbilt University Institute of Imaging Science (VUIIS), Nashville, TN 37232, USA
[b] Department of Radiology and Radiological Sciences, Vanderbilt University, Nashville, TN 37232, USA
[c] International Tomography Center SB RAS, 3A Institutskaya St., Novosibirsk, Russia
[d] Novosibirsk State University, 2 Pirogova St., Novosibirsk, Russia
[e] Department of Biomedical Engineering, Vanderbilt University, Nashville, TN 37232, USA
[f] Vanderbilt Ingram Cancer Center (VICC), Vanderbilt University, Nashville, TN 37232, USA
[g] Russian Academy of Sciences, Moscow, Russia

A R T I C L E   I N F O

A B S T R A C T

When parahydrogen reacts with propylene in low magnetic fields (*e.g.*, 0.05 T), the reaction product propane develops an overpopulation of pseudo-singlet nuclear spin states. We studied how the Spin-Lock Induced Crossing (SLIC) technique can be used to convert these pseudo-singlet spin states of hyperpolarized gaseous propane into observable magnetization and to detect ^{1}H NMR signal directly at 0.05 T. The theoretical simulation and experimental study of the NMR signal dependence on B_1 power (SLIC amplitude) exhibits a well-resolved dispersion, which is induced by the spin-spin couplings in the eight-proton spin system of propane. We also measured the exponential decay time constants (T_{LLSS} or T_S) of these pseudo-singlet long-lived spin states (LLSS) by varying the time between hyperpolarized propane production and SLIC detection. We have found that, on average, T_S is approximately 3 times longer than the corresponding T_1 value under the same conditions in the range of pressures studied (up to 7.6 atm). Moreover, T_S may exceed 13 s at pressures above 7 atm in the gas phase. These results are in agreement with the previous reports, and they corroborate a great potential of long-lived hyperpolarized propane as an inhalable gaseous contrast agent for lung imaging and as a molecular tracer to study porous media using low-field NMR and MRI.

© 2017 Elsevier Inc. All rights reserved.

1. Introduction

Low-field hyperpolarized (HP) nuclear magnetic resonance (NMR) spectroscopy and imaging (MRI) are quickly developing frontiers of magnetic resonance research [1]. The recent boost of interest in low-field NMR/MRI can be explained by three primary reasons. First, several hyperpolarization techniques rapidly emerged, which enhance NMR signals by orders of magnitude [2], thereby significantly improving the signal-to-noise ratio (SNR). Second, improvements in detection sensitivity of low-field NMR/MRI (*e. g.*, High-Quality-Factor-Enhanced NMR or EHQE-NMR [3]) enable approaching or even exceeding the sensitivity of conventional high-field NMR/MRI [4]. Third, the lifetime of the hyperpolarized state can be significantly enhanced at low magnetic

fields for protons and/or heteronuclei either through reduced contribution from chemical shift anisotropy or through long-lived spin states (LLSS) [5–13]. These advantages make low-field hyperpolarized NMR/MRI a promising modality for *in vivo* molecular spectroscopy and imaging [14–18]. Moreover, MRI in fields below 0.1 T offers the additional advantage of negligible Specific Absorption Rate (SAR), therefore providing enhanced patient safety and removing limitations on pulse sequence design and implementation [19]. While any hyperpolarization technique can be used in the context of low-field NMR/MRI, less expensive and more high-throughput parahydrogen-based hyperpolarization techniques, such as parahydrogen-induced polarization (PHIP) [20–22] and signal amplification by reversible exchange (SABRE) [23–28], are naturally more suited to go hand-in-hand with an inexpensive low-field MR modality rather than the more expensive (millions of dollars) and low-throughput technique of dissolution dynamic nuclear polarization (d-DNP) [29,30], currently the leading hyperpolarization technology [31–34]. It is also worth emphasizing that

the maximum polarization obtainable by d-DNP depends strongly on the applied magnetic field and spin temperature (since it is a phenomenon of polarization transfer from electrons to nuclei), whereas for PHIP and SABRE the maximum polarization is independent of these parameters. Furthermore, in addition to biomedical applications, the combination of hyperpolarization and low-field detection can be potentially useful for spectroscopic and imaging analysis of industrial-scale processes, where overpopulated pseudo-singlet spin states are conveniently created using chemical reactions involving parahydrogen [35].

Parahydrogen (p-H_2) is a naturally occurring nuclear spin singlet state that can be efficiently incorporated into certain molecules of interest via pairwise hydrogenation reaction [20,21,36]. When the reaction is carried out in a sufficiently low magnetic field, the singlet spin state of the nascent p-H_2 protons can be relatively long-lived if permitted by the symmetry of the nuclear spin Hamiltonian [37]. The p-H_2-induced singlet spin order can be converted into observable magnetization using various singlet-to-magnetization (S2M) transfer algorithms [38], including spin-lock induced crossing [39–41], and conveniently detected directly at low field [35].

Recently, we demonstrated that when parahydrogen is added to the propylene at a relatively low magnetic field (*i.e.*, in the strong-coupling regime, where chemical shift difference of $\sim$0.44 ppm between methylene and methyl protons in propane is less than their spin-spin coupling constant $^3J_{HH}$ of $\sim$7.4 Hz), the symmetry of the p-H_2-nascent singlet state is partially conserved and the resultant propane may potentially possess LLSS [42]. This is not straightforward, because, firstly, propane is a multi-spin system containing 8 strongly coupled protons at low magnetic field, which is a significantly more complex spin system than the isolated 2-spin pairs typically exploited as LLSS [43]. Secondly, the dominant relaxation mechanism for molecules in the gas phase is often the modulation of spin-rotation interactions rather than dipole-dipole interactions; only the latter are effectively "switched off" between spins in a singlet state [44–46]. Nevertheless, it has been shown theoretically [47,48] and experimentally [48–50] that LLSS can exist in multi-spin systems comprising more than two coupled spins.

Here, we present a systematic study of LLSS in the hyperpolarized gaseous propane molecule via (i) employing PHIP to produce gaseous propane at a low magnetic field and (ii) subsequently transforming the "hidden" pseudo-singlet spin order into observable magnetization using the Spin-Lock Induced Crossing (SLIC) technique [39,51] and performing signal detection directly at 0.05 T (Fig. 1a). Using a variable time delay (*i.e.*, waiting time) between hyperpolarized propane production and signal detection, we were able to measure the lifetime (T_S) of the pseudo-singlet LLSS for a wide range of pressures, and T_S was found to be approximately 3-fold greater than T_1 under the same conditions. The very high SLIC transformation efficiency, which is enabled by the use of a more homogeneous magnet than in our pioneering report [42], allowed us to demonstrate high-resolution ^1H NMR spectra and well-resolved dependence of the observable NMR signal on B_1 power (SLIC dispersion), which is clearly modulated by proton-proton J-couplings in the propane molecule. Finally, we performed spin dynamics simulations by solving the full Liouville–von Neumann equation, and demonstrated that the experimentally observed phenomena are in excellent agreement with theoretical calculations.

2. Materials and methods

2.1. Heterogeneous hydrogenation

The schematic of the experimental setup is shown in Fig. 1b. Propylene (>99%, Sigma-Aldrich, #295663) and ultra-pure hydrogen (>99.999%, A-L Compressed Gases Inc., Nashville, TN) were used as received. Preparation of the Rh/TiO_2 catalyst was described elsewhere [52]. Hydrogen gas was enriched with p-H_2 to $\sim$50% para-state using a home-built parahydrogen generator by passing normal H_2 through FeO(OH) powder (Sigma-Aldrich, P/N 371254, 30–50 mesh) maintained at liquid N_2 temperature (77 K) [53]. Alternatively, a home-built p-H_2 generator using cryocooling was employed to produce 80% p-H_2. Gas flow rates of p-H_2 and propylene (see SI for details regarding flow rates for different pressures) were regulated by mass flow controllers (Sierra Instruments, Monterey, CA, model #C50L-AL-DD-2-PV2-V0). The gases flowed through a long Teflon tube to ensure their efficient mixing and then to the 1/8 in. tubing copper reactor packed with Rh/TiO_2 catalyst located between two pieces of fiberglass wool. The reactor was heated to 100 °C using heating tape. The resultant gas mixture was directed either to the detection chamber (a plastic chamber or medium walled 5 mm NMR tube) located inside the RF probe connected to the NMR spectrometer (Kea2, Magritek, Wellington, New Zealand) or directly to the vent using a system of two manual shut-off valves (Western Analytical Products, #P-733). The total pressure in the reactor and in the detection chamber was the same, and it was controlled using a backpressure regulator (Fig. 1b).

2.2. Low-field (2 MHz) NMR detection

Two experimental arrangements were used to obtain data in the current study. The first experimental setup was similar to that described earlier [35]. The magnet ($\sim$2 MHz Magritek rock core analyzer, Halbach array, radial field direction) had homogeneity of $\sim$20 ppm over 4 cm diameter of spherical volume (DSV). A commercially available MR Kea2 spectrometer (Magritek, Wellington, New Zealand) was used for NMR detection as described by Waddell et al. [54]. The detection chamber (plastic, $\sim$2 mL) was placed in the home-built ^1H RF coil located in the magnet [55]. More experimental details of this experimental arrangement can be found in Ref. [35].

The second arrangement of the low-field NMR apparatus was comprised of a shimmed permanent magnet (SIGWA 0.0475T, Boston, MA) with an 80 cm gap and a homogeneity of <20 ppm across a 40 cm DSV (note that B_0 homogeneity over the relevant volume of the 5 mm NMR tube was better than 2 ppm) and a two channel RF probe consisting of an inner Tx/Rx detection coil and an outer Tx-only excitation coil. The two channel ^1H/^1H RF probe was designed to measure samples stored in standard 5 mm diameter NMR tubes (see SI). The inner Tx/Rx solenoid RF coil was decoupled from the outer transmit-only Helmholtz saddle coil by geometric orthogonality. The solenoid coil (8 mm diameter by 193 mm length) constructed to conform closely to the dimensions of the NMR sample in order to improve the coil filling factor and had a quality factor Q of 70. The outer saddle-shaped Tx-only excitation coil had 75 mm O.D. and 220 mm length. This experimental arrangement allowed attenuating the SLIC RF pulses from the output of the RF amplifier (BT00250-AlphaS, Tomco, Stepney, South Australia) without attenuating the detected NMR signal coming from the spin system after pulses. The coil was shielded from electric field interference and noise by housing it in an RF shield composed of a hollow copper cube made out of square copper clad PCB material (1 ft $\times$ 1 ft). A circular waveguide 50 mm in length protruded from the shield and served as an access port for insertion of the sample into the RF coil. The shielding provided an electric field suppression of 60 dB. Radio frequency calibration of the Tx/Rx coil using a 10 mM aqueous solution of $CuSO_4$ in a 5 mm medium walled NMR tube yielded a π/2 ^1H excitation pulse width of 26 µs at 0.6 W. Most of the experimental results presented in the study were obtained using the second arrangement (unless otherwise noted).
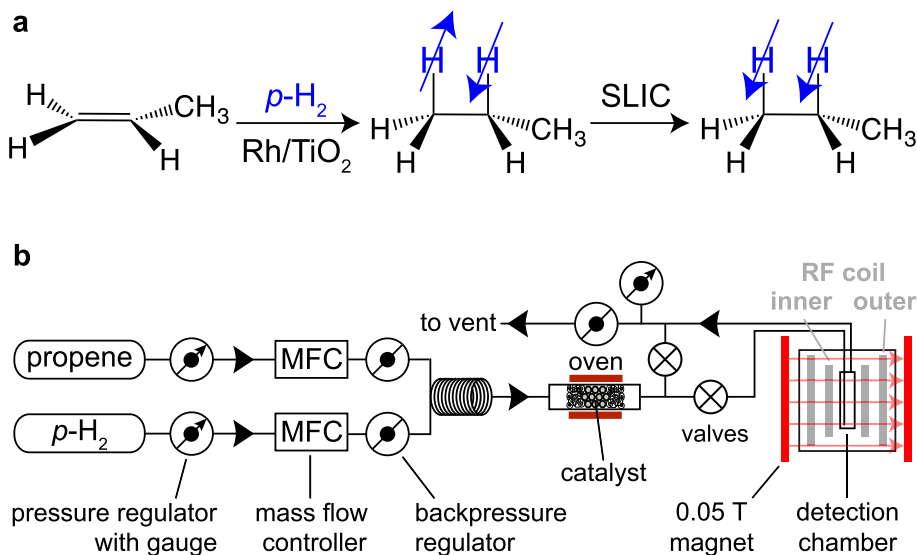
Fig. 1. (a) Molecular diagram of parahydrogen (p-H$_2$) addition to propylene over Rh/TiO$_2$ at 0.05 T resulting in the formation of pseudo-singlet long-lived spin states (LLSS) of propane, followed by the application of the Spin-Lock Induced Crossing (SLIC) sequence to transform LLSS into observable magnetization and to detect the NMR signal. (b) Schematic diagram of the experimental setup employed to perform p-H$_2$ addition to propylene and to detect LLSS of propane produced at 0.05 T using the SLIC sequence. Note that separate ^{1}H/^{1}H Rx and Tx coils were used, with the internal solenoid (Rx) geometrically decoupled from the outer saddle-shaped coil (Tx) by orienting them orthogonally (in addition to mutual orthogonality of B_1 fields of each RF coil to the main B_0 field, see SI).

2.3. SLIC RF pulse sequence

Spin order of p-H$_2$-nascent protons after chemical addition to propylene was converted to observable magnetization using the Spin-Lock Induced Crossing (SLIC) sequence developed by DeVience et al. [39]. In order to generate low-power ($\sim$30 µW) SLIC pulses, additional attenuators (Bird Technologies, 10 W, A series, male/female N connector, 30 and 20 dB) were inserted between the output of the RF amplifier and the RF input of the Tx coil. The SLIC pulse amplitude was calibrated by measuring the signal of a 10 mM aqueous solution of CuSO$_4$ (placed in a 5 mm medium walled NMR tube) on the Tx/Rx coil while transmitting on the Tx-only channel. Nutation experiments for the Tx-only coil at the power level of SLIC pulse (32 µW) with detection via the Tx/Rx coil yielded $\pi/2$ ^{1}H excitation pulse width of 22 ms. Acquisition of the ^{1}H NMR signal occurred directly during the flow of the propane gas through the NMR tube. The lifetime (T_S) of the pseudo-singlet LLSS of propane in 0.05 T field was measured by varying the time delay between the interruption of gas flow through the detection chamber and the application of the SLIC pulse. For T_1 measurements, the pulse sequence was applied immediately after the gas flow was stopped.

3. Results and discussion

The intensity of an NMR signal is directly proportional to the product of the nuclear spin polarization and the concentration of magnetic nuclei in the detection zone of the NMR spectrometer. Both of these parameters are very low for thermally polarized propane at a magnetic field of 0.05 T. Indeed, at such a low field the thermal polarization of ^{1}H nuclei is only $1.6 \cdot 10^{-5}\%$ and the concentration of hydrogen atoms in gaseous propane is $\sim$0.3 M, which is approximately two orders of magnitude lower than the proton concentration in liquid water. The PHIP hyperpolarization technique is suitable for direct ^{1}H NMR signal enhancement of the propane, when the chemical shift difference between p-H$_2$-nascent protons is significantly greater than the $^3J_{HH}$-coupling between them. This corresponds to the condition of the weak coupling regime for methyl and methylene protons in the propane molecule. Otherwise, in the strong coupling regime, the singlet state of p-H$_2$

is still conserved in the propane molecule produced by hydrogenation of propylene. This manifests itself in a relatively low NMR signal when measured at low magnetic field, because the PHIP-induced quantum state is nonmagnetic. Indeed, a direct detection of hyperpolarized (HP) propane using a hard $\pi/2$ pulse at 0.05 T results in a relatively low-intensity antiphase signal, showing a complex splitting pattern (Fig. 2a). This result is in agreement with the previously reported low-field NMR detection of HP norbornane [56]. We also note that this complex spectral pattern was not fully spectrally resolved earlier due to significantly worse B_0 magnetic field homogeneity [42]. We carried out spin dynamics simulations by numerically solving the Liouville–von Neumann equation for the density matrix of the spin system in order to analyze this pattern and to rationalize the observed splittings (see SI). The analysis revealed that the dominant contribution to the observed ^{1}H NMR signal is from the propane molecules containing ^{13}C nuclei at natural abundance (1.1%). The calculation included only a one-bond heteronuclear J-coupling of 125 Hz and three equally probable positions of the ^{13}C label with respect to the p-H$_2$-nascent protons in the propane molecule (Fig. 2b). The simulated spectrum reproduces very well the observed experimental features, and the resulting NMR spectrum is essentially dominated by the signal originating from ^{13}C-containing isotopomers. This is remarkable, because ^{13}C-containing isotopomers account for only $\sim$3.3% of all propane molecules, while the bulk of the propane ($\sim$96.7%) is free from magnetic nuclei other than protons. Nevertheless, this small population of ^{13}C-containing isotopomers produces the vast fraction of the observed NMR signal.

A much greater NMR signal intensity arising from ^{13}C-containing HP propane molecules (compared to those without ^{13}C nuclei) is explained by the presence of J-coupled heteronuclei. These heteronuclei break the near magnetic equivalence of strongly coupled hydrogens due to unequal spin-spin couplings to different protons in the molecule and reveal the otherwise "hidden" p-H$_2$-induced hyperpolarization [11,57,58]. This observation is similar to propane-d_6 produced via p-H$_2$ pairwise addition to propylene-d_6 demonstrating significantly stronger NMR signals than its non-deuterated analogue using direct detection and hard excitation RF pulses at 0.05 T [59]. Note that if a $\pi/4$ pulse is used
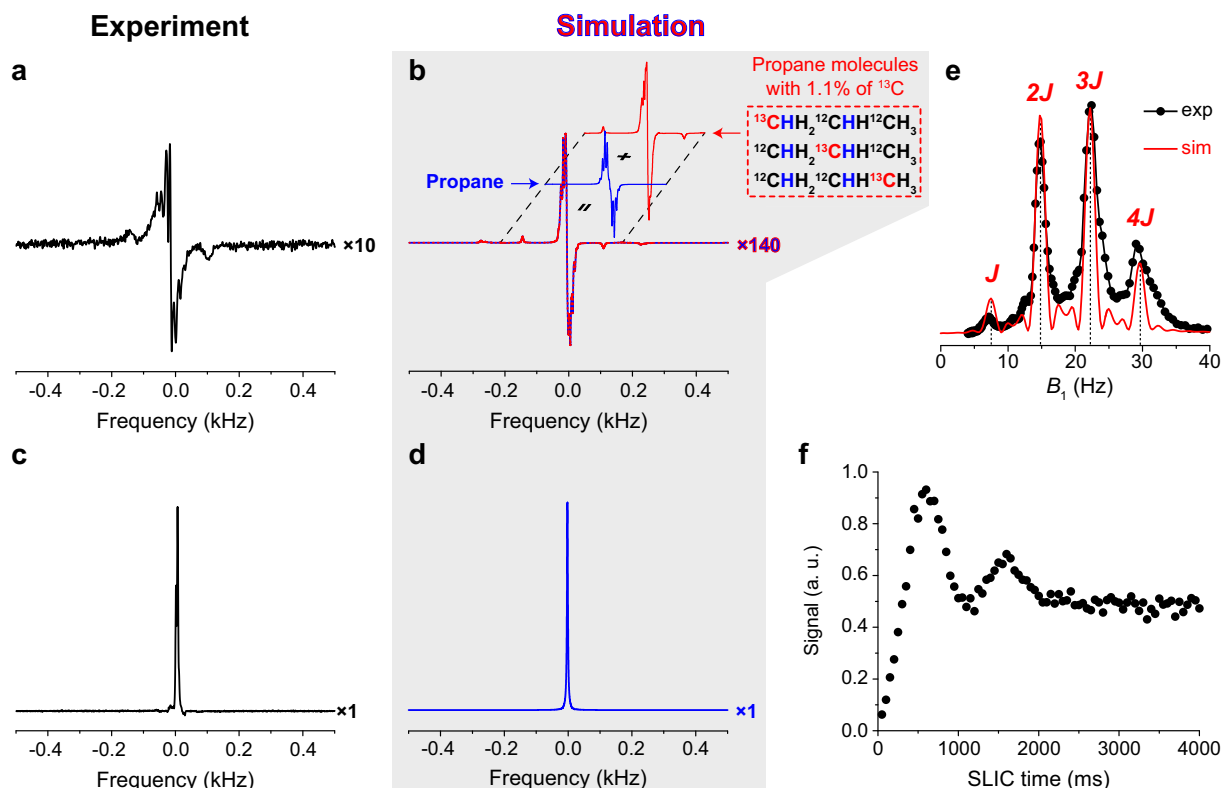
Fig. 2. (a) ^{1}H NMR spectrum of HP propane recorded at 0.05 T after application of a hard $\pi/2$ RF pulse; HP propane is obtained from propylene via pairwise p-H$_2$ addition over Rh/TiO$_2$ catalyst. (b) Simulation of ^{1}H NMR spectrum of HP propane (after application of a hard $\pi/2$ RF pulse): blue trace – HP propane population without ^{13}C nuclei; red trace – HP propane containing 1.1% (natural ^{13}C abundance) of randomly distributed ^{13}C nuclei; blue-red trace is the sum of blue and red traces shown behind it. (c) ^{1}H NMR spectrum (SNR ∼ 730) of HP propane recorded at 0.05 T after application of SLIC RF pulse with B_1 of 22.2 Hz; HP propane is obtained from propylene via pairwise p-H$_2$ addition over Rh/TiO$_2$ catalyst. (d) Simulation of ^{1}H NMR spectrum of HP propane using a SLIC RF pulse with B_1 of ∼22.2 Hz. Note the vertical scaling factor of 10 for spectrum (a) compared to spectrum (c), and the factor of 140 scaling for spectrum (b) compared to spectrum (d). (e) Experimentally measured (black circles and trace) and theoretically calculated (red trace) dependence of the SLIC induced HP propane signal on B_1 amplitude at the SLIC RF pulse duration (τ_{slic}) of 0.5 s at 0.05 T. (f) Experimentally measured dependence of the SLIC induced HP propane signal on the SLIC RF pulse duration at B_1 amplitude of 22.2 Hz. (For interpretation of the references to color in this figure legend, the reader is referred to the web version of this article.)

for signal detection, the observed ^{1}H NMR spectrum is slightly different (however, it can be very well simulated using a density matrix formalism), mainly because of the significantly altered spectral contribution of ^{13}C-containing isotopomers (Fig. S5).

When a SLIC RF pulse is used for excitation, it yields an NMR signal 1–2 orders of magnitude greater than that obtained using a hard RF pulse excitation (Fig. 2c). The SLIC RF pulse employed had a duration (τ_{slic}) of ∼0.5 s and a B_1 amplitude of ∼22.2 Hz. The latter corresponds to approximately $3 \cdot {}^3J_{HH}$, where ${}^3J_{HH}$ is the three-bond spin-spin coupling constant between methyl and methylene protons in propane. Spectral simulations support our experimental finding, i.e., the observation of the in-phase NMR signal of HP propane after SLIC RF excitation (Fig. 2d). The dominant fraction of this signal is the contribution from the most abundant HP propane molecules without ^{13}C nuclei. The experimentally observed NMR signal intensity was approximately 14 times lower than that predicted theoretically (if the corresponding spectra obtained with a $\pi/2$ pulse are normalized to have the same signal intensity, see Fig. 2a–d). This discrepancy cannot be explained by relaxation losses before acquisition; indeed, the time HP propane spent between production and the detection was the same in both detection protocols in which the hard pulse and the SLIC pulse were utilized (Fig. 2a and c). More than a factor of 14 difference in signal intensities may be partially explained by a non-ideal performance of the SLIC pulse, caused by inhomogeneity of B_1 and B_0 fields (most critical factor) and relaxation/decoherence during the

long RF SLIC excitation pulse (0.5 s) [35]. More importantly, these experiments were performed in a continuous flow mode, where gaseous propane was flowing through the NMR tube while the NMR signal was being acquired. As a result, a significant fraction of the produced HP propane might have migrated into or out of the RF coil during the SLIC pulse. This fact can additionally lower the resulting SLIC-induced signal. However, performing the experiment in the continuous flow regime is a clear advantage of the present study, because the critical parameters influencing the SLIC efficiency (i.e., τ_{slic} and B_1) can be conveniently studied in an automated fashion under nearly identical conditions.

Next, the B_1 amplitude of the SLIC pulse was varied under conditions of fixed τ_{slic} of ∼0.5 s. The resulting NMR signal peak intensity was plotted as a function of B_1 amplitude revealing a notable quartet splitting pattern (Fig. 2e). We name this spectral pattern 'SLIC dispersion' (in a manner similar to chemical shift dispersion), which is clearly mediated by the three-bond H-H spin-spin coupling ${}^3J_{HH}$ due to the peaks' positions at ∼7.4 Hz, ∼14.8 Hz, ∼22.2 Hz, and ∼29.6 Hz, respectively. It should also be emphasized that the asymmetry of this quartet (i.e., lower peak intensity at lower B_1 values) is likely the result of disproportionately greater signal losses due to B_1 and B_0 inhomogeneities. The observed pattern is also significantly more complex than the analogous one for a two-spin system (Fig. S6a), where (i) there are no additional spin-spin couplings, and (ii) a maximum is observed for B_1 value equal to the value of spin-spin coupling J [39]. Spin dynamics calcula-

tions using the density matrix formalism were carried out in order to explain the experimental results (see SI). We found that if the frequency (B_1 offset) of the SLIC pulse is set exactly at the average of the methyl and methylene proton resonances and $\tau_{slic} = 0.5$ s, the maxima in signal amplitude are observed at the frequencies $^3J_{HH}$, $2 \cdot ^3J_{HH}$, $3 \cdot ^3J_{HH}$, and $4 \cdot ^3J_{HH}$, where $^3J_{HH}$ is the spin-spin coupling constant between methyl and methylene protons (Fig. 2e). This result is reasonable, because nuclear spin level anti-crossings (spin-lock induced crossings) occur at specific nutation frequencies. At these frequencies chemical shift differences drive a polarization transfer between spin-locked states with $\Delta F = \pm 1$ and $\Delta m_F = \pm 1$ (where F and m_F are angular momentum quantum numbers, i.e. states $|F, m_F\rangle$), which is detected as a decrease in x-axis magnetization (observable signal) [60].

The dependence of the ^{1}H NMR signal of HP propane on the duration of the SLIC pulse is shown in Fig. 2f. It manifests itself as a decaying oscillation reaching a plateau at approximately half of the maximal intensity for τ_{slic} greater than 2 s. The main reason for this plateauing (vs. signal decaying to zero) is the experimental condition of continuous gas flow through the NMR tube during the series of acquisitions with variable SLIC duration. While a portion of the gas was pushed out by the inflowing gas, the freshly supplied HP propane portion experiences only a fraction of the SLIC pulse. After a certain duration of the SLIC pulse the observed signal becomes independent of τ_{slic} and a steady-state magnetization is achieved. An analytical solution for the SLIC signal vs. SLIC duration in the present experimental arrangement is in agreement with the observed phenomena and is presented in the SI (Fig. S8).

The T_S and T_1 of HP propane were measured at 0.05 T using optimal values of B_1 amplitude and τ_{slic} found for the SLIC RF pulse (Fig. 3a and b). Specifically, the pulse sequences shown in Fig. 3c–f were employed. The waiting time period between the injection of the gas into the detection chamber and the application of the SLIC pulse was varied in a consecutive series of experiments for T_S measurements. Since the SLIC RF pulse allows converting the singlet spin state directly into transverse magnetization, no additional RF pulses are needed for measuring T_S (Fig. 3c and d). In case of T_1 measurements, the SLIC RF pulse was applied directly after the injection of HP propane gas into the chamber, immediately followed by a $\pi/2$ pulse to convert transverse magnetization created by the SLIC pulse into a longitudinal one (parallel to the z-axis). Then two different strategies were used for the measurement. In the first approach, small-angle RF excitation pulses were employed to probe the T_1. The second strategy used a variable delay between rotating the magnetization toward the z-axis and applying the second $\pi/2$ pulse. Measured values are plotted in Fig. 3b, and in addition listed in Table S1. Two representative curves are shown in Fig. 3a for the pressure of ~7.6 atm.

Both T_1 and T_S of HP propane increase with the total gas pressure (up to $T_1 \sim 4$ s and $T_S \sim 13$ s at 7.6 atm). This is not surprising, because the correlation time is reduced when the time between collisions of gas molecules decreases. Another potential reason for T_1 and T_S becoming longer is the greater fraction of HP propane in the gas phase as pressure increases due to changes in propylene hydrogenation kinetics [61,62]. Indeed, additional ^{1}H 400 MHz NMR measurements using the same experimental setup demonstrated that propylene to propane conversion increases as the total pressure increases (see SI). This fact is in agreement with typically positive overall reaction orders for hydrogenation of alkenes above 300 K [61,63–67]. Notably, the experimentally determined ratio of T_S/T_1 is nearly constant and amounts to 3.1 ± 0.5 for all studied pressures, suggesting that the contribution of dipole-dipole interactions toward the relaxation mechanism for hydrocarbons in general, and for propane in particular, is significant. Future studies are certainly warranted to investigate theoretically the fundamental causes governing the observed behavior and multi-spin proton LLSS in the gas phase.

Analysis of static magnetic fields suitable for the SLIC transformation in propane was carried out. In general, the static magnetic field (B_0) should be low enough for p-H_2-nascent protons to reside in singlet spin states after hydrogenation. Straightforward analysis shows that for two p-H_2-nascent spins in methylene and methyl groups to be in the strong coupling regime, a magnetic field B_0 below $2\pi J/\gamma_{1H}(\delta_1 - \delta_2) \approx 0.4$ T is sufficient (here γ_{1H} is the proton gyromagnetic ratio, $J = 7.4$ Hz is the spin-spin coupling between methylene and methyl protons, and $\delta_1 = 1.34$ ppm and $\delta_2 = 0.90$ ppm are their chemical shifts, respectively). Our simulations show that the optimal duration of the SLIC pulse may be decreased from ~600 ms at 0.05 T down to ~70 ms at 0.4 T (see SI). This will undoubtedly improve the overall performance of the SLIC pulse in singlet-to-triplet conversion, because relaxation/decoherence losses during the spin-lock pulse will be reduced. Moreover, the ^{1}H NMR signal of propane obtained after the SLIC pulse may be increased at higher fields as well (Fig. S7). Moving to magnetic fields higher than 0.05 T as employed here has other advantages: MRI scanners operating in the low magnetic field region (i.e., 0.1–0.5 T) are readily available on the market. Given that relaxation times (T_1, T_2) of propane should not significantly depend on the static magnetic field strength (since the conditions of extreme narrowing apply for propane in the gas phase [63]), operation in the 0.1–0.5 T magnetic field region may additionally improve SLIC efficiency and signal detection sensitivity of HP gaseous propane for various applications.

It is worth noting that the singlet-to-triplet conversion efficiency can approach a theoretical limit of unity or 100% only in case of ideal isolated two-spin system (Fig. S6a), while the transformation efficiency of SLIC at 0.05 T was found to be only ~8% for eight-proton spin system of propane. While this value is significantly below 100%, it is a manifestation of a complex network of spin-spin interactions. Indeed, simplification of the system to five (vs. eight) proton spins of ethyl group results in the increase of the transformation efficiency to ~14% using otherwise the same simulation parameters (Fig. S6b). This observation is also in agreement with our previous SLIC studies of ethyl groups in the liquid state [35]. It should be pointed out that SLIC transformation efficiency can be more than doubled at higher magnetic fields, e.g., using 0.4 T vs. 0.05 T (Fig. S7).

The results presented here are important in the context of potential applications of HP propane and its LLSS created by pairwise addition of p-H_2 as an inhalable contrast agent for functional lung imaging. Several clinical research approaches for lung imaging using MRI that are currently being developed include imaging of heteronuclei, e.g. ^{19}F MRI of perfluorinated gases such as SF_6 and C_nF_{2n+2} (n = 1–3) [68,69] or HP noble gases, such as ^{3}He, ^{129}Xe, and others [31,70,71]. The production of HP noble gases has relatively high cost, and it also requires sophisticated hyperpolarizer instrumentation. The imaging of both HP noble gases and ^{19}F via MRI additionally requires multinuclear RF coil and transmitter/receiver capabilities. The above two factors significantly limit applications of these agents only to several privileged centers of excellence worldwide. The major advantage of using HP propane (and potentially other hydrocarbon gases) [72] in MRI is its very low cost (a few cents per liter excluding the cost of p-H_2 production) and production scalability. Moreover, any MRI system with proton transmit/receive circuitry is potentially capable of molecular imaging using HP propane; it should be noted though that LLSS may be currently utilized using low-field MRI scanners [35]. Furthermore, ^{1}H MRI of hydrocarbon gases may find various applications in materials science, studying porous media, imaging of chemical reactors, or other non-biomedical applications.
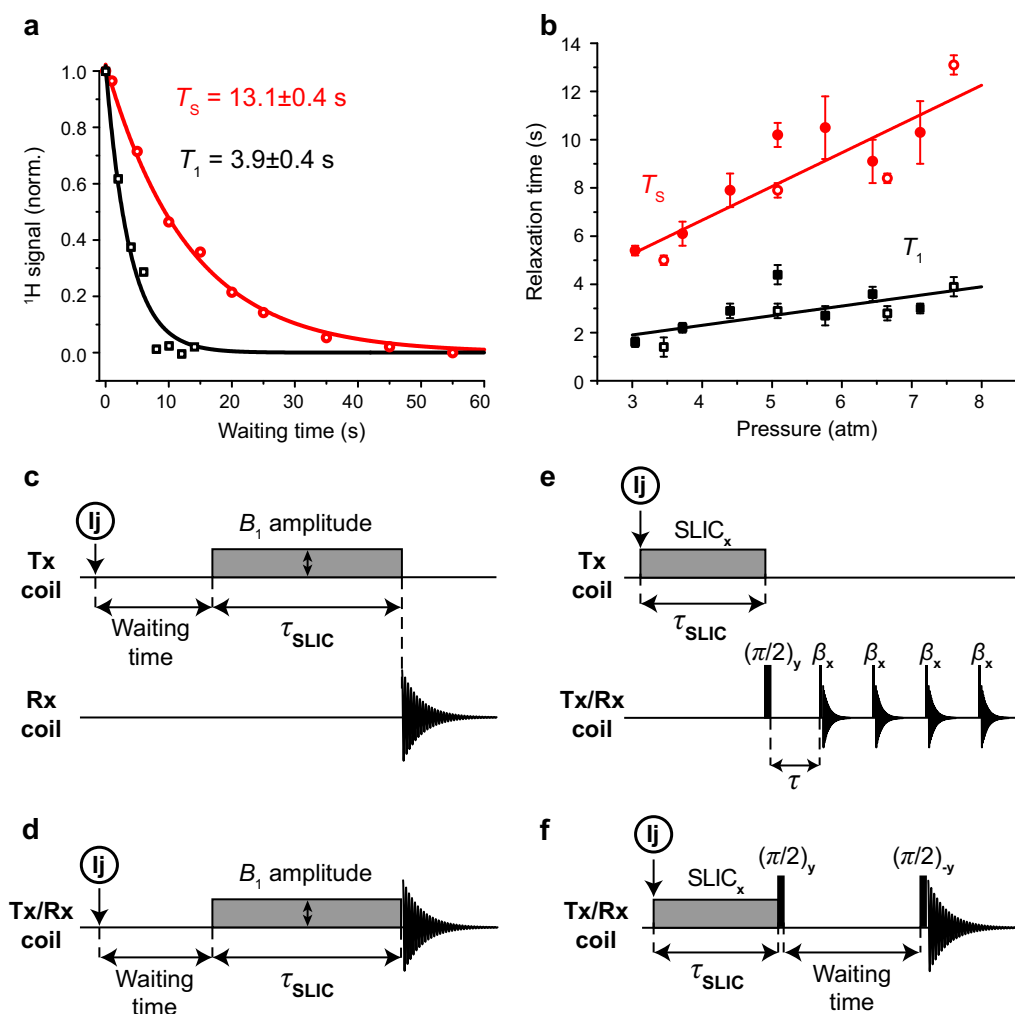
Fig. 3. (a) Examples of T_1 (black symbols and trace) and T_S (red symbols and trace) measurements of gaseous HP propane at ∼7.6 atm. (b) Measured T_1 (black symbols and trace) and T_S (red symbols and trace) of gaseous propane at various pressures. Empty circles and squares show the results obtained using the setup described in Fig. 1b (second experimental arrangement, see Section 2.2), filled circles and squares show results obtained using the first experimental arrangement (see Section 2.2). (c) Sequence of events for propane T_S measurements using the two channel ^{1}H/^{1}H probe (experimental data points are represented by empty red circles in (b)): Injection (Ij) of the propane into the detection chamber, flow cessation in the detection chamber and a waiting time period of variable duration, low-amplitude RF field irradiation (SLIC) for the time τ_{slic} on the transmit (Tx) coil followed by signal acquisition using the Tx/Rx coil. (d) Sequence of events for propane T_S measurement using a single-channel ^{1}H probe (experimental data points are represented by filled red circles in (b)). (e) Sequence of events for propane T_1 measurements using a two channel ^{1}H/^{1}H probe (experimental data points are represented by empty black squares in (b)): Injection (Ij) of HP propane into the detection chamber, flow cessation and immediate application of low-power irradiation (SLIC) for duration τ_{slic} on the transmit (Tx) coil followed by a $\pi/2$ pulse and a train of small-angle excitation pulses (β = 10°) with time delay τ on the Tx/Rx coil. (f) Sequence of events for propane T_1 measurement using a single-channel ^{1}H probe (experimental data points are represented by filled black squares in b). (For interpretation of the references to color in this figure legend, the reader is referred to the web version of this article.)

It is important to consider the key contrast agent characteristics influencing the detection sensitivity of HP propane compared to that of HP ^{129}Xe in the context of potential biomedical applications. Hyperpolarization of ^{129}Xe to nearly the theoretical maximum of unity (∼90%) has been demonstrated [73–75], while the highest propane polarization demonstrated to date is only 6% [76]. However, more than 3 times greater gyromagnetic ratio of protons compared to that of ^{129}Xe and the widespread availability of ^{1}H transmitter/detection hardware in MRI scanners make them much more favorable nuclei from the detection perspective for hyperpolarized gas NMR/MRI. We hope that this study will stimulate future work to further increase the level of hyperpolarization of propane via PHIP. Finally, SLIC efficiency of singlet-to-triplet transformation is another challenge that should be addressed in the future to maximize the imaging sensitivity of HP propane produced by PHIP.

4. Conclusion

In conclusion, the long-lived nuclear spin states of HP propane produced via pairwise addition of p-H$_2$ to propylene were systematically studied in the gas phase at pressures up to ∼7.6 atm. In particular, we created the LLSS in HP propane gas and measured its exponential decay constant (T_S) by using hydrogenation of propylene with p-H$_2$ and subsequent NMR detection at 0.05 T employing a SLIC RF pulse. The T_1 and T_S measurements were carried out in sufficiently low magnetic field (i.e., 0.05 T), where methyl and methylene protons of HP propane molecules are strongly coupled via three-bond spin-spin coupling $^3J_{HH}$. SLIC allows converting typically non-observable nuclear spin order of p-H$_2$-derived pseudo-singlet state of HP propane into readily observable transverse magnetization, and enables detecting ^{1}H NMR signal directly at low magnetic field. The lifetime of

pseudo-singlet nuclear spin states of PHIP-produced HP propane is approximately 3 times greater than the corresponding T_1 time under the same reaction conditions. Moreover, a T_S value of at least 13 s in the gas phase is reported. These results of a relatively long decay constant and the demonstration of SLIC conversion highlight the great potential of HP propane produced by PHIP technique as an inhalable gaseous contrast agent for MRI of lungs (in the context of molecular imaging immediately after inhalation of HP propane gas by a patient) and for other imaging applications with the use of low-field MR instruments.

Acknowledgments

Appendix A. Supplementary material

Supplementary data associated with this article can be found, in the online version, at http://dx.doi.org/10.1016/j.jmr.2017.01.014.

References

[1] B. Blümich, Virtual special issue: magnetic resonance at low fields, J. Magn. Reson. 274 (2017) 145–147.
[2] P. Nikolaou, B. Goodson, E. Chekmenev, NMR hyperpolarization techniques for biomedicine, Chem. Eur. J. 21 (2015) 3156–3166.
[3] M. Suefke, A. Liebisch, B. Blumich, S. Appelt, External high-quality-factor resonator tunes up nuclear magnetic resonance, Nat. Phys. 11 (2015) 767–771.
[4] A. Coffey, M. Truong, E. Chekmenev, Low-field MRI can be more sensitive than high-field MRI, J. Magn. Reson. 237 (2013) 169–174.
[5] M. Levitt, Singlet nuclear magnetic resonance, Annu. Rev. Phys. Chem. 63 (2012) 89–105.
[6] M. Carravetta, O.G. Johannessen, M.H. Levitt, Beyond the T_1 limit: singlet nuclear spin states in low magnetic fields, Phys. Rev. Lett. 92 (2004) 153003.
[7] M. Carravetta, M.H. Levitt, Theory of long-lived nuclear spin states in solution nuclear magnetic resonance. I. Singlet states in low magnetic field, J. Chem. Phys. 122 (2005) 214505.
[8] G. Pileio, M. Carravetta, E. Hughes, M.H. Levitt, The long-lived nuclear singlet state of ^{15}N-nitrous oxide in solution, J. Am. Chem. Soc. 130 (2008) 12582–12583.
[9] G. Pileio, M. Carravetta, M.H. Levitt, Storage of nuclear magnetization as long-lived singlet order in low magnetic field, Proc. Natl. Acad. Sci. U.S.A. 107 (2010) 17135–17139.
[10] T. Theis, G.X. Ortiz, A.W. Logan, K.E. Claytor, Y. Feng, W.P. Huhn, V. Blum, S.J. Malcolmson, E.Y. Chekmenev, Q. Wang, Direct and cost-efficient hyperpolarization of long-lived nuclear spin states on universal ^{15}N$_2$-diazirine molecular tags, Sci. Adv. 2 (2016) e1501438.
[11] P. Vasos, A. Comment, R. Sarkar, P. Ahuja, S. Jannin, J.-P. Ansermet, J. Konter, P. Hautle, B. Van den Brandt, G. Bodenhausen, Long-lived states to sustain hyperpolarized magnetization, Proc. Natl. Acad. Sci. U.S.A. 106 (2009) 18469–18473.
[12] W. Warren, E. Jenista, R. Branca, X. Chen, Increasing hyperpolarized spin lifetimes through true singlet eigenstates, Science 323 (2009) 1711–1714.
[13] S.S. Roy, P. Norcott, P.J. Raynern, G.G.R. Green, S.B. Duckett, A hyperpolarizable 1H magnetic resonance probe for signal detection 15 minutes after spin polarization storage, Angew. Chem. Int. Ed. 55 (2017) 15642–15645.
[14] S. Patz, I. Muradian, M.I. Hrovat, I.C. Ruset, G. Topulos, S.D. Covrig, E. Frederick, H. Hatabu, F. Hersman, J.P. Butler, Human pulmonary imaging and spectroscopy with hyperpolarized ^{129}Xe at 0.2 T, Acad. Radiol. 15 (2008) 713–727.
[15] J. Parra-Robles, A.R. Cross, G.E. Santyr, Theoretical signal-to-noise ratio and spatial resolution dependence on the magnetic field strength for hyperpolarized noble gas magnetic resonance imaging of human lungs, Med. Phys. 32 (2005) 221–229.
[16] W. Dominguez-Viqueira, J. Parra-Robles, M. Fox, W.B. Handler, B.A. Chronik, G.E. Santyr, A variable field strength system for hyperpolarized noble gas MR imaging of rodent lungs, Concepts Magn. Reson. B 33 (2008) 124–137.
[17] L. Tsai, R. Mair, M. Rosen, S. Patz, R. Walsworth, An open-access, very-low-field MRI system for posture-dependent ^{3}He human lung imaging, J. Magn. Reson. 193 (2008) 274–285.

[18] A. Coffey, R. Shchepin, M. Truong, K. Wilkens, W. Pham, E. Chekmenev, An open-source automated parahydrogen hyperpolarizer for molecular imaging using ^{13}C metabolic contrast agents, Anal. Chem. 88 (2016) 8279–8288.
[19] M. Hayden, C. Bidinosti, E. Chapple, Specific absorption rates and signal-to-noise ratio limitations for MRI in very-low magnetic fields, Concepts. Magn. Reson. 201 (40A) (2012) 281–294.
[20] C. Bowers, D. Weitekamp, Parahydrogen and synthesis allow dramatically enhanced nuclear alignment, J. Am. Chem. Soc. 109 (1987) 5541–5542.
[21] M.G. Pravica, D.P. Weitekamp, Net NMR alignment by adiabatic transport of parahydrogen addition products to high magnetic field, Chem. Phys. Lett. 145 (1988) 255–258.
[22] J. Natterer, J. Bargon, Parahydrogen induced polarization, Prog. Nucl. Magn. Reson. Spectrosc. 31 (1997) 293–315.
[23] R. Adams, J. Aguilar, K. Atkinson, M. Cowley, P. Elliott, S. Duckett, G. Green, I. Khazal, J. Lopez-Serrano, D. Williamson, Reversible interactions with para-hydrogen enhance NMR sensitivity by polarization transfer, Science 323 (2009) 1708–1711.
[24] J. Hovener, N. Schwaderlapp, T. Lickert, S. Duckett, R. Mewis, L. Highton, S. Kenny, G. Green, D. Leibfritz, J. Korvink, et al., A hyperpolarized equilibrium for magnetic resonance, Nat. Commun. 4 (2013) 2946.
[25] D. Barskiy, K. Kovtunov, I. Koptyug, P. He, K. Groome, Q. Best, F. Shi, B. Goodson, R. Shchepin, M. Truong, et al., In situ and ex situ low-field NMR spectroscopy and MRI endowed by SABRE hyperpolarization, ChemPhysChem 15 (2014) 4100–4107.
[26] V.V. Zhivonitko, I.V. Skovpin, I.V. Koptyug, Strong ^{31}P nuclear spin hyperpolarization produced via reversible chemical interaction with parahydrogen, Chem. Commun. 51 (2015) 2506–2509.
[27] M. Truong, T. Theis, A. Coffey, R. Shchepin, K. Waddell, F. Shi, B. Goodson, W. Warren, E. Chekmenev, ^{15}N hyperpolarization by reversible exchange using SABRE-SHEATH, J. Phys. Chem. C 119 (2015) 8786–8797.
[28] D.A. Barskiy, R.V. Shchepin, A.M. Coffey, T. Theis, W.S. Warren, B.M. Goodson, E.Y. Chekmenev, Over 20% 15N hyperpolarization in under one minute for metronidazole, an antibiotic and hypoxia probe, J. Am. Chem. Soc. 138 (2016) 8080–8083.
[29] J. Ardenkjaer-Larsen, B. Fridlund, A. Gram, G. Hansson, L. Hansson, M. Lerche, R. Servin, M. Thaning, K. Golman, Increase in signal-to-noise ratio of >10,000 times in liquid-state NMR, Proc. Natl. Acad. Sci. U.S.A. 100 (2003) 10158–10163.
[30] J. Ardenkjaer-Larsen, On the present and future of dissolution-DNP, J. Magn. Reson. 264 (2016) 3–12.
[31] D.A. Barskiy, A.M. Coffey, P. Nikolaou, D.M. Mikhaylov, B.M. Goodson, R.T. Branca, G.J. Lu, M.G. Shapiro, V.-V. Telkki, V.V. Zhivonitko, et al., NMR hyperpolarization techniques of gases, Chem. Eur. J. 23 (2017) 725–751.
[32] J. Ardenkjaer-Larsen, G. Boebinger, A. Comment, S. Duckett, A. Edison, F. Engelke, C. Griesinger, R. Griffin, C. Hilty, H. Maeda, et al., Facing and overcoming sensitivity challenges in biomolecular NMR spectroscopy, Angew. Chem. Int. Ed. 54 (2015) 9162–9185.
[33] M.C. Tayler, I. Marco-Rius, M.I. Kettunen, K.M. Brindle, M.H. Levitt, G. Pileio, Direct enhancement of nuclear singlet order by dynamic nuclear polarization, J. Am. Chem. Soc. 134 (2012) 7668–7671.
[34] I. Marco-Rius, M. Tayler, M. Kettunen, T. Larkin, K. Timm, E. Serrao, T. Rodrigues, G. Pileio, J. Ardenkjaer-Larsen, M. Levitt, et al., Hyperpolarized singlet lifetimes of pyruvate in human blood and in the mouse, NMR Biomed. 26 (2013) 1696–1704.
[35] D.A. Barskiy, O.G. Salnikov, R.V. Shchepin, M. Feldman, A.M. Coffey, K.V. Kovtunov, I.V. Koptyug, E.Y. Chekmenev, NMR SLIC sensing of hydrogenation reactions using parahydrogen in low magnetic fields, J. Phys. Chem. C 120 (2016) 29098–29106.
[36] C. Bowers, D. Weitekamp, Transformation of symmetrization order to nuclear spin magnetization by chemical reaction and nuclear magnetic resonance, Phys. Rev. Lett. 57 (1986) 2645–2648.
[37] E. Vinogradov, A.K. Grant, Hyperpolarized long-lived states in solution NMR: three-case study in low field, J. Magn. Reson. 194 (2008) 46–57.
[38] M. Tayler, M. Levitt, Singlet nuclear magnetic resonance of nearly-equivalent spins, Phys. Chem. Chem. Phys. 13 (2011) 5556–5560.
[39] S. DeVience, R. Walsworth, M. Rosen, Preparation of nuclear spin singlet states using spin-lock induced crossing, Phys. Rev. Lett. 111 (2013) 173002.
[40] T. Theis, Y. Feng, T.-L. Wu, W.S. Warren, Composite and shaped pulses for efficient and robust pumping of disconnected eigenstates in magnetic resonance, J. Chem. Phys. 140 (2014) 014201.
[41] A.N. Pravdivtsev, A.S. Kiryutin, A.V. Yurkovskaya, H.-M. Vieth, K.L. Ivanov, Robust conversion of singlet spin order in coupled spin-1/2 pairs by adiabatically ramped RF-fields, J. Magn. Reson. 273 (2016) 56–64.
[42] K. Kovtunov, M. Truong, D. Barskiy, I. Koptyug, A. Coffey, K. Waddell, E. Chekmenev, Long-lived spin states for low-field hyperpolarized gas MRI, Chem. Eur. J. 20 (2014) 14629–14632.
[43] E. Vinogradov, A.K. Grant, Long-lived states in solution NMR: selection rules for intramolecular dipolar relaxation in low magnetic fields, J. Magn. Reson. 188 (2007) 176–182.
[44] H. Gutowsky, I. Lawrenson, K. Shimomura, Nuclear magnetic spin-lattice relaxation by spin-rotational interactions, Phys. Rev. Lett. 6 (1961) 349–351.
[45] M. Bloom, M. Lipsicas, B. Muller, Proton spin-lattice relaxation in polyatomic gases, Can. J. Phys. 39 (1961) 1093–1109.
[46] J.-N. Dumez, P. Håkansson, S. Mamone, B. Meier, G. Stevanato, J.T. Hill-Cousins, S.S. Roy, R.C. Brown, G. Pileio, M.H. Levitt, Theory of long-lived nuclear spin states in methyl groups and quantum-rotor induced polarisation, J. Chem. Phys. 142 (2015) 044506.

[47] A.K. Grant, E. Vinogradov, Long-lived states in solution NMR: theoretical examples in three-and four-spin systems, J. Magn. Reson. 193 (2008) 177–190.

[48] G. Stevanato, S.S. Roy, J. Hill-Cousins, I. Kuprov, L.J. Brown, R.C. Brown, G. Pileio, M.H. Levitt, Long-lived nuclear spin states far from magnetic equivalence, Phys. Chem. Chem. Phys. 17 (2015) 5913–5922.

[49] P. Ahuja, R. Sarkar, P.R. Vasos, G. Bodenhausen, Long-lived states in multiple-spin systems, ChemPhysChem 10 (2009) 2217–2220.

[50] G. Pileio, M. Concistrè, M. Carravetta, M.H. Levitt, Long-lived nuclear spin states in the solution NMR of four-spin systems, J. Magn. Reson. 182 (2006) 353–357.

[51] S. DeVience, R. Walsworth, M. Rosen, Probing Scalar Coupling Differences via Long-Lived Singlet States, J. Magn. Reson. 262 (2016) 42–49.

[52] K. Kovtunov, D. Barskiy, A. Coffey, M. Truong, O. Salnikov, A. Khudorozhkov, E. Inozemtseva, I. Prosvirin, V. Bukhtiyarov, K. Waddell, et al., High-resolution 3D proton MRI of hyperpolarized gas enabled by parahydrogen and Rh/TiO_2 heterogeneous catalyst, Chem. Eur. J. 20 (2014) 11636–11639.

[53] K. Kovtunov, V. Zhivonitko, I. Skovpin, D. Barskiy, I. Koptyug, Parahydrogen-induced polarization in heterogeneous catalytic processes, Top. Curr. Chem. 338 (2013) 123–180.

[54] K. Waddell, A. Coffey, E. Chekmenev, In situ detection of PHIP at 48 mT: demonstration using a centrally controlled polarizer, J. Am. Chem. Soc. 133 (2011) 97–101.

[55] A. Coffey, R. Shchepin, K. Wilkens, K. Waddell, E. Chekmenev, A large volume double channel H-1-X RF probe for hyperpolarized magnetic resonance at 0.0475 T, J. Magn. Reson. 220 (2012) 94–101.

[56] K. Kovtunov, D. Barskiy, R. Shchepin, A. Coffey, K. Waddell, I. Koptyug, E. Chekmenev, Demonstration of heterogeneous parahydrogen induced polarization using hyperpolarized agent migration from dissolved Rh(I) complex to gas phase, Anal. Chem. 86 (2014) 6192–6196.

[57] L. Buljubasich, M. Franzoni, H.W. Spiess, K. Münnemann, Level anti-crossings in ParaHydrogen induced polarization experiments with Cs-symmetric molecules, J. Magn. Reson. 219 (2012) 33–40.

[58] M.C. Tayler, M.H. Levitt, Accessing long-lived nuclear spin order by isotope-induced symmetry breaking, J. Am. Chem. Soc. 135 (2013) 2120–2123.

[59] K. Kovtunov, M. Truong, D. Barskiy, O. Salnikov, V. Bukhtiyarov, A. Coffey, K. Waddell, I. Koptyug, E. Chekmenev, Propane-d_6 heterogeneously hyperpolarized by parahydrogen, J. Phys. Chem. C 118 (2014) 28234–28243.

[60] S.J. DeVience, Nuclear magnetic resonance with spin singlet states and nitrogen vacancy centers in diamond (Doctoral dissertation), 2014.

[61] G.C. Bond, Metal-Catalysed Reactions of Hydrocarbons, Springer, US, New York, 2005.

[62] O. Salnikov, K. Kovtunov, D. Barskiy, V. Bukhtiyarov, R. Kaptein, I. Koptyug, Kinetic study of propylene hydrogenation over Pt/Al_2O_3 by parahydrogen-induced polarization, Appl. Magn. Reson. 44 (2013) 279–288.

[63] D. Barskiy, O. Salnikov, K. Kovtunov, I. Koptyug, NMR signal enhancement for hyperpolarized fluids continuously generated in hydrogenation reactions with parahydrogen, J. Phys. Chem. A 119 (2015) 996–1006.

[64] M.E. Davis, R.J. Davis, Fundamentals of Chemical Reaction Engineering, Courier Corporation, 2012.

[65] R. Zhou, E. Zhao, W. Cheng, L. Neal, H. Zheng, R. Quinones, H. Hagelin-Weaver, C. Bowers, Parahydrogen-induced polarization by pairwise replacement catalysis on Pt and Ir nanoparticles, J. Am. Chem. Soc. 137 (2015) 1938–1946.

[66] R. Zhou, W. Cheng, L. Neal, E. Zhao, K. Ludden, H. Hagelin-Weaver, C. Bowers, Parahydrogen enhanced NMR reveals correlations in selective hydrogenation of triple bonds over supported Pt catalyst, Phys. Chem. Chem. Phys. 17 (2015) 26121–26129.

[67] E. Zhao, H. Zheng, K. Ludden, Y. Xin, H. Hagelin-Weaver, C. Bowers, Strong metal-support interactions enhance the pairwise selectivity of parahydrogen addition over Ir/TiO_2, ACS Catal. 6 (2016) 974–978.

[68] D.O. Kuethe, A. Caprihan, E. Fukushima, R.A. Waggoner, Imaging lungs using inert fluorinated gases, Magn. Reson. Med. 39 (1998) 85–88.

[69] D.O. Kuethe, A. Caprihan, H.M. Gach, I.J. Lowe, E. Fukushima, Imaging obstructed ventilation with NMR using inert fluorinated gases, J. Appl. Physiol. 88 (2000) 2279–2286.

[70] B. Goodson, Nuclear magnetic resonance of laser-polarized noble gases in molecules, materials, and organisms, J. Magn. Reson. 155 (2002) 157–216.

[71] D.M. Lilburn, G.E. Pavlovskaya, T. Meersmann, Perspectives of hyperpolarized noble gas MRI beyond ^{3}He, J. Magn. Reson. 229 (2013) 173–186.

[72] B. Vuichoud, E. Canet, J. Milani, A. Bornet, D. Baudouin, L. Veyre, D. Gajan, L. Emsley, A. Lesage, C. Copéret, et al., Hyperpolarization of frozen hydrocarbon gases by dynamic nuclear polarization at 1.2 K, J. Phys. Chem. Lett. 7 (2016) 3235–3239.

[73] P. Nikolaou, A. Coffey, L. Walkup, B. Gust, N. Whiting, H. Newton, S. Barcus, I. Muradyan, M. Dabaghyan, G. Moroz, et al., Near-unity nuclear polarization with an open-source Xe-129 hyperpolarizer for NMR and MRI, Proc. Natl. Acad. Sci. U.S.A. 110 (2013) 14150–14155.

[74] P. Nikolaou, A. Coffey, K. Ranta, L. Walkup, B. Gust, M. Barlow, M. Rosen, B. Goodson, E. Chekmenev, Multidimensional mapping of spin-exchange optical pumping in clinical-scale batch-mode ^{129}Xe hyperpolarizers, J. Phys. Chem. B 118 (2014) 4809–4816.

[75] M.S. Freeman, K. Emami, B. Driehuys, Characterizing and modeling the efficiency limits in large-scale production of hyperpolarized ^{129}Xe, Phys. Rev. A 90 (2014) 023406.

[76] O.G. Salnikov, D.A. Barskiy, A.M. Coffey, K.V. Kovtunov, I.V. Koptyug, E.Y. Chekmenev, Efficient batch-mode parahydrogen-induced polarization of propane, ChemPhysChem 17 (2016) 3395–3398.

Extending the Lifetime of Hyperpolarized Propane Gas through Reversible Dissolution

Dudari B. Burueva,[†,‡] Alexey S. Romanov,[†,‡] Oleg G. Salnikov,[†,‡] Vladimir V. Zhivonitko,[†,‡] Yu-Wen Chen,[§] Danila A. Barskiy,[∥,⊥] Eduard Y. Chekmenev,[∥,⊥,#] Dennis W. Hwang,[§] Kirill V. Kovtunov,*[,†,‡] and Igor V. Koptyug[†,‡]

[†]International Tomography Center SB RAS, 3A Institutskaya Street, 630090 Novosibirsk, Russia

[‡]Novosibirsk State University, 2 Pirogova Street, 630090 Novosibirsk, Russia

[§]Department of Chemistry and Biochemistry, National Chung Cheng University, 168 University Road, Min-Hsiung, Chiayi 62102, Taiwan

[∥]Department of Radiology, Vanderbilt University Institute of Imaging Science (VUIIS), 1161 21st Avenue South, Medical Center North, AA-1105, Nashville, Tennessee 37232-2310, United States

[⊥]Department of Biomedical Engineering and Physics, Vanderbilt-Ingram Cancer Center (VICC), 1301 Medical Center Drive, Nashville, Tennessee 37232-2310, United States

[#]Russian Academy of Sciences, 14 Leninskiy Prospekt, 119991 Moscow, Russia

S *Supporting Information*

ABSTRACT: Hyperpolarized (HP) propane produced by the parahydrogen-induced polarization (PHIP) technique has been recently introduced as a promising contrast agent for functional lung magnetic resonance (MR) imaging. However, its short lifetime due to a spin–lattice relaxation time T_1 of less than 1 s in the gas phase is a significant translational challenge for its potential biomedical applications. The previously demonstrated approach for extending the lifetime of the HP propane state through long-lived spin states allows the HP propane lifetime to be increased by a factor of ~3. Here, we demonstrate that a remarkable increase in the propane hyperpolarization decay time at high magnetic field (7.1 T) can be achieved by its dissolution in deuterated organic solvents (acetone-d_6 or methanol-d_4). The approximate values of the HP decay time for propane dissolved in acetone-d_6 are 35.1 and 28.6 s for the CH_2 group and the CH_3 group, respectively (similar values were obtained for propane dissolved in methanol-d_4), which are ~50 times larger than the gaseous propane T_1 value. Furthermore, we show that it is possible to retrieve HP propane from solution to the gas phase with the preservation of hyperpolarization.
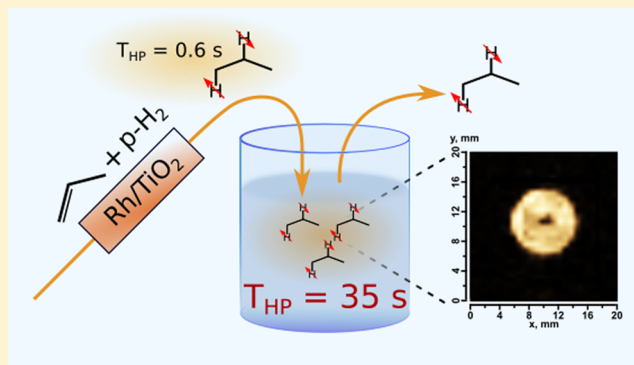
INTRODUCTION

Lung diseases have remained one of the major causes of human death during the past several decades. In particular, the most common lung disease is chronic obstructive pulmonary disease, which is responsible for ~2.75 million deaths annually according to the Global Burden of Disease estimates.[1] Currently, the chest radiography and X-ray computed tomography (CT) methods find wide practical application for functional lung imaging.[2] Nevertheless, magnetic resonance imaging (MRI) might be attractive for pulmonary visualization, which, unlike CT, does not suffer from limitations caused by maximum permissible radiation doses. However, despite the widespread application of MRI in daily medical practice, pulmonary MRI is still challenging. In brief, problems with lung MR imaging can be divided into two groups: (a) problems

related to the nature of lung tissue (fast signal decay due to the magnetic susceptibility differences at air–tissue interfaces[3] and loss of signal related to respiratory motion) and (b) problems related to the inherent properties of gas, namely, a low proton density and the resulting low signal-to-noise ratio. With regard to the first point, recent improvements in MRI technology have addressed these issues.

First, these problems can be addressed by using fast single-shot imaging with very short acquisition times. For this purpose, different pulse sequences such as steady-state free precession (SSFP) or half-Fourier acquisition single-shot turbo

spin-echo (HASTE) sequences have been employed.[4] Through the use of ultrafast MRI sequences, subsecond image acquisition can be achieved.[5] The second approach, based on the respiratory triggering/gating[6,7] of fast spin-echo sequences, increases the acquisition time but provides better spatial resolution.

Promising opportunities are revealed by a new rapidly developing sampling method in MRI: compressed sensing[8−10] or sparse MRI. It is claimed that, if the sampling grid of k-space is randomized, then the image of an object that is sampled below the Nyquist criterion can be recovered to the original quality by using a sparsifying nonlinear transform that is built by the minimization of the l_1 norm of the image data. This method was successfully applied for in vivo three-dimensional magnetic resonance spectroscopic imaging (MRSI) experiments[11,12] with the $t−k_x−k_y$ undersampling technique demonstrating significant reduction of the acquisition time.

Nevertheless, the low signal-to-noise ratio of proton nuclear magnetic resonance (^{1}H NMR) spectroscopy remains the main challenge for lung ^{1}H MRI. The most efficient way to significantly improve sensitivity in pulmonary MRI is to use contrast agents with nonequilibrium nuclear spin polarization or hyperpolarization.[13,14] The first approach for the hyperpolarization of gases is the spin-exchange optical pumping (SEOP)[15] of ^{129}Xe or ^{3}He, which enables signal enhancement by 5 orders of magnitude.[16] The possibility of using HP noble gases (^{129}Xe and ^{3}He) for MRI has been widely explored.[17] In fact, currently, HP noble-gas MRI is approved for use as a clinical research imaging modality for patients with pulmonary disease.[18] However, despite these promising results, the widespread application of HP noble gases in pulmonary MR imaging seems exceedingly complex because of the requirement of having heteronuclear radio-frequency (rf) channels and rf probes, which are not included in standard equipment in commercially available MRI scanners.

Therefore, the development of gaseous contrast agents for MR imaging with proton detection is highly desired. The easiest way to obtain proton-hyperpolarized gases is to use parahydrogen-induced polarization (PHIP).[19,20] PHIP is based on the generation of nonequilibrium magnetization through the use of parahydrogen, the spin isomer of the hydrogen molecule with zero nuclear spin. Parahydrogen itself cannot be detected by NMR spectroscopy because of its zero nuclear spin, so to obtain observable nonequilibrium magnetization, it is necessary to break the symmetry of the parahydrogen molecule, for example, through the use of a hydrogenation reaction.[21] If both atoms from a parahydrogen molecule are added to the same substrate molecule (pairwise hydrogen addition) and their positions in the product molecule are magnetically non-equivalent, the NMR signals of such product molecule become significantly enhanced (in theory, up to $\sim10^4–10^5$-fold).[19]

The first demonstration of the in vivo use of an HP contrast agent produced by the PHIP technique was a ^{13}C MR angiography study published in 2001.[5] Despite its several shortcomings (e.g., the presence of a toxic metal complex used as a homogeneous hydrogenation catalyst, the use of an organic solvent, and ^{13}C MRI acquisition), this work served as a catalyst for a large number of studies devoted to the development of the PHIP technique for MR imaging[22−26] through the use of HP contrast agents in solution. The pioneering works[27,28] that demonstrated the production of hyperpolarized gas (in that case, propane) through the use of PHIP technique were based on the utilization of heterogeneous hydrogenation catalysts.

This work motivated further research on MR imaging with HP propane. Recently, a number of studies have been conducted that demonstrated successfully the feasibility of HP propane in the two-dimensional[29−33] and three-dimensional[34,35] imaging of various model objects.

However, despite the exciting results on HP propane utilization in MR imaging, its biomedical use is complicated because of the relatively short lifetime of hyperpolarization governed by the spin−lattice relaxation time T_1. Typically, T_1 values are less than 1 s at standard temperature and pressure.[36]

The fast T_1 relaxation of gaseous propane is caused by the spin-rotation interaction.[37] In a rapidly rotating molecule (or part of a molecule, such as a methyl group), the local magnetic field fluctuations are generated by the rotational motion, leading to fast T_1 relaxation. The spin-rotation relaxation is important for nuclei of small molecules in the gas phase and for nuclei in highly mobile environments in large molecules in solution (e.g., protons of CH_3 groups in proteins).

In solution, the T_1 times of small molecules can often be increased by reducing the number of protons by deuterating the molecule. However, for gases this effect is quite small: for example, the T_1 value of the CHD_2 group of propane-d_6 at 9.4 T is 684 ± 27 ms, whereas the T_1 value of the CH_3 group of propane is 616 ± 16 ms.[38] This is consistent with the predominance of the spin-rotataion mechanism for nuclear spin relaxation in gaseous propane.

Another possibility for slowing down the decay of hyperpolarization is to store the molecules in a slowly relaxing singlet state (called a long-lived spin state, or LLSS).[39−41] The lifetime-limiting factors of singlet-state relaxations were investigated recently.[42,43] Furthermore, a relatively long hyperpolarization lifetime, T_{LLSS}, was achieved for HP propane-d_6 ($\sim$6.0 s)[38] and for HP propane (4.7−13.1 s)[34,44] at low magnetic fields.

Therefore, this work logically follows from a number of our previous studies[31,34,38] that concentrated on the development of ^{1}H magnetic resonance imaging of propane, including hyperpolarized (HP) propane, for potential application in functional lung imaging. Here, we address the issue of the short lifetime of HP propane and demonstrate that it is possible to extend the lifetime of the hyperpolarized state of propane at high magnetic fields by dissolving the propane in organic solvents. We found that the estimated values of hyperpolarization decay times for propane are 35.1 and 28.6 s for the CH_2 group and the CH_3 group, respectively, which are about 1−2 orders of magnitude greater than the T_1 times for gaseous propane.[38]

■ MATERIALS AND METHODS

NMR and MRI Experiments. Commercially available hydrogen, propylene, propane, acetone-d_6 (Astrachem, 99.7%), and methanol-d_4 (Astrachem, 99.7%) were used as received. Rh/TiO_2 catalyst with 1 wt % metal loading was provided by the group of Prof. V. I. Bukhtiyarov (Boreskov Institute of Catalysis, Novosibirsk, Russia) and was described in detail elsewhere.[34] For the production of hyperpolarized propane, hydrogen gas was first enriched with parahydrogen isomer up to 50% by passing it through an ortho−para conversion catalyst FeO(OH) maintained at 77 K (hereinafter, the resultant hydrogen gas is referred to as p-H_2). The propene/p-H_2 (1:4) mixture was passed through the Rh/TiO_2 catalyst held at 200 °C to form hyperpolarized propane, which was supplied through a $^1/_{16}$-in.-o.d. polytetrafluoroethylene

(PTFE) capillary to a 10-mm NMR tube located in the NMR spectrometer for detection [an adiabatic longitudinal transport after dissociation engenders nuclear alignment (ALTADENA)[45] experiment]. In the case of dissolution experiments, HP propane was supplied to the bottom of the NMR tube containing 2 mL of deuterated solvent (acetone-d_6 or methanol-d_4). The concentration of dissolved propane was calculated through the use of an internal standard method (toluene) and was approximately 50 mM. The HP NMR spectra of liquid solutions were acquired after a rapid interruption of gas flow to avoid magnetic field inhomogeneities caused by bubbles. The NMR spectra of liquids in thermal equilibrium were acquired after the complete relaxation of hyperpolarization with the gas flow stopped.

All dissolution experiments were carried out at 25 °C. The gas flow rate was varied from 1.89 to 3.13 mL/s through the use of an Aalborg rotameter. A scheme of the experimental setup is presented in Figure S1 (Supporting Information). T_1 measurements were carried out using the standard inversion−recovery sequence.

The extraction of dissolved HP propane to the gas phase was carried out as follows: First, the reaction mixture was supplied through the reactor with Rh/TiO$_2$ catalyst to an NMR tube containing 0.5 mL of acetone-d_6. The position of the NMR tube inside the NMR spinner turbine was adjusted for the detection of the gas phase just above the liquid (Figure S2). Next, the displacement of HP propane from the solution was achieved by switching the flow of the reaction mixture (propene/p-H$_2$) from the catalyst to a bypass line using two valves (Figure S2). During this experiment, the NMR spectra of the gas phase were acquired continuously through the use of a small-angle (10°) rf excitation pulse.

NMR spectra were acquired on a 300 MHz Bruker AV 300 NMR spectrometer. All MR images were obtained on a Bruker Avance III 400 MHz NMR spectrometer with microimaging accessories using ParaVision 5.1 software based on Bruker TopSpin 3.0 and a commercial 30-mm ^{1}H/^{31}P birdcage rf coil (Bruker). Before MRI experiments were conducted in Para-Vision, the magnetic field was shimmed in TopSpin to provide field homogeneity for the sample in a 10-mm NMR tube. The fast low-angle shot (FLASH)[46] pulse sequence was used for image acquisition; the spectral bandwidth was 50 kHz, and the pulse angle was 5°. The total time of the MRI experiment was 1.7 s, the echo time (TE) was 14.8 ms, and the repetition time (TR) was 26.8 ms. The field of view (FOV) was 5 × 5 cm for the axial slice orientation and 5 × 3 cm for the sagittal plane, and the slice thickness was equal to 50 mm for both experiments. This means that the sample was projected onto the XY and XZ planes for the axial and sagittal orientations, respectively. The matrix size was 64 × 64, so the image resolution was approximately 0.8 × 0.8 mm^2 for the axial slice orientation and 0.8 × 0.47 mm^2 for the sagittal slice orientation. Because the two polarized signals of propane have opposite phases in ALTADENA NMR spectra,[45] the net integral is approximately zero. Therefore, to avoid mutual cancelation of the two signals in an MRI experiment, we used a selective excitation rf pulse centered at the frequency of the ALTADENA peak of the propane CH$_3$ group.

RESULTS AND DISCUSSION

In this article, we address the issue of the preservation of propane hyperpolarization by its dissolution in deuterated organic solvents. Gaseous HP propane was obtained by passing
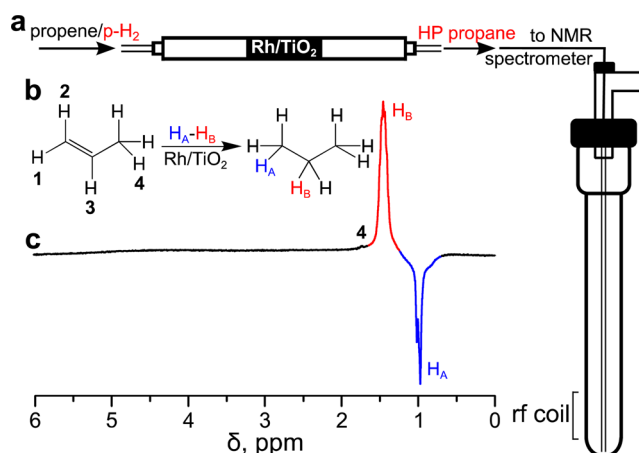

Figure 1. (a) Scheme of the experimental setup for HP propane production. (b) Reaction scheme of propene hydrogenation. (c) ALTADENA single-scan ^{1}H NMR spectrum acquired during gas-phase hydrogenation of propene with parahydrogen over 1 wt % Rh/TiO$_2$ catalyst.

a propene/p-H$_2$ gas mixture through a reactor with a Rh/TiO$_2$ catalyst (Figure 1), which usually provides both higher catalytic activity and higher PHIP levels than other heterogeneous catalysts.[34] Indeed, it was found that utilization of the Rh/TiO$_2$ catalyst allows ∼100% conversion of propene to be achieved. Also, as expected, pronounced PHIP effects with characteristic line patterns in the NMR spectra were observed for the propane molecule (Figure 1c), with one line in emission and another in enhanced absorption.

Next, dissolution experiments were carried out. For this purpose, HP propane was supplied to the bottom of the NMR tube containing acetone-d_6. As expected from our previous results,[47] we observed PHIP effects for propane dissolved in acetone-d_6 (Figure 2). It should be noted that the concentration of dissolved propane was virtually independent of the duration of bubbling and the average concentration was equal to 50 mM. We noticed that the hyperpolarization decay for dissolved propane was significantly slower than for propane in the gas phase. Therefore, hyperpolarization "lifetime" measurements of dissolved HP propane were carried out by recording ALTADENA signal decay curves through the acquisition of a set of ^{1}H NMR spectra at 1-s intervals using a small-angle rf excitation pulse (α = 10°). In a first approximation, the influence of the 10° rf excitation pulse on the longitudinal magnetization was neglected. In particular, correcting for the signal reduction caused by the influence of small-angle rf pulses would result in an increase in the hyperpolarization decay time (T_{HP}) for both the CH$_2$ and CH$_3$ groups of propane; therefore, the values shown here represent lower estimates. To confirm this conclusion, the results of experiments with 5° rf excitation pulses are presented in Figure S3. The hyperpolarization decay time measurements for dissolved HP propane yielded the values $T_{HP}(CH_2)$ = 35.1 ± 0.1 s and $T_{HP}(CH_3)$ = 28.6 ± 0.1 s (Figure 2d), which are ∼50 times greater than T_1 values for gaseous propane at the same 7.1 T magnetic field (∼0.6 s[36]). The obtained T_{HP} values are in a good agreement with the T_1 values obtained by the inversion−recovery technique for fully relaxed dissolved propane (Figure 2e).
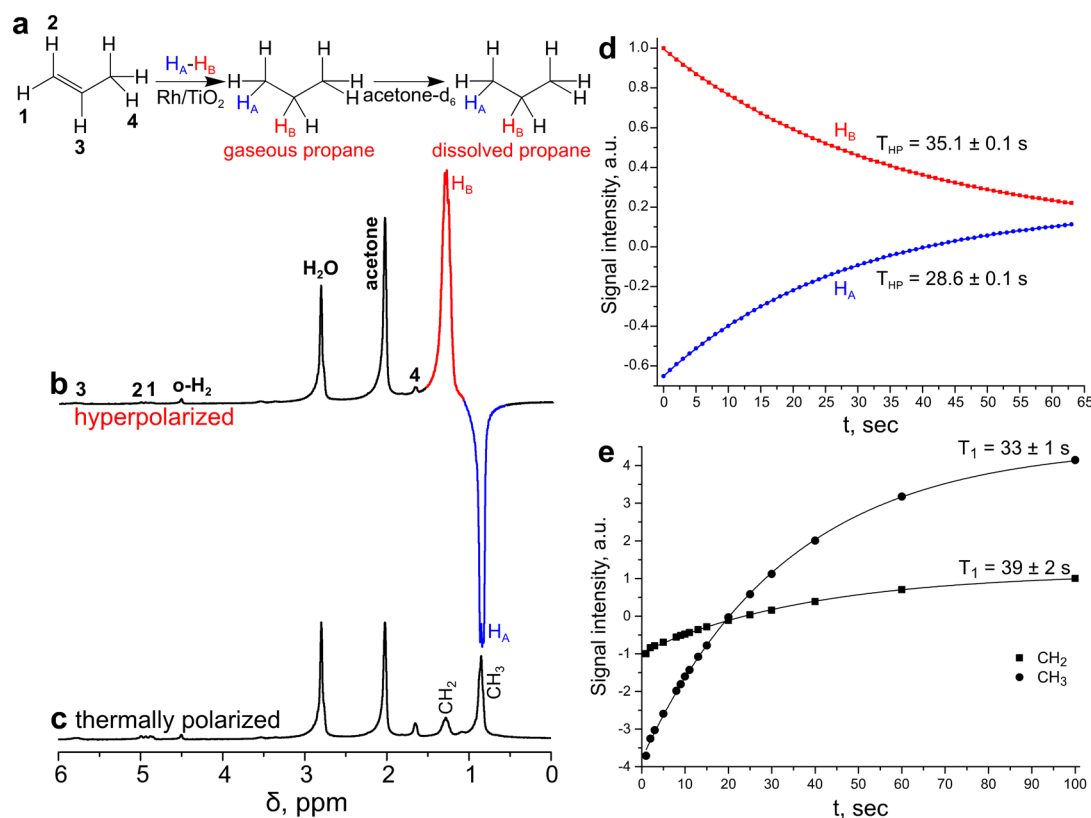
Figure 2. (a) Scheme showing the production of dissolved HP propane. (b) Single-scan ^{1}H NMR spectrum of dissolved HP propane produced by hydrogenation of propene with parahydrogen over 1 wt % Rh/TiO$_2$ catalyst and subsequent dissolution of HP propane in acetone-d_6. The signal enhancement was ~17-fold. (c) Corresponding ^{1}H NMR spectrum of the same solution as in panel b acquired after complete relaxation of hyperpolarization. (d) T_{HP} measurements for HP propane dissolved in acetone-d_6 through the use of 10° rf pulses. (e) T_1 measurements for thermally polarized propane dissolved in acetone-d_6 by the inversion–recovery sequence.

A reference inversion–recovery experiment with a concentrated solution of propane in acetone-d_6 at 25 °C obtained by bubbling pure propane from a gas tank provided comparable T_1 times for CH$_2$ (41.8 s) and CH$_3$ (35.6 s) protons (Figure S4). We note, however, that the results of inversion–recovery measurements are strongly dependent on the presence of dissolved oxygen, which is paramagnetic, with longest T_1 time being obtained after a sufficiently long bubbling (2 min) of pure propane through acetone-d_6. This resulted in the efficient removal of oxygen from the solution and a 5–6-fold elongation of T_1 times compared to the T_1 values obtained in the case of a short bubbling time (8 s). Similarly, bubbling of the reaction mixture in the experiments with hyperpolarized propane served to remove dissolved oxygen, which is important for obtaining the longest possible preservation of the hyperpolarization.

This dramatic elongation of the hyperpolarization decay time in the case of dissolved propane compared to gaseous propane is most likely due to the change in the dominant relaxation mechanism. This is confirmed by the fact that the hyperpolarization decay time is in a good agreement with the spin–lattice relaxation time in both cases. As discussed above, the main relaxation mechanism for small molecules (e.g., propane) in the gas phase is the spin-rotation mechanism,[48] the contribution of which depends on the time intervals between molecular collisions. However, in the liquid phase, molecular collisions are very frequent, leading to a dramatic decrease of the spin-rotation channel of relaxation. On the other hand, in solution, the dipole–dipole and intermolecular (including solute–solvent) interactions emerge as the prevailing mecha-

nism of relaxation. Thus, such a significant increase of the relaxation time in solution is explained by the changes in the relaxation mechanism.

The significant signal enhancement obtained for dissolved HP propane allowed fast MRI experiments to be performed using two-dimensional FLASH image acquisition. Here, we used the conventional FLASH pulse sequence to acquire two-dimensional slices with a spatial resolution of 0.8 × 0.8 mm^2 for axial slice orientations and 0.8 × 0.47 mm^2 for sagittal slice orientations and a short acquisition time (~1.7 s). Note that the signal enhancement obtained by the PHIP technique is crucial for the ^{1}H FLASH MRI of propane in the liquid phase. The signal enhancement for HP propane versus thermally polarized propane allows for the detection of images with a spatial resolution that is sufficient to visualize a $^1/_{16}$-in.-o.d. Teflon capillary (Figure 3a). Thermally polarized propane imaging does not yield an appreciable signal-to-noise ratio (SNR) to detect MR images for both slice orientations (Figures 3b and S5b).

Next, we aimed to determine the applicability of our approach to other deuterated solvents. For this purpose, we dissolved HP propane in methanol-d_4 (Figure 4). As expected, strong PHIP signals were observed for dissolved propane (Figure S6). The T_{HP} values for propane dissolved in methanol-d_4 were estimated as 34.6 ± 0.3 s for the CH$_2$ group and 28.3 ± 0.1 s for the CH$_3$ group (Figure 4b). These values are in agreement with the T_1 values for propane dissolved in methanol-d_4 (Figure 4c) and the values obtained previously for HP propane dissolved in acetone-d_6. This means that the
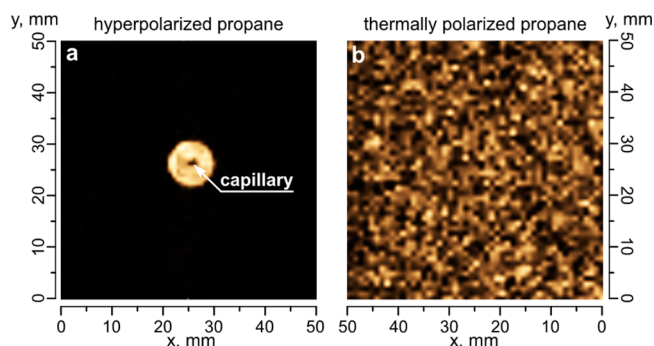
Figure 3. (a) MR image of a 10-mm NMR tube filled with solution of HP propane in acetone-d_6 in axial orientation. SNR = 17.2. (b) Corresponding MR image of fully relaxed solution shown in panel a. The field of view (FOV) was 5 × 5 cm, with a 64 × 64 matrix size and a slice thickness equal to the diameter of the NMR tube. The total acquisition time was 1.7 s.
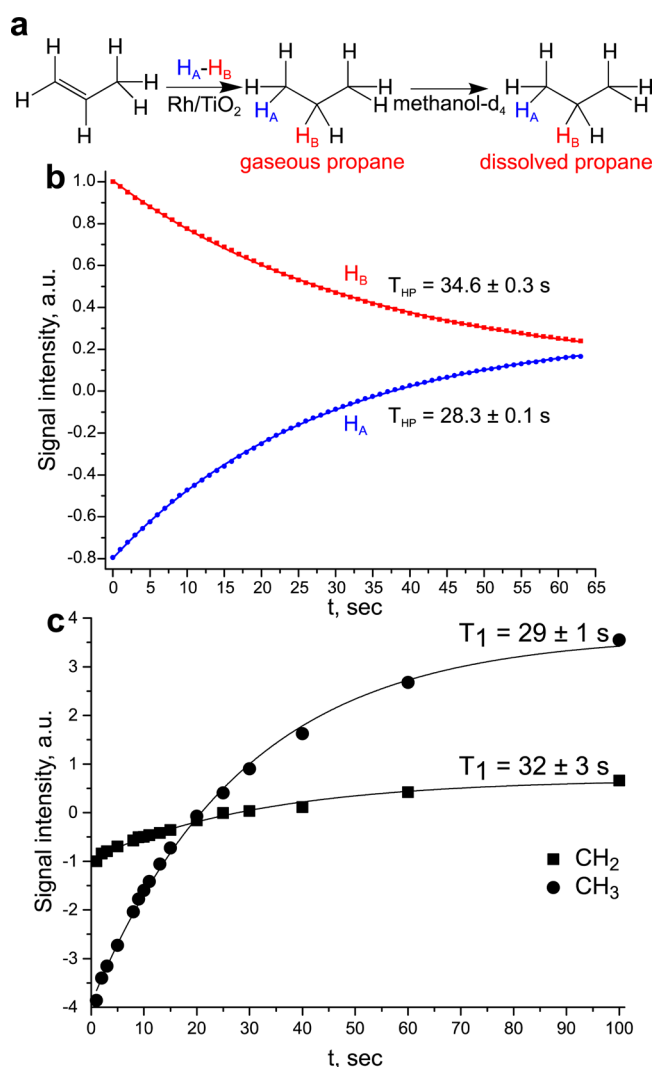

Figure 4. (a) Scheme showing the production of dissolved HP propane. (b) T_{HP} measurements for HP propane dissolved in methanol-d_4 through the use of 10° rf pulses. (c) T_1 measurements for thermally polarized propane dissolved in methanol-d_4 by the inversion−recovery sequence.

observed prolongation of the dissolved HP propane lifetime is a common feature for different deuterated organic solvents.

For potential applications of HP propane as a contrast agent in the MRI of lungs, one needs to retrieve the HP propane from solution to the gas phase. Therefore, we performed experiments to confirm the viability of our approach. To that end, we adjusted the position of the NMR tube in the rf probe to acquire NMR spectra of the gas phase just above the liquid. First, the propene/p-H$_2$ mixture was passed through the catalyst layer, and the resulting mixture of HP propane and residual p-H$_2$ was bubbled through acetone-d_6. Then, the gas flow was stopped for ~1−2 s, and next, the propene/p-H$_2$ mixture was bubbled directly into the acetone-d_6 solution, bypassing the reactor (see Figure S2 for the experimental setup). During all of these procedures, NMR spectra of the gas phase were acquired continuously in 1-s intervals. Thus, in the beginning, we observed NMR signals of HP propane in the gas phase; after the interruption of the gas flow, the HP propane gas above the solution rapidly relaxed to thermal equilibrium, and after the gas flow had been restarted, we observed NMR signals of both HP propane and propene (Figure S7). Thus, HP propane was successfully retrieved to the gas phase while retaining a substantial degree of hyperpolarization. Consequently, the developed approach is a very impressive technique for overcoming the lifetime limitations of HP propane usage as a potential hyperpolarized contrast gas agent for biomedical MRI applications caused by its extremely short spin−lattice relaxation time. Prolongation of the HP propane lifetime through its dissolution, followed by retrieval of the HP propane to the gas phase, not only allows the HP propane production and MRI investigations to be separated in time but also makes these two procedures (HP gas production and MRI studies) fully independent. In this way, the dissolved state can play the role of a temporary carrier for the polarization storage that allows for the transport of HP propane gas. Nevertheless, further investigations are undoubtedly needed, for example, to optimize the conditions for maximizing the hyperpolarization in both the liquid[49,50] and gas[51] phases.

CONCLUSIONS

The presented new approach based on the dissolution of HP propane enables one to preserve the hyperpolarization obtained by the PHIP technique for ca. 50 times longer than in the gas phase. This phenomenon can be explained by the switching of the main contribution to the relaxation mechanism from spin-rotation in the gas phase to dipole−dipole interactions in the liquid phase. Moreover, we demonstrated the successful retrieval of dissolved HP propane to the gas phase with a substantial retention of its hyperpolarized state. We hope that this new approach to the prolongation of the hyperpolarization lifetime can greatly expand the application of HP propane as a contrast agent in gas-phase MR imaging. Moreover, the future development of the reported approach might have synergism with LLSS technique that, without doubt, allows for the production of hyperpolarized molecules with extremely long relaxation times.

ASSOCIATED CONTENT

S Supporting Information

The Supporting Information is available free of charge on the ACS Publications website at DOI: 10.1021/acs.jpcc.7b00509.

Schemes of HP gas production and dissolution and T_1 relaxation measurements. Additional ^{1}H NMR spectra of HP propane dissolved in alcohol solution and ^{1}H NMR

spectrum of HP propane gas retrieved from the solution after $7T_1$ of propane gas. Sagittal MRI images of hyperpolarized and thermally polarized dissolved propane (PDF)

■ AUTHOR INFORMATION

Corresponding Author
*E-mail: kovtunov@tomo.nsc.ru.

ORCID ⓘ
Danila A. Barskiy: 0000-0002-2819-7584
Kirill V. Kovtunov: 0000-0001-7577-9619
Igor V. Koptyug: 0000-0003-3480-7649

Author Contributions
The manuscript was written through contributions of all authors. All authors have given approval to the final version of the manuscript.

Notes
The authors declare no competing financial interest.

■ ABBREVIATIONS

HP, hyperpolarization; MR, magnetic resonance; MRI, magnetic resonance imaging; NMR, nuclear magnetic resonance; PHIP, parahydrogen-induced polarization; rf, radiofrequency; SNR, signal-to-noise ratio; T_{HP}, hyperpolarization decay time

■ REFERENCES

(1) Lopez, A. D.; Shibuya, K.; Rao, C.; Mathers, C. D.; Hansell, A. L.; Held, L. S.; Schmid, V.; Buist, S. Chronic Obstructive Pulmonary Disease: Current Burden and Future Projections. *Eur. Respir. J.* **2006**, *27*, 397−412.

(2) Goldman, L. W. Principles of CT and CT Technology. *J. Nucl. Med. Technol.* **2007**, *35*, 115−128.

(3) Bergin, C. J.; Glover, G. H.; Pauly, J. M. Lung Parenchyima: Magnetic Susceptibility in MR Imaging. *Radiology* **1991**, *180*, 845−848.

(4) Failo, R.; Wielopolski, P. A.; Tiddens, H. A. W. M.; Hop, W. C. J.; Pozzi Mucelli, R.; Lequin, M. H. Lung Morphology Assessment Using MRI: A Robust Ultra-Short TR/TE 2D Steady State Free Precession Sequence Used in Cystic Fibrosis Patients. *Magn. Reson. Med.* **2009**, *61*, 299−306.

(5) Golman, K.; Axelsson, O.; Johannesson, H.; Mansson, S.; Olofsson, C.; Petersson, J. S. Parahydrogen-Induced Polarization in Imaging: Subsecond ^{13}C Angiography. *Magn. Reson. Med.* **2001**, *46*, 1−5.

(6) Larson, A. C.; White, R. D.; Laub, G.; Mcveigh, E. R.; Li, D.; Simonetti, O. P. Self-Gated Cardiac Cine MRI. *Magn. Reson. Med.* **2004**, *51*, 93−102.

(7) Serra, G.; Milito, C.; Mitrevski, M.; Granata, G.; Martini, H.; Pesce, A. M.; SfiKa, I.; Bonanni, L.; Catalano, C.; Fraioli, F.; et al. Lung MRI as a Possible Alternative to CT Scan for Patients With Primary Immune Defi Ciencies and Increased Radiosensitivity. *Chest* **2011**, *140*, 1581−1590.

(8) Donoho, D. L. Compressed Sensing. *IEEE Trans. Inf. Theory* **2006**, *52*, 1289−1306.

(9) Lustig, M.; Donoho, D.; Pauly, J. M. Sparse MRI: The Application of Compressed Sensing for Rapid MR Imaging. *Magn. Reson. Med.* **2007**, *58*, 1182−1195.

(10) King, K. F.; Kanwischer, A.; Peters, R. Imaging Industry Expectations for Compressed Sensing in MRI. *Proc. SPIE* **2015**, *9597*, 959705.

(11) Hu, S.; Lustig, M.; Chen, A. P.; Crane, J.; Kerr, A.; Kelley, D. A. C.; Hurd, R.; Kurhanewicz, J.; Nelson, S. J.; Pauly, J. M.; et al. Compressed sensing for resolution enhancement of hyperpolarized ^{13}C flyback 3D-MRSI. *J. Magn. Reson.* **2008**, *192*, 258−264.

(12) Hu, S.; Lustig, M.; Balakrishnan, A.; Larson, P. E. Z.; Bok, R.; Kurhanewicz, J.; Nelson, S. J.; Goga, A.; Pauly, J. M.; Vigneron, D. B. 3D Compressed Sensing for Highly Accelerated Hyperpolarized ^{13}C MRSI with in Vivo Applications to Transgenic Mouse Models of Cancer. *Magn. Reson. Med.* **2010**, *63*, 312−321.

(13) Nikolaou, P.; Goodson, B. M.; Chekmenev, E. Y. NMR Hyperpolarization Techniques for Biomedicine. *Chem. - Eur. J.* **2015**, *21*, 3156−3166.

(14) Barskiy, D. A.; Coffey, A. M.; Nikolaou, P.; Mikhaylov, D. M.; Goodson, B. M.; Branca, R. T.; Lu, G. J.; Shapiro, M. G.; Telkki, V.; Zhivonitko, V. V.; et al. NMR Hyperpolarization Techniques of Gases. *Chem. - Eur. J.* **2017**, *23*, 725−751.

(15) Walker, T. G.; Happer, W. Spin-Exchange Optical Pumping of Noble-Gas Nuclei. *Rev. Mod. Phys.* **1997**, *69*, 629−642.

(16) Raftery, D.; Long, H.; Meersmann, T.; Grandinetti, P. J.; Reven, L.; Pines, A. High-Field NMR of Adsorbed Xenon Polarized by Laser Pumping. *Phys. Rev. Lett.* **1991**, *66*, 584−587.

(17) Nikolaou, P.; Coffey, A. M.; Walkup, L. L.; Gust, B. M.; Whiting, N.; Newton, H.; Barcus, S.; Muradyan, I.; Dabaghyan, M.; Moroz, G. D.; et al. Near-Unity Nuclear Polarization with Open-Source ^{129}Xe Hyperpolarizer for NMR and MRI. *Proc. Natl. Acad. Sci. U. S. A.* **2013**, *110*, 14150−14155.

(18) *Hyperpolarized and Inert Gas MRI: From Technology to Application in Research and Medicine*; Albert, M. S., Hane, F., Eds.; Elsevier Inc.: London, 2017.

(19) Bowers, C. R.; Weitekamp, D. P. Parahydrogen and Synthesis Allow Dramatically Enhanced Nuclear Alignment. *J. Am. Chem. Soc.* **1987**, *109*, 5541−5542.

(20) Bowers, C. R. Sensitivity Enhancement Utilizing Parahydrogen. *Encycl. Magn. Reson.* **2007**, *9*, 750−770.

(21) Bowers, C. R.; Weitekamp, D. P. Transformation of Symmetrization Order to Nuclear-Spin Magnetization by Chemical Reaction and Nuclear Magnetic Resonance. *Phys. Rev. Lett.* **1986**, *57*, 2645−2648.

(22) Bhattacharya, P.; Harris, K.; Lin, A. P.; Mansson, M.; Norton, V. A.; Perman, W. H.; Weitekamp, D. P.; Ross, B. D. Ultra-Fast Three Dimensional Imaging of Hyperpolarized ^{13}C in Vivo. *MAGMA* **2005**, *18*, 245−256.

(23) Hövener, J.-B.; Chekmenev, E. Y.; Harris, K. C.; Perman, W. H.; Tran, T. T.; Ross, B. D.; Bhattacharya, P. Quality Assurance of PASADENA Hyperpolarization for ^{13}C Biomolecules. *MAGMA* **2009**, *22*, 123−134.

(24) Bhattacharya, P.; Chekmenev, E. Y.; Reynolds, W. F.; Wagner, S.; Zacharias, N.; Chan, H. R.; Bunger, R.; Ross, B. D. Parahydrogen-Induced Polarization (PHIP) Hyperpolarized MR Receptor Imaging in Vivo: A Pilot Study of ^{13}C Imaging of Atheroma in Mice. *NMR Biomed.* **2011**, *24*, 1023−1028.

(25) Zacharias, N. M.; Chan, H. R.; Sailasuta, N.; Ross, B. D.; Bhattacharya, P. Real-Time Molecular Imaging of Tricarboxylic Acid Cycle Metabolism in Vivo by Hyperpolarized 1−^{13}C Diethyl Succinate. *J. Am. Chem. Soc.* **2012**, *134*, 934−943.

(26) Coffey, A. M.; Shchepin, R. V.; Truong, M. L.; Wilkens, K.; Pham, W.; Chekmenev, E. Y. Open-Source Automated Parahydrogen Hyperpolarizer for Molecular Imaging Using ^{13}C Metabolic Contrast Agents. *Anal. Chem.* **2016**, *88*, 8279−8288.

(27) Koptyug, I. V.; Kovtunov, K. V.; Burt, S. R.; Anwar, M. S.; Hilty, C.; Han, S. I.; Pines, A.; Sagdeev, R. Z. Para-Hydrogen-Induced Polarization in Heterogeneous Hydrogenation Reactions. *J. Am. Chem. Soc.* **2007**, *129*, 5580−5586.

(28) Kovtunov, K. V.; Beck, I. E.; Bukhtiyarov, V. I.; Koptyug, I. V. Observation of Parahydrogen-Induced Polarization in Heterogeneous Hydrogenation on Supported Metal Catalysts. *Angew. Chem., Int. Ed.* **2008**, *47*, 1492−1495.

(29) Bouchard, L.-S.; Kovtunov, K. V.; Burt, S. R.; Anwar, M. S.; Koptyug, I. V.; Sagdeev, R. Z.; Pines, A. Para-Hydrogen-Enhanced Hyperpolarized Gas-Phase Magnetic Resonance Imaging. *Angew. Chem., Int. Ed.* **2007**, *46*, 4064−4068.

(30) Bouchard, L.-S.; Burt, S. R.; Anwar, M. S.; Kovtunov, K. V.; Koptyug, I. V.; Pines, A. NMR Imaging of Catalytic Hydrogenation in Microreactors with the Use of Para-Hydrogen. *Science* **2008**, *319*, 442−445.

(31) Kovtunov, K. V.; Romanov, A. S.; Salnikov, O. G.; Barskiy, D. A.; Chekmenev, E. Y.; Koptyug, I. V. Gas Phase UTE MRI of Propane and Propene. *Tomography* **2016**, *2*, 49−55.

(32) Telkki, V. V.; Zhivonitko, V. V.; Ahola, S.; Kovtunov, K. V.; Jokisaari, J.; Koptyug, I. V. Microfluidic Gas-Flow Imaging Utilizing Parahydrogen-Induced Polarization and Remote-Detection NMR. *Angew. Chem., Int. Ed.* **2010**, *49*, 8363−8366.

(33) Zhivonitko, V. V.; Telkki, V.-V.; Koptyug, I. V. Characterization of Microfluidic Gas Reactors Using Remote-Detection MRI and Parahydrogen-Induced Polarization. *Angew. Chem., Int. Ed.* **2012**, *51*, 8054−8058.

(34) Kovtunov, K. V.; Barskiy, D. A.; Coffey, A. M.; Truong, M. L.; Salnikov, O. G.; Khudorozhkov, A. K.; Inozemtseva, E. A.; Prosvirin, I. P.; Bukhtiyarov, V. I.; Waddell, K. W.; et al. High-Resolution 3D Proton MRI of Hyperpolarized Gas Enabled by Parahydrogen and Rh/TiO$_2$ Heterogeneous Catalyst. *Chem. - Eur. J.* **2014**, *20*, 11636−11639.

(35) Kovtunov, K. V.; Truong, M. L.; Barskiy, D. A.; Koptyug, I. V.; Coffey, A. M.; Waddell, K. W.; Chekmenev, E. Y. Long-Lived Spin States for Low-Field Hyperpolarized Gas MRI. *Chem. - Eur. J.* **2014**, *20*, 14629−14632.

(36) Barskiy, D. A.; Salnikov, O. G.; Kovtunov, K. V.; Koptyug, I. V. NMR Signal Enhancement for Hyperpolarized Fluids Continuously Generated in Hydrogenation Reactions with Parahydrogen. *J. Phys. Chem. A* **2015**, *119*, 996−1006.

(37) McClung, R. E. D. Spin-Rotation Relaxation Theory. *Encycl. Magn. Reson.* **2007**, *1961*, 1−5.

(38) Kovtunov, K. V.; Truong, M. L.; Barskiy, D. A.; Salnikov, O. G.; Bukhtiyarov, V. I.; Coffey, A. M.; Waddell, K. W.; Koptyug, I. V.; Chekmenev, E. Y. Propane-d_6 Heterogeneously Hyperpolarized by Parahydrogen. *J. Phys. Chem. C* **2014**, *118*, 28234−28243.

(39) Carravetta, M.; Levitt, M. H. Long Lived Nuclear Spin States in High-Field Solution NMR. *J. Am. Chem. Soc.* **2004**, *126*, 6228−6229.

(40) Warren, W. S.; Jenista, E.; Branca, R. T.; Chen, X. Increasing Hyperpolarized Spin Lifetimes Through True Singlet Eigenstates. *Science* **2009**, *323*, 1711−1714.

(41) Levitt, M. H. Singlet Nuclear Magnetic Resonance. *Annu. Rev. Phys. Chem.* **2012**, *63*, 89−105.

(42) Zhang, Y.; Basu, K.; Canary, J. W.; Jerschow, A. Singlet Lifetime Measurements in an All-Proton Chemically Equivalent Spin System by Hyperpolarization and Weak Spin Lock Transfers. *Phys. Chem. Chem. Phys.* **2015**, *17*, 24370−24375.

(43) Zhang, Y.; Duan, X.; Soon, P. C.; Sychrovsky, V.; Canary, J. W.; Jerschow, A. Limits in Proton Nuclear Singlet-State Lifetimes Measured with Para-Hydrogen-Induced Polarization. *ChemPhysChem* **2016**, *17*, 2967−2971.

(44) Barskiy, D. A.; Salnikov, O. G.; Romanov, A. S.; Feldman, M. A.; Coffey, A. M.; Kovtunov, K. V.; Koptyug, I. V.; Chekmenev, E. Y. NMR Spin-Lock Induced Crossing (SLIC) Dispersion and Long-Lived Spin States of Gaseous Propane at Low Magnetic Field (0.05 T). *J. Magn. Reson.* **2017**, *276*, 78−85.

(45) Pravica, M. G.; Weitekamp, D. P. Net NMR Alignment by Adiabatic Transport of Parahydrogen Addition Products to High Magnetic Field. *Chem. Phys. Lett.* **1988**, *145*, 255−258.

(46) Haase, A.; Frahm, J.; Matthaei, D.; Hanicke, W.; Merboldt, K.-D. FLASH Imaging. Rapid NMR Imaging Using Low Flip-Angle Pulses. *J. Magn. Reson.* **1986**, *67*, 258−266.

(47) Kovtunov, K. V.; Zhivonitko, V. V.; Skovpin, I. V.; Barskiy, D. A.; Salnikov, O. G.; Koptyug, I. V. Toward Continuous Production of Catalyst-Free Hyperpolarized Fluids Based on Biphasic and Heterogeneous Hydrogenations with Parahydrogen. *J. Phys. Chem. C* **2013**, *117*, 22887−22893.

(48) Bryant, R. G. NMR Relaxation Studies of Solute-Solvent Interactions. *Annu. Rev. Phys. Chem.* **1978**, *29*, 167−188.

(49) Allouche-Arnon, H.; Lerche, M. H.; Karlsson, M.; Lenkinski, R. E.; Katz-Brull, R. Deuteration of a Molecular Probe for DNP Hyperpolarization - A New Approach and Validation for Choline Chloride. *Contrast Media Mol. Imaging* **2011**, *6*, 499−506.

(50) Olsen, G.; Markhasin, E.; Szekely, O.; Bretschneider, C.; Frydman, L. Optimizing Water Hyperpolarization and Dissolution for Sensitivity-Enhanced 2D Biomolecular NMR. *J. Magn. Reson.* **2016**, *264*, 49−58.

(51) Mammoli, D.; Canet, E.; Buratto, R.; Miéville, P.; Helm, L.; Bodenhausen, G. Collisional Cross-Section of Water Molecules in Vapour Studied by Means of ^{1}H Relaxation in NMR. *Sci. Rep.* **2016**, *6*, 38492.

NMR Hyperpolarization Techniques of Gases

Top left to bottom right: B. M. Goodson, M. S. Rosen, D. Mikhaylov, E. Y. Chekmenev, M. Barlow, I. Hall, R. T. Branca, L. Schröder, M. G. Shapiro, I. V. Koptyug, V. I. Bukhtiyarov, V.-V. Telkki.

Invited for the cover of this issue is a group of researchers coordinated by E. Y. Chekmenev from Vanderbilt University. The image depicts hyperpolarized Xe-129 and parahydrogen gases and their MRI applications. Read the full text of the article at 10.1002/chem.201603884.

How would you describe to the layperson the most significant results of this study?

Over the last 20+ years, physicists and chemists have been working to improve the measurement capabilities of nuclear magnetic resonance (NMR) and magnetic resonance imaging (MRI) through the development of hyperpolarization techniques. Hyperpolarization can increase the nuclear spin polarization (i.e., the fractional alignment of nuclear spins with respect to the quantization direction), by 4–8 orders of magnitude, resulting in an equivalent gain in the detectable NMR and MRI signal. This enormous signal gain enables measurements to be performed in a few seconds that otherwise would take days, months, or even longer. Hyperpolarized gases, unlike liquids and solids, can be readily separated and purified from the auxiliary substances used to mediate the hyperpolarization processes. This advantage has enabled many novel MRI applications, including the visualization of void spaces in human lungs. Additionally, hyperpolarized gases can be dissolved in liquids and can be used as sensitive molecular probes and reporters of metabolic processes in living organisms.

What do you consider the exciting developments in the field?

Several advances in physics, chemistry, and engineering over the past ten years have led to significant improvement in the production of hyperpolarized gases. First, it has become possible to rapidly produce larger quantities of the hyperpolarized noble gas ^{129}Xe, upwards of several liters per hour. Second, the efficiency of this technology has improved, allowing polarizations approaching the theoretical limit of unity, that is, nearly complete alignment of nuclear spins with respect to the magnetic field. Third, the unique properties of hyperpolarized noble gases have enabled a new tool for pulmonary imaging, allowing the monitoring of lung structure, function, and response to treatment; hyperpolarized ^{129}Xe has already been tested in numerous clinical trials in volunteers with

lung diseases and control subjects. This technology may advise the diagnosis and monitoring of millions of patients with COPD and other pulmonary diseases. Moreover, new applications of HP gases continue to emerge, including the use of molecular biosensors based on hyperpolarized gases, the imaging of brown adipose tissue, and the development of genetically encoded reporters for gene expression imaging. Moreover, one of the recent developments in the field of hyperpolarization is the production of proton-hyperpolarized hydrocarbons, which can be visualized using conventional (i.e., proton-based) MRI scanners.

Front Cover Picture:
E. Y. Chekmenev et al.
NMR Hyperpolarization Techniques of Gases

High-resolution hyperpolarized in vivo metabolic ^{13}C spectroscopy at low magnetic field (48.7 mT) following murine tail-vein injection

Aaron M. Coffey [a,b,*], Matthew A. Feldman [a,b], Roman V. Shchepin [a,b], Danila A. Barskiy [a,b], Milton L. Truong [a,b], Wellington Pham [a,b,c,d], Eduard Y. Chekmenev [a,b,c,d,e,*]

[a] Vanderbilt University Institute of Imaging Science (VUIIS), Vanderbilt University, Nashville, TN 37232-2310, United States
[b] Department of Radiology, Vanderbilt University, Nashville, TN 37232-2310, United States
[c] Department of Biomedical Engineering, Vanderbilt University, Nashville, TN 37232-2310, United States
[d] Vanderbilt-Ingram Cancer Center (VICC), Vanderbilt University, Nashville, TN 37232-2310, United States
[e] Russian Academy of Sciences, Leninskiy Prospekt 14, Moscow 119991, Russia

A R T I C L E   I N F O

A B S T R A C T

High-resolution ^{13}C NMR spectroscopy of hyperpolarized succinate-1-^{13}C-2,3-d$_2$ is reported in vitro and in vivo using a clinical-scale, biplanar (80 cm-gap) 48.7 mT permanent magnet with a high homogeneity magnetic field. Non-localized ^{13}C NMR spectra were recorded at 0.52 MHz resonance frequency over the torso of a tumor-bearing mouse every 2 s. Hyperpolarized ^{13}C NMR signals with linewidths of $\sim$3 Hz (corresponding to $\sim$6 ppm) were recorded in vitro (2 mL in a syringe) and in vivo (over a mouse torso). Comparison of the full width at half maximum (FWHM) for ^{13}C NMR spectra acquired at 48.7 mT and at 4.7 T in a small-animal MRI scanner demonstrates a factor of $\sim$12 improvement for the ^{13}C resonance linewidth attainable at 48.7 mT compared to that at 4.7 T in vitro. ^{13}C hyperpolarized succinate-1-^{13}C resonance linewidths in vivo are at least one order of magnitude narrower at 48.7 mT compared to those observed in high-field ($\geq$3 T) studies employing HP contrast agents. The demonstrated high-resolution ^{13}C in vivo spectroscopy could be useful for high-sensitivity spectroscopic studies involving monitoring HP agent uptake or detecting metabolism using HP contrast agents with sufficiently large ^{13}C chemical shift differences.

© 2017 Elsevier Inc. All rights reserved.

1. Introduction

The emergence of several hyperpolarization techniques enhancing the detected signal from nuclear spins by orders of magnitude [1–5] have led to a wealth of opportunities to pursue in the developing arena of high sensitivity magnetic resonance research. In non-hyperpolarized methods, the magnetic field strength of the detection magnet serves to polarize the nuclear spins (usually protons) with polarization levels of $\leq$3.5 ppm/Tesla constraining the detection limit [6] to large ensembles of nuclear spins (conventionally bulk water in clinical MR applications). Hyperpolarization techniques, however, produce spin polarization independent of the readout magnet, and therefore, they provide freedom to select a magnetic field strength, and correspondingly a detection frequency, optimized to the nucleus observed [7,8] and the dielectric

properties of the sample [9–11]. Of particular interest is the quickly developing frontier of low-field magnetic resonance (NMR) and imaging (MRI) [12–14], due to its ability to strongly complement the study of hyperpolarized (HP) nuclei, and its potential for application in areas of study including heteronuclear spin-labeled metabolites [15,16] or other contrast agents [17–22] at low concentrations.

Key advantages have given rise to the desirability of pursuing low-field NMR and MRI. First, detection at low static magnetic field B_0 is known to yield far less vulnerability to magnetic susceptibility-induced field gradient artifacts in imaging, including those surrounding metallic implants [23] or interfaces between materials such as airways and tissues as occur in the lungs, inner ear, and nasal passages, thus significantly reducing the advanced shimming hardware requirements [24]. Second, the specific absorption rate (SAR) of energy deposited in the sample/subject during application of radiofrequency (RF) pulses scales $\propto B_0^2$. Consequently, lowering the field strength confers the benefit of reducing SAR to potentially negligible levels [11], which not only alleviates patient safety concerns, but can also lead to design and

---

implementation of faster pulse sequences by permitting use of RF pulses for echoes instead of gradient echoes [11]. Third, through utilizing long-lived spin states (LLSS) [25–36] or taking advantage of reduced contributions from chemical shift anisotropy particularly below 0.1 T [37], hyperpolarized state lifetimes can significantly extend for protons and/or heteronuclei at low magnetic fields. Fourth, experimental validation of the theoretical equations for low-field NMR and MRI [12,13] sensitivity for hyperpolarized states has favorably corroborated the weak frequency dependence of hyperpolarized state detection, where these theories indicate the potential for approaching or even exceeding the sensitivity of high-field NMR/MRI [12,13]. Lastly, utilization of low-field magnets provides significantly less expensive purchasing and maintenance costs, which can pair favorably with lower-cost methods of producing hyperpolarized spin states such as Spin Exchange Optical Pumping (SEOP) primarily focused on ^3He and ^{129}Xe [1,38–42] or the high-throughput parahydrogen-based methods [5,14,43] including parahydrogen-induced polarization (PHIP) [44–46] and signal amplification by reversible exchange (SABRE) [47–51].

In this communication, we demonstrate proof-of-principle high-resolution ^{13}C NMR spectroscopic detection of HP succinate-1-^{13}C-2,3-d_2 (^{13}C-SUX) at $B_0 = 48.7$ mT in vitro as well as in vivo. Here, we take advantage of the significantly more homogeneous B_0 field generated by a clinical-scale 80 cm-gap biplanar permanent magnet with ~13 ppm homogeneity over 40 cm diameter spherical volume (DSV) compared to a previously employed 8.9 cm-bore magnet with >20 ppm homogeneity over 4 cm [52]. Succinate was employed, because it finds potential application for cancer imaging [53–56]. With the improved DSV size and B_0 homogeneity, we report on in vivo high-resolution ^{13}C NMR spectroscopy capable of resolving splittings ≥4 Hz arising due to ^{13}C-^1H heteronuclear spin-spin couplings within the HP ^{13}C-SUX molecule (note that although ^{13}C-^2H two- and three-bond couplings are present in HP ^{13}C-SUX (Fig. 1), they are significantly weaker than the corresponding ^{13}C-^1H spin-spin couplings, and they are likely are manifested as line-broadening in the detected ^{13}C NMR spectra). We compare 48.7 mT ^{13}C in vitro and in vivo NMR spectra with those obtained at 4.7 T, and find at least one order of magnitude of ^{13}C linewidth (in the units of Hz) improvement at low magnetic field compared to high magnetic field.

2. Material and methods

2.1. PHIP hyperpolarizer

A PHIP hyperpolarizer used to prepare the 1-^{13}C-succinate-d_2 hyperpolarized contrast agent (HCA) was fully automated via open-source software and hardware and integrated with a dual-channel low-field NMR spectrometer (Kea2, Magritek, Wellington, New Zealand), with operations controlled by computer through a graphical user interface (GUI) [52]. The Helmholtz saddle configuration radiofrequency (RF) coils used for the RF polarization transfer sequence developed by Goldman and Johannesson [57] operate at the ^1H and ^{13}C resonances for $B_0 = 5.75$ mT when capacitively tuned and matched to 50 Ω and enclose a high pressure plastic reactor with ~56 mL volume kept at temperatures between 50 and 60 °C. Quality assurance of the produced agent before use is achieved via a small tipping angle RF pulse in order to establish the degree of polarization of the agent. The process of producing a dose of HCA takes less than a minute, and the routines for readying the system for the next dose, including cleaning, result in a total PHIP cycle time of less than 3 min. Full details of the PHIP polarizer instrumentation including schematics, software, and bill of materials are freely available elsewhere [52]. A home-built

parahydrogen (p-H_2) generator using a low-power cryocooler is used to produce continuously 90+% p-H_2 from bulk hydrogen at flow rates up to 150 sscm and 25 bar pressure. A 1 L double-ended 316 SS sample cylinder with PTFE lining (316L-50DF4-500-T-PD, Swagelok) and brass Yor-Lok tube fittings (5272K291, McMaster-Carr) provides a gas reservoir for p-H_2 collection between experiments (~0.4 L is consumed per production of HCA, coincidentally matching conveniently the PHIP cycle time).

2.2. PHIP hyperpolarization of 1-^{13}C-succinate-d_2 (^{13}C-SUX)

Preparation of aqueous Rh-based hydrogenation catalyst and fumaric acid-1-^{13}C-d_2 precursor used to produce HP succinate-1-^{13}C-d_2 (^{13}C-SUX) followed the fully described previously procedure [52]. Briefly, precursor stock solution of fumaric acid-1-^{13}C-d_2 (Cambridge Isotopes, CDLM-6062-PK, 1-^{13}C 99%, 2,3-D_2 98%, 3.00 mmol, 0.357 g) is prepared in D_2O, degassed, pH adjusted to 10.3, and mixed with the standard PHIP catalyst/ligand system of rhodium(I) catalyst, bis(norbornadiene) rhodium(I) tetrafluoroborate (0.200 g, 0.54 mmol, 45-0230, CAS 36620-11-8, Strem Chemicals, MA) and phosphorus ligand, disodium salt of 1, 4-bis[(phenyl-3-propanesulfonate)phosphine]butane (717347, Sigma-Aldrich-Isotec, 0.360 g, 0.64 mmol). Following preparation, the catalyst is stored in a plastic bottle attached to the gas/liquid manifold of the PHIP hyperpolarizer and kept under slight over-pressure (~2–5 psi gauge pressure) of ultra-high purity nitrogen or Argon (>99.999%, A-L Compressed Gases Inc., Nashville, TN) [52].

2.3. MRI magnet and RF coils

The upright biplanar permanent magnet clinical imaging system (Supporting Information (SI) and Fig. 2) generates B_0 field of 48.7 mT statically shimmed to ~13 ppm homogeneity over a 40 cm DSV (SIGWA 48.7 mT, Boston NMR, Boston, MA). The open-bore configuration achieves an 80 cm-gap between the planar XYZ gradient coil inserts mounted to the pole pieces. Heteronuclear NMR spectroscopic detection involving ^{13}C and ^{15}N on this system has been observed to approach ~1 Hz linewidths (determined as full width at half maximum or FWHM), when measuring NMR samples with μL volumes (e.g., samples in 5 mm NMR tubes). We note that this system is particularly well suited for the direct NMR measurement of J-couplings of hyperpolarized compounds given its low field strength and excellent field homogeneity [30]. While not utilized for shimming in the reported in vivo study, when used for MRI the XYZ planar gradient coil set is capable of reaching 20 mT/m in all axes with linearity within approximately ±6% across the full FOV of 40 cm. Further details of the imaging system (including the Tecmag Redstone console) are provided in the SI.

The RF coil built for use in this imaging system was designed to measure metabolic HP contrast agents in vivo in small animal studies involving mice. The solenoid coil was constructed to match the typical dimensions of the animal (17 mm diameter by up to 193 mm body length) to increase the coil filling factor and correspondingly the SNR. The coil had a quality factor of 55. The coil was tuned using 56H02 Johansen trimmer capacitors and ATC non-magnetic ceramic capacitors to tune the resonant frequency to ^{13}C resonance at 0.521 MHz or ^1H resonance at 2.074 MHz and match the coil impedance to the 50 Ω coaxial transmission line impedance. All component values are provided in Tables S1 and S2 in the SI. The resonant circuit for ^1H or ^{13}C detection was comprised of a parallel LC resonator with a series capacitive matching element (see Figs. S3 and S4, SI). The solenoid was constructed with 170 windings using 28 AWG gauge magnet wire with a measured inductance of 302 μH. The coil was enclosed in an RF shield constructed using square double-sided 1 oz. copper clad PCB materials
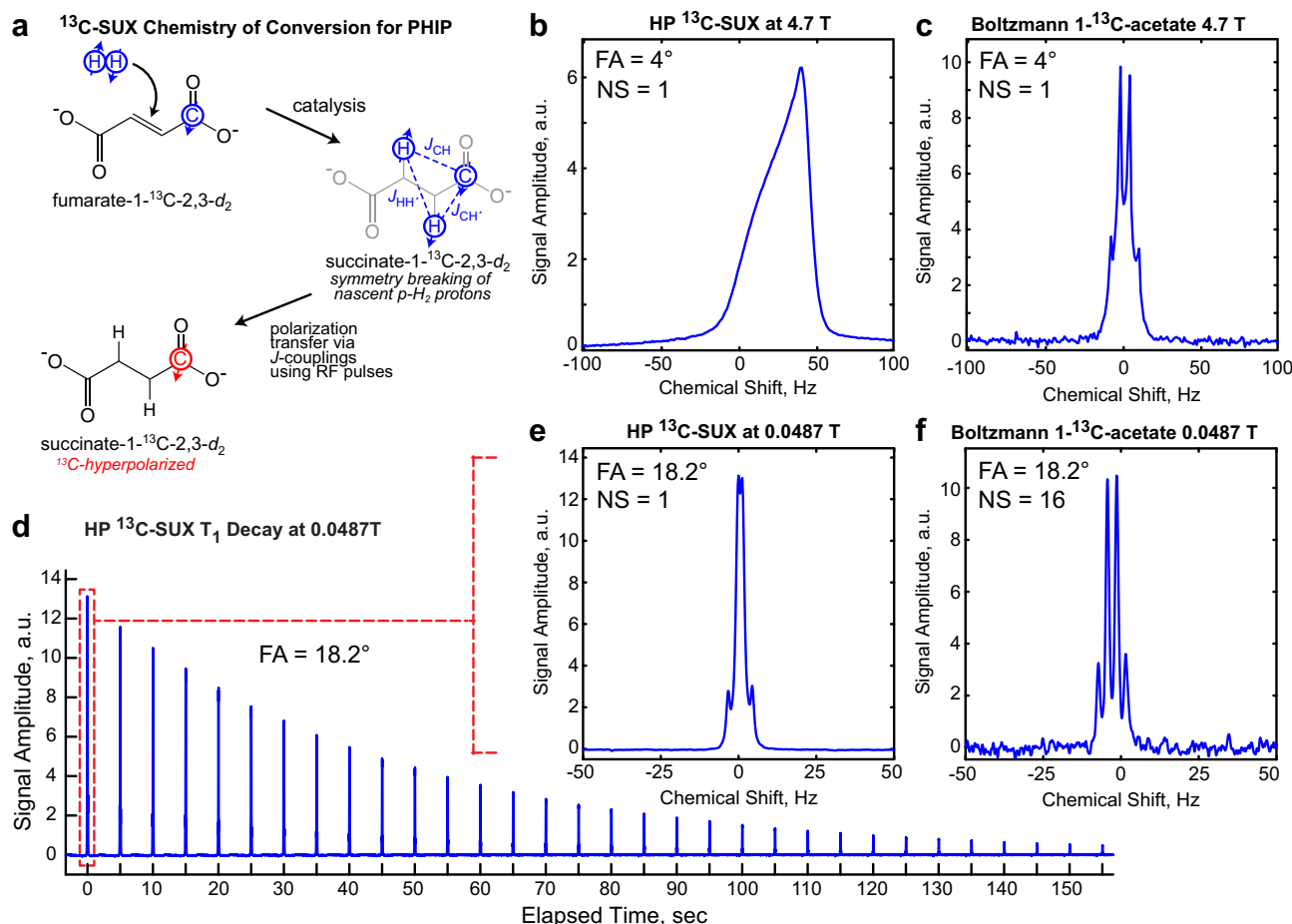
Fig. 1. Chemistry of ^{13}C-SUX hyperpolarization and NMR spectroscopy. (a) The conversion scheme of fumarate-1-^{13}C-2,3-d_2 to yield succinate-1-^{13}C-2,3-d_2 via the PHIP process. (b and e) ^{13}C NMR spectroscopy of HP ^{13}C-SUX in hollow plastic spheres (2.8 mL volume) at 4.7 T (best shim) and an HCA-filled syringe at 48.7 mT, respectively. (c and f) Thermal Boltzmann polarization reference of 1 g sodium 1-^{13}C-acetate in D$_2$O at 4.7 T (single average) and 5 g sodium 1-^{13}C-acetate in 15 mL D$_2$O at 48.7 mT (16 averages), respectively. (d) T_1 decay curve of HP ^{13}C-SUX at 48.7 mT with simulated T_1 of 88 ± 5 s. See additional details in the text.

(473-1007-ND, Digikey, Thief River Falls, MN) to form an enclosed cubic volume (1 ft × 1 ft × 1 ft). This shielding provided an electric field suppression of 60+ dB. The coil was calibrated via a nutation sequence on the Redstone console using variable flip angle via pulse length calibration for fixed power, and the $\pi/2$ tip angle was determined to be 115 µs for ^{1}H and 475 µs for ^{13}C for <1 W of applied RF power. Further description of the RF probe is provided in the SI.

2.4. ^{13}C HP NMR spectroscopy and ^{13}C NMR spectroscopy using thermal polarization

Sodium 1-^{13}C-acetate was used for Boltzmann thermal polarization analysis at 48.7 mT and 4.7 T for HP ^{13}C-SUX spectroscopic comparison given ~97-fold field strength ratio for B_0. HP ^{13}C-SUX spectroscopy was performed by injecting HCA into a 2.8 mL hollow plastic sphere situated inside the corresponding RF coil at either 4.7 T (best ^{1}H shim settings on the acetate phantom) or 48.7 mT (static magnet shim) followed by application of a small tipping angle hard RF pulse to observe the shimmed NMR resolution obtainable. For in vivo detection, a time series of NMR acquisitions to allow observation of HCA dynamics was commenced on the Redstone console at the start of the PHIP hyperpolarization sequence that produces a batch of HP ^{13}C-SUX.

2.5. ^{13}C spectroscopy in small rodents using HP ^{13}C-SUX

The feasibility of in vivo ^{13}C high-resolution detection of spin-spin couplings was tested in mice for HP ^{13}C-SUX at the low magnetic field of 48.7 mT. Procedurally, the 4T1 mammary carcinoma cells were maintained in RPMI-1640 medium supplemented with fetal bovine serum (10%, v/v) and the culture dish was incubated in a 37 °C, 5% CO$_2$. Eight-to ten-week-old female nude mice were purchased from Jackson Laboratory. All animal experimental protocols were approved by the Vanderbilt University Institutional Animal Care and Use Committee. Nude mice 6–8 weeks of age (from Jackson Laboratory, Bar Harbor, ME, USA) were implanted sub-cutaneously under anesthesia (isoflurane mixed with 2% oxygen) with 1.0×10^6 cells in the mammary fat pad using a 27-G needle. The progress of tumor growth was monitored via every-other-day measurement of tumor size and animal weight. When the tumors reached approximately 4 mm in diameter, in vivo ^{13}C spectroscopy study was performed.

In preparation for the NMR experiment, the mice were anesthetized using ketamine:xylazine (75 mg/kg: 5 mg/kg) via intraperitoneal injection. The anesthetic dose was designed to immobilize animals for approximately 60 min. After anesthetization, with the animal lying on a thin film carrier, a 28-gauge needle affixed to a catheter line was inserted into the lateral tail vein. The animal with catheter in place was then transported and placed
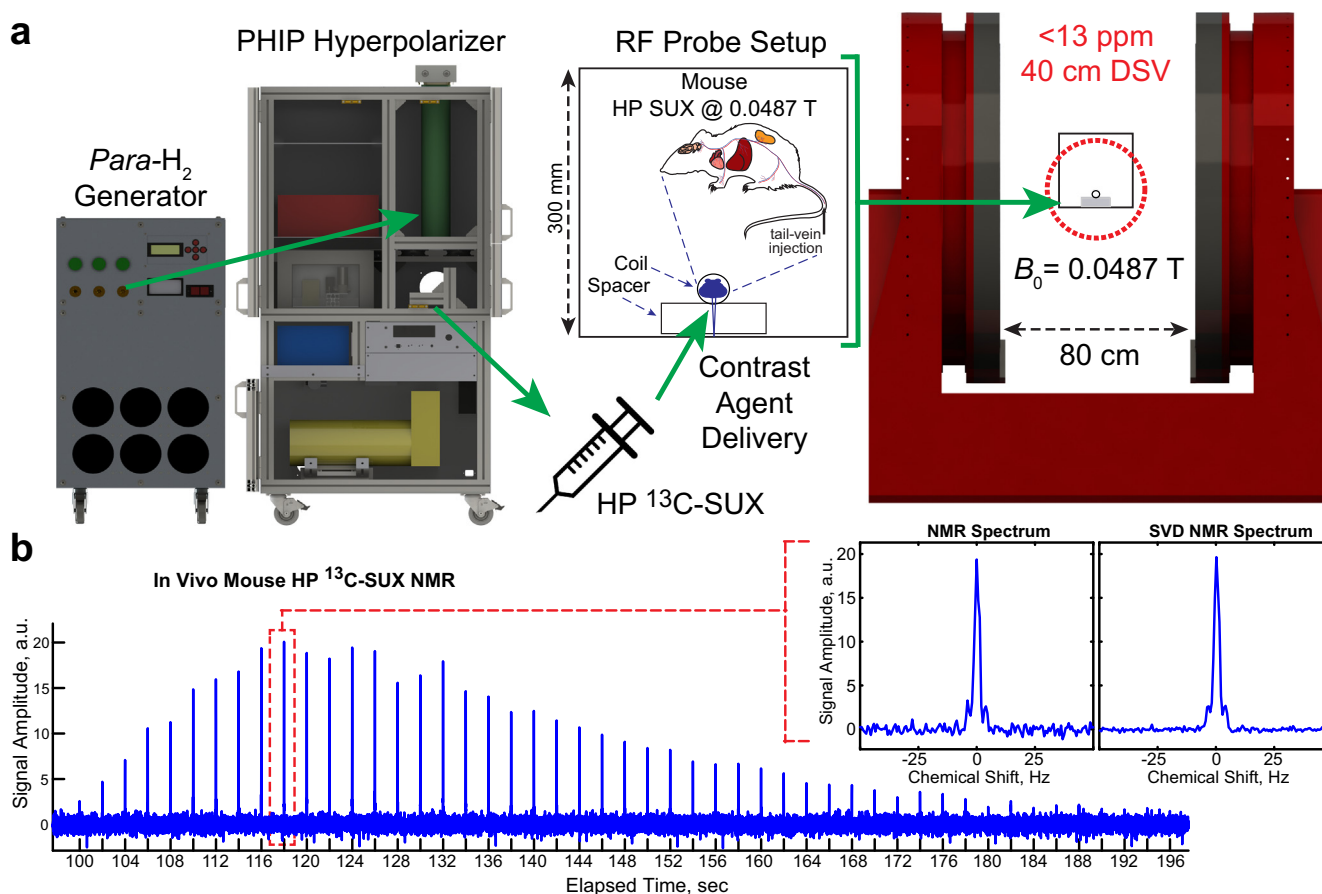
Fig. 2. Experimental setup and *in vivo* ^{13}C NMR spectroscopy. (a) Parahydrogen at ~80% purity was prepared with a home-built parahydrogen generator and used to produce HP ^{13}C-SUX from ^{13}C-FUM in a home-built PHIP hyperpolarizer. (b) Coinciding with the start of production of HP ^{13}C-SUX in the PHIP hyperpolarizer, NMR acquisitions every 2 s were acquired with FA = 18°, with (insets) showing a selected NMR spectrum from the series alongside the corresponding SVD de-noised spectrum (10 largest singular values). See additional details in the text and SI.

inside the RF probe with the catheter line fitting through the RF shield. Prior to acquiring NMR spectroscopy or MRI imaging, animals were slowly injected over ~5 s timespan with ~0.2 mL of HP ^{13}C-SUX via the catheter in performance of a tail-vein injection. After NMR spectroscopy, animals were retrieved from the scanner and placed back into a warm cage under constant observation until recovered from anesthesia.

3. Results and discussion

3.1. In vitro ^{13}C NMR spectroscopy at 4.7 T and 48.7 mT

^{13}C NMR spectra of thermally polarized sodium acetate-1-^{13}C (1 g dissolved in 2.8 mL D$_2$O DSV) were recorded using a 4.7 T Varian preclinical MRI scanner (Fig. 1c, 1 scan) and using a Tecmag Redstone console (Fig. 1c, 16 scans) at 50 MHz and 0.52 MHz ^{13}C resonance frequency, respectively. The high-field acquisition was performed using active shimming, while the low-field acquisition was performed without any additional magnet shimming. Acetate-1-^{13}C moiety results in a characteristic ^{13}C quartet appearance due to ~6.0 Hz ^{1}H-^{13}C two-bond spin-spin coupling. The quartet features are somewhat better resolved at 48.7 mT, Fig. 1c vs. f.

^{13}C spectroscopy of HP ^{13}C-SUX was performed at 4.7 T using the same type of hollow plastic spherical container. The resulting spectrum (Fig. 1b) shows one relatively broad line with FWHM ~36 Hz. ^{13}C spectroscopy of HP ^{13}C-SUX performed at 48.7 mT

was conducted in a plastic syringe container. The spectrum (Fig. 1e) shows a very well resolved multiplet pattern—a manifestation of complex network of two- and three-bond ^{13}C-^{1}H spin-spin couplings. The half-height line width (HHLW) was estimated to be <3 Hz, and the two outer peaks of the splitting pattern (~3.9 Hz away) are well differentiated. The ~12-fold narrower linewidth (and consequently better resolution in units of Hz) obtained at 48.7 mT is possible due to the fact that susceptibility-induced field gradients which scale linearly with B_0 are significantly reduced at 48.7 mT compared to 4.7 T (by the ratio of ~97 of the two field strengths). The chemical shift dispersion (in units of Hz) scales linearly with B_0, and as a result, it is reduced by a factor of ~97 at 48.7 mT compared to that at 4.7 T. The effective ~12-fold line narrowing (due to reduced susceptibility-induced B_0 field gradients) described above partially mitigates the above reduction in chemical shift dispersion, and the overall resolving power of ^{13}C spectroscopy at 48.7 mT was approximately 8 times worse than that at 4.7 T (*i.e.*, ~97:12).

Despite nominal reduction of spectral resolution, the significant *in vivo* ^{13}C line narrowing at 48.7 mT vs. 4.7 T provides a certain advantage from the perspective of the detection sensitivity, or SNR. Because the sensitivity for HP detection can scale as $B_0^{1/4}$ [12] or as $B_0^{0.14}$ in the range of 10–500 kHz [58] depending on coil geometry and construction and the means of detection, which is a very weak field dependence, the significant reduction in FWHM is an important contributing factor to the overall detection sensitivity argument for low-field MR. In particular, this may translate into more sensitive LF MR detection schemes of HP contrast agents

for some applications, which can take advantage of this significant narrowing of linewidth despite the commensurate reduction in the chemical shift dispersion, *e.g.* HP gas spectroscopy and imaging [5,59].

3.2. In vitro ^{13}C-SUX T_1 in deoxygenated D_2O

Previous measurement of ^{13}C-SUX hyperpolarized lifetime in D_2O at 47.5 mT yielded 75 ± 3 s *in vitro* [15]. At 48.7 mT, the lifetime of HP ^{13}C-SUX in D_2O was measured to be 88 ± 5 s *in vitro* according to the decay curve shown in Fig. 1 and accounting for using a RF pulse with flip angle (FA) ∼18°. This is in good agreement with previously reported value, and the minor discrepancy is likely caused by slight imprecision (<1°) in calibrating the low-field RF pulse and small variations in the pH of the produced HCA, which is known to modulate ^{13}C T_1 of HP SUX significantly [53,54,60]. ^{13}C chemical shift anisotropy (CSA) decreases significantly in units of Hz at 48.7 mT compared to that at ≥3 T. As a result, ^{13}C CSA likely has a negligible contribution to the T_1 relaxation of the ^{13}C HP state at 48.7 mT, and dipole-dipole interactions likely represent the dominant T_1 relaxation mechanism at such low magnetic fields.

3.3. In vivo ^{13}C NMR spectroscopy at 4.7 T and 48.7 mT

HP ^{13}C-SUX was injected as a bolus dose in the tail vein of anesthetized tumor-bearing mouse, which was positioned inside a RF coil placed in the center of 48.7 mT magnet (Fig. 1). Non-localized ^{13}C NMR spectra were recorded via the NMR console commencing at the start of HCA production on the PHIP hyperpolarizer every 2 s using a small angle pulse for every RF excitation. The time window for recording NMR spectra of HP ^{13}C-SUX was ∼80 s (Fig. 2b). We note that the entire dynamic ^{13}C *in vivo* scan was effectively completed ∼3 min after the beginning of contrast agent production in the PHIP hyperpolarizer. The ^{13}C NMR signal increases at the very beginning due to HCA entering the body of the animal, and it decreases after reaching a maximum post-injection due to (i) T_1 decay, (ii) RF pulse-associated losses, and (iii) possible metabolism. Despite the significant detection volume (whole mouse vs. a small syringe), the ^{13}C NMR linewidth remained largely unchanged: ∼3 Hz (*in vivo*, Fig. 2b) vs. ∼3 Hz (*in vitro*, see above). While this result is not surprising because the susceptibility-induced gradients are negligible, the demonstration of such high-spectral-resolution HP ^{13}C low-field NMR spectroscopy *in vivo* has been performed for the first time to the best of our knowledge. Most *in vivo* preclinical experiments with ^{13}C HP contrast agents are performed at 3 T and above, and ^{13}C FWHM is typically ≥1 ppm corresponding to ≥30 Hz [55,61–65]. The HP ^{13}C FWHM (in units of Hz) demonstrated here *in vivo* is at least an order of magnitude improvement compared to high-field *in vivo* studies of HP HCAs. Moreover, the FWHM of ∼3 Hz (corresponding to ∼6 ppm) is only a factor of ≤6 worse than that observed in high-field studies (*i.e.* ≥1 ppm) [55,61–65]. While the chemical shift resolution (in units of ppm) is certainly reduced at 48.7 mT, this reduction is offset through the gain in sensitivity via ^{13}C line-narrowing, which represents an interesting trade-off between the detection sensitivity (*i.e.* SNR) and resolution.

3.4. Imaging and biomedical translation

Although HP NMR spectroscopy has been reported in the ZULF regime [37,66,67] including frequency-selective RF excitation [67], the use of conventional MRI frequency encoding in ZULF potentially is challenging due to the very low resonance frequency, and new MRI encoding techniques likely need to be developed. However, ^{13}C (as well as ^{1}H, ^{3}He and ^{129}Xe) MRI imaging can be performed at $B_0 > 6$ mT (including ∼48.7 mT, the field studied here) as has been demonstrated by us [15,52,68–70] and others [8,19,20,71–75] previously using conventional MRI approaches. In particular, ^{13}C frequency encoding can still be accomplished at ∼0.5 MHz resonance frequency (f_0) as employed here and using a RF coil with suitable quality factor Q and reasonable choice of spectral width (SW) to satisfy the imaging bandwidth condition of $f_0/Q \gg$ SW [15]. The direct use of conventional encoding approaches is a clear translational advantage of LF MRI compared to the current status of ZULF due to the ready availability of commercial hardware and the wide range of already established pulse sequences.

The ^{13}C NMR spectroscopy demonstrated here at 48.7 mT with ∼6 ppm spectral resolution (∼3 Hz FWHM) could be useful for *in vivo* ^{13}C spectroscopic studies aiming to: (i) differentiate HP pyruvate-^{13}C and its main metabolic product in tumors of HP lactate-1-^{13}C, because their HP ^{13}C resonances have a sufficient chemical shift difference of ∼12 ppm [61,62]; (ii) pH imaging via spectroscopic detection of HP ^{13}C-bicarbonate and ^{13}CO$_2$, because their resonances are separated by ∼35 ppm [76]; and (iii) potentially other injectable ^{13}C HP contrast agents with sufficiently different chemical shifts of HP metabolites [65,77].

4. Conclusion

High-resolution (FWHM ∼3 Hz) ^{13}C NMR spectroscopy of HP ^{13}C-SUX has been successfully demonstrated at 0.521 MHz resonance frequency *in vitro* and *in vivo* using a homogeneous (13 ppm over 40 cm DSV) 80 cm-gap 48.7 mT magnet. Resolution of ^{13}C line splittings of ∼4 Hz were successfully observed *in vivo*. The *in vivo* ^{13}C linewidth (FWHM) obtained at 48.7 mT was ∼12 times better than that achieved with a 4.7 T small-animal MRI scanner using the same HCA. A significant gain in spectral linewidth for ^{13}C low-field *in vivo* NMR spectroscopy is advantageous for improving the detection sensitivity of LF NMR. Potential biomedical applications can include monitoring HP ^{13}C agent uptake as well as detecting metabolism of biomolecules with sufficiently different chemical shifts at such low fields including MRSI of HP pyruvate-1-^{13}C/lactate-1-^{13}C, HP bicarbonate-^{13}C/^{13}CO$_2$ and others [78–80].

Appendix A. Supplementary material

Supplementary data associated with this article can be found, in the online version, at http://dx.doi.org/10.1016/j.jmr.2017.06.009.

References

[1] P. Nikolaou, B.M. Goodson, E.Y. Chekmenev, NMR Hyperpolarization Techniques for Biomedicine, Chem. Eur. J. 21 (2015) 3156–3166.
[2] B.M. Goodson, Nuclear magnetic resonance of laser-polarized noble gases in molecules, materials, and organisms, J. Magn. Reson. 155 (2002) 157–216.
[3] D. Blazina, S.B. Duckett, J.P. Dunne, C. Godard, Applications of the parahydrogen phenomenon in inorganic chemistry, Dalton Trans. (2004) 2601–2609.
[4] K.V. Kovtunov, V.V. Zhivonitko, I.V. Skovpin, D.A. Barskiy, I.V. Koptyug, Parahydrogen-induced polarization in heterogeneous catalytic processes, Top. Curr. Chem. 338 (2013) 123–180.
[5] D.A. Barskiy, A.M. Coffey, P. Nikolaou, D.M. Mikhaylov, B.M. Goodson, R.T. Branca, G.J. Lu, M.G. Shapiro, V.-V. Telkki, V.V. Zhivonitko, I.V. Koptyug, O.G.

Salnikov, K.V. Kovtunov, V.I. Bukhtiyarov, M.S. Rosen, M.J. Barlow, S. Safavi, I.P. Hall, L. Schröder, E.Y. Chekmenev, NMR Hyperpolarization Techniques of Gases, Chem. Eur. J. 23 (2017) 725–751.

[6] H.D.W. Hill, R.E. Richards, Limits of measurement in magnetic resonance, J. Phys. E: Sci. Instrum. 1 (1968) 977–983.

[7] J. Parra-Robles, A.R. Cross, G.E. Santyr, Theoretical signal-to-noise ratio and spatial resolution dependence on the magnetic field strength for hyperpolarized noble gas magnetic resonance imaging of human lungs, Med. Phys. 32 (2005) 221–229.

[8] W. Dominguez-Viqueira, W. Berger, J. Parra-Robles, G.E. Santyr, Litz wire radiofrequency receive coils for hyperpolarized noble gas MR imaging of rodent lungs at 73.5 mT, Concept Magn. Res. B 37B (2010) 75–85.

[9] T. Yamashita, T. Oida, S. Hamada, T. Kobayashi, Thermal noise calculation method for precise estimation of the signal-to-noise ratio of ultra-low-field MRI with an atomic magnetometer, J. Magn. Reson. 215 (2012) 100–108.

[10] K.M. Gilbert, T.J. Scholl, B.A. Chronik, RF coil loading measurements between 1 and 50 MHz to guide field-cycled MRI system design, Concept Magn. Res. B 33B (2008) 177–191.

[11] M.E. Hayden, C.P. Bidinosti, E.M. Chapple, Specific absorption rates and signal-to-noise ratio limitations for MRI in very-low magnetic fields, Concept Magn. Res. A 40A (2012) 281–294.

[12] A.M. Coffey, M.L. Truong, E.Y. Chekmenev, Low-field MRI can be more sensitive than high-field MRI, J. Magn. Reson. 237 (2013) 169–174.

[13] M. Suefke, A. Liebisch, B. Blumich, S. Appelt, External high-quality-factor resonator tunes up nuclear magnetic resonance, Nature Phys. (2015) 767–771.

[14] B. Blümich, Virtual special issue: Magnetic resonance at low fields, J. Magn. Reson. 274 (2017) 145–147.

[15] A.M. Coffey, K.V. Kovtunov, D. Barskiy, I.V. Koptyug, R.V. Shchepin, K.W. Waddell, P. He, K.A. Groome, Q.A. Best, F. Shi, B.M. Goodson, E.Y. Chekmenev, High-resolution low-field molecular MR imaging of hyperpolarized liquids, Anal. Chem. 86 (2014) 9042–9049.

[16] R.V. Shchepin, A.M. Coffey, K.W. Waddell, E.Y. Chekmenev, Parahydrogen induced polarization of 1-^{13}C-phospholactate-d$_2$ for biomedical imaging with >30,000,000-fold NMR signal enhancement in water, Anal. Chem. 86 (2014) 5601–5605.

[17] K.V. Kovtunov, M.L. Truong, D.A. Barskiy, I.V. Koptyug, A.M. Coffey, K.W. Waddell, E.Y. Chekmenev, Long-lived spin states for low-field hyperpolarized gas MRI, Chem. Eur. J. 20 (2014) 14629–14632.

[18] K.V. Kovtunov, M.L. Truong, D.A. Barskiy, O.G. Salnikov, V.I. Bukhtiyarov, A.M. Coffey, K.W. Waddell, I.V. Koptyug, E.Y. Chekmenev, Propane-d$_6$ heterogeneously hyperpolarized by parahydrogen, J. Phys. Chem. C 118 (2014) 28234–28243.

[19] W. Dominguez-Viqueira, J. Parra-Robles, M. Fox, W.B. Handler, B.A. Chronik, G. E. Santyr, A variable field strength system for hyperpolarized noble gas MR imaging of rodent lungs, Concept Magn. Res. B 33B (2008) 124–137.

[20] L.L. Tsai, R.W. Mair, M.S. Rosen, S. Patz, R.L. Walsworth, An open-access, very-low-field MRI system for posture-dependent He-3 human lung imaging, J. Magn. Reson. 193 (2008) 274–285.

[21] J.B. Hovener, N. Schwaderlapp, T. Lickert, S.B. Duckett, R.E. Mewis, L.A.R. Highton, S.M. Kenny, G.G.R. Green, D. Leibfritz, J.G. Korvink, J. Hennig, D. von Elverfeldt, A hyperpolarized equilibrium for magnetic resonance, Nat. Commun. 4 (2013) 5.

[22] Y. Zhu, C.-H. Chen, Z. Wilson, I. Savukov, C. Hilty, Milli-tesla NMR and spectrophotometry of liquids hyperpolarized by dissolution dynamic nuclear polarization, J. Magn. Reson. 270 (2016) 71–76.

[23] R.D. Venook, N.I. Matter, M. Ramachandran, S.E. Ungersma, G.E. Gold, N.J. Giori, A. Macovski, G.C. Scott, S.M. Conolly, Prepolarized magnetic resonance imaging around metal orthopedic implants, Magn. Reson. Med. 56 (2006) 177–186.

[24] C. Juchem, T.W. Nixon, S. McIntyre, D.L. Rothman, R.A.d. Graaf, Magnetic field modeling with a set of individual localized coils, J. Magn. Reson. 204 (2010) 281–289.

[25] M. Carravetta, M.H. Levitt, Long-lived nuclear spin states in high-field solution NMR, J. Am. Chem. Soc. 126 (2004) 6228–6229.

[26] M.H. Levitt, Singlet nuclear magnetic resonance, Annu. Rev. Phys. Chem. 63 (2012) 89–105.

[27] M. Carravetta, O.G. Johannessen, M.H. Levitt, Beyond the T_1 limit: singlet nuclear spin states in low magnetic fields, Phys. Rev. Lett. 92 (2004) 153003.

[28] G. Pileio, M. Carravetta, E. Hughes, M.H. Levitt, The long-lived nuclear singlet state of ^{15}N-nitrous oxide in solution, J. Am. Chem. Soc. 130 (2008) 12582–12583.

[29] G. Pileio, M. Carravetta, M.H. Levitt, Storage of nuclear magnetization as long-lived singlet order in low magnetic field, Proc. Natl. Acad. Sci. USA 107 (2010) 17135–17139.

[30] D.A. Barskiy, O.G. Salnikov, A.S. Romanov, M.A. Feldman, A.M. Coffey, K.V. Kovtunov, I.V. Koptyug, E.Y. Chekmenev, NMR Spin-Lock Induced Crossing (SLIC) dispersion and long-lived spin states of gaseous propane at low magnetic field (0.05 T), J. Magn. Reson. 276 (2017) 78–85.

[31] Y.S. Feng, T. Theis, X.F. Liang, Q. Wang, P. Zhou, W.S. Warren, Storage of hydrogen spin polarization in long-lived C-13(2) singlet order and implications for hyperpolarized magnetic resonance imaging, J. Am. Chem. Soc. 135 (2013) 9632–9635.

[32] Y. Feng, T. Theis, T.-L. Wu, K. Claytor, W.S. Warren, Long-lived polarization protected by symmetry, J. Chem. Phys. 141 (2014) 134307.

[33] T. Theis, G.X. Ortiz, A.W.J. Logan, K.E. Claytor, Y. Feng, W.P. Huhn, V. Blum, S.J. Malcolmson, E.Y. Chekmenev, Q. Wang, W.S. Warren, Direct and cost-efficient

hyperpolarization of long-lived nuclear spin states on universal ^{15}N$_2$-diazirine molecular tags, Sci. Adv. 2 (2016) e1501438.

[34] M. Emondts, M.P. Ledbetter, S. Pustelny, T. Theis, B. Patton, J.W. Blanchard, M. C. Butler, D. Budker, A. Pines, Long-lived heteronuclear spin-singlet states in liquids at a zero magnetic field, Phys. Rev. Lett. 112 (2014) 077601.

[35] P. Turschmann, J. Colell, T. Theis, B. Blumich, S. Appelt, Analysis of parahydrogen polarized spin system in low magnetic fields, Phys. Chem. Chem. Phys. 16 (2014) 15411–15421.

[36] P.R. Vasos, A. Comment, R. Sarkar, P. Ahuja, S. Jannin, J.-P. Ansermet, J.A. Konter, P. Hautle, B. van den Brandt, G. Bodenhausen, Long-lived states to sustain hyperpolarized magnetization, Proc. Natl. Acad. Sci. USA 106 (2009) 18469–18473.

[37] M.C.D. Tayler, T.F. Sjolander, A. Pines, D. Budker, Nuclear magnetic resonance at millitesla fields using a zero-field spectrometer, J. Magn. Reson. 270 (2016) 35–39.

[38] P. Nikolaou, A.M. Coffey, L.L. Walkup, B.M. Gust, N. Whiting, H. Newton, S. Barcus, I. Muradyan, M. Dabaghyan, G.D. Moroz, M. Rosen, S. Patz, M.J. Barlow, E.Y. Chekmenev, B.M. Goodson, Near-unity nuclear polarization with an 'open-source' ^{129}Xe hyperpolarizer for NMR and MRI, Proc. Natl. Acad. Sci. USA 110 (2013) 14150–14155.

[39] B. Driehuys, G.D. Cates, E. Miron, K. Sauer, D.K. Walter, W. Happer, High-volume production of laser-polarized Xe-129, Appl. Phys. Lett. 69 (1996) 1668–1670.

[40] A.L. Zook, B.B. Adhyaru, C.R. Bowers, High capacity production of >65% spin polarized xenon-129 for NMR spectroscopy and imaging, J. Magn. Reson. 159 (2002) 175–182.

[41] I.C. Ruset, S. Ketel, F.W. Hersman, Optical pumping system design for large production of hyperpolarized Xe-129, Phys. Rev. Lett. 96 (2006) 053002.

[42] P. Nikolaou, A.M. Coffey, L.L. Walkup, B.M. Gust, N.R. Whiting, H. Newton, I. Muradyan, M. Dabaghyan, K. Ranta, G. Moroz, S. Patz, M.S. Rosen, M.J. Barlow, E.Y. Chekmenev, B.M. Goodson, XeNA: an automated 'open-source' ^{129}Xe hyperpolarizer for clinical use, Magn. Reson. Imaging 32 (2014) 541–550.

[43] T. Theis, P. Ganssle, G. Kervern, S. Knappe, J. Kitching, M.P. Ledbetter, D. Budker, A. Pines, Parahydrogen-enhanced zero-field nuclear magnetic resonance, Nat. Phys. 7 (2011) 571–575.

[44] C.R. Bowers, D.P. Weitekamp, Transformation of symmetrization order to nuclear-spin magnetization by chemical-reaction and nuclear-magnetic-resonance, Phys. Rev. Lett. 57 (1986) 2645–2648.

[45] C.R. Bowers, D.P. Weitekamp, Para-hydrogen and synthesis allow dramatically enhanced nuclear alignment, J. Am. Chem. Soc. 109 (1987) 5541–5542.

[46] T.C. Eisenschmid, R.U. Kirss, P.P. Deutsch, S.I. Hommeltoft, R. Eisenberg, J. Bargon, R.G. Lawler, A.L. Balch, Para hydrogen induced polarization in hydrogenation reactions, J. Am. Chem. Soc. 109 (1987) 8089–8091.

[47] R.W. Adams, J.A. Aguilar, K.D. Atkinson, M.J. Cowley, P.I.P. Elliott, S.B. Duckett, G.G.R. Green, I.G. Khazal, J. Lopez-Serrano, D.C. Williamson, Reversible interactions with para-hydrogen enhance NMR sensitivity by polarization transfer, Science 323 (2009) 1708–1711.

[48] M.J. Cowley, R.W. Adams, K.D. Atkinson, M.C.R. Cockett, S.B. Duckett, G.G.R. Green, J.A.B. Lohman, R. Kerssebaum, D. Kilgour, R.E. Mewis, Iridium N-heterocyclic carbene complexes as efficient catalysts for magnetization transfer from para-hydrogen, J. Am. Chem. Soc. 133 (2011) 6134–6137.

[49] T. Theis, M.L. Truong, A.M. Coffey, R.V. Shchepin, K.W. Waddell, F. Shi, B.M. Goodson, W.S. Warren, E.Y. Chekmenev, Microtesla SABRE enables 10% nitrogen-15 nuclear spin polarization, J. Am. Chem. Soc. 137 (2015) 1404–1407.

[50] M.L. Truong, T. Theis, A.M. Coffey, R.V. Shchepin, K.W. Waddell, F. Shi, B.M. Goodson, W.S. Warren, E.Y. Chekmenev, ^{15}N hyperpolarization by reversible exchange using SABRE-SHEATH, J. Phys. Chem. C 119 (2015) 8786–8797.

[51] D.A. Barskiy, R.V. Shchepin, A.M. Coffey, T. Theis, W.S. Warren, B.M. Goodson, E. Y. Chekmenev, Over 20% ^{15}N hyperpolarization in under one minute for metronidazole, an antibiotic and hypoxia probe, J. Am. Chem. Soc. 138 (2016) 8080–8083.

[52] A.M. Coffey, R.V. Shchepin, M.L. Truong, K. Wilkens, W. Pham, E.Y. Chekmenev, Open-source automated parahydrogen hyperpolarizer for molecular imaging using ^{13}C metabolic contrast agents, Anal. Chem. 88 (2016) 8279–8288.

[53] P. Bhattacharya, E.Y. Chekmenev, W.H. Perman, K.C. Harris, A.P. Lin, V.A. Norton, C.T. Tan, B.D. Ross, D.P. Weitekamp, Towards hyperpolarized ^{13}C-succinate imaging of brain cancer, J. Magn. Reson. 186 (2007) 150–155.

[54] E.Y. Chekmenev, J. Hovener, V.A. Norton, K. Harris, L.S. Batchelder, P. Bhattacharya, B.D. Ross, D.P. Weitekamp, PASADENA hyperpolarization of succinic acid for MRI and NMR spectroscopy, J. Am. Chem. Soc. 130 (2008) 4212–4213.

[55] N.M. Zacharias, H.R. Chan, N. Sailasuta, B.D. Ross, P. Bhattacharya, Real-time molecular imaging of tricarboxylic acid cycle metabolism in vivo by hyperpolarized 1-C-13 diethyl succinate, J. Am. Chem. Soc. 134 (2012) 934–943.

[56] J.-B. Hövener, E.Y. Chekmenev, K.C. Harris, W. Perman, T. Tran, B.D. Ross, P. Bhattacharya, Quality assurance of PASADENA hyperpolarization for ^{13}C biomolecules, Magn. Reson. Mater. Phys. 22 (2009) 123–134.

[57] M. Goldman, H. Johannesson, Conversion of a proton pair para order into C-13 polarization by rf irradiation, for use in MRI, C.R. Physique 6 (2005) 575–581.

[58] M. Suefke, A. Liebisch, B. Blümich, S. Appelt, External high-quality-factor resonator tunes up nuclear magnetic resonance, Nat. Phys. 11 (2015) 767–771.

[59] S. Patz, I. Muradian, M.I. Hrovat, I.C. Ruset, G. Topulos, S.D. Covrig, E. Frederick, H. Hatabu, F.W. Hersman, J.P. Butler, Human pulmonary imaging and

spectroscopy with hyperpolarized Xe-129 at 0.2 T, Acad. Radiol. 15 (2008) 713–727.

[60] E.Y. Chekmenev, V.A. Norton, D.P. Weitekamp, P. Bhattacharya, Hyperpolarized ^{1}H NMR employing low gamma nucleus for spin polarization storage, J. Am. Chem. Soc. 131 (2009) 3164–3165.

[61] S.E. Day, M.I. Kettunen, F.A. Gallagher, D.E. Hu, M. Lerche, J. Wolber, K. Golman, J.H. Ardenkjaer-Larsen, K.M. Brindle, Detecting tumor response to treatment using hyperpolarized C-13 magnetic resonance imaging and spectroscopy, Nat. Med. 13 (2007) 1382–1387.

[62] K. Golman, R. in't Zandt, M. Thaning, Real-time metabolic imaging, Proc. Natl. Acad. Sci. USA 103 (2006) 11270–11275.

[63] A. Comment, M.E. Merritt, Hyperpolarized magnetic resonance as a sensitive detector of metabolic function, Biochemistry 53 (2014) 7333–7357.

[64] P. Bhattacharya, E.Y. Chekmenev, W.F. Reynolds, S. Wagner, N. Zacharias, H.R. Chan, R. Bünger, B.D. Ross, Parahydrogen-induced polarization (PHIP) hyperpolarized MR receptor imaging in vivo: a pilot study of ^{13}C imaging of atheroma in mice, NMR Biomed. 24 (2011) 1023–1028.

[65] K.M. Brindle, Imaging metabolism with hyperpolarized ^{13}C-labeled cell substrates, J. Am. Chem. Soc. 137 (2015) 6418–6427.

[66] R. McDermott, A.H. Trabesinger, M. Muck, E.L. Hahn, A. Pines, J. Clarke, Liquid-state NMR and scalar couplings in microtesla magnetic fields, Science 295 (2002) 2247–2249.

[67] T.F. Sjolander, M.C.D. Tayler, J.P. King, D. Budker, A. Pines, Transition-selective pulses in zero-field nuclear magnetic resonance, J. Phys. Chem. A 120 (2016) 4343–4348.

[68] D.A. Barskiy, K.V. Kovtunov, I.V. Koptyug, P. He, K.A. Groome, Q.A. Best, F. Shi, B. M. Goodson, R.V. Shchepin, M.L. Truong, A.M. Coffey, K.W. Waddell, E.Y. Chekmenev, In situ and ex situ low-field NMR spectroscopy and MRI endowed by SABRE hyperpolarization, ChemPhysChem 15 (2014) 4100–4107.

[69] P. Nikolaou, A.M. Coffey, K. Ranta, L.L. Walkup, B. Gust, M.J. Barlow, M.S. Rosen, B.M. Goodson, E.Y. Chekmenev, Multi-dimensional mapping of spin-exchange optical pumping in clinical-scale batch-mode ^{129}Xe hyperpolarizers, J. Phys. Chem. B 118 (2014) 4809–4816.

[70] P. Nikolaou, A.M. Coffey, L.L. Walkup, B. Gust, C. LaPierre, E. Koehnemann, M.J. Barlow, M.S. Rosen, B.M. Goodson, E.Y. Chekmenev, A 3D-printed high power nuclear spin polarizer, J. Am. Chem. Soc. 136 (2014) 1636–1642.

[71] M. Sarracanie, B.D. Armstrong, J. Stockmann, M.S. Rosen, High speed 3D overhauser-enhanced MRI using combined b-SSFP and compressed sensing, Magn. Reson. Med. 71 (2014) 735–745.

[72] M. Sarracanie, C.D. LaPierre, N. Salameh, D.E.J. Waddington, T. Witzel, M.S. Rosen, Low-cost high-performance MRI, Sci. Rep. 5 (2015) 15177.

[73] M.F. Carias, W. Dominguez-Viqueira, G.E. Santyr, Improving signal-to-noise ratio of hyperpolarized noble gas MR imaging at 73.5 mT using multiturn litz wire radiofrequency receive coils, Concept Magn. Res. B 39B (2011) 37–42.

[74] E. Krjukov, S. Fichele, J.M. Wild, M.N.J. Paley, Design and evaluation of a low field system for hyperpolarized 3-He gas imaging of neonatal lungs, Concept Magn. Res. B 31B (2007) 209–217.

[75] A.K. Venkatesh, A.X. Zhang, J. Mansour, L. Kubatina, C.H. Oh, G. Blasche, M.S. Unlu, D. Balamore, F.A. Jolesz, B.B. Goldberg, M.S. Albert, MRI of the lung gas-space at very low-field using hyperpolarized noble gases, Magn. Reson. Imaging 21 (2003) 773–776.

[76] F.A. Gallagher, M.I. Kettunen, S.E. Day, D.E. Hu, J.H. Ardenkjaer-Larsen, R. in't Zandt, P.R. Jensen, M. Karlsson, K. Golman, M.H. Lerche, K.M. Brindle, Magnetic resonance imaging of pH in vivo using hyperpolarized C-13-labelled bicarbonate, Nature 453 (2008) 940–U973.

[77] J. Kurhanewicz, D.B. Vigneron, K. Brindle, E.Y. Chekmenev, A. Comment, C.H. Cunningham, R.J. DeBerardinis, G.G. Green, M.O. Leach, S.S. Rajan, R.R. Rizi, B.D. Ross, W.S. Warren, C.R. Malloy, Analysis of cancer metabolism by imaging hyperpolarized nuclei: prospects for translation to clinical research, Neoplasia 13 (2011) 81–97.

[78] R.V. Shchepin, D.A. Barskiy, A.M. Coffey, M.A. Feldman, L.M. Kovtunova, V.I. Bukhtiyarov, K.V. Kovtunov, B.M. Goodson, I.V. Koptyug, E.Y. Chekmenev, Robust imidazole-^{15}N$_2$ synthesis for high-resolution low-field (0.05 T) ^{15}N hyperpolarized NMR spectroscopy, ChemistrySelect 2 (2017) 4478–4483.

[79] R.V. Shchepin, M.L. Truong, T. Theis, A.M. Coffey, F. Shi, K.W. Waddell, W.S. Warren, B.M. Goodson, E.Y. Chekmenev, Hyperpolarization of "neat" liquids by NMR signal amplification by reversible exchange, J. Phys. Chem. Lett. 6 (2015) 1961–1967.

[80] R.V. Shchepin, D.A. Barskiy, A.M. Coffey, T. Theis, F. Shi, W.S. Warren, B.M. Goodson, E.Y. Chekmenev, ^{15}N hyperpolarization of imidazole-^{15}N$_2$ for magnetic resonance pH sensing via SABRE-SHEATH, ACS Sensors 1 (2016) 640–644.

Direct Hyperpolarization of Nitrogen-15 in Aqueous Media with Parahydrogen in Reversible Exchange

Johannes F. P. Colell,[†] Meike Emondts,[‡] Angus W. J. Logan,[†] Kun Shen,[†] Junu Bae,[†] Roman V. Shchepin,[§] Gerardo X. Ortiz, Jr.,[†] Peter Spannring,[‖] Qiu Wang,[†] Steven J. Malcolmson,[†] Eduard Y. Chekmenev,[§,⊥] Martin C. Feiters,[‖] Floris P. J. T. Rutjes,[‖] Bernhard Blümich,*[‡] Thomas Theis,*[†] and Warren S. Warren*[†,#]

[†]Department of Chemistry, Duke University, Durham, North Carolina 27708, United States

[‡]Institute for Technical and Macromolecular Chemistry, RWTH Aachen University, Worringerweg 2, 52072 Aachen, Germany

[§]Departments of Radiology and Radiological Sciences, Biomedical Engineering, Physics and Astronomy, Vanderbilt Institute of Imaging Science (VUIIS), Vanderbilt Ingram Cancer Center (VICC), Vanderbilt University, Nashville, Tennessee 37232, United States

[‖]Institute for Molecules and Materials, Radboud University, Heyendaalseweg 135, 6525 AJ Nijmegen, The Netherlands

[⊥]Russian Academy of Sciences, Moscow, Russia

[#]Departments of Physics, Radiology and Biomedical Engineering, Duke University, Durham, North Carolina 27707, United States

S *Supporting Information*
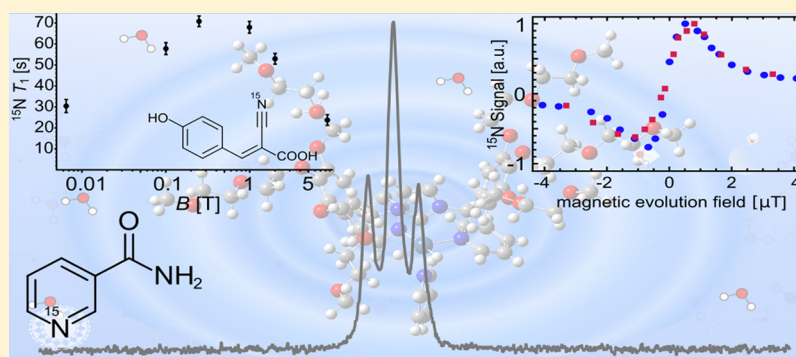
ABSTRACT: Signal amplification by reversible exchange (SABRE) is an inexpensive, fast, and even continuous hyperpolarization technique that uses *para*-hydrogen as hyperpolarization source. However, current SABRE faces a number of stumbling blocks for translation to biochemical and clinical settings. Difficulties include inefficient polarization in water, relatively short-lived ^1H-polarization, and relatively limited substrate scope. Here we use a water-soluble polarization transfer catalyst to hyperpolarize nitrogen-15 in a variety of molecules with SABRE-SHEATH (SABRE in shield enables alignment transfer to heteronuclei). This strategy works in pure H_2O or D_2O solutions, on substrates that could not be hyperpolarized in traditional ^1H-SABRE experiments, and we record ^{15}N T_1 relaxation times of up to 2 min.

INTRODUCTION

NMR and MRI are nondestructive methods to obtain information about molecular structure and spatial morphology. However, magnetic resonance is restricted mainly by the inherently low sensitivity as a result of low thermal polarization levels. For example, NMR spectroscopy and clinical MRI predominantly use highly abundant ^1H nuclei. Even so, observation of low concentration analytes remains challenging. Hyperpolarization methods (e.g., DNP, PHIP, SABRE, SEOP)[1−7] enhance MR signals by 4−5 orders of magnitude and overcome inherent sensitivity limitations.[9−12]

Traditionally, hyperpolarization methods require extensive optimization. Usually methods and optimization are associated with high experimental complexity and cost. In this regard,

signal amplification by reversible exchange (SABRE) stands out because it is simple, fast, and continuously repeatable.[4,13] SABRE uses readily available *para*-hydrogen (p-H_2) as a source of polarization. The transfer occurs in reversibly formed substrate−hydrogen adducts in a transition metal complex. The magnetic evolution field B_{evo} must be sufficiently low to mix energy levels between hydride-^1H and the target nucleus to establish a path for polarization transfer.[7,14] While protons in the substrate are targeted at magnetic fields around 65 G,[15] transfer to heteronuclei (e.g., ^{15}N, ^{13}C, ^{31}P) occurs at μT magnetic fields using a technique termed SABRE in shield

enables alignment transfer to heteronuclei (SABRE-SHEATH).[7,8] As shown in Scheme 1, the required hardware is relatively simple.

Scheme 1. A sample is hyperpolarized via SABRE-SHEATH for an evolution time t_{evo} at optimized matching field B_{evo} of ~0.5 μT established by a small solenoid coil in a magnetic shield that attenuates the Earth's magnetic field and transferred into a Benchtop (1 T) NMR spectrometer or conventional high-field (8.45 T) spectrometer for detection.
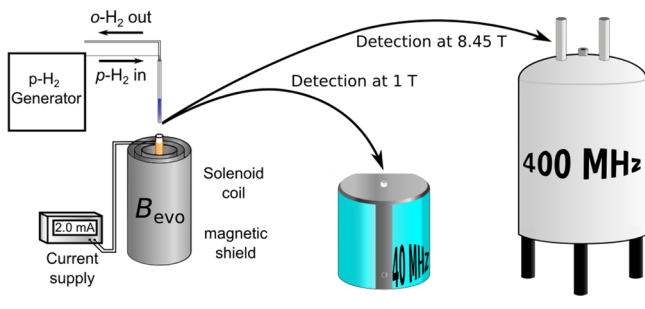
As a result of experimental simplicity and its promise, SABRE and SABRE-SHEATH are now attracting an increasing number of research groups contributing to its rapid development.[4,7,15−21] A milestone for SABRE was the transition from organic solvents to aqueous solutions, which was recently achieved for [1]H-SABRE.[22−28]

Still, for ^{1}H spin−lattice relaxation times are relatively short and the substrate scope is limited. Direct polarization transfer to heteronuclei has not been demonstrated in an aqueous environment. Hyperpolarizing nitrogen-15 via SABRE-SHEATH allows a wider range of structural motifs, and relaxation times are characteristically larger.

SABRE-SHEATH with ^{15}N targets is made accessible with the water-soluble [IrCl(IDEG)(COD)] precatalyst (**1a**). As shown in Scheme 2 the precatalyst is converted to the catalytically active species (**1**) in the presence of substrates under a hydrogen atmosphere.[22] At μT magnetic field hydride and ^{15}N energy levels match and the spin system coherently evolves with a rate given by J_{NH}- into ^{15}N-polarization on substrates.[29]

We investigate different molecular motifs found in medical drugs, biomolecules, and molecular tags. Structural motifs could be readily translated from the established [IrCl(IMes)(COD)] system.[16,30]

Pyridine (**2**), the canonical SABRE substrate,[4] was a logical first choice. Next, nitriles are often encountered in drugs,[31] polarize consistently well, tolerate complex backbones, and show large ^{15}N-SABRE-SHEATH enhancements, despite little to no [1]H-SABRE enhancements.[30,32] We selected benzonitrile (**3**) and α-cyano-4-hydroxycinnamic acid (**4**) (CHCA, buffered with NaOD to pH 7.5). Diazirines, which also do not exhibit ^{1}H enhancements, are common biomolecular tags that can replace CH_2 groups in many classes of biomolecules.[33] Here we use 2-cyano-3-(D_3-methyl-[15]N_2-diazirine)propanoic acid (**5**). Lastly, we focus on nicotinamide (**6**), the amide of vitamin B_3, which could be tolerated in vivo at detectable concentrations[34−36] and is a potential option for translation to biomedical studies.[20,37]

For these substrates we detail hyperpolarization levels, carefully characterize temperature and magnetic field dependencies, consider the effect of deuterated vs protonated solvents

Scheme 2. Precatalyst [IrCl(IDEG)(COD)] (1a) is transformed into the active species [Ir(IDEG)(H)$_2$Sub$_3$] (Sub = Substrate) (1) in presence of a substrate of choice (2−6) under a hydrogen atmosphere; reversible exchange leads to polarization buildup on ^{15}N within 30−120 s; the polarization transfer is primarily driven by the N−H coupling through the bonds that form a 180° angle as the N−H coupling through bonds forming a 90° angle is close to zero.
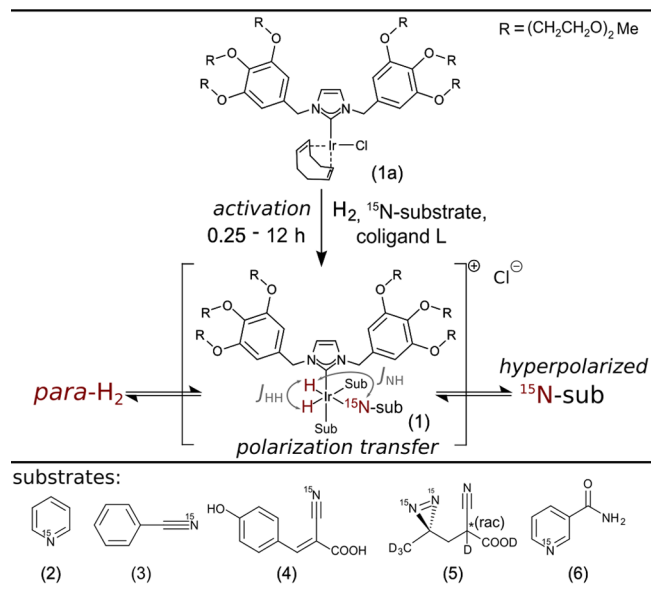
(D_2O vs H_2O), and measure relaxation time constants at various magnetic fields.

■ RESULTS AND DISCUSSION

In Figure 1 we show a comparison between single-scan spectra originating from compounds directly SABRE-SHEATH hyperpolarized in aqueous medium, referenced to thermally polarized neat ^{15}N-pyridine at 8.45 T. Concentrations of investigated compounds are different as a result of solubility as well as sample loss phenomena for benzonitrile and pyridine. Both pyridine and benzonitrile were initially prepared as 100 mM solutions, but after activation by H_2 bubbling the concentrations were significantly reduced.

A synopsis of experimental results and conditions is given in Table 1 (experimental details provided in Materials and Methods). Spectra are acquired at 1 T and 8.45 T (see Scheme 1) to study the field dependence of T_1 relaxation as detailed below. The 1 T measurements also demonstrate the feasibility of high-sensitivity single-scan ^{15}N detection with a benchtop NMR system. Furthermore, to determine the effect of proton-containing solvents, nicotinamide was investigated in H_2O.

We find that polarization levels in deuterated solvents are largely independent of the detection field; that is, enhancements simply scale with the thermal polarization. In contrast, for nicotinamide in H_2O (Table 1, entry 6), we observe lower apparent polarization levels at 8.45 T. This is caused by relaxation losses during transfer because it takes much longer to transfer the sample into the high-field magnet (~8 s) than into the benchtop device sitting right next to the magnetic shields (~2 s). The solvent protons (and deuterons) are in chemical exchange with the ^{15}N-substrate, where they cause spin−dipole
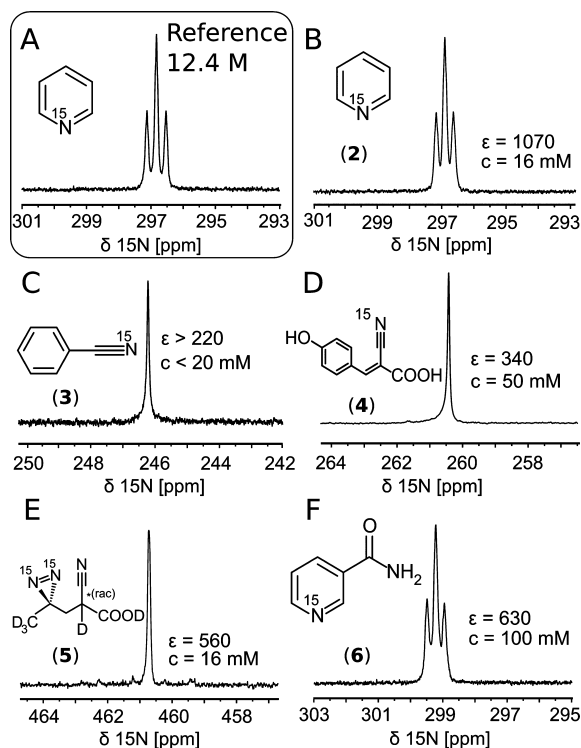
Figure 1. ^{15}N spectra of (A) thermally polarized reference at 8.45 T and (B−F) hyperpolarized compounds (in D$_2$O unless denoted otherwise). (A) Neat ^{15}N-pyridine, (B) ^{15}N-pyridine, (C) ^{15}N-benzonitrile, (D) ^{15}N-CHCA, (E) ^{15}N$_2$-diazirine, (F) ^{15}N-nicotinamide (in H$_2$O).

methanol and catalyst 1 in H$_2$O/D$_2$O as a function of these variables (T, B_{evo}).
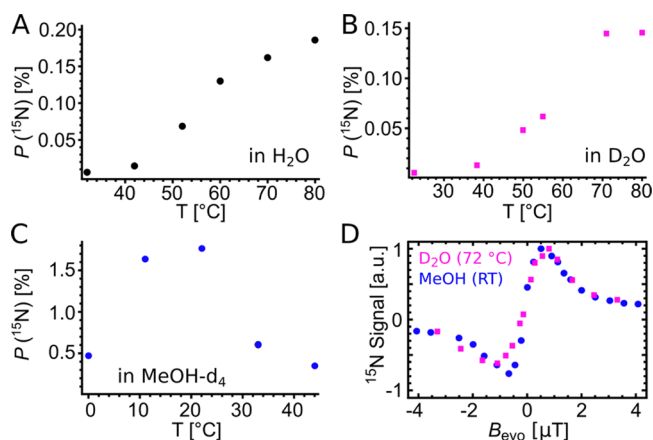
Figure 2. Comparison of ^{15}N polarization as a function of temperature in (A) H$_2$O, (B) D$_2$O, and (C) methanol-d$_4$ at $B_{evo} = 0.5$ μT. (D) Hyperpolarized signals as a function of μT field at the temperature corresponding to the maximum polarization in the respective solvents: 22 °C for ^{15}N-acetonitrile in methanol-d$_4$ and 72 °C for ^{15}N-CHCA in D$_2$O (blue: 5 mM [IrCl(IMes)(COD)], 30 mM pyridine, 100 mM ^{15}N-CH$_3$CN, methanol-d$_4$; magenta: 5 mM [IrCl(IDEG)(COD)], 30 mM pyridine, 50 mM ^{15}N-CHCA, D$_2$O).

relaxation. This relaxation mechanism scales with the distance between the relaxation partners r_{ij}^{-6} as well as the gyromagnetic ratio, which is 6.5 times smaller for deuterium,[38,39] explaining the observed differences between solvents.

SABRE-SHEATH in water gives rise to a new set of challenges. Water has significantly higher viscosity and surface tension than methanol, and at room temperature the solubility of hydrogen in water is 5 times lower.[40,41] We observed that some samples, specifically nonpolar liquid-state substrates (e.g., benzonitrile and pyridine), are extracted from the solvent when bubbling with hydrogen during the polarization buildup. Nicotinamide and CHCA, both crystalline solids when isolated, were used for systematic studies, as substrate loss did not occur.[20]

Of particular interest are the dependence of the ^{15}N polarization on temperature and magnetic evolution field B_{evo}. Figure 2 contrasts the established [IrCl(IMes)(COD)] in

The temperature dependence was studied using a 100 mM nicotinamide sample. For catalyst system 1 in H$_2$O (Figure 2A) and D$_2$O (Figure 2B) the ^{15}N polarization increases with temperature. In contrast, in methanol (Figure 2C, [IrCl(IMes)-(COD)] precursor) the largest polarization is recorded at room temperature.

The magnetic field dependence is shown in Figure 2D. We compare normalized data (max. ^{15}N polarization: 0.13% in D$_2$O, 1.7% in MeOH-d$_4$) of two nitrile/solvent systems: first, in blue, ^{15}N-acetonitrile in MeOH-d$_4$ with [IrCl(IMes)(COD)] and second, in magenta, ^{15}N-CHCA in D$_2$O with [IrCl-(IDEG)(COD)] (1a).

We note that nitriles are better suited for this study than nicotinamide, as enhancements are more robust and reproducible. Additionally, they exhibit inversion of the NMR signal upon inversion of B_{evo}. Variation of the temperature changes the dissociation rate constants of substrate and catalyst-bound H$_2$.[14,16,42] Optimal polarization transfer efficiency is expected when the exchange rate k_{diss} is on the order of the ^{15}N to hydride J_{NH}-coupling across the iridium center (see Scheme 2).[14,42] Figure 1A−C show that the IMes catalyst in methanol yields the largest ^{15}N polarization at room temperature,

Table 1. Synopsis of Experimental Conditions, Enhancements, and Polarization Levels[a]

substrate	activation time [h]	$c_{substrate}/c_{catalyst}$	$c_{Substrate}$ [mM]	enhancement 8.45 T (P [%])	enhancement 1 T (P [%])	enhancement ratio (1 T/ 8.45 T)
(2) pyridine	12	3.3	16.5[c]	1100	[d]	[d]
(3) benzonitrile	0.25	20	50[b,c]	90	[d]	[d]
(4) CHCA	12	10	50	440 (0.13)	3700 (0.13)	8.4
(5) diazirine	6	10	16.3	560 (0.16)	4700 (0.17)	8.4
(6) nicotinamide	12	20	100	520 (0.16)	6100 (0.21)	8.9
(6) nicotinamide H$_2$O	12	20	100	630 (0.2)	10 500 (0.37)	28

[a]Substrates are ^{15}N labeled, solvent is D$_2$O unless otherwise specified. Concentrations of liquid substrates are determined at the time of the experiment using ^{1}H spectroscopy. T = 75 °C. [b]Signal maximum obtained 30 min after activation, subsequent substrate loss due to evaporation. [c]Initial concentration 100 mM. [d]Insufficient S/N ratio.

whereas catalyst **1** requires significantly elevated temperatures to achieve comparable exchange rates leading to maximum polarization. On the basis of these insights it is reasonable to expect ^{15}N polarization in water to decrease at even higher temperatures, in analogy to methanol, as shown in Figure 2C.

As seen in Figure 2D, the methanol and water systems show very similar responses to B_{evo} at their respective optimized temperatures (22 and 72 °C). The response curves originate from two distinct matching conditions associated with overpopulation in ^{15}N-α or ^{15}N-β, giving either positive or negative NMR signal with identical polarization levels.[30] The matching conditions are given by[7]

$$B_{evo} = \pm \frac{J_{HH} + J_{NH}/2}{\gamma_H - \gamma_N} \quad (1)$$

where J_{HH} is the hydride to hydride J-coupling ($\sim$10 Hz) and J_{NH} the hydride to ^{15}N coupling ($\sim$20 Hz) in **1**. Experimentally, we observe maxima at $B_{evo} \approx \pm 0.5$ μT, which is slightly higher than the ± 0.3 μT predicted from eq 1, as the limited lifetime broadens the matching conditions.

Taken together, the observations of Figure 1A−D suggest that the activation energy of substrate dissociation from **1** is significantly larger than for the established [IrCl(IMes)-(COD)]−methanol systems. This is also supported by the fact that catalyst **1** in methanol at RT did not yield any enhancement.

The absolute polarization level in D_2O is about one order of magnitude smaller than for the methanol system, when compared at their respective optimized temperatures (^{15}N-CHCA in D_2O, $P(^{15}N) = 0.13\%$, ^{15}N-CH$_3$CN in d_4-MeOH, $P(^{15}N) = 1.7\%$). Interestingly, this difference in hyperpolarization level can simply be attributed to the difference in hydrogen solubility (factor 5) and the difference in solvent concentration ($c(H_2O) = 55$ mol/L, $c(MeOH) = 28$ mol/L, factor 2).

Current experimental data and theoretical considerations indicate that SABRE polarization levels are limited by the exchange of hydrides on the iridium center and the exchange kinetics of other ligand types (substrate/solvent), as well as both pressure and flow rate of *para*-hydrogen. Exchange of hydrogen restores the polarization source to the active complex species and the process proceeds via the mixed classical/nonclassical hydride [Ir(H)$_2$(η-H$_2$)(IMes)L$_2$], with arbitrary ligands L.[14,16] Formation of this species requires collision between a 16-electron complex and a hydrogen molecule, where collision with a *para*-hydrogen molecule may refresh the active species. As a result, the polarization is proportional to the concentration of *para*-hydrogen in solution, not the saturation concentration of hydrogen (*ortho* + *para*). Accordingly, the pressure dependence of polarizations is relatively weak, whereas dependence on the flow rate is significant. Depending on system composition, a linear or exponential dependence of ^{15}N polarization on the flow rate was reported.[30,43,44] We conclude that the *para*-hydrogen enrichment in solution is limited by the exchange at the gas−liquid interface.

Let us now consider the substrate exchange process. The rates of ligand dissociation k_{diss} and association k_{asso} determine not only the lifetime of the complex, where polarization transfer from the hydrides to the target nuclei occurs, but also the concentration of the 16-electron species required for the hydride exchange.[14] As a result ^{15}N polarization depends directly on the concentration of the 16-electron species.

Accordingly, the largest polarizations are observed at relatively low catalyst concentrations and high catalyst loadings. It is noteworthy that an exponential dependence of polarization on the substrate concentrations has been observed by Appleby et al.[45]

We point out that all reported polarization levels are not optimized with respect to sample composition, concentrations, hydrogen pressure, or flow rate. Optimization of catalyst concentration and loading afforded an 8−10-fold increase of ^{15}N polarization level for the methanol system. Maximum polarizations are recorded at low catalyst concentrations and high catalyst loadings (^{15}N-nicotinamide $P(^{15}N) = 7\%$, ^{15}N-benzonitrile $P(^{15}N) = 16\%$, metronidazole at natural abundance $P(^{15}N) = 20\%$).[7,14,18,43,46] We conclude that ^{15}N polarization can be increased by at least a factor 10 by using low substrate concentrations and high catalyst loading. Further improvements are expected by modifications to the experimental setup to allow for more effective mixing of hydrogen and solvent at higher pressures.

^{15}N Relaxation Times in Water. Of particular importance for hyperpolarization applications is the spin−lattice relaxation time T_1, which defines the viable time delay between preparation of hyperpolarization and detection. We examined the T_1 lifetime for ^{15}N-nicotinamide[46] and ^{15}N-CHCA, which constitute biocompatible compounds and contain ^{15}N in chemically different environments.[46−48] Table 2 shows the ^{15}N T_1 relaxation times in D_2O, which at 1 T exceed 1 min for both compounds.

Table 2. ^{15}N T_1 Times of 100 mM Nicotinamide and 50 mM CHCA in D_2O at Different Detection Fields

	T_1 [s] 1 T	T_1 [s] 8.45 T
^{15}N-CHCA	71 ± 15[a]	24 ± 3
^{15}N-nicotinamide	116 ± 10	32[b] ± 4

[a]Detected and stored at 1 T. Control by detection at 8.45 T: $T_1 = 68 \pm 2$ s. [b]In H_2O: 32 ± 5.5 s.

For ^{15}N-nicotinamide at 8.45 T we find the effect of proton-containing solvent (H_2O) on the T_1 time to be negligible. It should be noted that the ^{15}N T_1 time of nicotinamide at 8.45 T and room temperature is close to the T_1 reported for ^{13}C in the ^{13}C(1)-pyruvate markers currently in clinical use for prostate cancer diagnostics ($T_1 = 29.2$ s in vivo, $T_1 = 60$ s, ex vivo, 3 T).[9,10] It is noteworthy that the ^{13}C T_1 values in vivo are smaller than those ex vivo, characteristic for diffusion in constricted environments.

To elucidate this field dependence in more detail, we hyperpolarized ^{15}N-CHCA and held the sample at different fields for variable times prior to detection. The results are shown in Figure 3, displaying ^{15}N-relaxation time of CHCA (50 mM, pH 7.5, D_2O) at different magnetic fields. For this compound relatively low magnetic fields of about 0.2 T give the longest relaxation times. This is an intriguing finding in the context of low-field approaches to NMR and MRI,[49,50] which could be coupled with SABRE to establish low-cost spectroscopy and molecular imaging.

The scaling of signal-to-noise with magnetic field strongly depends on the exact experimental conditions. For traditional thermal NMR, the signal is proportional to polarization and the induction. Both terms are proportional to B_0; thus the signal scales with B_0^2.[38,51] In NMR, coil noise is typically dominant,
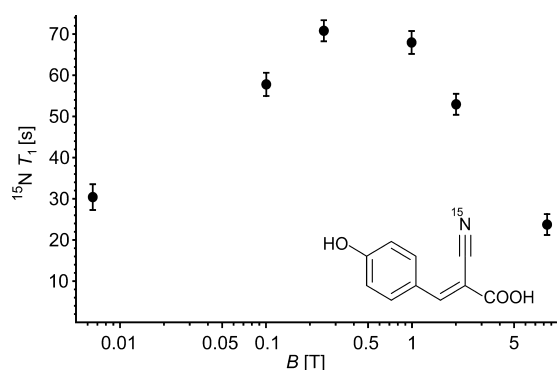
Figure 3. ^{15}N T_1 time constant of CHCA as a function of the magnetic field. The sample is hyperpolarized and stored at a given field for an incremented delay time and detected at 8.45 T.

which scales as $B_0^{1/4}$; hence signal-to-noise (S/N) is proportional to $B_0^{7/4}$.[51−53] However, with a hyperpolarized sample spin polarization is independent of B_0 and, thus, S/N scales with $B_0^{3/4}$.

Another scenario arises for human MRI. Here, dielectric losses dominate, which are proportional to B_0. Thus, S/N only increases proportional to B_0 for thermal MRI experiments.[52,54] Therefore, S/N is expected to be independent of B_0 for hyperpolarized human MRI.[55,56] MRI in low magnetic fields has significant advantages, as magnet and RF-circuit design are flexible, easy to construct, and relatively inexpensive.[56,57] For example, high-performance ^1H-MRI at 6.5 mT with thermal magnetization has already been reported.[49] It is noteworthy that recent advances in the low-field domain, such as "external high-quality-factor-enhanced NMR" (EHQE-NMR)[58] and others,[59] lead to S/N independent of B_0 even for spectroscopic applications.

■ MATERIALS AND METHODS

Solutions of substrates in D_2O/H_2O were added to [IrCl(IDEG)-(COD)] (IDEG = 1,3-bis(3,4,5-tris(diethyleneglycol)benzyl))-imidazole-2-ylidene), COD = 1,5-cyclooctadiene), stirred until a homogeneous solution of known concentration in catalyst is obtained, and transferred to a 5 mm medium wall pressure NMR tube (Wilmad 524-PV-7). The typical sample volume was 350 μL. The solution was bubbled with argon for 30 min and pressurized with 10 bar of para-H_2, and hydrogen flow was adjusted to obtain adequate bubbling. Catalyst activation times were 0.25−12 h depending on substrate, solvent (deuterated solvents require longer activation times), and temperature. Catalyst activation can be sped up significantly by raising the temperature. For SABRE-SHEATH experiments para-H_2 (Bruker BPHG 090, 38 K, 90%) was bubbled through a sample placed in a μT magnetic field. Hyperpolarization buildup is achieved in 0.5−2 min. The μT field is generated by a small solenoid inside a magnetic shield (see Scheme 1). The sample temperature was controlled with a water bath inside the magnetic shields. Measurements were performed with a Bruker Avance DX 360 (8.45 T) or Magritek Spinsolve ^1H/^{15}N spectrometer (1 T). Enhancements are calculated relative to neat ^{15}N-labeled pyridine. The concentration in the samples was monitored by ^1H spectroscopy.

■ CONCLUSIONS

We have demonstrated SABRE-SHEATH hyperpolarization of ^{15}N in aqueous media at moderate temperatures (20−80 °C) and achieve up to 1000-fold enhancements over thermal measurements at 8.45 T. We applied SABRE-SHEATH in water to biocompatible marker groups in different molecules (CHCA, nicotinamide, diazirine moieties). Hyperpolarization

of ^{15}N-nitrile and the $^{15}N_2$-diazirine exemplifies how SABRE-SHEATH is amenable to more substrate classes because ^{15}N is closer to the hyperpolarization source than protons in the molecular backbone.

Furthermore, we demonstrated T_1 times comparable to, or exceeding, clinically used DNP tracers.[9,10] For example, nicotinamide in D_2O exhibits a ^{15}N relaxation time of 2 min, which is significantly longer than typical ^1H-T_1 (seconds) of traditional ^1H-SABRE substrates. Still, recent advances have demonstrated long-lived ^1H singlet states with decay times of up to 4.5 min.[37] When such strategies are translated to ^{15}N, lifetimes in excess of 20 min become available.[60]

Imaging applications of SABRE hyperpolarized protons[25] as well as nitrogen-15 have already been reported.[43] Hyperpolarized heteronuclei are beneficial, as they are background free and have a large chemical shift range, which allows for easy chemical identification. Future developments may be expected to advance SABRE to in vivo molecular imaging complementing DNP-hyperpolarized ^{13}C tracers, which have quickly become an essential and routine tool, giving detailed and fundamental insight into in vivo metabolism and biochemistry.[9,10,61−65]

■ ASSOCIATED CONTENT

ⓢ Supporting Information

The Supporting Information is available free of charge on the ACS Publications website at DOI: 10.1021/jacs.7b00569.

> Relaxation time measurements, detailed description of experimental procedures, spectral data, physicochemical reference data for H_2O (PDF)

■ AUTHOR INFORMATION

Corresponding Authors
*bluemich@itmc.rwth-aachen.de
*thomas.theis@duke.edu
*warren.warren@duke.edu
ORCID ⓘ
Johannes F. P. Colell: 0000-0001-9020-344X
Qiu Wang: 0000-0002-6803-9556
Steven J. Malcolmson: 0000-0003-3229-0949
Eduard Y. Chekmenev: 0000-0002-8745-8801
Floris P. J. T. Rutjes: 0000-0003-1538-3852
Thomas Theis: 0000-0001-6779-9978
Notes
The authors declare no competing financial interest.

■ ACKNOWLEDGMENTS

■ REFERENCES

(1) Carver, T. R.; Slichter, C. P. Phys. Rev. **1956**, 102, 975−980.

(2) Cudalbu, C.; Comment, A.; Kurdzesau, F.; van Heeswijk, R. B.; Uffmann, K.; Jannin, S.; Denisov, V.; Kirik, D.; Gruetter, R. *Phys. Chem. Chem. Phys.* **2010**, *12*, 5818−5823.

(3) Shchepin, R. V.; Coffey, A. M.; Waddell, K. W.; Chekmenev, E. Y. *Anal. Chem.* **2014**, *86*, 5601−5605.

(4) Adams, R. W.; Aguilar, J. A.; Atkinson, K. D.; Cowley, M. J.; Elliott, P. I. P.; Duckett, S. B.; Green, G. G. R.; Khazal, I. G.; Lopez-Serrano, J.; Williamson, D. C. *Science* **2009**, *323*, 1708−1711.

(5) Bowers, C. R.; Weitekamp, D. P. *Phys. Rev. Lett.* **1986**, *57*, 2645−2648.

(6) Ben-Amar Baranga, A.; Appelt, S.; Romalis, M. V.; Erickson, C. J.; Young, A. R.; Cates, G. D.; Happer, W. *Phys. Rev. Lett.* **1998**, *80*, 2801−2804.

(7) Theis, T.; Truong, M. L.; Coffey, A. M.; Shchepin, R. V.; Waddell, K. W.; Shi, F.; Goodson, B. M.; Warren, W. S.; Chekmenev, E. Y. *J. Am. Chem. Soc.* **2015**, *137*, 1404−1407.

(8) Barskiy, D. A.; Shchepin, R. V.; Tanner, C.; Colell, J. F. P.; Goodson, B. M.; Theis, T.; Warren, W. S.; Chekmenev, E. Y. *ChemPhysChem* **2017**, DOI: 10.1002/cphc.201700416.

(9) Kurhanewicz, J.; Vigneron, D. B.; Brindle, K.; Chekmenev, E. Y.; Comment, A.; Cunningham, C. H.; DeBerardinis, R. J.; Green, G. G.; Leach, M. O.; Rajan, S. S.; Rizi, R. R.; Ross, B. D.; Warren, W. S.; Malloy, C. R. *Neoplasia* **2011**, *13*, 81−97.

(10) Nelson, S. J.; Kurhanewicz, J.; Vigneron, D. B.; Larson, P. E. Z.; Harzstark, A. L.; Ferrone, M.; van Criekinge, M.; Chang, J. W.; Bok, R.; Park, I.; Reed, G.; Carvajal, L.; Small, E. J.; Munster, P.; Weinberg, V. K.; Ardenkjaer-Larsen, J. H.; Chen, A. P.; Hurd, R. E.; Odegardstuen, L. I.; Robb, F. J.; Tropp, J.; Murray, J. A. *Sci. Transl. Med.* **2013**, *5*, 198ra108−198ra108.

(11) Eshuis, N.; van Weerdenburg, B. J. A.; Feiters, M. C.; Rutjes, F. P. J. T.; Wijmenga, S. S.; Tessari, M. *Angew. Chem., Int. Ed.* **2015**, *54*, 1372−1372.

(12) Eshuis, N.; Hermkens, N.; van Weerdenburg, B. J. A.; Feiters, M. C.; Rutjes, F. P. J. T.; Wijmenga, S. S.; Tessari, M. *J. Am. Chem. Soc.* **2014**, *136*, 2695−2698.

(13) Hövener, J.-B.; Schwaderlapp, N.; Lickert, T.; Duckett, S. B.; Mewis, R. E.; Highton, L. A. R.; Kenny, S. M.; Green, G. G. R.; Leibfritz, D.; Korvink, J. G.; Hennig, J.; von Elverfeldt, D. *Nat. Commun.* **2013**, *4*, 2946.

(14) Barskiy, D. A.; Pravdivtsev, A. N.; Ivanov, K. L.; Kovtunov, K. V.; Koptyug, I. V. *Phys. Chem. Chem. Phys.* **2015**, *89*, 89−93.

(15) Zeng, H.; Xu, J.; Gillen, J.; McMahon, M. T.; Artemov, D.; Tyburn, J.-M.; Lohman, J. A. B.; Mewis, R. E.; Atkinson, K. D.; Green, G. G. R.; Duckett, S. B.; van Zijl, P. C. M. *J. Magn. Reson.* **2013**, *237*, 73−78.

(16) Cowley, M. J.; Adams, R. W.; Atkinson, K. D.; Cockett, M. C. R.; Duckett, S. B.; Green, G. G. R.; Lohman, J. A. B.; Kerssebaum, R.; Kilgour, D.; Mewis, R. E. *J. Am. Chem. Soc.* **2011**, *133*, 6134−6137.

(17) Theis, T.; Truong, M.; Coffey, A. M.; Chekmenev, E. Y.; Warren, W. S. *J. Magn. Reson.* **2014**, *248*, 23−26.

(18) Barskiy, D. A.; Shchepin, R. V.; Coffey, A. M.; Theis, T.; Warren, W. S.; Goodson, B. M.; Chekmenev, E. Y. *J. Am. Chem. Soc.* **2016**, *138*, 8080−8083.

(19) Nikolaou, P.; Goodson, B. M.; Chekmenev, E. Y. *Chem. - Eur. J.* **2015**, *21*, 3156−3166.

(20) Shchepin, R. V.; Barskiy, D. A.; Coffey, A. M.; Theis, T.; Shi, F.; Warren, W. S.; Goodson, B. M.; Chekmenev, E. Y. *ACS Sensors* **2016**, *1*, 640−644.

(21) Shchepin, R. V.; Chekmenev, E. Y. *J. Labelled Compd. Radiopharm.* **2014**, *57*, 621−624.

(22) Spannring, P.; Reile, I.; Emondts, M.; Schleker, P. P. M.; Hermkens, N. K. J.; van der Zwaluw, N. G. J.; van Weerdenburg, B. J. A.; Tinnemans, P.; Tessari, M.; Blümich, B.; Rutjes, F. P. J. T.; Feiters, M. C. *Chem. - Eur. J.* **2016**, *22*, 9277−9282.

(23) Truong, M. L.; Shi, F.; He, P.; Yuan, B.; Plunkett, K. N.; Coffey, A. M.; Shchepin, R. V.; Barskiy, D. A.; Kovtunov, K. V.; Koptyug, I. V.; Waddell, K. W.; Goodson, B. M.; Chekmenev, E. Y. *J. Phys. Chem. B* **2014**, *18*, 13882−13889.

(24) Fekete, M.; Bayfield, O.; Duckett, S. B.; Hart, S.; Mewis, R. E.; Pridmore, N.; Rayner, P. J.; Whitwood, A. *Inorg. Chem.* **2013**, *52*, 13453−13461.

(25) Rovedo, P.; Knecht, S.; Bäumlisberger, T.; Cremer, A. L.; Duckett, S. B.; Mewis, R. E.; Green, G. G. R.; Burns, M. J.; Rayner, P. J.; Leibfritz, D.; Korvink, J. G.; Hennig, J.; Pütz, G.; von Elverfeldt, D.; Hövener, J.-B. *J. Phys. Chem. B* **2016**, *120*, 5670−5677.

(26) Hövener, J.-B.; Schwaderlapp, N.; Borowiak, R.; Lickert, T.; Duckett, S. B.; Mewis, R. E.; Adams, R. W.; Burns, M. J.; Highton, L. A. R.; Green, G. G. R.; Olaru, A.; Hennig, J.; von Elverfeldt, D. *Anal. Chem.* **2014**, *86*, 1767−1774.

(27) Zeng, H.; Xu, J.; McMahon, M. T.; Lohman, J. A. B.; van Zijl, P. C. M. *J. Magn. Reson.* **2014**, *246*, 119−121.

(28) Shi, F.; He, P.; Best, Q. A.; Groome, K.; Truong, M. L.; Coffey, A. M.; Zimay, G.; Shchepin, R. V.; Waddell, K. W.; Chekmenev, E. Y.; Goodson, B. M. *J. Phys. Chem. C* **2016**, *120*, 12149−12156.

(29) Barskiy, D. A.; Pravdivtsev, A. N.; Ivanov, K. L.; Kovtunov, K. V.; Koptyug, I. V. *Phys. Chem. Chem. Phys.* **2015**, *18*, 89−93.

(30) Colell, J. F. P.; Logan, A. W. J.; Zhou, Z.; Shchepin, R. V.; Barskiy, D. A.; Ortiz, G. X.; Wang, Q.; Malcolmson, S. J.; Chekmenev, E. Y.; Warren, W. S.; Theis, T. *J. Phys. Chem. C* **2017**, *121*, 6626.

(31) Fleming, F. F.; Yao, L.; Ravikumar, P. C.; Funk, L.; Shook, B. C. *J. Med. Chem.* **2010**, *53*, 7902−7917.

(32) Mewis, R. E.; Green, R. A.; Cockett, M. C. R.; Cowley, M. J.; Duckett, S. B.; Green, G. G. R.; John, R. O.; Rayner, P. J.; Williamson, D. C. *J. Phys. Chem. B* **2015**, *119*, 1416−1424.

(33) Dubinsky, L.; Krom, B. P.; Meijler, M. M. *Bioorg. Med. Chem.* **2012**, *20*, 554−570.

(34) Bergmann, F.; Wislicki, L. *Br. J. Pharmacol. Chemother.* **1953**, *8*, 49−53.

(35) Guyton, J. R.; Blazing, M. A.; Hagar, J.; Kashyap, M. L.; Knopp, R. H.; McKenney, J. M.; Nash, D. T.; Nash, S. D. *Arch. Intern. Med.* **2000**, *160*, 1177−1184.

(36) Libri, V.; Yandim, C.; Athanasopoulos, S.; Loyse, N.; Natisvili, T.; Law, P. P.; Chan, P. K.; Mohammad, T.; Mauri, M.; Tam, K. T.; Leiper, J.; Piper, S.; Ramesh, A.; Parkinson, M. H.; Huson, L.; Giunti, P.; Festenstein, R. *Lancet* **2014**, *384*, 504−513.

(37) Roy, S. S.; Norcott, P.; Rayner, P. J.; Green, G. G. R.; Duckett, S. B. *Angew. Chem., Int. Ed.* **2016**, *55*, 15642−15645.

(38) Abragam, A. *The Principles of Nuclear Magnetism*; Clarendon Press: Oxford, 1961.

(39) Halbach, K. *Nucl. Instrum. Methods* **1980**, *169*, 1−10.

(40) Crozier, T. E.; Yamamoto, S. *J. Chem. Eng. Data* **1974**, *19*, 242−244.

(41) Brunner, E. *J. Chem. Eng. Data* **1985**, *30*, 269−273.

(42) Knecht, S.; Pravdivtsev, A. N.; Hövener, J.-B.; Yurkovskaya, A. V.; Ivanov, K. L. *RSC Adv.* **2016**, *6*, 24470−24477.

(43) Truong, M. L.; Theis, T.; Coffey, A. M.; Shchepin, R. V.; Waddell, K. W.; Shi, F.; Goodson, B. M.; Warren, W. S.; Chekmenev, E. Y. *J. Phys. Chem. C* **2015**, *119*, 8786−8797.

(44) Shchepin, R. V.; Truong, M. L.; Theis, T.; Coffey, A. M.; Shi, F.; Waddell, K. W.; Warren, W. S.; Goodson, B. M.; Chekmenev, E. Y. *J. Phys. Chem. Lett.* **2015**, *6*, 1961−1967.

(45) Appleby, K. M.; Mewis, R. E.; Olaru, A. M.; Green, G. G. R.; Fairlamb, I. J. S.; Duckett, S. B. *Chem. Sci.* **2015**, *6*, 3981−3993.

(46) Shchepin, R. V.; Barskiy, D. A.; Mikhaylov, D. M.; Chekmenev, E. Y. *Bioconjugate Chem.* **2016**, *27*, 878−882.

(47) Wang, H.; Lanks, K. W. *Cancer Res.* **1986**, *46*, 5349−5352.

(48) Olaru, A. M.; Burns, M. J.; Green, G. G. R.; Duckett, S. B. *Chem. Sci.* **2016**, *8*, 2257−2266.

(49) Sarracanie, M.; LaPierre, C. D.; Salameh, N.; Waddington, D. E. J.; Witzel, T.; Rosen, M. S. *Sci. Rep.* **2015**, *5*, 15177.

(50) Danieli, E.; Mauler, J.; Perlo, J.; Blümich, B.; Casanova, F. *J. Magn. Reson.* **2009**, *198*, 80−87.

(51) Hoult, D. I.; Richards, R. E. *J. Magn. Reson.* **1976**, *24*, 71−85.

(52) Hoult, D. I.; Lauterbur, P. C. *J. Magn. Reson.* **1979**, *34*, 425−433.

(53) Hoult, D. I. Sensitivity of the NMR Experiment. In *eMagRes.*; John Wiley & Sons, Ltd, 2007.

(54) Hoult, D. I. *Enc. Magn. Reson.* **2007**, DOI: 10.1002/9780470034590.emrstm0491.

(55) Hoult, D. I.; Richards, R. E. *J. Magn. Reson.* **1976**, *24*, 71−85.

(56) Minard, K. R.; Wind, R. A. *Concepts Magn. Reson.* **2001**, *13*, 190−210.

(57) Danieli, E.; Perlo, J.; Blümich, B.; Casanova, F. *Phys. Rev. Lett.* **2013**, *110*, 180801−1−5.

(58) Suefke, M.; Liebisch, A.; Blumich, B.; Appelt, S. *Nat. Phys.* **2015**, *11*, 767−771.

(59) Coffey, A. M.; Truong, M.; Chekmenev, E. Y. *J. Magn. Reson.* **2013**, *237*, 169−174.

(60) Theis, T.; Ortiz, G. X.; Logan, A. W. J.; Claytor, K. E.; Feng, Y.; Huhn, W. P.; Blum, V.; Malcolmson, S. J.; Chekmenev, E. Y.; Wang, Q.; Warren, W. S. *Sci. Adv.* **2016**, *2*, e1501438−e1501438.

(61) Nelson, S. J.; Kurhanewicz, J.; Vigneron, D. B.; Larson, P. E.; Harzstark, A. L.; Ferrone, M.; van Criekinge, M.; Chang, J. W.; Bok, R.; Park, I.; Reed, G.; Carvajal, L.; Small, E. J.; Munster, P.; Weinberg, V. K.; Ardenkjaer-Larsen, J. H.; Chen, A. P.; Hurd, R. E.; Odegardstuen, L. I.; Robb, F. J.; Tropp, J.; Murray, J. A. *Sci. Transl. Med.* **2013**, *5*, 198ra108.

(62) Sriram, R.; Van Criekinge, M.; Hansen, A.; Wang, Z. J.; Vigneron, D. B.; Wilson, D. M.; Keshari, K. R.; Kurhanewicz, J. *NMR Biomed.* **2015**, *28*, 1141−1149.

(63) Keshari, K. R.; Sriram, R.; Van Criekinge, M.; Wilson, D. M.; Wang, Z. J.; Vigneron, D. B.; Peehl, D. M.; Kurhanewicz, J. *Prostate* **2013**, *73*, 1171−1181.

(64) Rodrigues, T. B.; Serrao, E. M.; Kennedy, B. W. C.; Hu, D.-E.; Kettunen, M. I.; Brindle, K. M. *Nat. Med.* **2013**, *20*, 93−97.

(65) Reile, I.; Eshuis, N.; Hermkens, N. K. J.; van Weerdenburg, B. J. A.; Feiters, M. C.; Rutjes, F. P. J. T.; Tessari, M. *Analyst* **2016**, *141*, 4001−4005.

Heterogeneous Microtesla SABRE Enhancement of ^{15}N NMR Signals

Kirill V. Kovtunov,* Larisa M. Kovtunova, Max E. Gemeinhardt, Andrey V. Bukhtiyarov, Jonathan Gesiorski, Valerii I. Bukhtiyarov, Eduard Y. Chekmenev, Igor V. Koptyug, and Boyd M. Goodson*

Abstract: The hyperpolarization of heteronuclei via signal amplification by reversible exchange (SABRE) was investigated under conditions of heterogeneous catalysis and microtesla magnetic fields. Immobilization of [IrCl(COD)(IMes)], [IMes = 1,3-bis(2,4,6-trimethylphenyl), imidazole-2-ylidene; COD = cyclooctadiene] catalyst onto silica particles modified with amine linkers engenders an effective heterogeneous SABRE (HET-SABRE) catalyst that was used to demonstrate a circa 100-fold enhancement of ^{15}N NMR signals in ^{15}N-pyridine at 9.4 T following parahydrogen bubbling within a magnetic shield. No ^{15}N NMR enhancement was observed from the supernatant liquid following catalyst separation, which along with XPS characterization supports the fact that the effects result from SABRE under heterogeneous catalytic conditions. The technique can be developed further for producing catalyst-free agents via SABRE with hyperpolarized heteronuclear spins, and thus is promising for biomedical NMR and MRI applications.

[*] Dr. K. V. Kovtunov, Prof. I. V. Koptyug
Laboratory of Magnetic Resonance Microimaging, International Tomography Center, SB RAS
3A Institutskaya St., Novosibirsk 630090 (Russia)
E-mail: kovtunov@tomo.nsc.ru

Dr. K. V. Kovtunov, Dr. L. M. Kovtunova, Prof. I. V. Koptyug
Novosibirsk State University
2 Pirogova St., Novosibirsk 630090 (Russia)

Dr. L. M. Kovtunova, Dr. A. V. Bukhtiyarov, Prof. V. I. Bukhtiyarov
Boreskov Institute of Catalysis SB RAS
5 Acad. Lavrentiev Pr., Novosibirsk 630090 (Russia)

M. E. Gemeinhardt, J. Gesiorski, Prof. B. M. Goodson
Department of Chemistry and Biochemistry, Southern Illinois University
Carbondale, IL 62901 (USA)
E-mail: bgoodson@chem.siu.edu

Prof. B. M. Goodson
Materials Technology Center, Southern Illinois University
Carbondale, IL 62901 (USA)

Prof. E. Y. Chekmenev
Vanderbilt University Institute of Imaging Science (VUIIS), Department of Radiology, Department of Biomedical Engineering, Department of Physics and Astronomy, Vanderbilt-Ingram Cancer Center (VICC)
Nashville, TN 37232-2310 (USA)
and
Russian Academy of Sciences
Leninskiy Prospekt 14, 119991 Moscow (Russia)

Supporting information and the ORCID identification number(s) for the author(s) of this article can be found under:
https://doi.org/10.1002/anie.201705014.

A variety of different methods have been developed over the years to achieve NMR signal enhancement via hyperpolarization (the generation of highly non-equilibrium nuclear spin polarization), thereby overcoming the sensitivity problems of standard NMR/MRI techniques.[1–4] One such technique is dissolution dynamic nuclear polarization (d-DNP),[5] which allows different ^{13}C- and ^{15}N-containing molecules to be hyperpolarized and used in biomedical investigations.[6–10] Alternatively, methods involving parahydrogen-induced polarization (PHIP)[11,12] and signal amplification by reversible exchange (SABRE)[13,14] have demonstrated the ability to provide significant polarization enhancements using simple, highly economical setups; moreover, these parahydrogen-based methods are of interest because they are rapid (acting in seconds or tens of seconds) and can potentially have high agent throughput with continuous agent generation.

In parahydrogen-based methods, an organometallic catalyst is used to form a coordination complex between the parahydrogen (para-H$_2$) and the target substrate molecule:[1] In traditional PHIP, this allows hydrogenation of unsaturated bonds and hence a transfer of spin order to the substrate; however in SABRE, spin order is transferred spontaneously through the *J*-coupling network without requiring permanent chemical change to the substrate.

Although great progress has been achieved over a relatively short period of time,[15–21] a limitation that continues to exist for both PHIP and SABRE is the presence of the organometallic catalyst in the solution after substrate polarization has been achieved, hindering a number of potential biological and biomedical applications that would be affected by such contamination. Furthermore, catalyst recovery would be highly desirable to permit later re-use. As such there has been interest in developing approaches that use heterogeneous catalysts (that is, where the catalyst is in a different phase from the substrate) to combat these issues and better enable implementation of parahydrogen-based approaches for medical/imaging applications. Recent work towards that end includes the immobilization of homogeneous complexes to solid supports for SABRE[22,23] and for PHIP[17,24,25] or supported/bulk metal/metal oxide catalysts use for PHIP.[17,26–29]

The nature of the hyperpolarized substrates is also important. For example, because of the long spin–lattice relaxation times (T_1) of many heteronuclei, hyperpolarization of heteronuclear spins can significantly extend the lifetime of the resulting non-equilibrium polarization compared to that of polarized protons.[30,31] Indeed, recent demonstrations of hyperpolarization of important nuclei (with reduced detection sensitivity compared to ^{1}H, but often greater spectral

sensitivity along with much longer T_1 values) as ^{15}N,[32–35] ^{13}C,[1,36–38] ^{31}P,[39–41] and even ^{119}Sn and ^{29}Si[42] are reported for both homogeneous SABRE[43] and homogeneous PHIP;[44] however, to date the transfer of polarization to heteronuclei under heterogeneous catalytic conditions (wherein the substrate is in a different phase than the catalyst) was reported only for the PHIP technique.[31,45,46] Nevertheless, the intrinsic advantages of the SABRE approach[13] would make the production of heteronuclear hyperpolarization via SABRE under heterogeneous catalytic conditions (that is, HET-SABRE)[22,23] highly desirable.

Toward that end, here we combine heterogeneous SABRE with the ability to polarize ^{15}N nuclei. A signal enhancement of about 100 was reached for the ^{15}N resonance of ^{15}N-pyridine molecules using a novel heterogeneous SABRE catalyst $(SiO_2)_x(C_3H_6)NH\ Ir(COD)(IMes)$, where IMes = 1,3-bis(2,4,6-trimethylphenyl), imidazole-2-ylidene, COD = cyclooctadiene.

The preparation of the HET-SABRE catalyst used in the present work is briefly summarized below: First, the homogeneous SABRE catalyst [Ir(COD)(IMes)Cl][47] was synthesized as previously reported.[18,47–49] Then 90 mg of this [Ir(COD)(IMes)Cl] powder and 400 mg of 3-aminopropyl-functionalized silica gel (ca. 40–63 µm; Millipore-Sigma 364258) were added in a Schlenk tube and dried under vacuum for 30 min. After back-filling with argon gas, 10 mL of dried and deoxygenated benzene was transferred to the Schlenk tube via syringe and the reaction mixture was stirred for 24 h. Three drops of triethylamine (Millipore-Sigma 121-44-8) were then added to the reaction mixture with stirring continued for an additional 6 h. The solid material was filtered and washed with benzene until the supernatant solution was colorless; the catalyst particles were then washed with methanol several times and dried under vacuum for 2 h to give the pre-activated heterogeneous SABRE (HET-SABRE) catalyst with tentative structure shown in Figure 1.
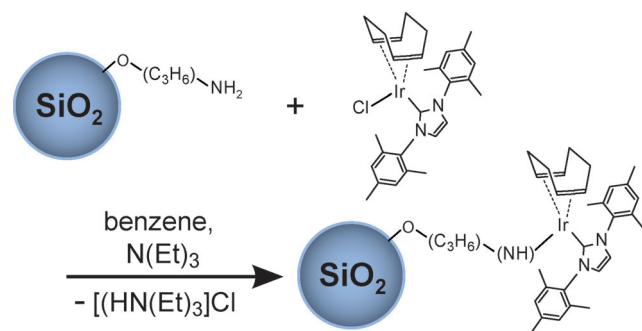
Figure 1. Tentative HET-SABRE catalyst structure with the summary of the catalyst synthesis via immobilization of Ir(COD)(IMes)Cl to NH$_2$-(CH$_2$)$_3$-modified silica particles (the COD is hydrogenated during activation and dissociates from the catalyst).

To test its viability to perform HET-SABRE, the catalyst was first investigated to see if it could be used to enhance ^{1}H NMR signals of pyridine. To this end, 10 mg of the HET-SABRE catalyst was placed inside a 5 mm NMR tube along with 15 µL of pyridine dissolved in 0.5 mL of CD$_3$OD. Parahydrogen gas (75 psi, enriched to 50% para-H$_2$ isomer) was then bubbled into the reaction mixture via Teflon capillary tubing, which extended to the bottom of the NMR tube. After 10 s of para-H$_2$ bubbling within the fringe field of the NMR spectrometer (ca. tens of Gauss), the sample was quickly transferred to the high field (9.4 T) of an NMR spectrometer and enhanced ^{1}H signals were detected from the free py substrate (Supporting Information, Figure S3). Although the observed ^{1}H polarization enhancement (ca. 2.6-fold) was smaller than that achieved in previous HET-SABRE efforts,[22,23] the point of this initial experiment was merely to qualitatively validate the catalyst for later studies of heteronuclear polarization enhancement, and no attempt was made to improve the enhancement by optimizing experimental parameters (such as para-H$_2$ fraction, SABRE mixing field, temperature, concentrations). Nevertheless, to ensure the heterogeneous nature of the observed ^{1}H polarization enhancement, the HET-SABRE catalyst particles were filtered out and the experiment was repeated with the supernatant solution; no detectable ^{1}H polarization enhancement was observed.

Observation of HET-SABRE enhancement of ^{1}H NMR signals enabled the catalyst to be tested for efficacy in generating heteronuclear (here, ^{15}N) polarization under heterogeneous catalytic conditions. Figure 2 shows successful enhancement of ^{15}N NMR signals from ^{15}N-labeled py (^{15}N-py) achieved by the so-called SABRE-SHEATH[30,32] (signal amplification by reversible exchange in shield enables alignment transfer to heteronuclei) approach. Here, 10 mg of the HET-SABRE catalyst was added to a (protonated) methanol solution containing 100 mM ^{15}N-py; the solvent was changed to MeOH because of mild concern that the quadrupolar ^{2}H nuclei in solvent molecules, which may transiently enter the inner sphere of the complex,[50,51] could reduce polarization efficiency inside the magnetic shield.[52–54] A strong polarized ^{15}N resonance was observed following 30 s bubbling of 50% para-H$_2$ inside a magnetic shield and rapid transfer to 9.4 T for detection (Figure 2d). Spectra resolution was sufficient to resolve the expected fine structure of the ^{15}N spectrum from scalar couplings with neighboring ^{1}H spins (Figure 2d, inset). A corresponding thermally polarized ^{15}N spectrum from the sample is shown in Figure 2b, indicating a circa 100-fold enhancement for the hyperpolarized signals in Figure 2d. This enhancement value is about 2.5 times higher than the best previously reported numbers for ^{1}H HET-SABRE,[23] although the better comparison is to the 5-fold enhancement values in Ref. [22], where the catalyst support particles were closer in size to those used here (indicating a larger enhancement than what would be explained simply by the circa 10-fold decrease in gyromagnetic ratio for ^{15}N compared to ^{1}H).

To verify the heterogeneous nature of the observed ^{15}N signal enhancement in Figure 2d, the HET-SABRE catalyst was removed by filtration and para-H$_2$ was bubbled through the supernatant liquid under the same experimental conditions (including use of the magnetic shield). The resulting spectrum (Figure 2c) exhibits no discernible SABRE enhancement of the ^{15}N signal. This lack of ^{15}N SABRE-SHEATH signal with the supernatant solution (in the absence
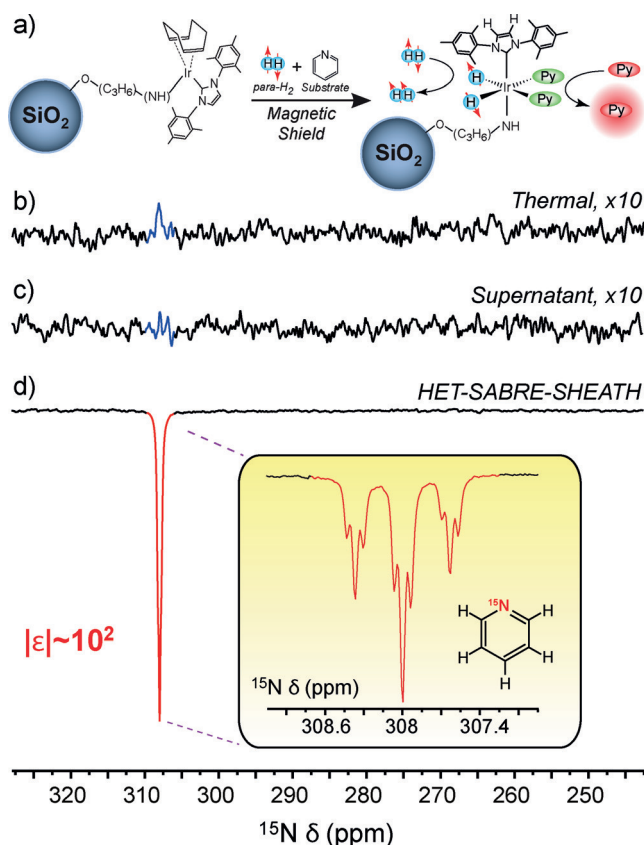
Figure 2. a) The heterogeneous SABRE-SHEATH experiment. b)–d) Selected ^{15}N spectra from "HET-SABRE-SHEATH" experiments (line broadening (l.b.): 10 Hz). b) Thermally polarized ^{15}N signal from 100 mм ^{15}N-py (10 mg catalyst/MeOH; 1 scan). c) ^{15}N NMR spectrum obtained from the supernatant solution recorded after HET-SABRE catalyst filtration, but otherwise conducted under the same SABRE-SHEATH experimental conditions in (d). Note the absence of enhanced ^{15}N signal in (c); the absence of thermally polarized ^{15}N signal similar to (b) is due to the fact that there is insufficient time for the ^{15}N spins of the substrate to thermally equilibrate with the NMR magnet during the rapid sample transfer from the magnetic shield (^{15}N $T_1 > 1$ min). d) HET-SABRE-SHEATH enhancement of ^{15}N signals from the from the ^{15}N-py substrate, achieved prior to catalyst particle filtration used for (c); the inset shows the resolved ^{15}N spectrum from free substrate (l.b. = 0.2 Hz).

of HET-SABRE catalyst particles) supports the conclusion that the observed ^{15}N enhancements are the result of HET-SABRE, and not homogeneous SABRE from leached catalyst moieties.

Additional supportive evidence comes from comparing the ^{15}N NMR spectrum obtained with the present heterogeneous catalyst with a corresponding spectrum obtained using homogeneous catalysts (Figure 3). Whereas both ^{15}N NMR spectra show clear hyperpolarized ^{15}N resonances assigned to free ^{15}N-py substrate, only the solution containing the homogeneous catalysts exhibits additional peaks in the 240–270 ppm range peaks that are attributed to equatorially and axially bound py, respectively.[30] If the enhanced signal in Figures 2d and 3a were obtained from leached homogeneous catalyst moieties, then corresponding peaks from catalyst-bound substrate would be expected; however, the peaks from
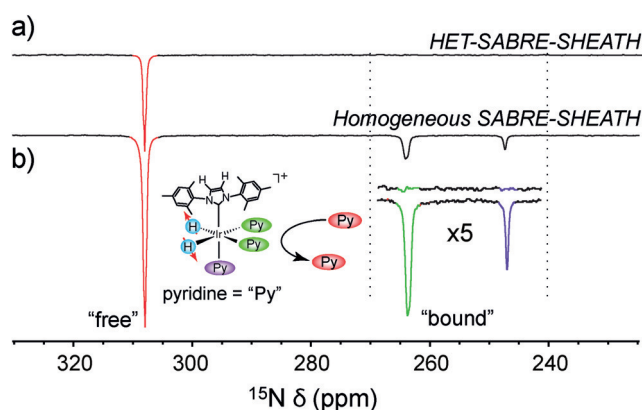
Figure 3. a) The ^{15}N HET-SABRE-SHEATH result in Figure 2d compared with b) a corresponding ^{15}N SABRE-SHEATH spectrum obtained with the standard homogenous catalyst. The ^{15}N-py concentrations were 100 mм and 50 mм, respectively, and both spectra are presented in the same vertical scale. The inset shows the expected presence of bound substrate resonances in the spectrum obtained with the homogeneous catalyst, and the apparent absence of bound substrate peaks for the heterogeneous system.

substrate bound to the heterogeneous catalyst particles are too weak (and/or too broadened) to manifest significantly in the observed spectra (consistent with previous ^1H results with microscale HET-SABRE particles).[22] While $\varepsilon_{15N} \approx 100$ fold is about 10 times lower than that using homogeneous variant of this catalyst (when taking into account para-H_2 enrichment),[32] no temperature or field optimization was performed here. Indeed, when the homogeneous catalyst was used for these experiments (Figure 3b), it showed about 4 times better SABRE polarization performance with 50 mм ^{15}N-py. We anticipate that future optimization of temperature, SABRE-SHEATH field, catalyst to substrate ratio, para-H_2 pressure, flow rate, and so on will allow for significant improvement of the performance of this catalyst material.[33,53]

Finally, the HET-SABRE catalyst was also studied via XPS and ICP-MS (inductively coupled plasma mass spectrometry; see the Supporting Information). It was shown by XPS (Figure S1) that the amount of iridium is the same before and after catalyst use in the SABRE-SHEATH experiments. Similarly, levels of Ir measured by ICP-MS were similar for a supernatant solution (collected after H_2 bubbling and subsequent catalyst filtration) and a reference solution of MeOH and pyridine (Supporting Information, Figure S3). These results thus provide additional support for the strong immobilization of the active (originally homogeneous) catalyst at the surfaces of the modified silica particles and a lack of leaching of the catalyst moieties into the solution-and hence, the conclusion that the enhancement in Figure 2d is truly the result of a heterogeneous catalytic process.

In conclusion, the enhancement of heteronuclear (^{15}N) NMR signals by SABRE-SHEATH under heterogeneous catalytic conditions is reported for the first time. A ^{15}N polarization enhancement of about 100 is demonstrated with 50% para-H_2 fraction using a novel HET-SABRE catalyst preparation, and NMR and XPS results are consistent with the conclusion that the enhancements are the result of the

HET-SABRE effect and not the result of homogeneous SABRE from any leached catalyst species. Given the fact that a variety of experimental conditions were not optimized (for example, support particle size and catalyst surface loading, in addition to those parameters listed farther above), and the fact that enhancements of the same order were observed for the homogeneous catalyst under the same conditions, much larger ^{15}N enhancements are anticipated to result from ongoing work. The catalyst described here also has the potential for future modifications to render its hyperpolarization in aqueous media,[55–57] which is highly synergistic with recent demonstrations of ^{15}N SABRE-SHEATH in an aqueous medium[58] and would ultimately pave the way to production of pure (from catalyst) ^{15}N hyperpolarized biomolecules in aqueous media for biomedical use.[59] Indeed, our efforts will be directed not only toward improving enhancements via such experimental optimization, but also preparation of biologically relevant agents (including the targeting of other nuclei), as well as agent separation and use (and catalyst re-use) for various biological or biomedical applications.

Acknowledgements

Conflict of interest

The authors declare no conflict of interest.

Keywords: heterogeneous catalysis · heteronuclei · het-SABRE · hyperpolarization · parahydrogen

[1] R. A. Green, R. W. Adams, S. B. Duckett, R. E. Mewis, D. C. Williamson, G. G. R. Green, *Prog. Nucl. Magn. Reson. Spectrosc.* **2012**, *67*, 1–48.

[2] D. A. Barskiy, A. M. Coffey, P. Nikolaou, D. M. Mikhaylov, B. M. Goodson, R. T. Branca, G. J. Lu, M. G. Shapiro, V. Telkki, V. V. Zhivonitko, et al., *Chem. Eur. J.* **2017**, *23*, 725–751.

[3] P. Nikolaou, B. M. Goodson, E. Y. Chekmenev, *Chem. Eur. J.* **2015**, *21*, 3156–3166.

[4] A. Comment, M. E. Merritt, *Biochemistry* **2014**, *53*, 7333–7357.

[5] J. H. Ardenkjaer-Larsen, B. Fridlund, A. Gram, G. Hansson, L. Hansson, M. H. Lerche, R. Servin, M. Thaning, K. Golman, *Proc. Natl. Acad. Sci. USA* **2003**, *100*, 10158–10163.

[6] J. Milani, B. Vuichoud, A. Bornet, R. Melzi, S. Jannin, G. Bodenhausen, *Rev. Sci. Instrum.* **2017**, *88*, 015109.

[7] S. J. Nelson, J. Kurhanewicz, D. B. Vigneron, P. E. Z. Larson, A. L. Harzstark, M. Ferrone, M. Van Criekinge, J. W. Chang, I. Park, G. Reed, et al., *Sci. Transl. Med.* **2013**, *5*, 198ra108.

[8] M. Durst, E. Chiavazza, A. Haase, S. Aime, M. Schwaiger, R. F. Schulte, *Magn. Reson. Med.* **2016**, *76*, 1900–1904.

[9] J. Kurhanewicz, D. B. Vigneron, K. Brindle, E. Y. Chekmenev, A. Comment, C. H. Cunningham, R. J. Deberardinis, G. G. Green, M. O. Leach, S. S. Rajan, et al., *Neoplasia* **2011**, *13*, 81–97.

[10] C. Cudalbu, A. Comment, F. Kurdzesau, R. B. Heeswijk, K. Uffmann, S. Jannin, V. Denisov, D. Kirike, R. Gruetter, *Phys. Chem. Chem. Phys.* **2010**, *12*, 5818–5823.

[11] C. R. Bowers, D. P. Weitekamp, *J. Am. Chem. Soc.* **1987**, *109*, 5541–5542.

[12] M. G. Pravica, D. P. Weitekamp, *Chem. Phys. Lett.* **1988**, *145*, 255–258.

[13] R. W. Adams, J. A. Aguilar, K. D. Atkinson, M. J. Cowley, P. I. P. Elliott, S. B. Duckett, G. G. R. Green, I. G. Khazal, J. López-Serrano, D. C. Williamson, *Science* **2009**, *323*, 1708–1711.

[14] R. W. Adams, S. B. Duckett, R. A. Green, D. C. Williamson, G. G. R. Green, *J. Chem. Phys.* **2009**, *131*, 194505.

[15] S. B. Duckett, N. J. Wood, *Coord. Chem. Rev.* **2008**, *252*, 2278–2291.

[16] J. B. Hövener, N. Schwaderlapp, R. Borowiak, T. Lickert, S. B. Duckett, R. E. Mewis, R. W. Adams, M. J. Burns, L. A. R. Highton, G. G. R. Green, et al., *Anal. Chem.* **2014**, *86*, 1767–1774.

[17] K. V. Kovtunov, V. V. Zhivonitko, I. V. Skovpin, D. A. Barskiy, I. V. Koptyug, *Top. Curr. Chem.* **2013**, *338*, 123–180.

[18] D. A. Barskiy, K. V. Kovtunov, I. V. Koptyug, P. He, K. A. Groome, Q. A. Best, F. Shi, B. M. Goodson, R. V. Shchepin, A. M. Coffey, et al., *J. Am. Chem. Soc.* **2014**, *136*, 3322–3325.

[19] R. Zhou, E. W. Zhao, W. Cheng, L. M. Neal, H. Zheng, R. E. Quiñones, H. E. Hagelin-Weaver, C. R. Bowers, *J. Am. Chem. Soc.* **2015**, *137*, 1938–1946.

[20] O. G. Salnikov, K. V. Kovtunov, I. V. Koptyug, *Sci. Rep.* **2015**, *5*, 13930.

[21] K. V. Kovtunov, D. A. Barskiy, A. M. Coffey, M. L. Truong, O. G. Salnikov, A. K. Khudorozhkov, E. A. Inozemtseva, I. P. Prosvirin, V. I. Bukhtiyarov, K. W. Waddell, et al., *Chem. Eur. J.* **2014**, *20*, 11636–11639.

[22] F. Shi, A. M. Coffey, K. W. Waddell, E. Y. Chekmenev, B. M. Goodson, *Angew. Chem. Int. Ed.* **2014**, *53*, 7495–7498; *Angew. Chem.* **2014**, *126*, 7625–7628.

[23] F. Shi, A. M. Coffey, K. W. Waddell, E. Y. Chekmenev, B. M. Goodson, *J. Phys. Chem. C* **2015**, *119*, 7525–7533.

[24] I. V. Koptyug, K. V. Kovtunov, S. R. Burt, M. S. Anwar, C. Hilty, S. I. Han, A. Pines, R. Z. Sagdeev, *J. Am. Chem. Soc.* **2007**, *129*, 5580–5586.

[25] S. Abdulhussain, H. Breitzke, T. Ratajczyk, A. Grünberg, M. Srour, D. Arnaut, H. Weidler, U. Kunz, H. J. Kleebe, U. Bommerich, et al., *Chem. Eur. J.* **2014**, *20*, 1159–1166.

[26] K. V. Kovtunov, I. E. Beck, V. I. Bukhtiyarov, I. V. Koptyug, *Angew. Chem. Int. Ed.* **2008**, *47*, 1492–1495; *Angew. Chem.* **2008**, *120*, 1514–1517.

[27] E. W. Zhao, H. Zheng, R. Zhou, H. E. Hagelin-Weaver, C. R. Bowers, *Angew. Chem. Int. Ed.* **2015**, *54*, 14270–14275; *Angew. Chem.* **2015**, *127*, 14478–14483.

[28] S. Glöggler, A. M. Grunfeld, Y. N. Ertas, J. McCormick, S. Wagner, P. P. M. Schleker, L. S. Bouchard, *Angew. Chem. Int. Ed.* **2015**, *54*, 2452–2456; *Angew. Chem.* **2015**, *127*, 2482–2486.

[29] D. B. Burueva, A. S. Romanov, O. G. Salnikov, V. V. Zhivonitko, Y.-W. Chen, D. A. Barskiy, E. Y. Chekmenev, D. W.-H. Hwang, K. V. Kovtunov, I. V. Koptyug, *J. Phys. Chem. C* **2017**, *121*, 4481–4487.

10436 www.angewandte.org

© 2017 Wiley-VCH Verlag GmbH & Co. KGaA, Weinheim

Angew. Chem. Int. Ed. **2017**, *56*, 10433–10437

[30] M. L. Truong, T. Theis, A. M. Coffey, R. V. Shchepin, K. W. Waddell, F. Shi, B. M. Goodson, W. S. Warren, E. Y. Chekmenev, *J. Phys. Chem. C* **2015**, *119*, 8786–8797.

[31] K. V. Kovtunov, D. A. Barskiy, R. V. Shchepin, O. G. Salnikov, I. P. Prosvirin, A. V. Bukhtiyarov, L. M. Kovtunova, V. I. Bukhtiyarov, I. V. Koptyug, E. Y. Chekmenev, *Chem. Eur. J.* **2016**, *22*, 16446–16449.

[32] T. Theis, M. L. Truong, A. M. Coffey, R. V. Shchepin, K. W. Waddell, F. Shi, B. M. Goodson, W. S. Warren, E. Y. Chekmenev, *J. Am. Chem. Soc.* **2015**, *137*, 1404–1407.

[33] D. A. Barskiy, R. V. Shchepin, A. M. Coffey, T. Theis, W. S. Warren, B. M. Goodson, E. Y. Chekmenev, *J. Am. Chem. Soc.* **2016**, *138*, 8080–8083.

[34] H. Nonaka, M. Hirano, Y. Imakura, Y. Takakusagi, K. Ichikawa, S. Sando, *Sci. Rep.* **2017**, *7*, 40104.

[35] F. Reineri, A. Viale, S. Ellena, D. Alberti, T. Boi, G. B. Giovenzana, R. Gobetto, S. S. D. Premkumar, S. Aime, *J. Am. Chem. Soc.* **2012**, *134*, 11146–11152.

[36] A. N. Pravdivtsev, A. V. Yurkovskaya, H. Zimmermann, H. Vieth, K. L. Ivanov, *RSC Adv.* **2015**, *5*, 63615–63623.

[37] K. Golman, O. Axelsson, H. Jóhannesson, S. Månsson, C. Olofsson, J. S. Petersson, *Magn. Reson. Med.* **2001**, *46*, 1–5.

[38] A. M. Coffey, R. V. Shchepin, M. L. Truong, K. Wilkens, W. Pham, E. Y. Chekmenev, *Anal. Chem.* **2016**, *88*, 8279–8288.

[39] V. V. Zhivonitko, I. V. Skovpin, I. V. Koptyug, *Chem. Commun.* **2015**, *51*, 2506–2509.

[40] M. J. Burns, P. J. Rayner, G. G. R. Green, L. A. R. Highton, R. E. Mewis, S. B. Duckett, *J. Phys. Chem. B* **2015**, *119*, 5020–5027.

[41] H. Jóhannesson, O. Axelsson, M. Karlsson, *C. R. Phys.* **2004**, *5*, 315–324.

[42] A. M. Olaru, A. Burt, P. J. Rayner, S. J. Hart, A. C. Whitwood, G. G. R. Green, S. B. Duckett, *Chem. Commun.* **2016**, *52*, 14482–14485.

[43] R. E. Mewis, *Magn. Reson. Chem.* **2015**, *53*, 789–800.

[44] L. T. Kuhn, J. Bargon, *Top. Curr. Chem.* **2007**, *276*, 25–68.

[45] K. V. Kovtunov, D. A. Barskiy, O. G. Salnikov, R. V. Shchepin, A. M. Coffey, L. M. Kovtunova, V. I. Bukhtiyarov, I. V. Koptyug, E. Y. Chekmenev, *RSC Adv.* **2016**, *6*, 69728–69732.

[46] S. Glöggler, A. M. Grunfeld, Y. N. Ertas, J. McCormick, S. Wagner, P. P. M. Schleker, L.-S. Bouchard, *Angew. Chem. Int. Ed.* **2015**, *54*, 2452–2456; *Angew. Chem.* **2015**, *127*, 2482–2486.

[47] M. J. Cowley, R. W. Adams, K. D. Atkinson, M. C. R. Cockett, S. B. Duckett, G. G. R. Green, J. B. Lohman, R. Kerssebaum, D. Kilgour, R. E. Mewis, *J. Am. Chem. Soc.* **2011**, *133*, 6134–6137.

[48] D. A. Barskiy, K. V. Kovtunov, I. V. Koptyug, P. He, K. A. Groome, Q. A. Best, F. Shi, B. M. Goodson, R. V. Shchepin, M. L. Truong, et al., *ChemPhysChem* **2014**, *15*, 4100–4107.

[49] L. D. Vazquez-Serrano, B. T. Owens, J. M. Buriak, *Inorg. Chim. Acta* **2006**, *359*, 2786–2797.

[50] K. X. Moreno, K. Nasr, M. Milne, A. D. Sherry, W. J. Goux, *J. Magn. Reson.* **2015**, *257*, 15–23.

[51] B. J. A. Van Weerdenburg, A. H. J. Engwerda, N. Eshuis, A. Longo, D. Banerjee, M. Tessari, F. Guerra, P. J. T. Rutjes, F. M. Bickelhaupt, M. C. Feiters, *Chem. Eur. J.* **2015**, *21*, 10482–10489.

[52] R. V. Shchepin, D. A. Barskiy, D. M. Mikhaylov, E. Y. Chekmenev, *Bioconjugate Chem.* **2016**, *27*, 878–882.

[53] R. V. Shchepin, M. L. Truong, T. Theis, A. M. Coffey, F. Shi, K. W. Waddell, W. S. Warren, B. M. Goodson, E. Y. Chekmenev, *J. Phys. Chem. Lett.* **2015**, *6*, 1961–1967.

[54] D. A. Barskiy, R. V. Shchepin, C. P. N. Tanner, J. F. P. Colell, B. M. Goodson, T. Theis, W. S. Warren, E. Y. Chekmenev, *ChemPhysChem* **2017**, *18*, 1493–1498.

[55] M. L. Truong, F. Shi, P. He, B. Yuan, K. N. Plunkett, A. M. Coffey, R. V. Shchepin, D. A. Barskiy, K. V. Kovtunov, I. V. Koptyug, et al., *J. Phys. Chem. B* **2014**, *118*, 13882–13889.

[56] F. Shi, P. He, Q. A. Best, K. Groome, M. L. Truong, A. M. Coffey, G. Zimay, R. V. Shchepin, K. W. Waddell, E. Y. Chekmenev, B. M. Goodson, *J. Phys. Chem. C* **2016**, *120*, 12149–12156.

[57] P. Spannring, I. Reile, M. Emondts, P. P. M. Schleker, N. K. J. Hermkens, N. G. J. van der Zwaluw, B. J. A. van Weerdenburg, P. Tinnemans, M. Tessari, B. Blümich, et al., *Chem. Eur. J.* **2016**, *22*, 9277–9282.

[58] J. F. P. Colell, M. Emondts, A. W. J. Logan, K. Shen, J. Bae, R. V. Shchepin, G. X. Ortiz, P. Spannring, Q. Wang, S. J. Malcolmson, et al., *J. Am. Chem. Soc.* **2017**, *139*, 7761–7767.

[59] L. B. Bales, K. V. Kovtunov, D. A. Barskiy, R. V. Shchepin, A. M. Coffey, L. M. Kovtunova, A. V. Bukhtiyarov, M. Feldman, V. I. Bukhtiyarov, E. Y. Chekmenev, I. V. Koptyug, B. M. Goodson, *J. Phys. Chem. C* **2017**, *121*, 15304–15309.

■ **Analytical Chemistry**

Robust Imidazole-^{15}N$_2$ Synthesis for High-Resolution Low-Field (0.05 T) ^{15}N Hyperpolarized NMR Spectroscopy

Roman V. Shchepin,[a] Danila A. Barskiy,[a] Aaron M. Coffey,[a] Matthew A. Feldman,[a] Larisa M. Kovtunova,[b, c] Valerii I. Bukhtiyarov,[b, c] Kirill V. Kovtunov,[b, d] Boyd M. Goodson,[e] Igor V. Koptyug,[b, d] and Eduard Y. Chekmenev*[a, f]

NMR hyperpolarization techniques have the potential to revolutionize the field of NMR spectroscopy and molecular MRI because they can transiently enhance nuclear spin polarization by 4–8 orders of magnitude, with corresponding gains in NMR signal-to-noise ratio (SNR). The SABRE-SHEATH (Signal Amplification By Reversible Exchange in SHield Enables Alignment Transfer to Heteronuclei) technique, first demonstrated in 2015, allows for direct, efficient ($>$ 20% nuclear spin polarization), and fast (in under one minute) hyperpolarization of ^{15}N sites. Several classes of biologically relevant ^{15}N hyperpolarized contrast agents have been efficiently hyperpolarized to date including pH sensors, which can be potentially useful for non-invasive pH imaging of cancer and other diseases with altered metabolism. Here, we report the optimized ^{15}N enrichment of imidazole-^{15}N$_2$ – a promising in vivo pH sensor with pKa ~ 7.0. A hyperpolarized 0.1 M aqueous solution (ε_{15N} ~ 146,000 fold, P_{15N} ~ 0.24%) was used to record ^{15}N NMR spectra at 0.05 T, demonstrating the feasibility of high-resolution (full width at half maximum ~ 1 Hz corresponding to 5 ppm at 0.05 T) NMR spectroscopy near its pKa (7.0) at ultra-low magnetic field. Given that proton-binding events modulate the chemical shift by ~ 30 ppm for this pH-sensing probe, our results demonstrate the feasibility of ultra-low-field pH sensing near its pKa (7.0) with SNR approaching that of high-field (9.4 T) MR.

[a] Prof. R. V. Shchepin, Dr. D. A. Barskiy, Dr. A. M. Coffey, M. A. Feldman, Prof. E. Y. Chekmenev
Vanderbilt University Institute of Imaging Science (VUIIS)
Department of Radiology, Department of Biomedical Engineering
Department of Physics and Astronomy
Nashville, Tennessee, 37232-2310 (United States)
E-mail: eduard.chekmenev@vanderbilt.edu

[b] Dr. L. M. Kovtunova, Prof. V. I. Bukhtiyarov, Dr. K. V. Kovtunov, Prof. I. V. Koptyug
Novosibirsk State University
2 Pirogova St., Novosibirsk 630090 (Russia)

[c] Dr. L. M. Kovtunova, Prof. V. I. Bukhtiyarov
Boreskov Institute of Catalysis SB RAS
5 Acad. Lavrentiev Pr., Novosibirsk 630090 (Russia)

[d] Dr. K. V. Kovtunov, Prof. I. V. Koptyug
Laboratory of Magnetic Resonance Microimaging
International Tomography Center (ITC), SB RAS
3 A Institutskaya St., Novosibirsk 630090 (Russia)

[e] Prof. B. M. Goodson
Southern Illinois University
Department of Chemistry and Biochemistry
Materials Technology Center
Carbondale, IL 62901 (United States)

[f] Prof. E. Y. Chekmenev
Russian Academy of Sciences
Leninskiy Prospekt 14, 119991 Moscow (Russia)

💻 Supporting information for this article is available on the WWW under https://doi.org/10.1002/slct.201700718

NMR hyperpolarization can increase nuclear spin polarization by 4–8 orders of magnitude, depending on the detection magnetic field and the type of nuclear spin.[1] The concomitant gains in the signal-to-noise ratio (SNR) enable new applications of NMR and MRI.[2] Importantly, the biomedical applications of hyperpolarized (HP) NMR and MRI have been the main driving force behind the development and the refinement of hyperpolarization techniques to date.[1f, 2b] Signal Amplification By Reversible Exchange (SABRE), pioneered by Duckett, Green, and co-workers in 2009,[3] is one of the newest hyperpolarization techniques. This technique is based on the Parahydrogen Induced Polarization (PHIP)[4] effect pioneered by Bowers and Weitekamp.[5] While SABRE was originally demonstrated for proton hyperpolarization, the in vivo proton spin-lattice relaxation time constant T_1 is generally significantly shorter than T_1's of heteronuclei (e.g., ^{13}C and ^{15}N): i.e. seconds vs. minutes.[6] Recently, direct hyperpolarization of longer-lived ^{15}N and ^{13}C sites in biomolecules has been demonstrated using the SABRE-SHEATH (SABRE in SHield Enables Alignment Transfer to Heteronuclei) technique.[7] The ^{15}N SABRE-SHEATH process is very efficient, and ^{15}N polarization exceeding 20% in ~ 1 minute has already been demonstrated.[8] The SABRE-SHEATH technique has been already successfully applied to pH sensors,[9] and HP imidazole-^{15}N$_2$[10] is one of the leading compounds for potential in vivo applications such as pH imaging of cancer and other diseases using HP contrast agents.[11]

From a chemical synthesis perspective, the design of ^{15}N HP contrast agents offers additional benefits over ^{13}C: isotopic enrichment is often considerably more straightforward for ^{15}N heterocycles and others (especially in the biological context because many biologically relevant biomolecules contain heterocycles: B vitamins, DNA bases, etc.),[12] and the source of ^{15}N enrichment (i.e. ^{15}NH$_4$Cl is cheap ($<$ $20/g). Moreover, ^{15}N may also offer greater T_1 lifetimes compared to those of ^{13}C nuclei: up to ~ 10 minutes,[13] which can be additionally increased via the use of long-lived spin-states[14] (up to 20 minute relaxation time constants have been already demonstrated[15]). Furthermore, low-field detection of HP contrast agents can yield more SNR compared to the high-field detection.[16] Therefore, HP low-field Magnetic Resonance (MR)

is a new frontier that can offer greater detection sensitivity at a fraction of the high-field MR cost and specific absorption rate.[17] Importantly, some HP contrast agents (including a small number of ^{15}N contrast agents[15]) exhibit longer lifetimes and T_1 at low magnetic fields, which is advantageous in the context of biomedical applications[18] because it would offer longer time windows for penetration of biochemical pathways and for MR detection.[2b]

Here, we report a robust synthetic procedure for preparation of isotopically enriched imidazole-^{15}N$_2$ and investigate the feasibility of high-resolution ^{15}N spectroscopy of aqueous solutions of ^{15}N HP imidazole-^{15}N$_2$ near its pKa (~ 7.0) at 0.05 T, an ultra-low field (ULF) from the perspective of clinical imaging.[17b] The demonstrated spectral resolution of ~ 1 Hz (full width at half maximum, FWHM) is sufficient for future use of this potent HP contrast agent as a pH sensor.

One potential drawback of direct ^{15}N detection is a relatively low gyromagnetic ratio (γ) of ^{15}N nucleus with γ_{15N} being approximately $\gamma_{1H}/10$. Since the detection sensitivity in conventional (i.e. non-hyperpolarized) NMR scales with γ^3 due to (i) equilibrium nuclear spin polarization, which is linearly proportional to γ, (ii) dipole moment and (iii) resonance frequency ω_0, which is also linearly proportional to γ,[19] nuclear spin hyperpolarization can only help overcoming the contribution due to nuclear spin polarization. As a result, even when hyperpolarization is employed, γ^2 dependence generally remains. Various approaches to maximize SNR in NMR have been developed through more intelligent design of the NMR detectors (i.e. radio-frequency (RF) coils). In our previous work, we have shown that low-frequency RF coils can benefit significantly, by maximizing the use of the conductor length; and as a result of such optimization, it is possible to mitigate the resonance frequency factor (mentioned above) to the power of $^1/_4$.[16a] So, for the same kind of HP nuclei (i.e. with identical γ), the overall detection sensitivity of NMR experiment (i.e. signal-to-noise ratio or SNR) can generally scale as $\omega_0^{1/4}$ or $B_0^{1/4}$.[16a, 20] Moreover, several works in the field of LF MRI ($<$ 5 MHz) have demonstrated that the use of Litz[21] and superconducting[22] wire can completely negate and potentially overpower the nominal $\omega_0^{1/4}$ or $B_0^{1/4}$ dependence, thereby making LF detection of HP compounds more sensitive than that using conventional high-field detection.[16a] However, as described above dipole moment of low-gamma nuclei such as ^{15}N studied here makes ^{15}N detection significantly less sensitive than that of ^{1}H by at least a factor of $\gamma^{5/4}$.[20] A solution to this challenge is indirect ^{1}H detection of HP compounds,[23] which has been successfully demonstrated for HP ^{15}N choline.[24] This approach has been extended to imaging[25] and more recently to MRI of the leading HP contrast agent ^{13}C hyperpolarized pyruvate in vivo.[26]

The overall synthesis of imidazole-^{15}N$_2$ is shown in Scheme 1a, and the detailed reaction mechanism is shown in Scheme 1b. The mechanism of imidazole-^{15}N$_2$ formation follows a typical acid catalyzed imine formation, which relies on the H$^+$ activation of carbonyls. The preparation allows for convenient ^{15}N enrichment of both ^{15}N sites using ^{15}NH$_4$Cl as the ^{15}N isotope source. The overall preparation is based on previous
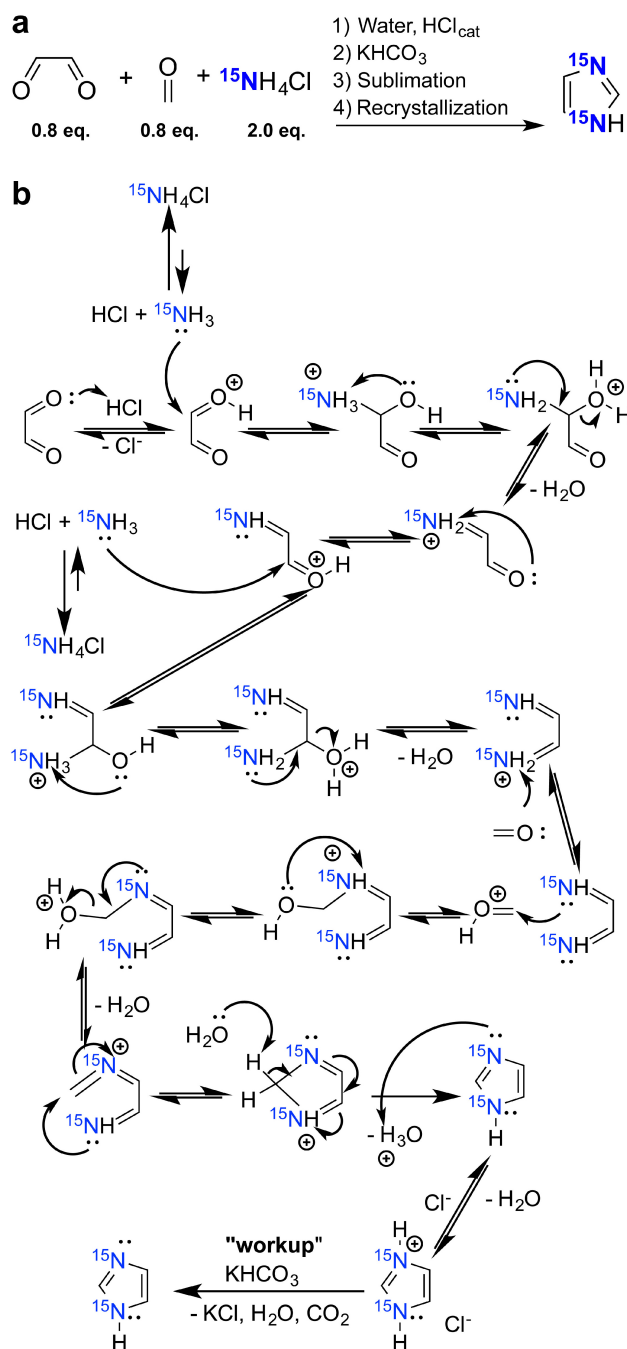
Scheme 1. Preparation scheme of imidazole-^{15}N$_2$. a) overall reaction scheme; b) detailed reaction mechanism.

work;[27] however, we found that the procedure developed by Alei and co-workers[27a] was challenging to reproduce. The key steps of our procedure (Scheme 1) include (i) cyclization under acidic rather than basic reaction conditions, (ii) use of a slight excess of readily available ^{15}NH$_4$Cl, and (iii) use of a sublimation setup. The described simple and robust synthesis offers the following advantages with respect to the recently described procedure:[27b] (i) the use of significantly simpler sublimation hardware (i.e. 1 mbar vs. 10^{-3} mbar), (ii) the use of milder

reaction conditions (i.e. 75 °C vs. 90 °C) and the use of potassium bicarbonate vs. potassium hydroxide for the neutralization step, and (iii) ~50–fold greater production scale (~0.25 mmol vs. ~0.005 mmol). All synthetic details are provided in the Supporting Information (SI).

The material synthesized in this fashion was used to study the feasibility of high-resolution ultra-low-field ^{15}N NMR spectroscopy using an 80 cm-gap permanent MRI magnet with B_0 homogeneity < 19 ppm over a 40 cm-diameter of spherical volume (DSV). A home-built single-channel RF probe was used to record ^{15}N signals with a Kea2 NMR spectrometer (Magritek, Wellington, New Zealand) at a ^{15}N resonance frequency of 210 kHz (see SI for details). ^{15}N hyperpolarization was performed as described previously[10] using samples of the IrIMes SABRE catalyst[28] in a 5 mm NMR tube high-pressure setup[29] at a magnetic field for polarization transfer B_T < 1 µT using a magnetic field shield[7a, b] (Figure 1a) or in situ[30] at B_T ~ 0.05 T in the MRI magnet. The latter conditions are suitable for hyperpolarization of the imidazole protons by traditional SABRE, where the polarization transfer is spontaneous (i.e. performed in static magnetic field with no RF pulses), and the resulting NMR line shape is anti-phase, in line with previous experiments where polarization transfer is performed at the Earth's field or a few milli-Tesla, i.e. the static magnetic field significantly exceeding 1 µT.[7a, b]

The ^{15}N spectrum recorded at 0.05 T using SABRE-SHEATH hyperpolarization at B_T < 1 µT (Figure 1b) exhibits a multiplet due to heteronuclear spin-spin couplings between ^{15}N and non-exchangeable hydrogens in the imidazole ring (Figure 1 g). The observed multiplet is in agreement with a previously reported high-field study by Whaley and co-workers: see spectral simulation in Figure 1c.[27a] In situ[30b] ^{15}N SABRE hyperpolarization inside the 0.05 T magnet yielded the ^{15}N spectrum (Figure 1d) exhibiting an anti-phase multiplet. While the in situ ^{15}N hyperpolarization yielded a spectrum with lower SNR than that of the spectrum shown in Figure 1b, it offers a convenient means for optimization of some SABRE-SHEATH parameters: e.g. temperature, parahydrogen (para-H$_2$) pressure, etc. (assuming that these parameters are not field dependent, i.e. the same in micro- and milli-Tesla regimes respectively), because the sample stays in the RF coil, and it may be continuously re-hyperpolarized.[30b, 31]

The ^{15}N multiplet shown in Figure 1b (and also simulated in Figure 1c) has a FWHM of ~ 1 Hz for the central peak corresponding to ~ 5 ppm at 210 kHz resonant frequency. While proton continuous wave (cw) decoupling was not available for our experimental purposes, we simulated this condition for protonated and non-protonated imidazole-^{15}N$_2$ forms corresponding to acidic (below pKa) and basic (above pKa) conditions in Figure 1e. CW proton decoupling effectively removes NMR line splitting originating from ^{15}N-^{1}H spin-spin couplings. The simulated spectra clearly indicate that HP ^{15}N spectroscopy can be potentially employed to differentiate chemical shifts of the protonated and non-protonated forms of aqueous imidazole-^{15}N$_2$ for pH sensing purposes. We estimate the spectral resolution of ~0.5 Hz (equivalent to ~2.5 ppm) corresponds to a sensitivity (i.e. resolution) of ~0.1 units of pH
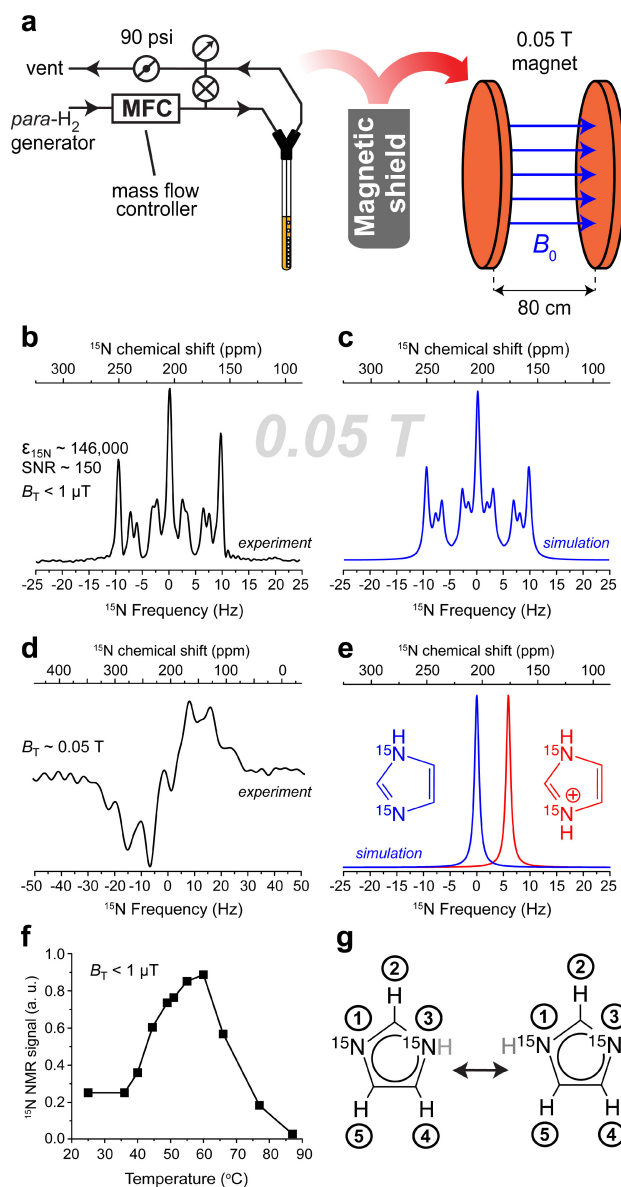
Figure 1. a) Schematic diagram of the SABRE-SHEATH[7a] experimental setup, which was connected to a home-built parahydrogen generator (producing ~80% para-H$_2$ fraction) located near a ~0.05 T MR instrument (~210 kHz ^{15}N resonance frequency) for ^{15}N signal detection. b) ^{15}N NMR spectrum of ~100 mM imidazole-^{15}N$_2$ hyperpolarized using the SABRE-SHEATH procedure (hyperpolarization ex situ at B_T < 1 µT; catalyst concentration is ~ 5 mM, see SI for details): note the multiplet splittings due to spin-spin coupling between ^{15}N and ^{1}H spins.[27a] c) Theoretically calculated ^{15}N NMR spectrum of imidazole-^{15}N$_2$. NMR parameters were taken from Ref. # [27a]. Note that the small difference between experimental and simulated NMR multiplet peaks in (b) and (c) is likely due to the deviation of polarization distribution induced by the SABRE-SHEATH process. d) ^{15}N NMR spectrum of imidazole-^{15}N$_2$ hyperpolarized using the SABRE procedure (hyperpolarization in situ at B_T ~ 0.05 T). e) Simulated ^{15}N NMR spectra of imidazole-^{15}N$_2$ under the conditions of continuous ^{1}H decoupling for deprotonated (blue) and protonated (red) forms of the molecule corresponding to basic and acidic solutions, i.e. above and below pKa of ~ 7.0 respectively. f) Temperature dependence of the ^{15}N SABRE-SHEATH signal intensity integrated over the full spectrum, and in which the spectral structure and relative peak amplitudes do not vary from one temperature point to the next). g) Molecular structure of imidazole-^{15}N$_2$ at pH above pKa (~ 7.0): note that one proton (gray) is in fast exchange between two nitrogen-15 sites.

near the pKa value of ~7.0. We note that the susceptibility-induced magnetic field gradients typical for in vivo conditions will likely have a negligible effect at this low magnetic field, and the above estimate for sensitivity of pH will likely be valid for future in vivo investigations.

The HP solution studied contained ~82% aqueous phosphate buffer (pH = 10, EMD Millipore Corporation, BX1642-1, 0.3 mL), ~18% methanol (see SI) and ~100 mM imidazole-$^{15}N_2$. Compared to the previous HP SABRE-SHEATH studies in neat methanol-d_4 solvent[7b]; whereas that original solution yielded the maximum ^{15}N hyperpolarization near room temperature, this solution yielded a clear maximum at ~60 °C (Figure 1f). The maximum ^{15}N signal enhancement (ε_{15N}) achieved was ca. 146,000 fold at 0.05 T using 80% para-H_2 (Figure 1b), corresponding to P_{15N} ~ 0.24%. The enhancement and polarization values were calculated using a separate reference HP sample of imidazole-$^{15}N_2$ at 0.05 T and 9.4 T and comparing it to the signal from a thermally polarized sample of 3.2 M $^{15}NH_4Cl$ in D_2O at 9.4 T with known ^{15}N nuclear spin polarization (Figure 2; see SI for details).
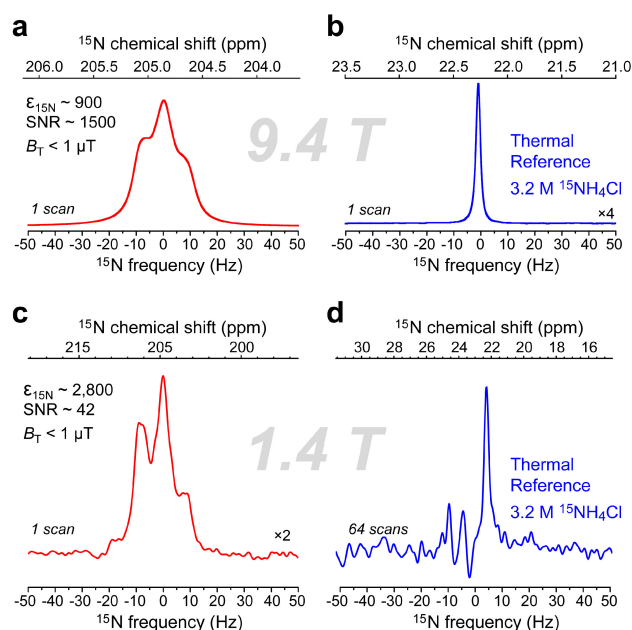
Figure 2. ^{15}N NMR spectroscopy at 9.4 T and 1.4 T. The same experimental conditions (i.e., catalyst, imidazole-$^{15}N_2$ concentration, etc.) were used except for p-H2 fraction (~50% vs. ~80% used in Figure 1. a) ^{15}N NMR spectrum of imidazole-$^{15}N_2$ hyperpolarized using the SABRE-SHEATH procedure (hyperpolarization at $B_T < 1$ μT) with the detection at 9.4 T (Bruker Avance III NMR spectrometer). b) ^{15}N NMR spectrum of a thermally polarized signal reference sample (3.2 M $^{15}NH_4Cl$ in D_2O) with detection at 9.4 T (Bruker Avance III NMR spectrometer). c) ^{15}N NMR spectrum of imidazole-$^{15}N_2$ hyperpolarized using SABRE-SHEATH procedure (hyperpolarization at $B_T < 1$ μT) with the detection at 1.4 T (Nanalysis NMRReady-60PRO spectrometer). d) ^{15}N NMR spectrum of thermally polarized signal reference sample (3.2 M $^{15}NH_4Cl$ in D_2O) using 64 scans (Nanalysis NMRReady-60PRO spectrometer). See SI for additional details.

Despite the relatively low P_{15N} achieved in this study compared to some of our other recent work, it was sufficient to

achieve ^{15}N spectra with good SNR (ca. 150) using a single scan. Significantly greater P_{15N} can be potentially achieved using ^{15}N SABRE-SHEATH through optimization of experimental conditions:[17b, 32] the use of near 100% p-H_2,[33] optimization of static magnetic field during polarization transfer in micro-Tesla field regime,[8, 34] increasing p-H_2 pressure (with corresponding increase of H_2 concentration in aqueous solution) and p-H_2 flow rate,[9] and others.[35] As a result of such future improvements, low-field hyperpolarized ^{15}N NMR is a potentially very promising frontier. Because there are no other (known to us) low-field ^{15}N reports (i.e. at $B_0 < 1$ T), we used this experiment to compare ^{15}N detection sensitivity of the HP state at high (9.4 T), intermediate (1.4 T), and very low (0.05 T) magnetic fields. Figure 2 shows the corresponding ^{15}N spectra obtained at 9.4 T and 1.4 T using two different NMR spectrometers. We have used the thermally polarized sample (with known values of equilibrium P_{15N} of $3.3 \cdot 10^{-4}$ % and $4.9 \cdot 10^{-5}$ % at 9.4 T and 1.4 T respectively) of 3.2 M $^{15}NH_4Cl$ in D_2O as a signal reference to determine ε_{15N} (~900 and ~2,800) and P_{15N} (0.29% and 0.14%) of HP imidazole-$^{15}N_2$ samples studied at these two fields. Because P_{15N} values were very similar at 0.05 T and 9.4 T (0.24% vs. 0.29%), the detection sensitivity or SNR can be easily compared. ^{15}N detection at 9.4 T provided ~10-fold greater SNR compared to that at 0.05 T. In part, the greater detection sensitivity is explained by ~2-fold smaller diameter of the RF coil (i.e., a 2-fold better filling factor, resulting in a corresponding factor of ~2 greater sensitivity[19]) and a factor of 1.2 greater ^{15}N spin polarization (0.29% vs. 0.24%). When these factors are taken into account, the SNR was effectively ~4 times greater at 9.4 T vs. 0.05 T. The latter is in good agreement with our theory predicting $B_0^{1/4}$ dependence of SNR for HP contrast media under conditions where the nuclear spin polarization is not induced by the applied field, but created via hyperpolarization.[16a] This result is remarkable in the context of the presented NMR spectra, because it demonstrates that ULF NMR can, perhaps counter to intuition, provide the benefits of high-resolution and high-sensitivity detection in the context of HP contrast agents—all while still providing useful spectral sensitivity to local chemistry as well. We hope that future optimization work will allow us to further enhance the detection SNR through not only improving ^{15}N polarization, but also by decreasing the RF coil diameter and the implementation of recently developed external high-quality-factor resonators for ULF NMR.[36]

The detection at 1.4 T was performed using hardware that has only recently become available to us, and it was not optimized. As a result the SNR (~42) was significantly lower than that at 9.4 T and 0.05 T. While future optimization work will hopefully improve the SNR, it should be emphasized that this is a bench-top portable spectrometer offering a tremendous advantage of streamlined workflow in the chemistry lab for development and optimization of SABRE-SHEATH hyperpolarization, because the prepared samples can be tested immediately in the lab with little preparation. It is also noteworthy to emphasize the effective ^{15}N line width improvement at 1.4 T vs. 9.4 T of the HP imidazole-$^{15}N_2$, which is not the result of better B_0 homogeneity at 1.4 T. Instead, the NMR line

width is the manifestation of the chemical exchange of the hopping proton (Figure 1 g).[10] The effect of this exchange is further reduced at 0.05 T (the sample is satisfying the NMR conditions of fast exchange at such low fields), which is manifested in the additional ^{15}N NMR line narrowing (Figure 1b) compared to the NMR lines at 9.4 T and 1.4 T (Figures 2a and 2c).

In conclusion, a robust ^{15}N synthetic enrichment procedure for production on imidazole-$^{15}N_2$ is reported using an inexpensive ^{15}N enrichment source ($^{15}NH_4Cl$, < $20/g). The resulting spin-labeled material enabled ^{15}N SABRE-SHEATH HP NMR studies at 0.05 T, 1.4 T, and 9.4 T. The feasibility of high-resolution ^{15}N NMR spectroscopy at 0.05 T is demonstrated with detection sensitivity that can potentially approach that of 9.4 T. The feasibility of ^{15}N HP NMR in a bench-top instrument allows for convenient optimization studies using ^{15}N SABRE-SHEATH. Future studies will need to address other translational challenges including increasing the ^{15}N polarization in aqueous solutions,[29,35,37] removal of the SABRE catalyst, or developing efficient heterogeneous SABRE catalysts for preparation of pure aqueous HP solutions[38] of this promising pH sensing probe.

Supporting Information Summary

Supporting Information (SI) is available: experimental details regarding imidazole-$^{15}N_2$ synthesis, sample preparation and SABRE hyperpolarization protocol, high-resolution NMR spectra of synthesized imidazole-$^{15}N_2$, simulation of ^{15}N NMR spectrum of imidazole-$^{15}N_2$, design of radio-frequency probe for ^{15}N experiments at 0.05 T, and calculations of P_{15N} and ε_{15N} at 9.4 T, 1.4 T and 0.05 T.

Acknowledgements

Conflict of Interest

The authors declare no conflict of interest.

Keywords: ^{15}N NMR spectroscopy · hyperpolarization · isotopic enrichment · parahydrogen · SABRE-SHEATH

[1] a) P. Nikolaou, A. M. Coffey, M. J. Barlow, M. Rosen, B. M. Goodson, E. Y. Chekmenev, *Anal. Chem.* **2014**, *86*, 8206–8212; b) P. Nikolaou, B. M. Goodson, E. Y. Chekmenev, *Chem. Eur. J.* **2015**, *21*, 3156–3166; c) J. H. Ardenkjaer-Larsen, B. Fridlund, A. Gram, G. Hansson, L. Hansson, M. H. Lerche, R. Servin, M. Thaning, K. Golman, *Proc. Natl. Acad. Sci. U. S. A.* **2003**, *100*, 10158–10163; d) J.-H. Ardenkjaer-Larsen, G. S. Boebinger, A. Comment, S. Duckett, A. S. Edison, F. Engelke, C. Griesinger, R. G. Griffin, C. Hilty, H. Maeda, G. Parigi, T. Prisner, E. Ravera, J. van Bentum, S. Vega, A. Webb, C. Luchinat, H. Schwalbe, L. Frydman, *Angew. Chem. Int. Ed.* **2015**, *54*, 9162–9185; e) J. H. Ardenkjaer-Larsen, *J. Magn. Reson.* **2016**, *264*, 3–12; f) D. A. Barskiy, A. M. Coffey, P. Nikolaou, D. M. Mikhaylov, B. M. Goodson, R. T. Branca, G. J. Lu, M. G. Shapiro, V.-V. Telkki, V. V. Zhivonitko, I. V. Koptyug, O. G. Salnikov, K. V. Kovtunov, V. I. Bukhtiyarov, M. S. Rosen, M. J. Barlow, S. Safavi, I. P. Hall, L. Schröder, E. Y. Chekmenev, *Chem. Eur. J.* **2017**, *23*, 725–751.

[2] a) B. M. Goodson, *J. Magn. Reson.* **2002**, *155*, 157–216; b) J. Kurhanewicz, D. B. Vigneron, K. Brindle, E. Y. Chekmenev, A. Comment, C. H. Cunningham, R. J. DeBerardinis, G. G. Green, M. O. Leach, S. S. Rajan, R. R. Rizi, B. D. Ross, W. S. Warren, C. R. Malloy, *Neoplasia* **2011**, *13*, 81–97; c) K. M. Brindle, *J. Am. Chem. Soc.* **2015**, *137*, 6418–6427; d) S. E. Day, M. I. Kettunen, F. A. Gallagher, D. E. Hu, M. Lerche, J. Wolber, K. Golman, J. H. Ardenkjaer-Larsen, K. M. Brindle, *Nat. Med.* **2007**, *13*, 1382–1387; e) K. Golman, O. Axelsson, H. Johannesson, S. Mansson, C. Olofsson, J. S. Petersson, *Magn. Reson. Med.* **2001**, *46*, 1–5; f) K. Golman, R. in't Zandt, M. Thaning, *Proc. Natl. Acad. Sci. U. S. A.* **2006**, *103*, 11270–11275.

[3] R. W. Adams, J. A. Aguilar, K. D. Atkinson, M. J. Cowley, P. I. P. Elliott, S. B. Duckett, G. G. R. Green, I. G. Khazal, J. Lopez-Serrano, D. C. Williamson, *Science* **2009**, *323*, 1708–1711.

[4] T. C. Eisenschmid, R. U. Kirss, P. P. Deutsch, S. I. Hommeltoft, R. Eisenberg, J. Bargon, R. G. Lawler, A. L. Balch, *J. Am. Chem. Soc.* **1987**, *109*, 8089–8091.

[5] a) C. R. Bowers, D. P. Weitekamp, *Phys. Rev. Lett.* **1986**, *57*, 2645–2648; b) C. R. Bowers, D. P. Weitekamp, *J. Am. Chem. Soc.* **1987**, *109*, 5541–5542; c) M. G. Pravica, D. P. Weitekamp, *Chem. Phys. Lett.* **1988**, *145*, 255–258.

[6] C. Cudalbu, A. Comment, F. Kurdzesau, R. B. van Heeswijk, K. Uffmann, S. Jannin, V. Denisov, D. Kirik, R. Gruetter, *Phys. Chem. Chem. Phys.* **2010**, *12*, 5818–5823.

[7] a) T. Theis, M. L. Truong, A. M. Coffey, R. V. Shchepin, K. W. Waddell, F. Shi, B. M. Goodson, W. S. Warren, E. Y. Chekmenev, *J. Am. Chem. Soc.* **2015**, *137*, 1404–1407; b) M. L. Truong, T. Theis, A. M. Coffey, R. V. Shchepin, K. W. Waddell, F. Shi, B. M. Goodson, W. S. Warren, E. Y. Chekmenev, *J. Phys. Chem. C* **2015**, *119*, 8786–8797; c) D. A. Barskiy, R. V. Shchepin, C. P. N. Tanner, J. F. P. Colell, B. M. Goodson, T. Theis, W. S. Warren, E. Y. Chekmenev *ChemPhysChem* **2017**, DOI: 10.1002/cphc.201700416.

[8] D. A. Barskiy, R. V. Shchepin, A. M. Coffey, T. Theis, W. S. Warren, B. M. Goodson, E. Y. Chekmenev, *J. Am. Chem. Soc.* **2016**, *138*, 8080–8083.

[9] R. V. Shchepin, M. L. Truong, T. Theis, A. M. Coffey, F. Shi, K. W. Waddell, W. S. Warren, B. M. Goodson, E. Y. Chekmenev, *J. Phys. Chem. Lett.* **2015**, *6*, 1961–1967.

[10] R. V. Shchepin, D. A. Barskiy, A. M. Coffey, T. Theis, F. Shi, W. S. Warren, B. M. Goodson, E. Y. Chekmenev, *ACS Sensors* **2016**, *1*, 640–644.

[11] a) F. A. Gallagher, M. I. Kettunen, S. E. Day, D. E. Hu, J. H. Ardenkjaer-Larsen, R. in't Zandt, P. R. Jensen, M. Karlsson, K. Golman, M. H. Lerche, K. M. Brindle, *Nature* **2008**, *453*, 940-U973; b) A. M. Olaru, M. J. Burns, G. G. R. Green, S. B. Duckett, *Chem. Sci.* **2017**, *8*, 2257–2266; c) W. Jiang, L. Lumata, W. Chen, S. Zhang, Z. Kovacs, A. D. Sherry, C. Khemtong, *Sci. Rep.* **2015**, *5*, 9104; d) D. J. Scholz, M. A. Janich, U. Köllisch, R. F. Schulte, J. H. Ardenkjaer-Larsen, A. Frank, A. Haase, M. Schwaiger, M. I. Menzel, *Magn. Reson. Med.* **2015**, *73*, 2274–2282; e) R. R. Flavell, C. von Morze, J. E. Blecha, D. E. Korenchan, M. Van Criekinge, R. Sriram, J. W. Gordon, H.-Y. Chen, S. Subramaniam, R. A. Bok, Z. J. Wang, D. B. Vigneron, P. E. Larson, J. Kurhanewicz, D. M. Wilson, *Chem. Comm.* **2015**, *51*, 14119–14122.

[12] a) T. W. Whaley, D. G. Ott, *J. Labelled Comp.* **1974**, *10*, 283–286; b) N. J. Oppenheimer, T. O. Matsunaga, B. L. Kam, *J. Labelled Comp. Radiopharm.* **1978**, *15*, 191–196; c) A. W. J. Logan, T. Theis, J. F. P. Colell, W. S. Warren, S. J. Malcolmson, *Chem. Eur. J.* **2016**, *22*, 10777–10781; d) R. V. Shchepin, D. A. Barskiy, D. M. Mikhaylov, E. Y. Chekmenev, *Bioconjugate Chem.* **2016**, *27*, 878–882; e) R. V. Shchepin, E. Y. Chekmenev, *J. Labelled Comp. Radiopharm.* **2014**, *57*, 621–624.

[13] a) H. Nonaka, M. Hirano, Y. Imakura, Y. Takakusagi, K. Ichikawa, S. Sando, *Sci. Rep.* **2017**, *7*, 40104; b) H. Nonaka, R. Hata, T. Doura, T. Nishihara, K. Kumagai, M. Akakabe, M. Tsuda, K. Ichikawa, S. Sando, *Nat. Commun.*

2013, *4*, 2411; c) R. Hata, H. Nonaka, Y. Takakusagi, K. Ichikawa, S. Sando, *Chem. Comm.* **2015**, *51*, 12290–12292.

[14] a) M. H. Levitt, *Annu. Rev. Phys. Chem.* **2012**, *63*, 89–105; b) M. H. Levitt, *J. Magn. Reson.* **2016**, *262*, 91–99; c) W. S. Warren, E. Jenista, R. T. Branca, X. Chen, *Science* **2009**, *323*, 1711–1714.

[15] T. Theis, G. X. Ortiz, A. W. J. Logan, K. E. Claytor, Y. Feng, W. P. Huhn, V. Blum, S. J. Malcolmson, E. Y. Chekmenev, Q. Wang, W. S. Warren, *Sci. Adv.* **2016**, *2*, e1501438.

[16] a) A. M. Coffey, M. L. Truong, E. Y. Chekmenev, *J. Magn. Reson.* **2013**, *237*, 169–174; b) W. Myers, D. Slichter, M. Hatridge, S. Busch, M. Mössle, R. McDermott, A. Trabesinger, J. Clarke, *J. Magn. Reson.* **2007**, *186*, 182–192.

[17] a) S. Appelt, S. Gloggler, F. W. Hasing, U. Sieling, A. G. Nejad, B. Blumich, *Chem. Phys. Lett.* **2010**, *485*, 217–220; b) B. Blümich, *J. Magn. Reson.* **2017**, *274*, 145–147; c) S. Gloggler, J. Colell, S. Appelt, *J. Magn. Reson.* **2013**, *235*, 130–142; d) M. E. Hayden, C. P. Bidinosti, E. M. Chapple, *Concept Magnetic Res. A* **2012**, *40 A*, 281–294; e) Y. Zhu, C.-H. Chen, Z. Wilson, I. Savukov, C. Hilty, *J. Magn. Reson.* **2016**, *270*, 71–76.

[18] a) K. V. Kovtunov, M. L. Truong, D. A. Barskiy, I. V. Koptyug, A. M. Coffey, K. W. Waddell, E. Y. Chekmenev, *Chem. Eur. J.* **2014**, *20*, 14629–14632; b) K. V. Kovtunov, M. L. Truong, D. A. Barskiy, O. G. Salnikov, V. I. Bukhtiyarov, A. M. Coffey, K. W. Waddell, I. V. Koptyug, E. Y. Chekmenev, *J. Phys. Chem. C* **2014**, *118*, 28234–28243; c) L. L. Tsai, R. W. Mair, M. S. Rosen, S. Patz, R. L. Walsworth, *J. Magn. Reson.* **2008**, *193*, 274–285; d) D. A. Barskiy, O. G. Salnikov, A. S. Romanov, M. A. Feldman, A. M. Coffey, K. V. Kovtunov, I. V. Koptyug, E. Y. Chekmenev, *J. Magn. Reson.* **2017**, *276*, 78–85.

[19] D. l. Hoult, R. E. Richards, *J. Magn. Reson.* **1976**, *24*, 71–85.

[20] A. M. Coffey, K. V. Kovtunov, D. Barskiy, I. V. Koptyug, R. V. Shchepin, K. W. Waddell, P. He, K. A. Groome, Q. A. Best, F. Shi, B. M. Goodson, E. Y. Chekmenev, *Anal. Chem.* **2014**, *86*, 9042–9049.

[21] a) A. W. Lotfi, F. C. Lee, in *Industry Applications Society Annual Meeting, Conference Record of the 1993 IEEE, Vol. 2*, **1993**, pp. 1169–1175; b) W. Dominguez-Viqueira, W. Berger, J. Parra-Robles, G. E. Santyr, *Concept Magnetic Res. B* **2010**, *37B*, 75–85; c) M. F. Carias, W. Dominguez-Viqueira, G. E. Santyr, *Concept Magnetic Res. B* **2011**, *39B*, 37–42; d) M. Sarracanie, C. D. LaPierre, N. Salameh, D. E. J. Waddington, T. Witzel, M. S. Rosen, *Sci. Rep.* **2015**, *5*, 15177.

[22] F. Resmer, H. C. Seton, J. M. S. Hutchison, *J. Magn. Reson.* **2010**, *203*, 57–65.

[23] a) E. Y. Chekmenev, V. A. Norton, D. P. Weitekamp, P. Bhattacharya, *J. Am. Chem. Soc.* **2009**, *131*, 3164–3165; b) J. A. Pfeilsticker, J. E. Ollerenshaw, V. A. Norton, D. P. Weitekamp, *J. Magn. Reson.* **2010**, *205*, 125–129; c) V. A. Norton, D. P. Weitekamp, *J. Chem. Phys.* **2011**, *135*, 141107.

[24] R. Sarkar, A. Comment, P. R. Vasos, S. Jannin, R. Gruetter, G. Bodenhausen, H. Hall, D. Kirik, V. P. Denisov, *J. Am. Chem. Soc.* **2009**, *131*, 16014–16015.

[25] a) M. Mishkovsky, A. Comment, R. Gruetter, *J. Cereb. Blood Flow Metab.* **2012**, *32*, 2108–2113; b) M. L. Truong, A. M. Coffey, R. V. Shchepin, K. W. Waddell, E. Y. Chekmenev, *Contrast Media Mol. Imaging* **2014**, *9*, 333–341.

[26] J. Wang, F. Kreis, A. J. Wright, R. L. Hesketh, M. H. Levitt, K. M. Brindle, *Magn. Reson. Med.* **2017**, DOI 10.1002/mrm.26725.

[27] a) M. Alei, L. O. Morgan, W. E. Wageman, T. W. Whaley, *J. Am. Chem. Soc.* **1980**, *102*, 2881–2887; b) S. Johannsen, N. Megger, D. Böhme, K. O. SigelRoland, J. Müller, *Nat. Chem.* **2010**, *2*, 229–234.

[28] M. J. Cowley, R. W. Adams, K. D. Atkinson, M. C. R. Cockett, S. B. Duckett, G. G. R. Green, J. A. B. Lohman, R. Kerssebaum, D. Kilgour, R. E. Mewis, *J. Am. Chem. Soc.* **2011**, *133*, 6134–6137.

[29] M. L. Truong, F. Shi, P. He, B. Yuan, K. N. Plunkett, A. M. Coffey, R. V. Shchepin, D. A. Barskiy, K. V. Kovtunov, I. V. Koptyug, K. W. Waddell, B. M. Goodson, E. Y. Chekmenev, *J. Phys. Chem. B* **2014**, *18* 13882–13889.

[30] a) D. A. Barskiy, K. V. Kovtunov, I. V. Koptyug, P. He, K. A. Groome, Q. A. Best, F. Shi, B. M. Goodson, R. V. Shchepin, A. M. Coffey, K. W. Waddell, E. Y. Chekmenev, *J. Am. Chem. Soc.* **2014**, *136*, 3322–3325; b) D. A. Barskiy, K. V. Kovtunov, I. V. Koptyug, P. He, K. A. Groome, Q. A. Best, F. Shi, B. M. Goodson, R. V. Shchepin, M. L. Truong, A. M. Coffey, K. W. Waddell, E. Y. Chekmenev, *ChemPhysChem* **2014**, *15*, 4100–4107; c) T. Theis, M. Truong, A. M. Coffey, E. Y. Chekmenev, W. S. Warren, *J. Magn. Reson.* **2014**, *248*, 23–26.

[31] a) J. B. Hovener, N. Schwaderlapp, T. Lickert, S. B. Duckett, R. E. Mewis, L. A. R. Highton, S. M. Kenny, G. G. R. Green, D. Leibfritz, J. G. Korvink, J. Hennig, D. von Elverfeldt, *Nat. Commun.* **2013**, *4*, 5; b) J.-B. Hövener, S. Knecht, N. Schwaderlapp, J. Hennig, D. von Elverfeldt, *ChemPhysChem* **2014**, *15*, 2451–2457.

[32] S. S. Zalesskiy, E. Danieli, B. Blümich, V. P. Ananikov, *Chem. Rev.* **2014**, *114*, 5641–5694.

[33] B. Feng, A. M. Coffey, R. D. Colon, E. Y. Chekmenev, K. W. Waddell, *J. Magn. Reson.* **2012**, *214*, 258–262.

[34] J. F. P. Colell, A. W. J. Logan, Z. Zhou, R. V. Shchepin, D. A. Barskiy, G. X. Ortiz, Q. Wang, S. J. Malcolmson, E. Y. Chekmenev, W. S. Warren, T. Theis, *J. Phys. Chem. C* **2017**, *121*, 6626–6634.

[35] J. F. P. Colell, M. Emondts, A. W. J. Logan, K. Shen, J. Bae, R. V. Shchepin, G. X. Ortiz, P. Spannring, Q. Wang, S. J. Malcolmson, E. Y. Chekmenev, M. C. Feiters, F. P. J. T. Rutjes, B. Bluemich, T. Theis, W. S. Warren, *J. Am. Chem. Soc.* **2017**, DOI 10.1021/jacs.1027b00569.

[36] M. Suefke, A. Liebisch, B. Blumich, S. Appelt, *Nature Phys.* **2015**, 767–771.

[37] a) F. Shi, P. He, Q. A. Best, K. Groome, M. L. Truong, A. M. Coffey, G. Zimay, R. V. Shchepin, K. W. Waddell, E. Y. Chekmenev, B. M. Goodson, *J. Phys. Chem. C* **2016**, *120*, 12149–12156; b) J.-B. Hövener, N. Schwaderlapp, R. Borowiak, T. Lickert, S. B. Duckett, R. E. Mewis, R. W. Adams, M. J. Burns, L. A. R. Highton, G. G. R. Green, A. Olaru, J. Hennig, D. von Elverfeldt, *Anal. Chem.* **2014**, *86*, 1767–1774; c) H. Zeng, J. Xu, M. T. McMahon, J. A. B. Lohman, P. C. M. van Zijl, *J. Magn. Reson.* **2014**, *246*, 119–121.

[38] a) F. Shi, A. M. Coffey, K. W. Waddell, E. Y. Chekmenev, B. M. Goodson, *Angew. Chem. Int. Ed.* **2014**, *53*, 7495–7498; b) F. Shi, A. M. Coffey, K. W. Waddell, E. Y. Chekmenev, B. M. Goodson, *J. Phys. Chem. C* **2015**, *119*, 7525–7533.

PHIP, SABRE, and SEOP: Low(er)-Cost Alternatives for the Rapid Creation of Pure, Long-Lived Hyperpolarized Agents

Boyd M. Goodson[1,2]

[1]Department of Chemistry and Biochemistry, Southern Illinois University, Carbondale, IL 62901;
[2]Materials Technology Center, SIUC.

Hyperpolarization[1]—the creation of highly non-equilibrium nuclear spin polarization—has been investigated for years as a way to dramatically improve the detection sensitivity of NMR and MRI. Potential biomedical applications are particularly exciting, where orders-of-magnitude sensitivity improvements can enable *in vivo* spectroscopy and imaging (*e.g.*) of relatively low-concentration metabolites in tissues and gases in pulmonary spaces—including at low magnetic fields. Although many hyperpolarization methods have been developed and pursued, one approach—dissolution dynamic nuclear polarization (d-DNP)[1,2]—has become increasingly dominant because of improved—and now commercially available—technology enabling preparation of hyperpolarized (HP) molecules with high (10s of percent) polarizations in various isotopes within a wide range of chemical and biological systems (as well as the means to separate these HP compounds from the auxiliary substances needed for hyperpolarization (persistent radicals in the case of d-DNP))—even enabling clinical trials using metabolic MRI contrast agents.[3] However, the high costs and infrastructure associated with d-DNP technology, combined with relatively small amounts produced and slow agent production rates, present a challenge for many potential applications and sites considering implementation of hyperpolarization methodologies.

Although possessing their own challenges, three other hyperpolarization approaches—respectively dubbed PHIP,[4] SABRE,[5] and SEOP[6]--embody attractive alternatives because of their significantly lower costs and instrumentation demands, much greater hyperpolarization rates (with run times from tens of minutes to seconds—even allowing continuous agent production), and potential for scalability. In PHIP (parahydrogen-induced polarization) the pure spin order from parahydrogen (pH_2) gas is transferred to a molecular substrate—generally involving a catalyst; whereas "traditional" PHIP involves hydrogenation of asymmetric unsaturated bonds with pH_2 to create hyperpolarization,[4] SABRE[5] (for Signal Amplification By Reversible Exchange) allows the pH_2 spin order to be transferred to a target molecule without requiring its permanent chemical change. Finally, SEOP enables hyperpolarization by irradiating an alkali metal vapor with high-intensity circularly polarized laser light in the presence of a target gas like xenon; although somewhat slower and more expensive than PHIP and SABRE—and limited to the production of HP noble gases—SEOP now enables clinical-scale production of HP Xe with nuclear spin polarization approaching unity (e.g. Ref. [7]).

This presentation will provide an overview of recent examples from our lab's various collaborations that endeavor to greatly expand the power and reach of SABRE, PHIP, and SEOP by growing the repertoire of target species/agents; improving biological compatibility; increasing polarizations, amounts, and hyperpolarization lifetimes of agents; and improving the cost and ease-of-use of associated technologies. For example, a collaboration with the labs of Eduard Chekmenev (Vanderbilt) and Igor Koptyug (ITC Novosibirsk, as well as scientists from Novosibirsk's Boreskov Institute of Catalysis) has recently demonstrated successful transfer of PHIP hyperpolarization to heteronuclei using heterogeneous catalysts and a simple magnetic shield--including within aqueous solutions, where hyperpolarized ^{15}N T_1 values of up to ~500 s were measured.[8] Next, following our recent work demonstrating heterogeneous (HET) SABRE (to potentially enable preparation of pure HP agents following catalyst separation, as well as catalyst reuse), this collaboration has developed new HET-SABRE catalysts and extended the approach to enhancing ^{15}N spin polarization using a magnetic shield to facilitate rapid and efficient ^{1}H-^{15}N polarization transfer—an approach based on that recently developed in a collaboration with the Chekmenev lab and Warren Warren and Thomas Theis of Duke (previously demonstrating efficient generation of ~10% polarization in ^{15}N spins under homogeneous catalytic conditions[11-13]). Indeed, under such conditions this SABRE approach has recently been used to demonstrate high ^{15}N polarizations in biologically relevant substrates that may be useful for both pH and hypoxia sensing / mapping *in vivo*.[14,15] Other recent improvements under homogeneous conditions include expanding SABRE to aqueous conditions[16] and taking the amenable substrates of SABRE beyond nitrogen heterocycles.[17] Finally, as time permits the efforts of our ongoing SEOP collaboration with the Chekmenev Lab, Mike Barlow (Nottingham), and Matt Rosen and Sam Patz (Harvard) will be discussed, including efforts to improve xenon hyperpolarization technologies (following the development of our open-source clinical-scale xenon "hyperpolarizer"[7]), to yield greater automation, ease of use, and polarizer performance, as well as more fundamental efforts to better understand SEOP processes under the demanding conditions of high Xe densities and resonant laser flux while hyperpolarizing both xenon-129 and xenon-131—the latter being an isotope attracting increasing interest for neutron scattering experiments probing fundamental symmetries.

References: [1]Nikolaou *et al., CEJ* **2015** *21*, 3156; [2]Ardenkjær-Larsen *et al.*, *PNAS* **2003** *100*, 10158; [3]Nelson, *et al. Sci. Transl. Med.* **2013**, 5, 198ra108; [4]Bowers & Weitekamp, *JACS*, **1987** *109*, 5541; [5]Adams *et al.*, *Science* **2009** *323*, 1708; [6]Walker & Happer *Rev. Mod. Phys*. **1997** *69*, 629; [7]Nikolaou, *et al. PNAS* **2013** *110*,14150 ; [8]Bales *et al.,* in preparation; [9]Shi *et al. Angew. Chem.* **2014** *126*, 7625; [10]Shi *et al. JPCC* **2015** *119*, 7525; [11]Theis *et al. JACS*, **2015** *137*, 1404; [12]Shchepin *et al.*, *JPCL* **2015** *6*, 1961; [13]Truong et al., *JPCB* **2014** *118*, 13882; [14]Shchepin *et al.*, *ACS Sens.* **2016**, *1*, 640; [15]Barskiy *et al., JACS 2016*, *138*, 8080; [16]Shi *et al.,JPCC* **2016**, *120*, 12149; [17]Shchepin *et al.*, *ChemSelect* **2016** *1*, 2552.

Potential For High-Resolution Hyperpolarized In Vivo Metabolic Heteronuclear Spectroscopy At Low Magnetic Fields

Aaron M. Coffey, Matthew A. Feldman, Roman V. Shchepin, Danila A. Barskiy, Milton L. Truong, Wellington Pham, Malcolm Avison, John C. Gore, and Eduard Y. Chekmenev

Background and Significance

The emergence of several hyperpolarization techniques enhancing the detected signal from nuclear spins by orders of magnitude have led to a wealth of opportunities to pursue in the developing arena of high sensitivity magnetic resonance research. In non-hyperpolarized methods, the magnetic field strength of the detection magnet serves to polarize the nuclear spins (usually protons) with polarization levels of ≤3.5 ppm/Tesla constraining the detection limit to large ensembles of nuclear spins (conventionally bulk water in clinical MR applications). Hyperpolarization techniques, however, produce spin polarization independent of the readout magnet, and therefore, they provide freedom to select a magnetic field strength, and correspondingly a detection frequency, optimized to the nucleus observed and the dielectric properties of the sample. Of particular interest is the quickly developing frontier of low-field magnetic resonance (NMR) and imaging (MRI), due to its strongly complementing the study of hyperpolarized (HP) nuclei, and its potential for application in areas of study including heteronuclear spin-labeled metabolites or other contrast agents at low concentrations.

Approach and Results

High-resolution ^{13}C NMR spectroscopy of hyperpolarized succinate-1-^{13}C was been performed *in vitro* and *in vivo* using a clinical-scale, biplanar (80 cm-gap) 48.7 mT permanent magnet with a high homogeneity magnetic field. Non-localized ^{13}C NMR spectra were recorded *in vivo* at 0.52 MHz resonance frequency over the torso of a tumor-bearing mouse every 2 seconds. Hyperpolarized ^{13}C NMR signals with linewidths of ~3 Hz (corresponding to ~6 ppm) were recorded *in vitro* (2 mL in a syringe) and *in vivo* (over a mouse torso). Comparison of the full width at half maximum (FWHM) for ^{13}C NMR spectra acquired at 48.7 mT and at 4.7 T in a small-animal MRI scanner demonstrates a factor of ~12 improvement for the ^{13}C resonance linewidth attainable at 48.7 mT compared to that at 4.7 T *in vitro*. ^{13}C HP succinate-1-^{13}C *in vivo* resonance linewidths are at least one order of

Figure 1. HP ^{129}Xe produced by a fully automated, stopped-flow regime clinical-scale polarizer or HP ^{13}C metabolic tracers by a fully automated, PHIP polarizer can be used to obtain metabolic information regarding various bodily tissues with high spectroscopic resolution at low magnetic fields (e.g. 48.7 mT) given a magnet with sufficient B_0 homogeneity (e.g. ~13 ppm over 40 cm DSV).

magnitude narrower at 48.7 mT compared to those observed in high-field (≥ 3 T) studies employing HP contrast agents. The high-resolution ^{13}C *in vivo* spectroscopy demonstrated could be useful for high-sensitivity spectroscopic studies involving monitoring HP agent uptake or detecting metabolism using HP contrast agents with sufficiently large ^{13}C chemical shift differences. For HP ^{129}Xe, the FWHM was ~6 Hz when dissolved in toluene and ~3.1 Hz in the gas phase. For an imaging matrix of 256×256, 2*FWHM for the dissolved ^{129}Xe (i.e. 12 Hz) yields an acquisition spectral width (SW) and effective coil bandwidth requirement of ~3 kHz, meaning the maximum permitted coil quality factor Q for imaging is $Q(256\times256) = B_1/SW = 573/3 = 191$. A ^{129}Xe surface coil for human imaging has been constructed with $Q_{loaded} = 126$ (and $Q_{unloaded} = 156$) when tuned and matched to the loaded condition.

3rd Generation Fully-Automated Stopped Flow Xenon-129 Hyperpolarizer

Panayiotis Nikolaou, Aaron M. Coffey, Eduard Y. Chekmenev

Background and Significance

Over the last two decades there have been many advances in the field of hyperpolarized (HP) noble gas production and imaging, largely enabled by the development of low-cost, high-power frequency-narrowed laser diode arrays (LDAs) and the improvement of ^{129}Xe polarizer technology in general. These recent developments in the field make HP ^{129}Xe an attractive and feasible diagnostic tool for a variety of potential biomedical applications. In particular, our team along with our collaborators previously has developed two generations of clinical-scale hyperpolarizers: an "open-source" prototype, and our "3D-printed" hyperpolarizer--each improving on the previous generation, with the ultimate goal to develop a relatively low-cost, high-capacity ^{129}Xe hyperpolarizer with fully automated operation that can deliver near-unity ^{129}Xe nuclear spin polarization—making it attractive for both biomedical and basic research (including for potential clinical use).

Methods

The new XeUS polarizer operates using a positive-pressure gas manifold with a pre-mixed ^{129}Xe/N$_2$ gas cylinder (*e.g.*, using a 50:50 mix or other compositions), which is employed to load a 0.5 L OP cell to >2000 Torr total gas pressure. This design allows the hyperpolarizer to generate up to 1 L/cycle of HP ^{129}Xe mixture every ~30 minutes. The device chassis is relatively compact: 0.55 m (width) x 1.25 m (length) x 1.35 m (height), and the hyperpolarizer runs on a dedicated single 220 V (20 Amp) circuit. This device utilizes a micro-channel cooled 795 nm, 180 W LDA module (QPC Lasers) with spectral width (FWHM) of <0.2 nm, and with 2" expanding telescope optics to provide homogeneous illumination of the OP cell. The new design employs an aluminum heating jacket (vs. circulating air) that has direct thermal contact with the OP cell housed within it, which in turn is aligned concentrically to the laser. The aluminum jacket offers several advantages over a conventional forced-air oven: (i) it heats and cools the OP cell significantly faster, thus reducing polarization cycle times, (ii) it provides rf-shielding for the integrated 40 kHz in-situ NMR coil, (iii) it eliminates the need

Figure 1. The 3D rendering of the 3rd generation ^{129}Xe fully automated stopped-flow hyperpolarizer.

for additional windows typically used in forced-air SEOP ovens (which can cause small but undesirable losses in laser intensity), and (iv) allows for more compact integration of in-situ near-IR and NMR sensors. The entire optical path resides in a "light-tight" portion of the chassis.

Instead of using multiple large coils (*e.g.* Helmoltz coil pair), this system employs a single solenoid B_0 NMR magnet that is 8" OD and 22" long with field homogeneity of ~300 ppm over a 5 cm sphere, and integrated RF shielding. This magnet (<10 kg) produces a B_0 of ~4 mT using < 0.2 kW. The XeUS polarizer runs on a custom-built micro-controller driver module allowing complete automation, monitoring, and control of all on-board devices, safety sensors/interlocks, and solenoid valves by using custom software. This device can be operated in fully automated or advanced-user (expert operating components individually) modes. Moreover, the hyperpolarizer software is web-browser based, and therefore can be run on a variety of computers (*e.g.*, laptop, tablet, etc.) connected locally via USB or Wi-Fi, or remotely. Finally, XeUS hyperpolarizer quality assurance data (e.g. %P_{Xe}) and other advanced reporting data (e.g., laser power output, errors, etc.) are stored locally as well as in the cloud.

Results & Conclusions

The combination of improved LDA technology, along with other improvements over previous generations, will result in a single push button and better performing xenon hyperpolarizer, ready for pre-clinical use.

Acknowledgments

Enhancement of ^{15}N NMR signals via Heterogeneous SABRE-SHEATH

Max Gemeinhardt,[1] Larisa M. Kovtunova,[2] Kirill Kovtunov,[3,4] Jonathan Gesiorski,[1*] Liana B. Bales,[1*] Igor V. Koptyug,[3,4] Valerii I. Bukhtiyarov,[2] Eduard Y. Chekmenev,[5,6,7,8] Boyd M. Goodson[1,9]

[1]Department of Chemistry and Biochemistry, Southern Illinois University, Carbondale, IL 62901; *Undergraduate Researcher; [2]Boreskov Institute of Catalysis, Novosibirsk, Russia; [3]International Tomography Center, [4]Novosibirsk State University, Novosibirsk 630090, Russia; [5]Department of Radiology, Vanderbilt University, Nashville, TN, 37232; [6]Department of Biomedical Engineering, Vanderbilt University, Nashville, TN, 37235; [7]Vanderbilt-Ingram Cancer Center, Vanderbilt University, Nashville, TN, 37205; [8]Russian Academy of Sciences, Moscow, Russia; [9]Materials Technology Center, SIUC.

While there are several ways to achieve hyperpolarization of nuclear spins to enhance NMR and MRI signals, the methods involving PHIP (ParaHydrogen Induced Polarization) and SABRE (Signal Enhancement by Reversible Exchange) have demonstrated the ability to provide reasonable enhancements in simple, economical set ups[1,2]; moreover, these parahydrogen-based methods are of interest because they are rapid (acting in seconds or 10s of seconds) and potentially can have high agent throughput with continuous agent generation. In these methods an organometallic catalyst is used to form a coordination complex between the *para*-hydrogen (*para*-H$_2$) and the target substrate molecule: In traditional PHIP, this allows hydrogenation of unsaturated bonds and hence a transfer of spin order to the substrate; however in SABRE, the complex is transient in nature and spin polarization is transferred through the J-coupling network without requiring permanent chemical change to the target substrate. Furthermore, while SABRE was originally demonstrated with enhancement of ^{1}H spins with magnetic "mixing" fields of ~10^2 Gauss (chosen to roughly match the frequency difference between source and target spins to the magnitude of the scalar couplings between them),[2] achieving efficient transfer to heteronuclei is harder because the difference in frequencies is ordinarily so much larger (e.g ~10-fold ratio of gyromagnetic ratios for ^{1}H versus ^{15}N). It was recently shown (in collaboration with Warren & Theis at Duke) use of a simple mu-metal magnetic shield allows the mixing field to be lowered to <1 μT—sufficient to enable efficient transfer of spin order from *para*-H$_2$ to ^{15}N spins and achieve NMR signal enhancements by orders of magnitude[3]–an approach dubbed "SABRE-SHEATH" (for SABRE in shield enables alignment transfer to heteronuclei).

One limitation of the SABRE approaches is the continued presence of the organometallic catalyst in the solution after agent hyperpolarization has been achieved—hindering a number of potential biological and biomedical applications. Moreover, recovery of the catalyst is desirable to permit later re-use. Thus, there has been interest in the development of effective heterogeneous catalysts (i.e. where the catalyst is in a different phase from the target substrate[4]) to combat such practical issues that could enable implementation of SABRE systems towards medical/imaging applications. Indeed, SABRE enhancement of ^{1}H spins was recently demonstrated with micro- and nanoscale supported catalysts.[5,6]

Here we provide the synthesis of a novel microscale HET-SABRE catalyst (Fig. 1 inset) and demonstrate its successful application to enhance ^{15}N spin polarization using the SABRE-SHEATH approach. Enhancements of up to ~100-fold were achieved with ~50% *para*-H$_2$ fraction (Fig. 1E), and separation of the catalyst from the supernatant solution prevented the observation of SABRE-SHEATH enhancement—showing that the effect is the result of the heterogeneous catalyst (and not the result of any homogeneous catalyst leaching from the supports). Ongoing efforts are directed to improving the efficiency of the effect and extension to biologically relevant agents.
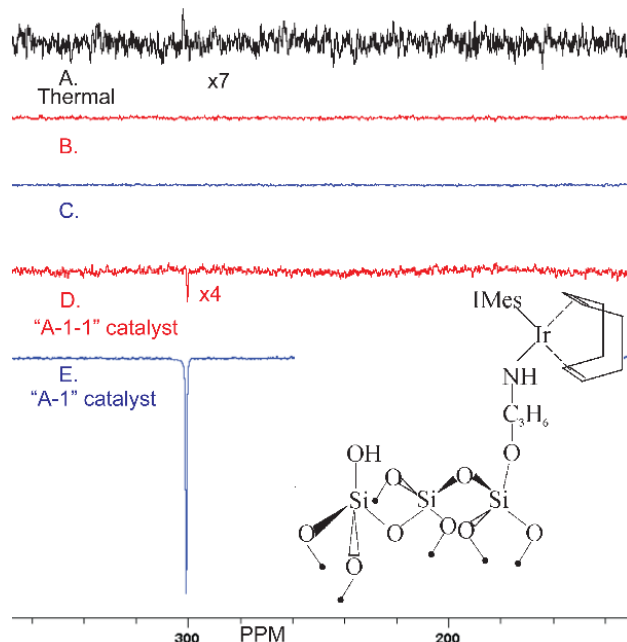

Figure 1. Selected ^{15}N spectra from "HET-SABRE-SHEATH" experiments. (A) Weak thermally-polarized ^{15}N signal from ~100 mM ^{15}N-labeled pyridine. (D & E) respectively show ^{15}N SABRE enhancement using two formulations ("A-1" and "A-1-1") of the catalyst shown in the *Inset* (ε~100 in E compared to A). Corresponding spectra in (B) and (C) attempting SABRE-SHEATH with the supernatant liquids from these HET-SABRE catalysts fail to exhibit any ^{15}N enhancement. *Inset* shows the structure of the HET SABRE catalyst "A-1" used in these experiments.

References[1]Bowers & Weitekamp, *JACS*, **1987** *109*, 5541, [2]Adams, et al. Science, 2009, 323 (5922), 1708; [3]Theis *et al*. *JACS*, **2015** *137*, 1404, [4]Hîbner *et al. Adv. Synth. Catal.,* **2016** 358, 3, [5]Shi, *et al. Angew. Chem. Int. Ed.* **2014,** 53, 1; [6]Shi, *et al. JPCC.* **2015,** *119*, 7525.

Hyperpolarization of 15N in aqueous Solution with SABRE SHEATH

Johannes F. P. Colell[a], Meike Emondts[b], Angus W. J. Logan[a], Kun Shen[a], Roman Shchepin[c], Peter Spannring[b,d], Qiu Wang[a], Steven J. Malcolmson[a], Eduard Y. Chekmenev[c], Martin Feiters[d], Floris Rutjes[d], Bernhard Blümich[b], Warren S. Warren[a] and Thomas Theis[a]

[a] Department of Chemistry, Duke University, Durham, NC 27708, USA. [b] Institut für Technische und Makromolekulare Chemie (ITMC), RWTH Aachen University, 52074 Aachen, Germany. [c] Vanderbilt Institute of Imaging Science (VUIIS), Department of Radiology, Department of Biomedical Engineering, Vanderbilt-Ingram Cancer Center (VICC), Vanderbilt University, Nashville, TN 37232, USA. [d] Radboud University Nijmegen, Cluster for Molecular Chemistry, 6525 AJ

SABRE and the heteronuclear SABRE-SHEATH variant (^{15}N, ^{31}P, ^{13}C), is undergoing rapid development. In SABRE a solution of a suitable transition metal catalyst and a substrate of interest is exposed to highly enriched in the para-hydrogen, the polarization transfer target nucleus depends on ambient magnetic field. Translation of SABRE to aqueous systems is of particular importance, as it significantly expands the flexibility of the method and hence application potential.[1, 2] To date, moderate enhancements on ^1H were demonstrated in N-heterocyclic aromatic systems by different approaches. Hyperpolarization in aqueous solution is especially relevant in light of recent advances in the field of imaging with hyperpolarized markers in clinical settings.[3]

Figure 1: [IrCl[COD](IDEG)] allows for polarization transfer to heteronuclei in water. The substrate scope of heteronuclear SABRE in water encompasses sp and sp^2 nitrogen.

We have expanded SABRE-SHEATH[4] to direct hyperpolarization of ^{15}N in water. Different structural moieties and molecules of biochemical interest can be readily polarized (see Fig.1). Hyperpolarization of heteronuclei is of special interest, as characteristically longer T_1 relaxation times allow for extended delays between creating hyperpolarization and readout. Larger viable time-delay prior to detection, and greater chemical shift dispersion result in enhanced sensitivity to chemical transformations.

Figure 2: Investigation and comparison of ^{15}N polarization as function of temperature and magnetic field in different solvent catalyst systems.

We performed a comparative study of the established [IrCl(IMes)(COD)] system in methanol and the aqueous system. As shown in Fig. 2, a comparison of polarization levels and correlation with system concentrations is illuminating, as it allows to understand mechanistic details and limiting factors to polarization buildup and maximization. For the novel [IrCl[COD](IDEG)] system maximum hyperpolarization is observed at elevated temperatures of 80 °C

With the presented approaches we overcome three major obstacles. First, we create significant enhancements in aqueous media, not methanol; second, we expand the substrate scope by targeting 15N which can be brought closer to the hyperpolarization source than 1H in the molecular backbone and lastly, we achieve significant hyperpolarization lifetime extensions by relying on 15N instead of protons.

1.   M. L. Truong, F. Shi, P. He, B. Yuan, K. N. Plunkett, A. M. Coffey, R. V. Shchepin, D. A. Barskiy, K. V. Kovtunov, I. V. Koptyug, K. W. Waddell, B. M. Goodson and E. Y. Chekmenev, *J. Phys. Chem. B*, 2014, **18** 13882–13889.
2.   P. Spannring, I. Reile, M. Emondts, P. P. M. Schleker, N. K. J. Hermkens, N. G. J. van der Zwaluw, B. J. A. van Weerdenburg, P. Tinnemans, M. Tessari, B. Blümich, F. P. J. T. Rutjes and M. C. Feiters, *Chem. Eur. J.*, 2016, DOI: 10.1002/chem.201601211, 9277-9282.
3.   S. J. Nelson, J. Kurhanewicz, D. B. Vigneron, P. E. Z. Larson, A. L. Harzstark, M. Ferrone, M. van Criekinge, J. W. Chang, R. Bok, I. Park, G. Reed, L. Carvajal, E. J. Small, P. Munster, V. K. Weinberg, J. H. Ardenkjaer-Larsen, A. P. Chen, R. E. Hurd, L. I. Odegardstuen, F. J. Robb, J. Tropp and J. A. Murray, *Sci. Transl. Med.*, 2013, **5**, 198ra108-198ra108.

4.	T. Theis, M. L. Truong, A. M. Coffey, R. V. Shchepin, K. W. Waddell, F. Shi, B. M. Goodson, W. S. Warren and E. Y. Chekmenev, *J. Am. Chem. Soc.*, 2015, **137**, 1404-1407.

[1]H SABRE and ^{15}N SABRE-SHEATH Enhancement and Competitive Binding of Primary DNA Nucleobases

Bryce E. Kidd,[1] Max E. Gemeinhardt,[1] Jamil Mashni,[1] Liana Bales,[1] Jonathan Gesiorski,[1] Eduard Y. Chekmenev,[2] and Boyd M. Goodson[1]

1.) Department of Chemistry and Biochemistry, Southern Illinois University, Carbondale, Illinois 62901
2.) Department of Radiology, Department of Biomedical Engineering, Department of Physics and Astronomy, Vanderbilt University Institute of Imaging Science (VUIIS), Nashville, Tennessee 37232 (United States) and Russian Academy of Sciences, Leninskiy Prospekt 14, 119991 Moscow (Russia)

With ΔE between nuclear spin states that is much less than kT, NMR only accesses ~0.003% of available molecules (for ^{1}H and B_0 = 9.4 T) and thus suffers from poor detection sensitivity. Hyperpolarization methods like signal amplification by reversible exchange (SABRE),[1] spin-exchange optical pumping (SEOP),[2] dynamic nuclear polarization (DNP)[3] produce non-Boltzmann spin populations to greatly enhance NMR signals. With hyperpolarization, rapid acquisition of less-sensitive and low-natural-abundance nuclei (e.g., ^{15}N) is greatly facilitated, making it feasible to perform NMR/MRI of low-concentration species. Among these hyperpolarization techniques, SABRE—a type of *para*hydrogen-induced polarization (PHIP)[4]—can be conducted inexpensively and merely requires the production of the spin isomer *para*hydrogen (*para*-H$_2$), an appropriate external field, and a catalyst to enable transfer of spin order from *para*-H$_2$ to a reversibly-ligating substrate through the *J*-coupling network.[1] SABRE has the potential to produce biologically-friendly hyperpolarized spectral probes and contrast agents for MRI.

While the field of SABRE has grown rapidly since its inception in 2009,[1] to date there are only a handful of substrates that are adequate for potential biological or clinical use. This limitation is due to the need of small (usually heterocyclic) molecules like N-heterocycles that can reversibly exchange with the catalyst. Ideally, the substrate of interest should also be soluble in a biologically-friendly solvent (e.g., ethanol and/or water) and undergo large polarization enhancements.

Deoxyribonucleic acid (DNA) consists of two opposing polynucleotides that hydrogen bond through nucleobase-pairs (Adenine:Thymine and Guanine:Cytosine) to form the well-known double helix that is crucial to life as we know it. Thus with inspiration from DNA (and following previous studies[5,6]), here we explore: 1) the efficacy of three primary nucleobases (3-methyladenine, 6-O-methylguanine, and cytosine) to undergo enhancement via ^{1}H SABRE (at ~2-8 mT) and ^{15}N SABRE (<1 μT, via SABRE in shield enables alignment transfer to heteronuclei, SABRE-SHEATH[7]) using the Ir(COD)(IMes)Cl catalyst; and 2) the
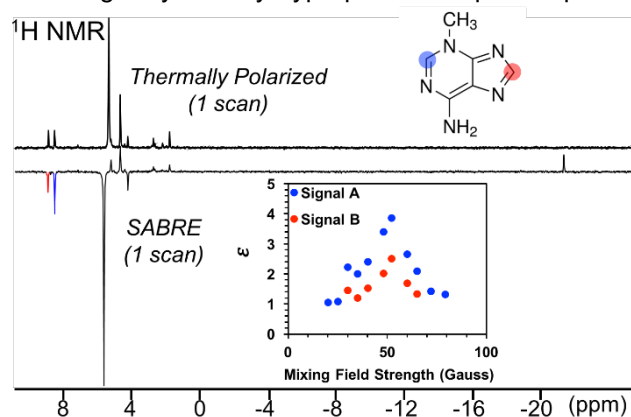

Figure 1. [1]H thermally-polarized (top) and SABRE-enhanced (bottom) spectra of 3-methyl adenine shows a maximum enhancement of ~4 at 52 G mixing field (solvent enhancement is also observed).
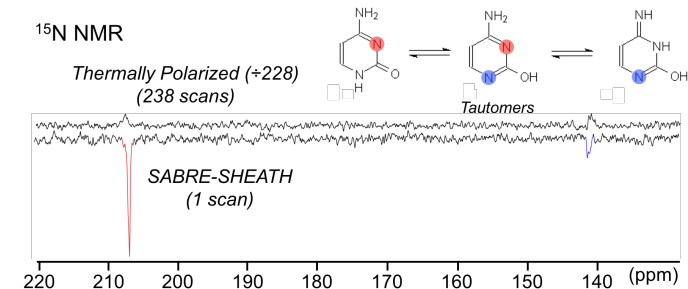
corresponding effects of competitive binding within DNA base mixtures. Upon activation of the catalyst (4 mM catalyst in Ethanol-d$_6$ or Ethanol-d$_6$/D$_2$O mixtures) with *para*-H$_2$ (47.6% enriched, 75 psi, and 150 sccm bubbling rate) and only one nucleobase (10:1 mol ratio of base:catalyst), we find that all three nucleobases exhibit at least weak SABRE enhancement (ε for 3-methyladenine (Figure 1) > 6-O-methylguanine > cytosine). Interestingly, we observe a time-dependent decrease in ε for 6-O-methylguanine and cytosine (^{1}H and ^{15}N); wherein the decay rate of ε depends on the amount of co-ligand present (e.g., mixtures of cytosine and 3-methyladenine). The decay in ε is potentially due to deamination (i.e., cytosine converting to uracil) in the presence of D$_2$O to afford a strong ligating nucleobase that may not reversibly exchange and thus may "deactivate" the catalyst. Finally, we show ^{15}N SABRE-SHEATH of cytosine (Figure 2) for the first time. Differences in the ^{15}N thermally polarized and SABRE-SHEATH spectra are consistent with preferential binding of one tautomer over the others.

References
(1) Adams, R. W. *et al. Science*, **2009**, *323 (5922)*, 1708 – 1711.
(2) Goodson, B. M. *J. Magn. Reson.*, **2002**, *155* (2), 157 – 216.
(3) Abragam, A.; Goldman, M. *Rep. Prog. Phys.*, **1978**, Volume 41.
(4) Bowers, R. C.; Weitekamp, D. P. *Phys. Rev. Lett.*, **1986**, *57 (21)*, 2645 – 2648.
(5) Hövener, J. *et al. Nat. Commun.*, **2013**, *4*, 1 – 5.
(6) Theis, T. *et al. Sci. Adv.*, **2016**, *2 (3)*, 1 – 7.
(7) Theis, T. *et al. J. Am. Chem. Soc.*, **2015**, *137*, 1404 – 1407.

Figure 2. [15]N thermally polarized (top) and SABRE-SHEATH enhanced (bottom) spectra of cytosine shows a maximum enhancement of ~60 at ≤ 1 μT mixing field and preferential binding of one tautomer.

Toward Hypoxia and pH Sensing ^{15}N Hyperpolarized Contrast Agents Using SABRE-SHEATH

Roman V. Shchepin [1], Danila A. Barskiy [1], Aaron M. Coffey [1], Thomas Theis [2], Kirill V. Kovtunov [3,4], Larisa M. Kovtunova [3,4], Igor V. Koptyug [3,4], Warren S. Warren [2], Boyd M. Goodson [5,6], Eduard Y. Chekmenev [1]

[1] Vanderbilt University Institute of Imaging Science (VUIIS), Department of Radiology, Nashville, TN, 37232; [2] Department of Chemistry, Duke University, Durham, North Carolina, 27708, United States; [3] Laboratory of Magnetic Resonance Microimaging International Tomography Center, [4] Novosibirsk State University, Novosibirsk 630090, Russia; [5] Department of Chemistry and Biochemistry, [6] Materials Technology Center, Southern Illinois University, Carbondale, Illinois 62901, United States

NMR hyperpolarization techniques increase nuclear spin polarization from thermal equilibrium levels of 10^{-6}-10^{-5} by orders of magnitude—in some cases approaching 100%. ^{15}N sites are particularly interesting because of their greater compared to ^{13}C polarization decay constants of up to 20 minutes [6]. Moreover, ^{15}N isotopic enrichment is frequently performed using relatively straightforward, chemical process and less expensive starting materials [3]. Direct hyperpolarization of heteronuclei with NMR Signal Amplification By Reversible Exchange (SABRE [4]) is possible via SABRE-SHEATH (SABRE in SHield Enables Alignment Transfer to Heteronuclei) [1,2]. SABRE-SHEATH is scalable, provides efficient hyperpolarization in seconds, and uses very simple and inexpensive hardware [5,6].

^{15}N nuclear spins of imidazole-^{15}N$_2$ were hyperpolarized using the NMR SABRE-SHEATH (Fig. 1a) [7]. A ^{15}N NMR signal enhancement of ~2 000 fold at 9.4 T is reported using parahydrogen gas (~50% para-H$_2$) and ~0.1 M imidazole-^{15}N$_2$ in aqueous buffer. Proton binding to a ^{15}N site of imidazole occurs at physiological pH (pKa ~ 7.0), and the binding event changes the ^{15}N isotropic chemical shift by ~30 ppm (Fig. 2b). Imidazole pKa is more suitable for *in vivo* pH sensing compared to pKas of previously studied ^{15}N-pyridine derivatives [9]. Moreover, ^{15}N$_2$-imidazole has a relatively low toxicity, and therefore ^{15}N-SABRE-SHEATH hyperpolarization potentially enables *in vivo* pH sensing at high (9.4 T) and low (0.05 T) fields. We also report robust ^{15}N synthesis of ^{15}N$_2$-imidazole based on ^{15}NH$_4$Cl.

Direct NMR hyperpolarization of ^{15}N sites in metronidazole using SABRE-SHEATH produced nuclear spin polarization P_{15N} of ~24% (Fig. 1d) using 80% para-H$_2$ gas corresponding to P_{15N}~32% if ~100% para-H$_2$ were employed [8]. In addition to this demonstration on the directly binding ^{15}N site (via $^2J_{H-15N}$), we also hyperpolarized more distant ^{15}N sites in metronidazole using longer-range spin-spin couplings ($^4J_{H-15N}$ and $^5J_{H-15N}$, Fig. 1c and 1e). Furthermore, this efficient (P_{15N}>20%) SABRE-SHEATH hyperpolarization is conducted in <1 minute, which is significantly more efficient and faster than ^{15}N d-DNP hyperpolarization of comparable compounds [8]. HP nitroimidazole and its derivatives are potentially imaging agents already used for *in vivo* hypoxia sensing using PET.

Taken together, ^{15}N-SABRE-SHEATH hyperpolarization of imidazole and metronidazole significantly expand the range of biologically relevant molecular structures and sites amenable to hyperpolarization via low-cost parahydrogen-based methods.

References: [1] Theis, T.; et al. *J. Am. Chem. Soc.* **2015,** *137*, 1404. [2] Truong, M. L.; et al. *J. Phys. Chem. C* **2015,** *119*, 8786. [3] Shchepin, R. V.; et al. *Bioconjugate Chem.* **2016,** *27*, 878. [4] Adams, R. W.; et al. *Science* **2009,** *323*, 1708. [5] Truong, M. L.; et al. *J. Phys. Chem. B* **2014,** *18*, 13882. [6] Theis, T.; et al. *Sci. Adv.* **2016,** *2*, e1501438. [7] Shchepin, et al. *ACS Sensors* **2016,** *1*, 640. [8] Barskiy, D. A.; Shchepin, R. V.; et al. *J. Am. Chem. Soc.* **2016,** *138*, 8080. [9] Shchepin, R. V.; et al. *J. Phys. Chem. Lett.* **2015**, *6,* 1961.
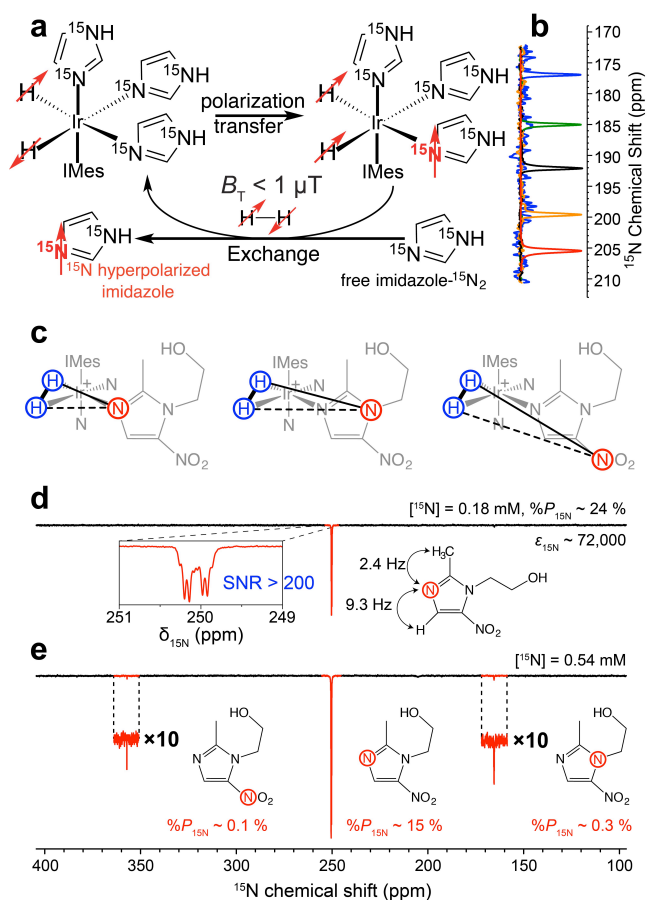
Figure 1. **a)** Structure of the activated Ir-IMes hexacoordinate complex after activation with H$_2$. The complex undergoes fast exchange with *para*-H$_2$ and free imidazole-^{15}N$_2$, which enables spontaneous polarization transfer from *para*-H$_2$ to ^{15}N nuclei of imidazole-^{15}N$_2$ in µT magnetic fields [1,2]. **b)** ^{15}N NMR spectra of imidazole-^{15}N$_2$ hyperpolarized via SABRE-SHEATH at pH values around pKa in aqueous buffer. **c)** Most-probable metronidazole-bound structures of the complex with relevant AA'B spin systems [8]. **d)** ^{15}N spectrum of HP natural abundance 50 mM metronidazole. Note the appearance of NMR resonances as a doublet of quartets due to spin-spin coupling of ^{15}N with aromatic and methyl protons (inset). **e)** ^{15}N spectrum of HP (SABRE-SHEATH) natural abundance 150 mM metronidazole. All ^{15}N spectra are recorded at 9.4 T.

3rd-Generation Fully-Automated Stopped-Flow Xenon-129 Hyperpolarizer

Panayiotis Nikolaou,[a] Aaron M. Coffey,[a] Bryce E. Kidd,[c] Megan Murphy,[c] Justin Porter,[c] Michael J. Barlow,[b] Boyd M. Goodson,[c] Eduard Y. Chekmenev[a]

[a]Vanderbilt University Institute of Imaging Science (VUIIS), Department of Radiology, Nashville, TN, USA
[b]Sir Peter Mansfield Magnetic Resonance Centre, University of Nottingham, Nottingham, UK
[c]Department of Chemistry & Biochemistry, Southern Illinois University Carbondale, IL, USA

Over the last two decades there have been many advances in the field of hyperpolarized (HP) noble gas production and imaging, largely enabled by the development of low-cost, high-power frequency-narrowed laser diode arrays (LDAs) and the improvement of ^{129}Xe polarizer technology in general. These recent developments in the field make HP ^{129}Xe an attractive and feasible diagnostic tool for a variety of potential biomedical applications. In particular, our team along with our collaborators previously has developed two generations of clinical-scale hyperpolarizers: an "open-source" prototype, and our "3D-printed" hyperpolarizer--each improving on the previous generation, with the ultimate goal to develop a relatively low-cost, high-capacity ^{129}Xe hyperpolarizer with fully automated operation that can deliver near-unity ^{129}Xe nuclear spin polarization—making it attractive for both biomedical and basic research (including for potential clinical use).

Here we present the development and features of the new 3rd-generation stopped-flow ^{129}Xe hyperpolarizer (**Fig. 1**) dubbed "XeUS". As with most previous ^{129}Xe polarizers, XeUS-3 utilizes Spin Exchange Optical Pumping (SEOP), a process in which resonant, circularly polarized photons optically pump Rb electrons, which in turn hyperpolarize the ^{129}Xe nuclear spins via hyperfine interactions (the "spin-exchange" process).

The new XeUS polarizer operates using a positive-pressure gas manifold with a pre-mixed ^{129}Xe/N_2 gas cylinder (*e.g.*, using a 50:50 mix or other compositions), which is employed to load a 0.5 L OP cell to >2000 Torr total gas pressure. This design allows the hyperpolarizer to generate up to 1 L/cycle of HP ^{129}Xe mixture every ~30 minutes. The device chassis is relatively compact: 0.55 m (width) x 1.25 m (length) x 1.35 m (height), and the hyperpolarizer runs on a dedicated single 220 V (20 Amp) circuit. This device utilizes a micro-channel cooled 795 nm, 180 W LDA module (QPC Lasers) with spectral width (FWHM) of <0.2 nm, and with 2" expanding telescope optics to provide homogeneous illumination of the OP cell. The new design employs an aluminum heating jacket (vs. circulating air) that has direct thermal contact with the OP cell housed within it, which in turn is aligned concentrically to the laser (**Fig. 2**). The aluminum jacket offers several advantages over a conventional forced-air oven: (i) it heats and cools the OP cell significantly faster, thus reducing polarization cycle times, (ii) it provides rf-shielding for the integrated 40 kHz in-situ NMR coil, (iii) it eliminates the need for additional windows typically used in forced-air SEOP ovens (which can cause small but undesirable losses in laser intensity), and (iv) allows for more compact integration of in-situ near-IR and NMR sensors. The entire optical path resides in a "light-tight" portion of the chassis.

Figure 1. The 3D rendering of the 3rd generation ^{129}Xe fully automated stopped-flow hyperpolarizer.

Instead of using multiple large coils (*e.g.* Helmoltz coil pair), this system employs a single solenoid B_0 NMR magnet that is 8" OD and 22" long with field homogeneity of ~300 ppm over a 5 cm sphere, and integrated RF shielding. This magnet (<10 kg) produces a B_0 of ~4 mT using < 0.2 kW. The XeUS polarizer runs on a custom-built micro-controller driver module allowing complete automation, monitoring, and control of all on-board devices, safety sensors/interlocks, and solenoid valves by using custom software. This device can be operated in fully automated or advanced-user (expert operating components individually) modes. Moreover, the hyperpolarizer software is web-browser based, and therefore can be run on a variety of computers (*e.g.*, laptop, tablet, etc.) connected locally via USB or Wi-Fi, or remotely. Finally, XeUS hyperpolarizer quality assurance data (e.g. %P_{Xe}) and other advanced reporting data (e.g., laser power output, errors, etc.) are stored locally as well as in the cloud.

References: [1] Goodson, B. M. *JMR* **2002**, *155*, 157. [2] Nikolaou, P.; et al. *PNAS* **2013**, *110*, 14150. [3] Nikolaou, P.; et al. *Magn. Reson. Imaging* **2014**, *32*, 541. [4] Nikolaou, P.; et al. *JACS* **2014**, *136* 1636. [5] Nikolaou, P.; et al. *J. Phys. Chem. B* **2014**, *118*, 4809. [6] Barskiy, D. A.; et al. *Chem. Eur. J.* **2016**, DOI 10.1002/chem.201603884.
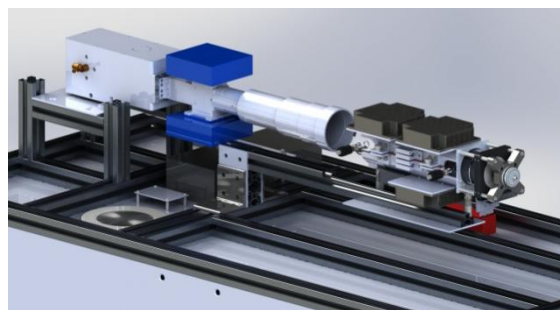
Figure 2. The new 180W frequency-narrowed LDA, and aluminum OP cell heating jacket, with integrated rf-shielded 40 kHz NMR coil, retro-reflection mirror, and IR sensor.

Hyperpolarized propane: relaxation, long-lived spin states, and spin-lock induced crossing (SLIC) dispersion

Danila A. Barskiy[1], Oleg G. Salnikov[2,3], Alexey S. Romanov[2,3], Matthew A. Feldman[1], Aaron M. Coffey[1], Kirill V. Kovtunov[2,3], Igor V. Koptyug[2,3], Eduard Y. Chekmenev[1]

[1]Vanderbilt University Institute of Imaging Science (VUIIS), Nashville, TN 37232, USA
[2]International Tomography Center, 3A Institutskaya st., Novosibirsk 630090, Russia
[3]Novosibirsk State University, 2 Pirogova st., Novosibirsk 630090, Russia

Hyperpolarization can enhance nuclear magnetic resonance signals by 4–8 orders of magnitude. This dramatic sensitivity increase enables the detection of dilute exogenous contrast media at low concentrations *in vivo*. The delivery of hyperpolarized (HP) contrast agents by inhalation for functional and molecular imaging is particularly attractive, because of its convenience and relative non-invasiveness. Hyperpolarized (HP) [129]Xe is currently the most promising agent for pulmonary imaging, because (i) it can be hyperpolarized to the order unity on a clinical scale [1], (ii) it is inert, and (iii) it has very large chemical shift dispersion useful for sensing the environment. However, HP [129]Xe technology has several major obstacles for widespread clinical translation: (i) low natural isotopic abundance of [129]Xe (~26%), (ii) the need for high-cost hyperpolarization equipment, (iii) the requirement for a customized multinuclear capability of MRI scanner. These obstacles currently limit this technology to only a few sites in the world.

Recently we showed that HP propane is good candidate for pulmonary imaging and other non-biomedical applications [2-3]. Indeed, propane is a non-toxic gas, it can be readily hyperpolarized via pairwise hydrogenation of propylene with parahydrogen (p-H_2), and it has much lower cost (few cents vs. tens of dollars per liter) compared to HP [129]Xe. Moreover, it can be imaged using conventional proton hardware universally available on clinical MRI scanners.

Here, we present a systematic relaxation study of the HP propane gas at high (9.4 T) and low (0.05 T) magnetic fields. Propane T_1 is linearly dependent on the fraction of the propane in the mixture with hydrogen and on the total gas pressure. Moreover, if propane is produced via parahydrogen-induced polarization (PHIP) at low magnetic fields (*i.e.*, under strong-coupling regime, where chemical shift difference between CH_2 and CH_3 protons is less than their spin-spin coupling constant J), the symmetry of p-H_2-nascent singlet state is partially conserved in the formed propane molecule, and produced in this fashion propane possesses long-lived spin states (LLSS). We investigated how spin-lock induced crossing (SLIC) technique [4] can be used to convert these LLSS of propane into observable magnetization to detect ^{1}H NMR signal directly at 0.05 T (Fig. 1A) [5-6]. The NMR signal dependence on SLIC amplitude exhibits a well-resolved dispersion, which is induced by the spin-spin couplings in the 8-proton spin system of propane (Fig. 1B). We also measured the lifetime (T_S) of the propane LLSS by varying the time between hyperpolarized propane production and SLIC detection: on average, T_S is approximately 3 times longer than the

Figure 1. (**a**) Molecular diagram of p-H_2 addition to propylene over Rh/TiO_2 at 0.05 T resulting in the formation of pseudo-singlet long-lived spin states (LLSS) of propane, followed by the application of spin-lock induced crossing (SLIC) sequence to transform LLSS into an observable magnetization and to detect the NMR signal. (**b**) Experimentally measured (black circles and trace) and theoretically calculated (red trace) dependence of the SLIC induced HP propane signal on B_1 amplitude at the SLIC RF pulse duration (τ_{slic}) of 0.5 s at 0.05 T. (**c**) Example of T_1 (black symbols and trace) and T_S (red symbols and trace) measurements of gaseous HP propane at ~7.6 atm.

corresponding T_1 value under the same conditions (Fig. 1C). Moreover, T_S exceeds 13 seconds at pressures above 7 atm in the gas phase. These results are in agreement with the previous reports, and they substantiate a great potential of long-lived HP propane as an inhalable gaseous contrast agent for lung imaging and other applications using low-field (<0.4 T) NMR and MRI.

1. D. A. Barskiy, et al. *Chem. Eur. J.*, DOI: 10.1002/chem.201603884 [journal cover].
2. K. V. Kovtunov, et al. *Chem. Eur. J.*, **2014**, 20 (45) 14629; *Chem. Eur. J.*, **2014**, 20 (37) 11636 [journal cover].
3. K. V. Kovtunov, et al. *J. Phys. Chem. C*, **2014**, *118*, 28234 [journal cover].
4. S. J. DeVience, et al. *Phys. Rev. Lett.*, **2013**, 111, 173002.
5. D. A. Barskiy, et al. *J. Phys. Chem. C*, DOI: 10.1021/acs.jpcc.6b07555 [journal cover].
6. D. A. Barskiy, et al. *J. Magn. Reson.*, under review.

New Developments in Stopped-Flow Spin-Exchange Optical Pumping of [129]Xe and [131]Xe

Megan N. Murphy[1], Justin Porter[1], Bryce E. Kidd[1], Michael J. Molway[1], Dustin Basler[1]
Kaili Ranta[1*], Max E. Gemeinhardt[1], Aaron M. Coffey[4], Panayiotis Nikolaou[4], Bamidele D. Falola[2,3], Ian I. Suni[1,2,3],
Matthew S. Rosen[5], Michael J. Barlow[6], Eduard Y. Chekmenev[4], and Boyd M. Goodson[1,3]

[1]Department of Chemistry & Biochemistry, [2]Department of Mechanical Engineering & Energy Processes, [3]Materials Technology Center, Southern Illinois University, Carbondale, IL; [4]Vanderbilt University Medical Center, Nashville, TN; [5]MGH/ Martinos Center for Biomedical Imaging, Boston, MA; [6]School of Medicine, University of Nottingham, Queens Medical Centre, Nottingham, UK; *present address: The Ohio State Medical School, Columbus, OH.

Spin exchange optical pumping (SEOP) is a noble gas hyperpolarization technique with applications in biomedical imaging,[1] NMR spectroscopy of molecules and materials,[1] and in tests of fundamental physics.[2] In SEOP, circularly polarized laser light depopulation pumps an alkali metal vapor (e.g. Rb) into an electronically spin-polarized ground state. This electronic spin polarization is transferred to the nuclei of noble gases during collisions. Of present interest are experimental aspects of clinical-scale production of hyperpolarized (HP) xenon by stopped-flow SEOP,[3,4] specifically SEOP cell design (including the use of alternative materials, coatings, and geometries), laser technology, and ultra-low field (*in situ*, ~1.6-5.8 mT) versus high-field (*ex situ*, 9.4 T) polarimetry of [129]Xe and [131]Xe.

We describe here progress on the use of Al-walled cells for stopped-flow SEOP production of HP [129]Xe. SEOP cells are usually made of boro- or aluminosilicate glass because of the need to operate at high temperature, resist chemical damage, and contain low levels of magnetic impurities. While Cu has been demonstrated in large *continuous*-flow cells,[5] long [129]Xe T_1 values are usually needed in order for high P_{Xe} to be achieved via the stopped-flow approach,[4,6] and with metal-based cells there are concerns of enhanced Xe relaxation from surface paramagnetic sites and Korringa relaxation.[7] Nevertheless, implementation of Al cells could be advantageous: First, while SEOP cells are hand-blown, Al cells could be mass-produced to high precision with cheap, inter-changeable, and disposable parts. Next, metal cells should allow access to higher combinations of pressure and temperature (for higher HPXe throughput). OP efficiency should
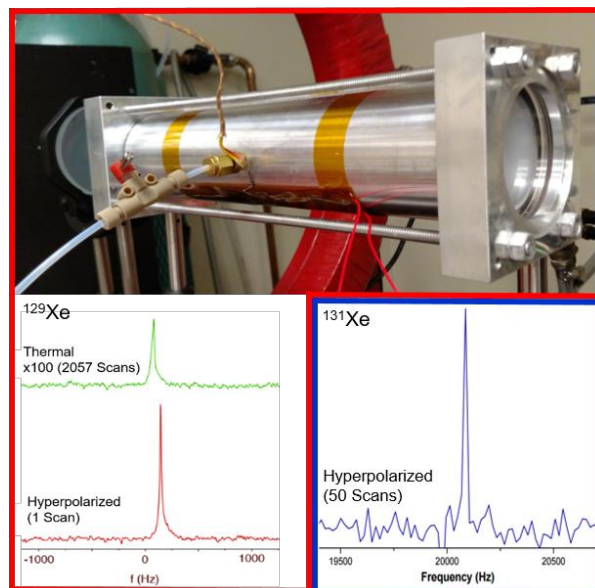

Fig. 1a. Al cell with polyimide heater seen on bottom; **Fig. 1b.** Thermal [129]Xe NMR signal (green), signal-averaged 2057 scans, 9.4 T, magnified 100x scaled against HP (red) [129]Xe (1 scan) from Al cell; **Fig. 1c.** Hyperpolarized [131]Xe (50 scans), ~5.7mT, 135 ºC.

be improved by the reduced number of optical surfaces, use of anti-reflection coatings, and the absence of warping of optical "flats" otherwise needed for glass cell structural integrity. Finally built-in heating/cooling could greatly simplify polarizer design (obviating the need for forced-air ovens) and that, combined with higher thermal conductivity, should allow more stable and agile temperature control—particularly important for automating stopped-flow SEOP (including for temperature ramping[8]) and reducing cycle times. In an initial feasibility study, batches of 1000/1000 Torr Xe/N_2 were hyperpolarized in a cylindrical ~600 cc Al-walled cell (alloy 6061, 2.5" OD, 2" ID, 12" length) using a 70 W spectrally-narrowed laser (QPC); the cell is heated with a flexible polyimide element fixed to its underside. *Ex situ* high-field measurement of the [129]Xe nuclear spin polarization (initially ~2%) with variable delays between SEOP cell cooling and gas ejection allowed an in-cell T_1 of ~25 min to be estimated. We are currently investigating the use of TiO_2 cell coatings created via galvanic deposition[9] to improve [129]Xe T_1 and better protect the chemical integrity of the Al walls, as well as the use of differential heating of the cell components to better facilitate Rb distribution in the cell and avoid Rb condensation onto optical surfaces.

In other work, we are continuing efforts to improve production of HP [131]Xe. Despite the fact that isotopes like [83]Kr (I=9/2) and [131]Xe (I=3/2) are harder to polarize because of quadrupolar relaxation, they may offer alternative contrast for functional pulmonary MRI[10,11]; [131]Xe is also of present interest because of its possible use as a HP nuclear target for probing CPT violation in spin-polarized neutron scattering experiments.[12] We previously found up to P_{Xe}~0.4%[13]; here we are investigating the use of an optimized cell geometry (3x3" O.D./length), higher temperatures (enabled by a Garolite-based forced-air oven), and higher laser power (~120 W) to improve the [131]Xe polarization (so far to ~0.6%). All of these efforts should be bolstered by a next-generation high-power (~180 W) ultra-narrow (FWHM~0.2 nm) MCC-cooled laser (QPC) and the implementation of new high-sensitivity noise-reducing surface detection coils.

Simulations of Xenon-Rich Stopped-Flow Spin-Exchange Optical Pumping at High Laser Fluxes

J.G. Skinner[1]*, K. Ranta[2]^, P. Nikolaou[3], A.M. Coffey[3], E. Chekmenev[3], B.M. Goodson[2], M.J. Barlow[1] & P. Morris[4]

[1]School of Medicine, University of Nottingham, Nottingham, UK
[2]Department of Chemistry and Biochemistry, Southern Illinois University, Carbondale, IL, USA
[3]Vanderbilt University Institute of Imaging Science (VUIIS), Department of Radiology, Nashville, TN, USA
[4]Sir Peter Mansfield Imaging Centre, University of Nottingham, Nottingham, UK
*Current address: Universitätsklinikum Freiburg, Freiburg, Germany
^Current address: School of Medicine, The Ohio State University, Columbus, OH, USA

Spin-exchange optical pumping (SEOP) [1], a method of hyperpolarisation (HP), can be used to enhance the NMR sensitivity of noble gases by up to five orders of magnitude at clinically relevant fields. SEOP-generated HP ^{129}Xe is showing great promise as a contrast agent for clinical lung imaging but an ongoing barrier to widespread clinical usage has been the challenge of economically producing clinically relevant quantities with high ^{129}Xe polarisation. Clinical-scale xenon-rich stopped-flow (SF) SEOP is now well-established in the literature [2,3] and has been used to produce very high P_{Xe} values (up to ~90% [3]); however, while previous simulation efforts have investigated SEOP (e.g., [4]), few have modelled the Xe-rich stopped-flow regime [5,6], particularly in the context of high resonant laser flux. Here, the so-called 'standard model' of SEOP, which has been previously used in the optimisation of continuous-flow Xe polarisers [7,8], is modified for– and validated against– two significant Xe-rich SF SEOP datasets [2,9]. The validated model is then used to identify practical steps that can be taken to modify the design of Xe polarisers to further increase the HPXe production efficiency. Additionally, the validated model provides further insight into the underlying physics at play in xenon-rich SF SEOP at high laser fluxes.

Two implementations of the SEOP model were used—a 2D (z,r) approach based on Mathematica ([5,6]) and a 1D (z) Python-based approach [10]—with comparisons to two literature datasets [2,9]; the approach was to include more and more features of SEOP phenomena to slowly increase model complexity in order to reproduce the experimental data. In the first experimental dataset [9], ^{129}Xe polarisation was measured as a function of temperature for a number of gas mixes (with Xe partial pressures ranging from 50-1400 torr and backfilled with N_2 to 2000 torr total pressure at loading). The gases were contained in a 1"-diameter cylindrical cell and pumped with a 29 W, 0.27 nm (spectral width) laser at ~795 nm. These experiments found an inverse relationship between the optimal (externally measured) cell temperature for SEOP (T_{opt}) and Xe density, an effect that was exploited to achieve high polarizations (~12-55% at those densities) [9]. The present simulations quantitatively reproduce these trends, and show that the magnitude of the effect is inversely related to the laser spectral linewidth. Furthermore, modulating the laser linewidth indicates that a differential gain in polarisation occurs at higher xenon densities when using narrowed lasers.

In the second experimental dataset [2], P_{Xe} was again measured as a function of temperature for a range of gas mixes (275 to 2000 torr) but also for a range of (much greater) laser powers (100, 125, 142 and 170 W) using a 0.3 nm (spectral width) laser at 795 nm and using a much larger 2"-diameter (500 cc) cell. Simulations for these conditions closely predicted peak P_{Xe} and γ_{SEOP} (a rate constant for P_{Xe} accumulation) across the full range of conditions (Fig. 1) (and also replicated the inverse relationship between T_{opt} and xenon density ([Xe])), though a slightly steeper negative gradient as a function of [Xe] in the optimal P_{Xe} values (relative to the model) may suggest thermal effects (not accounted for in the model) may be at play (Fig. 1(a)). These thermal effects may be exacerbated at higher laser powers by the increasing partial pressure of the poorly thermally conductive Xe, and therefore mitigated with the partial replacement of N_2 with more thermally conductive helium [11]. Indeed, our simulations indicate inclusion of He would have no detrimental impact on P_{Xe}. Additionally, both simulation and experiment indicate the system is laser-power limited. After validation, the model was used to investigate how to modify the design and operation of "XeUS-type" clinical-scale SF polarisers to further improve performance, including variations of cell geometry, laser linewidth, gas mixture/pressure, etc.—with results including that reduction of laser linewidth (and therefore increasing resonant intensity) improves P_{Xe} more at the higher Xe partial pressures tested. Finally, it was found that the simulations trended towards a "universally optimal" amount of laser absorption, providing an explanation for the above interplay of laser linewidth, T_{opt}, and [Xe] in the context of optimizing the photon to [Rb] ratio.
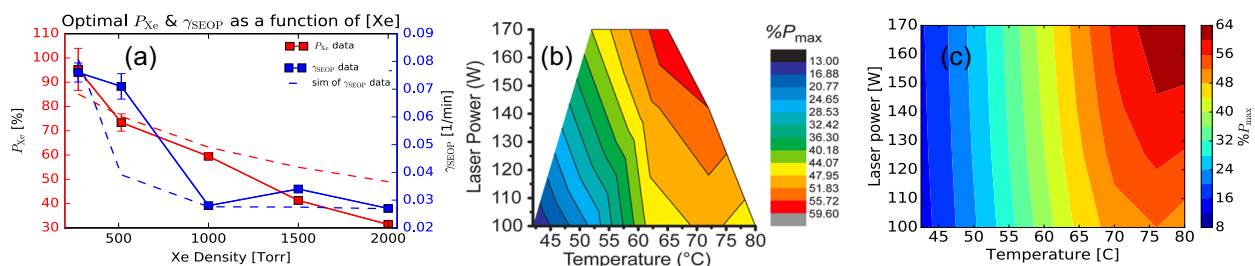

Fig.1.(a) Optimal P_{Xe} and γ_{SEOP} as a function of [Xe]. (b,c) exp. and sim. of P_{Xe} respectively at 1000 torr [Xe]. Exp. data from [2].

Feasibility Of Low-Field NMR (0.05T) Discrimination Of Spin-Spin Couplings In Vivo For Murine ^{13}C Metabolic Spectroscopy

Aaron M. Coffey,[a,b,*] Matthew A. Feldman,[a,b] Roman V. Shchepin,[a,b] Milton L. Truong,[a,b] Wellington Pham[a,b,c,d] and Eduard Y. Chekmenev[a,b,c,d,e,*]

[a]Vanderbilt University Institute of Imaging Science (VUIIS), [b]Department of Radiology, [c]Department of Biomedical Engineering, [d]Vanderbilt-Ingram Cancer Center (VICC), Vanderbilt University, Nashville, Tennessee 37232, United States [e]Russian Academy of Sciences, Leninskiy Prospekt 14, Moscow, 119991, Russia

We report on work involving low-field *in vivo* MR detection at $B_0 = 0.0487$ T of a hyperpolarized (HP) contrast agent (HCA) injected via tail-vein into a healthy wild-type mouse. At low magnetic field strengths there is no loss of SNR relative to high field for a well-designed radiofrequency (rf) coil,[1,2] and the chemical shift dispersion is potentially insufficient to differentiate hyperpolarized (HP) metabolites and contrast agents. However, if the magnetic field is sufficiently low, then magnetic susceptibility derived B_0 field inhomogeneity *in vivo* (the source of broad MRS lines at high field) becomes negligible. Consequently, direct spectroscopic resolution of spin-spin couplings or *J*-couplings, more commonly performed near zero field,[3] becomes feasible. Here we demonstrate with whole-body detection for a mouse the ability to resolve the ^{13}C multiplet of HP 1-^{13}C-succinate-d$_2$ (^{13}C-SUX) in a magnet with $B_0 = 0.0487$ T and inhomogeneity < 13 ppm over a 40 cm diameter spherical volume.

An open-source ^{13}C PHIP hyperpolarizer[4] (production cycle of 1 dose every 3 min, up to 28% ^{13}C-SUX polarization) was used to produce hyperpolarized ^{13}C-SUX contrast agent. Figure 1 shows the PHIP chemistry for production of ^{13}C-SUX and comparison of shimmed MRS at field strengths of $B_0 = 4.7$ T and $B_0 = 0.0487$ T. The presence of foam in the phantom illustrates the difficulties of susceptibility-induced magnetic field B_0 inhomogeneity at high fields. For the *in vivo* experiment, Figure 1, approximately 0.2 mL solution with ~30 mM concentration in D$_2$O of ^{13}C-SUX was slowly injected via tail vein into a catheterized mouse situated inside the solenoid coil of a rf probe capacitively tuned and matched to the ^{13}C resonance frequency for $B_0 = 0.0487$ T. Whole-body MRS acquisitions with flip angle (FA) = 18.2° every 2 s were started at the beginning of HCA production. The decay time constant for HP ^{13}C-SUX post-injection was ~35 s (not accounting for rf-pulse associated losses). The well-resolved ^{13}C spectrum of HP ^{13}C-SUX shows a complex ^{13}C multiplet: a result of spin-spin couplings between the hyperpolarized ^{13}C isotopic label and ^{1}H and ^{2}H sites of HP ^{13}C-SUX, Figure 1.[5] Moreover, the satellite peaks of the ^{13}C multiplet (also due to spin-spin couplings between ^{13}C and ^{1}H and ^{2}H nuclei) are also well resolved *in vivo*, Figure 1 because the corresponding peak splittings are clearly visible when compared to the phantom MR spectrum, Figure 1.
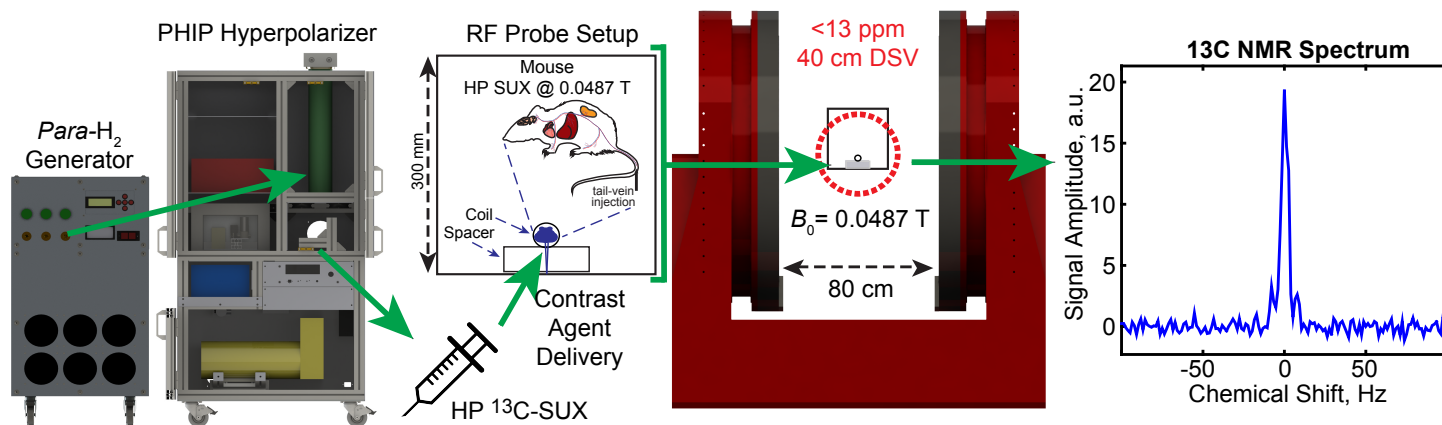

Figure 1. Experimental design. ^{13}C-SUX contrast agent is produced in a PHIP hyperpolarizer, injected via tail vein into a catheterized wild-type normal healthy mouse placed inside a shielded solenoid tuned to ^{13}C resonance, and MRS performed inside the homogenous DSV of a permanent magnet with $B_0 = 0.0487$ T. The NMR spectrum shows resolution *in vivo* of the ^{13}C *J*-couplings between the isotopic ^{13}C label and ^{1}H and ^{2}H sites. The magnet was only statically shimmed.

Acknowledgments

References

[1] Coffey, A.M., Truong, M.L. & Chekmenev, E.Y. *J Magn Reson* **237**, 169-174 (2013). [2] Suefke, M., Liebisch, A., Blümich, B. & Appelt, S. *Nat Phys* **11**, 767-771 (2015). [3] Sjolander, T.F., Tayler, M.C.D., King, J.P., Budker, D. & Pines, A. *The Journal of Physical Chemistry A* **120**, 4343-4348 (2016). [4] Coffey, A.M., Shchepin, R.V., Truong, M.L., Wilkens, K., Pham, W. & Chekmenev, E.Y. *Anal. Chem.* **88**, 8279-8288 (2016). [5] Chekmenev, E.Y., Hovener, J., Norton, V.A., Harris, K., Batchelder, L.S., Bhattacharya, P., Ross, B.D. & Weitekamp, D.P. *J Am Chem Soc* **130**, 4212-4213 (2008).

Resolving spin-spin couplings in hyperpolarized in vivo metabolic 13C spectroscopy at low magnetic field following murine tail-vein injection

Aaron M. Coffey[1], Matthew A. Feldman[1], Roman V. Shchepin[1], Milton L. Truong[1], Wellington Pham[1], and Eduard Y. Chekmenev[1]

[1]Radiology, Vanderbilt University Institute of Imaging Science, Nashville, TN, United States

Synopsis

We demonstrate murine whole-body MRS and the ability to resolve the ^{13}C multiplet of hyperpolarized 1-^{13}C-succinate-d_2 in a biplanar magnet with B_0 = 0.0487 T and inhomogeneity <13 ppm over 40 cm DSV. At low magnetic field strength no loss of SNR relative to high field for a well-designed radiofrequency coil occurs, but chemical shift dispersion is potentially insufficient to differentiate hyperpolarized metabolites and contrast agents. However, at sufficiently low field strength, magnetic susceptibility derived B_0 field inhomogeneity *in vivo* becomes negligible. Consequently, direct spectroscopic resolution of spin-spin couplings or *J*-couplings, more commonly performed near zero field, becomes feasible.

Overview

We report on work involving low-field *in vivo* MR detection at B_0 = 0.0487 T of a hyperpolarized (HP) contrast agent (HCA) injected via tail-vein into a healthy wild-type mouse. At low magnetic field strengths there is no loss of SNR relative to high field for a well-designed radiofrequency (rf) coil,[1,2] and the chemical shift dispersion is potentially insufficient to differentiate hyperpolarized (HP) metabolites and contrast agents. However, if the magnetic field is sufficiently low, then magnetic susceptibility derived B_0 field inhomogeneity *in vivo* (the source of broad MRS lines at high field) becomes negligible. Consequently, direct spectroscopic resolution of spin-spin couplings or *J*-couplings, more commonly performed near zero field,[3] becomes feasible. Here we demonstrate with whole-body detection for a mouse the ability to resolve the ^{13}C multiplet of HP 1-^{13}C-succinate-d_2 (^{13}C-SUX) in a magnet with B_0 = 0.0487 T and inhomogeneity < 13 ppm over a 40 cm diameter spherical volume.

Purpose

When injected into living organisms, hyperpolarized biomolecules can serve as metabolic contrast agents reporting on abnormal metabolism in cancer, heart diseases and other diseases and function as quantitative imaging biomarkers for these diseases. For example, efficient production of HP ^{13}C-SUX enables one to probe *in vivo* mechanisms and pathways for cancer imaging[4] using molecular imaging and spectroscopy.[5]

Methods and Results

An open-source ^{13}C PHIP hyperpolarizer[6] (production cycle of 1 dose every 3 min, up to 28% ^{13}C-SUX polarization) was used to produce hyperpolarized ^{13}C-SUX contrast agent. Figure 1 shows the PHIP chemistry for production of ^{13}C-SUX and comparison of shimmed MRS at field strengths of B_0 = 4.7 T and B_0 = 0.0487 T. The presence of foam in the phantom illustrates the difficulties of susceptibility-induced magnetic field B_0 inhomogeneity at high fields. For the *in vivo* experiment, Figure 2, approximately 0.2 mL solution with ~30 mM concentration in D_2O of ^{13}C-SUX was slowly injected via tail vein into a catheterized mouse situated inside the solenoid coil of a rf probe capacitively tuned and matched to the ^{13}C resonance frequency for B_0 = 0.0487 T. Whole-body MRS acquisitions with flip angle (FA) = 18.2° every 2 s were started at the beginning of HCA production. The decay time constant for HP ^{13}C-SUX post-injection was ~35 s (not accounting for rf-pulse associated losses). The well-resolved ^{13}C spectrum of HP ^{13}C-SUX shows a complex ^{13}C multiplet: a result of spin-spin couplings between the hyperpolarized ^{13}C isotopic label and ^{1}H and ^{2}H sites of HP ^{13}C-SUX, Figure 1c.[7] Moreover, the satellite peaks of the ^{13}C multiplet (also due to spin-spin couplings between ^{13}C and ^{1}H and ^{2}H nuclei) are also well resolved *in vivo*, Figure 3, inset, because the corresponding peak splittings are clearly visible when compared to the phantom MR spectrum, Figure 1c.

The use of HP ^{13}C-SUX was demonstrated for low-field *in vivo* MR paving the way for future low-field MRS and MRI of ^{13}C HCAs.

Acknowledgements

References

[1] Coffey, A.M., Truong, M.L. & Chekmenev, E.Y. Low-field MRI can be more sensitive than high-field MRI. *J Magn Reson* 237, 169-174 (2013).

[2] Suefke, M., Liebisch, A., Blümich, B. & Appelt, S. External high-quality-factor resonator tunes up nuclear magnetic resonance. *Nat Phys* 11, 767-771 (2015).

[3] Sjolander, T.F., Tayler, M.C.D., King, J.P., Budker, D. & Pines, A. Transition-Selective Pulses in Zero-Field Nuclear Magnetic Resonance. *J Phys Chem A* 120, 4343-4348 (2016).

[4] Zacharias, N.M., Chan, H.R., Sailasuta, N., Ross, B.D. & Bhattacharya, P. Real-time molecular imaging of tricarboxylic acid cycle metabolism in vivo by hyperpolarized 1-(13)C diethyl succinate. *J Am Chem Soc* 134, 934-943 (2012).

[5] Bhattacharya, P., Chekmenev, E.Y., Perman, W.H., Harris, K.C., Lin, A.P., Norton, V.A., Tan, C.T., Ross, B.D. & Weitekamp, D.P. Towards hyperpolarized (13)C-succinate imaging of brain cancer. *J Magn Reson* 186, 150-155 (2007).

[6] Coffey, A.M., Shchepin, R.V., Truong, M.L., Wilkens, K., Pham, W. & Chekmenev, E.Y. Open-Source Automated Parahydrogen Hyperpolarizer for Molecular Imaging Using ^{13}C Metabolic Contrast Agents. *Anal. Chem.* 88, 8279-8288 (2016).

[7] Chekmenev, E.Y., Hovener, J., Norton, V.A., Harris, K., Batchelder, L.S., Bhattacharya, P., Ross, B.D. & Weitekamp, D.P. PASADENA hyperpolarization of succinic acid for MRI and NMR spectroscopy. *J Am Chem Soc* 130, 4212-4213 (2008).
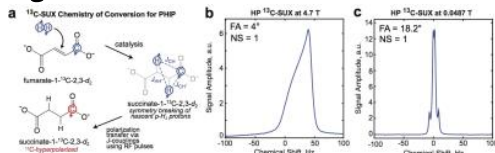
Figures

Figure 1. Hyperpolarized 1-^{13}C-succinate-d_2 synthesis and spectroscopy. (a) Steps for conversion to HP ^{13}C-SUX by fast pairwise addition of parahydrogen of ^{13}C-fumarate followed by rf polarization transfer. MR spectroscopy of HP ^{13}C-SUX in a phantom with the presence of bubbles due to agent foaming at (b) 4.7 T and (c) 0.0487 T.
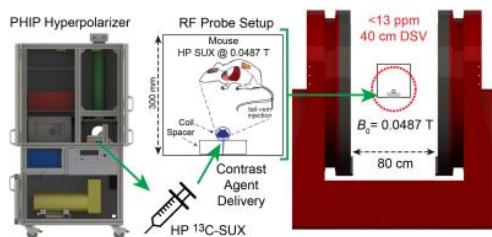

Figure 2. Experimental design. ^{13}C-SUX contrast agent is produced in a PHIP hyperpolarizer, injected via tail vein into a catheterized wild-type normal healthy mouse placed inside a shielded solenoid tuned to ^{13}C resonance, and MRS performed inside the homogenous DSV of a permanent magnet with B_0 = 0.0487 T. Magnet drawings and rf probe are to scale.
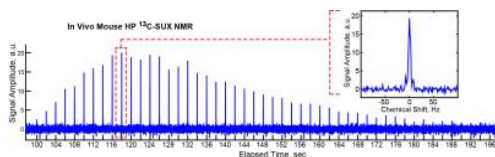
Figure 3. Hyperpolarized ^{13}C-SUX MRS. MRS acquisition was started at the beginning of contrast agent production. The contrast agent dynamics during and post tail-vein injection are reported by spectroscopic acquisition at 0.0487 T. The inset shows a closer view of a MR spectrum, showing resolution *in vivo* of the ^{13}C *J*-couplings between the isotopic ^{13}C label and ^{1}H and ^{2}H sites. The magnet was only statically shimmed.

Addendum: Current Performance Evaluation for QPC Laser ES- 8707-0003 (SN# 1611114)

Michael Molway, Megan Murphy, Bryce Kidd, Justin Porter, Dustin Basler, Boyd Goodson

Department of Chemistry and Biochemistry, Southern Illinois University, Carbondale, IL 62901

Based on the discussion between QPC and the SIUC team, further checks were conducted as an addendum to the 9 July 2017 report named "Current Performance Evaluation for QPC Laser". These checks included (1) looking at the cross sectional profile out of the 3 inch and 2 inch telescope and (2) looking at optical lens inside of optics train. Also the QPC suggested 0.2 micron air filter was attached in line from the purified air tank to the laser to prevent any small debris from entering the laser.

(1) Looking at the cross sectional profile out of the 3 inch and 2 inch telescope

The laser was directed at a black hardboard at 20 inches from the end of the telescope for both the 2 inch and 3 inch set ups and an image of the beam's cross sectional profile was captured through the use of a cell phone's camera.
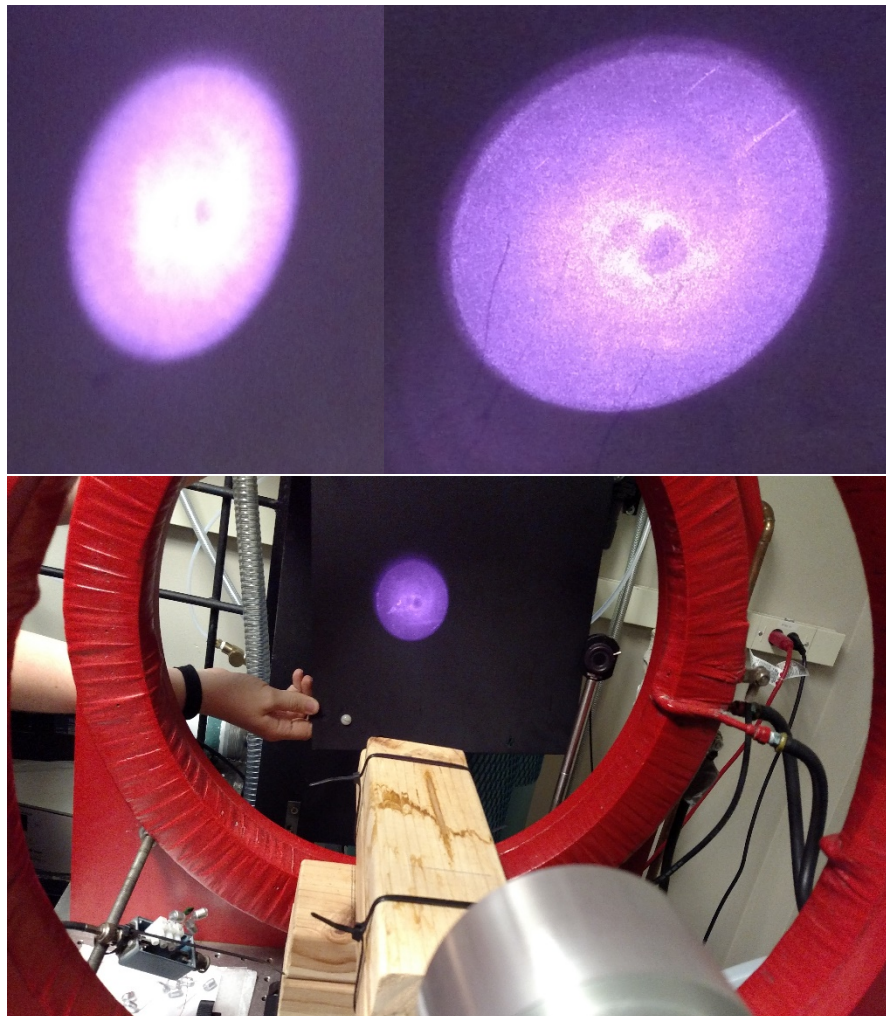
Figure 1. Images of cross sectional profile of laser beam out of 2 inch telescope (top-left) and 3 inch telescope (top-right), as well as an image (bottom) giving a relative distance from the end of the telescope to the black hardboard.

As can be seen in figure 1 (above), at the QPC suggested distance of 20 inches, the two holes in the cross sectional region of the laser were still present for the 3 inch telescope. When the 2 inch telescope is used, we are seeing only one hole in the cross sectional profile. The lens of the 2 inch telescope was checked for any visible damages and cleaned prior to use.

(2) Looking at optical lens inside of the optic train

The optical lens within the optical train was removed and examined for any visible dust, scratches, or other damages. A fluorescent illuminated tabletop magnifier was used in order to see damages more easily.

No dust, scratches, or other damages were observed on the optical lens. A picture of the current condition of the optical lens was not taken due to inability to focus camera clearly.
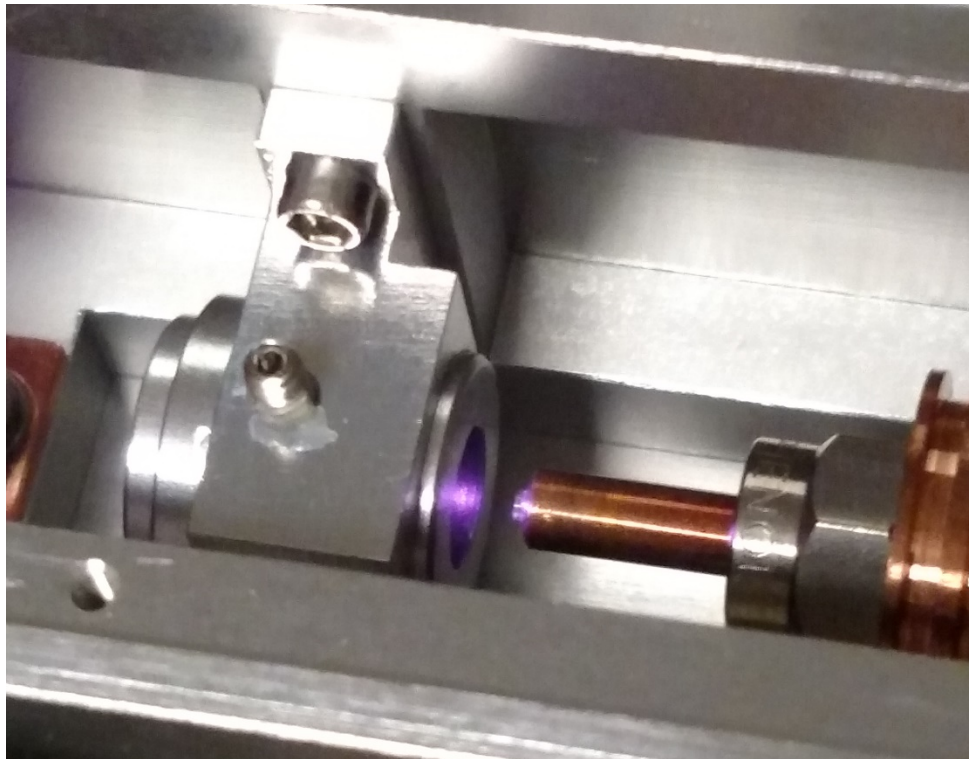
Figure 2. Image of inside the optical train as laser was in operation. Location of optical lens being examined was found within the cylindrical metal chassis bolted with a 2-56 set screw.

Addendum to Performance Evaluation for QPC Laser ES-8707-0003
(SN# 1611114)

(Supplement to QPC Product Test Report: 11/22/2016 and 03/24/2017)

Bryce Kidd, Michael Molway, Megan Murphy, Justin Porter, Dustin Basler, Max Gemeinhardt, Boyd Goodson

Department of Chemistry and Biochemistry, Southern Illinois University, Carbondale, IL 62901

Internal Document For: Hyperpolarized Xenon Technology Consortium (HXTC) & QPC Lasers

4 May 2017

Version 1.5

Based on the recommendation of QPC resulting from laser test data presented in SIUC's addendum to performance evaluation (Version 1.3) and conversations with Dr. Goodson and other consortium members, the laser to QPC for reworking some of its components.

Upon receiving the laser after QPC shipped it back to SIUC, two sets of experiments were performed to evaluate the new laser's performance in the context of the original specifications. (1) Comparison of QPC-reported specs (FWHM, peak centroid, and out-of-telescope (OT) output power) to corresponding in-house results at 26 °C water chiller temperature and nominal operating current (48.2 Amps); (2) Laser output as a function of operating current at fixed water chiller temperature (26 °C). These experiments were repeated several times (to rectify emerging issues) in order to ensure the most reliable data—and only the most recent / reliable sets are reported here (an attempt was also made to record the laser output with an ostensibly higher-resolution spectrometer, but it was later determined that the actual resolution was poorer than that of the Ocean Optics spectrometer used here).

Notes:

> *(a) "Telescope" optical construction was installed for all runs reported below.*
> *(b) For the runs in this addendum, a near-IR spectrometer (HR2000) was used that had a digital resolution given by its point spacing: 0.04 nm for wavelengths near the laser peak.*
> *(c) Wavelengths for spectra are referenced to Mike Barlow's portable light source; based on this calibration, a shift of 0.0375 nm was manually added to the raw data to give values and spectra show here. Spectra are air referenced.*
> *(d) Reported linewidths are FWHM; unless noted otherwise, centroids are of the main peak, carefully estimated by eye to true overall peak center (deemed more accurate than taking position of highest point on the peak). Confidence limits are p/m ~0.01 to ~0.02 nm.*

(1) Comparison of QPC reported FWHM, peak centroid, and OT output power to in-house results at 26 °C water chiller temperature and nominal operating current (48.2 Amps).

The laser was directed into a power meter, and the spectral profile (Ocean Optics HR2000 series) was recorded with a fiber-optic probe mounted to catch backscatter from the power meter.

A close-up of the spectrum recorded under these conditions is shown in **Fig. 1**; data are summarized in **Table 1**.
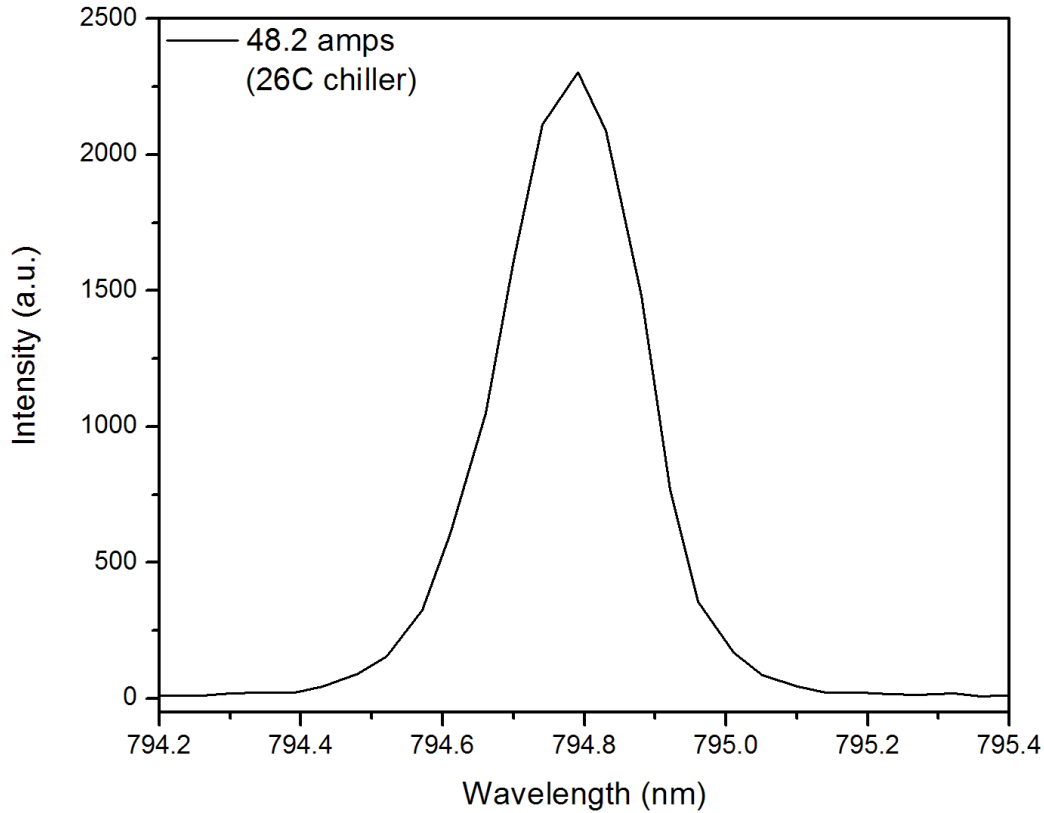
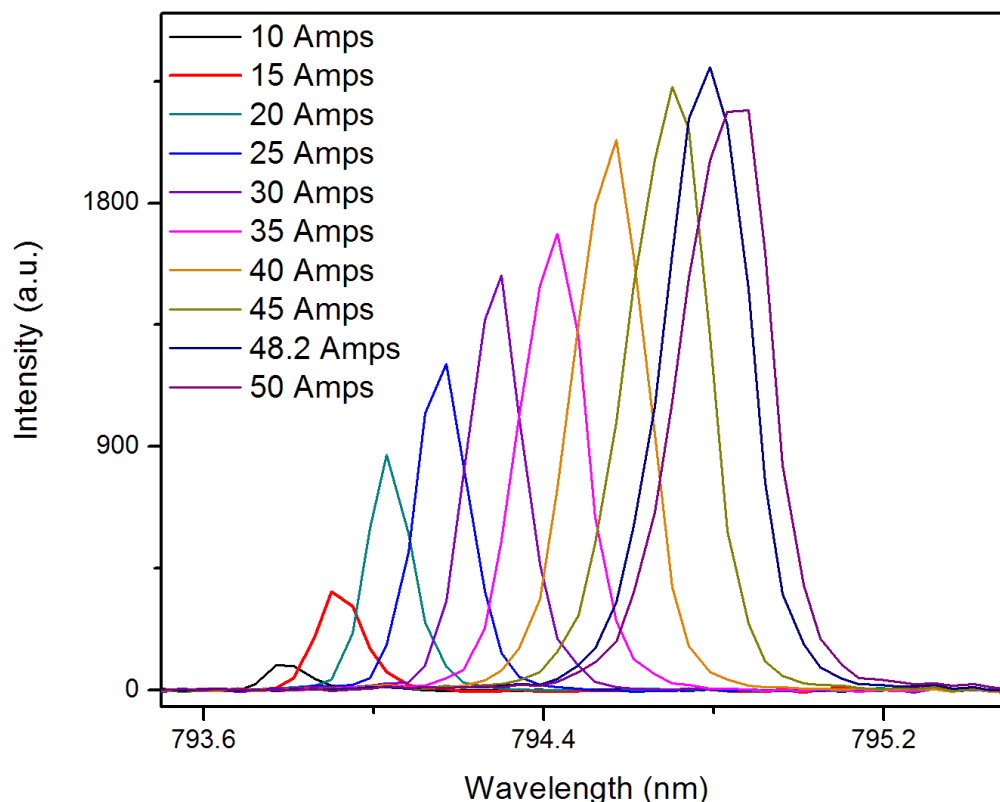**Fig. 1.** Close-up of near-IR spectral profiles of laser at a chiller temperature of 26 °C and max-nominal operating current (48.2 Amps). The spectrum was acquired after 1 hour of continuous operation. Details of data are below in Table 1.

Chiller Temp (C)	Laser Temp (C)	Current (A)	Power (W)	Voltage (V)	Centroid of Main Peak (nm)	FWHM (nm)
26	28.9	48.2	167	13.00	794.79	0.231

Table 1. Summary of data from fixed-chiller-temperature experiment.

The experiment was conducted at a water chiller temperature of 26 °C to compare laser FWHM, peak centroid, and OT output power to the results presented on Page 6 of QPC's "Product Test Report, 03/24/2017". We observe a 0.185 nm "blue shift" difference in peak centroid, 0.037 nm larger FWHM, and a negative difference of 3 W in OT output power when compared to QPC's reported peak centroid (794.975 nm), FWHM (0.194 nm), and output power (170 W), respectively. On the other hand, the laser showed stable output over time. Much of the difference in output wavelength likely reflects the difference between air and vacuum referencing. The FWHM issue may result from the 0.04 nm digital resolution of the near-IR spectrometer. If this number is subtracted, then the laser meets linewidth spec.

(2) Laser output as a function of current at fixed water chiller temperature (26 °C).

As before, the laser was directed into a power meter, and the spectral profile (Ocean Optics HR series) was recorded with a fiber-optic probe mounted to catch backscatter from the power meter; relative vertical scales in the graphs (i.e. of peak heights) should be directly comparable.

A close-up of the spectra recorded under these conditions is shown in **Fig. 2**; data are summarized in **Table 2**.

Fig. 2. Close-up of near-IR spectral profiles of laser as a function of operating current (10 – 50 amps) at fixed chiller temperature (26 °C). Details of data are below in Table 2.

Current (A)	Laser Temp (°C)	Chiller Temp (°C)	Power (W)	Voltage (V)	Centroid of Main Peak (nm)	FWHM (nm)
10	26.3	26	5.98	11.67	793.79	0.119
15	26.6	26	26.5	11.9	793.92	0.127
20	26.8	26	48.2	12.11	794.03	0.124
25	27.2	26	70	12.29	794.16	0.147
30	27.5	26	91.7	12.46	794.28	0.156
35	27.8	26	113	12.72	794.43	0.180
40	28.3	26	134	12.77	795.57	0.202
45	28.7	26	154	12.91	794.71	0.221

48.2	28.9	26	167	13	794.79	0.231
50	29.1	26	173	13.05	794.85	0.247

Table 2. Summary of data from variable-chiller-temperature experiment.

At this temperature, we obtain the Rb D1 resonance (794.766 nm) between an operating current of 45 to 48.2 amps.

Summary. The laser can be driven to Rb resonance under these conditions, in a manner that is ostensibly safe for long-term laser operation according to QPC (i.e., well within the required temperature range); importantly, unlocked output is also negligible under these conditions (not shown in the presented data), representing a significant improvement over the original embodiment for this laser. Two other key performance measures—output power and FWHM linewidth—appear to barely meet spec if a liberal correction factor of 0.04 nm (by direct subtraction) is applied. Moreover, slightly lower laser temperatures should allow higher currents (up to the nominal max of 50 A) and/or higher powers while slightly improving linewidth.

In any case, given the significant improvement in laser performance, SIUC personnel agree to say that the laser is within specifications and will now accept the laser as delivered/purchased.

Current Performance Evaluation for QPC Laser ES- 8707-0003 (SN# 1611114)

Michael Molway, Megan Murphy, Bryce Kidd, Justin Porter, Dustin Basler, Boyd Goodson

Department of Chemistry and Biochemistry, Southern Illinois University, Carbondale, IL 62901

Internal Document For: Hyperpolarized Xenon Technology Consortium (HXTC) & QPC Lasers

12 July 2017

Version 1.1

Based on the observations seen by the SIUC team and conversations with Dr. Goodson, the laser from QPC had two experiments completed to reevaluate its performance in-house. (1) Current in-house performance results, collected at 26.0 °C water chiller temperature and nominal operating current of 48.2 Amps, were compared to previously reported in-house results and QPC reported specs (FWHM, peak centroid, and out-of-telescope (OT) output power). (2) A camera phone was utilized to capture an image of the beam as it exited the telescope and hit a black hardboard to show inconsistences in the laser beam.

Notes:
    (a) "Telescope" optical construction was installed for all runs reported below.
    (b) For the runs in this report, a near-IR spectrometer (HR2000) was used that had a digital resolution given by its point spacing: 0.04 nm for wavelengths near the laser peak.
    (c) Wavelengths for spectra are referenced to Mike Barlow's portable light source; based on this calibration, a shift of 0.0508 nm was manually added to the raw data to give values and spectra shown here. Spectra are air referenced.
    (d) Reported linewidths are FWHM; unless noted otherwise, centroids are of the main and side peaks, carefully estimated by eye to true overall peak center (deemed more accurate than taking position of highest point on the peak). Confidence limits are p/m ~0.01 to ~0.02 nm.

(1) Current in-house performance results compared to previous in-house results

The laser was directed into a power meter, and the spectral profile was recorded with a mounted fiber-optic probe (Ocean Optics HR2000 series) to catch backscatter from the power meter.

A close-up of the spectrum recorded under these conditions is shown in Fig. 1; data from pages 5-6 of QPC's "Product Test Report, 03/24/2017", page 3 of SIUC's "Addendum to Performance Evaluation for QPC Laser ES-8707-0003, 4 May 2017" and the 12 July 2017 fixed-water-chiller experiment are summarized in Table 1.
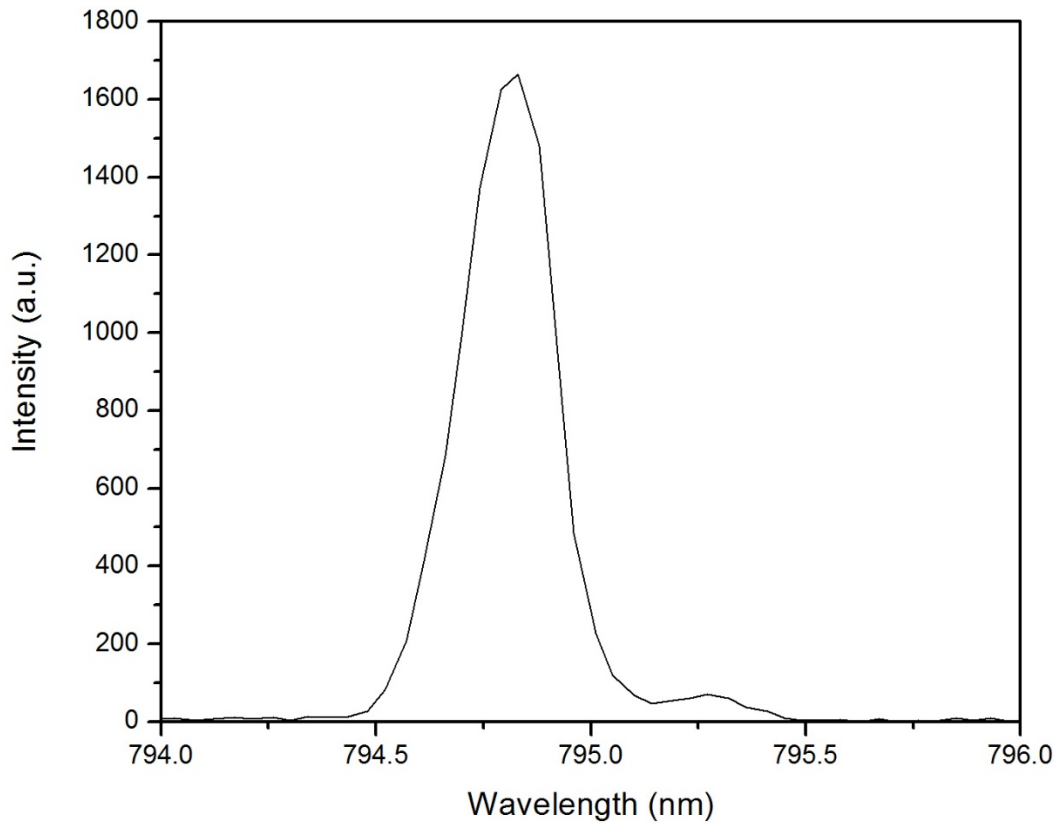
Fig. 1. Close-up of near-IR spectral profiles of laser at a chiller temperature of 26.0 °C and max-nominal operating current (48.2 Amps). The spectrum was acquired after 1 hour of continuous operation. Details of data are below in Table 1.

Data Name	Chiller Temp (C)	Laser Temp (C)	Current (A)	Power (W)	Voltage (V)	Centroid of Main Peak (nm)	Centroid of Side Peak (nm)	FWHM of Main peak (nm)
QPC	26.0	28.5	48.2	170	12.79	794.975	-	0.194
SIUC-OLD	26.0	28.9	48.20	167	13.00	794.79	-	0.231
SIUC-NEW	26.0	28.7	48.20	159	13.00	794.83	795.27	0.253

Table 1. Summary of data from QPC's "Product Test Report, 03/24/2017" (QPC), SIUC's "Addendum to Performance Evaluation for QPC Laser ES-8707-0003, 4 May 2017" (SIUC-OLD) and 12 July 2017 (SIUC-NEW) fixed-chiller-temperature experiments.

The experiment was conducted at a fixed water chiller temperature of 26.0 °C to compare laser's current main peak centroid, FWHM of main peak, and OT output power to (a) the results presented on Page 3 of SIUC's "Addendum to Performance Evaluation for QPC Laser ES-8707-0003, 4 May 2017" and (b) the results presented on page 6 of QPC's "Product Test Report, 03/24/2017".

(a) We observe a 0.041 nm "red shift" difference in peak centroid, 0.022 nm larger FWHM, and a negative difference of 8 W in OT output power when compared to our previous in-house results from 4 May 2017 (see Table 1 for summarized results).

(b) We observe a 0.145 nm "blue shift" difference in peak centroid, 0.059 larger FWHM, and a negative difference of 11 W in output power when compared to QPC's results from 24 March 2017 (see Table 1 for summarized results).

We also are observing a side peak at 795.27 nm that was not present in previous reports. A side by side comparison of the spectrum from SIUC's 4 May 2017 report and the spectrum collected on 12 July 2017 is shown in Fig. 2. A spectrum of increased intensity, to make observation of the side peak's centroid easier, is shown in Fig. 3.
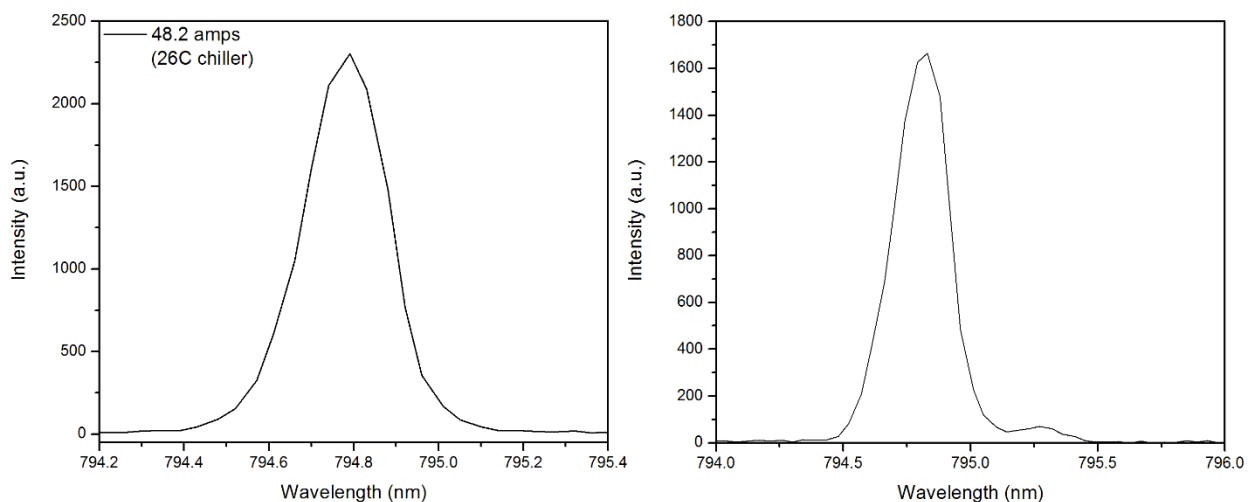
Fig. 2. A side by side comparison of the 4 May 2017 spectrum (left) and the 12 July 2017 spectrum (right). Both spectrums are a close up of near-IR spectral profiles of laser at a chiller temperature of 26.0 °C and max-nominal operating current (48.2 Amps) and were collected after 1 hour of continuous operation.
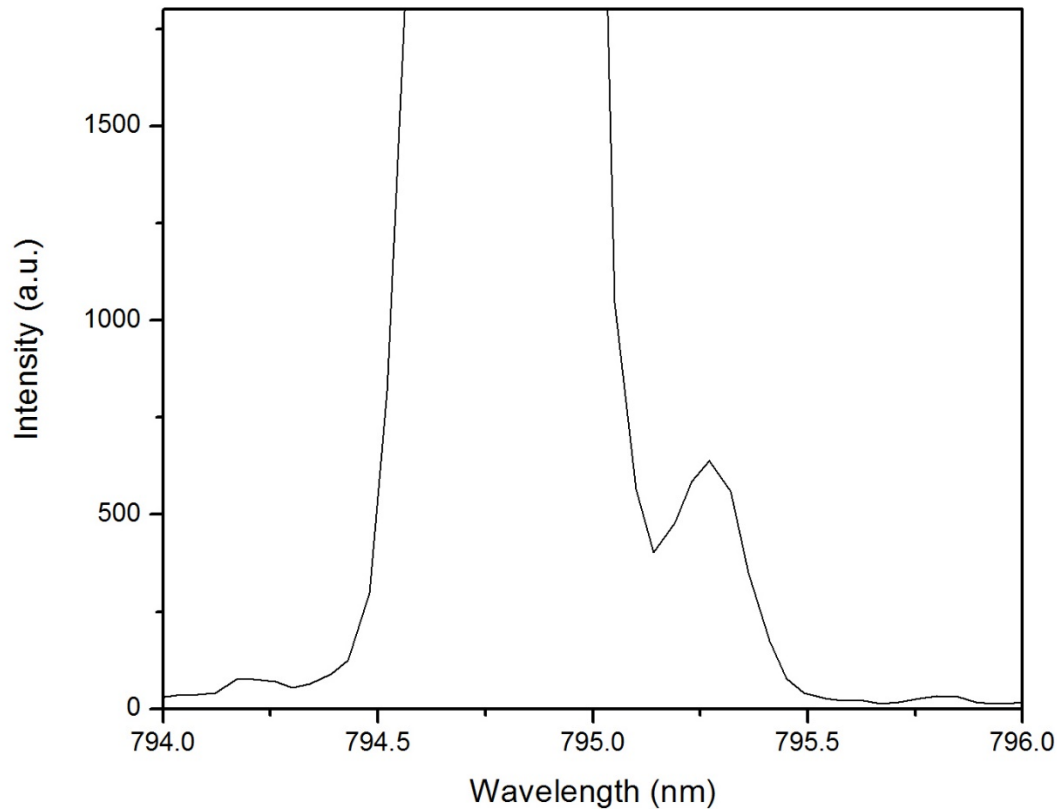

Fig. 3. Increased intensity of near-IR spectral profiles of laser at a chiller temperature of 26.0 °C and max-nominal operating current (48.2 Amps). The spectrum was acquired immediately following collection of the spectrum from Fig. 1. Intensity was increased by opening the "eye" of the fiber optic probe further. Details of data are above in Table 1.

(2) Image from camera phone of laser beam

The laser was directed at a black hardboard and an image of the beam was produced through the use of a camera phone.

Two "holes" in the center of laser beam (cross-sectional profile) as it hits the black hardboard can be seen in Fig. 4. Laser settings can be seen in Table 2.
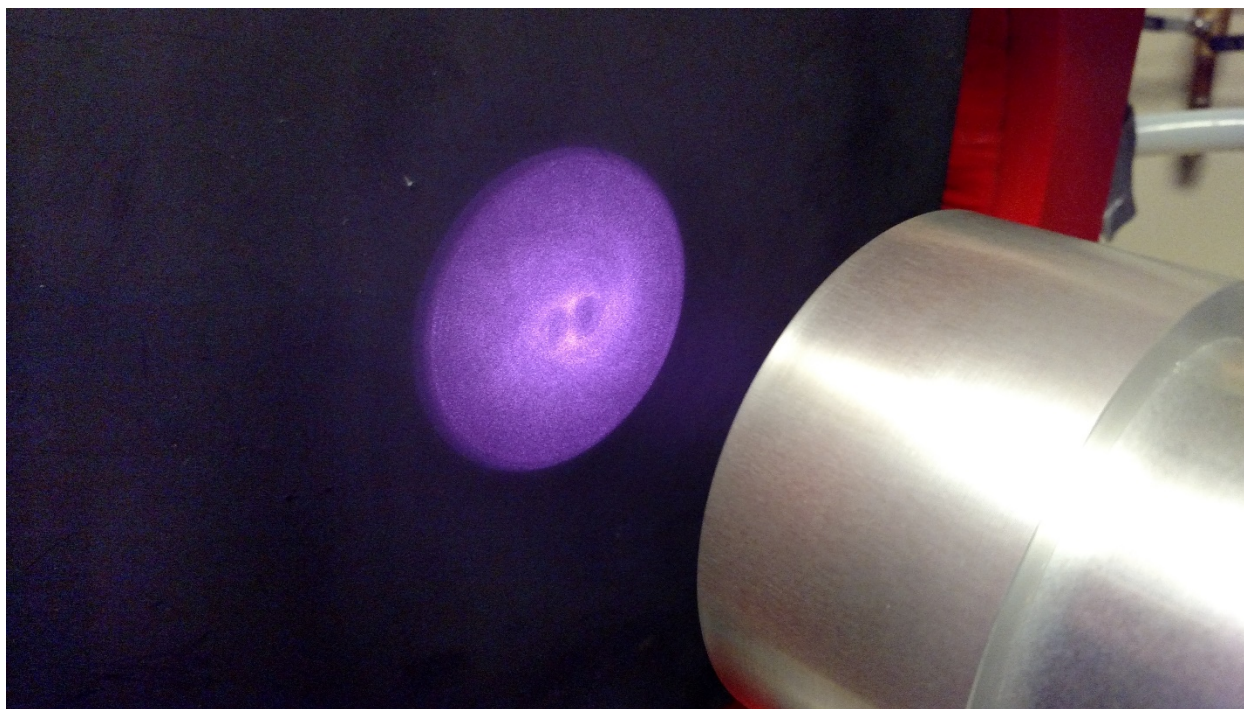
Fig. 4. Image from camera phone of laser beam as it hits a black hardboard

Chiller Temp (C)	Laser Temp (C)	Current (A)	Power (W)	Voltage (V)
26.0	28.7	48.20	159	13.00

Table 2. Summary of laser settings on 12 July 2017 during camera phone image experiment

Summary

The laser currently can still be driven to Rb resonance under these conditions; However, the growth of a side peak, an increase in FWHM and a decrease OT output power, as well as the presence of two "holes" in the laser beam cross-sectional profile, suggest that the laser is suffering from some sort of degradation in performance.

Current Performance Evaluation for QPC Laser ES- 8707-0003 (SN# 1703131)

Peter Nikolaou, Aaron Coffey, Eduard Chekmenev

Vanderbilt Institute of Imaging Science, Vanderbilt University, Nashville, TN 37232

**Internal Document For: Hyperpolarized Xenon Technology Consortium (HXTC) & QPC Lasers**

14 July 2017

Version 1.1

Brief History of Laser Operation:

Laser received at Vanderbilt, but and the power output was mapped by Bryce Kidd and Mike Barlow. Data is not included, but I will provide it once I find it.

We had issues with our Water Chiller. The flow rate was too low (4.1 L/min). Laser was shipped to SIU to be tested on their water Chiller.

| Current	Flow Rate (l/min)	Laser Temp (Celc.)	Power (W)	Voltage (V)	Wavelength (nm)
49	4.2	28.4	165	13.09	795.04
49	4.4	28.3	165	13.1	795.03
49	4.6	28.3	166	13.1	795.01
49	4.8	28.2	166	13.11	794.99
49	5	28.1	166	13.11	794.98
49	5.2	28.1	166	13.11	794.96
49	5.4	28	166	13.12	794.94
49	5.5	28	166	13.12	794.94
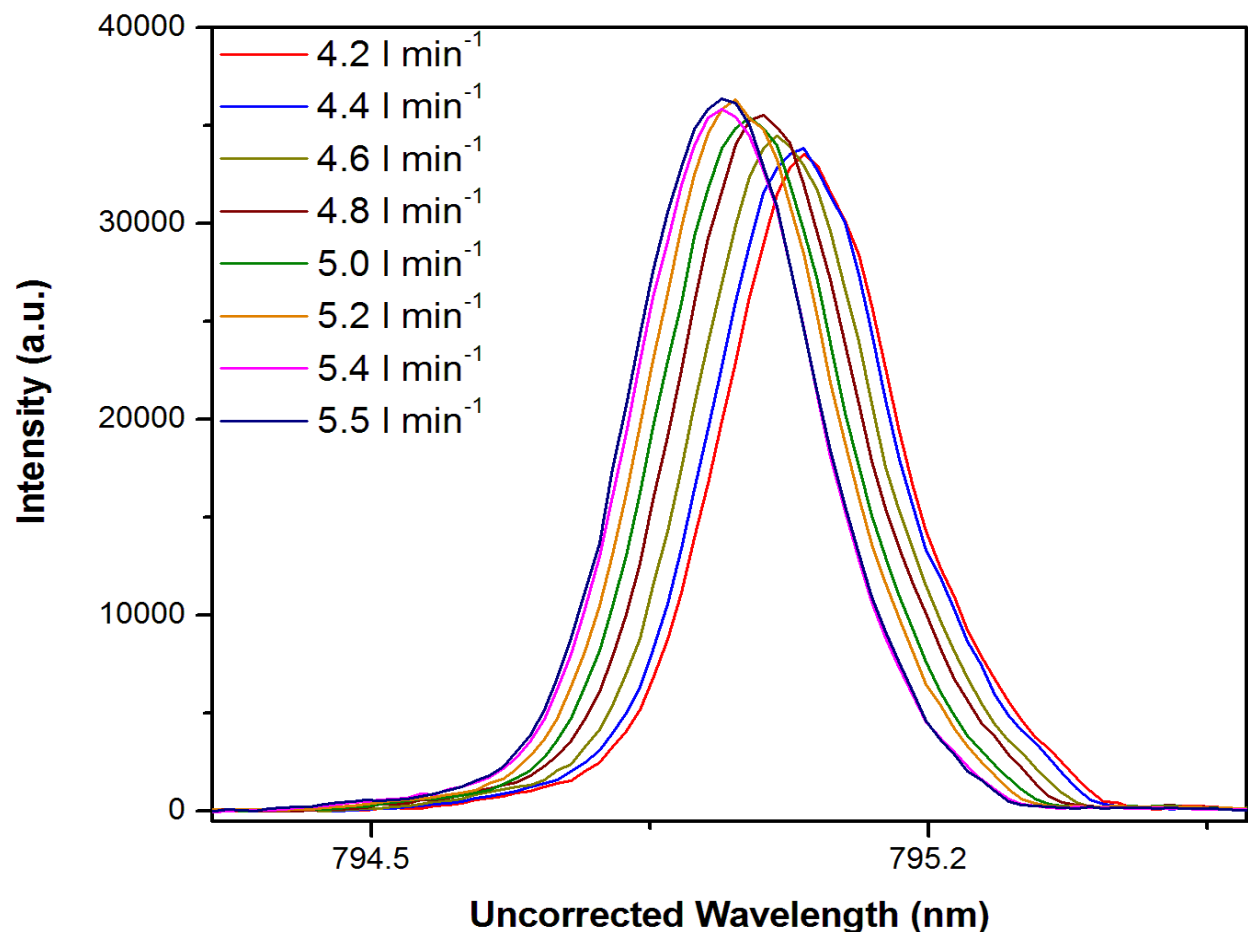
At that time the Power was recorded to be 166 Watts @ 49 Amps operating current.

Upon The return of the laser to Vanderbilt, it was not operated again until this week, because we were working on stand-alone air drying solution that we could use to operate the laser and be a part of the Polarizer.

We used the laser to hyperpolarized xenon and tune our NMR RF circuitry. Which took a couple of days of testing and approximately ~ 5-6 hrs of laser operation during that period of time.
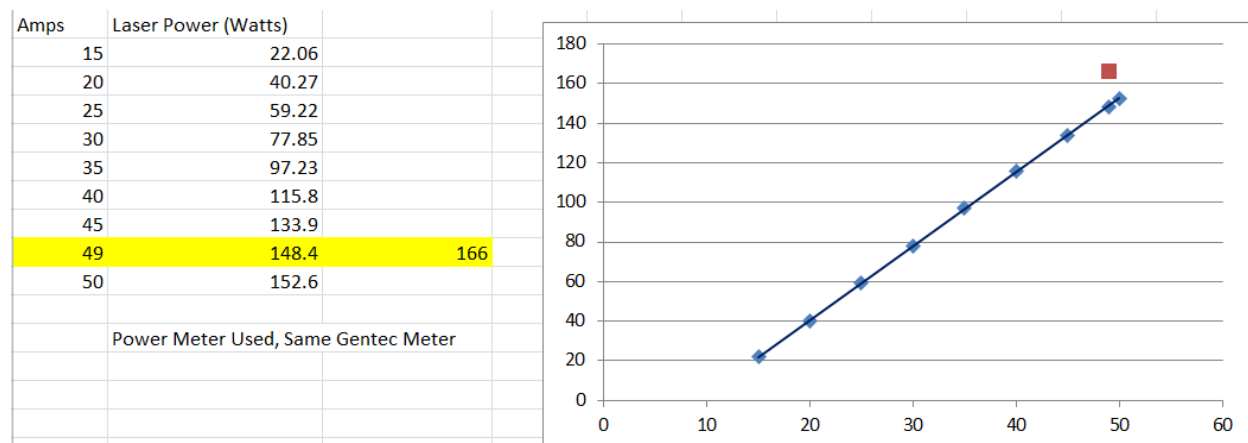
Another 1 hour operation was used to map out the Laser transmission as a function of Water chiller Flow Rate. (NOTE: Our Spectrometer is un-calibrated. 794.72 Rb D1 is actually represented at 795.18nm on our spectra. On resonance at 5.6L/min flow.
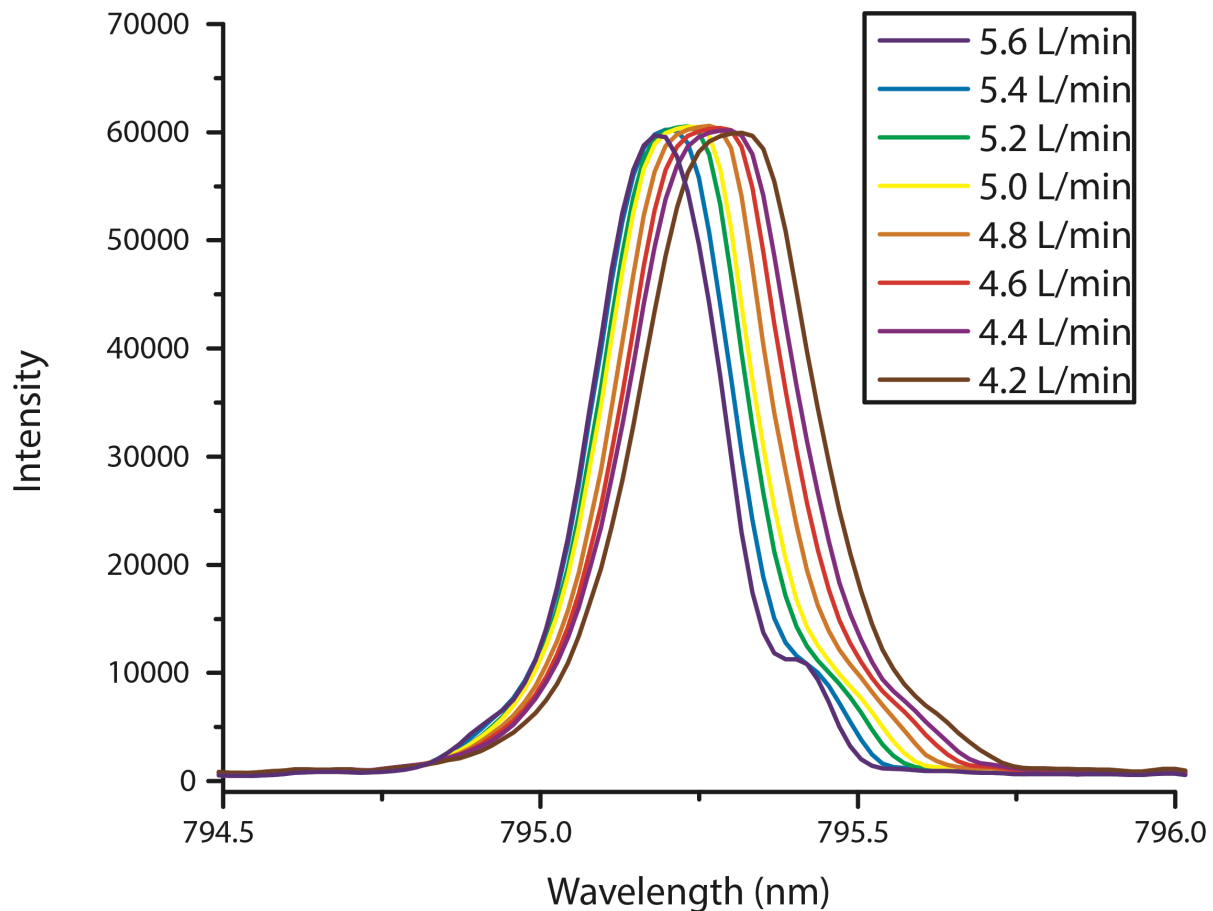
Below is the same specta, but with Data removed for better clarity.

FWHM @ 5.6L/min = 0.24nm
FWHM @ 4.2L/min = 0.31nm
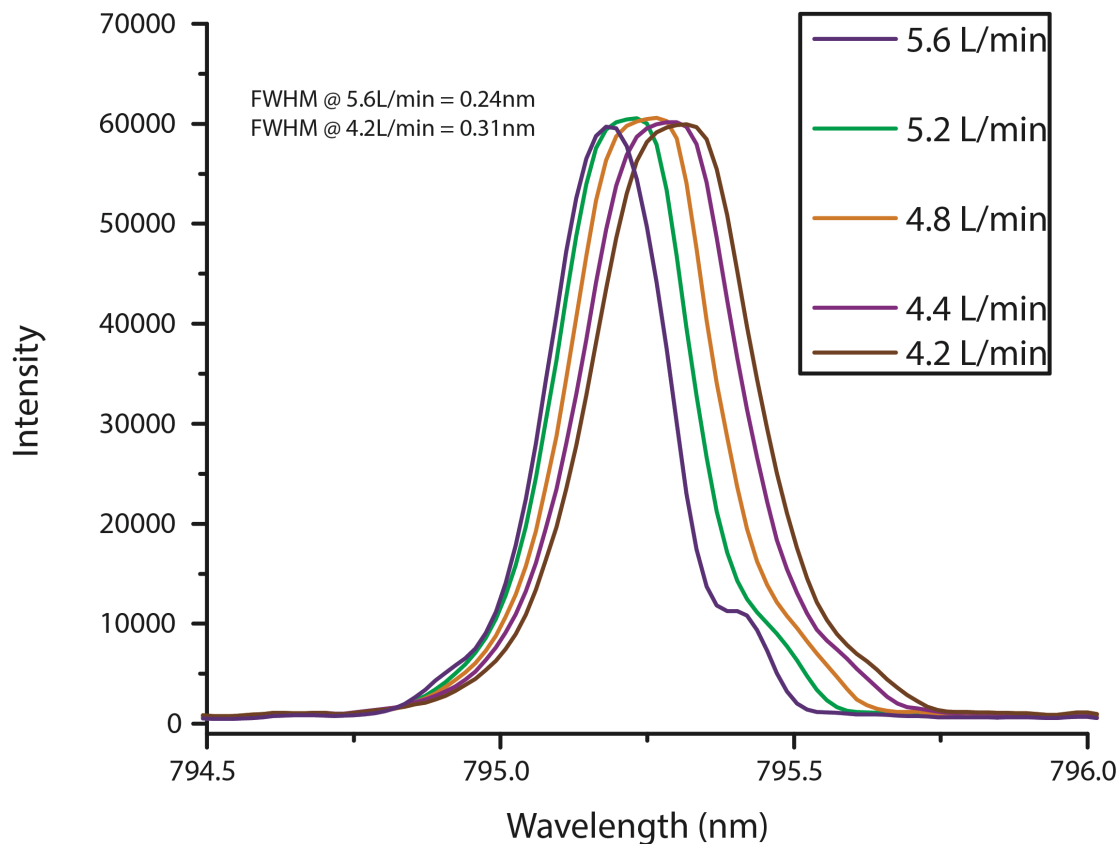
Upon hereing the issues from the SIUC Team, I performed power measurement experiments.
Laser Power Measurements Performed: 7/13/2017
Using Gentec Power Meter (Same as the one SIUC Uses).
Red Data Point: Power measurement from Bryce during Water Flow Rate Tests on Laser on April 13th

Amps	Laser Power (Watts)	
15	22.06	
20	40.27	
25	59.22	
30	77.85	
35	97.23	
40	115.8	
45	133.9	
49	148.4	166
50	152.6	
	Power Meter Used, Same Gentec Meter	

Laser Powered Measured Directly out of 800um Fiber (No Optical Telescope) @49Amps = 171.7 Amps